Submillimetre Studies of Pre-stellar and Starless Cores in the Ophiuchus, Taurus and Cepheus Molecular Clouds

Katherine Miranda Pattle

Jeremiah Horrocks Institute for Mathematics, Physics and Astronomy

University of Central Lancashire

February 2016

STUDENT DECLARATION FORM

Concurrent registration for two or more academic awards

I declare that while registered as a candidate for the research degree, I have not been a registered candidate or enrolled student for another award of the University or other academic or professional institution

Material submitted for another award

I declare that no material contained in the thesis has been used in any other submission for an academic award and is solely my own work

Collaboration

Where a candidate's research programme is part of a collaborative project, the thesis must indicate in addition clearly the candidate's individual contribution and the extent of the collaboration. Please state below:

I declare that all of the work in this thesis is my own original research carried out under the supervision of Professor Derek Ward-Thompson, with the following exceptions:

I reduced the SCUBA-2 data presented in Chapter 3 using methods developed by the JCMT Gould Belt Survey SCUBA-2 Data Reduction Team, of which I am a member. The Herschel data were provided by the Herschel Gould Belt Survey, of which I am a member. The HARP-B data were reduced by members of the JCMT Gould Belt Survey, of which I am a member. The IRAM data are archival. All of the data analysis is my own original research. The analysis in Chapter 3 has been published in Monthly Notices of the Royal Astronomical Society (2015, vol. 450 p. 1094), in a paper of which I am the first author, written in collaboration with members of the JCMT and Herschel Gould Belt Surveys.

The SCUBA-2 data used in Chapter 4 were reduced by members of the JCMT Gould Belt Survey SCUBA-2 Data Reduction Team. The Herschel data were provided by the Herschel Gould Belt Survey. The HARP-B data were reduced by members of the JCMT Gould Belt Survey. Green Bank Telescope ammonia data are taken from published measurements. All of the data analysis is my own original research.

The SCUBA-2 data presented in Chapter 5 were reduced by members of the JCMT Gould Belt Survey SCUBA-2 Data Reduction Team. The source temperatures quoted in Chapter 5 were provided by members of the Herschel Gould Belt Survey. The Nagoya 4-metre Telescope ^{13}CO data are taken from published measurements. All of the data analysis is my own original research.

All of the work in Chapter 6 is my own original research, including the analytical evolutionary model for starless cores which I present.

Signature of Candidate:

Type of Award: PhD in Astrophysics

School: Physical Sciences and Computing

Declaration

The work presented in this thesis was carried out at the Jeremiah Horrocks Institute for Mathematics, Physics and Astronomy, University of Central Lancashire.

I declare that while registered as a candidate for the research degree, I have not been a registered candidate or enrolled student for another award of the University or other academic or professional institution.

I declare that no material contained in the thesis has been used in any other submission for an academic award. Data and models used in this thesis that are not my own are clearly cited in the text.

I further declare that all of the work in this thesis is my own original research carried out under the supervision of Professor Derek Ward-Thompson, with the following exceptions:

I reduced the SCUBA-2 data presented in Chapter 3 using methods developed by the JCMT Gould Belt Survey SCUBA-2 Data Reduction Team, of which I am a member. The Herschel data were provided by the Herschel Gould Belt Survey, of which I am a member. The HARP-B data were reduced by members of the JCMT Gould Belt Survey, of which I am a member. The IRAM data are archival. All of the data analysis is my own original research. The analysis in Chapter 3 has been published in Monthly Notices of the Royal Astronomical Society (2015, vol. 450 p. 1094), in a paper of which I am the first author, written in collaboration with members of the JCMT and Herschel Gould Belt Surveys.

The SCUBA-2 data used in Chapter 4 were reduced by members of the JCMT

Gould Belt Survey SCUBA-2 Data Reduction Team. The Herschel data were provided by the Herschel Gould Belt Survey. The HARP-B data were reduced by members of the JCMT Gould Belt Survey. Green Bank Telescope ammonia data are taken from published measurements. All of the data analysis is my own original research.

The SCUBA-2 data presented in Chapter 5 were reduced by members of the JCMT Gould Belt Survey SCUBA-2 Data Reduction Team. The source temperatures quoted in Chapter 5 were provided by members of the Herschel Gould Belt Survey. The Nagoya 4-metre Telescope ^{13}CO data are taken from published measurements. All of the data analysis is my own original research.

All of the work in Chapter 6 is my own original research, including the analytical evolutionary model for starless cores which I present.

Signed

K. Pattle

- -

K. Pattle

Abstract

We identify, and characterise the properties of, starless cores in the Ophiuchus, Taurus and Cepheus molecular clouds. We identify sources in SCUBA-2 850-µm emission, and determine temperatures by fitting a modified blackbody model to their spectral energy distributions, measured using SCUBA-2, PACS and SPIRE data. We construct convolution kernels to accurately bring SCUBA-2 and Herschel data to a common resolution. Masses are calculated using best-fit temperatures and measured 850-µm flux densities.

In Ophiuchus, the mass distribution of starless cores is consistent with the expected shape of the Core Mass Function (CMF). We determine core masses from $C^{18}O$ and N_2H^+ measurements, and find some evidence for high-density N_2H^+ freeze-out. Virial analysis, including external pressure, shows that most cores are either bound or virialised. Gravitational potential and external pressure energies are found to be typically of a similar order of magnitude, with some variation between regions. Non-thermal linewidths decrease between $C^{18}O$-traced and N_2H^+-traced material, indicating dissipation of turbulence. Core properties vary with region, and hence we infer a south-west to north-east evolutionary gradient.

In Taurus, we identify starless cores in SCUBA-2 850-µm emission, Herschel 500-µm emission, and Herschel 500-µm emission filtered to remove large-scale structure. Cores detected and characterised using unfiltered Herschel 500-µm data have higher densities and temperatures than their equivalents in SCUBA-2 emission. SCUBA-2 detects only the densest starless cores relative to the filtered Herschel data, due

to a surface-brightness sensitivity limit, as both populations have similar ranges in temperature. Virial analysis shows that the SCUBA-2 cores are pressure-confined and that almost all are virially bound in the absence of an internal magnetic field. The magnetic field strengths required to bring our cores into virial equilibrium are consistent with those measured in dense gas in Taurus.

In Cepheus, we compare starless cores in the regions L1147/58, L1172/74, L1251 and L1228. Region CMFs generally show sub-Salpeter power-law indices. L1147/58 and L1228 have a high ratio of cores to protostars; L1251 and L1174 have a low ratio, suggesting that the latter are active sites of star formation, while in the former, star formation proceeds quiescently. Core external pressures are estimated; all but one of our cores are pressure-confined. We find a power-law relation between gravitational potential and external pressure energies. Cores which obey this relation are strongly pressure-dominated; those which do not are candidates for gravitational collapse.

Core temperatures and masses in each cloud are similar. Cores in Ophiuchus are significantly smaller and denser than in other regions. Ophiuchus shows strong evidence for clustering: a non-uniform surface density of sources, and small nearest-neighbour distances between sources. Taurus is a dispersed region, while Cepheus is intermediate. Ophiuchus shows the most variation of core properties with location. Cores in Taurus are extremely homogeneous; cores in Cepheus show a wide range of properties, but little correlation of properties with location.

We present a new analytical model for the evolution of starless cores. We find that not all pressure-confined and virially-bound cores will become gravitationally bound, with many instead collapsing to virial equilibrium. Hence, we state that only gravitationally bound starless cores can be definitively considered to be prestellar.

Contents

List of Tables

List of Figures

Acknowledgements

Firstly, I would like to thank my supervisor, Professor Derek Ward-Thompson, for giving me the chance to carry out this research, and for all the knowledge imparted along the way. Further thanks for reading this thesis in great detail, for coining the verb 'to quatermass', and for suggesting many excellent ways in which it could be made even longer.

Thanks to the star formation research group at the Jeremiah Horrocks Institute, particularly to Dr Jason Kirk for being an endless font of good advice, and to David Bresnahan for providing camaraderie and mockery in equal measure.

Thanks to Dr David Nutter (ex-Cardiff University) for teaching me how to reduce SCUBA-2 data, and to Dr Jenny Hatchell (University of Exeter) for teaching me how to observe with the JCMT.

Thanks to my examiners, Dr Toby Moore and Dr Dimitris Stamatellos, for being friendly while grilling me on the details.

I would like to acknowledge the STFC, as I have been the grateful recipient of an STFC-funded studentship throughout my PhD.

Thanks also to the many and various residents of the Maudland 208 office over the last three years, for the moral support, the distractions, and the stream-of-consciousness conversations over lunch.

Finally, and most importantly, my thanks and love to my family, especially my mum, my dad, and my brother Mark, without whom I wouldn't even have made it as far as the first hurdle, let alone to the finish line.

Chapter 1

Introduction

1.1   The Current Paradigm of the Star Formation Process

Stars form from the coldest, densest and smallest length-scale objects in the interstellar medium (ISM): prestellar cores. A thorough understanding of the properties of these cores and of the environments in which they form is essential to an understanding of the stars which will form from them. Prestellar cores are the gravitationally bound subset of starless cores – small-scale overdensities within larger molecular clouds. These molecular clouds are themselves the coldest and densest phase of the ISM, with the smallest filling factor.

1.1.1   The Interstellar Medium (ISM)

The ISM is generally treated as having three phases: the cold ISM, made up of molecular and atomic material at $< 300\,\mathrm{K}$, the warm ISM, which has both an atomic and an ionised component, at $\sim 10^4\,\mathrm{K}$, and the hot, ionised, ISM, at $\sim 10^6\,\mathrm{K}$. The three-phase model, proposed by McKee & Ostriker (1977), was developed in response to measurements of the soft X-ray background (e.g. Burstein et al. 1977), and of

A SMALL CLOUD

HIM
$T = 4.5 \times 10^5$ K
$n = 3.5 \times 10^{-3} cm^3$
$x = 1.0$

WNM
$T = 8,000$ K
$n = 0.37$ cm^{-3}
$x = 0.15$

WIM
$T = 8,000$ K
$n = 0.25$ cm^{-3}
$x = 0.68$

CNM
$T = 80$ K
$n = 42$ cm^{-3}
$x = 10^{-3}$

2.1pc
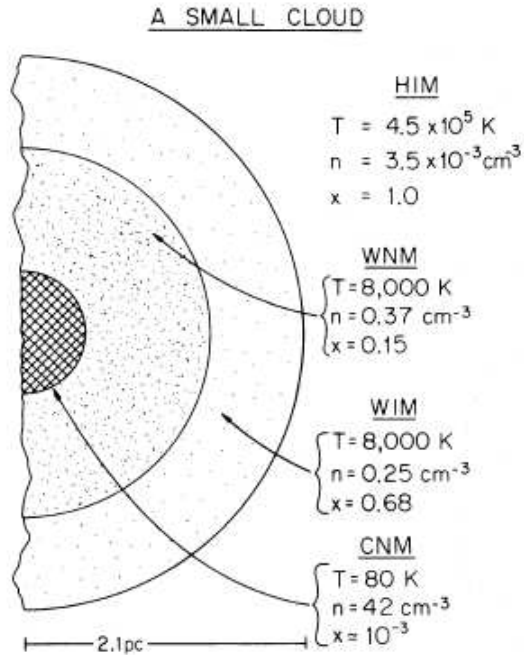
Figure 1.1: A cartoon of a cloud in the three-phase ISM, from McKee & Ostriker (1977). T is temperature, n is number density, and x is the ionisation fraction for each component.

the UV spectra of bright stars, showing broad absorption lines from highly ionised species, particularly Ovi and Nv (York 1974). Both of these indicated the presence of substantial amounts of hot, rarefied plasma in the Galactic disc, and replaced the previous two-phase model, proposed by Field et al. (1969), which did not have a hot component.

McKee & Ostriker (1977) proposed that the ISM is heated by supernova shocks, resulting in the majority ($\sim 70 - 80\%$) of the ISM by volume being hot, diffuse, highly turbulent gas (the Hot Interstellar Medium, or HIM). As the gas cools in the time between shocks, colder, dense clouds form. These clouds have a cold, neutral centre (the Cold Interstellar Medium, or CIM), and are surrounded by a warmer, partially photoionised, corona (the warm ISM). A cartoon of such a cold cloud is shown in Figure 1.1.

1.1.2 Molecular Clouds

Cold clouds in the ISM can exist on a wide variety of length scales, but a key type is the Giant Molecular Cloud (GMC). These clouds can have sizes of $\sim 10^2$ pc, might contain $10^5 - 10^7 \, \mathrm{M_\odot}$ in mass, and are typically confined to the spiral arms of the Galaxy, while clouds between the spiral arms are usually much smaller. This implies that molecular clouds form from the compressed ISM within the spiral arms, and that they have lifetimes of less than an arm crossing time, $\sim 10^7$ years – see Williams et al. (2000), and references therein. Star formation may be taking place at several different locations within a GMC.

GMCs are typically highly turbulent structures. Larson (1981) found a set of empirical relations which apply to molecular clouds over the majority of their length and size scales:

$$\sigma(\mathrm{kms^{-1}}) = 1.1 \, L(\mathrm{pc})^{0.38} \tag{1.1}$$

$$\sigma(\mathrm{kms^{-1}}) = 0.42 \, M(\mathrm{M_\odot})^{0.20} \tag{1.2}$$

$$\langle n(\mathrm{H_2}) \rangle (\mathrm{cm^{-3}}) = 3400 \, L(\mathrm{pc})^{-1.10} \tag{1.3}$$

where σ is the velocity dispersion, L is cloud size, M is cloud mass, and $\langle n(\mathrm{H_2}) \rangle$ is mean number density of $\mathrm{H_2}$ molecules. Similar scaling relations have been shown to apply to structure within clouds; Solomon et al. (1987) found

$$\sigma \propto L^{0.5} \tag{1.4}$$

within low-mass GMCs, while Caselli & Myers (1995) found

$$\sigma \propto L^{0.21} \tag{1.5}$$

in high-mass star-forming regions. However, these relations must break down on large scales, as GMCs are not infinite in extent, and on small scales, as at some point, self-similar behaviour must break down in order for stars to form.

While a GMC must be gravitationally bound on local scales if star formation is able to occur at all, whether or not GMCs are typically globally gravitationally bound is subject to debate (e.g. Heyer et al. 2009; Dobbs et al. 2011). At least some GMCs, particularly those at high galactic latitude, are gravitationally unbound (e.g. Dawson et al. 2015).

1.1.3   Turbulence and Magnetism in Molecular Clouds

As discussed above, molecular clouds are likely to be highly turbulent on all but the smallest length scales. There are a variety of mechanisms proposed for generating turbulence in clouds: on large scales (Galactic), differential Galactic rotation; on intermediate scales (GMC-scale), shocks from supernovae and stellar winds from OB associations; and on small scales, individual stellar winds and outflows (see, e.g. Elmegreen & Scalo 2004, and references therein). This turbulence must begin to decay in order for a region to undergo gravitational collapse.

Molecular clouds are also expected to be magnetised (e.g. Mestel & Spitzer 1956), as the Galactic magnetic field is thought to be frozen into the ionised material of the diffuse ISM (e.g. Davis & Greenstein 1951). The Galactic magnetic field is not strong enough to dominate the dynamics of the diffuse ISM and can thus be 'wound up' if the diffuse material to which it is frozen becomes part of the CNM. Magnetic fields in molecular clouds are typically significantly higher than in the diffuse ISM, due to this winding up of the magnetic field during the clouds' formation.

The relative importance of turbulent motion and magnetic fields to the formation and evolution of molecular clouds is a much-debated question (see Crutcher 2012 for a recent review). Theories of star formation can be divided into strong-field and weak-field models, depending on whether molecular clouds form with a mass greater or less than their magnetic critical mass, given by Nakano & Nakamura (1978) to

be

$$M_\Phi = \frac{\Phi}{2\pi\sqrt{G}}, \qquad (1.6)$$

where Φ is the magnetic flux in the cloud and G is the gravitational constant.

1.1.3.1 Strong-field models

In strong-field models, $M_{\mathrm{cloud}} < M_\Phi$; the molecular cloud is initially magnetically subcritical, and so the magnetic pressure in the cloud is strong enough to prevent gravitational collapse. The cloud slowly evolves to become gravitationally unstable through the process of ambipolar diffusion – the drift of neutral material across magnetic field lines (Mestel & Spitzer 1956). The ionisation fraction in a molecular cloud is by definition low ($\sim 10^{-7}$; e.g. Ward-Thompson 2002), as the majority of the cloud mass is in molecular form, and is (in the absence of UV flux from early-type stars) set by the cosmic ray ionisation rate. Only the ionised material is frozen into the magnetic field lines; the remainder of the material is free to contract gravitationally across the field lines. This is a slow process as particles in a molecular cloud have a short mean free path, and the scattering of neutral and ionised particles will result in well-coupled behaviour between the ionised and neutral material. However, the cloud, or regions within the cloud, will gradually increase in density until the magnetic critical mass is exceeded, and gravitational collapse will begin. This paradigm has been modelled extensively by, e.g. Mouschovias (1991); Mouschovias & Ciolek (1999).

An object undergoing ambipolar-diffusion-driven collapse is expected to do so on the ambipolar diffusion timescale,

$$t_{\mathrm{AD}} = \frac{L}{|\mathbf{v}_{\mathrm{drift}}|}, \qquad (1.7)$$

where L is the size of the object and $\mathbf{v}_{\mathrm{drift}}$ is the drift velocity of the neutrals relative to the ions.

As the gravitationally-unstable material collapses, the magnetic field remains frozen to the ions, and will be pulled in by the collapsing material. Cores which have undergone ambipolar-diffusion-driven collapse are expected to show a characteristic 'hour-glass' magnetic field shape. This has been observed in a single protostellar core by Girart et al. (2006), suggesting that the ambipolar-diffusion-driven paradigm is relevant in at least some cases.

1.1.3.2 Weak-field models

In weak-field models, $M_{\mathrm{cloud}} > M_\Phi$; the molecular cloud is initially magnetically supercritical, and cannot be supported against collapse by magnetic pressure. In this paradigm, molecular clouds form at 'stagnant' points at the intersection of supersonic turbulent flows in the ISM, and are short-lived ($\sim 10^6$ years) and generally gravitationally unbound. Stars form in regions in which turbulence has dissipated. According to the classical theory of turbulence, energy injected into a system on large scales 'cascades' to smaller scales, where it then dissipates due to viscous effects (Kolmogorov 1941; Kolmogorov 1991). In molecular clouds, this is expected to happen on a freefall timescale (e.g. Elmegreen & Scalo 2004; see Section 1.4 for a discussion of freefall time). The turbulence-dominated star-formation paradigm has been modelled by, e.g. Padoan & Nordlund (1999); Mac Low & Klessen (2004). In the weak-field model, magnetic fields cannot stop collapse, but can contribute more to the support of a collapsing region than turbulent pressure in the later stages of core collapse.

1.1.3.3 Synthesis of magnetism and turbulence

The observational evidence for whether molecular clouds are magnetically subcritical or supercritical is very mixed, and it is likely that neither turbulence nor magnetic fields can be neglected when attempting to successfully model the star formation

process. In addition to this, the M/M_Φ ratio may vary within a molecular cloud: a cloud which is magnetically subcritical in one location may be supercritical elsewhere (e.g. Crutcher 2012). More recent star-formation simulations (e.g. Nakamura & Li 2005; Tilley & Pudritz 2007; Vázquez-Semadeni et al. 2011) have included both magnetic fields and turbulence.

Further evidence that neither turbulence nor magnetism can be neglected when studying the dynamics of the ISM comes from the discovery of empirical relations between the two quantities; Basu (2000) found a relation between magnetic field strength, number density, and non-thermal velocity dispersion σ_{NT} in the ISM of

$$B \propto n^{\frac{1}{2}}\sigma_{\mathrm{NT}}. \tag{1.8}$$

In summary, the importance of turbulence to the formation and large-scale dynamics of molecular clouds is generally accepted. The rôle and relative importance of the magnetic field in these processes is less well-understood. It seems likely that while in individual cases one or other of turbulence and magnetism may dominate the evolution of a local region, neither turbulence nor magnetic fields can be neglected in a complete theory of star formation.

1.1.4 Filamentary Structure

It is well established that GMCs contain filamentary structure (see, e.g., Loren 1989; Loren 1989). However, recent high-resolution observations of molecular clouds, particularly those from the Herschel Space Observatory (see Chapter 2, below), have revealed that all molecular clouds show detailed filamentary structure, regardless of whether they are forming stars (André et al. 2010). For example, filaments are seen in both the quiescent Polaris Flare (Ward-Thompson et al. 2010; see also Panopoulou et al. 2015) and the actively star-forming Aquila Rift (Könyves et al. 2010). This implies that the formation of filaments precedes the formation of stars, and that the formation of filaments may be a necessary step in the star formation process.
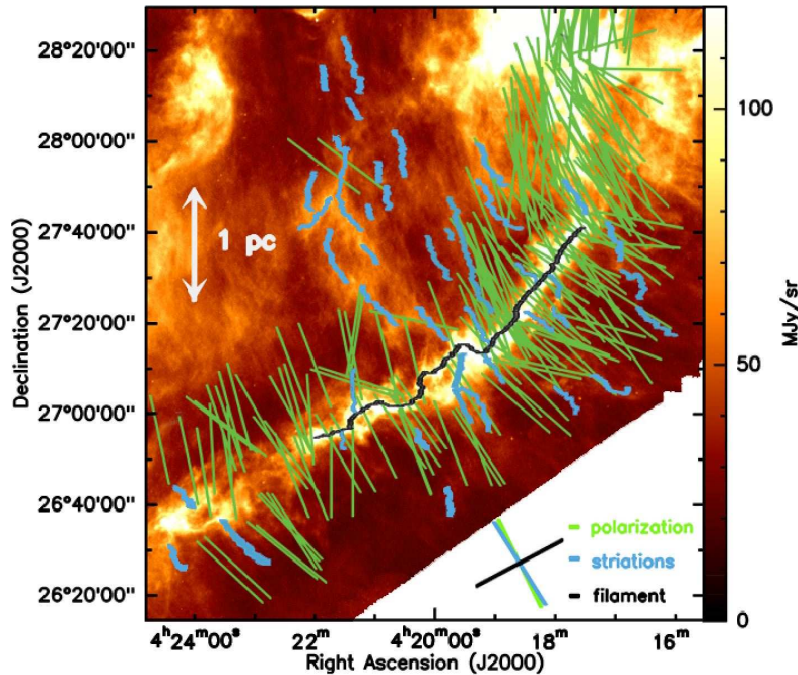
Figure 1.2: The Taurus B211/B213/L1495 filament observed with Herschel, with striations marked in blue, and polarisation vectors marked in green. From Palmeirim et al. (2013).

There appear to be some consistent properties of filaments, regardless of the parent molecular cloud in which they form. In particular, Arzoumanian et al. (2011) find a width of the 'inner plateau' of filaments of $\sim 0.1\,\mathrm{pc}$ in many local molecular clouds. However, it should be noted that these are all regions of low-to-intermediate mass star formation; whether these results can be generalised to sites of high-mass star formation is unclear.

André et al. (2010) found that most ($> 60\%$) of the prestellar cores in star-forming regions are found within gravitationally unstable filaments. A filament is gravitationally unstable if its mass per unit length exceeds a critical value (Ostriker 1964):

$$M_{\mathrm{line,crit}} = \frac{2c_s^2}{G} \tag{1.9}$$

where c_s is the isothermal sound speed, which, for a particle with temperature T
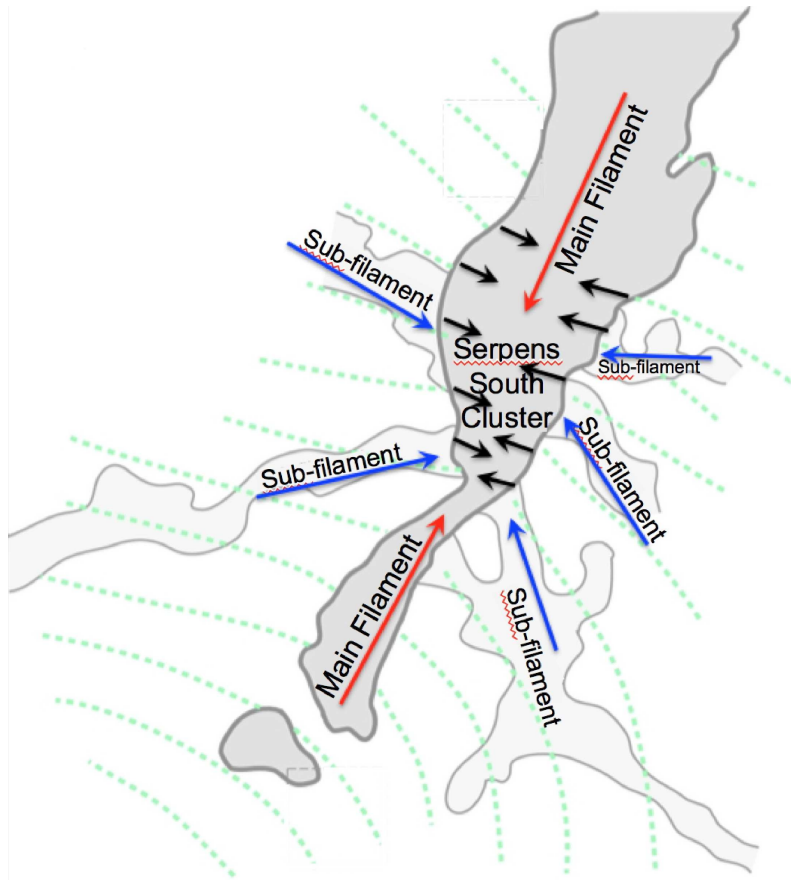
Figure 1.3: An illustration of the model of magnetically-regulated filament formation. From André et al. (2014).

and mass m is given by

$$c_s = \sqrt{\frac{k_{\mathrm{B}}T}{m}}. \tag{1.10}$$

André et al. (2010) find $M_{\mathrm{line,crit}}$ to be $\sim 15 \mathrm{M}_\odot \mathrm{pc}^{-1}$, for a typical temperature of $T \sim 10\,\mathrm{K}$ in molecular clouds.

Palmeirim et al. (2013) showed that faint 'striations' can be seen perpendicular to the prominent B211/B213/L1495 filament in the Taurus molecular cloud, but parallel to the the local polarization vectors, suggesting that material is being accreted onto the filament along magnetic field lines. These observations are shown in Figure 1.2.

André et al. (2014) proposed a theory of magnetically-regulated star formation

in which material flows onto filaments along magnetic field lines. Once the filament mass per unit length exceeds the critically stable line mass, it begins to fragment into a series of starless cores. These cores will continue to accrete mass until they become gravitationally stable (prestellar). They will then collapse under their own gravity to form stars. This model is illustrated in Figure 1.3.

1.2 Physical Properties of Starless and Prestellar Cores

A prestellar core is a gravitationally bound accumulation of material in the cold interstellar medium from which, barring external disruption, an individual stellar system will form. This system might be a single star, a binary, or a higher-order multiple system. Prestellar cores are the gravitationally-bound subset of a larger population of starless cores, with a starless core being any cold over-density in the molecular ISM, either gravitationally bound or otherwise. The original detection of a prestellar core was made by Ward-Thompson et al. (1994).

The observational definition of a starless core varies, but typically, they might be defined as an accumulation of material with number density $n(\mathrm{H_2}) > 10^4\,\mathrm{cm^{-3}}$, which is not detected in near-infrared emission. Historically, the density criterion was judged by whether the core was detected in high-density molecular tracers such as $\mathrm{NH_3}$ (Benson & Myers 1989). Beichman et al. (1986) discussed the requirement for non-detection in infrared emission, specifically, in IRAS observations.

Once a core has formed a hydrostatic central object, it is considered to be a protostar. The protostar then evolves to the main sequence through the Class 0-I-II-III evolutionary stages (Lada 1987; André et al. 1993), described below, before arriving at the Main Sequence.

1.2.1 Temperature

Low-mass prestellar cores are expected to be low-temperature objects, with mean line-of-sight temperatures in the range $\sim 10-20\,\mathrm{K}$ (e.g. Leung 1975). High-mass prestellar cores are expected to have higher temperatures, of up to $50\,\mathrm{K}$ (e.g. Wilson et al. 1999). Prestellar cores are expected to have a radial temperature gradient, with the centres colder than the edges (e.g. Leung 1975; Evans et al. 2001; Stamatellos & Whitworth 2003). This is because the edges will be heated by the local interstellar radiation field (ISRF), from which the centres should be shielded. In the absence of any embedded source, a starless core should be optically thin to its own radiation, and hence only heated externally. Stamatellos et al. (2007), modelling starless cores in the Ophiuchus molecular cloud, found central temperatures $\sim 7\,\mathrm{K}$ and edge temperatures $\sim 12\,\mathrm{K}$. Radial temperature gradients have been observed in starless cores by, e.g. Ward-Thompson et al. (2002).

Cores may be heated non-uniformly by nearby hot stars – typically, stars of spectral type A or earlier, i.e. emitting a non-negligable fraction of their photons above the Lyman limit. These non-uniform effects may lead to temperature gradients across a core (e.g. Nutter et al. 2009).

1.2.2 Mass

The mass M of a starless core can be determined from its submillimetre flux density F_ν using the Hildebrand (1983) formulation

$$M = \frac{F_\nu D^2}{\kappa B_\nu(T)},\tag{1.11}$$

where D is the distance to the core, T is the core temperature, κ is the dust opacity (discussed below), and $B_\nu(T)$ is the Planck function,

$$B_\nu(T) = \frac{2h\nu^3}{c^2}\frac{1}{e^{h\nu/k_\mathrm{B}T}-1},\tag{1.12}$$

where symbols take their usual meanings. The distribution of masses of prestellar cores is discussed in Section 1.5 below.

1.2.3 Magnetic Fields

There have been few direct measurements of the magnetic fields in starless cores; those measurements which have been made have varied from $\sim 1\,\mu$G (Troland et al. 1996) to up to $\sim 150\,\mu$G (Shinnaga et al. 1999), with magnetic field strength on the order of a few tens of μG being typical (e.g. Levin et al. 2001; Kirk et al. 2006; Troland & Crutcher 2008). It should be noted that no single observational technique can probe more than one component (either line-of-sight or plane-of-sky) of the magnetic field strength at a time.

The magnetic field of a starless core provides support against gravitational collapse (Chandrasekhar & Fermi 1953a). The magnetic energy Ω_{B} internal to a starless core is given, for a uniform magnetic field strength B, over a volume V, by

$$\Omega_{\mathrm{B}} = \frac{1}{2\mu_0} B^2 V, \tag{1.13}$$

where μ_0 is the permeability of free space.

1.2.4 External Pressure

The definition of a starless core as an over-density in the ISM requires that starless cores exist within more rarefied surroundings. The shielding of starless cores from the local ISRF also implies that starless cores are colder than their surroundings. Assuming the material of a molecular cloud can be approximated as an ideal gas, and in the absence of non-thermal motions, these two effects should counteract one another, and mitigate changes of pressure as density increases:

$$P = n k_{\mathrm{B}} T, \tag{1.14}$$

where P is the pressure, n is the number density of the gas, k_B is Boltzmann's constant and T is the temperature. However, as discussed above, turbulent motion is expected to dissipate in the dense gas of starless cores. Starless cores often show transonic or supersonic linewidths, suggesting a non-negligible fraction of their support against collapse comes from non-thermal motions. However, the non-thermal contribution to the linewidth in the more rarefied surrounding material is considerably higher. The thermal and non-thermal motions of the material immediately surrounding the starless core will typically produce a confining pressure on the core. For a uniform pressure P acting on a core of volume V, the energy due to external pressure Ω_P will be

$$\Omega_P = -3PV, \tag{1.15}$$

where the energy is negative as the external pressure force is confining the core (see, eg. Spitzer 1978). The validity of approximating turbulent motions as a hydrostatic confining pressure is debated (e.g. Elmegreen & Scalo 2004). However, the external pressure is often a dominant term in the energy balance of starless cores (e.g. Johnstone et al. 2000; Maruta et al. 2010), and so it is necessary to parameterise this effect, typically in the manner described herein.

1.2.5 Morphology

A number of different morphologies have been proposed for starless cores. Analytic or semi-analytic models of prestellar cores are generally very idealised, requiring a core to be spherically symmetric, isothermal and in hydrostatic equilibrium, the key equations being:

$$\frac{dP(r)}{dr} = -\frac{GM(r)\rho(r)}{r^2} = -\frac{d\Phi}{dr}\rho(r), \tag{1.16}$$

$$P(r) = \frac{\rho(r)k_B T}{\mu m_H} = \rho(r)c_s^2, \tag{1.17}$$

$$\frac{1}{r^2}\frac{d}{dr}\left(r^2\frac{d\Phi(r)}{dr}\right) = 4\pi G\rho(r), \tag{1.18}$$

which are, respectively, the equation of hydrostatic equilibrium, the ideal gas equation of state, and the gravitational potential energy equation, where r is radius, P is pressure, ρ is density, M is mass, Φ is gravitational potential, and c_s is the isothermal sound speed. There are various solutions to these equations, of varying complexity and physical applicability. Most modern models of starless core morpologies have an approximately flat central region of constant density, and a power-law drop-off in density at large radii.

One of the simplest models for the morphology of starless cores is the singular isothermal sphere (SIS – Shu 1977; Shu et al. 1987), which treats cores as isothermal objects with an inverse square radial density profile:

$$\rho(r) = \frac{c_s^2}{2\pi G r^2}. \tag{1.19}$$

This model, while consistent with core density profiles at large radii, must fail at the smallest radii, as it suggests $\rho(r) \to \infty$ as $r \to 0$.

A useful alternative is the Plummer density profile (Plummer 1911),

$$\rho(r) = \rho_{\mathrm{flat}} \left(\frac{R_{\mathrm{flat}}}{\sqrt{R_{\mathrm{flat}}^2 + r^2}} \right)^{\eta} \tag{1.20}$$

where R_{flat} is the radius of the flattened central plateau, ρ_{flat} is the uniform central density found at $r \ll R_{\mathrm{flat}}$, and η is the exponent of the power-law drop-off in density seen at large radii; when $r \gg R_{\mathrm{flat}}$, $\rho(r)$ tends to $\rho_{\mathrm{flat}} R_{\mathrm{flat}} r^{-\eta}$. For a true Plummer distribution, $\eta = 5$. However, Whitworth & Ward-Thompson (2001), who were the first to use a Plummer-like sphere as a model for the initial density distribution of a prestellar core, used $\eta = 4$, as the exponent necessary to recreate the observed relative accretion rates of Class 0 and Class I protostars. This is a particularly useful model, as it has only three free parameters: ρ_{flat}, R_{flat} and η.

Another frequently-used model is the Bonnor-Ebert sphere (Ebert 1955; Bonnor 1956). This model is discussed further in Section 1.3.3. However, a useful, and analytically tractable, approximation to the density profile of starless cores is the

Gaussian density distribution,

$$\rho = \rho_0 e^{-\frac{1}{2}\left(\frac{r}{\alpha}\right)^2}, \tag{1.21}$$

for a central density of ρ_0 and a Gaussian width α.

1.2.6   Environment

The physical properties of starless cores may depend upon their local environment. Starless cores may exist in near-total isolation (e.g. high-latitude 'lonely cores'; Quinn 2013), or in dense clusters in the centres of high-mass star-forming regions (e.g. in the Orion molecular cloud; c.f. Ward-Thompson et al. 2006). If a core exists in an area with high local A_V – i.e. within a molecular cloud – it will be shielded from the interstellar radiation field (ISRF), and hence should, in the absence of local heating (discussed below), have a lower mean temperature than an equivalent core existing in isolation (e.g. Stamatellos et al. 2007). Cores in molecular clouds might also be expected to have a smaller size than their isolated counterparts. According to some theoretical models of molecular clouds, regions of clustered star formation may show evidence of competitive accretion (e.g. Bonnell et al. 1998; Bate et al. 2003); however, observational evidence for this is lacking (e.g. André et al. 2007).

As discussed above, starless cores are local over-densities in the ISM: thus, starless cores within molecular clouds are likely to be denser than their isolated counterparts, as they represent an over-density within an already-dense molecular cloud, rather than an over-density within the diffuse ISM. This might also be considered to be a result of the smaller size of cores within molecular clouds: a core in a molecular cloud is likely to be denser than an equivalent core in the diffuse ISM.

Not all molecular clouds are alike: typically, molecular clouds are considered to be forming stars in either a clustered or a dispersed manner. An example of a nearby site of clustered star formation is the central region of the Ophiuchus molecular cloud (e.g. Wilking et al. 2008 – see Chapter 3), while a nearby site of
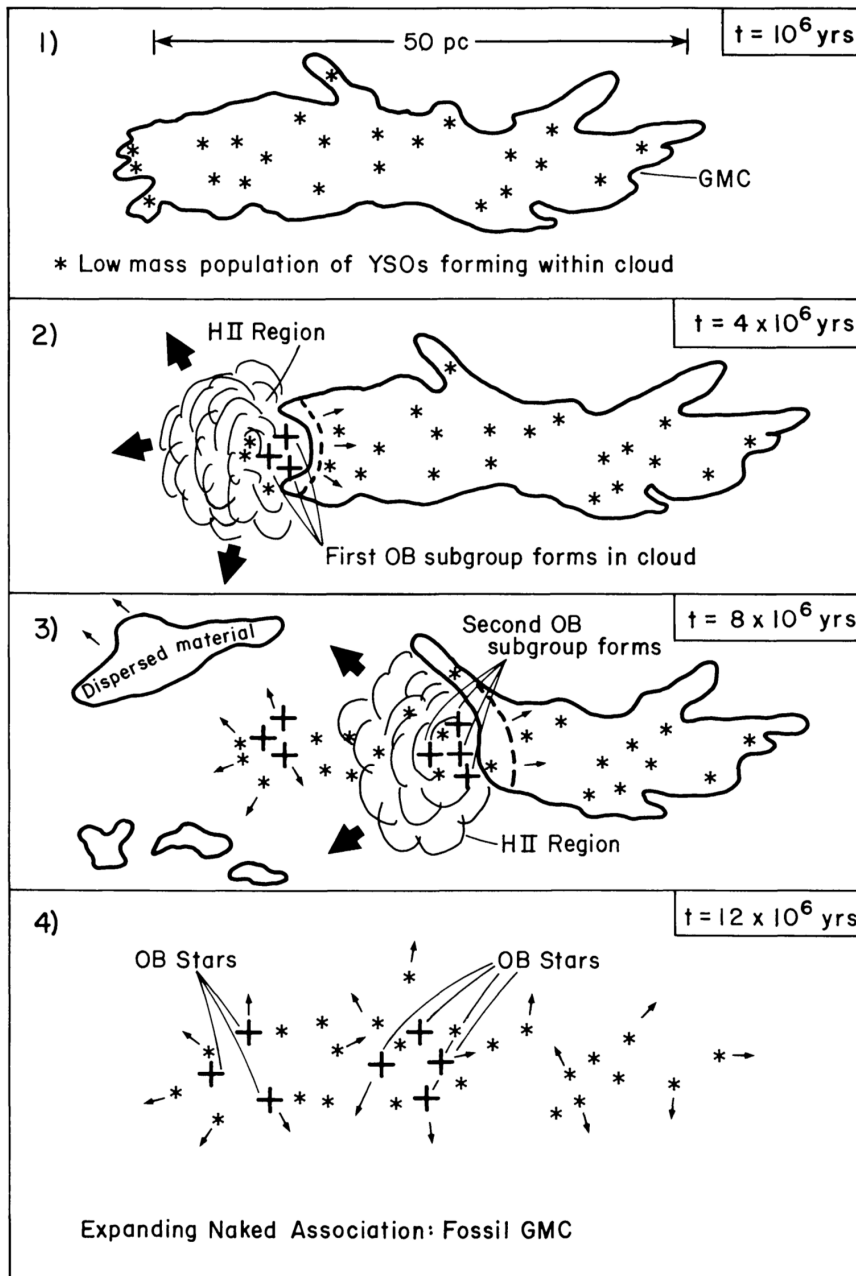
Figure 1.4: Cartoon of the sequential star formation process, from Lada (1987).
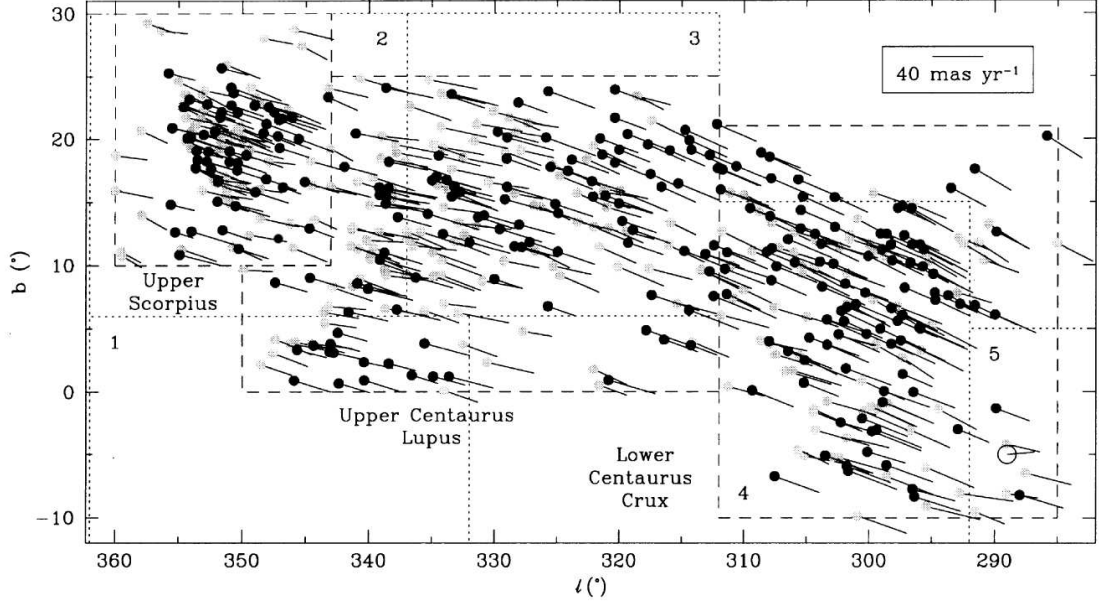
Figure 1.5: Stars in the Scorpius-Centaurus OB association, with their proper motions shown – from de Zeeuw et al. (1999). The Lower-Centaurus Crux, Upper-Centaurus Crux, and Upper Scorpius sub-groups are labelled. The Ophiuchus molecular cloud, not shown, has approximate Galactic coordinates $l = 353°$, $b = 16.5°$, south-east of the Upper Scorpius sub-group.

dispersed star formation is the Taurus molecular cloud (e.g. Kenyon et al. 2008 – see Chapter 4). In the absence of local heating – effectively, in the case of low-mass star formation – cores forming in a clustered environment are expected to be smaller and denser than those forming in a dispersed manner.

1.2.6.1 Sequential star formation

The local star formation history has a profound effect on the evolution of a star-forming region, as alluded to in the section above. Particularly, the formation of an OB association – a co-eval group of stars, a significant number of which are of spectral type B or earlier – can dominate the energy balance of, and control the subsequent evolution of, the local ISM. The model of sequential star formation grew out of observations of 'chains' of OB associations, in which the member associations are separated from one another by distances $\sim 10 - 40\,\text{pc}$, and in which there is

17

an age gradient, with the oldest OB association at one end of the chain, and the youngest at the other (Blaauw 1964). Elmegreen & Lada (1977) proposed a mechanism of sequential star formation, in which a young group of high-mass stars inject mechanical energy, momentum and material into the local ISM through outflows, stellar winds and, after a time delay of a few Myr, supernovae. This has the effect of clearing the local volume of dense molecular material, effectively ceasing local star formation, and producing a 'shell' of low-density material around the association (in extreme cases, this shell may be partially ionised). However, the density enhancement in the swept-up material on the edges of the shell will induce new star formation, as the increase in density reduces the Jeans mass in the swept-up material (see Section 1.3.1 for a discussion of Jeans mass). If this new site of star formation produces high-mass stars then the process will repeat itself. A cartoon of the sequential star formation process is shown in Figure 1.4.

Observational evidence exists for the sequential star formation process in action: here, we describe the evidence for a nearby example of the sequential star formation process, the Scorpius-Centaurus OB association. This is a series of groups of OB stars of decreasing age, each of which has an associated HI shell (e.g. Preibisch & Mamajek 2008, and references therein). The series of OB associations culminates in the Ophiuchus molecular cloud, in which star formation is ongoing. De Geus (1992) proposed that star formation proceeded through the three sub-groups of the Scorpius-Centaurus OB association, beginning in the Lower-Centaurus Crux group, followed by the Upper-Centarus Lupus group, and continuing into the Upper Scorpius group. It has long been suggested that the material in the Ophiuchus molecular cloud is being compressed by interaction with a subset of the Upper Scorpius group, the Sco OB2 association (Vrba 1977); furthermore, Loren (1989) ascribes the extended filamentary streamers in the Ophiuchus molecular cloud to the effects of the Sco OB2 association, $\sim 11\,\mathrm{pc}$ distant (Mamajek 2008). Nutter

et al. (2006) find that the regions of Ophiuchus in closest proximity to the Sco OB2 association have the most active star formation history, and suggest that this is a result of sequential star formation in the region. The Scorpius-Centaurus OB association is shown in Figure 1.5.

1.2.6.2   Triggered star formation

Triggered star formation is a phenomemon largely restricted to regions of high-mass star formation, in which star formation is directly induced by the interaction of molecular gas with an expanding HII region. The mechanism was proposed under the name 'radiation-driven implosion' by Klein et al. (1980), and is in a sense an extreme case of sequential star formation. An HII region is a bubble of gas, partially ionised by interaction with at least one early-type star, interior to the bubble (Strömgren 1939). Examples of triggered star formation include the Orion Nebula (e.g. Sugitani et al. 1989; Ward-Thompson et al. 2006); the famous 'Pillars of Creation' in the Eagle Nebula (e.g. White et al. 1999; Williams et al. 2001); and the 30 Doradus star-forming region in the Large Magellanic Cloud (e.g. Walborn et al. 2002).

1.3   Stability of Starless and Prestellar Cores

1.3.1   The Jeans Mass

Jeans (1928) demonstrated that if a uniform isothermal cloud, which is supported by thermal pressure, is to collapse under its own self-gravity, its mass must exceed the critical value

$$M_J = \frac{4\pi}{3} \frac{c_s^3}{\sqrt{G^3 \rho}} \qquad (1.22)$$

where c_s is the sound speed in the gas, and ρ is the gas density. This mass, known as the thermal Jeans Mass, is typically an under-estimate of the minimum mass

required for collapse; internal support from either or both of non-thermal motions and magnetic fields may inhibit collapse (see above).

1.3.2 The Virial Theorem

A prestellar core is a starless core which is gravitationally bound. The bound state of a core can be estimated using the virial theorem (Clausius 1870), of which we give a brief derivation here.

The moment of inertia $\mathcal{I}$ of a group of particles of mass m_i, position $\mathbf{r}_i$ and velocity $\mathbf{v}_i$ is given by

$$\mathcal{I} = \sum_i m_i \mathbf{r}_i.\mathbf{r}_i. \tag{1.23}$$

If the group of particles is in equilibrium, then the time derivative of $\mathcal{I}$, $\dot{\mathcal{I}}$ equals zero, so

$$\dot{\mathcal{I}} = 2 \sum_i m_i \mathbf{v}_i.\mathbf{r}_i = 0, \tag{1.24}$$

as $\dot{m}_i = 0$, $\dot{\mathbf{r}}_i = \mathbf{v}_i$ and $\mathbf{r}_i.\mathbf{v}_i = \mathbf{v}_i.\mathbf{r}_i$. In equilibrium, the second time derivative of $\mathcal{I}$ must also be zero,

$$\ddot{\mathcal{I}} = 2 \sum_i m_i (\dot{\mathbf{v}}_i.\mathbf{r}_i + \mathbf{v}_i.\mathbf{v}_i) = 0. \tag{1.25}$$

From Newton's second law the force $\mathbf{F}_i$ on the ith particle is

$$\mathbf{F}_i = m_i \dot{\mathbf{v}}_i. \tag{1.26}$$

Using this, and the formula for the kinetic energy of a system,

$$\Omega_{\text{K}} = \frac{1}{2} \sum_i m_i |\mathbf{v}_i|^2, \tag{1.27}$$

equation 1.25 becomes

$$\ddot{\mathcal{I}} = 2 \sum_i \mathbf{F}_i.\mathbf{r}_i + 4\Omega_{\text{K}} = 0. \tag{1.28}$$

For a system of particles, the force $\mathbf{F}_i$ on the ith particle is the sum of the forces between the ith particle and every other particle in the system,

$$\mathbf{F}_i = \sum_{i \neq j} \mathbf{F}_{ij}. \tag{1.29}$$

Then, the first term on the right-hand side of Equation 1.28 becomes

$$2\sum_i \mathbf{F}_i.\mathbf{r}_i = \sum_i \sum_{j\neq i} \mathbf{F}_{ij}.\mathbf{r}_i + \mathbf{F}_{ji}.\mathbf{r}_j \tag{1.30}$$

$$= \sum_i \sum_{j\neq i} \mathbf{F}_{ij}.(\mathbf{r}_i - \mathbf{r}_j) \tag{1.31}$$

$$= \sum_i \sum_{j\neq i} \mathbf{F}_{ij}.\mathbf{r}_{ij} \tag{1.32}$$

where $\mathbf{r}_{ij} = \mathbf{r}_i - \mathbf{r}_j$.

The three forces, other than the internal energy, which we consider to be significant to the virial balance of starless cores are the gravitational force (Clausius 1870), the electro-magnetic force (Chandrasekhar & Fermi 1953b), and the force due to external pressure on the core (Spitzer 1978). The first two of these are conservative forces, and can hence be described by the gradient of a potential, V, i.e.

$$\mathbf{F} = \nabla V(\mathbf{r}) \tag{1.33}$$

and

$$\sum_i \sum_{j\neq i} \mathbf{F}_{ij}.\mathbf{r}_{ij} = \sum_i \sum_{j\neq i} \mathbf{r}_{ij}.\nabla V(\mathbf{r}_{ij}). \tag{1.34}$$

For a generalised conservative power-law force,

$$V(\mathbf{r}_{ij}) = k|\mathbf{r}_{ij}|^n = kr_{ij}^n, \tag{1.35}$$

where hereafter, $|\mathbf{r}_{ij}| = r_{ij}$. Then,

$$\sum_i \sum_{j\neq i} \mathbf{F}_{ij}.\mathbf{r}_{ij} = \sum_i \sum_{j\neq i} \mathbf{r}_{ij}.nkr_{ij}^{n-1}\hat{\mathbf{r}}_{ij} \tag{1.36}$$

$$= \sum_i \sum_{j\neq i} nkr_{ij}^n \tag{1.37}$$

$$= n\sum_i \sum_{j\neq i} kr_{ij}^n \tag{1.38}$$

$$= n\Omega, \tag{1.39}$$

where Ω is the total potential energy due to the force in the system. Both the gravitational and magnetic forces obey inverse-square power-law behaviour, and so in both cases, $n = -2$. This result was shown by Chandrasekhar & Fermi (1953b).

The third force we consider, the force due to external pressure, can be determined by considering the core to be a sphere with total area A and volume V, acted upon by a constant external pressure P. Spitzer (1978) showed that the force exerted by gas pressure on an area of the wall $\mathrm{d}A$ is

$$\mathrm{d}\mathbf{F} = -\hat{\mathbf{r}}P\,\mathrm{d}A \tag{1.40}$$

where the sign is negative as the force is inward, and $\hat{\mathbf{r}}$ is a radial unit vector. Then,

$$2\sum_i \mathbf{F}_i.\mathbf{r}_i = -2\iint_A \hat{\mathbf{r}}.\mathbf{r}P\,\mathrm{d}A. \tag{1.41}$$

Using the divergence theorem

$$\iint_A \hat{\mathbf{r}}.\mathbf{Q}\,\mathrm{d}A = \iiint_V \nabla.\mathbf{Q}\,\mathrm{d}V, \tag{1.42}$$

here stated for an arbitrary vector quantity $\mathbf{Q}$, this can be converted into an integral over a volume V. Thus, Equation 1.41 becomes

$$2\sum_i \mathbf{F}_i.\mathbf{r}_i = 2 \times \left(-P\iiint_V \nabla.\mathbf{r}\,\mathrm{d}V\right) \tag{1.43}$$

$$= 2 \times \left(-3P\iiint_V \mathrm{d}V\right) \tag{1.44}$$

$$= -6PV. \tag{1.45}$$

As a result of the above, Equation 1.28 can be written as

$$\ddot{\mathcal{I}} = 4\Omega_{\mathrm{K}} + 2\Omega_{\mathrm{G}} + 2\Omega_{\mathrm{M}} - 6PV \tag{1.46}$$

and the virial theorem is given in its standard form by

$$\frac{1}{2}\ddot{\mathcal{I}} = 2\Omega_{\mathrm{K}} + \Omega_{\mathrm{G}} + \Omega_{\mathrm{M}} + \Omega_{\mathrm{P}}, \tag{1.47}$$

22

where Ω_{G} is the gravitational potential energy, Ω_{M} is the magnetic energy, and $\Omega_{\mathrm{P}} = -3PV$ is the energy due to external pressure acting on the core. If $\ddot{\mathcal{I}} < 0$, a core's net energy is negative, and hence the core is collapsing. Conversely, a core with $\ddot{\mathcal{I}} > 0$ will be dispersing, and the virially stable mass of a core is the mass at which $\ddot{\mathcal{I}} = 0$. However, not all virially-confined cores are prestellar cores. A prestellar core is a core which is gravitationally bound, i.e. where $\ddot{\mathcal{I}} < 0$ and $\Omega_{\mathrm{G}}/\Omega_{\mathrm{P}} > 1$ (Pattle et al. 2015).

1.3.3 Bonnor-Ebert Stability Criterion

Evaluation of the virial state of a starless core requires, as a minimum, a measure of the core's mass, and a measure of its internal velocity dispersion. The latter quantity cannot be determined without kinematic data. A frequently-used proxy for the virial balance of a core is the core's Bonnor-Ebert stability.

The Bonnor-Ebert (BE) model (Ebert 1955; Bonnor 1956) is a density distribution parameterised by its central density and characterised by a plateau of slowly decreasing density at small radii, and a power-law decrease at large radii. For a standard Bonnor-Ebert sphere, the power-law index is -2. The BE model treats a core as an isothermal, self-gravitating, polytropic sphere bounded by external pressure. The mass at which a BE sphere at temperature T, with sound speed $c_s(T)$, and bounded by external pressure P_{EXT}, is critically stable against gravitational collapse is given by

$$M_{\mathrm{BE},crit} = 1.18 \frac{c_s(T)^4}{P_{\mathrm{EXT}}^{1/2} G^{3/2}}, \tag{1.48}$$

or, equivalently, by

$$M_{\mathrm{BE},crit} = 2.4 \frac{c_s(T)^2}{G} R, \tag{1.49}$$

where R is the radius at which the BE sphere is confined by external pressure.

The critical BE mass is often considered a useful proxy for virial mass. If the critically-stable BE model is appropriate and the radius at which cores are bounded
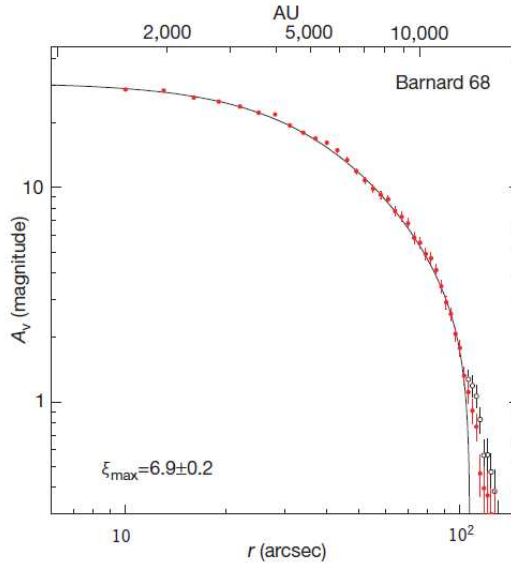
Figure 1.6: The azimuthally averaged visual extinction (as a proxy for column density) profile of the Bok Globule B68; Figure 2 from Alves et al. (2001), with the best-fitting Bonnor-Ebert sphere plotted. The value of $\xi_{\max}$ shown indicates that B68 is marginally over-dense, and hence marginally unstable against collapse.

by external pressure can be estimated, the stability of a core can be estimated without velocity dispersion data, as cores with observed masses greater than their critically-stable BE mass (i.e. $M/M_{\mathrm{BE},crit} > 1$) will be undergoing gravitational collapse.

An example of a core which is extremely well-fitted by a Bonnor-Ebert profile is shown in Figure 1.6. This core, B68, is an example of a Bok globule (Bok & Reilly 1947), and is located within an HII region (Alves et al. 2001).

This method, however, does not unambiguously identify virially stable cores. As noted by Ballesteros-Paredes et al. (2003), it is possible to fit stable Bonnor-Ebert distributions to cores which are in fact not in equilibrium, and for different projections of the same core to give very different values of the Bonnor-Ebert fitting parameters.

1.4 Evolution and Lifetime of Starless Cores

Whether or not prestellar and starless cores are part of the same population, with starless cores having the possibility of evolving to become gravitationally bound prestellar cores, has been subject to debate (see, e.g. Ward-Thompson et al. 2007, and references therein). Prior to Herschel studies of nearby molecular clouds, starless and prestellar cores were found to occupy separate regions of the mass/size plane (shown in Figure 1.7), suggesting that the two populations were separate (Motte et al. 2001). However, Könyves et al. (2010) and Kirk et al. (2013) find cores occupying the intermediate regions of the mass/size plane, suggesting that prestellar and starless cores are all part of the same population. Simpson et al. (2011) proposed that starless cores follow evolutionary tracks across the mass-size plane, accumulating mass and increasing in radius until they become gravitationally bound prestellar cores, and collapse. An example of a set of cores detected by Herschel, spanning the mass-size plane, is shown in Figure 1.7.

The lifetime of a prestellar core is not well-known, but is typically related to the time required for a core to collapse under its own gravity in the absence of internal support, known as the freefall time:

$$t_{ff} = \left(\frac{3\pi}{32G\rho} \right)^{1/2}, \tag{1.50}$$

for a core of uniform density ρ. Jessop & Ward-Thompson (2000) showed that starless core lifetimes can be inferred to be between 1 and 10 times the freefall time for the core, with core lifetime decreasing as average density increases (see Figure 1.8). A lifetime of $10 \times t_{ff}$ is consistent with the ambipolar diffusion timescale.

Starless core lifetimes are estimated by comparing the number of starless cores in a region to the number of embedded protostellar sources (Beichman et al. 1986; protostellar sources are discussed in Section 1.6). Provided that the star formation rate in the region has remained constant over a time $\sim t_{\text{starless}} + t_{\text{embedded}}$, where t_{starless}
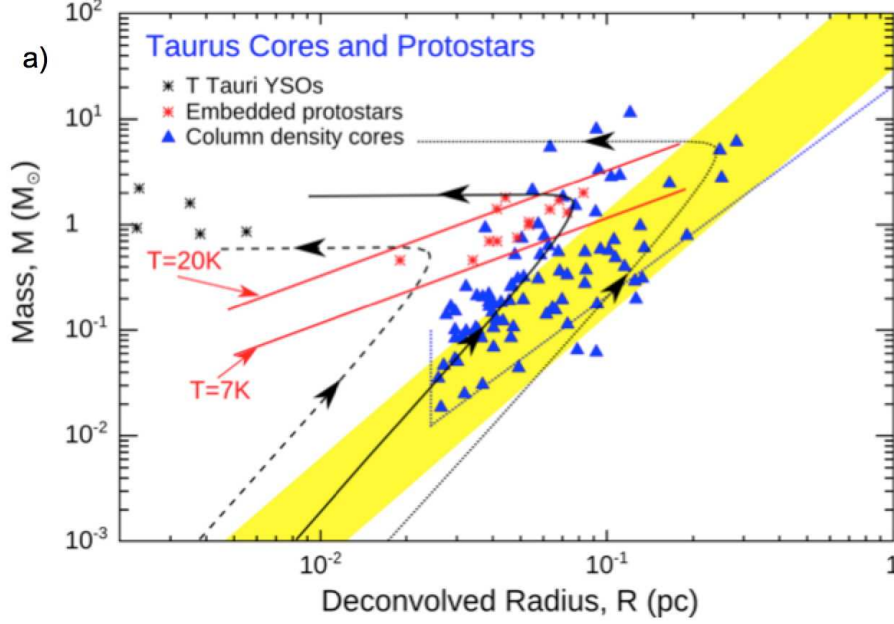
Figure 1.7: Mass-size diagram for cores and protostars in the Taurus molecular cloud (Kirk et al. 2013) with model evolutionary tracks from Simpson et al. (2011) overlaid, from André et al. (2014).

is the starless core lifetime and t_{embedded} is the lifetime of an embedded protostar, then

$$t_{\mathrm{starless}} \sim \frac{N_{\mathrm{starless}}}{N_{\mathrm{embedded}}} \times t_{\mathrm{embedded}}, \qquad (1.51)$$

where N_{starless} and N_{embedded} are the numbers of starless and embedded sources in the region, respectively. However, this relation assumes that all observed starless cores will eventually undergo gravitational collapse and evolve to become protostars. The assumption that the number ratio of two different source types is representative of the ratio of their lifetimes is valid only while the two types of source in question lie on a continuous evolutionary sequence. This is not a valid assumption if all starless cores do not evolve into protostars. However, this effect can be ameliorated by considering only those starless cores which are gravitationally bound (prestellar) when applying equation 1.51. Prestellar cores can be selected using a stability analysis (see Section 1.3, above), or, more approximately, by only considering cores with densities above a chosen threshold value to be likely to be gravitationally bound.

This method also implicitly assumes that all starless cores form a single population, and that a single characteristic lifetime can be determined. Observations of starless cores will, in a steady-state system, be biased towards observing longer-lived objects, as more longer-lived objects will be present at any given point in time at which the system is observed. Hence, inferred starless core lifetimes will be biased toward the lifetimes of the longest-lived objects, regardless of whether the longest-lived objects are likely to go on to form stars.

Estimates of starless core lifetimes vary from $\sim 10^5 - 10^7$ years with region (Jessop & Ward-Thompson 2000). The 'typical' lifetime of a starless core is typically considered to be $\sim 10^6$ years (Beichman et al. 1986; Lee & Myers 1999).

What fraction of its lifetime a starless core spends in the prestellar stage (i.e. undergoing gravitational collapse) is not certain. Lifetime estimates can be made from consideration of the infall rate in prestellar sources. Evidence for infall in a prestellar core or protostellar envelope can be found in blue-skewed asymmetry in optically thick emission lines from the source (Leung & Brown 1977; Walker et al. 1986). Tafalla et al. (1998) inferred an infall speed of up to $0.1\,\mathrm{km/s}$ in the prestellar core L1544, too high for the core to be undergoing ambipolar diffusion. Lee et al. (2001) surveyed 53 starless cores and identified 19 strong candidates for infall; they found that their cores had infall radii of $0.06 - 0.14\,\mathrm{pc}$ and one-dimensional infall speeds in the range $0.05 - 0.09\,\mathrm{km/s}$. A crude estimate of the lifetime can thus be made, assuming a constant infall rate:

$$t_{\mathrm{prestellar}} \sim \frac{R_{\mathrm{infall}}}{v_{\mathrm{infall}}}, \qquad (1.52)$$

suggesting a prestellar core lifetime $\sim 0.5 - 3 \times 10^6$ years.
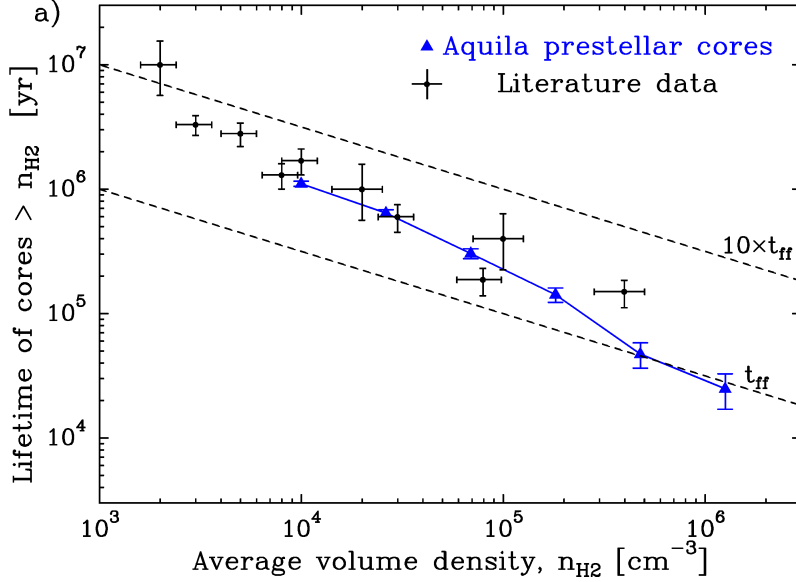
Figure 1.8: A 'JWT' plot, showing the relation between core volume density and lifetime, from André et al. (2014). The dashed lines show $1\times$ and $10\times$ the freefall time as a function of density.

1.5 The Initial Mass Function

A key constraint on any model of star formation is that it must be able to reproduce the distribution of zero-age main-sequence masses in a stellar population, known as the Initial Mass Function (IMF – Salpeter 1955). The functional form of the IMF is not absolutely determined. The two most commonly-used forms are the log-normal, or Chabrier, IMF (Chabrier 2003):

$$\Phi(M) \propto \begin{cases} \frac{1}{M}e^{-(\log M - \log 0.08)^2} & M/M_\odot < 1 \\ M^{-2.3\pm0.3} & M/M_\odot > 1 \end{cases} \tag{1.53}$$

or alternatively the broken power law, or Kroupa, IMF (Kroupa 2001):

$$\Phi(M) \propto \begin{cases} M^{-0.3\pm0.7} & 0.01 \le M/M_\odot < 0.08 \\ M^{-1.3\pm0.5} & 0.08 \le M/M_\odot < 0.50 \\ M^{-2.3\pm0.3} & 0.50 \le M/M_\odot < 1.0 \\ M^{-2.3\pm0.7} & 1.00 \le M/M_\odot \end{cases} \tag{1.54}$$

where $\Phi(M)dM$ is the number of single stars in the mass range M to $M + dM$.

28

A similarity between the high-mass IMF and the distribution of prestellar core masses was first shown by Motte et al. (1998). The distribution of prestellar core masses is known as the Core Mass Function (CMF). An IMF-like CMF – a power-law distribution at high masses, with a turnover at low masses – has been found in all nearby star-forming molecular clouds for which a CMF has been observed, including Ophiuchus (Motte et al. 1998; Johnstone et al. 2000; Enoch et al. 2007), Serpens (Testi & Sargent 1998; Enoch et al. 2007), Perseus (Enoch et al. 2007), Orion (Nutter & Ward-Thompson 2007), Aquila (Könyves et al. 2010), and the Pipe Nebula (Alves et al. 2007). The marked similarity between the CMF and IMF, shown for Aquila in Figure 1.9, suggests that the mass of a star, or a system of stars, is set at the prestellar core stage. The mass at which the CMF turns over is typically ~ 3 times that of the IMF, suggesting that, if there is a direct link between the CMF and the IMF, the process of conversion of a prestellar core into a main-sequence star is $\sim 33\%$ efficient (Offner et al. 2014).

Results from Herschel studies of nearby molecular clouds have shown that gas mass in molecular clouds which are not actively forming stars obeys a log-normal probability density function (PDF), e.g. the Polaris Flare – Ward-Thompson et al. (2010), whereas the PDFs of clouds in which significant numbers of stars are forming have both a log-normal low-mass PDF and a power-law tail at high masses (e.g. the Aquila Rift – Könyves et al. 2010; Könyves et al. 2015). André et al. (2010) interpret this result as meaning that turbulence-dominated, quiescent, molecular clouds will obey a log-normal mass distribution, while those clouds within which self-gravity becomes significant enough to allow stars to form will develop a high-mass power-law tail.

Whether the similarity between the CMF and the IMF is the result of a causal link between the two is still uncertain (see, e.g. Offner et al. 2014 for a recent review). Various theoretical models for the functional form of the CMF have been
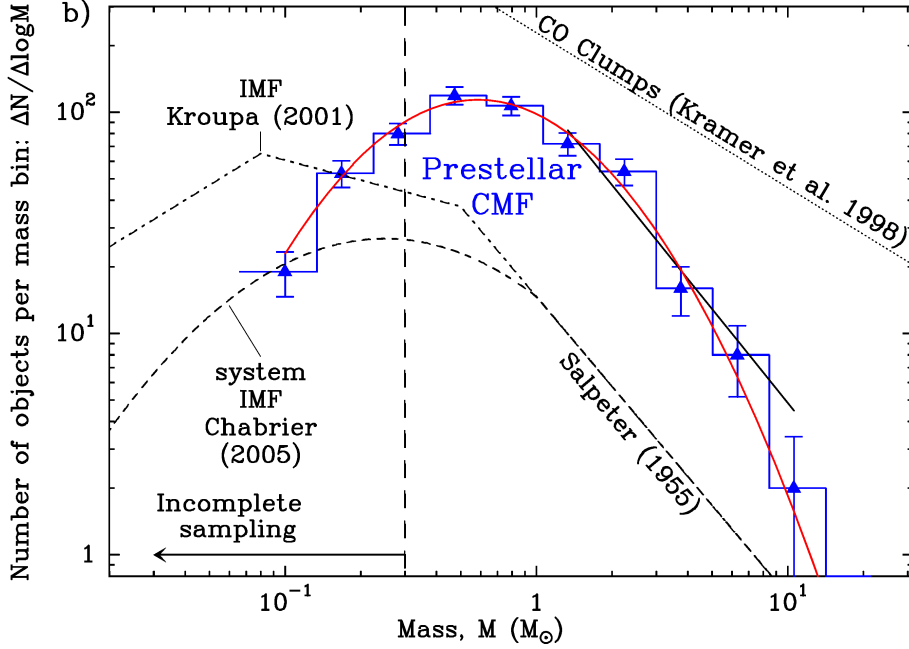
Figure 1.9: The core mass function for prestellar cores in the Aquila molecular cloud, from Könyves et al. (2010).

developed, typically showing the CMF to develop as a result of turbulence in the ISM. Turbulent motion is ubiquitous across almost all length scales in the ISM (see, e.g. Mac Low & Klessen 2004). Vazquez-Semadeni (1994) and Padoan et al. (1997) show that these turbulent motions will lead to a log-normal density distribution in molecular clouds, the width of which increases with the Mach number of the turbulence. The log-normally distributed probability density function (PDF) for density is given by

$$p(\ln x)\, \mathrm{d}\ln x = \frac{1}{\sqrt{2\pi\sigma^2}}\, \exp\left[-\frac{1}{2}\left(\frac{\ln x - \overline{\ln x}}{\sigma}\right)^2\right]\mathrm{d}\ln x, \qquad (1.55)$$

where p is the probability density function and x is the density contrast $\rho/\bar{\rho}$, and σ is the standard deviation of the distribution.

Power-law probability distributions have the functional form

$$p(x)\, \mathrm{d}x \propto x^{-\alpha}\, \mathrm{d}x \qquad (1.56)$$

where α is a constant, and $\alpha > 0$.

Turbulence is an inherently scale-free process (Kolmogorov 1941); the power-law behaviour of the CMF at high masses indicates a departure from turbulence-dominated behaviour and that self-gravity has become the dominant factor in determining the distribution of core masses. Accurately modelling the high-mass power-law slope is a key test of CMF models. Padoan et al. (1997) presented an early model of the CMF, in which they assumed an isothermal ISM which obeys a log-normal density PDF. By considering over-densities which exceed their local Jeans mass to be starless cores, they were able to reproduce the log-normal behaviour of the CMF, but could not accurately reproduce the power-law tail.

An important tool in recent theoretical models of the CMF has been the Press-Schechter formalism (Press & Schechter 1974). Originally developed for calculating the mass functions of dark matter haloes, the Press-Schechter formalism was first applied to the CMF by Inutsuka (2001). This method models the gas density of the ISM as a Gaussian random field, and uses the gas density PDF to evaluate the density of the ISM on all size scales. Thus, the fluctuations in density on each size scale can be compared to their local Jeans mass, and a mass function for gravitationally-bound turbulent over-densities can be constructed. Hennebelle & Chabrier (2008) used the Press-Schecter formalism to predict a CMF with a log-normal distribution at low masses, and a Salpeter power law at high masses, with the change in behaviour occuring at the mass at which the local Jeans mass is exceeded. This work has been extended by Hopkins (2012a) and Hopkins (2012b), who reconstructed the CMF from a rotationally-supported turbulent Galactic disc. In these studies, the largest scale on which objects within the disc are self-gravitating is referred to as the 'first crossing', and the smallest scale on which objects are self-gravitating is defined as the 'last crossing'. Hopkins (2012a) showed that the distribution of last-crossing structures matches the CMF, and can in some cases be reduced to the Hennebelle & Chabrier (2008) CMF model, while the mass spectrum,

Table 1.1: The observational classification criteria for protostellar sources

Class	IR Spectral Index	Bolometric Temperature (K)
0	$-$	$T_{bol} < 70$
I	$\alpha_{\mathrm{IR}} \geq 0.3$	$70 < T_{bol} < 650$
Flat	$-0.3 \leq \alpha_{\mathrm{IR}} < 0.3$	$350 < T_{bol} < 950$
II	$-1.6 \leq \alpha_{\mathrm{IR}} < -0.3$	$650 < T_{bol} < 2880$
III	$\alpha_{\mathrm{IR}} < -1.6$	$T_{bol} > 2880$

size-mass relations and linewidth-size relations of the first-crossing structures agree with those of molecular clouds.

1.6 Protostars

Once a prestellar core has collapsed to the point that a hydrostatic central object has formed, the object is considered to be a protostar. There is a well-defined set of evolutionary stages for low-mass ($< 8\,\mathrm{M_\odot}$) protostars as they evolve toward the main sequence: Class 0, Class I, Class II, and Class III, where Class 0 protostars are the least evolved and Class III are the most evolved. The Class I-III sequence was proposed by Lada (1987), and was extended by André et al. (1993) to include the Class 0 stage. Figure 1.10 shows the low-mass protostellar evolutionary sequence.

The evolutionary state of a protostellar object can determined using its infrared spectral index

$$\alpha_{\mathrm{IR}} = \frac{\mathrm{d}\log(\lambda F_\lambda)}{\mathrm{d}\log(\lambda)}, \tag{1.57}$$

where F_λ is the monochromatic flux density at wavelength λ.

The evolutionary state of a protostellar source can be inferred from its spectral index using the system proposed for Class I-III sources by Wilking et al. (1989), and extended to Class 0 (André et al. 1993; André 1994), and to sources with flat spectral indices, which lie between Class I and Class II (Greene et al. 1994). Alternatively, a source can be classified using its bolometric temperature, as calculated

for a blackbody distribution with the same mean frequency as the source's spectral energy distribution (Chen et al. 1995). The two methods of classification are shown in Table 1.6.

1.6.1 Class 0

While the mass of the central hydrostatic object (the protostar) is less than that of the surrounding envelope, the protostar is considered to be a Class 0 object (André et al. 1993). At this stage, material is being accreted very rapidly ($\sim 10^{-6} - 10^{-7}\,\mathrm{M_\odot}/\mathrm{yr}$; Pudritz et al. 1996) onto the central object, and the system has strong bipolar outflows. This is the main accretion phase of the protostar's evolution. Class 0 systems are relatively short-lived; Barsony (1994) estimated the Class 0 lifetime to be of the order 10^4 years based on protostellar masses and infall rates. More recent measurements based on the observed ratio of Class 0 to Class I sources have suggested a somewhat longer lifetime, of 1.5×10^5 years (Dunham et al. 2014, and references therein), but the Class 0 stage remains the briefest stage of protostellar evolution.

At this stage, the majority of the emission from the system is from the envelope surrounding the protostar, and the bolometric temperature of the system is less than 70 K. This means that Class 0 sources cannot be distinguished from Class I sources using their infrared spectral indices, as the majority of the envelope emission is at longer (submillimetre) wavelengths (e.g. Enoch et al. 2009). The original observational definition of a Class 0 protostar was an object whose submillimetre luminosity (at wavelengths $\lambda > 350\mathrm{\mu m}$) contributed greater than 0.5% to its total bolometric luminosity, i.e. $L_{\lambda>350\mathrm{\mu m}}/L_{bol} > 0.005$ (André et al. 1993).
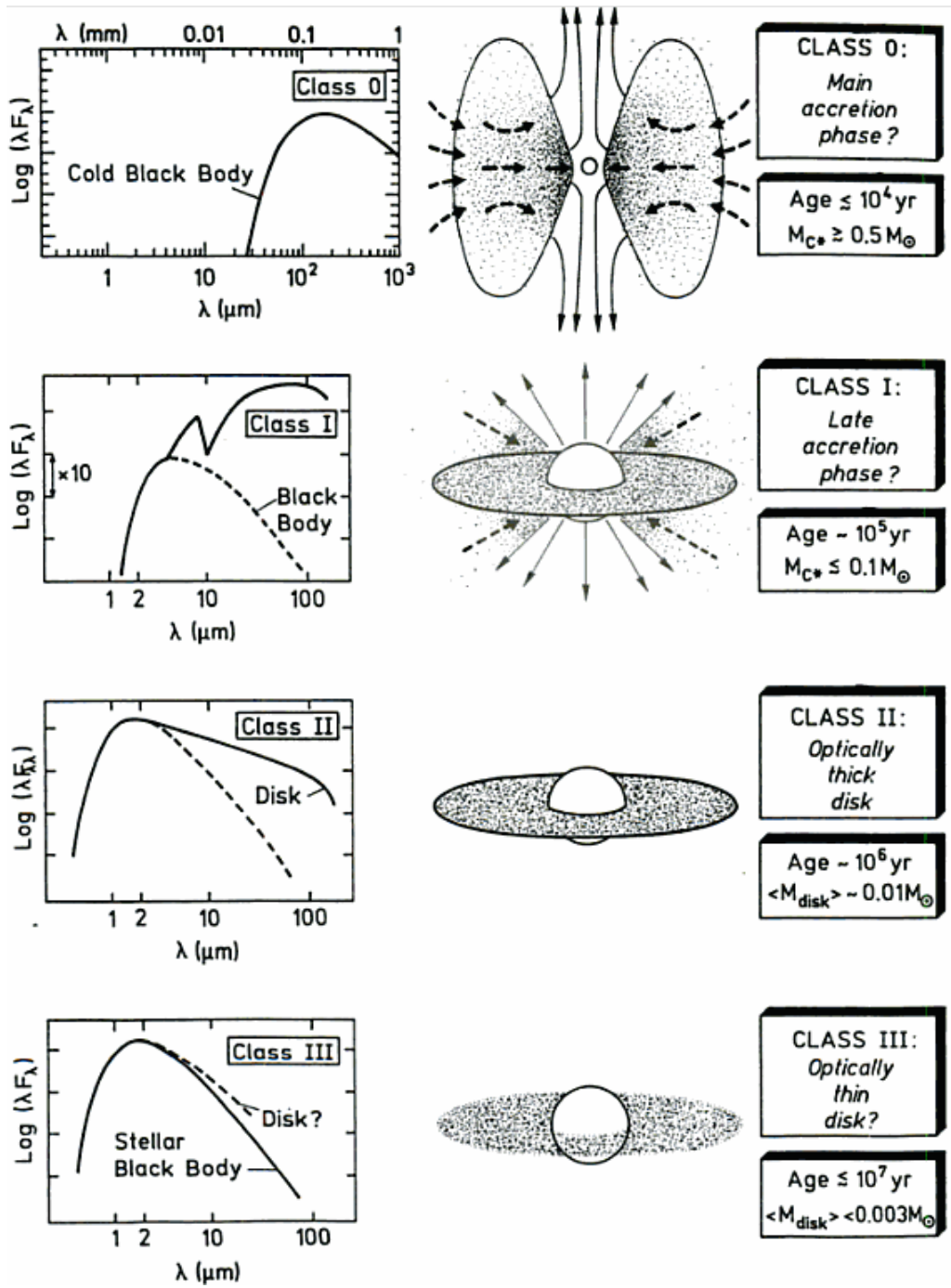
Figure 1.10: The low-mass protostellar evolutionary sequence, from André (1994).

1.6.2 Class I

This is the late accretion phase, in which the protostar is still acquiring a substantial fraction of its mass. The system is detectable in infrared emission, but the protostar is deeply embedded and the emission is still dominated by the envelope. A Class I source has a lifetime $\lesssim 5 \times 10^5$ years, determined from the observed ratio of Class I sources to T Tauri stars (Wilking et al. 1989; Dunham et al. 2014 and references therein).

A Class I source has an infrared spectral index $\alpha_{IR} \geq 0.3$. This indicates that the SED of a Class I sources rises longward of $2\mu m$, i.e. the source has a substantial infrared excess over a blackbody distribution. This infrared excess is from the envelope surrounding the protostar. The protostar itself is still deeply embedded in its envelope throughout the Class I stage.

1.6.3 Flat

A protostellar source with a flat spectral index has a spectrum intermediate between the embedded (Class 0 and I) and T Tauri (Class II and III) stages (Greene et al. 1994). An equivalent range in bolometric temperature, 350–950 K, was suggested by Evans et al. (2009). 'Flat' is not a distinct evolutionary stage, but an indication that the source is likely to be in the process of emerging from its envelope, and cannot be classified with certainty as either embedded or T Tauri.

1.6.4 Class II

A low-mass protostellar source in the Class II stage is otherwise known as a Classical T Tauri star (Joy 1945; Herbig 1962; Bastian et al. 1983). At this stage, the protostar has emerged from its envelope, and can for the first time be observed in visible light; it has reached its 'birthline' on the Hertzsprung-Russell Diagram (Hertzsprung 1911; Russell 1913; Stahler 1983). Formally, T Tauri stars are stellar objects associated

with regions of high A_V, with broad hydrogen Balmer lines ($\Delta\lambda(H_\alpha) > 5\,\text{Å}$) and calcium H and K lines appearing in emission in their spectra, and no supergiant or early-type photospheric absorption spectrum (Bastian et al. 1983) – i.e. T Tauri stars are low-mass late-type pre-main-sequence stars found in star-forming regions, with broad emission lines in their spectra. T Tauri stars have masses $< 3\,\text{M}_\odot$ (e.g. Appenzeller & Mundt 1989); their high-mass equivalents are Herbig Ae/Be stars (Herbig 1960).

T Tauri stars have not begun nuclear fusion; they radiate as they undergo Kelvin-Helmholtz contraction (Helmholtz 1854; Kelvin 1861). T Tauri stars have nearly fully convective interiors (Hayashi & Hoshi 1961). They appear on the Hertzsprung-Russell diagram as high-luminosity objects and follow Hayashi tracks (Hayashi 1961) toward the main sequence, contracting while maintaining a near-constant surface temperature, and hence decreasing significantly in luminosity. This continues until they either develop a radiative zone (and thus begin to evolve in radiative equilibrium; Henyey et al. 1955), or begin nuclear fusion. The lifetime of Class II protostars can be derived from the Kelvin-Helmholtz contraction timescale to be approximately 2×10^6 years (Stahler 1983).

There continues to be an excess in infrared emission from the star during this stage; this is from the optically thick protoplanetary disc surrounding the star. While the star may be accreting small amounts of material from the disc, the vast majority of its mass has already been acquired. The star has a bolometric temperature in the range $650 - 2880\,\text{K}$. A Class II object has a broader-than-blackbody energy distribution with flat or decreasing emission long-ward of 2μm (e.g. Wilking et al. 1989).

1.6.5 Class III

Class III objects, or Weak-Line T Tauri stars, are protostars which are approaching the main sequence. These stars have only a slight infrared excess, and this excess comes from the optically thin debris disc surrounding the star. These objects have bolometric temperatures $> 2880\,\mathrm{K}$. The name 'Weak-Line' T Tauri comes from the emission lines in a Class III star's spectrum, which are weaker than those seen in Class II spectra. This indicates lower levels of accretion from the debris disc than is occurring in earlier stages. Class III lifetimes, as derived from counting statistics, are found to be similar to Class II objects, on the order of 10^6 years (Wilking et al. 1989). A Class III object has an IR spectral index $\alpha \lesssim 2$: it can be modelled as a reddened blackbody (Wilking et al. 1989).

1.7 The Gould Belt

The Gould Belt is a ring of molecular clouds and OB associations $\sim 1\,\mathrm{kpc}$ in diameter and inclined at $\sim 20°$ to the Galactic Plane, centred on a position $\sim 200\,\mathrm{pc}$ from the Sun. The Gould Belt was originally observed in the Southern Hemisphere by Herschel (1847), who noted that the majority of the O and B type stars lie in a band inclined to the Galactic Plane. The Northern-Hemisphere portion of the Gould Belt was identified by Gould (1879). The approximate extent of the Gould Belt, as viewed from above the Galactic plane, is shown in Figure 1.11. The projection of the Gould Belt onto the plane of the sky is shown in Figure 1.12.

The stars of the Gould Belt have been shown to be kinematically distinct from other stars in the local solar neighbourhood, and to be expanding (e.g. Westin 1985; Lindblad et al. 1997). However, the stars of the Gould Belt do not appear to be expanding from a common centre. The OB stars of the Gould Belt have been linked both kinematically and in terms of their distance to nearby molecular

clouds (e.g. Dame et al. 1987), and to the Hɪ gas in which the molecular clouds are embedded (Lindblad et al. 1973). The presence of OB stars implies that there are also significant numbers of later-type stars present (see the discussion of the IMF in Section 1.5) – Guillout et al. (1998) found a late-type stellar population associated with the Gould Belt. The Gould Belt is relatively young, with an age $< 30 - 60\,\mathrm{Myr}$.

The mechanism by which the Gould Belt was formed is debated. The two proposed formation mechanisms are (1) an expanding shell, possibly caused by stellar winds and supernovae in the Cas-Tau fossil OB association (Blaauw 1956; Blaauw 1991) and (2) the impact of a high-velocity cloud on the Galactic disc (Comeron et al. 1992; Comeron & Torra 1992; Comeron & Torra 1994). Neither mechanism can be fully reconciled with the observed features of the Gould Belt. The expanding shell model cannot explain the tilt of the Gould Belt relative to the Galactic Plane; the lack of a common centre of expansion for the Belt; or the lack of pressure-driven asymmetry in the Taurus molecular cloud, which is located in the interior of the Gould Belt (see Figure 1.11). However, there is no observational evidence for any remnant of a high-velocity cloud – see Pöppel (2001) for a detailed discussion of the proposed formation mechanisms.

The location of the Taurus molecular cloud, inside the radius of expansion of the Gould Belt but kinematically associated with the other Belt clouds and of comparable age, is not well-understood. A possible mechanism by which the Taurus molecular cloud could have been ejected from the main Gould Belt $\sim 18\,\mathrm{Myr}$ after the Belt's formation was posited by Olano & Pöppel (1987).

The Gould Belt is considered a 'laboratory' for the study of low-mass star formation, as most of the low-mass star-forming regions within $500\,\mathrm{pc}$ of the Earth are associated with it. This has led to surveys aimed at mapping substantial fractions of the Gould Belt being undertaken using the JCMT (Ward-Thompson et al. 2007), the *Herschel* Space Observatory (André et al. 2010), and the *Spitzer* Space Telecope
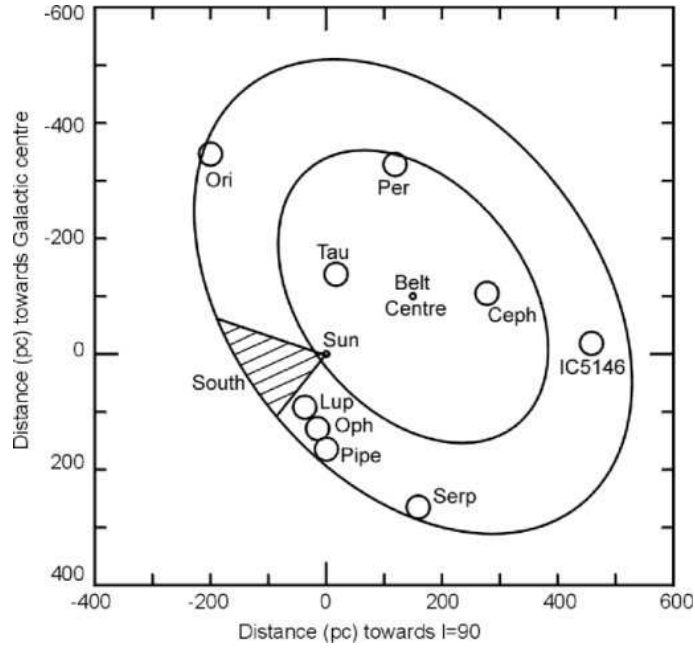
Figure 1.11: The Gould Belt, as viewed from above the Galactic Plane – from Ward-Thompson et al. (2007). The hatched region is not observable at the latitude of the JCMT.

(Evans et al. 2009).

1.7.1 JCMT Gould Belt Legacy Survey

The JCMT Gould Belt Legacy Survey (GBS; Ward-Thompson et al. 2007) was awarded approximately 500 hours of JCMT observing time, and aimed to map all of the well-known low- and intermediate-mass star-forming regions within 0.5 kpc of the Solar System accessible from the JCMT using SCUBA-2, HARP and the JCMT polarimeter, POL-2. The original aim of the SCUBA-2 survey was to map approximately $700 \, \text{deg}^2$ of the sky with SCUBA-2, split into two survey depths. A shallow survey, mapping areas with $A_V > 1$ to a depth of $1\sigma = 10 \, \text{mJy} \, \text{beam}^{-1}$ at 850μm, was intended to cover an area of approximately $400 \, \text{deg}^2$ within the Gould Belt and approximately $120 \, \text{deg}^2$ outside the main Gould Belt star-forming regions. A deep survey, mapping regions with $A_v > 3$ to a depth of $1\sigma = 3 \, \text{mJy} \, \text{beam}^{-1}$ at 850μm, was intended to cover a total area of approximately 64 deg^2.
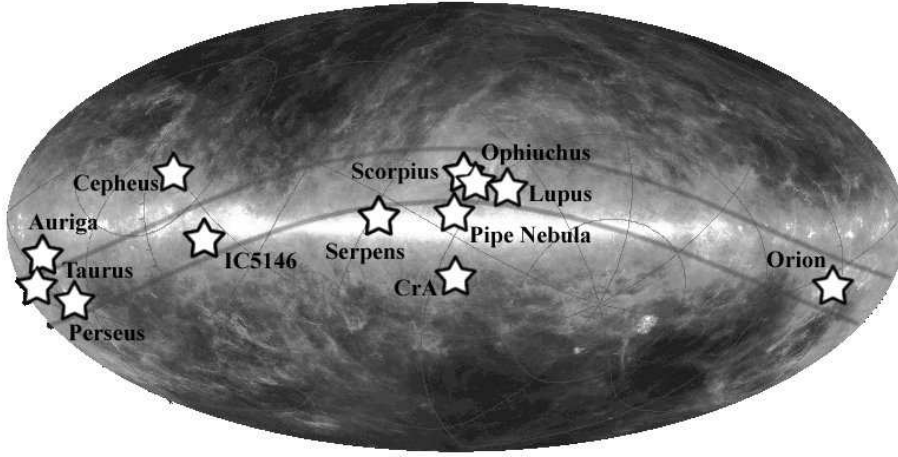
Figure 1.12: The Gould Belt, projected onto the Galactic Plane – from Ward-Thompson et al. (2007).

In 2011, subsequent to the announcement that the JCMT was not going to remain under UK/Canadian management, the survey was rescoped to a total of 412 hours of SCUBA-2 observing time. This resulted in the prioritisation of regions of high A_V. As yet, POL-2 has not been fully commissioned, and polarimetry observations have not been taken. Upon handover of the JCMT to the East Asian Observatory (EAO) in January 2015, the GBS came to an end, with near-total completion of the rescoped observations.

1.7.2 Herschel Gould Belt Survey

The Herschel Gould Belt Survey (HGBS; André et al. 2010) was designed to observe all of the densest regions of the Gould Belt at five wavelengths: 70μm, 160μm, 250μm, 350μm, and 500μm. To achieve this, the target regions were observed with the SPIRE and PACS cameras on the Herschel Space Observatory (discussed in Section 2.2). The survey goal was to map all of the $A_V > 3$ regions of the Gould Belt homogeneously with SPIRE and PACS simultaneously and, as this 'parallel mode' results in a non-diffraction-limited PACS beam (see Section 2.2), to map all of the $A_V > 6$ regions of the Gould Belt with PACS alone. Representative areas

with $A_V \sim 1 - 3$ were also to be observed with both instruments. The 'parallel mode' observations were completed before the telescope ran out of coolant in April 2013; the PACS-only observations were not completed.

1.8 Thesis Outline

Chapter 2 discusses the telescopes used to take the observations presented and used in this work. The data reduction processes for SCUBA-2 data and Herschel observations are described, as are the methods used to make data from SCUBA-2 and Herschel comparable.

Chapter 3 discusses the Ophiuchus molecular cloud. The SCUBA-2 Gould Belt Survey data of the region are presented. Sources are extracted from the SCUBA-2 850-µm data, and characterised using SCUBA-2 and Herschel data. The core masses derived from continuum measurements are compared to those derived from HARP $C^{18}O$ and IRAM N_2H^+ observations. A virial stability analysis is performed on those cores for which data are available. The virial stability of the cores is compared to their predicted stability according to the Bonnor-Ebert criterion. The variation of core properties and the effectiveness of dissipation of turbulence with region across Ophiuchus is discussed.

Chapter 4 discusses the Taurus molecular cloud. Sources are extracted from the SCUBA-2 850-µm data, Herschel 250-µm data, and Herschel 250-µm data filtered to match the spatial scales detectable with SCUBA-2. The sources are characterised using SCUBA-2 and Herschel data. The three sets of sources are compared, and the criteria distinguishing a core seen in Herschel data which is detectable with SCUBA-2 from those which are not are discussed. A virial analysis is performed on those SCUBA-2 cores for which data are available, and the energy balance in starless cores in Taurus is discussed.

Chapter 5 discusses the Cepheus Flare molecular clouds. Sources are extracted

from the SCUBA-2 850-μm data and characterised using flux densities measured from the 850-μm data and temperatures provided by the Herschel GBS. The number statistics of starless, embedded and Class II sources are discussed. The Bonnor-Ebert critically-stable masses and external pressures are estimated for each core. External pressures and the energy balance between gravity and external pressure are estimated using archive ^{13}CO data. An upper limit on the degree to which the cores in Cepheus are virially bound is determined.

Chapter 6 compares the Ophiuchus, Taurus and Cepheus Flare regions. An evolutionary model for initially pressure-confined starless cores is proposed and discussed. Chapter 7 summarises our conclusions.

1.9 Summary

In this chapter we have introduced prestellar cores as the densest and smallest length-scale objects in the interstellar medium. We discussed the properties of molecular clouds, and introduced the current paradigm of the star-formation process. We discussed the properties of starless cores: their masses, temperatures, external pressures, magnetic field strengths, and morphologies, and the dependence of the properties of molecular cores on their local environment. The stability of starless cores was discussed and the virial theorem was derived for a core in which gravitational potential energy, internal kinetic energy, internal magnetic energy, and energy due to external pressure contribute to the stability of the core. The Jeans and Bonnor-Ebert stability criteria were also discussed. We introduced the Initial Mass Function and Core Mass Function, and considered the possible causal link between the two. We discussed the low-mass protostellar evolutionary sequence. We described the Gould Belt of star-forming regions, and recent wide-area surveys intended to map a large fraction of its area. Finally, we outlined the structure and contents of this work.

Chapter 2

Instrumentation

2.1   The James Clerk Maxwell Telescope

The James Clerk Maxwell Telescope (hereafter, JCMT), located near the summit of Mauna Kea, Hawai'i, is an altitude-azimuth-mounted Cassegrain/Nasmyth telescope with a 15m parabolic primary antenna, and as such is the largest single-dish submillimetre observatory in the world. The telescope is shown in Figure 2.1. The JCMT is optimised to operate in the $\sim 350 - 1000\mu m$ wavelength range. The JCMT has a rotating tertiary mirror which allows the beam to be directed to a variety of instruments. There are currently four fully commissioned instruments operating at the JCMT: SCUBA-2, HARP-B, Receiver A and Receiver W. Data from two of these, SCUBA-2 and HARP-B, are used in this work.

The JCMT has historically been operated by the Joint Astronomy Centre in Hilo, Hawaii and funded by the UK, Canada and the Netherlands. In early 2015 telescope operations were taken over by the East Asian Observatory (EAO), a consortium of universities from Taiwan, China, Japan and South Korea. The UK and Canada remain partners in the JCMT.
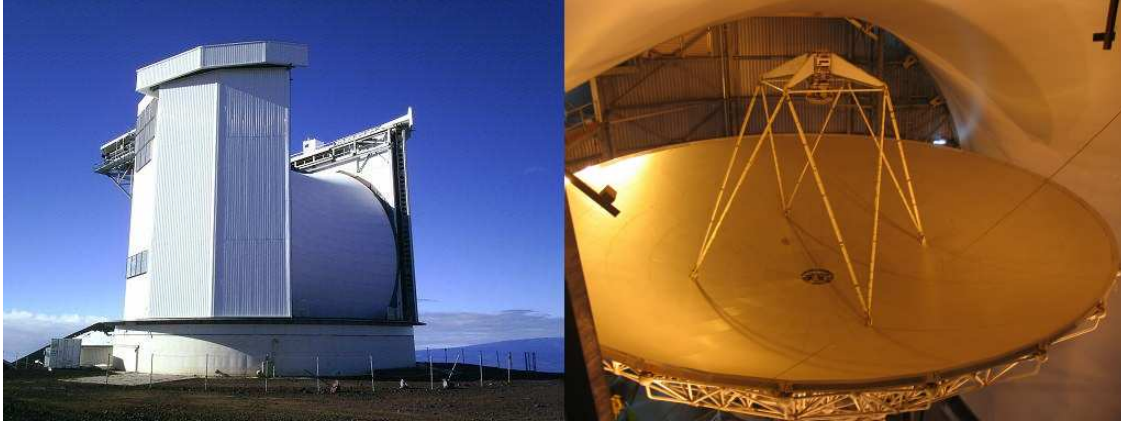
Figure 2.1: Exterior (left) and interior (right) views of the James Clerk Maxwell Telescope. Exterior view shows the Goretex shield protecting the telescope, and the rotating carosel on which the telescope is mounted. Interior view shows the telescope primary antenna and secondary mirror. Images from the East Asian Observatory.

2.1.1 SCUBA-2

The SCUBA-2 (Submillimetre Common-User Bolometer Array 2) instrument is a 10 000 pixel camera on the JCMT. SCUBA-2 observes in two wide wavelength bands, centred on 450μm and 850μm, at effective resolutions of 9.6″ and 14.1″ respectively (Holland et al. 2013). The two wavebands are observed simultaneously by means of a dichroic beam splitter. The key components of SCUBA-2, and their operating temperatures, are shown in Figure 2.2. Incoming light is directed into SCUBA-2 by the JCMT tertiary mirror. It is then passed through a series of thermal edge (TE) filters and low-pass (LP) frequency filters: a 5μm TE filter at room temperature; 10μm and 20μm TE filters; a 270μm (1.1 THz) LP filter at 50 K; a 30μm TE filter; and a 303μm (990 GHz) LP filter at 4 K. Finally, the light enters the 1 K box. The light is then passed through 345μm (870 GHz) and 310μm (967 GHz) LP filters, before being passed through the dichroic beam splitter. The transmitted portion of the light (with wavelength range 769−1000μm) is then passed through a 714μm (420 GHz) LP filter and an 850μm bandpass filter before reaching the 850μm focal plane of the camera. The reflected (400 − 526μm) portion of the light is passed through a
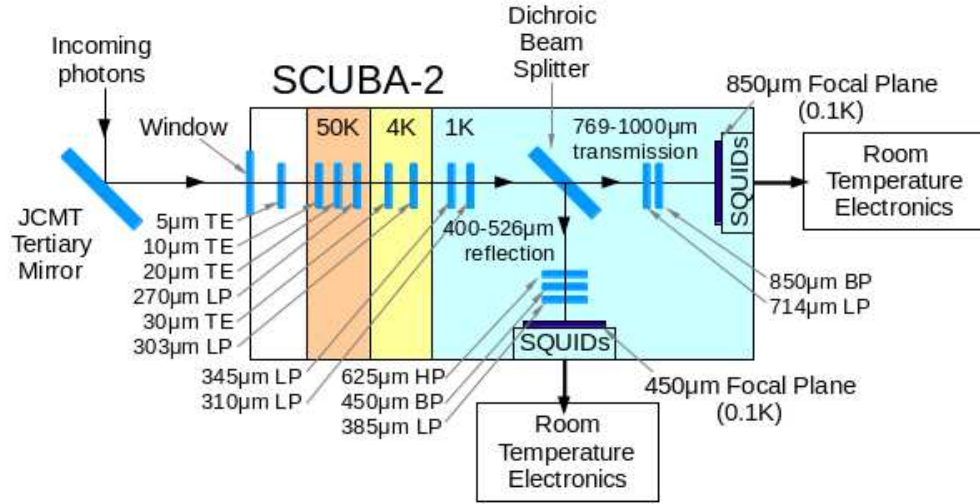
Figure 2.2: A schematic diagram of SCUBA-2, showing the operating temperatures of the principal components.

625µm (480 GHz) high-pass frequency filter, a 450µm bandpass filter and a 385µm (779 GHz) LP filter before reaching the 450µm focal plane. The focal planes have an operating temperature of approximately 0.1 K. The spectral responses of the SCUBA-2 450µm and 850µm cameras are shown in Figure 2.8, below.

2.1.1.1   Data acquisition

A SCUBA-2 focal plane unit is shown in Figure 2.3, and the focal plane bolometer arrays are shown in Figure 2.4. The focal planes at each wavelength are populated with four rectangular sub-arrays, each of which contains 40×32 bolometers. The total focal plane array footprint on the sky is approximately $600'' \times 600''$. Each bolometer is a thermal absorber coupled to a superconducting transition edge sensor (TES). A TES is a thin superconducting film kept at a temperature very near to its transition temperature. If raised above its transition temperature it ceases to be

45

ceramic PCB
(~100 mK)

sub-array
(~100 mK)

SQUID
series array
amplifiers
(~1 K)

cable interface to
room temperature
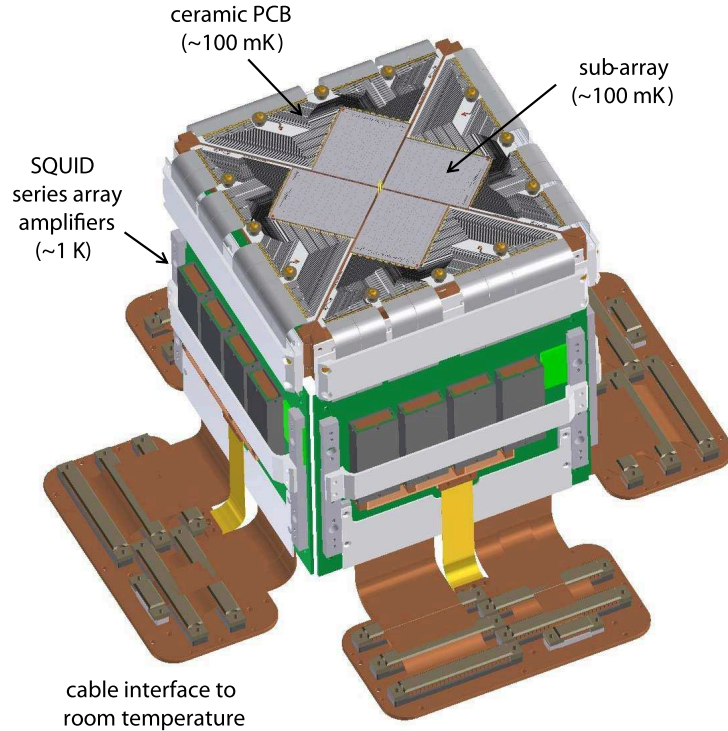
Figure 2.3: Layout of a SCUBA-2 focal plane unit (from Holland et al. 2013).

a superconductor, and hence its resistance increases substantially, and the current in the circuit decreases equivalently. The TES is connected in parallel with a fixed resistor and in series with an inductor; this inductor is inductively coupled to a superconducting quantum interference device (SQUID; a sensitive magnetometer which utilises the Josephson effect to produce a voltage proportional to an applied magnetic field). The changing magnetic field resulting from the change in current in the TES circuit is detected by the SQUID.

A fixed resistor and inductor are connected in parallel with the SQUID, and the circuit is inductively coupled to a further SQUID circuit, so that the changing voltage across the SQUID can be amplified. The initial magnetic field is amplified by a chain of 100 SQUIDs, creating an output current large enough to be digitised. Each bolometer has its own TES and SQUID; thereafter, each column of 32 bolometers has a common chain of SQUIDs. Figure 2.5 shows a simplified circuit diagram
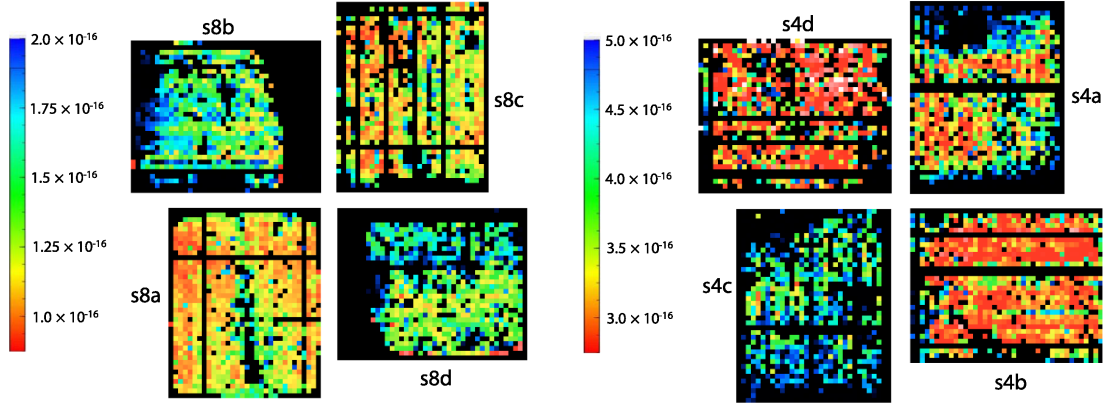
Figure 2.4: An extract from Figure 9 of Holland et al. 2013 showing the SCUBA-2 focal plane arrays, with each pixel representing one bolometer on the 850μm array (left) and 450μm array (right). The typical noise equivalent power (NEP; units of $Ws^{1/2}$) for each bolometer is shown. Note that each bolometer has a different NEP, which must be accounted for in the data reduction process (see below), and that each subarray has dead pixels.

indicating the layout of components within a subarray. The signal from each of the 40 rows is read in turn, at a frequency of 12 kHz, and then resampled to 200 Hz, i.e. a sample is taken every $3''$ at the maximum scanning speed of $600''/s$. This ensures that there are approximately 3 samples per 450μm diffraction-limited FWHM, and hence that the 450μm data is better than Nyquist-sampled.

Along with the 40 rows of detectors on each focal sub-array, there is an additional 41st row of SQUIDs which are not connected to TESs. These 'dark SQUIDs' measure and track non-thermal noise common to each of the sub-array's amplifier chains.

The conversion between input power and output current is determined by flat-field observations, taken immediately before each set of science observations. In a flat-field observation, the pixel heaters are ramped, and for these known input power values, the output current response is measured.

After being amplified, the signal is passed to room-temperature electronics known as Multi-Channel Electronics (MCE), before being passed to a data acquisition computer (one for each sub-array), along with information about the state of the

Figure 2.5: A simplified circuit diagram (after Holland et al. 2013), showing the configuration of components within each subarray of SCUBA-2. The area enclosed by the box shows the components associated with one pixel.

Table 2.1: SCUBA-2 beam properties, from Dempsey et al. (2013).

	450µm	850µm
FWHM Primary Beam (arcsec)	7.9	13.0
FWHM Secondary Beam (arcsec)	25	48
Primary Beam Amplitude	0.94	0.98
Secondary Beam Amplitude	0.06	0.02
Primary Beam Volume	0.6	0.75
Secondary Beam Volume	0.4	0.25
Beam FCF ($\mathrm{Jy\,pW^{-1}\,arcsec^{-1}}$)	4.71 ± 0.50	2.34 ± 0.08
Peak FCF ($\mathrm{Jy\,pW^{-1}}$)	491 ± 67	537 ± 26

instrument. From there, the data are archived, prior to reduction.

The output power must be corrected for atmospheric extinction. This is determined using the JCMT Water Vapour Monitor (WVM) to track opacity variation along the line of sight.

Finally, a flux conversion factor (FCF) must be applied to convert from power to astrophysical flux. Standard calibrators are regularly measured for this purpose. The primary calibrators for SCUBA-2 are Mars and Uranus, buth of which have a $\sim 5\%$ uncertainty in their model fluxes (Dempsey et al. 2013). There are a number of secondary calibrators, which are observed when the primary calibrators are not visible. The standard peak FCF values are 491 ± 67 Jy/pW at 450µm and 537 ± 26 Jy/pw at 850µm (Dempsey et al. 2013).

2.1.1.2 PONG observing mode

Observations made as part of the JCMT GBS used fully sampled circular regions. Other than some data taken as part of the Science Verification programme, observations were $30'$ in diameter. All observations were taken using the 'PONG' observing mode (Holland et al. 2013), in which the area of even coverage within the observation is maximised. This is done by defining the map as a square region and tracking the telescope across this region, 'bouncing' off the walls of the square as shown in Figure 2.6. Once the pattern is completed and the square has been covered, the
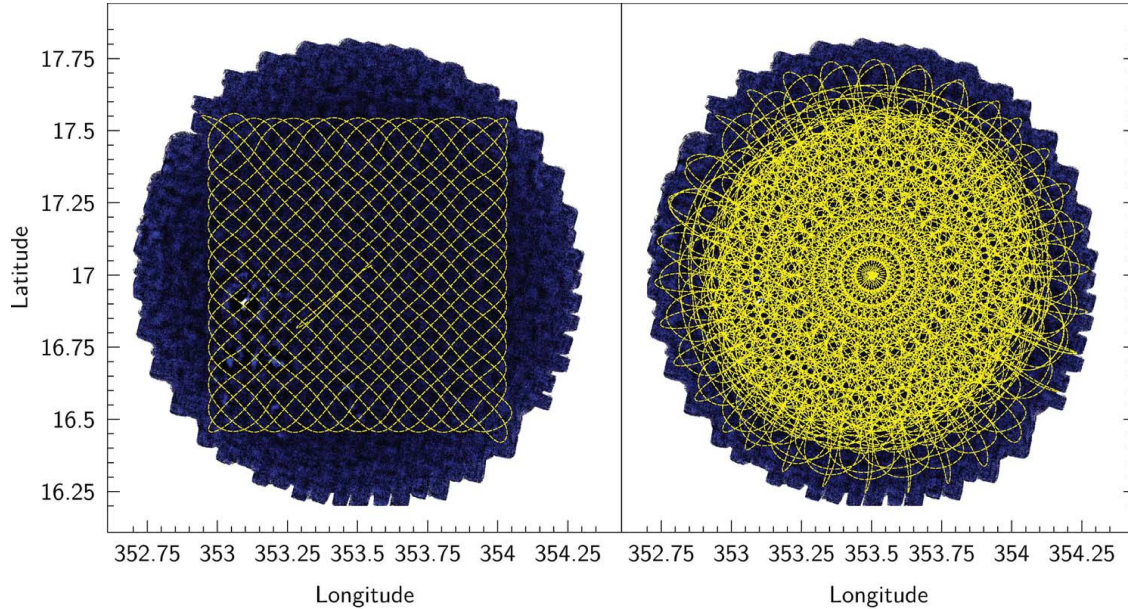
Figure 2.6: An extract from Figure 11 of Holland et al. (2013), showing the PONG observing mode on a 30 arcminute diameter field. The left-hand panel shows the telescope track for a single pong pattern; the right-hand panel shows the track for a full PONG1800 observation.

map is rotated and the pattern is repeated.

This observing mode allows large areas to be mapped, and permits the robust recovery of structure on scales up to the array size ($600''$). Figure 2.7 shows the region of even coverage of a PONG1800 observation (a $30'$-diameter region). Overlapping observations can be mosaiced in order to create continuous maps with large areas of even coverage. The PONG observating pattern is designed to modulate the sky signal as much as possible, both spatially (i.e. by scanning the same region at different position angles) and temporally (by scanning the same region at different speeds). This modulation is necessary in order to maximise the recovery of large-scale structure, due to the presence of slowly-varying signals, both spatially and temporally, in the data. These slowly-varying signals - atmospheric signal, variations in extinction, and instrumental $1/f$ noise - can be confused with astrophysical emission, hence the necessity for signal modulation. The methods by which the astrophysical signal is
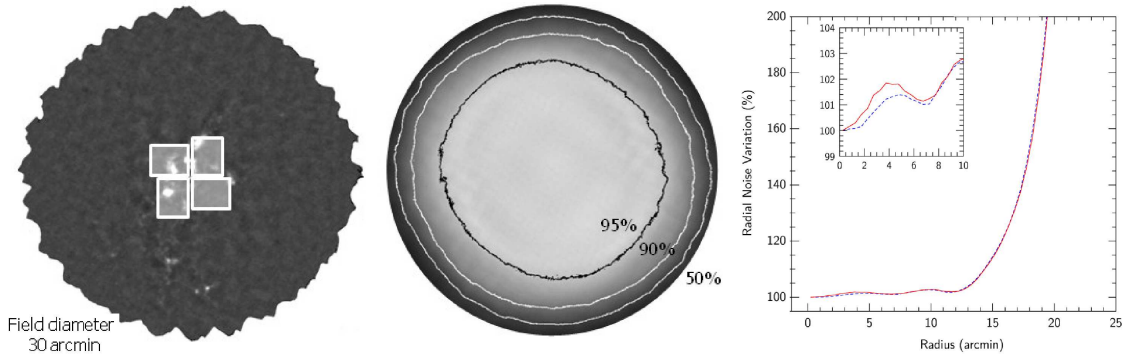
Figure 2.7: An extract from Figure 12 of Holland et al. (2013). The leftmost panel shows a 30 arcmin PONG observation, with the array size overlaid. The central panel shows the exposure time of the observations, with contours showing the radii of 95%, 90% and 50% of the peak value. The rightmost panel shows the percentage increase in RMS map noise as a function of radius.

distinguished from these other components are discussed in Section 2.1.2, below.

2.1.1.3 Weather bands

The JCMT measures weather quality in terms of the atmospheric opacity at 225 GHz, and categorises weather quality into five grades, with Grade 1 being the best observing conditions. The definitions of the different weather bands in terms of 225 GHz opacity (τ) and millimetres of precipitable water vapour along the telescope's line of sight (PWV) are listed in Table 2.2. All GBS data were taken in Grade 1 or Grade 2 weather. Grade 1 weather gives atmospheric transmission of better than 82% at 850μm and better than 28% at 450μm, and is necessary for observing faint structure at 450μm. Only key regions were observed in this weather grade. Grade 2 weather might typically give atmospheric transmissions of $\sim$ 77% at 850μm and $\sim$ 19% at 450μm; these transmission values allow high-quality 850μm observations, but only bright 450μm emission will be recoverable.

Typical atmospheric transmission on Mauna Kea at submillimetre wavelengths for 1mm of PWV is shown in Figure 2.8. The 450μm and 850μm bandpass filter
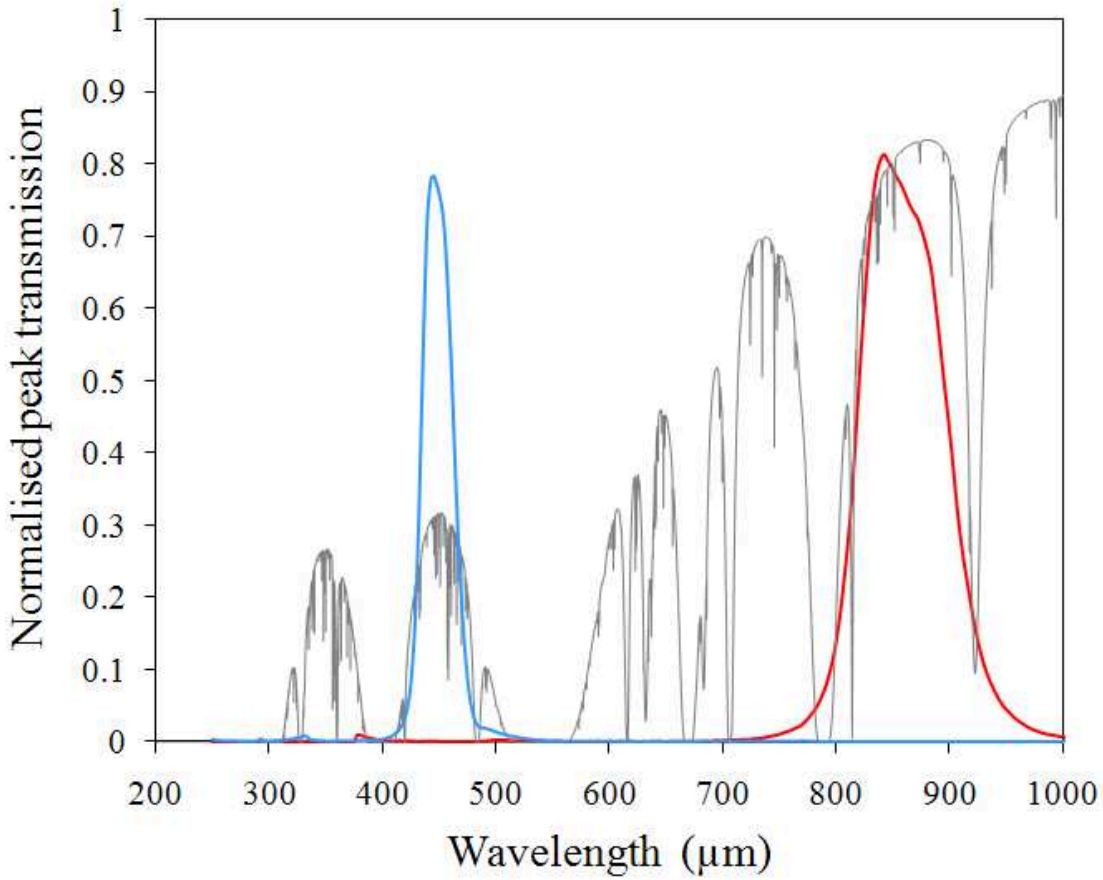
Figure 2.8: SCUBA-2 bandpass filter profiles at 450μm (blue) and 850μm (red), superimposed on the atmospheric transmission curve for Mauna Kea for 1mm of precipitable water vapour (Holland et al. 2013).

Table 2.2: JCMT weather bands

Grade	Definition	τ	PWV (mm)
1	Very dry	< 0.05	< 0.83
2	Dry	$0.05 - 0.08$	$0.83 - 1.58$
3	Medium	$0.08 - 0.12$	$1.58 - 2.58$
4	Wet	$0.12 - 0.2$	$2.58 - 4.58$
5	Very wet	> 0.2	> 4.58

profiles, shown on the same figure, are chosen to exploit the atmospheric transmission windows. Note that atmospheric transmission at 850µm is higher than that at 450µm.

2.1.2   SCUBA-2 Data Reduction

SCUBA-2 data reduction is performed using an iterative mapmaking routine, *makemap* in SMURF (Chapin et al. 2013). The data reduction process is described in detail by Chapin et al. (2013), and summarised here. An overview of the process is shown in Figure 2.9.

The first step in the mapmaking process is to read the data files into memory and concatenate them into a set of continuous time series for each subarray. A flat-field correction is then applied, determined by the closed-shutter instrument response measurements taken immediately prior to the observation (see above). The data are then down-sampled to match the requested pixel size in the final map. The data are then cleaned: noise spikes in the data are identified and removed, steps in the time series (likely the result of cosmic ray events) are corrected for, and any gaps in the time series are filled. Gaps are filled by interpolating between the start and end values of the gap, with Gaussian noise added to the interpolated values.

The total sky signal observed by SCUBA-2 is modelled as having four components: astrophysical signal (AST), atmospheric, or common-mode, signal (COM), low-frequency $1/f$ noise (FLT), and other noise (NOI). The astrophysical signal is recovered by iteratively modelling each of these components.

$$\text{Cleaned Value} = \text{COM} + \text{FLT} + \text{AST} + \text{Residuals} \qquad (2.1)$$

The degeneracy between these components makes it necessary to iteratively model each of these components, in order to minimise the residuals. The residual term consists of both uncorrelated white noise (NOI), which cannot be minimised,
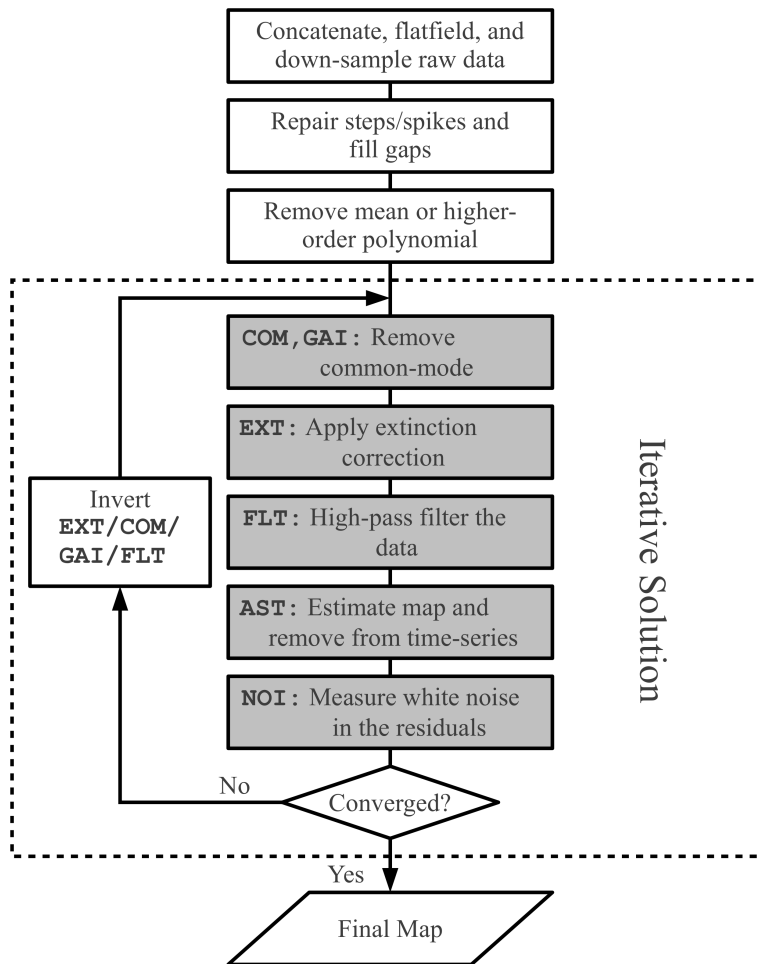
Figure 2.9: Data reduction process (Chapin et al. 2013).

and correlated components, which should in fact be assigned to the COM, AST or FLT models. The atmospheric (COM) signal is the mean of all bolometer values at each time-slice, on the assumption that there is no variation in signal from the atmosphere across the array footprint. The COM is then converted into a gain model (GAI), being weighted by the gain and zero-level offset for each bolometer. This GAI model is then subtracted from the cleaned data.

After the common-mode signal has been removed from the data, the extinction correction (EXT) is applied. This is a constant multiplicative scaling factor derived from the WVM, but is applied in each iteration after the COM model has been applied in order to avoid amplifying small errors.

The low-frequency noise (FLT) is estimated for each bolometer. This is done by Fourier transforming the time series data for each bolometer, applying a high-pass filter, and inverting the Fourier transform. This step removes residual $1/f$ noise remaining after the common-mode signal has been removed.

The signal map is then estimated, along with an associated variance map. The data are nearest-neighbour resampled onto a map grid: for each pixel, the brightness is estimated to be the weighted average of the good bolometer data samples that fall within that pixel. For the first iteration of the mapmaker, the weights of each bolometer data sample are set to 1; thereafter, the weights are given by the inverse variance expected from the bolometer white noise level.

For the ith pixel in the map, contributed to by bolometer data samples b_j with weights w_j, the brightness $M(x_i, y_i)$ is given by

$$M(x_i, y_i) = \frac{\sum_j w_j b_j}{\sum_j w_j} \tag{2.2}$$

and the variance $v(x_i, y_i)$ in the pixel is given by

$$v(x_i, y_i) = \frac{\sum_j w_j \sum_j w_j b_j - \left(\sum_j w_j b_j\right)^2}{N \left(\sum_j w_j\right)^2} \tag{2.3}$$

where N is the total number of bolometer samples that fall within the pixel.

The white noise (NOI) component is estimated from the residuals in the second iteration after the AST model has been subtracted from the time series data. The NOI model is then fixed, to prevent the weights of each bolometer diverging, and to allow a fixed reference against which to estimate the χ^2 value of the map.

This is the final stage in the iterative part of the mapmaking process. To begin the next iteration, the FLT, EXT and COM models are inverted, leaving the initial cleaned data with the current AST model subtracted. Unless the map convergence criterion has been met (discussed below), the iterative process then begins again with modelling of the common mode.

2.1.2.1 Convergence

After the ith iteration of the mapmaker, the signal map is given by

$$\text{Map}_i = (\text{Cleaned Data} - \text{AST}_{i-1}) - \text{COM}_i - \text{FLT}_i + \text{AST}_i \tag{2.4}$$

and the mean map change is given by

$$(\text{Mean Map Change})_i = \frac{1}{N_i} \sum_j \left| \frac{M_{j,i} - M_{j,i-1}}{\sqrt{v_{j,i}}} \right| \tag{2.5}$$

where $M_{j,i}$ is the map signal in the jth pixel enclosed by the mask (discussed below) after the ith iteration of the mapmaker, $\sigma_{j,i}$ is the standard deviation in this pixel, and N_i is the total number of pixels enclosed by the mask in iteration i. The mapmaking process is ended when the mean map change reaches a specified value; in the case of the GBS, this is 0.001, or a mean change of 0.1% across the map.

2.1.2.2 Masking

The degeneracy between AST, COM and FLT signal can, without some constraints placed on the mapmaker, lead to several defects in the output map. The degeneracy between AST and COM can lead to what is in fact common-mode signal being

assigned to the AST model. This causes the AST model to diverge, resulting in large 'blooms' of emission across the map. The FLT high-pass filtering applied to the time-stream data can also lead to ringing around bright sources, if they are not correctly assigned to the AST model.

The solution to these issues is to provide a 'mask' for the data: information as to whether or not any given pixel is expected to contain astrophysical signal. At the end of each iteration, all pixels in the map outside the masked region are set to zero, and the AST model is updated accordingly. This prevents small amounts of COM signal mistakenly assigned to the AST model in poorly constrained low signal-to-noise regions of the map from diverging in subsequent iterations. On the final iteration of the mapmaker, the pixels outside the mask are not set to zero.

In order to be able to define a mask without requiring *a priori* knowledge of the astrophysical signal, the GBS method for data reduction requires the data reduction process to be repeated. For the first reduction, an 'automask' is generated as a part of the mapmaking process. Here, the mask is determined iteratively, based on the signal-to-noise in the data. In each iteration, for each pixel, the signal-to-noise is taken to be

$$\text{Signal-to-Noise}(x_i, y_i) = \frac{M(x_i, y_i)}{\sqrt{v(x_i, y_i)}}. \tag{2.6}$$

Pixels with a signal-to-noise greater than 5 are included in the mask.

The map resulting from this process provides a good first approximation to the real astrophysical signal. However, the mask can be improved by using the repeat observations taken at each observing position. Once all the available data have been automask-reduced, the observations can be co-added and, if overlapping observing positions have been chosen, mosaiced. From this mosaic, a higher-quality signal-to-noise mask can be created. With this fixed 'external' mask (or 'extmask'), the data reduction process is repeated for each observation, now with a clear and consistent definition of the pixels which contain signal which may be assigned to the AST

57
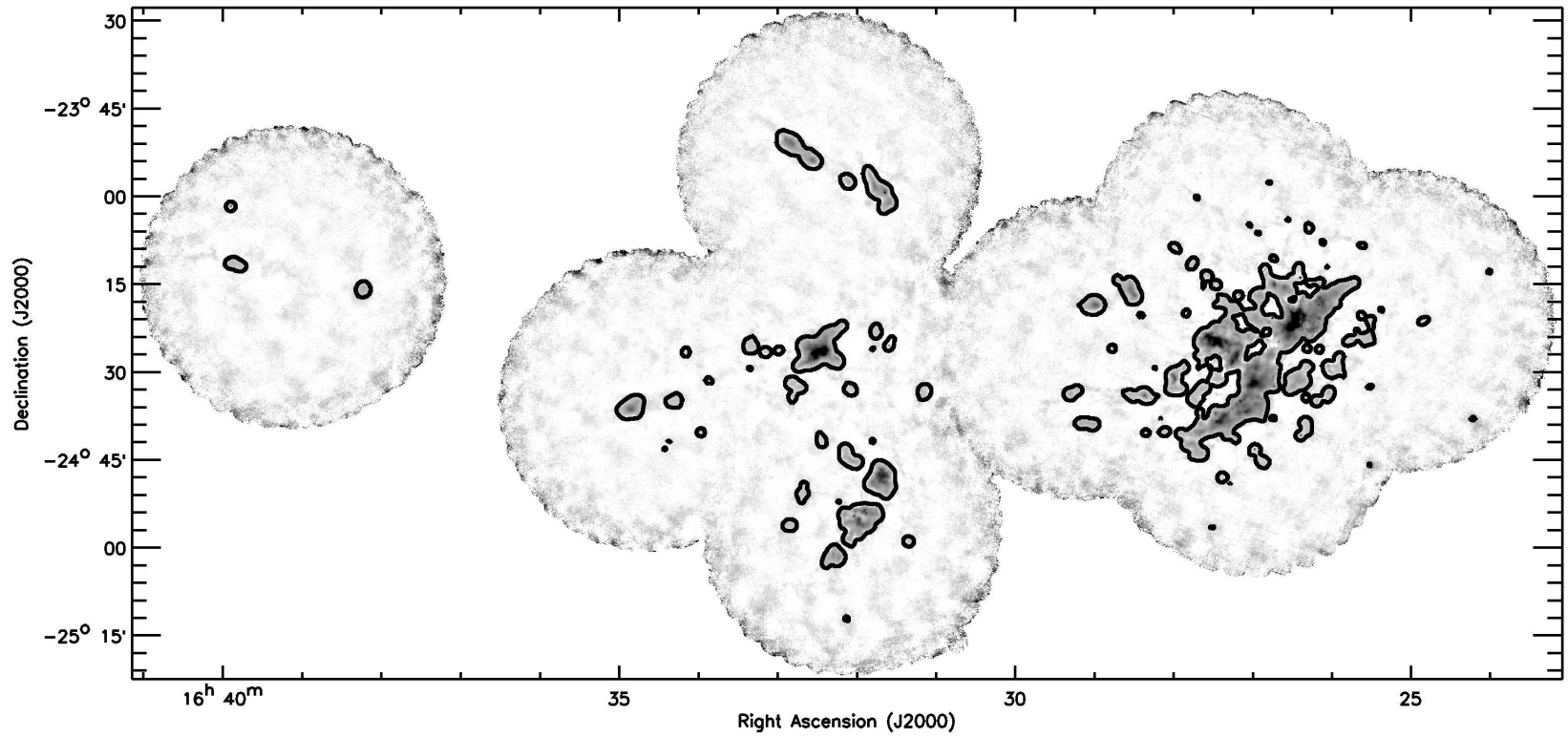
Figure 2.10: The black contour shows the edges of the IR1 mask for Ophiuchus, defining regions of significant emission.
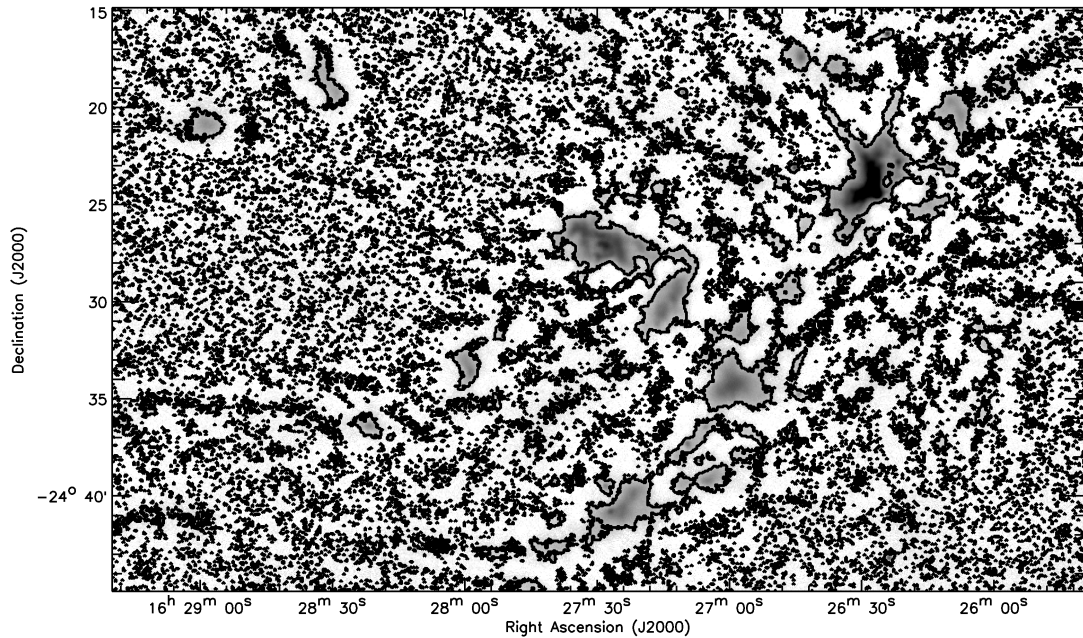
Figure 2.11: The black contour shows the edges of the IR2 mask for the L1688 region of Ophiuchus, defining regions of significant emission.

model.

   For the GBS Internal Release 1 data, the typical mask-making process was

1. Create a signal-to-noise map from the automask-reduced signal and variance maps.

2. Threshold the signal-to-noise map at a chosen value (typically 5, for IR1), setting everything above this value to 1 and everything below it to 0.

3. Smooth this mask with a Gaussian kernel, typically in the range FWHM= $5 - 10$ pixels.

4. Threshold the mask again at a chosen value, typically 0.05, setting everything above this value to 1 and everything below it to zero.

5. Inspect the mask, manually removing any masked regions that are the result of noise spikes (typically, these are found around the map edges).

As part of the testing for the Internal Release 2 reduction, it was found that smoothing the mask could in some fields produce defects in the map where in regions of lower signal-to-noise, included in the mask due to the smoothing, spurious AST signal was allowed to grow. For the IR2 reduction, typically only the first and second steps of the above process were applied, with a signal-to-noise cut of zero being used.

The external mask used in the IR1 reduction of the SCUBA-2 Ophiuchus data is shown in Figure 2.10. A subsection of the mask used in the IR2 reduction of the same data, for the subregion L1688, is shown in Figure 2.11.

The data used in Chapters 3 and 4 of this work – observations of the Ophiuchus (Chapter 3) and Taurus (Chapter 4) molecular clouds – were reduced using the IR1 method. The data used in Chapter 5 – observations of the Cepheus region – were reduced using the IR2 method. This situation arose for historical reasons, since the first two data sets were published before IR2 was available.

2.1.3   HARP-B and ACSIS

HARP-B (Heterodyne Array Receiver Program for the B-Band) is a 4×4 element heterodyne focal plane array receiver, sensitive in the range 325–375 GHz (~ 800–925 µm), with an angular resolution of $14''$ at 345 GHz, or 879µm (Buckle et al. 2009). Its backend is the Auto-Correlation Spectral Imaging System, ACSIS. The spectral range of HARP-B is shown in Figure 2.12, along with astrophysically important observable transitions.

The 16 HARP-B detectors are arranged in a 4×4 grid with a spacing of $30''$ between the detectors, resulting in an undersampled field of view of $104''\times104''$ at 345 GHz. In order to produce fully-sampled maps of large areas, a scanning (also known as on-the-fly mapping or rastering) observing mode is used, in which the telescope is moved steadily across the target field, with data being integrated continuously. The HARP-B array is rotated $14.48°$ relative to the scan direction,
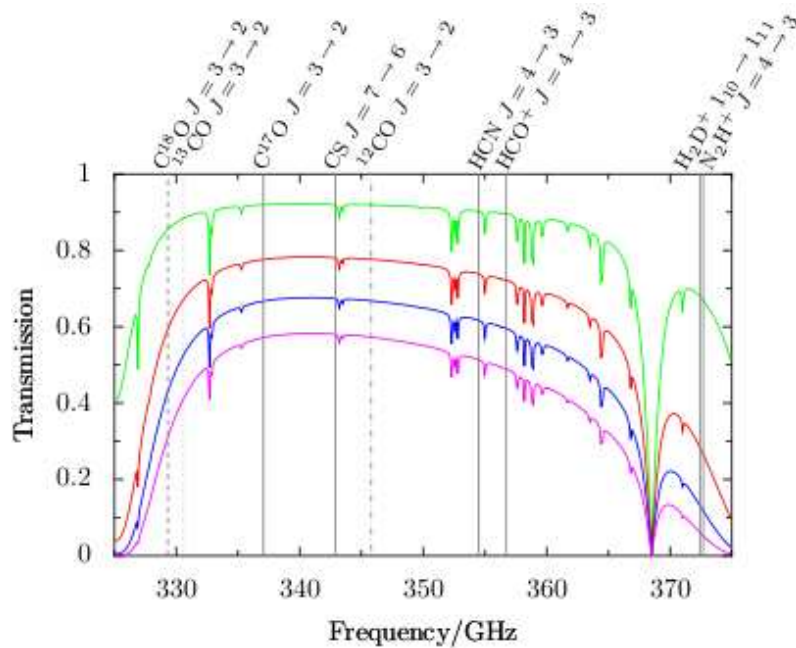
Figure 2.12: Atmospheric transmission in JCMT weather bands 1-4 across the HARP-B observing range (325–375 GHz; 800–925 μm), with frequently-observed transition frequencies marked (Buckle et al. 2009).

resulting in a sample spacing of 7.3″ perpendicular to the scan direction. The array and scan pattern are shown in Figure 2.13.

HARP-B covers the whole target field as rapidly as possible in order to minimise the effect of variations in sky transmission, pointing changes and calibration drifts. Each observation is repeated multiple times, and the resulting maps are co-added to increase the signal-to-noise ratio. Co-adding several rapidly-observed maps reduces calibration uncertainties across the final map. At the end of every one or every few rows in an observation, the telescope is 'nodded' to a specified off-source reference position, at which an off-source signal is observed simultaneously for each pixel. Using these off-source observations, most instrumental and atmospheric effects can be removed from the data. HARP-B operates as a single-sideband instrument; the unwanted frequency range is filtered (attenuated by a factor of $10 - 50$) before the signal reaches the mixer. This is done in order to decrease system temperatures and to increase calibration accuracy.
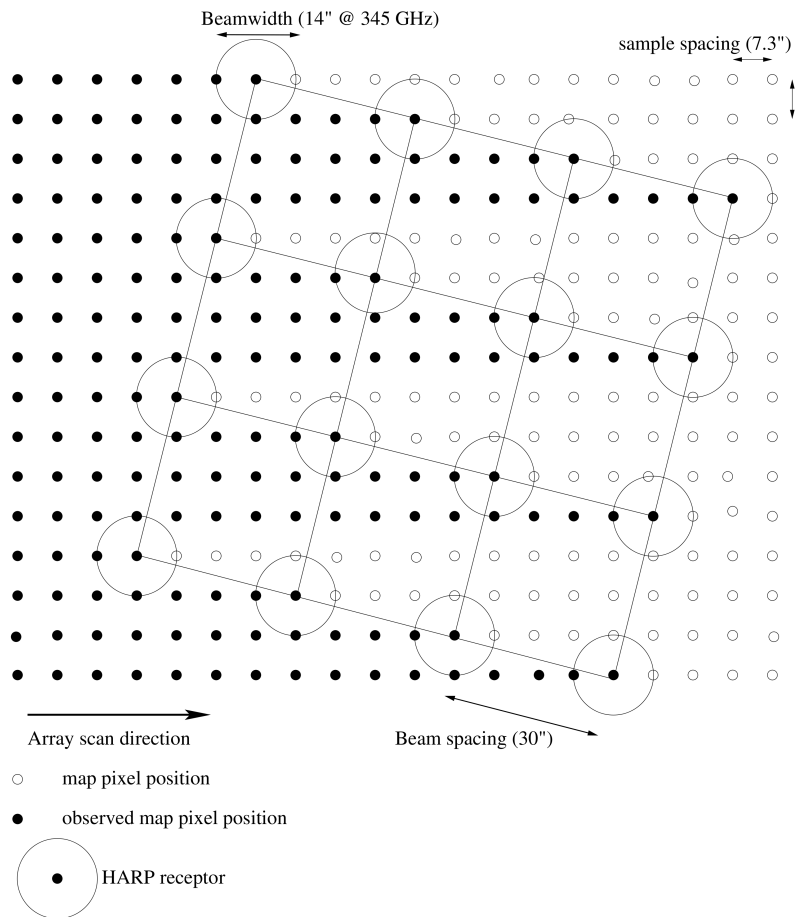
Figure 2.13: HARP-B scanning observing mode, demonstrating how fully sampled coverage is achieved using an undersampled array (from Buckle et al. 2009).

In order to mitigate noise variations due to missing detectors or variations in detector performance, two independent maps can be made of a field, with the telescope scanning in orthogonal directions. These maps are then co-added. This technique, used in GBS HARP-B observations, is known as basket-weaving.

ACSIS allows either wide-band or high-resolution spectra to be observed, and also allows the frequency range to be split into sub-bands. HARP-B has 16 outputs while ACSIS has 32 inputs: this allows two transitions with similar frequencies to be observed simultaneously (e.g. the ^{13}CO J= $3 \rightarrow 2$ and C^{18}O J= $3 \rightarrow 2$ transitions), or for a transition to be simultaneously observed in both wide-band and high-resolution modes.

HARP-B data are reduced using Starlink project software. The data reduction process is described in detail by Curtis et al. (2010). Starlink KAPPA routines (Currie et al. 2008) are used to mask poorly performing detectors. The data cube is made using the SMURF routine *makecube* (Jenness et al. 2008). It is necessary to perform a 'self-flat' or 'de-striping' of the data, where systematic calibration differences between HARP-B detectors are eliminated – described in detail by Curtis et al. (2010). Finally, KAPPA routines are used to remove linear baselines from the cube and to crop the map edges.

HARP-B CO data are calibrated relative to the sources IRC+10216, CRL2688 and CRL618. Buckle et al. (2009) estimate a calibration accuracy for HARP-B of $\sim 20\%$.

2.1.4 Carbon Monoxide Contamination of SCUBA-2 Data

SCUBA-2 850-μm data may be substantially contaminated by the CO J= $3 \rightarrow 2$ transition (Drabek et al. 2012) which, with a rest wavelength of 867.6 μm, is covered by the SCUBA-2 850-μm filter – half-power bandwith 85μm (Holland et al. 2013). The SCUBA-2 850-μm filter is a broad-band filter, intended to measure continuum

emission (see Figure 2.8). However, the CO J$=3\rightarrow2$ transition is excited in the low-to-medium-density material in molecular clouds (Bolatto et al. 2013, and references therein), and hence can contribute a significant fraction of the measured emission in the 850-μm band in SCUBA-2 observations of molecular clouds. Drabek et al. (2012) estimate that the contribution to the measured 850-μm continuum emission from CO is generally $\leq20\%$ in GBS SCUBA-2 850-μm observations, but can reach $\sim80\%$ in outflow-dominated regions.

Where SCUBA-2 and HARP-B CO data exist for the same observing position, CO contamination can be corrected for by re-reducing each of the 850-μm observations with the integrated ^{12}CO data added to the SCUBA-2 bolometer time series as a negative signal.

2.2   The Herschel Space Observatory

The Herschel Space Observatory (hereafter, Herschel) was a space observatory with a 3.5m diameter Cassegrain telescope, which orbited the second Sun-Earth Lagrangian point (Pilbratt et al. 2010). The telescope, a European Space Agency (ESA) mission with contributions from the National Aeronautics and Space Administration (NASA), was launched in May 2009 and ceased operations upon running out of helium coolant in April 2013. Herschel is shown in Figure 2.14.

Herschel carried three instruments: SPIRE (Spectral and Photometric Imaging REceiver – Griffin et al. 2010); PACS (Photodetector Array Camera and Spectrometer – Poglitsch et al. 2010) and HIFI (Heterodyne Instrument for the Far Infrared – de Graauw et al. 2010). Data taken using SPIRE and PACS are used in this work. SPIRE consisted of a photometer operating simultaneously at 250μm, 350μm and 500μm at resolutions of 18″, 25″ and 36″ respectively, and a Fourier-transform spectrometer covering the range 194–671μm (Griffin et al. 2010). PACS consisted of a photometer which could observe at 160μm and either 70μm or 100μm
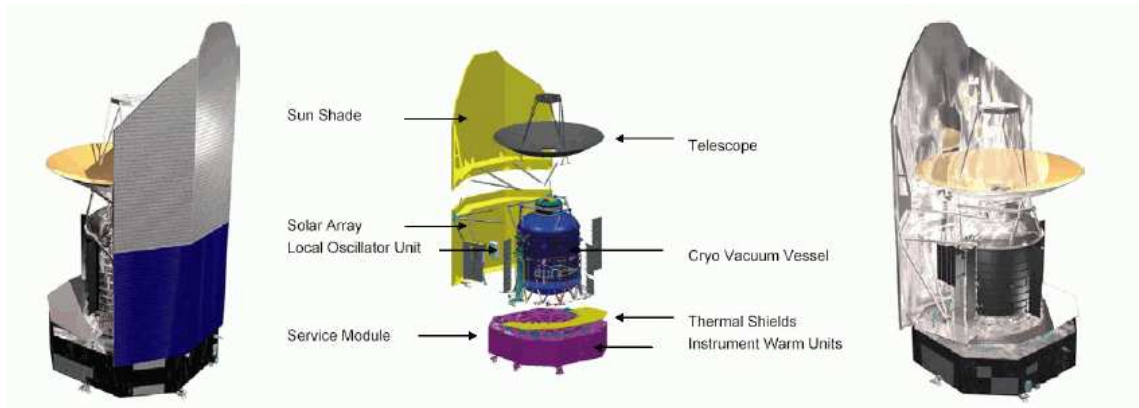
Figure 2.14: Components of the Herschel Space Observatory. Left: warm side of the telescope. Heat shield shown in grey; solar panels shown in blue. Centre: exploded diagram showing principal components of the spacecraft. The SPIRE, PACS and HIFI instruments are housed within the Cryo Vacuum Vessel. Right: cool side of the telescope, assembled (Herschel Observers' Manual 2014).

Table 2.3: Herschel beam properties. PACS beam sizes are given for a telescope scanning speed of $60'' \, \mathrm{s}^{-1}$. SPIRE effective beam areas are for conversion between 'per-beam' units and surface brightness units.

	PACS		SPIRE		
	70μm	160μm	250μm	350μm	500μm
Primary Beam FWHM (arcsec)	5.8×12.1	11.6×15.4	18.1	25.2	36.6
Effective Beam Area (sq. arcsec)	–	–	447	816	1711
Detectors	64×32	32×16	139	88	43

simultaneously, and a spectrometer covering 55–210μm (Poglitsch et al. 2010). The Herschel Gould Belt Survey (HGBS) used the SPIRE and PACS photometers in 'parallel mode', mapping all three SPIRE bands and the PACS 70μm and 160μm bands simultaneously, although the fast scanning speed ($60''$/s) prevented the PACS data from being taken at optimal resolution, and resulted in a substantially elliptical PACS beam: $5.8'' \times 12.1''$ and $11.6'' \times 15.4''$ at 70μm and 160μm respectively (Poglitsch et al. 2010).

Parallel mode observations were taken in a scanning observing mode (referred

to as scan-map mode in Herschel documentation). Each field was mapped twice, with orthogonal scan directions. The two scans were reduced separately, and then co-added. This procedure was used in order to minimise the effect of $1/f$ noise, which will introduce a slowly-varying component into the detector time series, on the output map (see e.g., the SPIRE Data Reduction Guide 2014).

Herschel data are typically reduced using the Herschel Interactive Processing Environment (HIPE; Ott 2010). Different methods are applied for the reduction of SPIRE and PACS data.

2.2.1 SPIRE Data Reduction

The data reduction process for SPIRE is described in detail in the SPIRE Data Reduction Guide (2014), and summarised here. SPIRE data are processed to one of a number of levels:

Level 0 Raw time series data

Level 0.5 Time series data calibrated in physical units

Level 1 Processed time series data calibrated in $\mathrm{Jy\,beam^{-1}}$

Level 2 Flux calibrated maps for signal, error and coverage

The first step in the reduction process is to convert Level 0 (raw) data into physical units (Level 0.5 data). In order to process the data to Level 1, corrections are then applied to the time series: correcting for interference between detector components; accounting for bolometer drifts and temperature jumps; identifying and removing glitches caused by cosmic rays; correcting for low-pass filtering of the data; converting the data into astrophysical units; and finding and correcting 'cooler burps' (SPIRE recycled coolant on approximately a 2-day cycle; a cooler burp is a steep temperature rise which reaches a plateau 6 or 7 hours after the end of such a cycle).

Pointing angles on the sky are determined for the detector time-lines. For regions dominated by extended emission, such as those in this work, an extended emission gain factor must be applied to each bolometer time series. These gain factors represent the ratio of the response of each bolometer to extended emission and the average response.

Taking the data from Level 1 to Level 2 is the 'mapmaking' step. The default mapmaking mode for SPIRE, known as 'naïve' mapmaking, is to project the full power seen by each detector into the nearest map pixel. Signal, signal squared and coverage maps are created. For each bolometer series at each time step in the observation, the signal measurement is added to the signal map, the signal measurement squared is added to the signal squared map, and 1 is added to the coverage map. The signal map is then divided by the coverage map, in order to return a flux density map (a mean signal map). The signal squared, signal, flux density and coverage maps are used to create a variance map, the square root of which is the error map. While this process can be performed in a non-iterative manner, it is generally necessary to iteratively 'destripe' SPIRE data. This process removes zero-level offsets in the bolometer time series by creating an average 'map' time series from the Level 2 signal map, determining the differences between this timeline and each individual bolometer time series, subtracting these offsets, and repeating the process until convergence between the map time series and each of the bolometer time series is reached. The destriping convergence parameter χ^2 is given, for the ith iteration of the destriper, by

$$\chi_i^2 = \sum_j \left([\text{Map Timeline}]_i - [\text{Input Signal Timeline}]_j + [\text{Offset}]_{i,j}\right)^2 \qquad (2.7)$$

where $[\text{Map Timeline}]_i$ is the average map time-line for iteration i, $[\text{Input Signal Timeline}]_j$ is the input bolometer time series for the jth bolometer, and $[\text{Offset}]_{i,j}$ is the zero-level offset determined between the ith average map time-line and the jth bolometer time series. Note that this is not the usual definition of the χ^2 parameter, but we use

this notation to be consistent with Herschel documentation. Convergence is deemed to be reached when the difference between χ^2 values in two successive iterations is less than a specified value. The standard condition for destriper convergence is

$$|\chi_i^2 - \chi_{i-1}^2| < 1 \times 10^{-10}. \tag{2.8}$$

The destriping process is described in detail in the SPIRE Data Reduction Guide (2014).

SPIRE data are by default mapped onto $6''$, $10''$ and $14''$ pixels at $250\mu\text{m}$, $350\mu\text{m}$ and $500\mu\text{m}$ respectively, and are calibrated in units of Jy beam^{-1}. The maps can be converted into surface brightness units using the effective beam areas listed in Table 2.3.

2.2.2 PACS Data Reduction

The data reduction process for PACS is structured similarly to the process for SPIRE, and is described in detail in the PACS Data Reduction Guide: Photometry (2014). In processing PACS data from Level 0.5 to Level 1, corrections include calibration into astrophysical units; masking bad and saturated pixels; a flat field correction; a non-linearity correction, as PACS bolometers display a non-linear response for flux densities greater than 100 mJy/beam in all bands; and removal of glitches caused by cosmic rays.

Processing Level 1 time series data into a map can be performed in HIPE. However, HGBS PACS mapmaking is performed using the *Scanamorphos* map-maker (Roussel 2013), written in the Interactive Data Language (IDL). This algorithm uses the multiple detections of each observing position (both within one scan, and in the orthogonal repeat observation) to model and subtract thermal and non-thermal low-frequency drifts in the bolometer time series (assuming a constant underlying source signal, similar to the AST model in SCUBA-2 data reduction). Scanamorphos additionally detects and masks glitches and brightness discontinuities, before

making a map projection where, as with SPIRE data reduction, the full power of each detector is projected into the nearest map pixel.

PACS data are by default calibrated in units of $\mathrm{Jy\,pixel^{-1}}$, and are mapped onto $3''$ pixels.

2.2.3   Absolute Calibration of Herschel Data

SPIRE and PACS detectors are sensitive to relative variations in signal, and so the absolute calibration of the Herschel maps is determined by comparison to the all-sky maps produced by the Planck satellite (Planck Collaboration 2011). The maps used to calculate the Herschel calibrations are those taken by the Planck High Frequency Instrument (Planck-HFI; Planck HFI Core Team 2011). Planck-HFI is itself calibrated relative to the sky brightness measured by COBE-FIRAS at the Galactic poles (Planck Collaboration 2014, and references therein).

Planck-HFI has two channels overlapping with the SPIRE wavebands: 545 GHz (550µm) and 857 GHz (350µm). Differences in filter profiles and central wavelengths between the SPIRE and Planck-HFI bands are accounted for using scalings which are applied to the Planck data. These scalings, described in detail in the SPIRE Handbook (2014), require an assumption about the shape of the underlying spectral energy distribution of the large-scale ISM emission. The typical assumption used in calculating scaling factors is that the ISM emission can be represented across the Herschel wavelengths by a modified blackbody distribution, i.e.

$$I_\nu \propto \nu^\beta B_\nu(T) \tag{2.9}$$

where I_ν is the ISM emission at frequency ν, β is the dust emissivity spectral index and $B_\nu(T)$ is the Planck function,

$$B_\nu(T) = \frac{2h\nu^3}{c^2} \left(e^{h\nu/k_\mathrm{B}T} - 1\right)^{-1}. \tag{2.10}$$

This requires assumptions both about the temperature and the dust properties of

the ISM. The standard background offsets used by the HGBS are 27.7, 159.8, 169.6, 94.4 and 41.1 MJy/sr at 70, 160, 250, 350 and 500μm respectively, as determined by Bernard et al. (2010).

The primary point source calibrator for the Herschel photometers is Neptune. Point source calibration uncertainty for the SPIRE bands is $\lesssim 5\%$, and is dominated by the uncertainty in the model of Neptune's submillimetre flux (Bendo et al. 2013). For extended sources, the SPIRE calibration accuracy is $\lesssim 10\%$ (Griffin et al. 2013). The point source calibration uncertainty of PACS is 3% at 70μm and 5% at 160μm (Balog et al. 2014; Müller et al. 2014). Extended source calibration accuracy for PACS is uncertain; the HGBS typically adopts calibration uncertainties of 10% and 20% at 70μm and 160μm respectively (e.g. Könyves et al. 2015).

2.3   IRAM 30m Telescope

The Institut de Radioastronomie Millimétrique (IRAM) 30-metre telescope is a 30 m single-dish parabolic antenna located on Pico Veleta in the Spanish Sierra Nevada. The telescope has various heterodyne receivers as well as continuum cameras operating at 3, 2, 1, and 0.9 mm. The IRAM 30 m observations of the N_2H^+(1-0) transition at ~ 3 mm used in this work are presented in André et al. (2007). The observations were taken using four SIS (superconductor-insulator-superconductor) heterodyne receivers simultaneously, with an autocorrelation spectrometer as a backend. The FWHM of the IRAM 30 m beam at 3mm is $26''$.
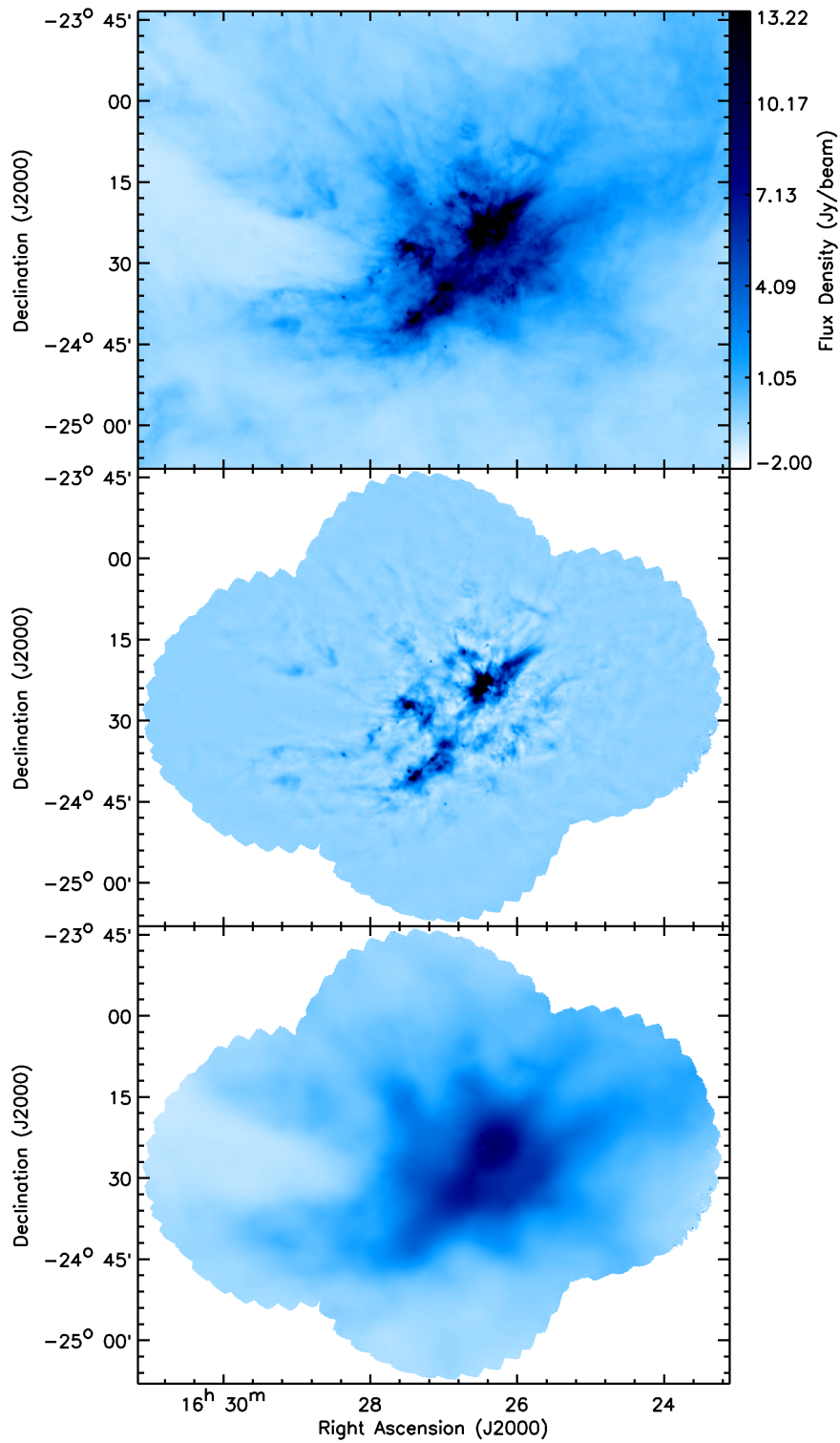
Figure 2.15: The effect of spatial filtering on the SPIRE 250μm map of L1688. Top panel: SPIRE map. Middle panel: filtered map. Bottom panel: difference map. The same colour scaling applies to all panels.

2.4 SCUBA-2 and Herschel Compatibility

2.4.1 Spatial Filtering

In order to make meaningful comparisons between SCUBA-2 and Herschel data, the large-scale structure to which SCUBA-2 is not sensitive must be removed from the Herschel observations. This is accomplished using the method developed by Sadavoy et al. (2013). Herschel data are added to the SCUBA-2 bolometer time series for a SCUBA-2 observation which has previously been reduced in the normal manner. The Herschel observations are scaled by a multiplicative factor such that they represent a small but non-negligible perturbation to the SCUBA-2 signal. The data reduction process is then repeated, using the same set of parameters which were used in the original reduction of the field. The original SCUBA-2 reduction of the data is then subtracted from the Herschel+SCUBA-2 map, leaving the spatially-filtered Herschel signal. Finally, the scaling applied the Herschel observation is reversed. For Herschel data 'H' scaled by a factor α and SCUBA-2 data 'S2', the filtering process can be summarised as

$$\text{Filtered Map} = \frac{\text{Map}(\text{S2} + \alpha\text{H}) - \text{Map}(\text{S2})}{\alpha}. \tag{2.11}$$

This process can be used either for a field for which both Herschel and SCUBA-2 data exist, or to create SCUBA-2-like observations for a field observed by Herschel alone. In the latter case, the SCUBA-2 field chosen as a background must contain minimal emission, and an automask reduction must be performed. In the former case – that of this work – the external mask applied to the SCUBA-2 reduction must also be applied to the Herschel data, in order to make the two observations of the field comparable. When the spatial filtering process is performed on a field for which there is both SCUBA-2 and Herschel data, the process will be repeated once for each SCUBA-2 observing position for which there is corresponding Herschel data, and the resulting spatially-filtered maps will then be combined to form a mosaic.
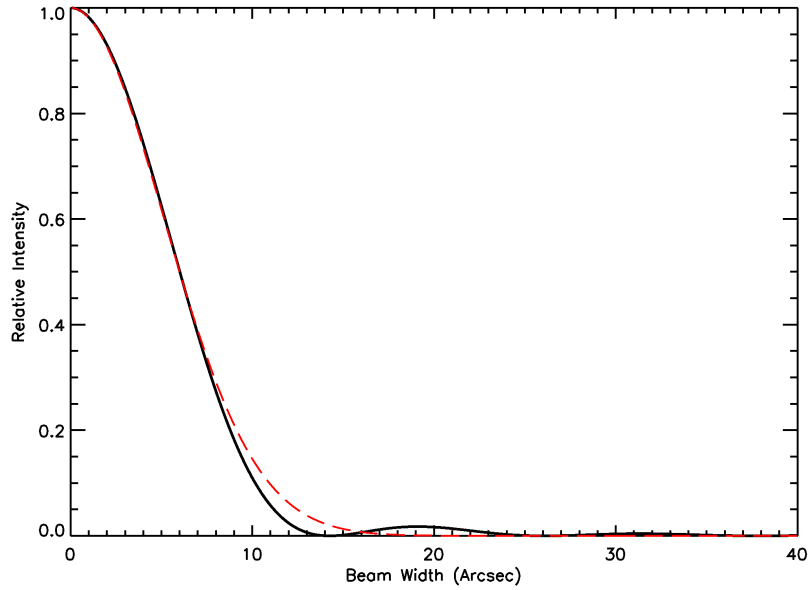
Figure 2.16: Fraunhofer diffraction pattern for a 15m-diameter aperture at 850μm. Overlaid in red is a 12″ FWHM Gaussian distribution, for purposes of comparison.

The effect of spatial filtering on Herschel data is shown in Figure 2.15. This shows the SPIRE 250μm map of the L1688 region of Ophiuchus, before and after being passed through the SCUBA-2 data reduction pipeline, using IR1 data reduction parameters and the mask shown in Figure 2.10. The bottom panel of Figure 2.15 shows the difference of the original and filtered maps, showing the extended emission which is lost in the filtering process.

2.4.2   Common-Resolution Convolution Kernels

In order to compare two telescope data sets, the two data sets must be brought to a common resolution. Each data set will have a resolution, and a beam pattern, determined by the instrument point spread function (PSF) at the wavelength under consideration. Typically, the data set at the higher resolution (that with the
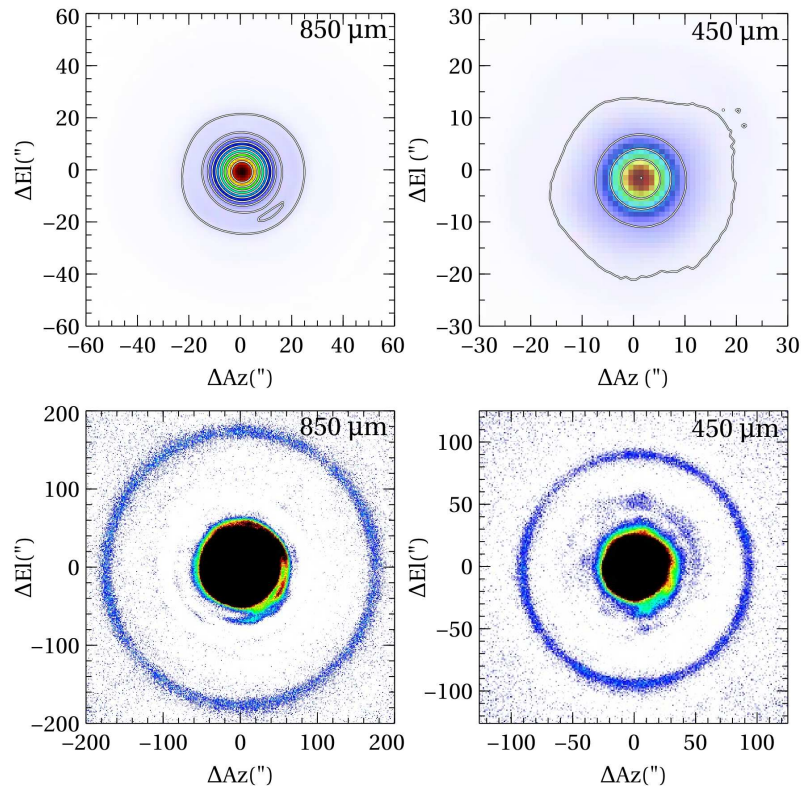
Figure 2.17: SCUBA-2 450μm and 850μm coadded observations of Uranus. Figure 4, Dempsey et al. (2013).
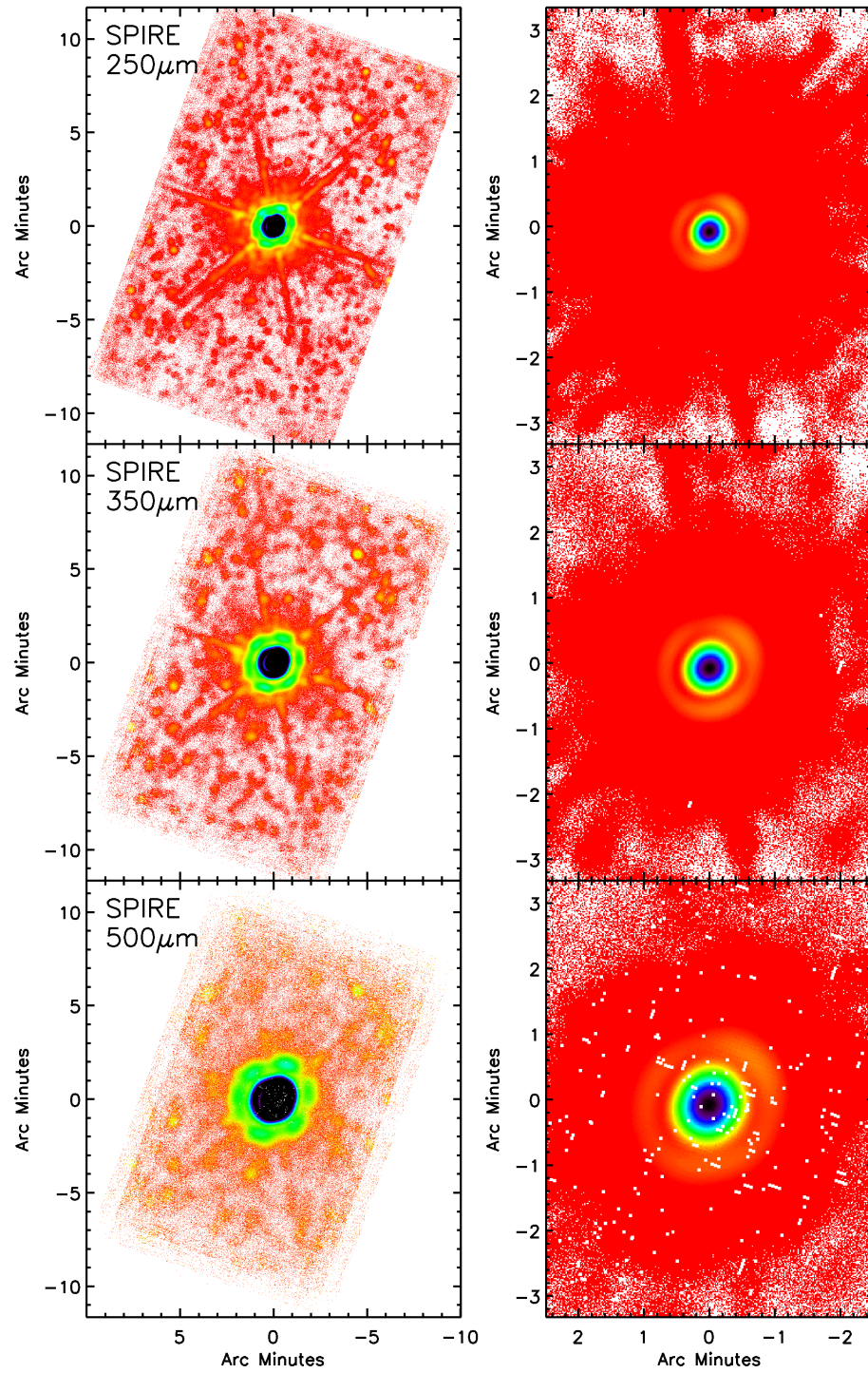
Figure 2.18: SPIRE beam patterns, square-root scaled.
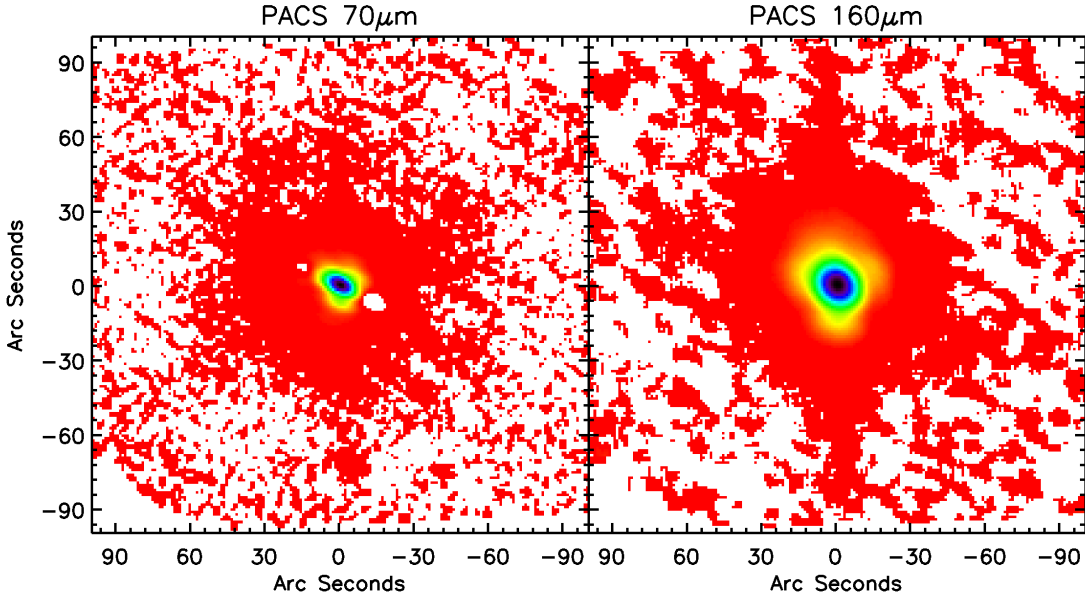
Figure 2.19: PACS beams at $60'' \, \mathrm{s}^{-1}$ scanning speed, square-root scaled.

narrower PSF) must have a smoothing function applied in order to match the resolution of the other data set. Each of the SCUBA-2 and Herschel photometric bands used here has a different point spread function. In order to reconstruct the lower-resolution beams as accurately as possible, for the results presented in this work, convolution kernels were constructed. This section discusses the methods considered for bringing the SCUBA-2 and Herschel data sets to a common resolution, and describes the method decided upon in detail.

The Fraunhofer diffraction pattern formed by plane waves from a point source passing through a circular aperture will be an Airy disc; a radially symmetric pattern with a bright central peak, with successive maxima and minima of emission at increasing radii (see, e.g. Hecht 2001). The intensity I of an Airy disc at diffraction angle θ is given by

$$I(\theta) = I_0 \left(\frac{2J_1(x)}{x} \right)^2 \qquad (2.12)$$

where I_0 is the peak intensity of the distribution, J_1 is a first-order Bessel function

of the first kind, and the dimensionless parameter x is

$$x = \frac{\pi D}{\lambda} \sin \theta \qquad (2.13)$$

where D is the aperture diameter and λ is the wavelength of the incoming light. The Airy diffraction pattern for light at 850μm for a telescope with a diameter of 15m is shown in Figure 2.16. As shown in Figure 2.16, the central maximum of an Airy disc can be well-approximated by a Gaussian distribution, and the primary beam width of a telescope is typically given as a Gaussian FWHM.

The resolution of a diffraction-limited circular aperture is determined by Rayleigh's criterion: two sources are considered marginally resolved when the central maximum of one source falls on the first minimum of the other. The angular separation of the first minimum from the central maximum in an Airy disc is

$$\theta = 1.22 \frac{\lambda}{D} \qquad (2.14)$$

where λ is the wavelength of the light and D is the diameter of the aperture, i.e. the diameter of the telescope's primary antenna.

In practice, no telescope beam is a perfect Airy disc. In the case of a reflecting telescope, obscuration of the primary mirror by the secondary focus and its supporting struts, as well as deformation of the primary mirror and other imperfections in the optical system, will alter the beam pattern. For ground-based telescopes such as the JCMT, the atmospheric seeing will alter the beam pattern. The PSF of a telescope is determined in practice by observations of standard calibrators. The beam patterns, or point spread functions, of the JCMT at 450μm and 850μm are shown in Figure 2.17. The beam patterns of SPIRE at 250μm, 350μm and 500μm are shown in Figure 2.18; the diffraction pattern resulting from the struts supporting the secondary mirror can be seen. The PACS 70-μm and 160-μm parallel-mode ($60'' \, \mathrm{s}^{-1}$ scanning speed) beam patterns are shown in Figure 2.19. The ellipticity of the beam pattern can be clearly seen.

2.4.2.1 Fourier Transform Operators

In order to map point spread function (PSF) A onto a lower-resolution PSF B, a convolution kernel $K(A \Rightarrow B)$ must be chosen, such that

$$\text{PSF}_B = K(A \Rightarrow B) * \text{PSF}_A. \tag{2.15}$$

The convolution kernel $K(A \Rightarrow B)$ is the function for which

$$\text{FT}[\text{PSF}_B] = \text{FT}[K(A \Rightarrow B)] \times \text{FT}[\text{PSF}_A] \tag{2.16}$$

where FT represents the Fourier Transform operator,

$$\text{FT}[f(x)] = \hat{f}(k) = \int_{-\infty}^{\infty} f(x)e^{-2\pi i k x} dx \tag{2.17}$$

and FT^{-1} represents the inverse Fourier Transform operator,

$$\text{FT}^{-1}[\hat{f}(k)] = f(x) = \int_{-\infty}^{\infty} \hat{f}(k)e^{2\pi i k x} dk. \tag{2.18}$$

Equation 2.16 follows from the definition of the convolution theorem. The convolution $f * g$ of functions $f(x)$ and $g(x)$ is defined to be

$$f * g \equiv \int_{-\infty}^{\infty} g(x')f(x-x')dx'. \tag{2.19}$$

If $f(x)$ and $g(x)$ have Fourier transforms $\hat{f}(k)$ and $\hat{g}(k)$ respectively, then Equation 2.19 can be rewritten as

$$f * g = \int_{-\infty}^{\infty} g(x') \left[\int_{-\infty}^{\infty} \hat{f}(k)e^{2\pi i k(x-x')}dk \right] dx' \tag{2.20}$$

$$= \int_{-\infty}^{\infty} \hat{f}(k) \left[\int_{-\infty}^{\infty} g(x')e^{-2\pi i k x'}dx' \right] e^{2\pi i k x} dk \tag{2.21}$$

$$= \int_{-\infty}^{\infty} \hat{f}(k)\hat{g}(k)e^{2\pi i k x} dk \tag{2.22}$$

$$= \text{FT}^{-1}[\hat{f}(k)\hat{g}(k)] \tag{2.23}$$

$$= \text{FT}^{-1}[\text{FT}(f)\text{FT}(g)] \tag{2.24}$$

78

and hence,

$$\text{FT}(f * g) = \text{FT}(f) \times \text{FT}(g). \tag{2.25}$$

For our purposes, $f = \text{PSF}_A$, and we wish to choose $g = K(A \Rightarrow B)$ such that $f * g = \text{PSF}_B$. See, e.g., Riley et al. (2006), Chapter 13 for a derivation and discussion of these results.

2.4.2.2 Single-Gaussian Beam Models

If all of the telescope beams can be adequately modelled as single Gaussians, then a simple analytical solution exists for the convolution kernel, as the Fourier transform of a Gaussian is another Gaussian. For the case where

$$\text{PSF}_A \propto e^{-8\ln2\left(\frac{r}{2\text{FWHM}_A}\right)^2} \tag{2.26}$$

and

$$\text{PSF}_B \propto e^{-8\ln2\left(\frac{r}{2\text{FWHM}_B}\right)^2} \tag{2.27}$$

where r is the radial distance from the beam centre and $FWHM_B > FWHM_A$, the Gaussian FWHM width $\text{FWHM}_{A \to B}$ necessary to bring data set A to the resolution of data set B will be

$$\text{FWHM}_{A \to B} = \sqrt{(\text{FWHM}_B)^2 - (\text{FWHM}_A)^2} \tag{2.28}$$

as Gaussians add in quadrature. Then, the Gaussian function which maps A onto B will be

$$K(A \Rightarrow B) = Ce^{-8\ln2(r/2\text{FWHM}_{A \to B})^2} \tag{2.29}$$

where C is a normalisation constant. For example, a SCUBA-2 850-μm map at 14.1″ resolution would require smoothing with a 33.8″ Gaussian kernel to bring the map to the 36.6″ resolution of the Herschel-SPIRE 500-μm band.

SCUBA-2 450-μm fluxes have previously been noted to show an excess over the values expected from interpolation of the Herschel 160-μm, 250-μm, 350-μm and

500-µm bands (Sadavoy et al. 2013). This discrepancy was also seen in our data sets when they were brought to a common resolution by smoothing the lower-resolution maps with simple Gaussian kernels.

2.4.2.3 Double-Gaussian SCUBA-2 Beam Models

As approximating the beams as single Gaussians appears to result in the overestimation of 450-µm flux densities at 500-µm resolution, an alternative is to use the two-component Gaussian SCUBA-2 450µm beam model described by Dempsey et al. (2013), and continue to approximate the Herschel beams as single Gaussians. In this case, one would typically cross-convolve both A and B to a common, lower, resolution, $A * B$.

In this model, to cross-convolve PSF_B with the two-component PSF_A, two Gaussian convolutions are needed. For the primary beam, the convolution needed is

$$K(\mathrm{A_{primary}}) = C_{\mathrm{A,primary}} e^{-8\ln2\left(r/2\mathrm{FWHM_{A,primary}}\right)^2} \tag{2.30}$$

and for the secondary beam, the same model applies. Then, the output map is given by

$$\mathrm{PSF}_{A*B} = (\text{Primary Beam Volume}) \times (K(\mathrm{A_{primary}}) * \mathrm{PSF}_B)+$$
$$(\text{Secondary Beam Volume}) \times (K(\mathrm{A_{secondary}}) * \mathrm{PSF}_B). \tag{2.31}$$

The SCUBA-2 450-µm primary and secondary beam volumes are listed in Table 2.1.

To convolve PSF_A with the single-component PSF_B, the convolution needed is

$$K(\mathrm{B}) = C_{\mathrm{B}} e^{-8\ln2(r/2\mathrm{FWHM_B})^2} \tag{2.32}$$

and the output map is given by

$$\mathrm{PSF}_{B*A} = K(\mathrm{B}) * \mathrm{PSF}_A. \tag{2.33}$$

Note that convolution is a commutative process, so $\mathrm{PSF}_{A*B} = \mathrm{PSF}_{B*A}$. However, when this model is applied to SCUBA-2 450-µm and Herschel 500-µm data, it proves

not to be a good enough approximation, as, as shown in Figure 2.20 (below), it does not remove the 450-µm excess seen at 500-µm resolution.

2.4.2.4   Beam-Map Convolution Kernels

As a part of this work, a set of convolution kernels were made using the Herschel and SCUBA-2 beam maps, following the method of Aniano et al. (2011). This was done to test the hypothesis that the apparent 450-µm excess was caused by the approximation of the 450-µm beam secondary component as a Gaussian (Dempsey et al. 2013). The method described by Aniano et al. (2011) can be applied to either measured beam maps or model telescope beams, and involves constructing a convolution kernel $K(A \Rightarrow B)$ empirically. In principle, $K(A \Rightarrow B)$ is derived using

$$K(A \Rightarrow B) = \text{FT}^{-1}\left(\frac{\text{FT}(\text{PSF}_B)}{\text{FT}(\text{PSF}_A)}\right). \tag{2.34}$$

In practice, however, the division by $\text{FT}(\text{PSF}_A)$ leads to $K(A \Rightarrow B)$ being dominated by noise, unless the high-frequency (i.e. high wavenumber k) components of PSF A are filtered. Firstly, high-frequency noise is filtered from both PSFs using a filter ϕ which takes the form

$$\phi(k) = \begin{cases} 1 & \text{for } k \leq k_\alpha \\ \frac{1}{2}\left(1 + \left(1.8249 \times \frac{k-k_\alpha}{k_\beta-k_\alpha}\right)\right) & \text{for } k_\alpha < k \leq k_\beta \\ 0 & \text{for } k_\beta < k \end{cases} \tag{2.35}$$

where $k_\alpha = 0.9k_\beta$ and $k_\beta = 8\pi/\text{FWHM}$ where FWHM is the FWHM of the instrument primary beam. Hereafter, $\text{FT}_\phi = \phi \times \text{FT}$. The highest-frequency components of PSF A are further filtered: Equation 2.34 becomes

$$K(A \Rightarrow B) = \text{FT}^{-1}\left(\frac{\text{FT}_\phi(\text{PSF}_B)}{\text{FT}_\phi(\text{PSF}_A)} \times f_\text{A}\right) \tag{2.36}$$

and the filter f_A takes the form

$$
f_\mathrm{A}(k) = \begin{cases} 1 & \text{for } k \leq k_\mathrm{L,A} \\ \frac{1}{2}\left(1 + \cos\left(\pi \times \frac{k - k_\mathrm{L,A}}{k_\mathrm{H,A} - k_\mathrm{L,A}}\right)\right) & \text{for } k_\mathrm{L,A} < k \leq k_\mathrm{H,A} \\ 0 & \text{for } k_\mathrm{H,A} < k \end{cases} \tag{2.37}
$$

where $k_\mathrm{H,A}$ is the highest wavenumber at which $\mathrm{FT}(\mathrm{PSF}_A)$ is appreciable:

$$
\mathrm{FT}(\mathrm{PSF}_A)(k_\mathrm{H,A}) = 0.005 \times \mathrm{FT}(\mathrm{PSF}_A)_\mathrm{max} \tag{2.38}
$$

and $k_\mathrm{L,A} = 0.7 k_\mathrm{H,A}$. Prior to constructing the convolution kernel, the PSFs are centroided, resampled to a common grid of 3645×3645 $0.2''$ pixels, and circularly averaged. The SCUBA-2 and SPIRE beams are already approximately circular and are largely unchanged by this circular averaging. The PACS beams, which are substantially elliptical in parallel-mode observations (see Figure 2.19), are more affected, and the convolution process may produce some distortion in convolved 70-μm and 160-μm maps. However, as both the circular averaging process and the convolution process conserve flux, provided that the PACS beams are smaller along both their axes than the beam to which they are being convolved, then total beam-map-kernel-convolved PACS flux densities measured inside an aperture the same size as or larger than the target beam size will be accurate. It should also be noted that all of the SCUBA-2, SPIRE and PACS instruments scan in more than one direction on the sky while taking an observation, and hence the beam pattern is rotated several times within each observation. This means that the beam pattern is to some extent circularly averaged even before the convolution is applied.

The kernels created for this work were generated using a routine written in Interactive Data Language (IDL), implementing the method described above. The SPIRE and PACS beam maps shown in Figures 2.18 and 2.19 were used as input for the Herschel beam patterns. SCUBA-2 beam maps were generated by co-adding
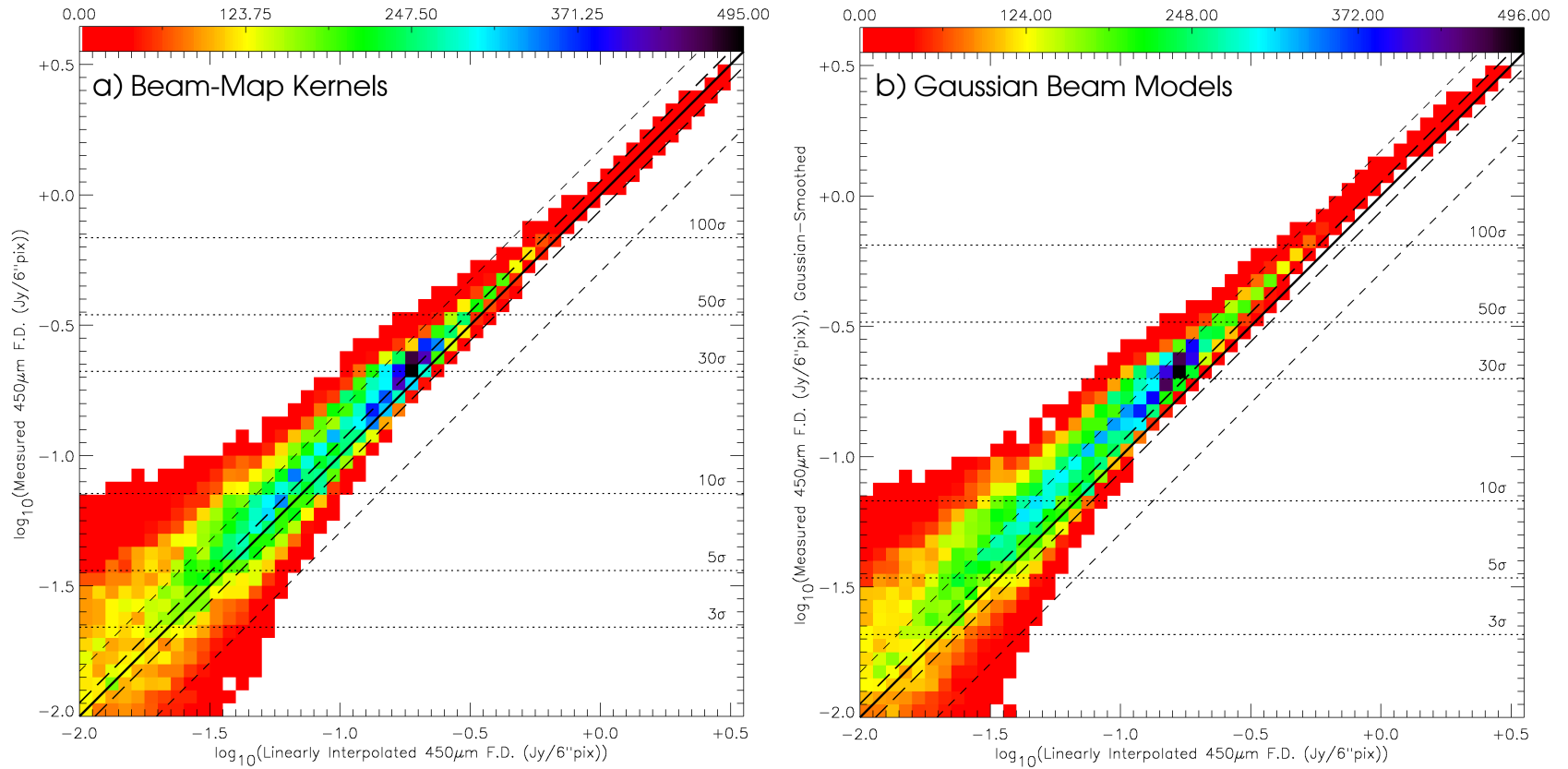
Figure 2.20: Histograms showing the agreement between predicted and measured 450-μm flux densities in the CO-subtracted region of L1688, for maps brought to a common resolution using (a) the beam-map convolution kernels and (b) double-Gaussian model for the 450-μm beam. Colour scale shows the number of map pixels in each box in the grid. Thick black lines show 1:1 agreement; long-dashed lines show 13% calibration error; short-dashed lines show 50% calibration error.
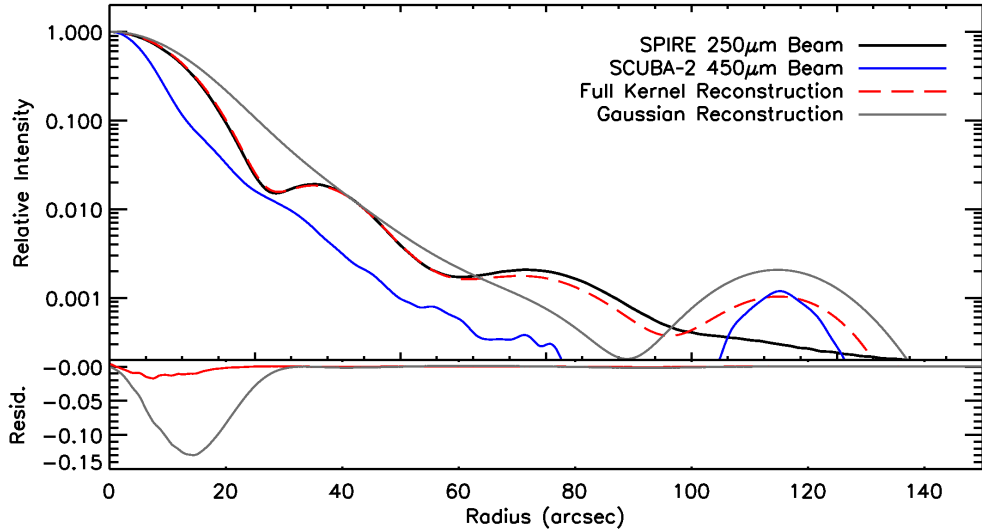
Figure 2.21: Comparison between the beam-map kernel (red) and single-Gaussian (grey) reconstructions of the SPIRE 250-μm beam (black) from the SCUBA-2 450-μm beam (blue). Residuals are shown below.

high-quality calibration observations of Uranus taken at 450μm and 850μm. Convolutions were performed using a separate routine, also written in IDL, supplied by Aniano et al. (2011).

Using the convolution kernels improves reconstruction of the beam, as shown in Figure 2.20. These plots compare the measured SCUBA-2 450-μm flux density for each pixel in the map (y axis) to the 450-μm flux density predicted by linear interpolation between the SPIRE 350-μm and SPIRE 500-μm data for the same pixel (x axis). Figure 2.20a shows this at SPIRE 500-μm resolution, for maps convolved using the beam-map kernels described above. Figure 2.20b shows this at (SPIRE 500-μm ∗ SCUBA-2 450-μm) resolution, with maps smoothed using the double-Gaussian beam model for the SCUBA-2 450-μm beam described above, and a single-Gaussian beam model for the SPIRE 350-μm and 500-μm beams. Both with and without the convolution kernels, there is a clear upward skew to the distribution of measured against predicted 450-μm flux densities, particularly at lower signal-to-noise. However, in Figure 2.20b, a systematic offset from the 1:1 line can be seen

at the highest signal-to-noise values. This offset is not seen in Figure 2.20a, and in Figure 2.20, the upward skew is less pronounced. This suggests that use of the beam-map convolution kernels improves reconstruction of the lower-resolution beams from the 450-μm beam, without entirely resolving the issue. It must be noted that the low-power portions of the 450-μm beam at large radii are substantially affected by atmospheric conditions, and hence are likely to vary between observations. Any beam model or average beam map must necessarily be an approximation to the true beam pattern when the observations were taken.

An example of the reconstruction of a beam using the beam-map convolution kernels is shown in Figure 2.21. The reconstruction of the SPIRE 250-μm beam from the SCUBA-2 450-μm beam is shown, along with the beam reconstruction resulting from treating both beams as single Gaussians. Note the flux excess resulting from approximating the beams as single Gaussians (grey line in main plot and residuals). The second and third Airy peaks of the SPIRE beam are recovered well using the beam-map kernel.

The improvement in agreement between fluxes measured at different wavelengths through use of beam-map kernels is shown in Figure 2.22. This figure shows some example SEDs for sources detected in the L1688 region of Ophiuchus, brought to SPIRE 350-μm resolution using beam-map kernels (left-hand columns) and brought to (SPIRE 350-μm $*$ SCUBA-2 450-μm) resolution using a double-Gaussian beam model for the SCUBA-2 450-μm beam and single-Gaussian beam models for the other beams (right-hand columns). At (SPIRE 350-μm $*$ SCUBA-2 450-μm) resolution, the Gaussian model typically causes an apparent excess at 350μm – as opposed to (SPIRE 500-μm $*$ SCUBA-2 450-μm) resolution, where the apparent excess is seen at 450μm – see Figure 2.20. This excess is removed by convolving the data to a common resolution using the beam map kernels, although a slight 450-μm excess typically then becomes apparent in the beam-map-kernel-convolved
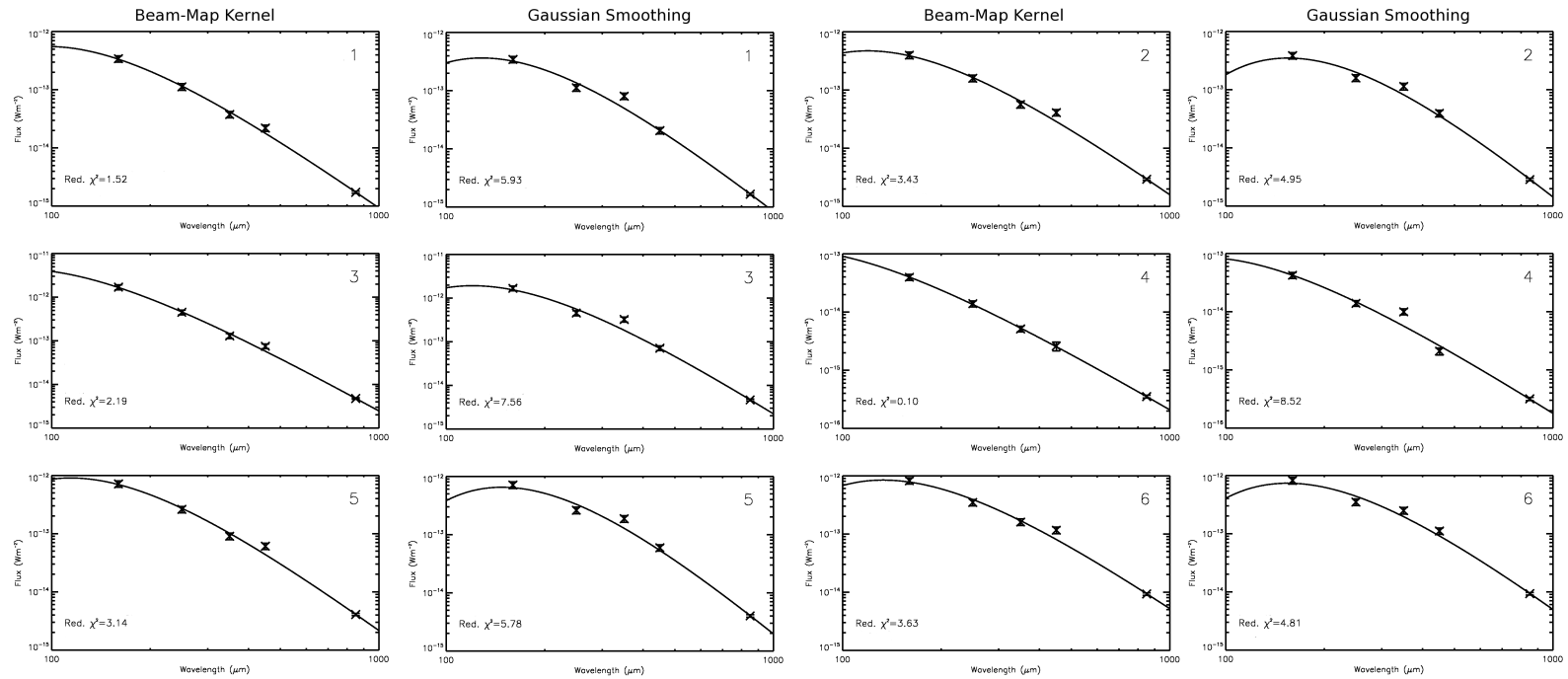
Figure 2.22: Some example SEDs for sources detected in the L1688 region of Ophiuchus. The left-hand columns show the fluxes measured when the data are convolved to SPIRE 350-μm resolution using the beam-map kernels. The right-hand columns show the fluxes measured when the data are convolved to SPIRE 350-μm resolution using single-Gaussian beam models.

maps. This is not surprising, since, as discussed above, the beam-map kernels do not entirely account for the variations in the SCUBA-2 450-μm beam, and SCUBA-2 450-μm fluxes remain slightly above their predicted values.

2.5 Summary

We have introduced and discussed the telescopes with which data used in this work were taken: the James Clerk Maxwell Telescope (JCMT), the Herschel Space Observatory and the IRAM 30-metre telescope. We discussed the SCUBA-2 and HARP instruments on the JCMT, and the SPIRE and PACS instruments on Herschel. We discussed methods by which data from SCUBA-2 and Herschel can be meaningfully compared.

The JCMT is a 15m-diameter submillimetre telescope located at the summit of Mauna Kea. Data taken using two instruments on the JCMT – the camera SCUBA-2 and the heterodyne receiver HARP-B – are used in this work. SCUBA-2 is a $10\,000$-pixel submillimetre camera which takes data simultaneously at $450\mu m$ and $850\mu m$, with effective resolutions of $9.6''$ and $14.1''$ respectively. HARP-B is a 16-pixel heterodyne receiver which operates in the frequency range 325–$375\,\mathrm{GHz}$ (~ 800–$925\,\mu m$), with an angular resolution of $14''$ at $345\,\mathrm{GHz}$.

SCUBA-2 data reduction requires iterative modelling of the astrophysical and atmospheric signal received by the telescope, as well as correlated low-frequency noise. In order to prevent atmospheric signal being spuriously assigned as astrophysical emission in low signal-to-noise regions, a signal-to-noise based 'mask' is used to define regions of significant astrophysical emission. In order to avoid the necessity for *a priori* knowledge of the astrophysical signal, the data reduction process is repeated twice. Firstly, the mask is defined based on simple signal-to-noise cuts in each iteration. A mask is then defined based on a signal-to-noise cut in the co-added and mosaiced first set of reductions. The fields observed are then re-reduced using

this mask.

The SCUBA-2 850-µm window can be significantly contaminated by the CO J = 3 → 2 transition. Where the ^{12}CO emission in a SCUBA-2 field has been observed with HARP-B, this is corrected for by re-reducing the SCUBA-2 data with the integrated HARP-B ^{12}CO emission included as a negative signal.

Herschel was a 3.5m-diameter submillimetre space observatory, observing in the wavelength range 70–500µm. Data taken using the SPIRE and PACS photometers are used in this work. SPIRE observed at 250µm, 350µm and 500µm, at resolutions of 18″, 25″and 36″ respectively. Data were taken simultaneously using the PACS photometer, operating at 70µm and 160µm, at resolutions of 5.8″×12.1″and 11.6″×15.4″respectively.

The IRAM 30-metre telescope is a 30 m-diameter millimetre telescope located on Pico Veleta. The telescope operates in the wavelength range ∼ 0.9–3 mm, and has both continuum and heterodyne observing modes. IRAM 30 m observations of the N_2H^+ J = 1 → 0 transition at 3 mm are used in this work.

Due to the necessity of removing atmospheric signal from SCUBA-2 data, SCUBA-2 is not sensitive to emission on spatial scales larger than its own array size (600″), and further spatial filtering is introduced by the mask used to constrain the data reduction process. In order to compare SCUBA-2 and Herschel data, it is necessary to spatially filter the Herschel data in the same manner as the SCUBA-2 data. This is done by re-reducing a SCUBA-2 field with the Herschel observations of the same region included, scaled to be a small perturbation on the SCUBA-2 data. The original SCUBA-2 reduction of the field is then subtracted, leaving the filtered Herschel data.

When bringing SCUBA-2 and Herschel data to a common resolution, it is necessary to use convolution kernels based on the true telescope beams, rather than Gaussian approximations. The SCUBA-2 450-µm beam, in particular, has a substantial

fraction of its power in the secondary beam, and cannot be modelled adequately as either a single- or a double-Gaussian, for the purposes of convolving the data to a common resolution with a Herschel data set. The empirically-derived convolution kernels used in this work significantly improve the previously-noted discrepancies between Herschel and SCUBA-2 450-µm flux densities.

Chapter 3

The Ophiuchus molecular cloud

The Ophiuchus molecular cloud is a nearby (139 ± 6 pc, Mamajek 2008), well-studied (Wilking et al. 2008), site of low-mass star formation (Wilking & Lada 1983). It consists of two submillimetre-bright central regions, L1688 and L1689, each of which has extensive filamentary streamers (see, e.g., Loren 1989). Ophiuchus is considered to be the nearest site of clustered star formation (Wilking & Lada 1983; Motte et al. 1998). Star formation in Ophiuchus is heavily influenced by the nearby Sco OB2 association (Vrba 1977), the centre of which is at a distance of 11 ± 3 pc from Ophiuchus (Mamajek 2008). The southwest/northeast-aligned filamentary streamers from each of the central regions are thought to be due to the effects of this association (Vrba 1977; Loren 1989). The L1688 cloud shows a much more active star formation history than the neighbouring L1689 cloud to the east, supporting this scenario (Nutter et al. 2006, hereafter NWA06). There have been many previous wide-field millimetre and submillimetre studies of the starless core population in the L1688 cloud (e.g. Motte et al. 1998, hereafter MAN98; Johnstone et al. 2000; Enoch et al. 2008; Simpson et al. 2008, hereafter S08; Simpson et al. 2011).

3.1 Observations

3.1.1 SCUBA-2

The SCUBA-2 (Holland et al. 2013) observations presented here form part of the JCMT GBS (Ward-Thompson et al. 2007). Continuum observations at 850 μm and 450 μm were made using fully sampled 30′ diameter PONG1800 observations at resolutions of 14.1″ and 9.6″ respectively, as described in Section 2.1.1.1. The SCUBA-2 data of Ophiuchus are shown in Figures 3.1 and 3.2, for the regions of the map with significant emission. The full maps, along with the variance arrays, are shown in Figures 3.4–3.7.

The data were reduced as described in Section 2.1.2, using the Internal Release 1 method. The mask used in the reduction can be seen in Figure 2.10.

Four overlapping subsections of the L1688 region were each observed four times between 2012 May 6 and 2012 July 4 in very dry (Grade 1; $\tau_{225\,GHz} < 0.05$) weather. Three overlapping subsections of the L1689 region were each observed six times between 2012 June 10 and 2013 June 30 in dry (Grade 2; $0.05 < \tau_{225\,GHz} < 0.08$) weather. One section of the L1709 region was observed six times in Grade 2 weather between 2013 July 18 and 2013 July 27, as was one section of the L1712 region between 2013 July 28 and 2013 July 29. We found a typical 1σ noise level of $1.73\,\mathrm{mJy}/6″$ pixel in the 850-μm SCUBA-2 data and $14.9\,\mathrm{mJy}/4″$ pixel in the 450-μm SCUBA-2 data.

3.1.2 HARP

The L1688 region of Ophiuchus was observed as part of the JCMT GBS (Ward-Thompson et al. 2007), in three isotopologues of the CO J=3→2 transition: ^{12}CO, ^{13}CO and C^{18}O, at a resolution of 14″. These data were presented by White et al. (2015). The region of the SCUBA-2 map for which ^{12}CO data are available (an area
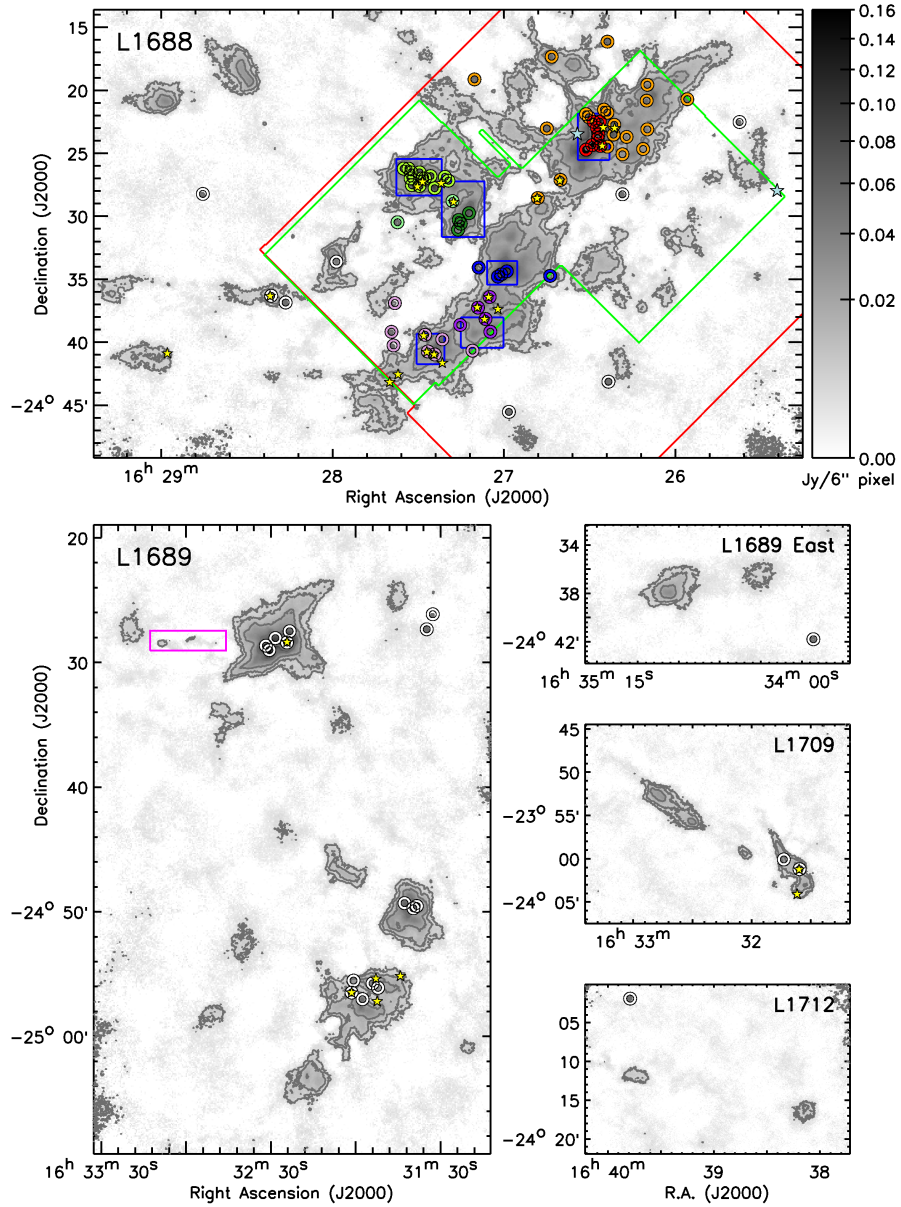
Figure 3.1: 850-μm flux density data, shown in square root scaling, for each of the sub-regions of Ophiuchus (see text for details). ^{12}CO data are available in the area outlined in red; ^{13}CO and C^{18}O data are available in the area outlined in green; N$_2$H$^+$ data are available in the areas outlined in blue. The CO outflow associated with IRAS 16293-2422 is marked in magenta. Open circles mark the sources we extract from the 850-μm data (see text for details of colour coding). Yellow stars mark the embedded protostars (Enoch et al. 2009). Blue stars mark the B stars HD 147889 and S1.
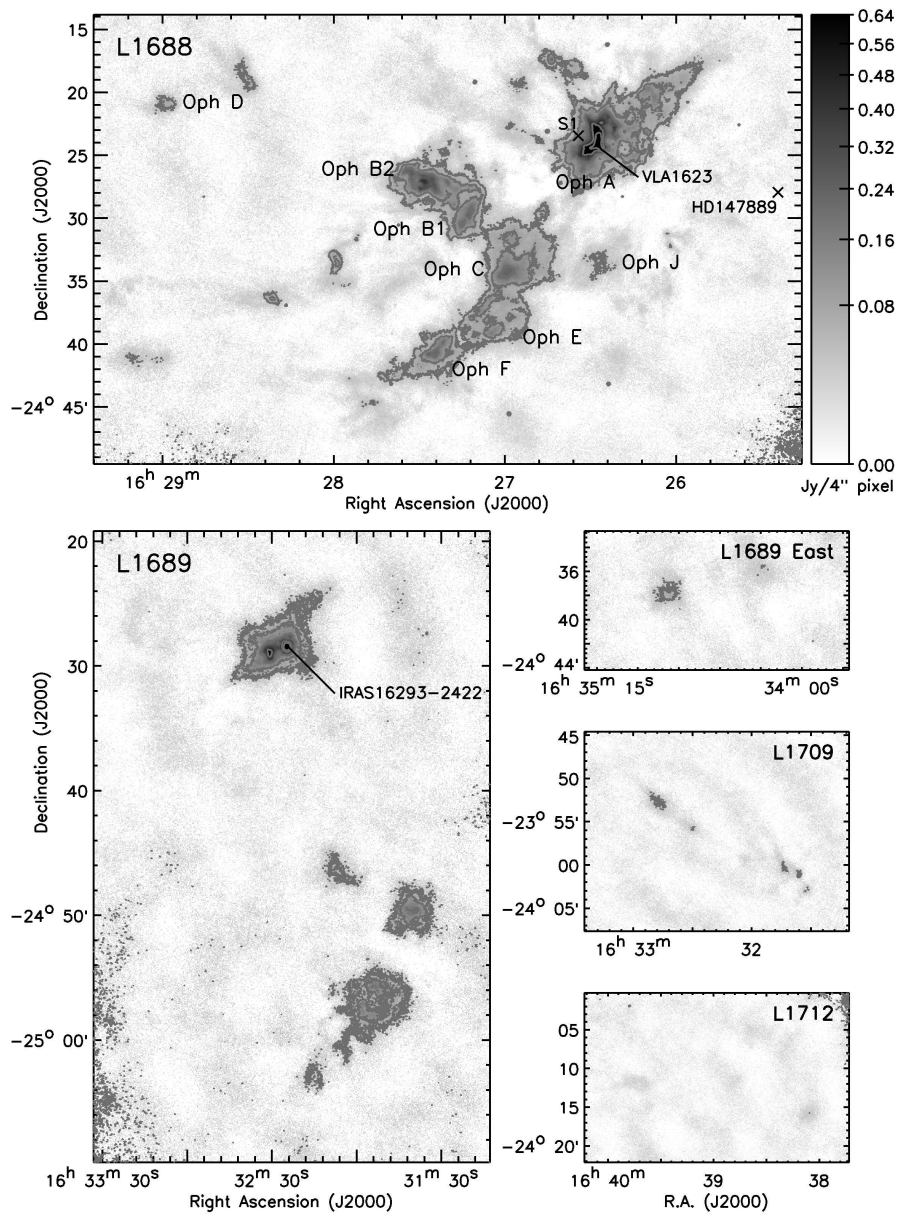
Figure 3.2: 450-μm flux density data, shown in square root scaling, for each of the sub-regions of Ophiuchus (see text for details). The B stars HD 147889 and S1 are marked, along with the Class 0 protostars VLA 1623 and IRAS 16293-2422. The sub-regions of the L1688 cloud are labelled.

94
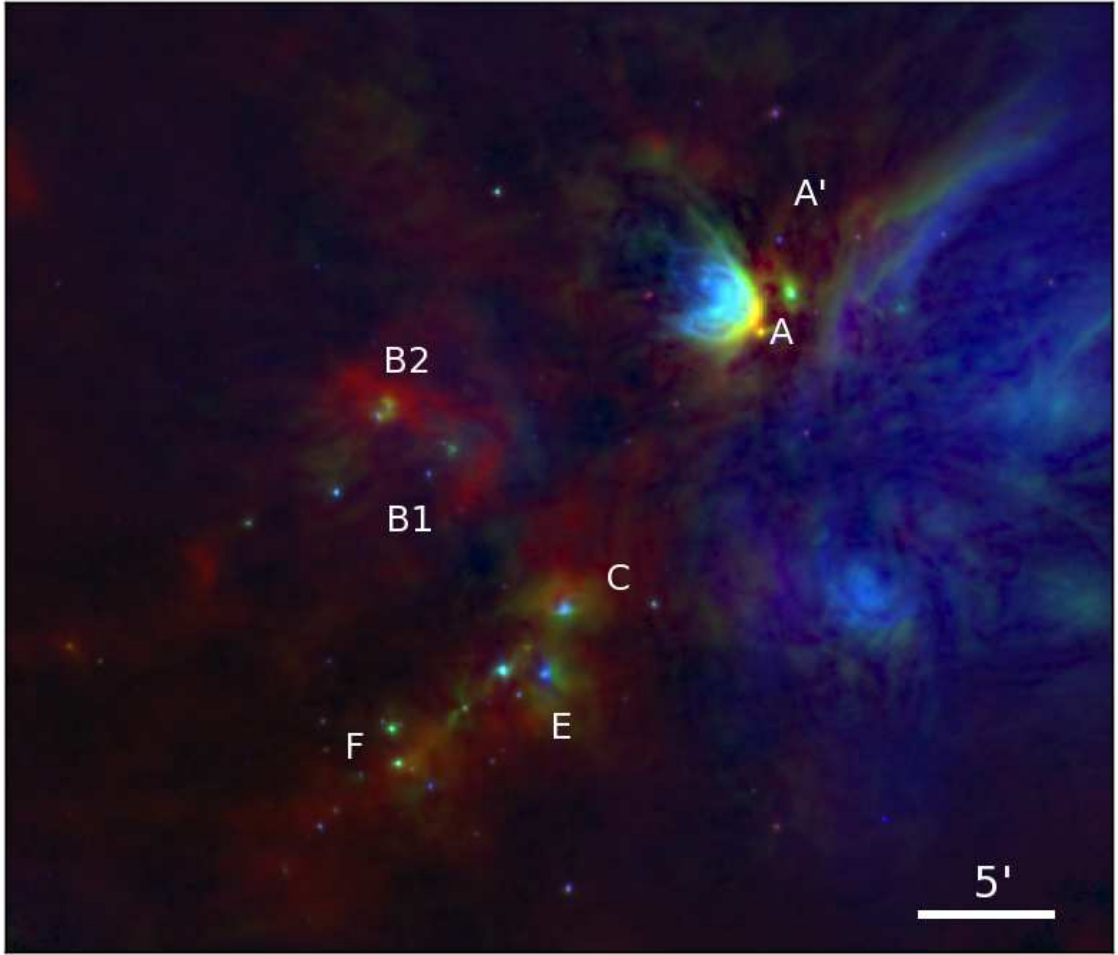
Figure 3.3: Three-colour image of L1688, with regions labelled. Red channel: SCUBA-2 850-μm data (this work). Green channel: *Herschel* 100-μm data (Ladjalate et al. 2015). Blue channel: *Spitzer* 8-μm data (Evans et al. 2003).
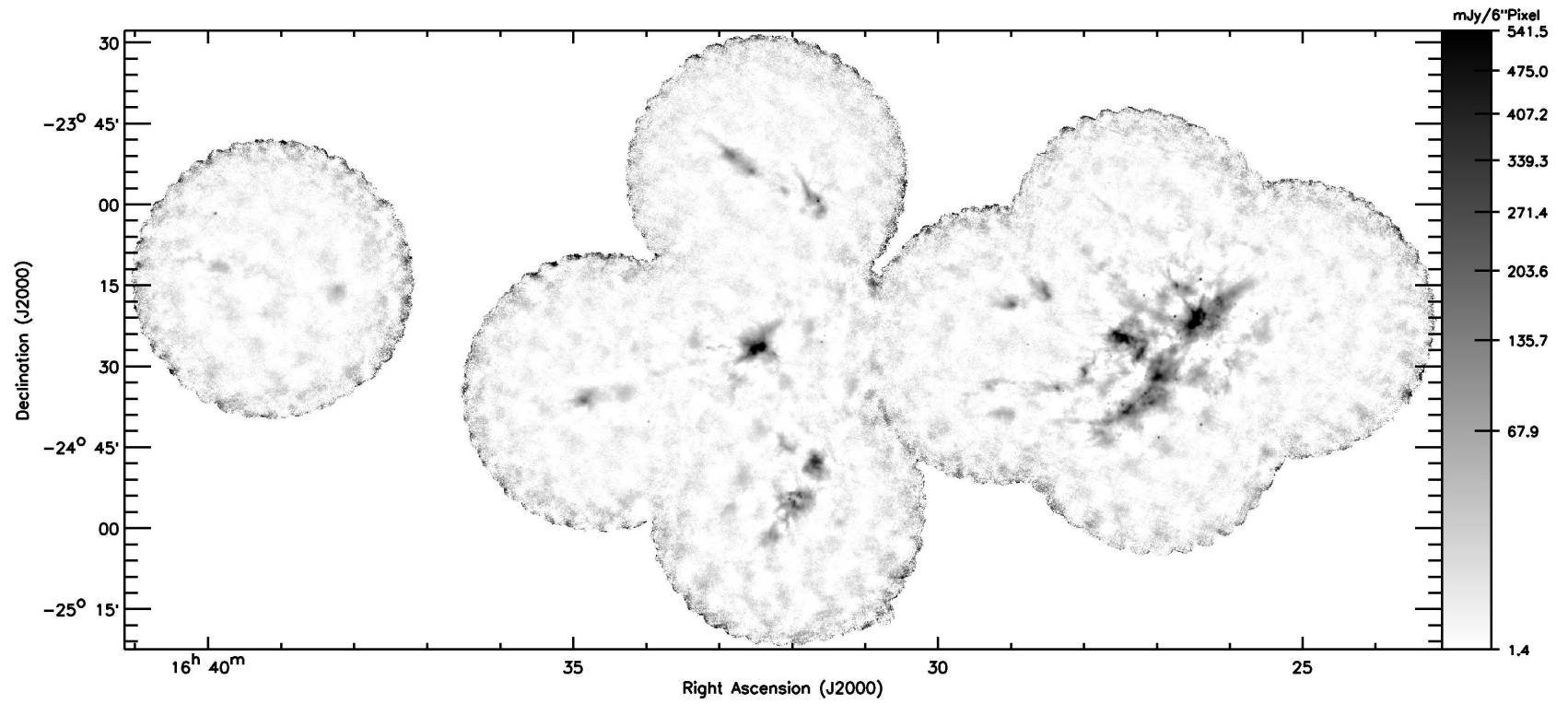
Figure 3.4: SCUBA-2 data of Ophiuchus at 850µm, shown in square root scaling.
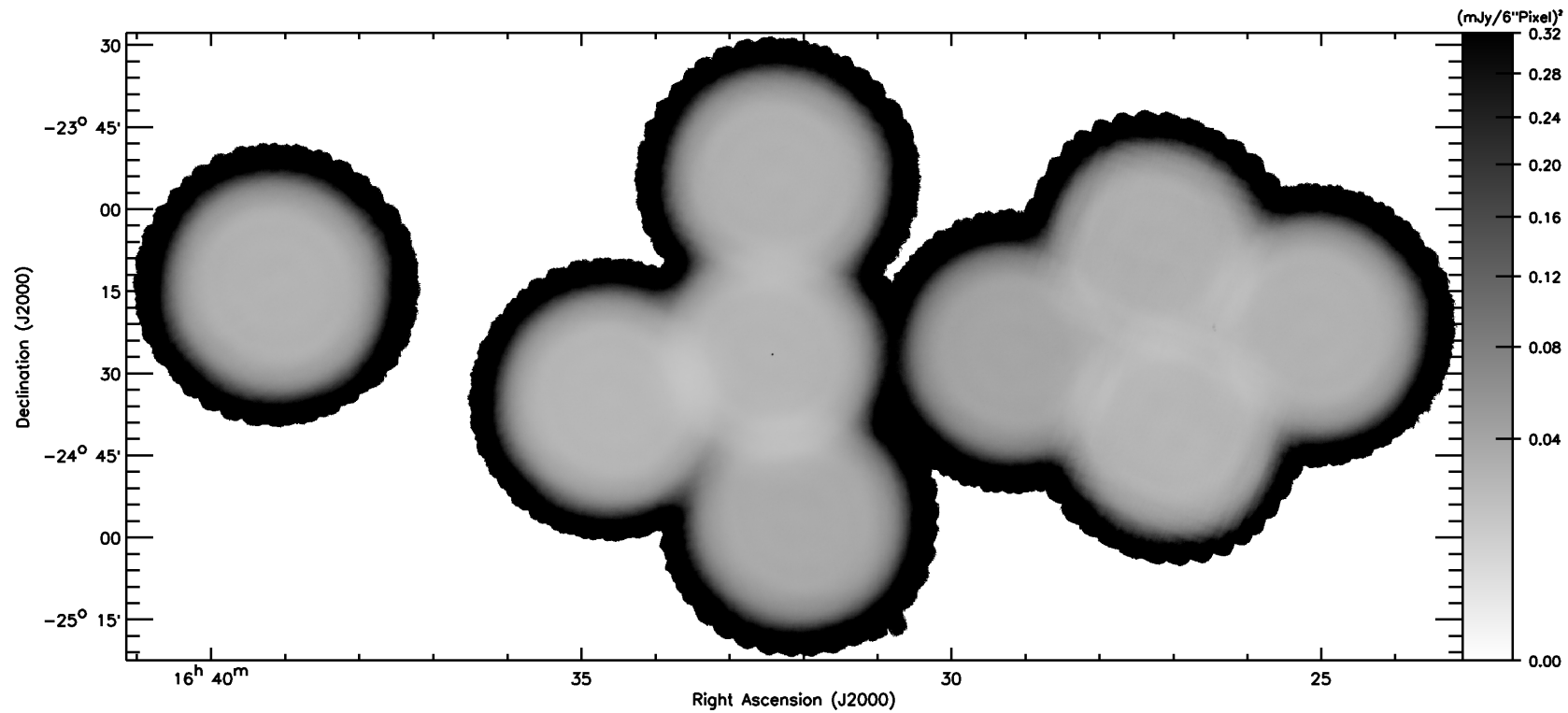
Figure 3.5: Variance of the SCUBA-2 data of Ophiuchus at 850μm, shown in square root scaling.
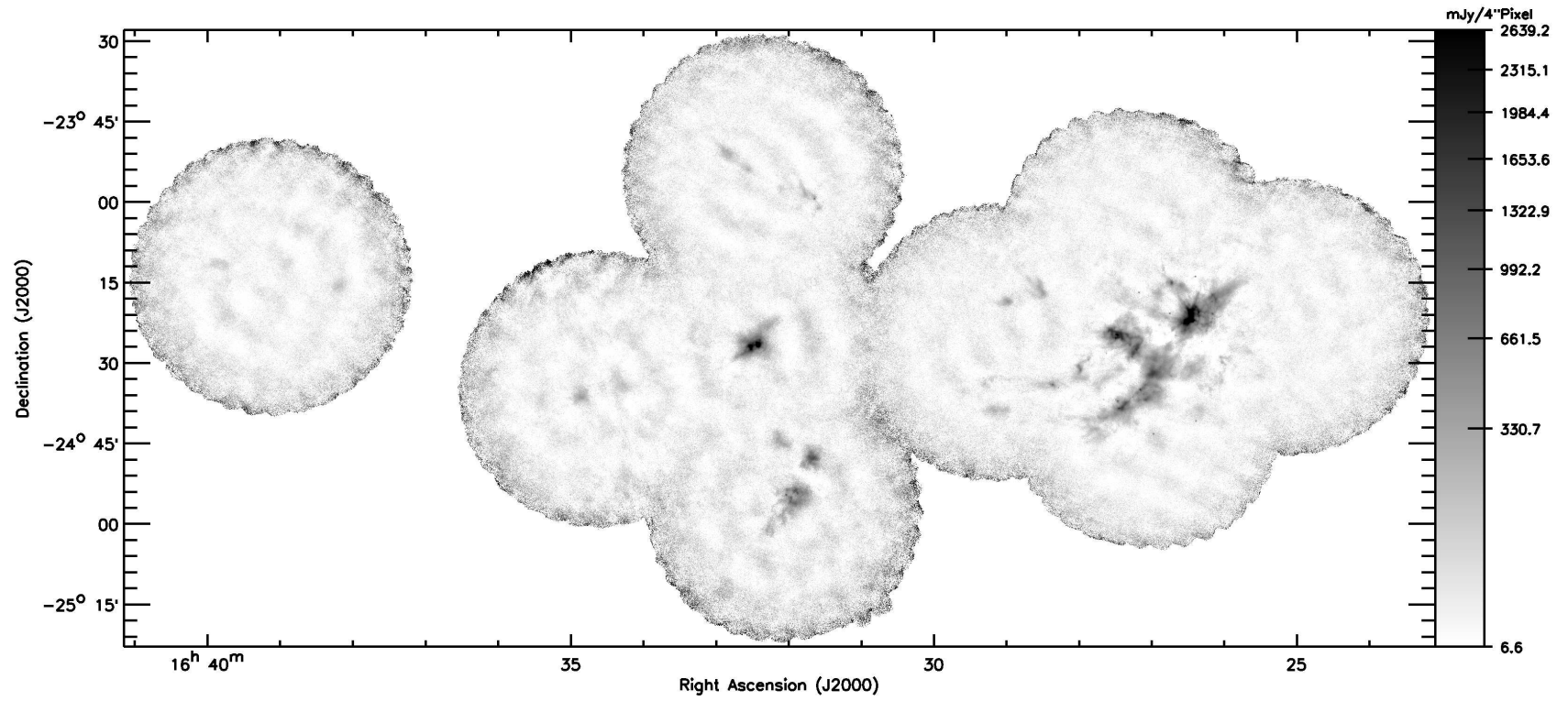
Figure 3.6: SCUBA-2 data of Ophiuchus at 450μm, shown in square root scaling.
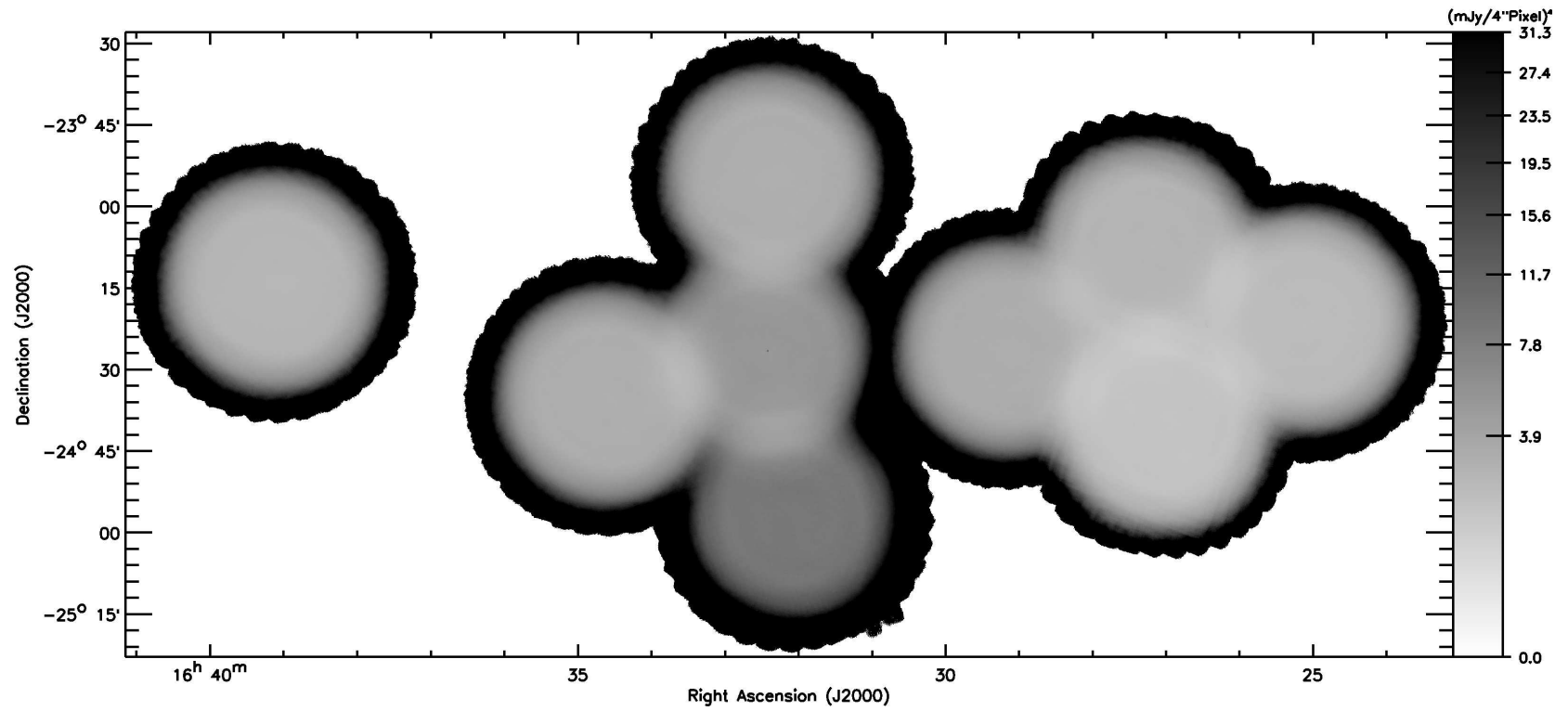
Figure 3.7: Variance of the SCUBA-2 data of Ophiuchus at 450μm, shown in square root scaling.

approximately $2050'' \times 2500''$, centred on L1688) is outlined in red on Figure 3.1, while the region for which both ^{13}CO and C^{18}O data are available (two overlapping regions, each with an area approximately $1000'' \times 1000''$) is outlined in green.

3.1.3 IRAM

Archival N$_2$H$^+$ J$=1 \rightarrow 0$ data are also used (Di Francesco et al. 2004; André et al. 2007). These observations were carried out with the IRAM 30m telescope at Pico Veleta, Spain, in 1998 June, 2000 July, and 2005 June. The FWHM of the IRAM beam at 3mm is $\sim 26''$. For the purposes of improving signal-to-noise, we binned the data to a $15''$ pixel grid. The regions of the area mapped with SCUBA-2 for which IRAM data are available are outlined in blue on Figure 3.1.

3.2 Data Processing

3.2.1 CO contamination

SCUBA-2 850-μm data may be substantially contaminated by the CO J$= 3 \rightarrow 2$ transition, as discussed in Section 2.1.4 above. Some CO contamination in the 850-μm data is expected for L1688, primarily due to the bright and extended outflow from the Class 0 protostar VLA1623 (André et al. 1993).

The total contribution of CO emission to the total observed flux density in L1688 was found to be 4.6%. However, the fractional CO contamination varies significantly across L1688. In the dense centres of Oph A, B, C and F the CO contamination fraction is typically $< 1\%$, while in Oph E, located along the same line of sight as the edge of the outflow from VLA 1623, the contamination reaches up to 10%. However, in the brightest regions of CO emission from the outflow from VLA 1623 and the PDR associated with HD 147889 – both regions of low 850-μm continuum emission – the contamination fraction reaches almost 100%. HARP CO data are

only available for the central L1688 region; other regions cannot be corrected in the same manner. However, it is only in L1688 that there is likely to be substantial contamination, and as even in L1688 the mean contribution of the CO emission is less than 5%, dropping to $< 1\%$ in the dense, 850-μm-bright regions in which the majority of our sources lie, it is unlikely that measured 850-μm flux densities outside of this region are significantly affected.

As a caveat, we note that a CO outflow can be seen in the 850-μm data of L1689, to the east of the northernmost part of the region. This outflow, marked in magenta on Figure 3.1, was previously identified as submillimetre condensation SMM21 by NWA06, and is likely to be the outflow known to be associated with the protostar(s) IRAS 16293-2422 (Mizuno et al. 1990). This indicates that there is likely to be some CO contamination associated with IRAS 16293-2422 in the L1689 North region. Flux densities, and hence masses, in this region may be over-estimated as a result.

3.2.2 Spatial filtering

In order to make SCUBA-2 and Herschel observations comparable, the large-scale structure must be removed from the Herschel observations, as discussed in Section 2.4.1 above. The filtering process described in Section 2.4.1 was repeated once for each SCUBA-2 observing position for which there were corresponding Herschel data, and the resulting spatially-filtered maps were combined to form a mosaic. The only region in the SCUBA-2 mosaic of Ophiuchus not covered by Herschel is L1712.

3.3 Results

3.3.1 Source extraction

Source extraction was performed on the CO-subtracted SCUBA-2 850-μm map of L1688, and the non-CO-subtracted SCUBA-2 850-μm map of the remainder of the field. Sources were identified using the curvature-based CuTEx algorithm (Molinari et al. 2011) in its detection mode. CuTEx identifies sources through signal in the second derivative of the input map, effectively removing background and large-scale structure from the map, and leaving the sharp changes in gradient associated with compact sources. CuTEx was chosen after extensive testing of various different methods as the algorithm best able to break apart the emission in crowded regions of the map (Oph A and Oph B), and which was in the most agreement with previous studies.

CuTEx identified 70 sources in the CO-subtracted L1688 region and 23 sources in the rest of the observed field: 4 in the remainder of L1688, 7 in L1689 North, 8 in L1689 South, 1 in L1689 East, 2 in L1709 and 1 in L1712. All but one of our sources are within the masked areas shown in Figure 2.10. Source 74/L1688N SMM1, which lies outside the mask, is the known protostellar object DoAr 4 (see Table 3.2 and discussion on source classification below).

Of the 70 sources in the CO-subtracted L1688 region, 46 were uniquely associated with a source in the S08 catalogue. A source is considered to be uniquely identified in the S08 catalogue if its FWHM area overlaps with that of an S08 source, and if it is the only source in our catalogue to do so. The S08 catalogue identifies 93 sources in SCUBA observations of L1688, of which 91 are within the CO-subtracted SCUBA-2 field. In Oph A, all of our sources have a unique counterpart in the S08 catalogue. In Oph B2 we identify 13 sources while S08 identify 12. The discrepancies between the two catalogues are mostly in low signal-to-noise regions and are likely to be due

Table 3.1: Results from multiple Gaussian fitting. Sources 1-70 are from the CO-subtracted section of L1688; 71-93 are from the remainder of L1688, L1689, L1709 and L1712. Position angles are measured east of north. FWHMs are as measured, without deconvolution. Sources are named following the conventions of MAN98/S08 for L1688, and NWA06 for L1689.

Source Index	Full Name JCMTLSG	Source Name	RA 16^h: (J2000)	Dec −24^h: (J2000)	FWHM ($''$)	Angle (°)	$F^{peak}_{\nu(850\mu m)}$ (Jy/pix)	$F^{total}_{\nu(850\mu m)}$ (Jy)	IR assn	Type	S08/ NWA06	Region
1	J162627.4-242352	SM1	26:27.36	23:52.8	20.4×16.2	178.7	0.651	6.762	S1	C	SM1	A
2	J162627.1-242334	SM1N	26:27.12	23:34.8	19.6×15.5	170.0	0.546	5.215	S1	C	SM1N	A
3	J162629.3-242425	SM2	26:29.28	24:25.2	29.0×17.2	139.0	0.279	4.389	S1	C	SM2	A
4	J162626.4-242428	VLA 1623	26:26.40	24:28.8	20.0×18.9	100.0	0.465	5.555	Y	P	VLA 1623	A
5	J162626.6-242233	A-MM5	26:26.64	22:33.6	36.2×18.0	106.2	0.074	1.519	S1	C?	A-MM5?	A
6	J162627.6-242302	A-MM6	26:27.60	23:02.4	30.9×22.1	169.6	0.209	4.474	S1	C?	A-MM6	A
7	J162628.8-242233	A-MM7	26:28.80	22:33.6	28.3×19.2	24.3	0.113	1.929	S1	C?	A-MM7	A
8	J162631.4-242446	A-MM8	26:31.44	24:46.8	27.2×17.7	88.3	0.105	1.589	S1	C	A-MM8	A
9	J162621.8-242334	A-MM1	26:21.84	23:34.8	26.5×19.2	3.6	0.026	0.424	N?	C?	A-MM1?	A′
10	J162624.0-242150	A-MM4	26:24.00	21:50.4	27.2×17.7	88.3	0.035	0.525	N	C	A-MM4	A′
11	J162625.2-242136	A-MM4a	26:25.20	21:36.0	14.3×15.7	100.0	0.027	0.191	N	C	-	A′
12	J162645.1-242306	A-MM9	26:45.12	23:06.0	17.1×16.0	80.0	0.063	0.544	Y	P	A-MM9	A′
13	J162621.6-242247	A-MM10	26:21.60	22:48.0	17.8×19.1	174.9	0.085	0.911	Y	P?	A-MM10	A′
14	J162640.3-242710	A-MM15	26:40.32	27:10.8	17.3×15.8	79.5	0.028	0.241	Y	P	A-MM15	A′
15	J162643.4-241724	A-MM18	26:43.44	17:24.0	29.7×22.4	71.0	0.059	1.230	N	C	A-MM18	A′
16	J162624.0-241612	A-MM19	26:24.00	16:12.0	17.6×16.5	80.0	0.070	0.640	N	P	A-MM19	A′
17	J162610.3-242052	A-MM24	26:10.32	20:52.8	17.3×15.8	79.5	0.035	0.306	Y	P	A-MM24	A′
18	J162556.2-242045	A-MM25	25:56.16	20:45.6	17.3×15.8	99.5	0.016	0.139	Y	P	A-MM25	A′
19	J162610.1-241937	A-MM30	26:10.08	19:37.2	22.8×14.5	41.8	0.024	0.247	N	C	A-MM30	A′
20	J162630.5-242212	A-MM31	26:30.48	22:12.0	31.9×19.9	80.7	0.035	0.691	N?	C?	-	A′
21	J162624.0-242432	A-MM32	26:24.00	24:32.4	22.4×14.3	26.1	0.030	0.304	Y	P?	-	A′
22	J162617.3-242345	A-MM33	26:17.28	23:45.6	20.9×15.6	175.1	0.021	0.218	Y	P	-	A′
23	J162631.4-242157	A-MM34	26:31.44	21:57.6	30.0×20.6	90.9	0.038	0.736	S1	C?	-	A′
24	J162648.2-242837	A-MM35	26:48.24	28:37.2	17.3×15.8	99.5	0.007	0.065	Y	P	-	A′
25	J162710.3-241911	A-MM36	27:10.32	19:12.0	17.3×15.8	79.5	0.036	0.313	Y	P	-	A′

Table 3.1: – continued.

Source Index	Full Name JCMTLSG	Source Name	RA 16^h (J2000)	Dec $-$24^h (J2000)	FWHM ($''$)	Angle ($°$)	$F^{peak}_{\nu(850\mu m)}$ (Jy/pix)	$F^{total}_{\nu(850\mu m)}$ (Jy)	IR assn	Type	S08/ NWA06	Region
26	J162611.5-242443	A2-MM1	26:11.52	24:43.2	25.7×16.7	109.1	0.018	0.246	N	C	A2-MM1	A$'$
27	J162618.7-242508	A2-MM2	26:18.72	25:08.4	16.8×16.0	78.8	0.016	0.134	N	C	-	A$'$
28	J162610.1-242309	A3-MM1	26:10.08	23:09.6	29.4×20.1	94.9	0.025	0.474	N?	C?	A3-MM1	A$'$
29	J162712.2-242949	B1-MM3	27:12.24	29:49.2	26.9×19.2	136.6	0.048	0.779	N	C	B1-MM3	B1
30	J162715.1-243039	B1-MM4a	27:15.12	30:39.6	26.2×19.2	114.9	0.050	0.796	N	C	B1-MM4	B1
31	J162715.8-243021	B1-MM4b	27:15.84	30:21.6	19.5×12.9	38.4	0.021	0.165	N	C	-	B1
32	J162716.1-243108	B1-MM5	27:16.08	31:08.4	25.1×17.6	98.3	0.033	0.462	N	C	B1-MM5	B1
33	J162718.0-242851	B1B2-MM2	27:18.00	28:51.6	40.1×14.4	107.7	0.018	0.324	Y	P?	B1B2-MM2	B1B2
34	J162737.2-243032	B1B2-MM3	27:37.20	30:32.4	17.6×19.4	177.7	0.014	0.156	Y	P	-	B1B2
35	J162719.4-242714	B2-MM2a	27:19.44	27:14.4	27.1×18.2	26.8	0.028	0.441	N	C	B2-MM2	B2
36	J162720.6-242656	B2-MM2b	27:20.64	26:56.4	29.6×17.4	172.2	0.032	0.524	N	C	-	B2
37	J162724.2-242750	B2-MM4	27:24.24	27:50.4	14.3×15.7	80.0	0.052	0.365	N	C	B2-MM4	B2
38	J162725.7-242652	B2-MM6	27:25.68	26:52.8	32.6×18.0	156.2	0.077	1.412	N	C	B2-MM6	B2
39	J162727.6-242703	B2-MM8a	27:27.60	27:03.6	27.2×16.6	97.8	0.060	0.844	Y	P?	B2-MM8	B2
40	J162728.6-242703	B2-MM8b	27:28.56	27:03.6	39.1×17.7	152.6	0.043	0.929	Y	P?	B2-MM8	B2
41	J162729.5-242634	B2-MM9	27:29.52	26:34.8	34.5×20.6	150.1	0.072	1.607	N	C	B2-MM9	B2
42	J162729.5-242739	B2-MM10	27:29.52	27:39.6	33.2×18.0	141.6	0.084	1.571	Y	P	B2-MM10	B2
43	J162733.4-242616	B2-MM13	27:33.36	26:16.8	34.9×14.3	38.2	0.083	1.298	N	C	B2-MM13	B2
44	J162732.4-242634	B2-MM14	27:32.40	26:34.8	36.6×19.1	23.3	0.080	1.764	N	C	B2-MM14	B2
45	J162732.6-242703	B2-MM15	27:32.64	27:03.6	25.9×16.3	112.9	0.071	0.945	N	C	B2-MM15	B2
46	J162735.0-242616	B2-MM16	27:35.04	26:16.8	14.3×15.7	100.0	0.076	0.536	N	C	B2-MM16	B2
47	J162732.2-242735	B2-MM17	27:32.16	27:36.0	32.7×20.7	144.3	0.044	0.928	N	P?	-	B2
48	J162659.0-243426	C-MM3	26:59.04	34:26.4	28.8×19.5	117.0	0.041	0.718	N?	C	C-MM3	C
49	J162701.0-243440	C-MM6a	27:00.96	34:40.8	24.5×14.3	151.7	0.022	0.242	N?	C	C-MM6	C
50	J162702.2-243451	C-MM6b	27:02.16	34:51.6	28.3×19.2	48.3	0.018	0.311	N?	C	C-MM6	C

Table 3.1: – continued.

Source Index	Full Name JCMTLSG	Source Name	RA 16^h (J2000)	Dec −24^h (J2000)	FWHM ($''$)	Angle ($°$)	$F_{\nu(850\mu m)}^{peak}$ (Jy/pix)	$F_{\nu(850\mu m)}^{total}$ (Jy)	IR assn	Type	S08/ NWA06	Region
51	J162643.9-243447	C-MM11	26:43.92	34:48.0	17.8×19.1	74.9	0.025	0.271	Y	P?	C-MM11	C
52	J162708.9-243408	C-MM13	27:08.88	34:08.4	17.8×15.6	175.1	0.009	0.078	Y	P	-	C
53	J162704.8-243914	E-MM2d	27:04.80	39:14.4	28.1×15.8	148.4	0.037	0.522	N	C	E-MM2d	E
54	J162709.1-243719	E-MM6	27:09.12	37:19.2	23.2×19.2	155.7	0.035	0.489	Y	P?	E-MM6	E
55	J162705.0-243628	E-MM7	27:05.04	36:28.8	20.9×19.5	80.0	0.025	0.318	Y	P?	E-MM7	E
56	J162706.5-243813	E-MM9	27:06.48	38:13.2	17.6×16.7	80.0	0.020	0.185	Y	P?	E-MM9	E
57	J162715.4-243842	E-MM10	27:15.36	38:42.0	17.3×15.8	79.5	0.018	0.153	Y	P	E-MM10	E
58	J162721.6-243950	F-MM1	27:21.60	39:50.4	14.3×15.7	100.0	0.033	0.232	N	C	F-MM1	F
59	J162724.2-244102	F-MM2b	27:24.24	41:02.4	14.3×15.7	100.0	0.018	0.125	Y	P	F-MM2b	F
60	J162726.6-244048	F-MM3	27:26.64	40:48.0	17.1×19.5	100.0	0.047	0.498	Y	P	F-MM3	F
61	J162727.6-243928	F-MM4	27:27.60	39:28.8	19.8×19.1	175.1	0.030	0.360	Y	P	F-MM4	F
62	J162739.4-243914	F-MM5	27:39.36	39:14.4	17.3×15.8	99.5	0.016	0.139	Y	P	F-MM5	F
63	J162711.0-244044	F-MM10	27:11.04	40:44.4	21.3×13.6	150.1	0.011	0.101	Y	P?	-	F
64	J162738.6-244019	F-MM11	27:38.64	40:19.2	17.6×15.9	80.0	0.009	0.080	Y	P	-	F
65	J162738.2-243657	F-MM12	27:38.16	36:57.6	17.6×15.9	171.5	0.008	0.072	Y	P	-	F
66	J162618.7-242819	J-MM1	26:18.72	28:19.2	17.6×15.9	80.0	0.023	0.207	Y	P	J-MM1	J
67	J162537.9-242233	J-MM7	25:37.92	22:33.6	17.3×15.8	99.5	0.021	0.178	Y	P	J-MM7	J
68	J162623.5-244311	J-MM8	26:23.52	43:12.0	17.3×15.8	86.4	0.051	0.444	Y	P	-	J
69	J162658.3-244536	J-MM9	26:58.32	45:36.0	17.6×15.5	93.6	0.049	0.422	Y	P	-	J
70	J162758.6-243339	H-MM1	27:58.56	33:39.6	29.2×18.5	38.6	0.050	0.845	N	C	-	88
71	J162816.3-243653	H-MM2	28:16.32	36:54.0	17.6×15.9	10.0	0.018	0.160	Y	P	-	88
72	J162821.4-243621	H-MM3	28:21.36	36:21.6	21.8×19.1	105.1	0.036	0.473	Y?	P?	-	88
73	J162845.1-242815	D/H-MM1	28:45.12	28:15.6	17.6×16.4	80.0	0.016	0.141	Y?	P	-	88
74	J162739.1-235819	88N SMM1	27:39.12	58:19.2	19.4×13.3	32.8	0.008	0.066	Y?	?	-	88
75	J163157.1-245714	SMM 8	31:57.12	57:14.4	28.3×19.2	65.7	0.037	0.638	N	C	SMM 8	89S

Table 3.1: – continued.

Source Index	Full Name JCMTLSG	Source Name	RA 16^h (J2000)	Dec −24^h (J2000)	FWHM ($''$)	Angle (°)	$F^{peak}_{\nu(850\mu m)}$ (Jy/pix)	$F^{total}_{\nu(850\mu m)}$ (Jy)	IR assn	Type	S08/ NWA06	Region
76	J163201.0-245641	SMM 9	32:00.96	56:42.0	18.8×16.8	92.8	0.049	0.483	Y	P	SMM 9	89S
77	J163151.6-245620	SMM 11	31:51.60	56:20.4	28.9×19.2	82.8	0.029	0.517	Y	P	SMM 11	89S
78	J163153.5-245558	SMM 12	31:53.52	55:58.8	22.8×14.5	158.2	0.036	0.378	N?	C	SMM 12	89S
79	J163200.2-245544	SMM 13	32:00.24	55:44.4	14.3×15.7	86.2	0.025	0.179	N	C	SMM 13	89S
80	J163137.7-244947	SMM 16a	31:37.68	49:48.0	29.2×18.5	161.4	0.021	0.363	N	C	SMM 16	89S
81	J163138.9-244958	SMM 16b	31:38.88	49:58.8	14.3×15.7	80.0	0.019	0.137	N	C	SMM 16	89S
82	J163142.0-244933	SMM 16c	31:42.00	49:33.6	28.1×16.1	109.9	0.026	0.365	N	C	SMM 16	89S
83	J163355.7-244203	SMM 17	33:55.68	42:03.6	17.8×16.3	15.1	0.017	0.152	Y	P	SMM 17	89E
84	J163228.8-242909	SMM 19	32:28.80	29:09.6	14.3×15.7	80.0	0.154	1.093	N?	C?	SMM 19	89N
85	J163222.6-242833	SMM 20	32:22.56	28:33.6	21.2×19.0	79.5	1.489	18.846	Y?	P	SMM 20	89N
86	J163230.0-242847	SMM 22	32:30.00	28:48.0	23.5×14.3	44.7	0.058	0.611	N?	C	-	89N
87	J163226.6-242811	SMM 23	32:26.64	28:12.0	25.6×21.4	23.6	0.003	0.046	N	C	-	89N
88	J163221.6-242739	SMM 24	32:21.60	27:39.6	22.1×18.8	74.3	0.023	0.295	N?	C	-	89N
89	J163133.4-242735	SMM 25	31:33.36	27:36.0	17.6×16.1	80.0	0.018	0.161	Y?	P	-	89N
90	J163131.2-242624	SMM 26	31:31.20	26:24.0	17.6×15.5	80.0	0.013	0.110	Y?	P	-	89N
91	J163135.5-240126	1709 SMM1	31:35.52	1:26.4	21.0×15.9	82.6	0.073	0.772	Y?	P	-	09
92	J163143.4-240017	1709 SMM2	31:43.44	0:18.0	18.1×16.8	93.5	0.023	0.217	N?	C	-	09
93	J163945.4-240202	1712 SMM1	39:45.36	2:02.4	17.6×17.4	80.0	0.037	0.353	-	P	-	12

in part to the different source-finding criteria used (see discussion on completeness in Section 3.3.2).

Of the sixteen sources in L1689, 13 were uniquely identified sources in the NWA06 catalogue, while the remaining 3 sources were substructure within NWA06 SMM16.

The sources identified by CuTEx were characterised using a custom multiple-Gaussian-fitting code, which models the flux density of sources in crowded regions by fitting a two-dimensional Gaussian to each of a set of associated sources simultaneously. This method uses the source positions and sizes provided by CuTEx as initial input to the fitting routine *mpfit* (Markwardt 2009), along with the model:

$$F(x, y) = a + bx + cy + \sum_{n=1}^{N} A_n e^{-\frac{1}{2}\left(\left(\frac{x'_n}{\sigma_{x,n}}\right)^2 + \left(\frac{y'_n}{\sigma_{y,n}}\right)^2\right)} \tag{3.1}$$

where

$$x'_n = (x - x_{0,n})\cos(\theta_n) - (y - y_{0,n})\sin(\theta_n) \tag{3.2a}$$

$$y'_n = (x - x_{0,n})\sin(\theta_n) + (y - y_{0,n})\cos(\theta_n) \tag{3.2b}$$

and N is the number of sources to be fitted simultaneously.

Sources are considered to be neighbours if they are separated by less than twice the FWHM of the larger source. Groups to be fitted simultaneously are defined such that each source in a group is a neighbour to at least one other source in the group, and no source has any neighbours outside of the group, with isolated sources considered as being in a one-member group. For each group, the local background is fitted as an inclined plane with coefficients a, b and c, while for each Gaussian, the peak flux density A, central coordinates x_0 and y_0, semi-major and semi-minor axes σ_x and σ_y, and position angle θ, are fitted. In order to accurately fit $6N + 3$ parameters for each group, *mpfit* was constrained such that for each source, $A > 0$, Δx_0 and $\Delta y_0 \leq 6''$, $\Delta \sigma_x$ and $\Delta \sigma_y \leq 10\%$, and $\Delta \theta \leq 5°$, where Δ signifies the amount that the quantity is allowed to vary from its initial value supplied by CuTEx. The fitted quantities do not hit the borders of the allowed parameter space. CuTEx

Table 3.2: Protostellar sources in Ophiuchus, with alternate identifications and classes, where known. EESG09 – Enoch et al. 2009; WGA08 – Wilking et al. 2008; AM94 – André & Montmerle 1994; DoAr – Dolidze & Arakelyan 1959; VSSG – Vrba et al. 1975; WL – Wilking & Lada 1983; YLW – Young et al. 1986, LFAM – Leous et al. 1991; GY – Greene & Young 1992; GWAYL – Greene et al. 1994; ISO-Oph – Bontemps et al. 2001; EESG09 Oph-emb – Enoch et al. (2009); EDJ2009 – Evans et al. 2009. Note that in WGA08 classifications, Arabic numerals indicate a class determined from an IRAC SED while Roman numerals indicate a class determined from a 3.6-24μm spectral index. F indicates a flat spectrum.

Source Index	Source ID	Alternative ID	Class	Class Reference
4	VLA 1623	EESG09 Oph-emb 3	0	EESG09
12	A-MM9	GY 116, VSSG 28, ISO-Oph 67	2,II	WGA08
13	A-MM10	LFAM 1, ISO-Oph 31	F,-	WGA08
14	A-MM15	GY 91, ISO-Oph 54, EESG09 Oph-emb 22	I	EESG09
16	A-MM19	YLW 32 ISO-Oph 40	II	AM94
17	A-MM24	ISO-Oph 17	2,II	WGA08
18	A-MM25	DoAr 20, YLW 25, ISO-Oph 6	II	AM94
21	A-MM32	GY 21, LFAM 3, ISO-Oph 37	F,F	WGA08
22	A-MM33	ISO-Oph 21	1,I	WGA08
24	A-MM35	GY 128, ISO-Oph 7, EESG09 Oph-emb 23	I	EESG09
25	A-MM36	SR 21(A?), YLW 8(A?), ISO-Oph 110	2,-	WGA08
33	B1B2-MM2	YLW 12A/B?, ISO-Oph 124/125?, EESG09 Oph-emb 11	I	EESG09
34	B1B2-MM3	YLW 46, GY 304, ISO-Oph 159	2,-	WGA08
39	B2-MM8a	GPJ2008 8		
40	B2-MM8b	YEE2006 20		
42	B2-MM10	GY 279, ISO-Oph 147, EESG09 Oph-emb 26	I	EESG09
47	B2-MM17	WLY 1-17?		
51	C-MM11	WL 12, YLW 2, ISO-Oph 65	1,-	WGA08
52	C-MM13	WL10, GY 211, ISO-Oph 105	2,II	WGA08
54	E-MM6	WL 15, ISO-Oph 108, EESG09 Oph-emb 16	I	EESG09
55	E-MM7	GY 197, ISO-Oph 99, EESG09 Oph-emb 6	1,I	WGA08
56	E-MM9	GY 205, ISO-Oph 103, EESG09 Oph-emb 12	I	EESG09
57	E-MM10	WL 20W/E?, GY 240A/B? ISO-Oph 121	-,-/2,-	WGA08
59	F-MM2b	GY 263, EESG09 Oph-emb 12	I	EESG09
60	F-MM3	GY 265, ISO-Oph 141, EESG09 Oph-emb 14	I	EESG09

Table 3.2: – continued.

Source Index	Source ID	Alternative ID	Class	Class Reference
61	F-MM4	GY 269, ISO-Oph 143, EESG09 Oph-emb 13	I	EESG09
62	F-MM5	GY 314, ISO-Oph 166	2,F	WGA08
63	F-MM10	GY 224, ISO-Oph 112	F,F	WGA08
64	F-MM11	GY 312, ISO-Oph 165	1,I	WGA08
65	F-MM12	YLW 47, GY 308, ISO-Oph 163	2,II	WGA08
66	J-MM1	YLW31, VSSG 1, ISO-Oph 24	F,II	WGA08
67	J-MM7	ISO-Oph 2		
68	J-MM8	DoAr 25, YLW 34, ISO-Oph 38	II	AM94
69	J-MM9	DoAr 29, ISO-Oph 88	II	AM94
71	H-MM2	YLW 58, ISO-Oph 196	II	AM94
72	H-MM3	EDJ2009 954, EESG09 Oph-emb 1	0	EESG09
73	D/H-MM1	DoAr40	II	AM94
74	88N SMM1	DoAr 33	II?	AM94
76	SMM 9	GWAYL 6, ISO-Oph 209, EESG09 Oph-emb 10	I	EESG09
77	SMM 11	GWAYL 5?, ISO-Oph 204? LDN 1689 IRS 5?		
83	SMM 17	EDJ2009 1013		
85	SMM 20	IRAS 16293-2422B, EESG09 Oph-emb 2	0	EESG09
89	SMM 25	DoAr 44	II	AM94
90	SMM 26	EDG2009 984		
91	1709 SMM1	GWAYL 4, EDJ2009 989, EESG09 Oph-emb 17	I	EESG09
93	1712 SMM1	IRAS 16367-2356, EDJ2009 989		

detects signal in the second derivatives of the input map, and hence can determine source sizes and orientations accurately, as it is sensitive to changes in gradient.

Our sources are listed in Table 3.1. In L1688, we continue the naming convention introduced by MAN98 and used by S08, while in L1689 we continue the naming convention of NWA06. For each source, we list: the index of the source; the name of the source using the official IAU naming convention; the name by which we refer to the source in the text; central right ascension and declination; position angle of the ellipse fitted to the source measured east of north; major and minor FWHMs; best-fit model peak flux density and total 850-µm flux density of the background-subtracted source; whether the source has associated emission in the *Herschel* 70-µm data (a listing of 'S1' indicating that the IR emission at the source location is likely to be due to the reflection nebula associated with the star S1); our evaluation of whether the source is starless or protostellar ('C' indicating a starless core and 'P' indicating a protostellar source; classification criteria and question-marked sources are discussed below); the source's identity in the S08 or NWA06 catalogues (if relevant); and the region in which the source is located. Our sources are marked on Figure 3.1 as open circles, coloured according to region: red for the central Oph A region, (defined as the region contiguous with the prestellar source SM1 where $F^{peak}_{\nu(850\mu\mathrm{m})} > 0.6\,\mathrm{Jy}/6''\,\mathrm{pixel}$); orange for the more diffuse material around Oph A, hereafter referred to as Oph A′; dark green for Oph B1; light green for Oph B2; blue-green for the intermediate region Oph B1B2; blue for Oph C; dark purple for Oph E; light purple for Oph F; and white for all other regions. This identification of region by colour is used throughout the rest of this chapter, except that cores marked in white in Figure 3.1 are elsewhere marked in black.

We judge whether a source is starless or protostellar by considering whether its morphology appears to be point-like or extended at 850µm, whether it has associated 70-µm emission (see, e.g. Könyves et al. 2010), and the shape of its spectral energy

distribution. The first two criteria are of the most importance, as in principle a protostellar source detectable at 850μm should have a point-like morphology at both 850μm and 70μm. The SED shape should then confirm the identification. However, in practice, each of these criteria has limitations. While a point-like morphology is a good indicator of an unresolved protostellar source, an extended morphology at 850-μm does not preclude the presence of a protostar, deeply embedded or otherwise confused with emission from cold gas along the same line of sight. Extended emission from warm gas may confuse identification of protostars by the presence of 70-μm emission at their position, particularly in the dense gas in Oph A being heated at its surface by the star S1 (there is a reflection nebula at this location when observed at shorter wavelengths – see the 8-μm emission in Figure 3.3). 70-μm associations likely to be caused by material heated by S1 are noted in Table 3.1. Similarly, a rising SED at short wavelengths indicates a high-temperature object, possibly a protostellar envelope, but may also be caused by the presence of warm material along the line of sight not directly associated with the source. In order to clarify these identifications, we also investigated whether there is a previously-identified protostar present within one 850-μm JCMT beam size (14.1″) of each of our source positions. This criterion was generally used only to confirm the identification made using the observational criteria listed above. However, in some cases it became necessary to use the presence or absence of a previously-identified protostar as the deciding criterion when classifying a source, particularly in crowded regions with substantial IR contamination. Previously-known protostars were located using the SIMBAD astronomical database (Wenger et al. 2000). Those sources we identify as protostellar are listed in Table 3.2, with alternative identifications and, where known, evolutionary class. Source 93/L1712 SMM1, for which *Herschel* data are not available, was catagorised as protostellar based on its 850-μm morphology and identification with the protostar IRAS 16367-2356 (see Table 3.2).

For the majority of our sources, a consistent classification can be made from each of our criteria. However, where this is not the case, our classifications in Table 3.1 are followed by question marks. In the case of a 'C?' listing, this indicates that while all other criteria suggest that this is a starless core, there is some 70-μm emission at the location of the source. In the case of a 'P?' listing, this indicates that while the source can be identified with a known protostar, one or more of the selection criteria – typically, a non-point-like morphology – suggests that the source might be extended. A queried classification indicates a slight conflict between our classification criteria, rather than substantial doubt about the nature of the source.

Hereafter, 'source' refers to any object in our catalogue, regardless of its classification; 'protostar' refers to an object in our catalogue identified either as a pre-main-sequence star or as containing an embedded protostellar source (those sources listed as 'P' or 'P?' in Table 3.1); and 'core' refers exclusively to those objects in our catalogue identified as starless cores ('C' or 'C?' in Table 3.1).

3.3.2 Source completeness

CuTEx detects sources through signal in the second derivative of the original map. As a result, source detection is a function of both peak flux density and source FWHM, with sharply peaked sources being recovered better than extended sources with the same peak flux density. To test the completeness of our set of sources, we injected 50 identical Gaussian sources at random positions in the CO-subtracted SCUBA-2 850-μm map of L1688, and attempted to recover these with CuTEx. We repeated this process for various source sizes and peak flux densities. For each source size and peak flux density, we repeated the source injection and recovery process ten times, and took the completeness fraction to be the mean fraction of sources recovered.

For our mean non-deconvolved source FWHM of 19.7″, CuTEx recovered 50% of

injected sources with a peak flux density of 0.011 Jy/6″ pixel, and 80% with a peak flux density of 0.020 Jy/6″ pixel. At our mean source temperature of ~ 13.5 K, these peak flux densities are equivalent to masses of 0.040 M$_\odot$ (50%) and 0.051 M$_\odot$ (80%) (see Section 3.3.3 for a discussion of determination of temperatures and derivation of masses). The 80% completeness limit at 13.5 K as a function of deconvolved source FWHM is shown as a solid line on Figure 3.8, below.

The completeness limit in crowded regions of emission will be slightly higher and less certain than the completeness limit in sparsely populated regions, as in crowded regions tightly-packed or superimposed sources must be separated. In regions of the SCUBA-2 850-µm map where $F_\nu > 10\sigma$, we found a 50% mass completeness limit of 0.047 ± 0.005 M$_\odot$ at 13.5 K, approximately consistent with, but slightly more uncertain than, the completeness limit across the map as a whole. We note that completeness is likely to vary somewhat across the map, and that the completeness limits given above and shown on Figure 3.8 are average values.

3.3.3 Source characterisation from continuum data

Table 3.3 lists the properties of our set of sources derived from SCUBA-2 and *Herschel* continuum data. The deconvolved FWHMs of the sources were determined using the SCUBA-2 850-µm equivalent beam size of 14.1″ (Dempsey et al. 2013). The equivalent radius of each source was calculated as the geometric mean of the two deconvolved FWHMs.

The data at 160 µm, 450 µm and 850 µm were convolved to the 250-µm resolution of 18″ using the convolution kernels described above. Flux densities were measured from the spatially filtered *Herschel* 160-µm and 250-µm data and the two sets of SCUBA-2 data using elliptical apertures with major and minor axis diameters of twice the measured (i.e. non-deconvolved) major and minor FWHMs of each of the sources (enclosing 99.5% of the total flux density in a Gaussian distribution). The
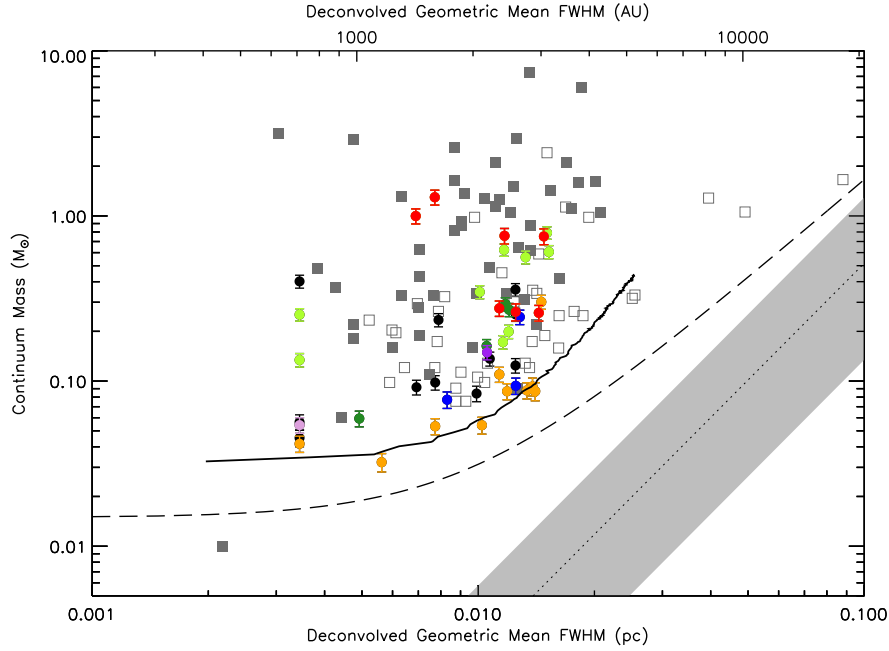
Figure 3.8: Comparison of the masses of our starless cores, calculated from the continuum data, with their deconvolved radii. Circles with error bars: this study. Open squares: MAN98. Filled squares: S08. Grey band: $M_{\mathrm{co}} \propto R_{\mathrm{co}}^{2.35}$ relation (Elmegreen & Falgarone 1996). Solid line: 80% completeness limit. Dashed line: 5σ sensitivity limit. Both limits assume a temperature of $13.5\,\mathrm{K}$. Red symbols are cores in Oph A; orange, Oph A′; dark green, Oph B1; light green, Oph B2; blue, Oph C; dark purple, Oph E; light purple, Oph F; black, elsewhere in the cloud.

resulting SED of each source was fitted with a modified blackbody distribution, in order to determine the mean column-density-weighted line-of-sight dust temperature of our sources. The monochromatic flux density F_ν at frequency ν is given by

$$\nu F_\nu = \lambda F_\lambda = \nu \Omega f B_\nu(T) \left(1 - e^{-\left(\frac{\nu}{\nu_c}\right)^\beta}\right), \tag{3.3}$$

where $B_\nu(T)$ is the Planck function at dust temperature T, Ω is the solid angle of the aperture, f is the filling factor of the source in the aperture, $\nu_c = 6\,\text{THz}$ is the frequency at which the optical depth is taken to become unity (Ward-Thompson et al. 2002), and β is the dust emissivity index, here taken to be 2.0. This value is consistent with recent studies of nearby molecular clouds (e.g. André et al. 2010; Kirk et al. (2013)) and produces SED fits which are a good model for both the SCUBA-2 and the Herschel data.

This process allows determination of the average temperature of the material within the aperture. There will be be some line-of-sight confusion between cold dust associated with the source (which will itself not be isothermal) and warmer foreground and background emission, possibly leading to an overestimation of source temperatures. However, the spatial filtering introduced by the SCUBA-2 data reduction process should reduce the contamination from extended emission. In crowded regions in which sources overlap significantly, the measured flux densities may be contaminated by emission from neighbouring sources. We emphasise that the temperatures reported here are line-of-sight averages.

Masses were calculated from the best-fit model 850-μm flux densities and dust temperatures of our sources following the Hildebrand (1983) formulation

$$M = \frac{F_{\nu(850\mu m)} D^2}{\kappa_{\nu(850\mu m)} B_{\nu(850\mu m)}(T)}, \tag{3.4}$$

where $F_{\nu(850\mu m)}$ is the modelled total flux density at 850-μm, D is the distance to Ophiuchus ($139 \pm 6\,\text{pc}$; Mamajek 2008), $B_{\nu(850\mu m)}(T)$ is the value of the Planck function at 850μm, and $\kappa_{\nu(850\mu m)}$ is the total 850μm dust mass opacity, as parameterised by Beckwith et al. (1990): $\kappa_\nu = 0.1(\nu/10^{12}\text{Hz})^\beta\,\text{cm}^2\text{g}^{-1}$ (assuming a standard

dust-to-gas ratio of 1:100). Again, the dust emissivity index β was taken to be 2.0.

For the protostellar sources in our catalogue, the temperatures, and hence the masses, determined from the dust emission, are those of the protostellar envelope, and not of the protostar itself. The modified blackbody model used to fit temperatures is applicable only to envelope-dominated sources; the temperatures and masses determined for the Class II protostars in our catalogue (listed in Table 3.2) may not be representative.

The mean volume density for each source was calculated assuming that the third axis of each source is the geometric mean of its major and minor axes. Then, the number density of molecular hydrogen $n(\text{H}_2)$ is calculated as

$$n(\text{H}_2) = \frac{M}{\mu m_{\text{H}}} \frac{1}{\frac{4}{3}\pi R^3}, \tag{3.5}$$

where R is the equivalent deconvolved radius, as defined above. Similarly, the column density of molecular hydrogen $N(\text{H}_2)$ of each source is calculated as

$$N(\text{H}_2) = \frac{M}{\mu m_{\text{H}}} \frac{1}{\pi R^2}, \tag{3.6}$$

and in both cases, the mean molecular weight μ is taken to be 2.86, assuming that the gas is $\sim 70\%$ H_2 by mass (Kirk et al. 2013). Hereafter, 'number density' and 'column density' refer to the number density and column density of molecular hydrogen, unless specifically stated otherwise.

One of our sources, SMM 23, located in the centre of L1689N, has a very low best-fit peak flux density, 0.003 Jy/6″ pixel. This is due to SMM 23 being located between SMM 20/IRAS 16293-2422 and SMM 19, the brightest and second-brightest sources in L1689N respectively, leading to the majority of flux at SMM 23's position being assigned to the two nearby bright sources in the fitting process. We consider SMM 23 to be robustly detected by CuTEx, and so determine its temperature and mass. However, due to its properties being poorly constrained by the fitting process, we exclude SMM 23 from all subsequent analysis, leaving 46 starless cores for further study.

3.3.4 Source mass distribution

Figure 3.8 shows the distribution of mass with size for the starless cores (those objects marked 'C' and 'C?' in Table 3.1) in our sample, compared with previous studies of the same region: MAN98 (with their masses and radii scaled to account for their assumption of a distance of 160 pc) and S08. Our cores are comparable in size to those found in previous studies. The masses of the cores in our sample are comparable to those found by MAN98, while the masses found by S08 are typically higher.

The grey band shown in Figure 3.8 indicates the behaviour expected for transient, gravitationally unbound CO clumps (Larson 1981; Elmegreen & Falgarone 1996). Gravitationally-bound prestellar cores are expected to occupy the upper part of the mass/size diagram (Motte et al. 2001), being over-dense compared to transient, unbound structures.

Before Herschel, there was discussion of whether starless and prestellar cores are two different populations, separated in the mass/size plane (see, e.g. Ward-Thompson et al. 2007, and references therein). Herschel studies have found cores occupying intermediate locations in the mass/size plane (Könyves et al. 2010; Kirk et al. 2013), indicating that prestellar and unbound starless cores are all part of the same population. Our cores are restricted to the 'prestellar' region in which previous studies have found the cores in L1688 to lie (MAN98, S08). The limit on our ability to recover faint sources is the CuTEx completeness limit. The 80% completeness limit, as a function of source size (at a temperature of 13.5 K), is shown as a solid line on Figure 3.8. However, the 5σ sensitivity limit of the SCUBA-2 850-μm data (again for a temperature of 13.5 K), shown as a dashed line on Figure 3.8, is such that regardless of our choice of source extraction algorithm, we are not sensitive to material occupying the 'unbound' regions of the mass/size plane.

Figure 3.9 shows the mass distribution of our cores. The mass distribution is
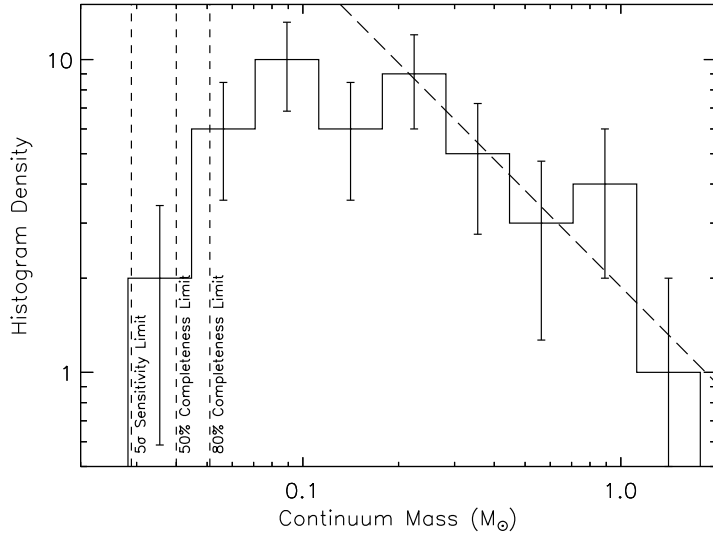
Figure 3.9: Core mass distribution, with best-fitting power-law index $\alpha = 2.0 \pm 0.4$ for cores with masses $> 0.2 \, M_\odot$ plotted as a dashed line. The 5σ sensitivity limit and 50% and 80% completeness limits for a temperature of $13.5 \, K$ are also shown.

consistent with the log-normal + power-law distribution expected for core mass functions (CMFs – Chabrier 2003), and previously seen in Ophiuchus by MAN98 and S08. We fitted a function of the form $N \propto M^{-\gamma}$ to the mass distribution, and found that, for bins centred on masses greater than or equal to 0.2 $M_\odot$, the best-fitting power-law index was $\gamma = 1.0 \pm 0.4$, equivalent to a CMF power-law index of $\alpha = \gamma + 1 = 2.0 \pm 0.4$.

Figure 3.9 shows an apparent flattening of the mass distribution at lower core masses. This flattening occurs at core masses above the completeness limit determined in Section 3.3.2. While the deviation of the mass distribution from power-law behaviour at low masses is not highly significant (see the error bars on Figure 3.9), we consider it to be real, as the onset of the flattening occurs at $\sim 0.2 \, M_\odot$, significantly above our 80 percent completeness limit of $0.051 \, M_\odot$, and because the flattening is consistent with both the expected behaviour of the low-mass core mass function (e.g. Chabrier 2003; Offner et al. 2014) and the observed behaviour of the core mass function determined in previous studies of Ophiuchus (MAN98; S08).

The traditional method of determining the power-law index of the CMF by fitting to binned data is liable to lead to a loss of accuracy in the fitted model. We attempted to ameliorate this issue by also analysing the cumulative distribution function of core masses using the maximum likelihood estimator for an infinite power-law distribution (Koen 2006; Maschberger & Kroupa 2009), calculated over the same mass range ($M \geq 0.2 M_{\odot}$). The cumulative distribution and fits are shown in Figure 3.10. The empirical cumulative distribution function $\hat{F}$ is given, for the ith data point in our sample, by

$$\hat{F}(X_i) \equiv \frac{i}{n+1}, \tag{3.7}$$

where n is the number of data points X. The maximum likelihood (ML) estimator for the exponent α of an infinite power-law distribution is

$$\alpha_{ml} = 1 + \frac{n}{\left(\sum_{i=1}^{n} X_i\right) - n\ln\left(\min(X)\right)}. \tag{3.8}$$

The unbiased maximum likelihood (UML) estimator, α_{uml} is then

$$\alpha_{uml} = 1 + \frac{n-1}{n}(\alpha_{ml} - 1). \tag{3.9}$$

The CMF power-law index found by this method was $\alpha_{uml} = 2.7 \pm 0.4$. Uncertainties were estimated by performing a set of Monte Carlo experiments, drawing a set of data points randomly from our distribution of masses, from which α_{ml} was recalculated. The error quoted is the standard deviation of the distribution of α_{uml} which results from this procedure.

The mean of α and α_{uml} is 2.35±0.3, in agreement with the power-law index of the high-mass tail of the IMF, $\alpha = 2.35$ (Salpeter 1955; Kroupa 2001.) In both cases, the power-law index is consistent with the high-mass power-law tail of the IMF. That our two estimators for the power-law index only marginally agree with one another is likely to be a result of low number statistics.

Previous studies of the starless core population of Ophiuchus have found similar slopes for the high-mass distribution of core masses. MAN98 found a slope of $\alpha \sim 2.5$
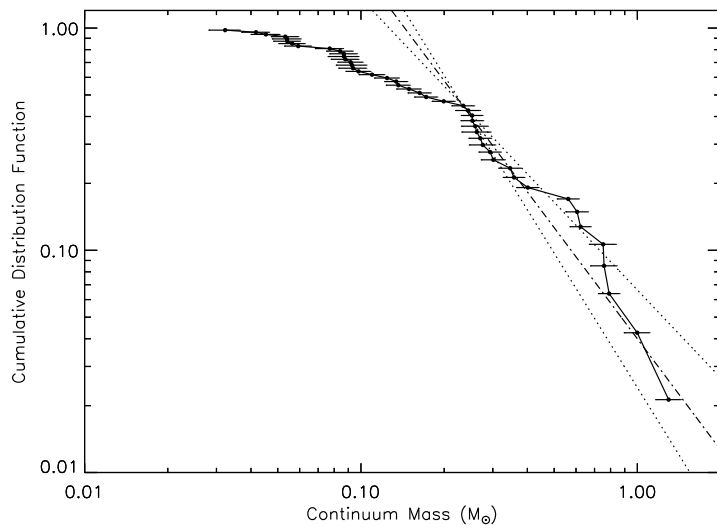
Figure 3.10: Cumulative mass distribution function, with unbiased maximum likelihood estimator power-law index $\alpha_{uml} = 2.7$ for cores with masses $> 0.2\,\mathrm{M}_\odot$ plotted as a dot-dashed line, and its $1\sigma \pm 0.4$ error limits plotted as dotted lines.

in the mass range 0.5–$3.0\,\mathrm{M}_\odot$. Johnstone et al. (2000) found a similar behaviour: $\alpha = 2.0 - 2.5$ for $M > 0.6\,\mathrm{M}_\odot$. Sadavoy et al. (2010) found a power-law slope of $\alpha = 2.26 \pm 0.20$ in the mass range $0.3\,\mathrm{M}_\odot < M < 5\,\mathrm{M}_\odot$. Our mass functions are consistent with the behaviour found by MAN98, Johnstone et al. (2000), and Sadavoy et al. (2010).

We conclude that our CMF is consistent with having a high-mass slope similar to that of the IMF, and with the CMFs found by previous studies of the same region. The similarity between the CMF and IMF has been noted in many recent studies of molecular clouds (e.g. Nutter & Ward-Thompson 2007), leading to suggestions that the form of the IMF is caused by cloud fragmentation prior to the prestellar core stage of star formation (see, e.g., André et al. 2014, and references therein).

Table 3.3: Properties derived from SCUBA-2 and Herschel data (see text for discussion).

Source Index	Source ID	Temperature (K)	850-μm Mass ($M_\odot$)	H_2 Column Density ($\times 10^{22}$ cm^{-2})	H_2 Volume Density ($\times 10^6$ cm^{-3})
1	SM1	17.2 ± 0.6	1.298 ± 0.134	30.520 ± 3.161	9.609 ± 0.995
2	SM1N	17.3 ± 0.6	0.999 ± 0.104	29.477 ± 3.077	10.398 ± 1.085
3	SM2	18.5 ± 0.7	0.758 ± 0.082	7.758 ± 0.837	1.612 ± 0.174
4	VLA 1623	16.4 ± 0.5	1.158 ± 0.117	19.788 ± 2.006	5.311 ± 0.538
5	A-MM5	18.6 ± 0.7	0.259 ± 0.028	1.761 ± 0.192	0.298 ± 0.032
6	A-MM6	18.8 ± 0.8	0.752 ± 0.083	4.810 ± 0.529	0.790 ± 0.087
7	A-MM7	21.7 ± 1.0	0.262 ± 0.031	2.348 ± 0.278	0.456 ± 0.054
8	A-MM8	18.4 ± 0.7	0.276 ± 0.030	3.003 ± 0.322	0.643 ± 0.069
9	A-MM1	16.6 ± 0.6	0.087 ± 0.010	0.860 ± 0.096	0.176 ± 0.020
10	A-MM4	16.3 ± 0.5	0.110 ± 0.011	1.194 ± 0.125	0.256 ± 0.027
11	A-MM4a	15.9 ± 0.5	0.042 ± 0.005	4.918 ± 0.555	3.468 ± 0.392
12	A-MM9	10.2 ± 0.2	0.268 ± 0.025	11.071 ± 1.053	4.621 ± 0.440
13	A-MM10	19.5 ± 0.9	0.144 ± 0.017	3.137 ± 0.360	0.950 ± 0.109
14	A-MM15	13.6 ± 0.4	0.069 ± 0.008	2.812 ± 0.311	1.167 ± 0.129
15	A-MM18	14.8 ± 0.4	0.301 ± 0.029	1.988 ± 0.194	0.332 ± 0.032
16	A-MM19	9.3 ± 0.3	0.382 ± 0.042	12.759 ± 1.399	4.788 ± 0.525
17	A-MM24	15.5 ± 0.5	0.070 ± 0.008	2.858 ± 0.309	1.186 ± 0.128
18	A-MM25	16.2 ± 0.6	0.030 ± 0.004	1.206 ± 0.172	0.501 ± 0.071
19	A-MM30	16.0 ± 0.5	0.053 ± 0.006	1.245 ± 0.139	0.391 ± 0.044
20	A-MM31	22.9 ± 1.2	0.087 ± 0.011	0.616 ± 0.077	0.106 ± 0.013
21	A-MM32	15.5 ± 0.5	0.069 ± 0.008	1.740 ± 0.197	0.568 ± 0.064
22	A-MM33	16.0 ± 0.5	0.047 ± 0.006	1.144 ± 0.134	0.365 ± 0.043
23	A-MM34	22.8 ± 1.2	0.093 ± 0.012	0.680 ± 0.085	0.119 ± 0.015
24	A-MM35	10.0 ± 0.2	0.033 ± 0.006	1.368 ± 0.238	0.568 ± 0.099
25	A-MM36	14.7 ± 0.5	0.078 ± 0.009	3.188 ± 0.366	1.324 ± 0.152

Table 3.3: – continued.

Source Index	Source ID	Temperature (K)	850-μm Mass ($M_\odot$)	H_2 Column Density ($\times 10^{22}$ cm^{-2})	H_2 Volume Density ($\times 10^6$ cm^{-3})
26	A2-MM1	15.8 ± 0.5	0.054 ± 0.006	0.724 ± 0.085	0.172 ± 0.020
27	A2-MM2	15.0 ± 0.4	0.032 ± 0.004	1.429 ± 0.183	0.618 ± 0.079
28	A3-MM1	17.6 ± 0.7	0.088 ± 0.010	0.687 ± 0.077	0.125 ± 0.014
29	B1-MM3	12.2 ± 0.3	0.270 ± 0.025	2.618 ± 0.240	0.529 ± 0.049
30	B1-MM4a	11.8 ± 0.2	0.293 ± 0.026	2.972 ± 0.267	0.614 ± 0.055
31	B1-MM4b	11.9 ± 0.3	0.059 ± 0.006	3.431 ± 0.375	1.695 ± 0.185
32	B1-MM5	12.1 ± 0.3	0.163 ± 0.015	2.066 ± 0.193	0.477 ± 0.045
33	B1B2-MM2	15.8 ± 0.5	0.071 ± 0.008	0.580 ± 0.066	0.107 ± 0.012
34	B1B2-MM3	16.4 ± 0.8	0.032 ± 0.005	0.693 ± 0.107	0.208 ± 0.032
35	B2-MM2a	11.4 ± 0.2	0.172 ± 0.016	1.795 ± 0.169	0.376 ± 0.035
36	B2-MM2b	11.6 ± 0.2	0.199 ± 0.019	1.941 ± 0.180	0.393 ± 0.037
37	B2-MM4	11.8 ± 0.3	0.134 ± 0.013	15.826 ± 1.481	11.162 ± 1.045
38	B2-MM6	11.3 ± 0.2	0.562 ± 0.050	4.477 ± 0.399	0.820 ± 0.073
39	B2-MM8a	13.5 ± 0.4	0.243 ± 0.024	2.975 ± 0.289	0.676 ± 0.066
40	B2-MM8b	13.8 ± 0.4	0.258 ± 0.025	1.613 ± 0.159	0.262 ± 0.026
41	B2-MM9	11.6 ± 0.3	0.606 ± 0.055	3.651 ± 0.334	0.582 ± 0.053
42	B2-MM10	15.8 ± 0.5	0.345 ± 0.035	2.676 ± 0.268	0.484 ± 0.049
43	B2-MM13	10.3 ± 0.2	0.623 ± 0.053	6.408 ± 0.546	1.334 ± 0.114
44	B2-MM14	10.7 ± 0.2	0.791 ± 0.068	4.875 ± 0.421	0.786 ± 0.068
45	B2-MM15	11.8 ± 0.3	0.346 ± 0.031	4.763 ± 0.431	1.147 ± 0.104
46	B2-MM16	10.4 ± 0.2	0.252 ± 0.022	29.785 ± 2.584	21.008 ± 1.823
47	B2-MM17	13.4 ± 0.3	0.272 ± 0.026	1.756 ± 0.168	0.290 ± 0.028
48	C-MM3	12.3 ± 0.3	0.244 ± 0.025	2.083 ± 0.210	0.395 ± 0.040
49	C-MM6a	12.8 ± 0.4	0.077 ± 0.009	1.564 ± 0.179	0.457 ± 0.052
50	C-MM6b	13.2 ± 0.4	0.094 ± 0.011	0.837 ± 0.095	0.163 ± 0.018

Table 3.3: – continued.

Source Index	Source ID	Temperature (K)	850-μm Mass ($M_\odot$)	H_2 Column Density ($\times 10^{22}$ cm^{-2})	H_2 Volume Density ($\times 10^6$ cm^{-3})
51	C-MM11	13.5 ± 0.4	0.078 ± 0.008	1.694 ± 0.180	0.513 ± 0.054
52	C-MM13	15.0 ± 0.5	0.019 ± 0.003	0.720 ± 0.129	0.291 ± 0.052
53	E-MM2d	13.6 ± 0.4	0.149 ± 0.015	1.879 ± 0.187	0.433 ± 0.043
54	E-MM6	20.1 ± 0.9	0.074 ± 0.009	0.933 ± 0.111	0.215 ± 0.025
55	E-MM7	16.1 ± 0.6	0.068 ± 0.008	0.999 ± 0.113	0.249 ± 0.028
56	E-MM9	15.0 ± 0.5	0.045 ± 0.005	1.433 ± 0.173	0.528 ± 0.064
57	E-MM10	16.3 ± 0.6	0.032 ± 0.004	1.306 ± 0.172	0.542 ± 0.071
58	F-MM1	15.3 ± 0.5	0.054 ± 0.006	6.381 ± 0.691	4.501 ± 0.488
59	F-MM2b	15.6 ± 0.5	0.028 ± 0.004	3.307 ± 0.427	2.333 ± 0.301
60	F-MM3	16.7 ± 0.6	0.101 ± 0.011	2.294 ± 0.246	0.711 ± 0.076
61	F-MM4	20.0 ± 0.9	0.055 ± 0.007	0.952 ± 0.114	0.257 ± 0.031
62	F-MM5	11.1 ± 0.3	0.057 ± 0.008	2.344 ± 0.321	0.973 ± 0.133
63	F-MM10	12.9 ± 0.3	0.031 ± 0.005	1.066 ± 0.155	0.403 ± 0.059
64	F-MM11	8.7 ± 0.2	0.055 ± 0.010	2.093 ± 0.367	0.836 ± 0.146
65	F-MM12	13.5 ± 0.4	0.021 ± 0.004	0.788 ± 0.147	0.315 ± 0.059
66	J-MM1	8.3 ± 0.2	0.161 ± 0.020	6.099 ± 0.756	2.435 ± 0.302
67	J-MM7	8.9 ± 0.3	0.116 ± 0.015	4.741 ± 0.628	1.968 ± 0.261
68	J-MM8	10.3 ± 0.3	0.212 ± 0.022	8.656 ± 0.911	3.593 ± 0.378
69	J-MM9	11.8 ± 0.3	0.155 ± 0.017	6.519 ± 0.700	2.747 ± 0.295
70	H-MM1	11.0 ± 0.2	0.358 ± 0.031	3.214 ± 0.282	0.626 ± 0.055
71	H-MM2	11.5 ± 0.3	0.062 ± 0.007	2.340 ± 0.282	0.934 ± 0.113
72	H-MM3	12.5 ± 0.3	0.156 ± 0.015	2.216 ± 0.213	0.542 ± 0.052
73	D/H-MM1	10.5 ± 0.3	0.065 ± 0.009	2.234 ± 0.296	0.850 ± 0.113
74	88N SMM1	8.2 ± 0.3	0.053 ± 0.011	2.800 ± 0.605	1.322 ± 0.286
75	SMM 8	11.3 ± 0.2	0.253 ± 0.023	2.263 ± 0.207	0.440 ± 0.040

Table 3.3: – continued.

Source Index	Source ID	Temperature (K)	850-μm Mass ($M_\odot$)	H_2 Column Density ($\times 10^{22}$ cm^{-2})	H_2 Volume Density ($\times 10^6$ cm^{-3})
76	SMM 9	19.0 ± 0.8	0.080 ± 0.009	2.125 ± 0.245	0.712 ± 0.082
77	SMM 11	14.6 ± 0.4	0.131 ± 0.013	1.126 ± 0.114	0.215 ± 0.022
78	SMM 12	14.3 ± 0.4	0.098 ± 0.010	2.292 ± 0.230	0.720 ± 0.072
79	SMM 13	12.8 ± 0.3	0.056 ± 0.006	6.654 ± 0.712	4.693 ± 0.502
80	SMM 16a	12.3 ± 0.3	0.124 ± 0.013	1.116 ± 0.112	0.217 ± 0.022
81	SMM 16b	12.5 ± 0.3	0.045 ± 0.005	5.341 ± 0.624	3.767 ± 0.440
82	SMM 16c	11.7 ± 0.3	0.136 ± 0.013	1.664 ± 0.162	0.377 ± 0.037
83	SMM 17	10.5 ± 0.3	0.070 ± 0.009	2.357 ± 0.295	0.886 ± 0.111
84	SMM 19	11.8 ± 0.3	0.402 ± 0.036	47.367 ± 4.264	33.409 ± 3.007
85	SMM 20	17.4 ± 0.7	3.555 ± 0.393	53.954 ± 5.961	13.649 ± 1.508
86	SMM 22	11.5 ± 0.3	0.235 ± 0.022	5.274 ± 0.485	1.624 ± 0.149
87	SMM 23	12.8 ± 0.3	0.015 ± 0.005	0.128 ± 0.040	0.025 ± 0.008
88	SMM 24	13.6 ± 0.4	0.084 ± 0.009	1.200 ± 0.130	0.295 ± 0.032
89	SMM 25	9.6 ± 0.2	0.090 ± 0.011	3.253 ± 0.406	1.269 ± 0.158
90	SMM 26	11.0 ± 0.3	0.046 ± 0.007	1.950 ± 0.293	0.820 ± 0.123
91	1709 SMM1	12.9 ± 0.4	0.240 ± 0.025	5.436 ± 0.573	1.681 ± 0.177
92	1709 SMM2	11.0 ± 0.2	0.092 ± 0.009	2.684 ± 0.275	0.942 ± 0.096
93	1712 SMM1	5.8 ± 0.1	0.716 ± 0.089	20.386 ± 2.534	7.064 ± 0.878

3.3.5 Source characterisation from spectral data

The typical column densities, masses and velocity dispersions derived from N_2H^+ and $C^{18}O$ data were estimated for each core for which data were available. For each core, the velocity dispersion was taken to be the average of the velocity dispersions in each good pixel covered by the aperture used for source continuum photometry, while the mass was taken to be the average of the masses in the good pixels in the aperture, multiplied by the total number of pixels in the aperture. The starless core properties derived from N_2H^+ and $C^{18}O$ data are listed in Table 3.5.

Of the emission from the three isotopologues of CO mapped by HARP-B, that of $C^{18}O$ was chosen as it has the lowest optical depth, typically < 0.5, but reaching ~ 2 in high-density regions (White et al. 2015). $C^{18}O$ emission can only probe the outer envelopes of starless cores; the freeze-out of heavy molecules onto dust grains at high densities and low temperatures means that CO (or its isotopologues) cannot be considered a reliable tracer for densities $n(H_2) > 10^5\,cm^{-3}$ (see, e.g. Di Francesco et al. 2007, and references therein). Although Ophiuchus is known to have low average levels of CO depletion (Christie et al. 2012), $C^{18}O$ linewidths can only be used as a conservative measure of the bound state of a core, providing information on the behaviour of the moderately dense cloud material.

N_2H^+ emission is a better tracer of the bound state of the densest parts of starless cores than $C^{18}O$, with significant depletion not occurring until core densities exceed $\sim 10^6\,cm^{-3}$ (Di Francesco et al. 2007, and references therein) . However, due to the low abundance of N_2H^+ relative to H_2 ($X(N_2H^+) = 5.2 \pm 0.5 \times 10^{-10}$ – Pirogov et al. 2003), it is only detectable in regions of the highest H_2 column density.

Each pixel was fitted using an IDL routine utilising *mpfit* (Markwardt 2009). For $C^{18}O$, a single Gaussian was fitted to each pixel, and fits with signal-to-noise ratio (SNR) ≥ 5 were accepted. For N_2H^+, a seven-component set of Gaussians was fitted to the multiplet line, and fits were accepted for pixels where the weakest

component had SNR ≥ 2.

Column densities, and hence masses, were calculated for each core, using the CO and N_2H^+ data sets. Column densities were calculated following Garden et al. (1991):

$$N = \frac{3k_{\mathrm{B}}}{8\pi^3 B\mu_{\mathrm{D}}^2} \frac{e^{hBJ(J+1)/k_{\mathrm{B}}T_{\mathrm{ex}}}}{J+1} \frac{T_{\mathrm{ex}} + \frac{hB}{3k_{\mathrm{B}}}}{1 - e^{-h\nu/k_{\mathrm{B}}T_{\mathrm{ex}}}} \int \tau \mathrm{d}v,$$
(3.10)

where N is the column density of the species in question, B and μ_{D} are the rotational constant and permanent dipole moment of the molecule respectively, and J is the lower rotational level of the transition. This equation, and the analysis that follows, assumes that the species under consideration is in local thermodynamic equilibrium (LTE) – i.e. that the species is in thermodynamic equilibrium with its surroundings, and its behaviour and level populations can be characterised by a single kinetic temperature, which can be equated to the excitation temperature T_{ex}.

The approximation of LTE in a transition in a species in the ISM – i.e. that the kinetic temperature of the gas can be equated to the excitation temperature T_{ex} (equivalent to the statement that the transition is thermalised) – holds while the transition is collisionally, rather than radiatively, excited, i.e. $C_{ji} \gg A_{ji}$, where C_{ji} and A_{ji} are the collisional and radiative de-excitation respectively. As the rates of collisional excitation and de-excitation are directly proportional to the number density of colliding particles, a critical density can be defined at which $C_{ji}/A_{ji} = 1$. When the density of material in the ISM is greater than the critical density of a transition, the transition will appear in emission, and as the density of the ISM increases, the line will become thermlalised, and LTE will apply. See, e.g. Emerson (1999) for a detailed discussion of the critical densities of transitions in the ISM.

The critical density of the $C^{18}O$ $J = 3 \rightarrow 2$ transition is a few times $10^4 \, \mathrm{cm}^{-3}$ (see Graves et al. 2010 and references therein), while the critical density of the N_2H^+ $J = 1 \rightarrow 0$ transition is $\sim 2 \times 10^5 \, \mathrm{cm}^{-3}$ (see Di Francesco et al. 2004 and references therein).

The excitation temperature, T_{ex}, can be calculated as follows (see, e.g., Pineda et al. 2008):

$$T_{ex} = \frac{T_0}{\ln\left(1 + T_0\left(\frac{T_R}{1-e^{-\tau}} + \frac{T_0}{e^{T_0/T_{bg}}-1}\right)^{-1}\right)}, \quad (3.11)$$

where $T_0 = h\nu/k_B$, T_{bg} is the cosmic microwave background temperature, $2.73\,K$, and T_R is the radiation temperature of the spectral line.

The integral in Equation 3.10 can be written as (see, e.g., Buckle et al. 2010):

$$\int \tau(v)dv = \frac{1}{J(T_{ex}) - J(T_{bg})}\int \frac{\tau(v)}{1-e^{-\tau(v)}}T_{MB}dv \quad (3.12)$$

$$\approx \frac{1}{J(T_{ex}) - J(T_{bg})}\frac{\tau(v_0)}{1-e^{-\tau(v_0)}}\int T_{MB}dv \quad (3.13)$$

where v_0 is the central velocity of the line, T_{MB} is the observed main beam temperature and $J(T)$ is the source function,

$$J(T) = \frac{T_0}{e^{T_0/T} - 1} \quad (3.14)$$

with T_0 defined as above.

Excitation temperatures and optical depths for $C^{18}O$ were calculated under the assumption that the ^{13}CO and $C^{18}O$ emission trace material with the same excitation temperature, and that ^{13}CO is optically thick everywhere that $C^{18}O$ is detected. The excitation temperature is calculated using Equation 3.11 in the limit $\tau_{^{13}CO} \gg 1$, with $T_R = T_{max,^{13}CO}$. The optical depth of $C^{18}O$ is determined using the relation

$$\frac{T_{max,C^{18}O}}{T_{max,^{13}CO}} = \frac{1 - e^{-\tau_{C^{18}O}}}{1 - e^{-\tau_{^{13}CO}}}, \quad (3.15)$$

and the abundance ratio $[^{13}CO/C^{18}O]=5.5$ (Frerking et al. 1982), i.e. $\tau_{^{13}CO} = 5.5\tau_{C^{18}O}$.

For $C^{18}O$, B and μ_D were taken from the NIST database (Johnson 2013): $B = 5.79384 \times 10^{10}\,s^{-1}$, and $\mu_D = 0.112\,D$. Thus, Equation 3.10 becomes

$$N(C^{18}O) = 7.94 \times 10^8 e^{16.88/T_{ex}}\frac{T_{ex} + 0.927}{1 - e^{-16.88/T_{ex}}} \times$$

$$\frac{1}{J(T_{ex}) - J(2.73\,K)}\frac{\tau}{1-e^{-\tau}}\Delta v \sum_i T_i\,cm^{-2}, \quad (3.16)$$
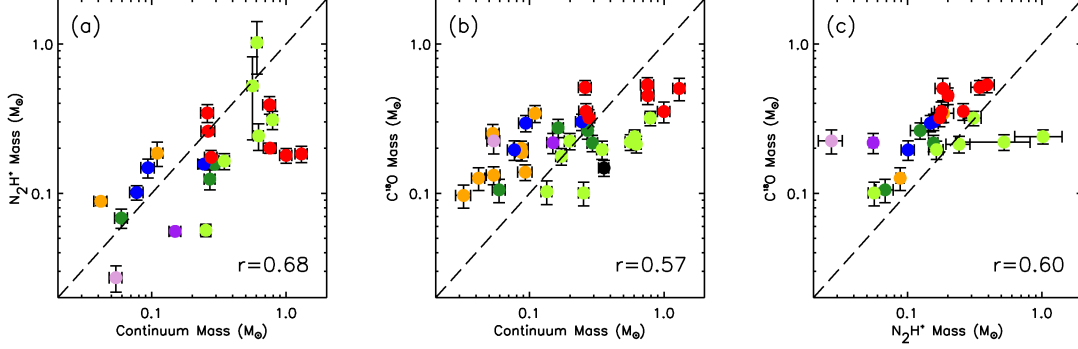
Figure 3.11: Comparison of masses calculated from continuum, N_2H^+ and $C^{18}O$ emission. Panel (a) compares continuum- and N_2H^+-derived masses, for the 23 cores for which N_2H^+ data are available. Panel (b) compares continuum- and $C^{18}O$-derived masses, for the 35 cores for which $C^{18}O$ data are available. Panel (c) compares N_2H^+- and $C^{18}O$-derived masses, for the 23 N_2H^+ cores. Colour coding is as in Figure 3.8. The dashed line is the line of unity. Spearman's rank correlation coefficients r are given for each set of masses. It can be seen that panel (a) provides the best correlation, with $r = 0.68$ (see text for discussion).

where Δv is the velocity channel width in $\mathrm{cm\,s^{-1}}$, and T_i is the best-fit main beam temperature in the ith velocity channel. The equivalent H_2 column density is found using the conversion factor $X(C^{18}O) = 2.635 \times 10^{-7}$. This value of $X(C^{18}O)$ was determined from the relations $N(H_2)/A_v = 9.4 \times 10^{20}\,\mathrm{cm^2\,mag^{-1}}$ (Pineda et al. 2010, and references therein), and $N(^{12}CO)/A_v = 1.01 \times 10^{17}\,\mathrm{cm^2\,mag^{-1}}$ (Pineda et al. 2010), i.e. $N(H_2)/N(^{12}CO) = 1.1 \times 10^4$. For the abundance ratios $[^{13}CO/C^{18}O]=5.5$ (Frerking et al. 1982) and $[^{12}CO/^{13}CO]=69$ (Wilson 1999), this leads to the value of $X(C^{18}O)$ given above. The accuracy of the H_2 column densities calculated using this abundance ratio depends on all of the above relations being valid in Ophiuchus and consistent across all of our cores. The total uncertainty resulting from all of these relations is difficult to quantify, but we state conservatively that our column densities determined from $C^{18}O$ emission are likely to be accurate to within a factor of a few.

The hyperfine splitting of the N_2H^+ multiplet allows for the direct calculation of optical depth. The optical depths of any pair of hyperfine transitions $j \to i$

and $m \rightarrow l$ are related to one another by their statistical weights and Einstein A coefficients (see, e.g., Emerson 1999, p. 308):

$$\frac{\tau_{ji}}{\tau_{ml}} = \frac{g_j A_{ji}}{g_m A_{ml}}.$$ (3.17)

Neglecting any background contribution, the relative strengths of the two lines will be

$$\frac{T_{\max,ji}}{T_{\max,ml}} = \frac{T_{\text{ex},ji}}{T_{\text{ex},ml}} \frac{1 - e^{-\tau_{ji}}}{1 - e^{-\tau_{ml}}}.$$ (3.18)

Assuming that the excitation temperature is the same for all of the hyperfine transitions, the relative strengths of each of the components can be expressed as a function of optical depth, and hence optical depth can be fitted as a free parameter. The excitation temperature can then be calculated using equation 3.11. For each of the 15 hyperfine components, equation 3.10 becomes

$$N_i = 3.10 \times 10^6 \frac{T_{\text{ex}} + 0.745}{1 - e^{-h\nu_i/k_B T_{\text{ex}}}} \times$$

$$\frac{1}{J(T_{\text{ex}}) - J(2.73\,\text{K})} \frac{\tau_i}{1 - e^{-\tau_i}} \Delta v \sum_j T_j \,\text{cm}^{-2}, (3.19)$$

where T_j is the best-fit model main-beam temperature of the ith hyperfine component in the jth velocity channel. The frequencies and Einstein A coefficients of the transitions are taken from Daniel et al. (2006), while the parameters $B = 4.65869 \times 10^{10}\,\text{s}^{-1}$ and $\mu_{\text{D}} = 3.40\,\text{D}$ are taken from the CDMS database (Müller et al. 2001). Summing over all components, the total N_2H^+ column density is

$$N(N_2H^+) = \sum_{i=1}^{15} N_i.$$ (3.20)

The equivalent H_2 column density is found using the conversion factor $X(N_2H^+) = 5.2 \times 10^{-10}$ (Pirogov et al. 2003). We note that Pirogov et al. (2003) determined this value of $X(N_2H^+)$ by considering the mean N_2H^+ abundance across 36 massive molecular cloud cores; the applicability of this abundance to a low-to-intermediate mass star-forming region such as Ophiuchus is not certain. Friesen et al. (2010)

find N_2H^+ abundances in the range $2.5 - 17 \times 10^{-10}$ in Oph B, while Di Francesco et al. (2004) find a mean N_2H^+ abundance of 1.3×10^{-10} in Oph A, indicating N_2H^+ depletion in the Oph A region. These results suggest that the Pirogov et al. (2003) value of $X(N_2H^+)$ is applicable to our cores, but that a wide scatter about this abundance is to be expected, and hence our H_2 column densities determined using this abundance are likely to be accurate to within a factor of $2-3$ in regions without significant N_2H^+ depletion.

Figure 3.11 compares the masses derived from each of our tracers, and shows that the masses of cores measured in N_2H^+ and in continuum emission correlate fairly well (Spearman's rank correlation coefficient $r = 0.68$), although with significant scatter about the line of unity, whereas those from $C^{18}O$ do not ($r = 0.57$). This correlation indicates that N_2H^+ and dust are tracing the same material. The excess in continuum mass over N_2H^+ mass in the most massive cores in Oph A indicates that N_2H^+ is not tracing the very innermost regions of the densest cores. As discussed above, depletion of N_2H^+ in the densest regions of Oph A has been previously noted by Di Francesco et al. (2004). There is also considerable variation in core mass from region to region, as shown by the coloured symbols. We return to a discussion of this variation in Section 3.5.

It should be noted that different subsets of our set of starless cores are shown in each panel of Figure 3.11. $C^{18}O$ data are available at the positions of 35 of the 46 starless cores which we are analysing (as shown in Figure 3.11b). N_2H^+ data are available for 23 of these 35 cores (shown in Figure 3.11a). There are no cores for which N_2H^+ data are available and $C^{18}O$ data are not (i.e. the samples shown in Figures 3.11a and 3.11c are identical, and are a subset of those in Figure 3.11b). The $C^{18}O$ and N_2H^+ masses of all cores for which data are available are listed in Table 3.5. The virial analysis in Section 3.4 is performed only on those 23 cores for which continuum, $C^{18}O$ and N_2H^+ data are all available.

130

3.4 Energy balance and stability

We now estimate the magnitude of each of the terms in the virial equation, in order to determine the energy balance, and hence the stability against collapse, of the cores in our sample. We consider the virial equation in the form

$$\frac{1}{2}\ddot{\mathcal{I}} = 2\Omega_{\mathrm{K}} + \Omega_{\mathrm{G}} + \Omega_{\mathrm{M}} + \Omega_{\mathrm{P}} \tag{3.21}$$

where $\ddot{\mathcal{I}}$ is the second derivative of the moment of inertia $\mathcal{I}$, Ω_{K} is the internal energy, Ω_{G} is the gravitational potential energy, Ω_{M} is the magnetic energy, and Ω_{P} is the energy due to external pressure acting on the core. If $\ddot{\mathcal{I}} < 0$, a core's net energy is negative, and hence the core is collapsing. Conversely, a core with $\ddot{\mathcal{I}} > 0$ will be dispersing, and the virially stable mass of a core is the mass at which $\ddot{\mathcal{I}} = 0$.

3.4.1 Gravitational and internal energy

The first two terms on the right-hand side of Equation 3.21 can be estimated from directly-measured quantities. The internal kinetic energy of a core of mass M and one-dimensional velocity dispersion σ is given by the relation

$$\Omega_{\mathrm{K}} = \frac{3}{2}M\sigma^2 \tag{3.22}$$

where σ is the line-of-sight velocity dispersion for the mean gas particle, related to the line-of-sight velocity dispersion in the tracer molecule $(\sigma_{\mathrm{N_2H^+}})$ by

$$\sigma^2 = \sigma_{\mathrm{N_2H^+}}^2 + k_{\mathrm{B}}T_{gas}\left(\frac{1}{\mu m_{\mathrm{H}}} - \frac{1}{m_{\mathrm{N_2H^+}}}\right) \tag{3.23}$$

where T_{gas} is the typical gas temperature of the material traced by $\mathrm{N_2H^+}$ (see Fuller & Myers 1992). We assume that $\mathrm{N_2H^+}$ traces material at $T_{gas} \approx 7\,\mathrm{K}$ (Stamatellos et al. 2007). We apply a similar correction to the $\mathrm{C^{18}O}$ linewidths, there taking T_{gas} to be the mean line-of-sight temperature of the core. However, as discussed below, $\mathrm{C^{18}O}$ linewidths are significantly supersonic, making the effect of this correction minimal.

The non-thermal component of the linewidth, σ_{NT}, can be derived using the gas temperature T_{gas}, and the relation $\sigma^2 = \sigma_{\text{T}}^2 + \sigma_{\text{NT}}^2$, where the sound speed, σ_{T}, is given by $\sqrt{k_{\text{B}} T_{gas}/m}$, and m is the mass of the molecule being considered ($m_{\text{C}^{18}\text{O}} = 30$ atomic mass units (amu); $m_{\text{N}_2\text{H}^+} = 29$ amu). Figure 3.12 compares the non-thermal N_2H^+ and C^{18}O linewidths of our cores, with the sound speed in gas at $7\,\text{K}$ (the typical gas temperature we assume for material traced by N_2H^+; c.f. Stamatellos et al. 2007) marked as a vertical line.

All of our cores have supersonic non-thermal velocity dispersions in C^{18}O. The non-thermal velocity dispersions in N_2H^+ are consistently smaller than those measured in C^{18}O, typically being transonic or mildly supersonic. This indicates a loss of turbulence between the material traced by C^{18}O and the denser material traced by N_2H^+. Transitions from supersonic turbulence at low densities to coherence at high densities have been observed in dense cores both in molecular clouds (e.g. Goodman et al. 1998; Caselli et al. 2002; Pineda et al. 2010) and in isolation (Quinn 2013). This behaviour is consistent with models of turbulent dissipation (e.g. Klessen et al. 2005; Offner et al. 2008). The ratio between the non-thermal velocity dispersion in C^{18}O and the non-thermal velocity dispersion in N_2H^+ varies from region to region: in Oph B, $\sigma_{\text{NT}}(\text{C}^{18}\text{O})/\sigma_{\text{NT}}(\text{N}_2\text{H}^+) \sim 2.5$ while in Oph C, the ratio is ~ 5, suggesting that turbulence has been dissipated more in Oph C than in Oph B.

In keeping with the model used to characterise our sources, the gravitational potential energy is that of a spherically symmetric Gaussian density distribution, $\rho(r) = \rho_0 e^{-r^2/2\alpha^2}$ ($\alpha = \text{FWHM}/\sqrt{8\ln 2}$):

$$\Omega_{\text{G}} = -\frac{1}{2\sqrt{\pi}} \frac{GM^2}{\alpha}. \tag{3.24}$$

We take α to be the geometric mean of the deconvolved Gaussian widths of each of our cores.

We give here a brief derivation of the gravitational potential energy of a Gaussian distribution, as used in our virial analysis. For a radially symmetric potential, the

132
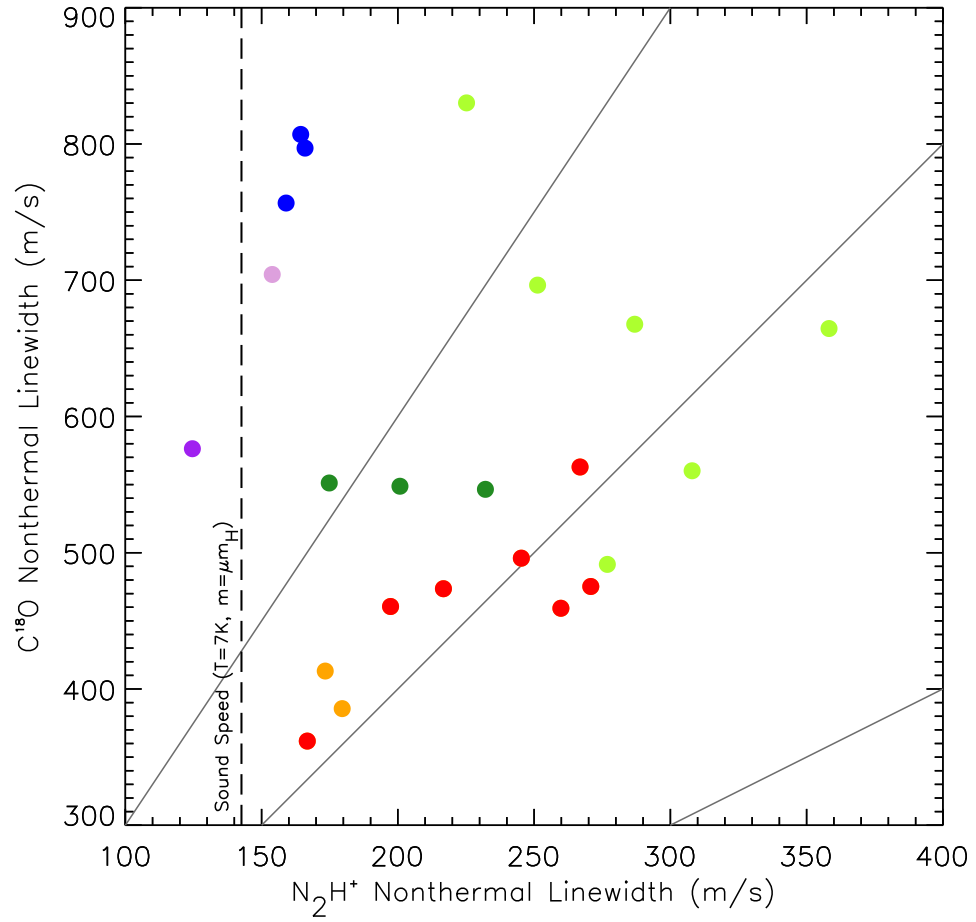
Figure 3.12: Comparison of mean non-thermal linewidths for the 23 cores for which N_2H^+ data are available, as measured in $C^{18}O$ and N_2H^+. The dashed line shows the mean gas sound speed at a temperature of 7 K. Grey lines show the 1:1, 2:1 and 3:1 $C^{18}O:N_2H^+$ linewidth ratios. Colour coding is as in Figure 3.8.

gravitational potential energy Ω_G is given by

$$\Omega_\mathrm{G} = -4\pi G \int_0^\infty \mathrm{d}r\, r\, \rho(r) M(r), \tag{3.25}$$

where $\rho(r)$ and $M(r)$ are the density and mass at radius r, respectively. $M(r)$ is given by

$$M(r) = 4\pi \int_0^r \mathrm{d}r'\, r'^2 \rho(r'). \tag{3.26}$$

We assume a radially symmetric Gaussian density distribution

$$\rho(r) = \rho_0 e^{-r^2/2\alpha^2}, \tag{3.27}$$

for which the total mass at radius r is given by

$$M(r) = 4\pi\rho_0 \int_0^r \mathrm{d}r'\, r'^2\, e^{-r'^2/2\alpha^2} \tag{3.28}$$

$$= 4\pi\rho_0 \left[\alpha^3 \sqrt{\frac{\pi}{2}} \,\mathrm{erf}\left(\frac{r}{\alpha\sqrt{2}}\right) - \alpha^2 r e^{-r^2/2\alpha^2} \right], \tag{3.29}$$

and the total mass summed over all radii is given by

$$M = 4\pi\rho_0 \int_0^\infty \mathrm{d}r'\, r'^2\, e^{-r'^2/2\alpha^2} \tag{3.30}$$

$$= 2\sqrt{2}\pi^{3/2}\rho_0\alpha^3. \tag{3.31}$$

Using equations 3.25 and 3.29, Ω_G is given by

$$\Omega_\mathrm{G} = -16\pi^2 G \rho_0^2 \alpha^2 \times$$

$$\int_0^\infty \mathrm{d}r\, r\, e^{-r^2/2\alpha^2} \left[\alpha\sqrt{\frac{\pi}{2}}\,\mathrm{erf}\left(\frac{r}{\alpha\sqrt{2}}\right) - r e^{-r^2/2\alpha^2} \right] \tag{3.32}$$

$$= -16\pi^2 G \rho_0^2 \alpha^2 \times \left(\frac{\alpha^3\sqrt{\pi}}{4}\right) \tag{3.33}$$

$$= -4\pi^{5/2} G \rho_0^2 \alpha^5. \tag{3.34}$$

Combining equations 3.31 and 3.34, the gravitational potential energy of a Gaussian distribution of characteristic width α and total mass M is

$$\Omega_\mathrm{G} = -\frac{1}{2\sqrt{\pi}} \frac{GM^2}{\alpha}. \tag{3.35}$$

134

For our mean core mass, $0.27\,\mathrm{M_\odot}$, and deconvolved size, $\mathrm{FWHM} = 0.01\,\mathrm{pc}$, the gravitational potential energy $|\langle\Omega_\mathrm{G}\rangle| \approx 4 \times 10^{41}\,\mathrm{erg}$, and for our mean one-dimensional $\mathrm{N_2H^+}$ velocity dispersion, $225\,\mathrm{ms^{-1}}$ (equivalent to $\sigma = 262\,\mathrm{ms^{-1}}$), the kinetic energy term in the virial equation is $2\langle\Omega_\mathrm{K}\rangle \approx 11 \times 10^{41}\,\mathrm{erg}$. Hence, these two terms are of similar order to one another, with the kinetic term slightly dominant.

3.4.2   External gas pressure

Previous studies of starless cores in Ophiuchus have suggested that external gas pressure might be instrumental in confining dense cores. Maruta et al. (2010) estimate a typical surface pressure on cores in Ophiuchus of $\langle P_\mathrm{EXT}\rangle/k_\mathrm{B} \approx 3 \times 10^6\,\mathrm{K\,cm^{-2}}$, sufficient to influence the energy balance of the cores. Similarly, Johnstone et al. (2000) estimate core surface pressures $P_\mathrm{EXT}/k_\mathrm{B} \sim 10^{6-7}\,\mathrm{K\,cm^{-3}}$ by treating the starless cores they identify in Ophiuchus as pressure-confined Bonnor-Ebert spheres.

We consider the gas pressure in material traced by $\mathrm{C^{18}O}$ to be the external pressure acting on our starless cores, since CO becomes significantly depleted through freeze-out onto dust grains at densities $\gtrsim 10^5\,\mathrm{cm^{-3}}$ (Di Francesco et al. 2007), and as such is expected to trace the outer layers, or envelopes, of starless cores. Higher-density tracers such as $\mathrm{N_2H^+}$ are expected to trace the denser inner material of the cores themselves.

The external pressure term in the virial equation, Ω_P, is given by

$$\Omega_\mathrm{P} = -3P_\mathrm{EXT}V = -4\pi P_\mathrm{EXT}R^3 \tag{3.36}$$

for a core of volume V being acted on by an external pressure P_EXT. P_EXT can be estimated from the ideal gas law:

$$P_\mathrm{EXT} \approx \rho_\mathrm{C^{18}O}\langle\sigma^2_{gas,\mathrm{C^{18}O}}\rangle, \tag{3.37}$$

where $\rho_\mathrm{C^{18}O}$ is the density at which the transition between $\mathrm{C^{18}O}$ and $\mathrm{N_2H^+}$ being effective tracers occurs, and $\langle\sigma^2_{gas,\mathrm{C^{18}O}}\rangle$ is the mean gas velocity dispersion in material

traced by $C^{18}O$. We assume that $C^{18}O$ does not trace densities higher than $10^5\,\mathrm{cm}^{-3}$. We must estimate a radius at which core density drops to $10^5\,\mathrm{cm}^{-3}$ in order to determine the volume over which this surface pressure acts. We continue to assume that our cores are characterised by Gaussian density distributions, in which case the radius at which the density drops to $\rho_{C^{18}O}$ is given by

$$r_{C^{18}O} = \alpha\sqrt{2\ln\left(\frac{\rho_0}{\rho_{C^{18}O}}\right)}.\tag{3.38}$$

The peak core density ρ_0 can be estimated from the measured mean density $\langle\rho_{\mathrm{FWHM}}\rangle$ of each core (listed in Table 3.3), which is determined over an area of radius $1\times$FWHM:

$$\rho_0 = \frac{\langle\rho_{\mathrm{FWHM}}\rangle}{3}(8\ln 2)^{3/2}\left(\sqrt{\frac{\pi}{2}}\,\mathrm{erf}\left(2\sqrt{\ln 2}\right) - \frac{\sqrt{2\ln 2}}{8}\right)^{-1}.\tag{3.39}$$

These equations give typical $r_{C^{18}O}$ values in the range $\sim 0.7 - 1.5$ FWHM.

The mean energy due to external gas pressure on the material traced by N_2H^+ estimated from this method is 9×10^{41} erg, roughly the same order of magnitude as the mean internal kinetic energy of our cores. This is equivalent to $\langle P_{\mathrm{EXT}}\rangle/k_B \approx 1.8\times 10^7\,\mathrm{K\,cm}^{-3}$, an order of magnitude higher pressure than that found by Maruta et al. (2010), but similar to the total pressure in Ophiuchus $P/k_B \sim 2\times 10^7\,\mathrm{K\,cm}^{-3}$ estimated by Johnstone et al. (2000).

3.4.3 External pressure from ionising photons

In Ophiuchus, the effects of the B2V star HD 147889 dominate the effects of the interstellar radiation field (Stamatellos et al. 2007). According to the cloud geometry model of Liseau et al. (1999), Oph A is the region of the cloud closest to HD 147889, at a distance of 1.1 pc. Furthermore, the B3-B5 star S1 appears to be influencing Oph A. We estimate the pressure on cores in Oph A from ionising photons from these B stars, as being indicative of the maximum external pressure acting on any of the cores in our sample.

Table 3.4: Adopted B star properties

Star	Luminosity (L$_\odot$)	T$_{\text{eff}}$ (K)	Radius (R$_\odot$)	$\log_{10}(\dot{N}^0_{\text{LyC}})$ (cm^{-2}s^{-1})
HD 147889	4700	22300	4.6	20.4
S1	1500	17200	4.4	18.5

It must be noted that the following analysis holds precisely only if the cores are being directly hit by ionising photons. Many of the ionising photons emitted by HD 147889 and S1 will be absorbed before reaching our starless cores, which are deeply embedded within the molecular cloud. Hence, the pressure due to ionising photons determined in this section is an upper limit on the true value. The lower-density material surrounding the starless cores will be heated by the absorption of these ionising photons; the heating effect of these photons on the material surrounding the starless cores will contribute to the external gas pressure acting on the cores, discussed in the section above.

The pressure term of the virial equation due to ionising photons from an early-type star irradiating one side of a starless core is given by Ward-Thompson et al. (2006) as

$$|\Omega_{\text{P}}| \approx 2\pi R^3 P_{\text{ext}} \sim \frac{4R^2 k_{\text{B}} T_{\text{II}}}{D} \left(\frac{3\pi \dot{N}_{\text{LyC}} R}{\alpha_*} \right)^{1/2}, \qquad (3.40)$$

where R is the radius of the core; D is the distance from the core to the exciting star; $T_{\text{II}} \sim 10^4$ K is the canonical temperature for gas in an H$_{\text{II}}$ region; $\alpha_* \approx 2 \times 10^{-13}$ cm^{3}s^{-1} is the recombination coefficient for atomic hydrogen into excited states at T_{II} and $\dot{N}_{\text{LyC}}$ is the rate at which Lyman continuum photons are emitted from the exciting star.

The recombination rate into excited states is used in accordance with the on-the-spot approximation – the approximation that the reflection nebula is optically thick and that each new photon which is emitted by a recombination into the ground state is absorbed close to the location at which it was created. Thus, each recombination into the ground state immediately causes the ionisation of another atom, and

recombinations into the ground state have no net effect on the ionisation balance of the region.

We take the number of Lyman continuum photons emitted per unit surface area of the star, $\dot{N}_{\mathrm{LyC}}^{0}$, from Dottori (1980), assuming in both cases $\log g \sim 4.25$ (Strom & Peterson 1968). The total rate of ionising photons is then $\dot{N}_{\mathrm{LyC}} = 4\pi R_{\mathrm{star}}^{2} \dot{N}_{\mathrm{LyC}}^{0}$, where the stellar radii are listed in Table 3.4. We take the distance to HD 147889 to be 1.1 pc, and the distance to S1 to be 0.06 pc, the plane-of-sky distance between the star S1 and the core SM1 at our assumed distance to Ophiuchus. For a core radius equal to our mean deconvolved core FWHM, 0.01 pc, the external pressure terms for a core in Oph A in close proximity to S1 will be

$$\Omega_{\mathrm{P,S1}} \sim -6.6 \times 10^{40} \, \mathrm{erg} \tag{3.41}$$

due to the star S1, and

$$\Omega_{\mathrm{P,HD}} \sim -3.4 \times 10^{40} \, \mathrm{erg} \tag{3.42}$$

due to the star HD 147889. Hence, the maximum value we expect the ionising photon pressure term to take anywhere in Oph A is $\Omega_{\mathrm{P}} \lesssim 10^{41}$ erg, and outside Oph A, where the effect of HD 147889 will be lessened, and the effect of S1 will be minimal, we expect $\Omega_{\mathrm{P}} \sim 10^{40}$ erg. Hence, we conclude that ionising photon pressure represents a small correction to the virial balance of our cores, typically being one to two orders of magnitude smaller than the gravitational and kinetic energy terms, and that we are justified in neglecting it in our virial analysis.

3.4.4 Magnetic energy density

Neither the strength nor the relative importance of magnetic fields in Ophiuchus are well known. There have to date been only a few reliable measurements of magnetic fields in the cloud (Goodman & Heiles 1994; Crutcher et al. 1993; Troland et al. 1996). The magnetic field at intermediate densities, measured through Zeeman

splitting in OH (Crutcher et al. 1993; Troland et al. 1996), is what we consider in the subsequent analysis, as more representative of the magnetic field in the molecular gas. Troland et al. (1996) find the line of sight magnetic field strength $|B_{los}|$ to be $10\,\mu G$ at a density of $10^{3.2}\,cm^{-3}$, and find a 1D velocity dispersion in OH of $\sim 0.57\,km\,s^{-1}$.

The magnetic field strength in the turbulent ISM is commonly related to the non-thermal velocity dispersion and density of the ISM (see, e.g. Basu 2000, and references therein):

$$B = B_0 \frac{\sigma_{NT}}{\sigma_{NT,0}} \left(\frac{n}{n_0}\right)^{1/2},$$ (3.43)

where the subscript '0' indicates the reference (measured) value of each quantity. We note that this relation implies a constant ratio between turbulent and magnetic energy. The magnetic energy can be expressed as

$$\Omega_M = \frac{B^2 V}{2\mu_0} = \frac{1}{2\mu_0} \left(\frac{B_0^2}{\rho_0 \sigma_{0,NT}^2}\right) M\sigma_{NT}^2,$$ (3.44)

while the non-thermal component of the kinetic energy, $\Omega_{K,NT}$, is given by $1.5 M\sigma_{NT}^2$ (see Equation 3.22). Thus, the ratio between turbulent and magnetic energy is given by

$$\frac{\Omega_M}{\Omega_{K,NT}} = \frac{1}{3\mu_0} \frac{B_0^2}{\rho_0 \sigma_{0,NT}^2},$$ (3.45)

which, for the values of B_0, ρ_0 and $\sigma_{0,NT}$ given by Crutcher et al. (1993) and Troland et al. (1996), gives a ratio of $\Omega_M/\Omega_{K,NT} = 0.11$ for the Ophiuchus molecular cloud. Therefore, for our cores (if Equation 3.43 holds) the magnetic energy of a core cannot exceed $\sim 10\%$ of the core's internal energy. In the case of transonic or subsonic motions within the core, the fraction will be smaller still. Furthermore, the internal energy term in the virial equation is $2\Omega_K$, while the magnetic energy term is merely Ω_M. Consequently, the contribution of magnetic energy to core stability will in this case be $\sim 5\%$ that of the turbulent kinetic energy. Therefore, we also neglect the magnetic energy term in our virial analysis. We note the need for further

Table 3.5: Properties of starless cores, derived from spectral line data, virial arguments, and the Bonnor-Ebert criterion.

Source Index	Source Name	N_2H^+ Mass ($M_\odot$)	$C^{18}O$ Mass ($M_\odot$)	Bonnor-Ebert Mass ($M_\odot$)	$-\Omega_G$	Ω_K	$-\Omega_P$	$\frac{1}{2}\ddot{\mathcal{I}}$
					($\times 10^{41}$ erg)			
1	SM1	0.184 ± 0.023	0.503 ± 0.086	0.261 ± 0.196	124.2	36.3	5.9	-57.4
2	SM1N	0.179 ± 0.020	0.353 ± 0.056	0.221 ± 0.168	82.4	27.3	5.9	-33.7
3	SM2	0.201 ± 0.016	0.450 ± 0.057	0.308 ± 0.244	27.9	13.4	11.3	-12.4
5	A-MM5	0.345 ± 0.048	0.511 ± 0.056	0.305 ± 0.242	2.7	5.2	10.1	-2.3
6	A-MM6	0.391 ± 0.053	0.532 ± 0.061	0.297 ± 0.239	21.7	18.1	19.9	-5.5
7	A-MM7	0.260 ± 0.013	0.354 ± 0.045	0.425 ± 0.374	3.1	6.9	8.0	$+2.6$
8	A-MM8	0.174 ± 0.019	0.321 ± 0.042	0.387 ± 0.303	3.8	4.0	4.4	-0.3
9	A-MM1	–	0.188 ± 0.024	0.180 ± 0.136	0.4	–	7.2	–
10	A-MM4	0.186 ± 0.035	0.343 ± 0.045	0.288 ± 0.207	0.6	1.7	3.0	-0.2
11	A-MM4a	0.088 ± 0.006	0.126 ± 0.022	0.255 ± 0.179	0.3	0.6	0.3	$+0.7$
19	A-MM30	–	0.251 ± 0.038	0.151 ± 0.107	0.2	–	4.2	–
20	A-MM31	–	0.200 ± 0.023	0.580 ± 0.530	0.3	–	2.7	–
23	A-MM34	–	0.138 ± 0.017	0.624 ± 0.569	0.4	–	2.5	–
26	A2-MM1	–	0.132 ± 0.018	0.202 ± 0.145	0.2	–	3.0	–
27	A2-MM2	–	0.097 ± 0.017	0.143 ± 0.098	0.1	–	1.7	–
28	A3-MM1	–	0.187 ± 0.023	0.220 ± 0.169	0.3	–	6.6	–
29	B1-MM3	0.124 ± 0.019	0.263 ± 0.033	0.113 ± 0.067	3.5	4.1	10.8	-6.1
30	B1-MM4a	0.156 ± 0.012	0.217 ± 0.028	0.107 ± 0.062	4.2	6.5	10.7	-1.9
31	B1-MM4b	0.068 ± 0.010	0.105 ± 0.019	0.109 ± 0.064	0.4	1.1	1.2	$+0.5$
32	B1-MM5	–	0.274 ± 0.038	0.121 ± 0.071	1.4	–	5.8	–
35	B2-MM2a	–	0.177 ± 0.023	0.116 ± 0.066	1.5	–	6.0	–
36	B2-MM2b	–	0.223 ± 0.028	0.092 ± 0.054	1.9	–	11.3	–
37	B2-MM4	–	0.103 ± 0.018	0.101 ± 0.060	3.0	–	0.8	–
38	B2-MM6	0.523 ± 0.296	0.220 ± 0.026	0.081 ± 0.047	13.6	25.0	25.8	$+10.6$
41	B2-MM9	1.021 ± 0.394	0.240 ± 0.026	0.085 ± 0.051	13.7	18.6	33.8	-10.4

Table 3.5: – continued.

Source Index	Source Name	N_2H^+ Mass $(M_\odot)$	$C^{18}O$ Mass $(M_\odot)$	Bonnor-Ebert Mass $(M_\odot)$	$-\Omega_\mathrm{G}$	Ω_K	$-\Omega_\mathrm{P}$	$\frac{1}{2}\ddot{\mathcal{I}}$
						$(\times 10^{41}$ erg$)$		
43	B2-MM13	0.242 ± 0.049	0.213 ± 0.027	0.079 ± 0.043	18.9	21.4	15.2	$+8.7$
44	B2-MM14	0.310 ± 0.044	0.319 ± 0.035	0.069 ± 0.038	23.6	19.7	40.7	-24.9
45	B2-MM15	0.164 ± 0.020	0.196 ± 0.028	0.071 ± 0.042	6.8	7.3	20.3	-12.3
46	B2-MM16	0.057 ± 0.005	0.100 ± 0.018	0.092 ± 0.050	10.5	7.3	0.7	$+3.4$
48	C-MM3	0.157 ± 0.011	0.301 ± 0.038	0.084 ± 0.055	2.6	3.3	21.2	-17.2
49	C-MM6a	0.101 ± 0.011	0.195 ± 0.029	0.085 ± 0.058	0.4	1.1	7.1	-5.3
50	C-MM6b	0.148 ± 0.022	0.295 ± 0.037	0.091 ± 0.063	0.4	1.3	12.2	-10.0
53	E-MM2d	0.056 ± 0.004	0.218 ± 0.034	0.134 ± 0.088	1.2	1.6	7.2	-5.2
58	F-MM1	0.027 ± 0.005	0.224 ± 0.041	0.139 ± 0.097	0.5	0.7	0.9	$+0.0$
70	H-MM1	$-$	0.148 ± 0.018	0.223 ± 0.124	5.8	$-$	2.2	$-$

measurements of magnetic field strengths in high-density regions, in order to test the validity of analyses of this kind.

3.4.5 Core stability

On average, for those cores in our sample for which N_2H^+ and $C^{18}O$ data are available, the gravitational potential energy and the external pressure energy are of similar magnitude, and together slightly dominate over the internal energy. However, there is a wide variation from core to core. Table 3.5 lists the values of gravitational potential energy, internal energy, external pressure energy and the virial parameter for all 23 of those cores for which sufficient data are available.

Figure 3.13 shows the ratio of Ω_G to Ω_P plotted against $-(\Omega_G + \Omega_P)/2\Omega_K$, the virial stability criterion. The vertical dashed line marks the locus of virial stability. It can be seen that the majority of our cores lie to the right of this line, indicating that they are virially bound. Of the 23 cores for which N_2H^+ data are available, 22 are either bound or virialised, having a virial ratio $-(\Omega_G + \Omega_P)/2\Omega_K \geq 1$. However, as can be seen in Figure 3.13, 1 core, in Oph A$'$, is marginally unbound, with virial ratio < 1, but with uncertainty on this ratio such that a ratio of 1 is consistent.

The horizontal dashed line on Figure 3.13 marks the division between those cores that are gravitationally bound (above the line) and those that are pressure-confined (below the line). There is a wide variation from region to region, with Oph A being the most gravitationally bound and Oph C being the most highly pressure-confined. These differences are discussed further in Section 3.5. It should be noted that a full virial analysis has only been performed on those cores located in regions targeted for N_2H^+ observations, i.e. the regions of highest column density. The results of this analysis cannot necessarily be generalised to the cores for which N_2H^+ data are not available.
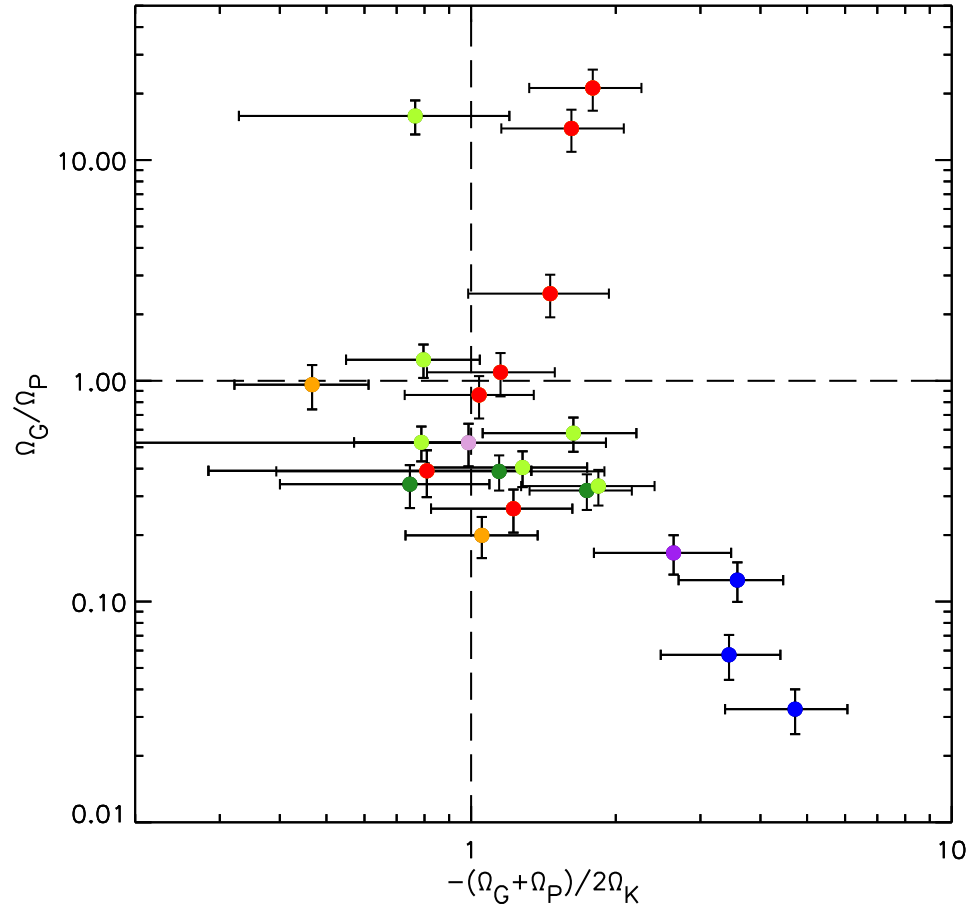
Figure 3.13: Virial stability of the 23 cores in our catalogue for which N_2H^+ data are available, compared to the ratio of gravitational energy and external pressure terms in the virial equation. The vertical dashed line indicates the line of virial stability, with the right-hand side of the plot being bound and the left-hand side being unbound. The horizontal dashed line marks equipartition between external pressure energy and gravitational potential energy; cores above the line are gravitationally bound, while cores below the line are pressure-confined. Colour coding is as in Figure 3.8.

3.4.6   Bonnor-Ebert critical mass

The Bonnor-Ebert (BE) model of a starless core (Bonnor 1956; Ebert 1955) is frequently used as a measure of the stability of starless cores, as discussed in Section 1.3.3 (e.g. Alves et al. 2001).

We investigated whether the critical BE stability criterion ($M/M_{\mathrm{BE},crit}$) can accurately predict the virial balance of starless cores in L1688, and hence whether it can be reliably used as a proxy for virial mass in regions for which line data are not available. We determined the critically stable masses of our cores by considering the external pressure, P_{EXT}, on our cores to be the gas pressure in $C^{18}O$. The critically stable BE masses and continuum masses of the subset of our cores for which N_2H^+ data are available are compared in Figure 3.14. Critically-stable BE masses for the remainder of the set of cores for which $C^{18}O$ data are are available are listed in Table 3.5, but are excluded from Figure 3.14 in order to aid comparison with Figure 3.13.

Figure 3.14 shows that there is no correlation between observed mass and critical BE mass, indicating that, as would be expected for a set of virially unstable cores, our cores cannot be modelled as static, critically-stable, BE spheres. Moreover, the critical BE stability criterion does not reliably predict either the virially bound state or the energy balance of the N_2H^+ cores. A core lying to the right of the line of unity on Figure 3.14 has no stable BE solution and must, according to BE analysis, be collapsing under its own gravity, while a core lying to the left of the line of unity may be modelled as a stable, pressure-confined BE sphere.

We find that the BE criterion typically over-predicts the degree to which our cores are gravitationally unstable. Of the 15 cores predicted to be collapsing under gravity according to Figure 3.14, 9 are in fact found to pressure-confined. However, there are no cases where the BE analysis suggests a core is pressure-confined and it is found to be gravitationally bound. The degree to which cores are virially bound
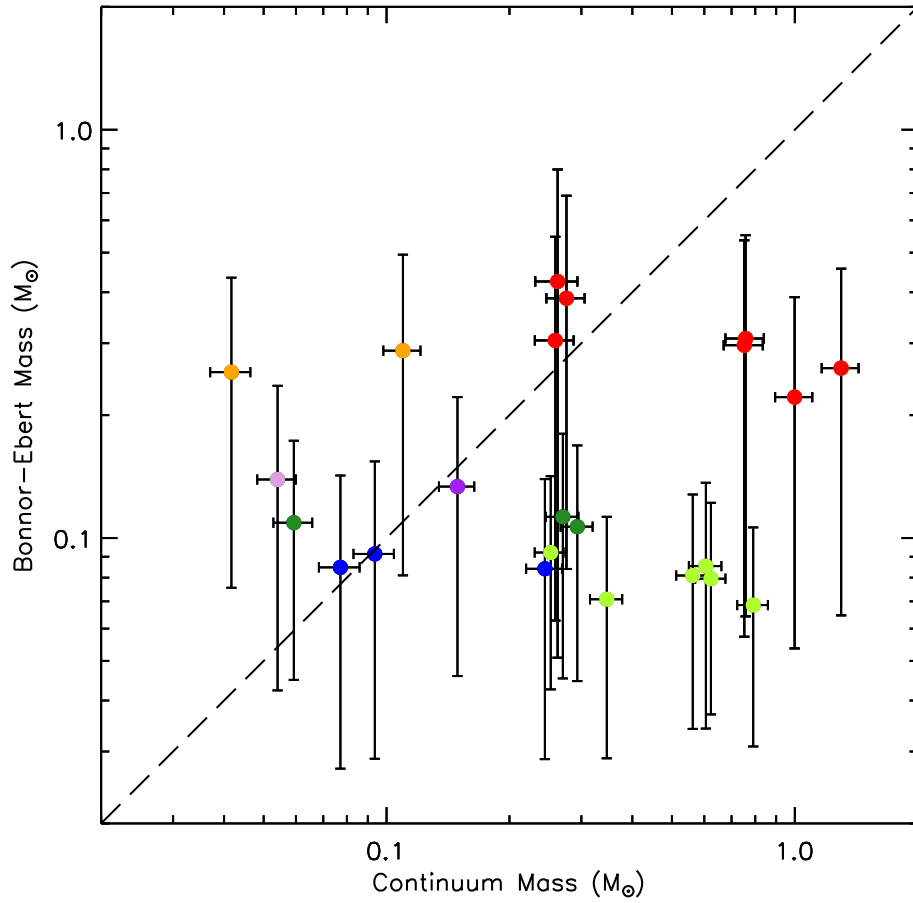
Figure 3.14: Comparison of continuum-derived mass and Bonnor-Ebert critical mass for the 23 cores for which N_2H^+ data are available. Cores to the right of the dashed line are collapsing according to the critical Bonner-Ebert criterion. Colour coding is as in Figure 3.8.

is in many cases also overestimated. For example, the BE criterion predicts that all 6 of the cores in Oph B2 will be strongly gravitationally bound, whereas Figure 3.13 shows that of these 6 cores, 4 are approximately virialised, and the other 2, while virially bound, are confined by external pressure.

A possible explanation for these discrepancies is that in this analysis we have used the standard BE mass formula (equation 1.48), which does not account for the contribution of non-thermal motion to internal support. However, as shown in Figure 3.12, our cores typically have transonic or mildly supersonic internal motions at the radii traced by N_2H^+, and hence assuming all support against collapse is thermal is likely to overestimate the degree to which our cores are both gravitationally unstable and virially bound. An accurate parameterisation of the effect of non-thermal internal motion on core support might improve the accuracy of the BE analysis.

We used the standard (i.e. thermal) BE mass formula in order to make our BE stability analysis comparable to other BE stability analyses, such as those performed by the Herschel GBS (e.g. Könyves et al. 2015), in which only thermal pressures are considered.

Another important consideration is that while in principle the 8 cores lying to the left of the line of unity in Figure 3.14 can be modelled as stable, pressure-confined BE spheres, Figure 3.13 shows that many of our cores, whether confined by pressure or by gravity, are not in virial equilibrium. Caution must be exercised when applying an equilibrium model such as a BE sphere to a non-equilibrium set of objects such as the cores in this sample.

3.5 Regional variations in core properties

Figure 3.13 shows that most of the cores in our sample for which N_2H^+ data are available are either bound or virialised. Figure 3.8 shows that our cores occupy the

part of the mass/size plane in which prestellar cores are expected to lie. However, whether our cores are gravitationally bound (i.e. prestellar) or confined by pressure varies from region to region. Gravity strongly dominates over external pressure in the most massive cores in Oph A, the well-known prestellar cores SM1, SM1N and SM2 (Ward-Thompson et al. 1989). Cores in Oph A' and B are typically in approximate equipartition between gravitational and pressure energy or marginally dominated by pressure. However, cores in Oph C and E are strongly dominated by pressure and virially bound.

It is noticeable from all of the above that the properties of the starless cores, including the degree to which cores are bound, as well as whether they are gravitationally bound or pressure-confined, and the extent to which turbulence is dissipated, varies more between regions than within them. This suggests that the local environment has a significant effect on the nature of the starless cores. Enoch et al. (2009) provide a catalogue of deeply embedded Class 0 and Class I protostars in L1688 and L1689, marked as yellow stars on Figure 3.1. We refer to this catalogue in the following discussion.

3.5.1 Oph A

Oph A is the only region in L1688 within which substantially gravitationally bound cores are found (see Figure 3.13). Temperatures in Oph A are higher than in other parts of the cloud. The Oph A region is also the part of the cloud most clearly being influenced by stars that have already formed: the B2 star HD 147889 drives a PDR at the western edge of Oph A, while on the eastern side of Oph A there is a reflection nebula associated with the B4 star S1, both of which can be seen in Figure 3.3. This suggests a morphology in the region in which the dense gas that makes up the central, submillimetre-bright cores of Oph A is being influenced by its local environment. However, as shown in Figure 3.13, cores in the densest regions

of Oph A do not appear to be dominated by external pressure. Enoch et al. (2009) list only one protostar embedded in Oph A: the Class 0 protostar VLA 1623 (the only Class 0 source in L1688). This is consistent with star formation in this dense clump being in its early stages.

3.5.2   Oph A$'$

The cores in Oph A$'$ are at similar temperatures to those in Oph A, but are among the least bound of the cores in our sample. Gravity and external pressure appear to be contributing approximately equally to the confinement of these cores. This region is confused, particularly along its western edge, where much of the emission is from the PDR associated with HD 147889. Enoch et al. (2009) list three embedded Class I protostars in Oph A$'$.

3.5.3   Oph B

The Oph B region appears to be relatively quiescent: it is the coldest of the regions; there are few embedded protostars; and the cores are typically virialised or marginally bound. Enoch et al. (2009) list four embedded Class I protostars in Oph B: none in Oph B1; one in Oph B1B2; and three in Oph B2, of which one is the outflow-driving source IRS 47 (White et al. 2015). Cores in Oph B1 and B2 typically show similar behaviour, although the ratio of gravitational to pressure energy is consistently in the range 0.3–0.4 in B1, and more varied in B2. As shown in Figure 3.12, cores in B2 have the highest non-thermal linewidths measured in N_2H^+, suggesting that turbulence is not being effectively dissipated in this region. We hypothesise that this could be due to the influence of the outflow from IRS 47, as protostellar outflows have been shown to inject and sustain turbulence on small scales in molecular clouds (Duarte-Cabral et al. 2012).

We note that the pre-brown dwarf candidate Oph B-11 (Pound & Blitz 1995;

Greaves et al. 2003; André et al. 2012), located between Oph B1 and B2, is detected in SCUBA-2 850-μm emission. Oph B-11 is discussed in detail in 3.5.4.

3.5.4   Oph B-11

We investigated whether the pre-brown dwarf source Oph B-11 was detectable in our 850-μm map of Ophiuchus. Originally detected and identified as a pre-brown dwarf candidate in a DCO^+ search (Pound & Blitz 1995), Oph B-11 was observed using SCUBA by Greaves et al. (2003), who classed the source as a very young 'isolated planet'. André et al. (2012) observed Oph B-11 using the IRAM Plateau de Bure Interferometer (PdBI), determining that the source was in fact a gravitationally bound pre-brown dwarf, with mass 0.02-0.03 $M_\odot$.

When observed by Greaves et al. (2003), the integration time for the 2.7′ diameter field was 2 hours, resulting in a very sensitive SCUBA map with 1σ RMS noise of 6 mJy/15″ beam. The 1σ RMS noise in our SCUBA-2 map of the same region is 6.3 mJy/15″ beam, almost identical. This was achieved using 4×PONG1800 observations, taking a total of 2 hours 40 minutes (i.e. essentially the same integration time as with SCUBA) to cover a field of 30′ diameter, compared to 2.7′ with SCUBA (i.e. roughly 120 times the area in the same time).

In order to detect this extremely faint source, we repeated the unsharp masking process used by Greaves et al. (2003) on their SCUBA map of the region. We smoothed the SCUBA-2 map with a 30″ Gaussian filter, and subtracted the smoothed emission from the original map, removing all structure significantly more extended than the 14.1″ beam. The data were then smoothed to a 15″ beam to match the SCUBA data of Greaves et al. (2003). The unsharp-masked SCUBA-2 data are shown in Figure 3.15. The SCUBA data used by Greaves et al. (2003) are shown in Figure 3.16.

After removing the extended structure in this way from the SCUBA-2 map,
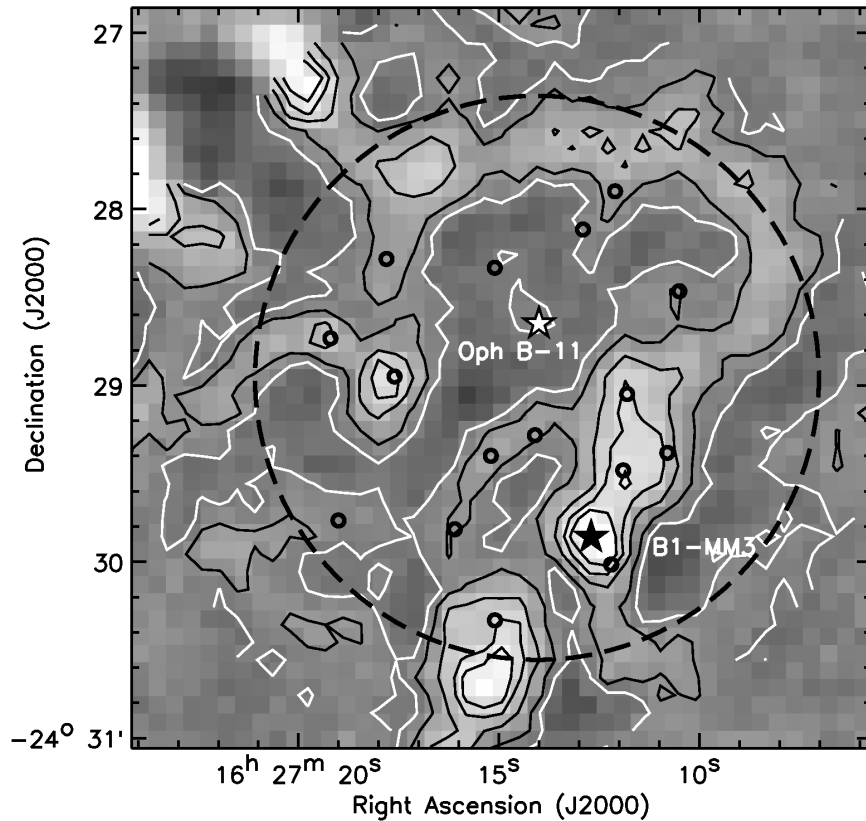
Figure 3.15: Unsharp-masked SCUBA-2 850-µm image of the region surrounding Oph B-11, smoothed to 15″ resolution. Our peak position for Oph B-11 is marked as a white star. B1-MM3 is marked as a black star. Other sources identified by Greaves et al. (2003) are marked as black circles. The approximate area observed by Greaves et al. (2003) is enclosed by the dashed line. Contour levels are 28, 66, 94, 115 and 129 mJy/15″ beam above the local minimum, to approximately match the contours of Greaves et al. (2003).

150
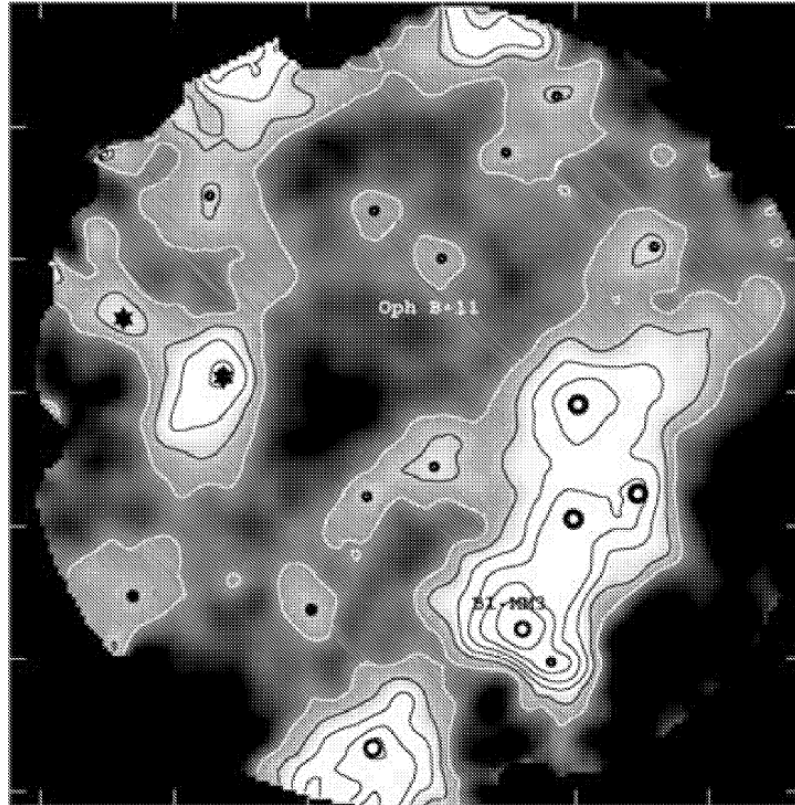
Figure 3.16: Greaves et al. (2003) SCUBA observations of Oph B-11, and the surrounding region.

we were able to detect Oph B-11. The emission peaks at R.A. = 16^{h}:27^{m}:14^{s}.0, Dec. = $-24°$:$28'$:$39''$. Greaves et al. (2003) found the source position to be R.A. = 16^{h}:27^{m}:14^{s}.0 Dec. = $-24°$:$28'$:$31''$, while André et al. (2012) give the source position as R.A. = 16^{h}:27^{m}:13^{s}.96 Dec. = $-24°$:$28'$:$29.3''$. All of these positions are consistent within the quoted errors.

We measure a peak flux density above the local background for Oph B-11 of $55 \pm 6\,\mathrm{mJy}/15''$ beam with an uncertainty on the local background of $\pm 9\,\mathrm{mJy}/15''$ beam. Greaves et al. (2003) find a peak 850-μm flux density for Oph B-11 of $39 \pm 6\,\mathrm{mJy}/15''$ beam, with an uncertainty on their local background of $\pm 5\,\mathrm{mJy}/15''$ beam. Thus, our measurement of the peak flux density of Oph B-11 is consistent with that of Greaves et al. (2003). We converted our peak flux density to a mass using the Greaves et al. (2003) temperature estimate of $12 - 20$ K, taking $\kappa_{850\mu\mathrm{m}} = 0.01\,\mathrm{cm}^2\mathrm{g}^{-1}$, and assuming a distance of 139 pc. We find a mass range for Oph B-11 of $0.012 - 0.024\,\mathrm{M}_\odot$. Thus, our data are consistent with the IRAM mass estimate (André et al. 2012), and hence with the pre-brown dwarf interpretation of Oph B-11.

The brightest source in the Greaves et al. (2003) field is the starless core B1-MM3. Greaves et al. (2003) measure a peak flux density of $177 \pm 6\,\mathrm{mJy}/15''$ beam for B1-MM3, with a background uncertainty of $\pm 5\,\mathrm{mJy}/15''$ beam. Our measured peak flux density for Oph B1-MM3 in the unsharp-masked SCUBA-2 data is $166 \pm 6\,\mathrm{mJy}/15''$ beam, with a background uncertainty of $\pm 9\,\mathrm{mJy}/15''$ beam. Thus, the flux density we measure for B1-MM3 is consistent with that measured by Greaves et al. (2003).

3.5.5 Oph C

Oph C appears to be extremely quiescent, and substantially less evolved than the rest of the Oph C-E-F 'filament' of which it appears to be a part. The three cores we

identify within Oph C are all substantially bound and pressure-confined, with broad $C^{18}O$ linewidths, as shown in Figure 3.12. The N_2H^+ linewidths, however, indicate that the cores in Oph C are among the least supersonic in N_2H^+. The reason for this apparently very effective dissipation of turbulence is not clear, although the lack of embedded sources driving outflows might be a possibility. The lack of embedded sources in Oph C, along with its considerably lower aspect ratio than its neighbours Oph E and Oph F, lead us to suggest that Oph C may have a slightly different line-of-sight distance than other regions, possibly being further from influences such as HD 147889. There are no embedded protostars in Oph C listed by Enoch et al. (2009).

3.5.6   Oph E and F

We consider Oph E and Oph F together, due to the low number of cores detected in these regions, along with the similarities between the two regions. These appear to be the most evolved regions of L1688, with a high ratio of embedded sources to starless cores: Oph E has four embedded Class I sources, while Oph F has six. Cores in Oph F are at a similar temperature to those in Oph A and A′, although without any obvious external heating. The core in Oph F for which an energy balance can be determined appears to be gravitationally bound, while the core in Oph E is pressure-confined. $C^{18}O$ linewidths show substantial turbulence, similar to Oph C, while these cores are the least supersonic in N_2H^+. Again, we hypothesise that this effective dissipation of turbulence may be the result of a lack of outflows in either of these regions.

3.5.7   L1689 and L1709

The starless cores we find in L1689 and L1709 are typically of similar mass to those in Oph B, C and E. We find six starless cores in L1689S; four in L1689; and one

in L1709. Enoch et al. (2009) list four embedded Class I protostars in L1689S; one Class 0 source in L1689N; and two Class I sources in L1709. The low number of cores relative to L1688, the low ratio of embedded sources to starless cores, and the presence of the Class 0 source IRAS 16293-2422 suggests that L1689 and L1709 are likely to be less evolved than, or forming stars less efficiently than, L1688. This was explained by NWA06 as due to L1689 being further from the Sco OB2 association than L1688, and hence less active.

3.5.8 Gradients across the cloud

It is clear from the discussion above that the different regions of the L1688 cloud do not show the same properties or evolutionary stage, despite being in close proximity both to one another and to HD 147889. There is a marked variation in temperature across the cloud, with Oph A and A′ being the warmest regions, followed by Oph F, E, C, B1, and B2, respectively. Oph A and A′ are clearly being influenced by the nearby B stars. As discussed in Section 3.4.3, the flux of ionising photons from the two B stars is not a dominant term in the virial equation in Oph A. However, these stars will be heating the gas and dust within Oph A.

Figure 3.3 shows in blue the warm dust traced by *Spitzer* 8-μm emission (Evans et al. 2003; Enoch et al. 2009), which surrounds Oph A and A′ on two sides. It should be noted that while the relative influence of HD 147889 on L1688 as a whole must be much greater than that of S1, the flux of ionising photons from S1 on Oph A is approximately twice that of HD 147889; the S1 reflection nebula is likely to have at least as much influence on Oph A as the PDR driven by HD 147889, even though the former is much smaller.

Oph A and Oph B appear to be at similar evolutionary stages, despite their marked difference in temperature. Both regions have embedded sources driving outflows, which may be hindering the dissipation of turbulence within the region.

However, while Oph A shows the influence of local effects, Oph B appears to be evolving in a more quiescent location: it is the coldest of the regions, and Figure 3.3 shows no sign of it being bordered by PDRs or reflection nebulae.

Cores in Oph A and Oph B are typically of similar mass (see Figure 3.11). However, as shown in Figure 3.13, while some of the cores in Oph A are strongly gravitationally dominated, the cores in Oph B are close to equipartition between gravitational potential energy and pressure. It is possible that material in Oph A might have been swept up by the PDR and the reflection nebula, increasing local density and hence leading to the strongly gravitationally bound prestellar cores in this region.

Oph E and F appear to be at a later evolutionary stage than Oph A and B, with a high ratio of protostars to starless cores, several embedded sources, and no embedded sources young enough to be driving outflows. Those starless cores that are found are among the least massive in L1688 (see Figure 3.11). These regions are both at an intermediate temperature. There is no obvious source of external heating, similar to Oph B, suggesting that the embedded sources in Oph E and F might be heating their surroundings. What might have led these regions to begin forming stars earlier than Oph A and B is not clear.

Oph C is noticeably different from the other regions in L1688, being an apparently entirely quiescent region, with only a few low-mass, pressure-confined cores and no embedded sources. As discussed above, this leads us to suggest that Oph C might be at a slightly different line-of-sight distance than the neighbouring regions.

There appears to be a general gradient in evolutionary stage from southwest to northeast across the cloud (except for Oph C). This could be due to the influence of the Sco OB2 association, located behind and to the southwest of Ophiuchus (Mamajek 2008); HD 147889, also behind Ophiuchus (Liseau et al. 1999), appears to be primarily of importance in Oph A, and to have relatively limited influence

elsewhere.

While a global southwest/northeast gradient in evolutionary stage can be inferred, and is consistent with previous studies (Loren 1989; NWA06), it must be emphasised that the properties of regions within L1688 appear to be determined substantially by local effects. In particular, the differences in temperature and energy balance between cores in Oph A and Oph B, two regions apparently at similar evolutionary stages, but with different immediate local environments (Oph A being heavily influenced by two B stars, and Oph B evolving in a less disturbed location), indicate the importance of local effects in determining the properties of starless cores.

3.6   Summary

In this chapter, we have extracted a set of sources from the SCUBA-2 850-μm map of the Ophiuchus molecular cloud, and have characterised the properties of these cores using SCUBA-2, Herschel, IRAM and HARP-B data sets.

We identified sources using the CuTEx curvature-based soure extraction algorithm, which gave us a catalogue of 93 sources, 70 of which were in the central region of the L1688 sub-cloud. Of these 93 sources, 46 were identified as protostellar, and 47 were identified as starless cores. Of the 70 sources in L1688, 47 were uniquely identified with a source in the S08 catalogue.

We determined the dust temperature of each source by SED fitting, which allowed an accurate mass determination to be made for each source. The distribution of masses of the starless cores is consistent with the expected shape of the core mass function. The low counting statistics of our sample did not allow us to accurately determine the power-law index of our core mass function, although the two slope values determined, $\alpha = 2.0 \pm 0.4$ and $\alpha = 2.7 \pm 0.4$ are both consistent with the expected behaviour of the high-mass Initial Mass Function.

We calculated the masses of our cores from N_2H^+ and $C^{18}O$ emission. We found that the mass of a core determined from 850-μm continuum emission and the mass determined from N_2H^+ emission correlate well, indicating that N_2H^+ and continuum emission are tracing the same material. The most massive cores, those in Oph A, have consistently higher continuum masses than N_2H^+ masses, indicating that, as expected, N_2H^+ emission does not trace the very densest material in prestellar cores.

We performed full virial stability analyses for the 23 cores for which both $C^{18}O$ and N_2H^+ data were available, estimating the contributions of gravitational energy, internal pressure (both thermal and non-thermal) and external pressure to the energy balance of the cores. Existing measurements of the magnetic field strength in Ophiuchus suggest that magnetic energy is unlikely to significantly alter the energy balance of our cores. We found that most of our cores are bound or virialised, with a virial ratio ≥ 1.

We calculated the Bonnor-Ebert critically-stable masses for each of the 23 cores for which N_2H^+ data are available. We found that our cores cannot be modelled as critically-stable Bonnor-Ebert spheres, and that the Bonnor-Ebert critically-stable mass is not a good estimator of the bound state of the cores for which we can perform a full virial analysis, typically overestimating the degree to which cores are gravitationally bound.

We found that whether our cores are gravitationally bound or pressure-confined depends strongly on the region in which they are located. Cores in the centre of Oph A are gravitationally bound, while cores in Oph C and E are pressure-confined. Cores in Oph A', B and F are in approximate equipartition between gravitational potential energy and external pressure energy, with pressure typically slightly dominating.

We see a loss of turbulence between core linewidths measured in $C^{18}O$ and core

linewidths measured in N_2H^+. This supports a picture in which dissipation of turbulence occurs in the dense centres of starless cores. At the radii traced by N_2H^+ emission, turbulence is dissipating, but is not yet fully dissipated, with a transonic or mildly supersonic non-thermal component to the core linewidth still present even when the core is on the brink of gravitational collapse. The degree to which turbulence is dissipated varies between regions, with turbulence being dissipated more within Oph C, E and F than within Oph A, A′ and B.

These results show that starless cores in the Ophiuchus molecular cloud are non-equilibrium objects with complex relationships with their local environments, and that a detailed analysis of their energy balance, of the sort we have carried out here, is required in order to accurately determine their virial state. In particular, we have shown that external pressure is of key importance to the energy balance of most of the densest starless cores in Ophiuchus, and thus cannot be neglected in a virial analysis.

Chapter 4

The Taurus molecular cloud

The Taurus molecular cloud (hereafter, Taurus) is a nearby (140 pc; Elias 1978), well-studied (see, e.g. Kenyon et al. 2008) site of low-mass star formation. Taurus is a quiescent region with well-defined filaments, in which star formation appears to be occurring in a dispersed mode (Kenyon et al. 2008). A particularly prominent filament is the L1495/B213/B211 filament in the northwest of Taurus, the head of which was observed as part of the JCMT GBS (Buckle et al. 2015). This extremely well-defined filament has been the subject of many studies, attempting to explain its formation and to determine its evolutionary state (e.g. Palmeirim et al. 2013; Hacar et al. 2013). Palmeirim et al. (2013) proposed that material is accreting onto the L1495 filament along 'striations' – thin streams of emission running perpendicular to the filament's length. Palmeirim et al. (2013) further noted that these striations lie parallel to the local magnetic field vectors – as determined by Goldsmith et al. (2008) – and proposed a mechanism whereby accretion onto filaments in Taurus is magnetically regulated, and hence – assuming that the dominant mode of star formation is filamentary (c.f. André et al. 2014 and discussion in Chapter 1) – that star formation in Taurus is also magnetically regulated.
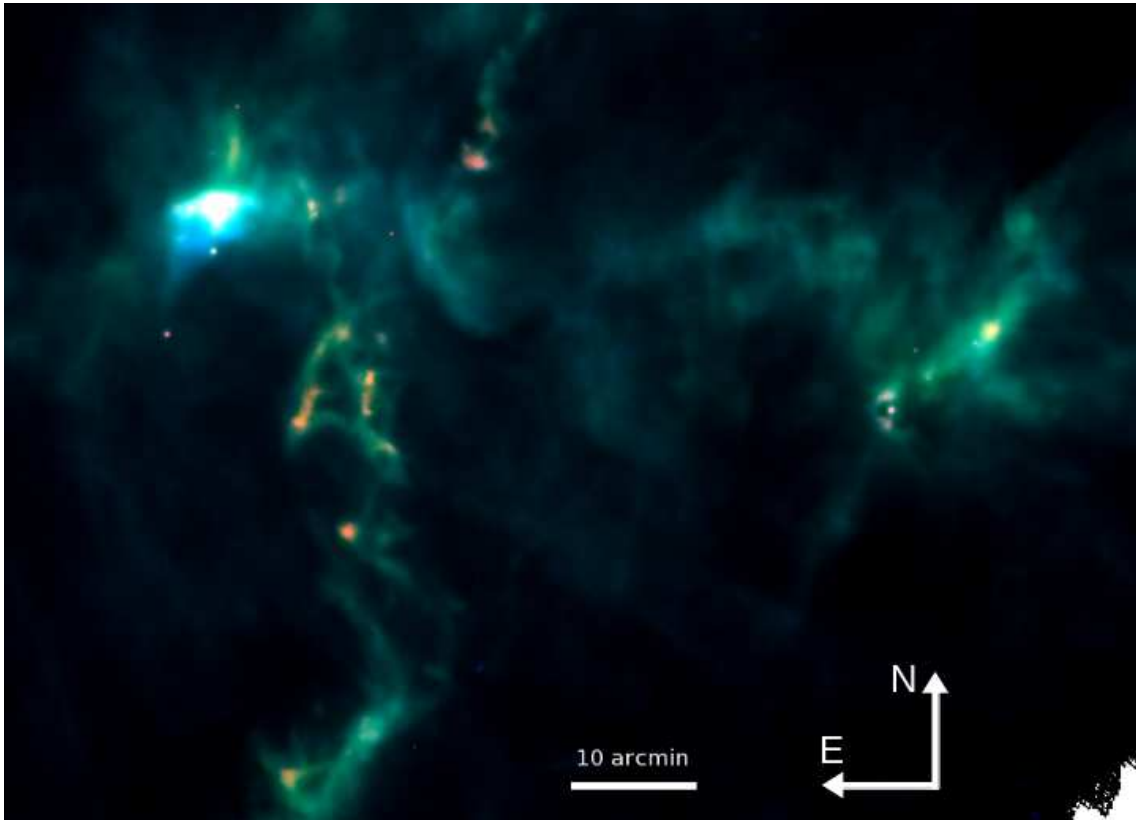
Figure 4.1: The L1495 region, as observed using SCUBA-2 and Herschel. Red channel: SCUBA-2 850-µm emission. Green channel: SPIRE 500-µm emission. Blue channel: SPIRE 250-µm emission. Note the red cores in the blue-green filaments.

4.1 Observations

4.1.1 SCUBA-2

The SCUBA-2 (Holland et al. 2013) observations used here form part of the JCMT GBS (Ward-Thompson et al. 2007). The L1495 region of the Taurus molecular cloud was observed with SCUBA-2 in 22 observations taken between October 2011 and July 2013.

The data were reduced as described in Section 2.1.2, using the Internal Release 1 method (Buckle et al. 2015). Continuum observations at 450 and 850 µm were made using fully sampled 15-, 30-, and 60-arcmin diameter circular regions (PONG900, 1800 and 3600 mapping modes – Bintley et al. 2014). Larger regions were covered

using overlapping scans. The final output map is centred at a position of R.A. (2000) = 04^h 17^m 54^s, Dec. (2000) = $+28°$ $05'$ $24''$. These data were first presented by Buckle et al. (2015), who provide full details of the observations. We only use the 850-μm data here.

4.1.2   Herschel Space Observatory

The comparison Herschel data used in this chapter were taken as part of the Herschel Gould Belt Survey (André et al. 2010) and were first presented by Marsh et al. (2015). They were taken simultaneously with the Photodetector Array Camera and Spectrometer, PACS (Poglitsch et al. 2010), and the Spectral and Photometric Imaging Receiver, SPIRE (Griffin et al. 2010; Swinyard et al. 2010) using the combined fast-scanning ($60''$/s) SPIRE/PACS parallel mode – see André et al. (2010) and Marsh et al. (2015) for details of the observations and the data reduction process – see also Chapter 2. The whole of the submillimetre-bright, high-column-density region of Taurus was observed as part of the HGBS (a region more than 10° across). In this chapter, we consider only the subset of this field which was also observed as part of the JCMT GBS. We removed large-scale structure from the Herschel observations by passing it through the SCUBA-2 pipeline in the manner described in Section 2.4.1. There are no positions observed by the JCMT GBS in Taurus which do not have corresponding HGBS observations.

4.2   Results

We here investigate what distinguishes those sources detected in both SCUBA-2 850-μm and Herschel-SPIRE 250-μm emission from those detected in 250-μm emission alone. We restrict our analysis to extended, starless sources, in order to be able to accurately characterise them using only data at wavelengths $>100\,\mu m$. We
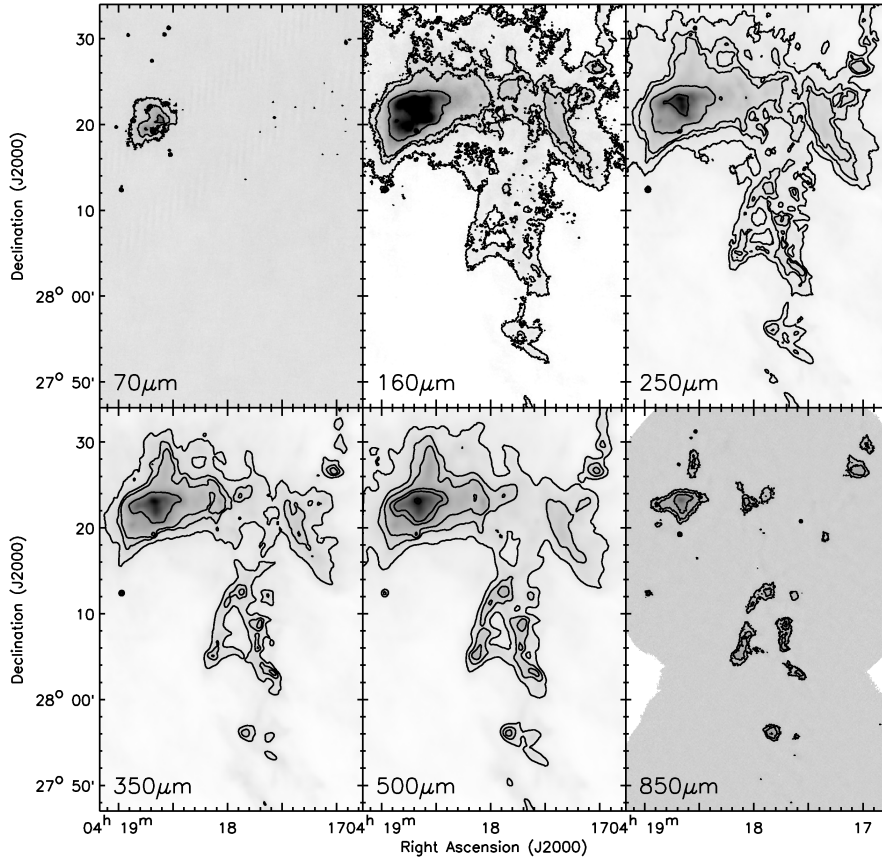
Figure 4.2: The centre of the L1495 region, as observed at the five Herschel wavelengths, 70, 160, 250, 350 and 500μm (Marsh et al. 2014; Marsh et al. 2015) and SCUBA-2 850 μm (Buckle et al. 2015). Contour levels – 70μm: 0.01, 0.02, 0.05, 0.5 Jy/6-arcsec pixel; 160μm: 0.05, 0.08, 0.1, 0.2, 0.5, 1.0 Jy/6-arcsec pixel; 250μm: as 160μm; 500μm: 0.02, 0.035, 0.05, 0.08, 0.1, 0.2, 0.5 Jy/6-arcsec pixel; 850μm: 0.005, 0.01, 0.02 Jy/6-arcsec pixel.

characterise our sources using a modified blackbody emission model.

The requirement for a SCUBA-2 detection of any source is a peaked 850-μm surface brightness, as SCUBA-2 loses sensitivity to flux on larger spatial scales (see Chapter 2). Thus, we hypothesise that the likely requirements for a SCUBA-2 detection of a starless core are for the core to have high density (thus having a high surface brightness), low temperature (i.e. having a high ratio of long-wavelength to short-wavelength flux), and compactness (i.e. being small enough not to lose emission to the SCUBA-2 spatial filtering). These properties are related to one

another: for starless cores of the same mass, in the absence of local heating, a dense core is expected to be colder than a rarefied core; and, trivially, a compact core will be denser than an extended core of the same mass. A dense core is expected to be colder than a rarefied core as its interior will be better shielded from the heating effects of the ISRF, and from cosmic ray heating. The aim of this study is to distinguish which, if any, of these properties is of most importance in determining whether a starless core identified in Herschel data will also be detectable in SCUBA-2 850-μm emission in the JCMT GBS.

Figure 4.1 shows a three-colour image of the region mapped with SCUBA-2, in which the SCUBA-2 850-μm emission is shown in red, Herschel 500-μm emission in green, and Herschel 250-μm is shown in blue. Both filamentary structure and starless cores can be seen in Figure 4.1. The majority of the cloud structure, including filaments, is detected by Herschel, and appears blue-green in Figure 4.1. The parts of the cloud detected by SCUBA-2 – hypothesised to be dense starless cores – appear red in Figure 4.1. These SCUBA-2 sources appear to lie exclusively on the filaments detected by Herschel, consistent with the hypothesis that core formation on filaments is the dominant mode of star formation (André et al. 2010).

The bright, extended source visible in Figure 4.1 at the north-eastern end of the L1495 filament is known as L1495A (Benson & Myers 1989; Lee et al. 2001). Figure 4.2 shows an enlargement of L1495A and the 'head' of the L1495 filament at six wavelengths: PACS 70μm, PACS 160μm, SPIRE 250μm, SPIRE 350μm, SPIRE 500μm and SCUBA-2 850μm. It can be seen from Figure 4.2 that only some of the sources and structures seen at other wavelengths are detected by SCUBA-2. The full area covered at high signal-to-noise ratio by SCUBA-2 at 850μm is shown in Figures 4.3 and 4.4.

L1495A can be seen clearly at all wavelengths in Figures 4.1 and 4.2, including with SCUBA-2 at 850 μm. The brightest peak coincides with the southern part

of L1495, known as L1495A-S (Benson & Myers 1989; Lee et al. 2001). The much fainter northern extension of L1495A is known as L1495A-N (Lee et al. 2001).

The bright point source visible to the south of L1495A-S in Figures 4.1 and 4.2 is V892 Tau (IRAS04155+2812). This star has a point source flux density in the IRAS Catalogue of 30 Jy at 12 microns and 100 Jy at 25 microns, which declines slightly to 70 Jy at 60 μm, before climbing again to 170 Jy at 100 μm. The 100-μm flux density almost certainly includes a contribution from L1495A-S, but otherwise, this SED is consistent with a Herbig Ae/Be star, and it is clearly heating L1495A-S, which is otherwise starless (Benson & Myers 1989). In the three-colour images in Figure 4.1, a colour gradient can be seen from south to north across L1495A, from blue to green. This would tend to indicate a temperature gradient across this core, with the hotter material in the south, consistent with the notion that the core is being externally heated by V892 Tau. A similar pattern of an externally heated core was modeled in Cepheus by Nutter et al. (2009), based on a combination of SCUBA and Akari data. Nutter et al. (2009) cautioned that temperature gradients could affect the appearance of starless cores at long wavelengths.

4.2.1   Source extraction

Three sets of sources were identified: sources in the 850-μm SCUBA-2 data (hereafter referred to as SCUBA-2 sources), sources in the 250-μm Herschel-SPIRE data (hereafter referred to as Herschel sources) and sources in the spatially-filtered 250-μm data (hereafter referred to as filtered-Herschel sources). Sources were identified using the source-finding algorithm CSAR (Kirk et al. 2013). CSAR is a dendrogram-based source-finding algorithm, which was run in its non-hierarchical mode on each of the three data sets. In its non-hierarchical mode, CSAR identifies a source based on a peak in the emission map, and assigns neighbouring pixels to that source if those pixels are above an assigned signal-to-noise criterion, and continues to do so

until the contour level at which the source becomes confused with its neighbours is reached. In its hierarchical mode, it continues to track the sources below the level at which they become confused with their neighbours, and assigns each group of neighbouring sources to a single 'root source'. These root sources are then themselves assessed in the same manner, and the process continues until all the significant emission in the map has been assigned to a structure of sources. However, for the purposes of identifying potentially prestellar starless cores, and due to the lack of extended structure in SCUBA-2 maps, we use CSAR in its non-hierarchical mode, identifying only peaks in emission.

The criteria chosen for a robustly-detected source were a peak flux density $F_\nu^{peak} \geq 4\sigma$ and a minimum of a 3σ drop in flux density between adjacent sources, where σ is the RMS noise level of the data (see Kirk et al. 2013). These stringent criteria were chosen in order to ensure that the sources we identified could be well-characterised, so that accurate comparisons could be made between cores detected in the different data sets.

CSAR is an appropriate choice of source extraction algorithm for Taurus because the sources are widely spaced and have closed contours around them. They are also significantly extended relative to the JCMT 850µm and SPIRE 250µm beams. The choice of CuTEx for source extraction in Ophiuchus (see Chapter 3) was due to the clustered nature of the distribution of cores in that region; a requirement for contours to close around sources was not appropriate there. However, the requirement of significant changes in gradient for a CuTEx detection are not typically met by the extended cores in Taurus, making CuTEx a poor choice of source extraction algorithm for this region. We discuss this further in Chapter 6 when we compare the two regions.

We measured the $1 - \sigma$ RMS noise on the low-variance regions of the SCUBA-2 850-µm map to be 0.9 ± 0.2 mJy/6-arcsec pixel and on the unfiltered 250-µm map
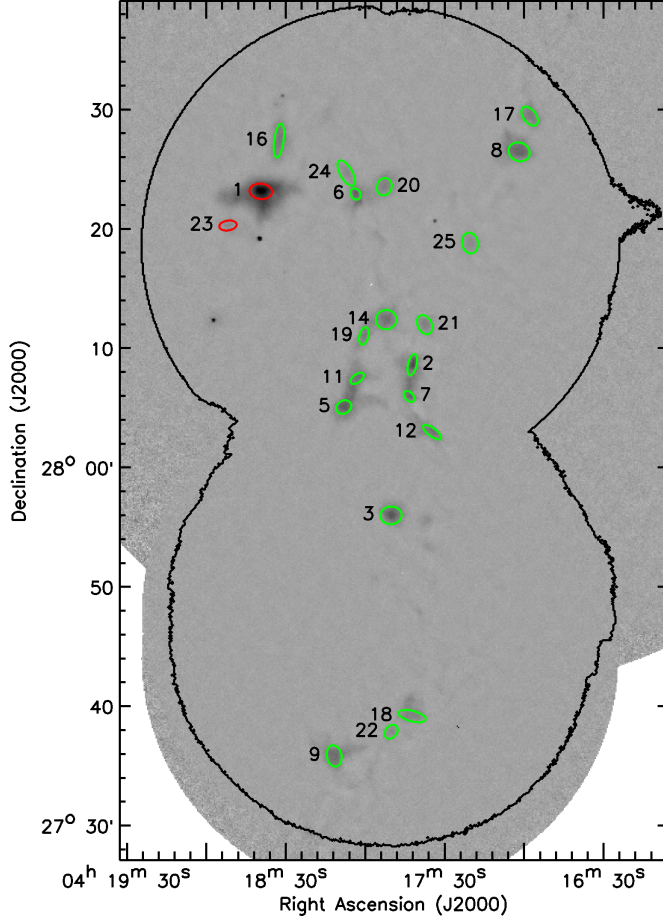
Figure 4.3: Grey-scale image of the head of the L1495 filament, as mapped by SCUBA-2 at 850 μm. Sources detected in emission by SCUBA-2 are marked by small green and red ellipses. Cores marked in red show signs of local heating (see text for details). The large-scale contour surrounds the region of lowest variance (c.f. Buckle et al. 2015). Cores are numbered as in Table 4.1.

to be 1.0 ± 0.2 mJy/6-arcsec pixel. Measuring the noise on the filtered 250-μm map produced values in the range 1.1–1.6 mJy/6-arcsec pixel. We adopted a value of 1.4 ± 0.2 mJy/6-arcsec pixel for the filtered 250-μm map, as being representative.

The regions of the SCUBA-2 map upon which source extraction was performed were those where the variance, as measured in the variance array, was ≤ 2 (Jy/6-arcsec pixel)^2. These are the two large regions marked on Figures 4.3 and 4.4. Noise levels across the Herschel maps are more uniform than those across the SCUBA-2 map. However, all sources detected in the Herschel data which were not fully
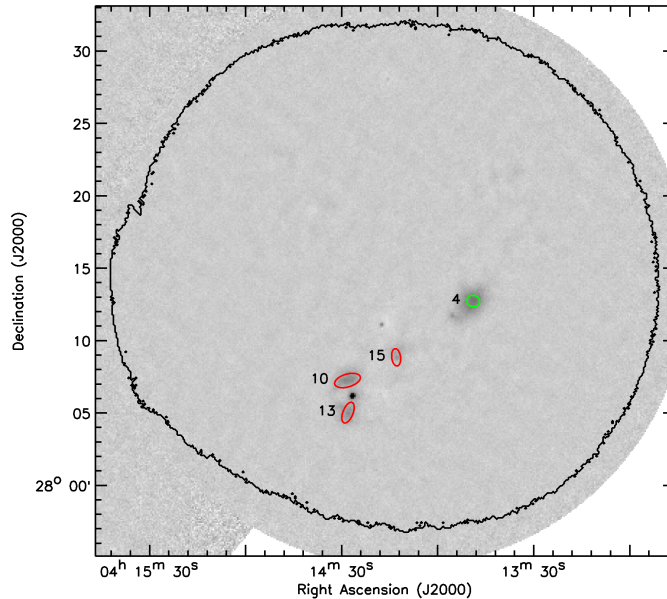
Figure 4.4: As Figure 4.3, for the L1495 West region.

located within one of the low-variance SCUBA-2 regions were excluded from further analysis, in order to allow an accurate comparison of the sources detected by the two instruments.

We identified 26 sources in the 850-µm map, 211 sources in the 250-µm map and 140 sources in the filtered 250-µm map. Sources smaller than the beam were rejected in the source extraction process. We examined the source samples to determine whether any sources contained protostars, based on whether they contained point sources at 70µm. One protostellar source was identified in the SCUBA-2 sample, along with 3 in the 250-µm sample and 2 in the filtered 250-µm sample. These sources were excluded from further analysis, leaving us with 25 sources in the 850-µm map (shown on Figures 4.3 and 4.4), 208 sources in the unfiltered 250-µm map (shown on Figures 4.5 and 4.6), and 138 sources in the filtered 250-µm map (shown on Figures 4.7 and 4.8). The 25 SCUBA-2 sources (named S1–S25) are listed in Table 4.1, while the Herschel sources (H1–H208) and filtered Herschel sources (F1–F138) are listed in Tables 4.2 and 4.3. For each SCUBA-2 source, Table 4.1 lists the name, right ascension and declination, measured major and minor FWHM sizes,
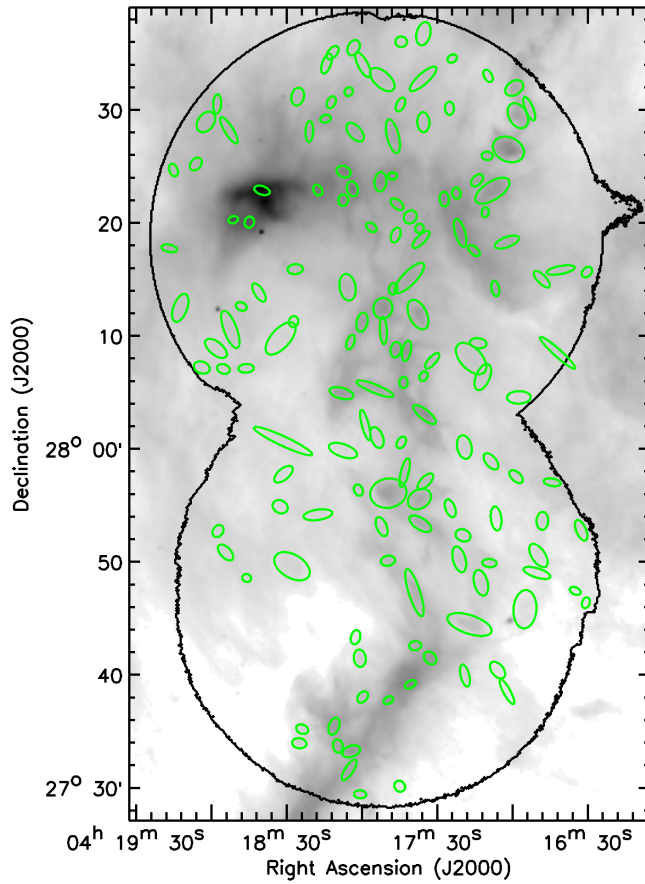
Figure 4.5: Grey-scale image of the head of the L1495 filament, in Herschel 250μm emission. Sources detected in Herschel 250μm emission are marked by small green ellipses. The large-scale contour surrounds the region of lowest SCUBA-2 variance (c.f. Buckle et al. 2015).
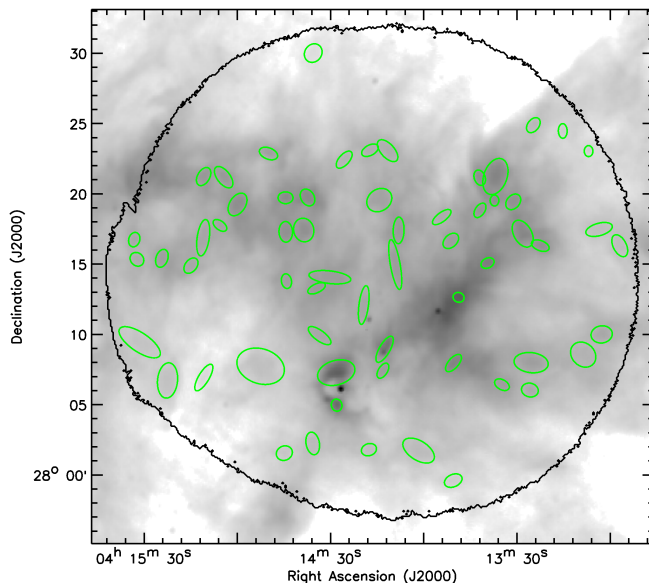
Figure 4.6: As Figure 4.5, for the L1495 West region.

position angle, flux densities as measured in filtered Herschel 160μm, 250μm, 350μm and 500μm and SCUBA-2 850μm emission, and the equivalent source numbers in the Herschel and filtered-Herschel catalogues.

For the Herschel sources, Table 4.2 lists the name, right ascension and declination, measured major and minor FWHM sizes, position angle, flux densities as measured in Herschel 160-μm, 250-μm, 350-μm and 500-μm emission, an extrapolated SCUBA-2 850-μm flux density (given in brackets), and the equivalent source in the Marsh et al. (2015) catalogue. Many of the sources found in the unfiltered Herschel data do not have counterparts in the Marsh et al. (2015) catalogue. Marsh et al. (2015) identify sources using the *getsources* algorithm (Men'shchikov et al. 2012), and produce two catalogues: a raw catalogue, and a catalogue of only robustly detected cores – inclusion of a core into the robust catalogue requires a stringent set of criteria to be met (Marsh et al. 2015). The Marsh et al. (2015) sources listed in the final column of Table 4.2 are from the robust catalogue. We find that, when comparing our sources with the full Marsh et al. (2015) catalogue, approximately half of

169
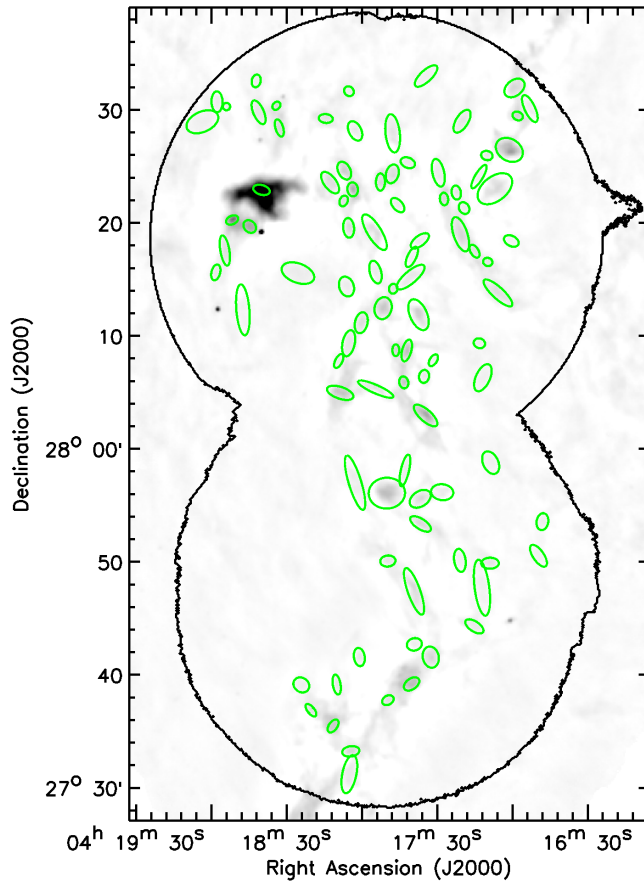
Figure 4.7: Grey-scale image of the head of the L1495 filament, in filtered Herschel 250μm emission. Sources detected in filtered Herschel 250μm emission are marked by small green ellipses. The large-scale contour surrounds the region of lowest SCUBA-2 variance (c.f. Buckle et al. 2015).

Table 4.1: Sources found by the CSAR algorithm in its non-hierarchical mode in the 850-μm SCUBA-2 data – see text for details.

Source Index	RA (J2000)	Dec (J2000)	FWHM (arcsec)	Angle (deg) (E of N)	F_ν^{total} (Jy)					Counterpart Sources
					160μm	250μm	350μm	500μm	850μm	
S1	4:18:40.00	+28:23:15.6	57.0 × 39.0	84.0	30.99	45.27	32.86	18.70	5.21	H1, F1
S2	4:17:42.10	+28:08:44.4	54.6 × 21.4	167.0	0.74	3.15	3.80	2.79	1.08	H26, F15
S3	4:17:50.18	+27:56:05.5	53.4 × 44.2	93.0	2.39	7.51	7.80	5.44	2.07	H47, F14
S4	4:13:48.01	+28:12:38.3	26.4 × 24.1	74.0	1.11	3.00	3.13	2.47	0.80	H6, F9
S5	4:18:08.17	+28:05:10.3	39.6 × 32.0	121.0	0.96	3.69	4.30	3.43	1.40	H40, F16
S6	4:18:03.83	+28:23:03.5	30.0 × 23.3	33.0	0.93	2.17	2.19	1.60	0.62	H7, F12
S7	4:17:43.31	+28:06:04.5	32.4 × 20.7	45.0	0.48	1.60	1.70	1.22	0.51	H28, F17
S8	4:17:01.36	+28:26:36.0	54.6 × 46.0	66.0	5.28	8.93	6.69	3.99	2.29	H15, F8
S9	4:18:11.60	+27:35:54.4	54.0 × 36.9	11.0	2.19	5.80	6.22	4.58	1.65	H41, F19
S10	4:14:27.63	+28:07:11.6	55.2 × 26.2	106.0	5.19	8.56	6.45	3.82	1.03	H8, F4
S11	4:18:03.08	+28:07:35.2	39.0 × 20.5	126.0	0.30	1.28	1.57	1.24	0.69	–
S12	4:17:34.58	+28:03:05.0	55.2 × 20.3	53.0	1.98	4.39	3.85	2.51	0.74	H19, F10
S13	4:14:27.53	+28:04:58.1	45.6 × 20.8	158.0	3.20	4.76	3.28	1.89	0.64	H11, F5
S14	4:17:52.08	+28:12:31.1	51.6 × 48.7	93.0	2.21	5.24	5.28	4.08	1.75	H23, F18
S15	4:14:12.33	+28:08:46.6	36.0 × 18.4	7.0	2.24	2.78	2.06	1.17	0.27	H9, F6
S16	4:18:33.13	+28:27:31.0	85.8 × 24.0	172.0	1.03	3.17	3.34	2.34	0.91	–
S17	4:16:57.34	+28:29:35.6	54.6 × 32.0	38.0	1.44	2.96	2.61	1.84	1.04	H58, F22
S18	4:17:42.09	+27:39:15.0	70.8 × 26.0	75.0	2.70	4.94	4.01	2.97	0.86	H13, F13
S19	4:18:00.55	+28:11:08.7	45.0 × 22.2	165.0	0.55	1.70	1.74	1.23	0.52	H45, F43
S20	4:17:52.87	+28:23:40.0	44.4 × 37.1	160.0	1.16	2.08	1.78	1.28	0.89	H18, F36
S21	4:17:37.42	+28:12:06.0	51.0 × 35.4	27.0	1.40	3.06	2.61	1.67	0.73	H44, F21
S22	4:17:50.02	+27:37:56.1	38.4 × 28.8	140.0	0.58	1.31	1.09	0.81	0.36	H34, F46
S23	4:18:52.50	+28:20:23.0	44.4 × 24.8	99.0	5.47	4.95	2.75	1.53	0.33	H3, F3
S24	4:18:07.41	+28:24:48.7	70.8 × 30.9	30.0	1.92	3.87	3.15	1.94	0.64	H10, F20
S25	4:17:20.14	+28:18:56.5	52.8 × 40.1	12.0	2.76	3.84	2.51	1.42	0.71	H16, F27
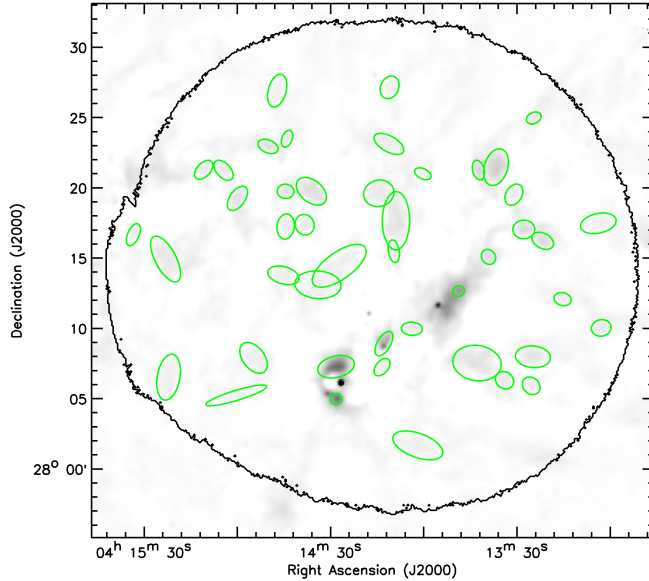
Figure 4.8: As Figure 4.7, for the L1495 West region.

the Herschel sources without Marsh et al. (2015) counterparts can be identified with a source in the raw Marsh et al. (2015) catalogue. The remainder of the sources are typically highly elongated and have a low signal-to-noise ratio, suggesting that with our chosen parameters for CSAR (optimised for detection of sources in the SCUBA-2 data), we are detecting striations such as those identified by Palmeirim et al. (2013). Table 4.3 lists the same properties for the filtered-Herschel sources as given in Table 4.2, except the 160-μm, 250-μm, 350-μm and 500-μm flux densities are measured in filtered Herschel emission, and the equivalent source in the Herschel catalogue is listed.

4.2.2 Source characterisation

We derived temperatures and masses for each of our sources using the spectral energy distribution (SED) measured from the Herschel and, in the case of the SCUBA-2 sources, the SCUBA-2 continuum data. The flux densities of the SCUBA-2 sources were measured across 5 wavebands (160μm, 250μm, 350μm, 500μm and 850μm),

Table 4.2: CSAR output for Herschel sources.

Source Index	RA (J2000)	Dec (J2000)	FWHM (arcsec)	Angle (deg) (E of N)	F_ν^{total} (Jy)					Counterpart Marsh Source
					160μm	250μm	350μm	500μm	850μm	
H1	4:18:40.43	+28:22:60.0	42.6 × 22.4	72.0	46.36	52.41	34.09	16.34	(4.54)	455
H2	4:18:51.98	+28:20:23.4	25.8 × 18.2	105.0	14.64	12.64	7.27	3.23	(0.83)	468
H3	4:18:45.48	+28:20:10.4	30.0 × 25.2	165.0	27.95	19.83	10.61	4.56	(1.11)	–
H4	4:18:17.93	+28:23:01.9	30.6 × 21.5	32.0	9.31	11.54	7.70	3.75	(1.07)	416
H5	4:13:47.92	+28:12:32.4	24.0 × 20.8	72.0	4.50	8.36	7.15	4.19	(1.33)	103
H6	4:18:03.97	+28:23:08.6	39.6 × 28.7	16.0	11.40	16.74	12.58	6.75	(2.00)	381
H7	4:14:27.64	+28:07:13.7	81.6 × 52.1	106.0	30.55	48.33	37.04	19.72	(6.01)	138
H8	4:14:11.95	+28:08:52.4	63.0 × 23.2	150.0	8.48	14.55	12.14	6.96	(2.15)	–
H9	4:18:07.51	+28:24:40.6	39.0 × 29.3	65.0	11.25	15.95	11.44	5.92	(1.74)	390
H10	4:14:27.56	+28:04:54.8	26.4 × 22.7	14.0	4.34	6.88	4.92	2.49	(0.76)	139
H11	4:17:40.47	+27:39:14.3	31.8 × 19.1	120.0	5.01	8.11	6.22	3.38	(1.03)	314
H12	4:18:07.67	+28:22:08.6	31.2 × 26.1	173.0	7.76	10.53	7.42	3.79	(1.10)	391
H13	4:17:01.06	+28:26:38.4	85.8 × 63.7	65.0	34.38	46.25	32.68	16.86	(4.88)	252
H14	4:17:20.52	+28:19:15.0	76.8 × 26.2	16.0	18.89	23.81	15.83	7.75	(2.22)	277
H15	4:17:26.94	+28:22:14.2	39.0 × 24.4	4.0	9.31	11.06	7.02	3.34	(0.94)	285
H16	4:17:52.66	+28:23:47.1	51.6 × 31.6	175.0	14.13	18.68	13.08	6.66	(1.92)	349
H17	4:17:34.84	+28:03:08.9	74.4 × 25.4	52.0	10.98	17.90	14.10	7.87	(2.40)	299
H18	4:17:47.80	+28:24:17.4	23.4 × 18.5	90.0	4.17	5.04	3.37	1.67	(0.47)	335
H19	4:13:38.45	+28:14:58.2	29.4 × 21.0	115.0	3.98	6.84	5.34	2.90	(0.90)	89
H20	4:17:22.08	+28:22:46.2	30.0 × 22.8	9.0	5.86	7.23	4.70	2.24	(0.64)	281
H21	4:17:51.64	+28:12:34.2	55.2 × 50.1	169.0	16.46	25.99	21.38	12.48	(3.73)	345
H22	4:17:14.97	+28:17:40.7	37.2 × 20.2	49.0	6.06	7.88	5.26	2.59	(0.75)	273
H23	4:17:42.08	+28:08:47.5	55.2 × 22.9	168.0	6.30	11.14	9.73	5.96	(1.83)	321
H24	4:13:49.70	+28:07:51.5	45.0 × 21.4	139.0	6.23	9.47	6.95	3.56	(1.08)	105
H25	4:17:43.32	+28:05:59.3	30.0 × 22.3	0.0	3.38	5.80	4.79	2.84	(0.87)	324
H26	4:18:04.11	+27:33:17.9	49.2 × 28.9	109.0	7.10	12.57	9.98	5.53	(1.73)	384

Table 4.2: – continued.

Source Index	RA (J2000)	Dec (J2000)	FWHM (arcsec)	Angle (deg) (E of N)	F_{ν}^{total} (Jy)					Counterpart Marsh Source
					160μm	250μm	350μm	500μm	850μm	
H27	4:17:32.58	+27:41:34.6	38.4 × 29.5	41.0	7.16	10.52	7.61	3.99	(1.18)	294
H28	4:17:07.54	+28:22:59.5	103.8 × 47.3	123.0	33.22	42.68	28.99	14.43	(4.14)	259
H29	4:13:35.68	+28:21:08.3	80.4 × 49.3	160.0	19.23	34.22	26.67	14.21	(4.50)	84
H30	4:17:49.27	+27:37:49.7	27.6 × 18.3	120.0	2.93	4.91	3.85	2.12	(0.65)	339
H31	4:17:46.41	+28:08:53.6	40.8 × 27.4	169.0	6.77	10.36	8.03	4.46	(1.33)	331
H32	4:17:56.28	+28:19:44.6	31.2 × 20.6	51.0	4.39	5.88	3.95	1.94	(0.56)	360
H33	4:13:26.99	+28:17:02.8	62.4 × 38.3	29.0	14.38	20.65	14.41	7.28	(2.16)	75
H34	4:17:45.97	+28:21:47.6	40.2 × 22.4	51.0	6.90	8.23	5.27	2.51	(0.71)	329
H35	4:18:08.25	+28:05:02.2	65.4 × 28.5	74.0	8.25	14.78	12.83	7.84	(2.42)	392
H36	4:18:11.03	+27:35:30.9	46.8 × 26.8	160.0	5.29	10.73	9.80	6.11	(1.97)	399
H37	4:14:43.72	+28:19:43.3	31.8 × 25.2	90.0	4.66	6.89	5.04	2.62	(0.78)	155
H38	4:14:36.59	+28:19:44.0	38.4 × 28.5	31.0	6.86	9.78	7.04	3.61	(1.07)	146
H39	4:17:37.51	+28:12:00.6	84.6 × 45.9	26.0	19.92	26.86	19.08	9.98	(2.88)	310
H40	4:18:00.04	+28:11:19.5	51.0 × 28.4	168.0	7.18	11.49	9.65	5.71	(1.71)	372
H41	4:18:14.86	+28:29:21.4	28.2 × 19.9	106.0	3.64	4.94	3.38	1.68	(0.49)	409
H42	4:17:49.39	+27:56:10.7	96.6 × 77.3	100.0	27.66	42.50	33.46	18.92	(5.63)	340
H43	4:14:59.27	+28:19:15.8	53.4 × 34.1	147.0	10.59	14.15	9.79	4.88	(1.42)	164
H44	4:13:40.77	+28:21:03.6	34.2 × 23.4	20.0	3.55	6.25	4.87	2.60	(0.82)	97
H45	4:17:47.51	+28:14:17.0	30.0 × 22.8	171.0	3.75	5.44	3.91	2.05	(0.61)	333
H46	4:13:36.04	+28:19:25.8	23.4 × 18.5	0.0	2.25	3.54	2.62	1.37	(0.42)	85
H47	4:13:21.33	+28:16:11.0	40.2 × 21.8	69.0	4.72	6.61	4.52	2.25	(0.66)	66
H48	4:17:47.68	+28:27:48.6	92.4 × 31.5	14.0	16.94	19.09	12.14	5.79	(1.60)	334
H49	4:17:06.39	+28:14:19.0	41.4 × 20.4	11.0	5.40	6.83	4.50	2.19	(0.63)	–
H50	4:13:29.97	+28:19:19.3	37.2 × 27.3	139.0	5.37	8.15	5.83	2.95	(0.89)	78
H51	4:14:37.89	+28:17:24.9	51.0 × 42.9	14.0	11.38	16.70	12.20	6.34	(1.89)	147
H52	4:14:43.71	+28:17:17.5	44.4 × 28.9	2.0	6.78	10.07	7.40	3.88	(1.16)	154

Table 4.2: – continued.

Source Index	RA (J2000)	Dec (J2000)	FWHM (arcsec)	Angle (deg) (E of N)	F_ν^{total} (Jy) 160μm	250μm	350μm	500μm	850μm	Counterpart Marsh Source
H53	4:16:57.24	+28:29:38.3	71.4 × 48.0	30.0	14.35	20.37	15.43	8.40	(2.45)	248
H54	4:17:40.65	+28:20:39.7	36.6 × 32.1	136.0	7.97	9.26	5.87	2.80	(0.78)	319
H55	4:17:13.73	+28:23:55.0	38.4 × 24.0	136.0	5.96	7.11	4.64	2.26	(0.63)	272
H56	4:17:36.29	+28:18:40.2	60.0 × 22.1	135.0	8.56	10.31	6.78	3.31	(0.93)	305
H57	4:18:21.38	+28:28:13.7	55.2 × 20.3	178.0	6.52	8.80	6.02	3.01	(0.88)	424
H58	4:17:36.95	+28:19:39.1	25.2 × 22.0	160.0	3.58	4.31	2.79	1.35	(0.38)	307
H59	4:17:10.46	+28:21:04.8	27.6 × 18.6	172.0	2.91	4.00	2.82	1.43	(0.42)	264
H60	4:17:54.82	+28:05:26.1	105.6 × 21.0	68.0	9.24	12.76	9.16	4.84	(1.40)	359
H61	4:18:04.91	+27:31:38.9	64.2 × 21.9	148.0	6.26	10.66	8.29	4.53	(1.40)	–
H62	4:18:02.93	+28:28:10.2	60.0 × 32.6	42.0	11.95	13.91	8.97	4.30	(1.20)	–
H63	4:18:09.46	+27:33:45.3	35.4 × 26.0	11.0	3.57	6.85	5.70	3.28	(1.05)	–
H64	4:17:41.00	+28:15:14.7	107.4 × 36.6	136.0	21.04	27.37	18.62	9.36	(2.69)	315
H65	4:13:40.77	+28:18:44.0	34.8 × 20.4	146.0	3.32	5.13	3.69	1.88	(0.57)	96
H66	4:17:36.91	+27:55:39.4	66.0 × 49.0	122.0	14.01	18.88	13.73	7.23	(2.09)	304
H67	4:17:36.53	+27:53:28.3	66.0 × 30.1	58.0	8.50	11.94	8.74	4.60	(1.35)	306
H68	4:15:03.74	+28:21:12.8	54.0 × 27.6	38.0	7.63	9.99	6.87	3.42	(0.99)	165
H69	4:15:10.22	+28:21:15.8	42.0 × 25.8	150.0	5.81	7.55	5.17	2.57	(0.74)	170
H70	4:17:51.45	+28:10:35.2	72.6 × 17.6	3.0	6.44	8.54	6.26	3.36	(0.96)	–
H71	4:16:58.70	+28:32:05.4	52.2 × 36.2	123.0	8.11	11.25	8.31	4.45	(1.29)	250
H72	4:18:04.64	+28:09:34.0	40.8 × 20.1	160.0	3.61	5.42	4.28	2.44	(0.72)	382
H73	4:14:07.15	+28:17:20.8	57.0 × 23.6	178.0	6.52	8.91	6.24	3.18	(0.93)	–
H74	4:14:33.83	+28:13:15.1	40.8 × 18.6	115.0	3.42	5.42	4.26	2.30	(0.70)	–
H75	4:17:09.64	+28:26:05.0	29.4 × 21.6	82.0	3.45	4.01	2.60	1.27	(0.35)	266
H76	4:14:29.51	+28:14:02.2	90.0 × 28.1	83.0	10.53	16.61	12.96	6.98	(2.12)	–
H77	4:17:01.71	+28:18:26.2	67.8 × 26.6	110.0	8.90	11.91	8.17	4.12	(1.19)	254
H78	4:14:08.33	+28:14:54.8	108.0 × 21.5	10.0	9.70	13.55	9.71	4.98	(1.46)	–

Table 4.2: – continued.

Source Index	RA (J2000)	Dec (J2000)	FWHM (arcsec)	Angle (deg) (E of N)	F_ν^{total} (Jy) 160μm	250μm	350μm	500μm	850μm	Counterpart Marsh Source
H79	4:14:12.54	+28:07:20.7	36.0×19.0	148.0	2.42	4.50	3.77	2.11	(0.67)	124
H80	4:17:35.27	+28:06:32.6	26.4×20.1	148.0	2.34	3.29	2.37	1.24	(0.36)	300
H81	4:17:38.87	+27:47:22.2	131.4×31.9	18.0	11.21	16.62	11.37	5.77	(1.71)	313
H82	4:13:34.10	+28:06:17.3	34.2×21.4	61.0	2.80	4.73	3.51	1.82	(0.57)	82
H83	4:19:17.68	+28:17:49.9	42.0×19.2	79.0	3.48	5.15	3.74	1.91	(0.57)	483
H84	4:13:50.28	+28:16:34.2	39.0×26.7	134.0	4.70	6.69	4.81	2.45	(0.73)	106
H85	4:17:38.58	+27:42:39.8	32.4×23.8	97.0	3.54	4.99	3.44	1.77	(0.52)	–
H86	4:18:12.54	+28:30:49.0	33.6×21.4	154.0	3.58	4.66	3.20	1.60	(0.46)	404
H87	4:13:24.61	+28:07:50.6	73.2×42.9	83.0	12.55	17.45	12.05	6.03	(1.77)	72
H88	4:14:43.57	+28:13:46.5	31.8×21.4	10.0	3.33	4.24	2.92	1.46	(0.42)	153
H89	4:14:49.16	+28:22:53.0	40.8×23.9	68.0	3.76	5.38	3.89	1.99	(0.59)	161
H90	4:15:23.85	+28:15:26.7	39.6×25.3	160.0	4.10	6.14	4.34	2.20	(0.66)	179
H91	4:17:46.52	+28:19:03.5	40.8×23.9	160.0	5.21	6.07	3.89	1.86	(0.52)	–
H92	4:18:53.82	+28:28:18.6	80.4×22.5	32.0	9.37	11.10	7.35	3.52	(0.99)	–
H93	4:18:05.48	+28:31:46.1	24.6×21.2	140.0	2.61	3.14	2.10	1.03	(0.29)	388
H94	4:14:13.35	+28:19:31.0	56.4×46.3	125.0	11.92	15.02	10.36	5.20	(1.48)	127
H95	4:15:05.01	+28:17:46.5	33.6×18.7	53.0	3.00	3.72	2.51	1.24	(0.35)	167
H96	4:19:07.13	+28:25:18.5	37.8×27.0	140.0	4.85	5.77	3.80	1.84	(0.52)	–
H97	4:18:58.60	+28:30:39.1	50.4×20.9	177.0	5.31	6.00	3.84	1.81	(0.50)	–
H98	4:18:05.87	+28:14:25.5	70.8×42.5	10.0	14.55	15.94	10.04	4.76	(1.30)	–
H99	4:19:03.11	+28:29:02.6	60.6×42.1	142.0	11.48	14.40	9.59	4.62	(1.32)	–
H100	4:15:10.45	+28:16:54.0	78.6×26.8	172.0	8.79	11.03	7.34	3.60	(1.03)	–
H101	4:18:26.11	+28:31:18.8	48.0×32.8	166.0	6.47	8.85	6.26	3.18	(0.93)	438
H102	4:14:18.61	+28:12:02.5	83.4×20.3	172.0	5.93	9.01	7.01	3.78	(1.14)	–
H103	4:15:32.79	+28:16:47.2	31.2×23.4	163.0	2.79	3.75	2.54	1.26	(0.37)	187
H104	4:14:32.95	+28:09:52.6	58.2×22.8	54.0	3.99	6.94	5.49	2.96	(0.93)	–

Table 4.2: – continued.

Source Index	RA (J2000)	Dec (J2000)	FWHM (arcsec)	Angle (deg) (E of N)	F_ν^{total} (Jy) 160µm	250µm	350µm	500µm	850µm	Counterpart Marsh Source
H105	4:15:14.46	+28:14:54.8	37.2 × 24.6	141.0	3.79	4.91	3.31	1.62	(0.47)	–
H106	4:17:42.84	+27:57:59.8	78.6 × 22.0	166.0	5.37	6.98	4.75	2.39	(0.68)	–
H107	4:13:01.72	+28:09:48.9	45.6 × 36.8	98.0	6.30	8.03	5.31	2.59	(0.74)	58
H108	4:17:49.49	+27:50:11.5	38.4 × 26.2	100.0	2.76	4.61	3.40	1.79	(0.55)	338
H109	4:13:25.07	+28:05:53.4	36.0 × 29.1	77.0	3.20	4.88	3.46	1.76	(0.53)	73
H110	4:16:52.67	+28:30:15.8	67.2 × 21.0	22.0	5.14	6.83	4.78	2.45	(0.71)	–
H111	4:17:31.80	+28:07:54.4	52.2 × 20.5	138.0	4.09	5.07	3.36	1.69	(0.48)	293
H112	4:17:44.62	+28:30:37.6	39.6 × 20.9	155.0	3.75	4.07	2.56	1.21	(0.33)	–
H113	4:15:31.93	+28:15:22.9	31.8 × 27.2	45.0	2.57	3.96	2.81	1.42	(0.43)	–
H114	4:13:53.17	+28:18:16.4	47.4 × 19.7	127.0	3.36	4.46	3.01	1.49	(0.43)	–
H115	4:19:16.13	+28:24:46.2	34.8 × 21.8	21.0	2.80	3.51	2.32	1.12	(0.32)	482
H116	4:18:26.97	+28:16:01.0	40.8 × 26.0	95.0	4.49	5.09	3.16	1.47	(0.41)	–
H117	4:14:10.56	+28:23:02.1	57.0 × 29.1	42.0	6.07	7.61	5.07	2.48	(0.71)	–
H118	4:17:35.39	+28:29:03.4	52.8 × 32.4	3.0	7.24	7.83	4.81	2.26	(0.62)	–
H119	4:17:34.50	+27:57:13.4	54.0 × 24.6	136.0	4.36	5.79	4.00	2.05	(0.59)	297
H120	4:17:59.58	+27:38:06.8	33.6 × 23.7	139.0	2.41	3.45	2.56	1.37	(0.40)	369
H121	4:14:16.27	+28:23:04.5	39.0 × 22.3	118.0	3.29	3.90	2.58	1.26	(0.35)	–
H122	4:17:51.97	+28:32:50.1	79.8 × 42.0	48.0	12.59	14.68	9.46	4.51	(1.26)	–
H123	4:17:35.49	+28:32:54.4	92.4 × 28.9	132.0	9.93	11.06	7.01	3.33	(0.92)	–
H124	4:16:40.08	+28:15:57.4	76.2 × 21.3	101.0	5.92	6.63	4.14	2.00	(0.55)	–
H125	4:16:47.69	+28:15:08.3	57.0 × 22.3	44.0	4.66	5.36	3.37	1.64	(0.45)	–
H126	4:17:16.82	+27:44:32.5	123.0 × 48.2	72.0	13.57	16.99	11.68	5.96	(1.68)	274
H127	4:18:03.57	+28:35:39.6	42.6 × 29.6	153.0	4.49	5.30	3.52	1.72	(0.48)	–
H128	4:13:07.74	+28:08:23.1	58.8 × 48.3	46.0	9.63	11.99	7.77	3.77	(1.07)	–
H129	4:16:29.52	+28:15:46.0	31.8 × 23.3	135.0	2.85	3.04	1.87	0.89	(0.24)	–
H130	4:14:24.65	+28:22:24.9	45.0 × 22.2	138.0	3.08	3.94	2.64	1.29	(0.37)	135

Table 4.2: – continued.

Source Index	RA (J2000)	Dec (J2000)	FWHM (arcsec)	Angle (deg) (E of N)	F_ν^{total} (Jy) 160μm	250μm	350μm	500μm	850μm	Counterpart Marsh Source
H131	4:19:13.16	+28:12:33.3	78.0 × 37.0	160.0	8.79	11.03	7.20	3.44	(0.98)	–
H132	4:17:44.21	+28:00:40.5	34.2 × 21.8	149.0	2.36	2.82	1.82	0.90	(0.25)	–
H133	4:18:48.62	+28:12:42.0	30.0 × 21.4	68.0	2.01	2.46	1.55	0.73	(0.21)	–
H134	4:17:08.78	+27:49:59.2	38.4 × 21.4	86.0	2.05	2.57	1.74	0.88	(0.25)	262
H135	4:17:59.78	+28:34:08.6	72.6 × 26.7	28.0	6.54	7.08	4.54	2.18	(0.60)	–
H136	4:18:00.53	+27:29:29.1	32.4 × 21.1	87.0	1.35	2.31	1.70	0.91	(0.28)	371
H137	4:17:13.31	+28:09:28.3	45.0 × 26.4	83.0	3.76	4.17	2.51	1.19	(0.32)	270
H138	4:13:23.26	+28:24:46.8	36.0 × 24.2	142.0	1.75	2.88	2.14	1.10	(0.34)	71
H139	4:17:24.87	+28:30:17.4	34.8 × 23.8	0.0	3.08	3.13	1.93	0.91	(0.24)	–
H140	4:18:12.02	+28:35:13.1	40.8 × 23.4	142.0	3.21	3.54	2.37	1.15	(0.32)	–
H141	4:18:53.00	+28:10:39.8	105.0 × 32.8	20.0	10.68	11.90	7.41	3.45	(0.95)	–
H142	4:18:14.48	+28:34:14.5	55.8 × 23.1	161.0	3.91	4.58	3.06	1.50	(0.42)	–
H143	4:18:01.39	+27:56:26.9	31.2 × 22.6	22.0	1.90	2.44	1.53	0.73	(0.21)	–
H144	4:14:35.36	+28:02:11.5	48.6 × 28.5	11.0	2.86	4.64	3.35	1.70	(0.52)	145
H145	4:17:52.05	+27:53:12.8	53.4 × 26.3	22.0	3.83	4.87	3.29	1.65	(0.47)	–
H146	4:16:43.63	+27:57:08.6	45.6 × 19.9	81.0	2.58	2.98	1.81	0.85	(0.24)	–
H147	4:17:16.15	+28:08:06.9	101.4 × 56.6	43.0	17.53	18.98	11.49	5.49	(1.48)	–
H148	4:17:20.93	+27:50:19.1	70.8 × 33.6	15.0	5.96	7.09	4.70	2.33	(0.65)	280
H149	4:14:01.19	+28:01:38.0	75.6 × 41.0	57.0	6.57	9.72	6.74	3.30	(0.99)	115
H150	4:17:11.46	+28:06:28.2	73.8 × 36.4	157.0	7.65	8.50	5.13	2.44	(0.67)	–
H151	4:12:55.60	+28:16:07.6	51.0 × 28.4	27.0	3.71	4.56	2.95	1.44	(0.41)	–
H152	4:17:23.74	+28:34:42.2	26.4 × 20.1	122.0	1.63	1.67	1.04	0.50	(0.13)	–
H153	4:18:00.74	+27:41:32.9	46.2 × 31.6	8.0	1.77	3.11	2.23	1.15	(0.36)	374
H154	4:18:41.52	+28:13:56.4	55.2 × 24.1	32.0	3.37	4.04	2.55	1.19	(0.34)	–
H155	4:13:02.25	+28:17:18.0	58.2 × 26.5	106.0	3.84	4.55	2.91	1.41	(0.39)	–
H156	4:14:17.23	+28:01:43.3	33.0 × 25.6	108.0	1.48	2.53	1.85	0.95	(0.29)	–

Table 4.2: – continued.

Source Index	RA (J2000)	Dec (J2000)	FWHM (arcsec)	Angle (deg) (E of N)	F_ν^{total} (Jy) 160µm	250µm	350µm	500µm	850µm	Counterpart Marsh Source
H157	4:17:54.00	+28:01:06.6	58.2 × 31.6	21.0	4.84	5.24	3.36	1.63	(0.44)	–
H158	4:17:44.37	+28:36:11.3	31.2 × 28.2	90.0	2.27	2.58	1.67	0.80	(0.22)	–
H159	4:14:52.07	+28:07:42.9	103.8 × 74.1	72.0	13.82	19.79	14.18	7.19	(2.12)	163
H160	4:16:41.40	+28:08:37.3	124.8 × 17.6	48.0	5.74	6.33	4.02	1.91	(0.52)	–
H161	4:17:12.25	+27:48:14.4	69.6 × 35.5	15.0	5.62	6.50	4.22	2.08	(0.57)	269
H162	4:18:46.60	+28:07:12.9	41.4 × 23.1	94.0	2.19	2.56	1.58	0.73	(0.20)	–
H163	4:17:35.37	+28:36:54.1	63.0 × 36.1	166.0	5.71	6.57	4.18	2.00	(0.55)	–
H164	4:18:55.71	+28:07:09.4	34.8 × 24.9	71.0	2.08	2.41	1.47	0.68	(0.19)	–
H165	4:15:22.19	+28:06:43.9	75.6 × 42.2	175.0	5.72	7.90	5.50	2.73	(0.80)	177
H166	4:17:19.41	+27:52:26.6	41.4 × 31.1	68.0	2.80	3.37	2.09	1.00	(0.28)	–
H167	4:15:31.16	+28:09:27.7	103.2 × 40.4	56.0	8.10	11.01	7.63	3.81	(1.11)	–
H168	4:19:04.40	+28:07:16.7	43.2 × 30.9	72.0	3.41	3.43	2.08	0.95	(0.25)	–
H169	4:17:58.65	+28:02:13.1	83.4 × 16.6	15.0	3.93	4.02	2.58	1.25	(0.33)	–
H170	4:16:58.11	+27:57:38.7	43.2 × 24.1	48.0	2.14	2.57	1.61	0.77	(0.22)	–
H171	4:16:47.56	+27:53:43.2	47.4 × 30.8	177.0	2.75	3.05	1.85	0.87	(0.24)	240
H172	4:17:09.29	+28:33:10.1	35.4 × 20.8	29.0	1.85	1.92	1.17	0.55	(0.15)	–
H173	4:18:58.73	+28:08:58.6	69.6 × 34.3	51.0	5.44	6.10	3.78	1.75	(0.48)	–
H174	4:17:08.19	+27:58:59.9	51.6 × 27.2	41.0	2.89	3.48	2.16	1.03	(0.29)	–
H175	4:17:24.52	+27:54:50.6	49.2 × 25.1	20.0	2.66	2.91	1.82	0.87	(0.24)	–
H176	4:18:24.93	+27:34:00.1	38.4 × 27.0	82.0	1.10	1.95	1.36	0.70	(0.22)	437
H177	4:17:18.88	+28:00:16.2	63.6 × 38.2	12.0	4.49	5.80	3.57	1.69	(0.48)	–
H178	4:16:32.03	+27:52:52.7	58.2 × 25.4	23.0	3.26	3.53	2.10	0.97	(0.26)	–
H179	4:18:57.69	+27:52:47.4	34.2 × 26.3	146.0	2.07	2.18	1.27	0.57	(0.15)	–
H180	4:14:44.55	+28:01:30.6	35.4 × 30.7	114.0	1.89	2.56	1.76	0.87	(0.25)	–
H181	4:18:23.75	+27:35:15.1	33.0 × 23.9	67.0	0.89	1.62	1.16	0.60	(0.19)	434
H182	4:18:54.63	+27:50:53.6	52.2 × 27.5	43.0	3.20	3.38	1.96	0.89	(0.24)	–

Table 4.2: – continued.

Source Index	RA (J2000)	Dec (J2000)	FWHM (arcsec)	Angle (deg) (E of N)	F_ν^{total} (Jy) 160μm	250μm	350μm	500μm	850μm	Counterpart Marsh Source
H183	4:17:18.63	+27:40:01.0	59.4 × 23.3	14.0	2.60	2.73	1.70	0.84	(0.22)	–
H184	4:18:32.74	+28:09:52.7	105.6 × 50.2	138.0	10.08	11.58	7.17	3.37	(0.93)	–
H185	4:18:27.97	+27:49:41.4	103.8 × 62.3	59.0	12.15	12.40	7.29	3.33	(0.88)	–
H186	4:18:27.58	+28:11:22.5	28.8 × 24.8	165.0	1.52	1.57	0.96	0.44	(0.12)	–
H187	4:18:31.69	+28:00:46.8	171.0 × 24.1	65.0	6.97	7.88	4.60	2.09	(0.57)	–
H188	4:18:46.13	+27:48:38.2	24.0 × 20.8	72.0	1.04	1.01	0.59	0.27	(0.07)	–
H189	4:13:05.42	+28:22:53.7	23.4 × 18.5	0.0	0.61	0.74	0.50	0.25	(0.07)	–
H190	4:16:56.97	+28:04:40.1	63.0 × 33.2	91.0	3.68	4.19	2.54	1.21	(0.33)	–
H191	4:18:17.63	+27:54:15.3	77.4 × 26.4	98.0	3.11	4.07	2.40	1.09	(0.31)	–
H192	4:13:13.74	+28:24:21.0	31.2 × 18.7	1.0	0.78	1.15	0.85	0.45	(0.13)	–
H193	4:16:49.15	+27:50:39.0	70.8 × 34.9	34.0	4.11	4.01	2.40	1.13	(0.29)	–
H194	4:13:50.06	+27:59:28.5	39.6 × 26.2	114.0	1.27	1.94	1.32	0.63	(0.19)	–
H195	4:18:07.63	+27:59:57.2	78.0 × 34.0	71.0	4.32	4.48	2.78	1.32	(0.35)	–
H196	4:18:32.77	+27:54:57.6	41.4 × 33.1	62.0	2.02	2.50	1.46	0.66	(0.19)	–
H197	4:18:31.46	+27:57:50.6	59.4 × 29.3	130.0	2.18	2.83	1.67	0.77	(0.22)	–
H198	4:16:54.59	+27:45:53.7	102.0 × 61.2	176.0	7.92	7.39	4.29	2.04	(0.52)	–
H199	4:16:49.76	+27:49:06.6	74.4 × 25.4	73.0	2.13	2.34	1.41	0.66	(0.18)	–
H200	4:15:10.46	+28:06:55.9	65.4 × 22.3	149.0	1.35	1.64	1.09	0.55	(0.15)	–
H201	4:17:05.59	+27:40:29.9	51.6 × 31.0	39.0	1.69	1.78	1.01	0.47	(0.12)	–
H202	4:17:06.13	+27:53:56.4	64.2 × 28.0	7.0	1.87	1.94	1.11	0.53	(0.14)	–
H203	4:14:34.48	+28:30:01.7	41.4 × 35.9	144.0	1.42	1.67	1.16	0.57	(0.16)	–
H204	4:16:30.16	+27:46:27.7	29.4 × 20.1	160.0	0.56	0.62	0.38	0.18	(0.05)	–
H205	4:18:02.45	+27:43:24.1	38.4 × 24.5	166.0	0.57	0.83	0.51	0.24	(0.07)	–
H206	4:16:34.43	+27:47:30.3	30.6 × 18.8	67.0	0.68	0.56	0.33	0.15	(0.04)	–
H207	4:17:01.84	+27:38:35.2	74.4 × 18.1	28.0	1.28	1.24	0.70	0.32	(0.08)	–
H208	4:17:44.73	+27:30:12.5	30.6 × 26.8	40.0	0.83	0.74	0.47	0.23	(0.06)	–

Table 4.3: CSAR output for filtered-Herschel sources.

Source Index	RA (J2000)	Dec (J2000)	FWHM (arcsec)	Angle (deg) (E of N)	F_ν^{total} (Jy) 160μm	250μm	350μm	500μm	850μm	Counterpart Herschel Source
F1	4:18:40.60	+28:23:02.3	45.0 × 25.8	75.0	23.27	29.52	20.02	10.88	(3.02)	H1
F2	4:18:52.41	+28:20:21.6	34.2 × 22.2	115.0	4.43	3.88	2.13	1.16	(0.28)	H3
F3	4:14:27.71	+28:07:13.3	79.8 × 45.7	103.0	11.80	16.50	12.04	7.35	(2.03)	H8
F4	4:14:27.69	+28:04:54.4	25.2 × 24.7	90.0	2.46	3.76	2.60	1.46	(0.43)	H11
F5	4:14:12.18	+28:08:50.9	58.2 × 27.6	150.0	3.89	5.39	4.13	2.38	(0.68)	H9
F6	4:17:00.73	+28:26:36.5	76.8 × 57.7	58.0	7.01	11.69	8.62	5.19	(1.54)	H15
F7	4:13:47.92	+28:12:33.1	25.2 × 22.0	110.0	1.01	2.70	2.80	2.19	(0.73)	H6
F8	4:17:34.44	+28:03:04.1	79.8 × 31.3	48.0	3.41	7.39	6.38	4.25	(1.36)	H19
F9	4:18:45.31	+28:19:47.4	37.2 × 29.5	45.0	11.18	3.62	0.95	0.56	(0.07)	H4
F10	4:18:03.87	+28:23:06.0	37.2 × 27.9	7.0	1.25	2.84	2.85	2.09	(0.66)	H7
F11	4:17:40.00	+27:39:16.3	46.2 × 28.3	126.0	2.13	3.89	3.09	2.26	(0.64)	H13
F12	4:17:49.98	+27:56:10.9	96.6 × 81.9	92.0	4.10	12.14	11.84	8.28	(2.96)	H47
F13	4:17:42.03	+28:08:49.4	59.4 × 24.6	165.0	0.93	3.75	4.45	3.23	(1.30)	H26
F14	4:18:08.76	+28:05:04.1	73.2 × 31.9	71.0	1.84	5.39	5.65	4.38	(1.50)	H40
F15	4:17:43.23	+28:05:59.9	31.8 × 23.9	12.0	0.53	1.73	1.82	1.30	(0.48)	H28
F16	4:17:51.56	+28:12:34.6	59.4 × 45.1	165.0	2.30	5.43	5.38	4.14	(1.30)	H23
F17	4:18:11.39	+27:35:32.3	39.0 × 21.8	144.0	1.05	2.76	2.99	2.20	(0.75)	H41
F18	4:18:07.27	+28:24:45.7	50.4 × 32.2	28.0	1.63	3.20	2.58	1.60	(0.50)	H10
F19	4:17:37.30	+28:11:59.9	87.6 × 44.7	24.0	2.05	4.00	3.22	2.09	(0.64)	H44
F20	4:16:57.33	+28:29:36.7	28.2 × 21.9	66.0	0.63	1.37	1.21	0.83	(0.26)	H58
F21	4:13:35.48	+28:21:22.6	81.0 × 49.7	163.0	3.06	6.69	5.57	3.96	(1.23)	H33
F22	4:17:32.33	+27:41:39.2	57.0 × 42.8	12.0	1.82	2.73	2.01	1.72	(0.39)	H31
F23	4:17:46.43	+28:08:50.9	31.2 × 18.3	0.0	0.69	1.39	1.21	0.72	(0.23)	H35
F24	4:17:20.42	+28:19:07.8	95.4 × 37.4	19.0	3.75	5.11	3.25	1.84	(0.51)	H16
F25	4:18:04.31	+27:33:17.7	46.2 × 27.1	99.0	0.96	1.83	1.41	0.94	(0.28)	H29
F26	4:17:39.05	+27:47:29.0	130.8 × 31.8	20.0	2.00	3.98	2.81	1.42	(0.47)	H87

Table 4.3: – continued.

Source	RA	Dec	FWHM	Angle (deg)	F_ν^{total} (Jy)					Counterpart
Index	(J2000)	(J2000)	(arcsec)	(E of N)	160μm	250μm	350μm	500μm	850μm	Herschel Source
F27	4:16:58.63	+28:32:05.6	60.6×41.4	129.0	2.03	3.88	3.05	1.89	(0.59)	H76
F28	4:17:27.06	+28:22:15.4	33.6×22.2	6.0	0.83	1.16	0.72	0.41	(0.11)	H17
F29	4:18:33.49	+28:28:31.8	48.0×19.9	17.0	0.58	1.94	2.06	1.51	(0.56)	–
F30	4:13:41.19	+28:21:10.7	42.6×24.4	14.0	0.72	1.50	1.25	0.84	(0.26)	H49
F31	4:18:34.69	+28:30:30.0	24.0×18.8	135.0	0.47	0.73	0.61	0.42	(0.11)	–
F32	4:17:52.67	+28:23:45.3	46.2×24.3	179.0	0.89	1.60	1.36	0.95	(0.27)	H18
F33	4:17:06.56	+28:23:09.8	105.6×64.7	128.0	4.41	6.32	4.27	2.26	(0.66)	H32
F34	4:13:26.63	+28:16:55.0	46.8×40.0	91.0	1.40	1.99	1.32	0.94	(0.23)	H37
F35	4:17:36.43	+27:53:27.3	63.0×27.5	57.0	1.40	2.42	1.89	1.15	(0.35)	H72
F36	4:17:36.58	+27:55:40.9	61.2×39.8	123.0	1.60	2.65	2.11	1.51	(0.41)	H71
F37	4:18:05.49	+28:19:41.3	52.8×28.6	5.0	1.35	1.82	1.15	0.59	(0.17)	–
F38	4:18:12.97	+28:23:41.8	67.2×31.9	37.0	2.64	2.86	1.72	0.96	(0.24)	–
F39	4:18:00.34	+28:11:17.0	57.0×33.4	167.0	0.85	2.64	2.63	1.88	(0.68)	H45
F40	4:17:47.91	+28:24:28.8	51.0×33.7	164.0	2.19	2.83	2.00	1.18	(0.32)	H20
F41	4:13:20.57	+28:16:05.9	49.8×32.4	63.0	1.59	2.27	1.55	0.91	(0.25)	H52
F42	4:17:49.49	+27:37:49.9	32.4×23.8	120.0	0.47	1.10	0.93	0.67	(0.21)	H34
F43	4:17:55.05	+28:19:18.5	109.2×37.3	32.0	1.91	3.06	2.22	1.29	(0.38)	H36
F44	4:18:55.30	+28:17:39.5	81.6×22.8	10.0	1.75	1.77	1.01	0.32	(0.10)	–
F45	4:14:35.35	+28:19:44.9	73.8×46.2	50.0	3.62	5.51	3.90	1.95	(0.60)	H43
F46	4:13:38.15	+28:14:59.0	33.6×28.9	35.0	0.67	1.63	1.33	0.89	(0.29)	H21
F47	4:18:07.50	+28:22:04.5	29.4×21.0	155.0	0.60	0.92	0.68	0.47	(0.12)	H14
F48	4:17:05.34	+28:13:55.7	100.8×31.5	47.0	2.50	3.48	2.40	1.62	(0.42)	H54
F49	4:14:49.31	+28:22:57.7	45.0×27.0	67.0	0.86	1.55	1.12	0.59	(0.19)	H95
F50	4:18:20.26	+27:36:56.0	40.2×18.3	38.0	0.31	0.89	0.76	0.51	(0.18)	–
F51	4:18:14.74	+28:29:22.6	37.2×23.3	84.0	0.92	1.49	1.07	0.53	(0.17)	H46
F52	4:14:43.71	+28:19:45.0	36.0×30.7	87.0	0.72	1.31	1.01	0.58	(0.18)	H42

Table 4.3: – continued.

Source Index	RA (J2000)	Dec (J2000)	FWHM (arcsec)	Angle (deg) (E of N)	F_ν^{total} (Jy) 160μm	250μm	350μm	500μm	850μm	Counterpart Herschel Source
F53	4:17:54.49	+28:05:23.9	102.6 × 20.4	66.0	0.43	0.64	0.33	0.07	(0.05)	H65
F54	4:17:14.76	+28:17:37.6	38.4 × 20.8	31.0	0.79	1.17	0.75	0.43	(0.12)	H25
F55	4:13:42.12	+28:07:25.1	103.8 × 75.1	81.0	3.23	6.05	4.81	3.35	(0.97)	–
F56	4:14:59.31	+28:19:15.9	58.8 × 32.8	145.0	1.51	2.18	1.46	0.76	(0.22)	H48
F57	4:14:08.01	+28:17:36.3	124.8 × 59.3	179.0	3.54	5.80	4.25	2.73	(0.78)	H78
F58	4:17:47.78	+28:28:04.5	102.6 × 37.7	6.0	1.86	2.75	1.72	0.71	(0.22)	H53
F59	4:17:47.50	+28:14:17.6	26.4 × 22.7	166.0	0.40	0.80	0.55	0.33	(0.10)	H50
F60	4:17:09.43	+28:16:40.5	25.2 × 22.0	70.0	0.36	0.68	0.53	0.35	(0.10)	–
F61	4:13:24.02	+28:07:49.9	75.0 × 46.0	85.0	1.98	2.81	1.92	1.28	(0.33)	H93
F62	4:17:49.56	+27:50:09.8	40.8 × 29.5	96.0	0.68	1.51	1.20	0.69	(0.23)	H118
F63	4:17:08.60	+27:49:58.2	46.8 × 29.3	91.0	0.78	1.22	0.87	0.57	(0.16)	H147
F64	4:17:19.78	+28:29:09.0	69.0 × 32.8	148.0	1.95	2.39	1.55	0.79	(0.22)	H117
F65	4:17:22.11	+28:22:49.2	37.8 × 24.6	9.0	0.54	0.91	0.58	0.31	(0.10)	H22
F66	4:18:41.87	+28:29:55.1	67.8 × 28.1	24.0	1.56	2.22	1.36	0.78	(0.22)	–
F67	4:15:22.67	+28:14:58.0	108.6 × 45.0	28.0	2.26	3.57	2.59	2.07	(0.50)	H96
F68	4:14:03.11	+28:09:53.8	45.0 × 28.2	87.0	0.11	0.89	0.93	0.86	(0.35)	–
F69	4:18:05.41	+28:09:27.9	70.2 × 32.0	168.0	1.14	2.22	1.72	0.92	(0.30)	H77
F70	4:14:43.14	+28:23:30.2	37.8 × 21.6	160.0	0.43	0.81	0.56	0.33	(0.10)	–
F71	4:15:03.78	+28:21:16.5	51.6 × 30.3	43.0	1.11	1.48	0.96	0.47	(0.14)	H73
F72	4:18:00.94	+27:41:39.2	48.6 × 28.5	9.0	0.65	1.68	1.31	0.37	(0.15)	H169
F73	4:17:35.06	+28:06:31.8	34.8 × 26.7	170.0	0.54	0.93	0.65	0.30	(0.10)	H86
F74	4:18:09.98	+27:39:12.6	54.0 × 21.2	10.0	0.49	0.84	0.54	0.12	(0.07)	–
F75	4:18:04.86	+27:31:16.5	103.2 × 37.9	168.0	2.11	3.61	2.63	1.57	(0.47)	H66
F76	4:13:01.85	+28:09:50.9	42.6 × 35.3	101.0	0.99	1.53	0.99	0.58	(0.17)	H115
F77	4:18:58.92	+28:15:42.9	43.2 × 22.8	166.0	0.96	1.16	0.73	0.33	(0.10)	–
F78	4:17:09.77	+28:26:06.5	31.2 × 24.2	75.0	0.40	0.64	0.39	0.14	(0.06)	H81

Table 4.3: – continued.

Source Index	RA (J2000)	Dec (J2000)	FWHM (arcsec)	Angle (deg) (E of N)	F_ν^{total} (Jy) 160μm	250μm	350μm	500μm	850μm	Counterpart Herschel Source
F79	4:17:14.86	+27:44:22.4	55.2 × 26.2	56.0	1.00	2.04	1.56	0.76	(0.26)	H138
F80	4:17:41.66	+28:25:28.2	39.6 × 27.1	68.0	0.87	1.23	0.80	0.39	(0.12)	–
F81	4:17:40.50	+28:15:19.5	93.6 × 31.9	131.0	1.63	2.57	1.77	0.99	(0.29)	H69
F82	4:14:37.60	+28:17:21.9	45.0 × 40.4	22.0	0.89	1.64	1.16	0.65	(0.20)	H56
F83	4:13:23.12	+28:24:51.7	33.6 × 23.7	116.0	0.57	0.92	0.62	0.30	(0.10)	H152
F84	4:18:02.92	+28:28:17.2	55.2 × 33.1	26.0	0.98	1.35	0.94	0.40	(0.13)	H67
F85	4:15:10.20	+28:21:18.8	48.6 × 28.5	137.0	0.77	0.92	0.64	0.45	(0.10)	H74
F86	4:14:13.52	+28:19:34.3	65.4 × 55.9	105.0	2.13	2.68	1.78	1.47	(0.31)	H100
F87	4:14:08.78	+28:15:26.0	49.2 × 23.4	9.0	0.75	1.21	0.86	0.31	(0.11)	H84
F88	4:13:33.27	+28:06:10.8	41.4 × 35.1	54.0	0.54	1.18	0.92	0.72	(0.21)	H88
F89	4:18:54.86	+28:30:25.0	19.8 × 19.8	90.0	0.24	0.13	0.05	0.03	(0.01)	–
F90	4:17:29.36	+28:24:35.0	75.0 × 31.1	13.0	0.93	1.27	0.83	0.43	(0.12)	–
F91	4:17:42.73	+27:58:11.8	86.4 × 21.0	167.0	0.34	0.52	0.31	0.15	(0.05)	H114
F92	4:18:09.36	+28:07:53.3	40.2 × 18.3	153.0	0.51	0.72	0.41	0.19	(0.06)	–
F93	4:13:29.76	+28:19:24.3	48.6 × 33.7	149.0	0.59	0.94	0.63	0.41	(0.11)	H55
F94	4:14:44.57	+28:13:45.7	68.4 × 37.1	75.0	1.56	1.82	1.09	0.58	(0.16)	H94
F95	4:18:05.43	+28:31:48.2	27.6 × 24.1	45.0	0.41	0.57	0.42	0.31	(0.07)	H99
F96	4:17:18.99	+28:21:27.0	33.0 × 26.1	33.0	0.29	0.87	0.67	0.40	(0.15)	–
F97	4:18:25.87	+28:15:40.2	90.6 × 50.5	70.0	3.89	5.49	3.45	1.69	(0.50)	H128
F98	4:14:10.12	+28:23:05.4	70.2 × 33.3	61.0	0.97	1.27	0.83	0.76	(0.14)	H129
F99	4:17:54.64	+28:15:46.5	62.4 × 29.6	16.0	0.62	1.12	0.93	0.51	(0.17)	–
F100	4:17:27.76	+27:56:16.1	59.4 × 42.4	83.0	0.71	1.40	1.00	0.51	(0.18)	–
F101	4:16:52.44	+28:30:16.1	78.6 × 26.8	25.0	0.94	1.39	0.95	0.72	(0.17)	H120
F102	4:17:45.74	+28:21:42.8	45.6 × 25.4	42.0	0.63	1.00	0.63	0.23	(0.09)	H39
F103	4:18:02.75	+27:57:06.0	150.6 × 30.0	17.0	2.10	3.54	2.45	1.36	(0.42)	H158
F104	4:18:06.30	+28:14:29.3	54.0 × 38.0	19.0	1.26	1.14	0.63	0.39	(0.08)	H104

Table 4.3: – continued.

Source Index	RA (J2000)	Dec (J2000)	FWHM (arcsec)	Angle (deg) (E of N)	F_ν^{total} (Jy) 160µm	250µm	350µm	500µm	850µm	Counterpart Herschel Source
F106	4:13:24.67	+28:05:46.0	41.4×34.3	46.0	0.23	0.48	0.36	0.40	(0.07)	H119
F107	4:14:33.41	+28:13:04.6	99.0×59.4	86.0	1.74	3.46	2.99	2.49	(0.66)	H80
F108	4:18:58.65	+28:30:50.1	55.8×29.4	1.0	0.84	1.09	0.71	0.42	(0.11)	H103
F109	4:14:43.74	+28:17:14.3	54.0×37.5	174.0	0.37	1.08	0.89	0.66	(0.22)	H57
F110	4:16:47.55	+27:53:39.0	45.6×31.2	170.0	0.81	1.34	0.82	0.32	(0.11)	H191
F111	4:18:42.87	+28:32:41.8	34.2×23.7	168.0	0.41	0.62	0.40	0.25	(0.07)	–
F112	4:14:12.83	+28:07:10.3	43.2×25.9	140.0	0.60	1.13	0.82	0.28	(0.11)	H85
F113	4:17:36.78	+28:18:33.0	57.0×27.1	127.0	0.83	1.38	1.02	0.46	(0.16)	H61
F114	4:17:12.82	+28:09:28.0	30.6×25.6	70.0	0.46	0.70	0.45	0.25	(0.07)	H151
F115	4:15:33.06	+28:16:42.5	50.4×23.9	156.0	0.66	0.96	0.61	0.21	(0.08)	H110
F116	4:14:01.45	+28:01:34.6	112.2×51.2	70.0	1.99	3.13	2.12	1.62	(0.39)	H165
F117	4:14:54.36	+28:07:53.2	75.6×46.4	38.0	1.78	2.74	2.00	1.15	(0.34)	H176
F118	4:17:40.01	+28:17:07.1	58.8×23.0	155.0	0.68	1.06	0.69	0.29	(0.10)	–
F119	4:17:38.89	+27:42:46.9	40.2×32.5	104.0	0.48	0.84	0.50	0.24	(0.08)	H91
F120	4:19:04.54	+28:29:03.6	89.4×53.6	114.0	1.97	3.66	2.67	1.58	(0.49)	H105
F121	4:13:14.28	+28:11:55.7	37.2×27.3	77.0	0.40	0.71	0.50	0.32	(0.09)	–
F122	4:18:24.14	+27:39:10.4	44.4×37.4	54.0	0.65	1.34	0.89	0.49	(0.16)	–
F123	4:14:59.95	+28:05:13.0	136.2×19.2	107.0	0.96	1.33	0.85	0.52	(0.14)	–
F124	4:15:21.86	+28:06:32.3	99.0×48.8	170.0	1.84	3.00	2.05	1.03	(0.32)	H183
F125	4:17:34.32	+28:33:09.4	76.8×30.1	133.0	1.12	1.37	0.90	0.64	(0.14)	H135
F126	4:17:11.41	+28:06:24.8	77.4×38.2	156.0	1.75	2.40	1.55	0.81	(0.23)	H166
F127	4:13:59.20	+28:20:56.6	37.8×21.6	64.0	0.39	0.69	0.45	0.21	(0.07)	–
F128	4:17:08.31	+27:58:53.1	63.6×39.8	26.0	1.29	2.15	1.37	0.69	(0.22)	H194
F129	4:17:11.82	+27:47:48.2	150.0×36.5	8.0	1.45	1.82	1.11	0.63	(0.16)	H178
F130	4:17:31.31	+28:07:57.8	34.8×18.9	148.0	0.26	0.34	0.18	0.05	(0.03)	H121

Table 4.3: – continued.

| Source | RA | Dec | FWHM | Angle (deg) | F_ν^{total} (Jy) | | | | | Counterpart |
Index	(J2000)	(J2000)	(arcsec)	(E of N)	160µm	250µm	350µm	500µm	850µm	Herschel Source
F131	4:16:59.95	+28:18:31.9	42.0×27.3	63.0	0.58	0.85	0.62	0.29	(0.09)	H83
F132	4:17:12.95	+28:24:14.6	71.4×20.0	149.0	0.47	0.72	0.40	0.13	(0.06)	H60
F133	4:17:20.67	+27:50:13.6	61.8×30.5	8.0	0.84	1.18	0.77	0.39	(0.12)	H164
F134	4:14:46.26	+28:26:56.2	72.0×37.9	165.0	0.81	1.37	0.86	0.67	(0.16)	–
F135	4:14:09.78	+28:27:07.5	50.4×38.3	156.0	0.80	1.37	0.84	0.35	(0.12)	–
F136	4:13:02.49	+28:17:18.6	77.4×42.0	102.0	2.01	2.92	1.80	0.63	(0.20)	H171
F137	4:18:47.99	+28:12:24.1	136.2×33.1	5.0	2.52	3.42	2.16	1.08	(0.31)	H146
F138	4:16:49.15	+27:50:37.8	67.2×27.9	34.0	1.02	1.16	0.74	0.36	(0.10)	H216

all convolved to the SPIRE 500-µm resolution of 36 arcsec, while the flux densities of the Herschel and filtered-Herschel sources were measured across the 160-µm, 250-µm, 350-µm and 500-µm wavebands, also at 36-arcsec resolution. The maps were convolved to a common SPIRE 500-µm(36-arcsec) resolution using the Herschel→Herschel and SCUBA-2→Herschel convolution kernels described in Section 2.4.2. Flux densities for each source were measured using elliptical apertures with major and minor axes of twice the major and minor FWHM returned by CSAR, enclosing 99.5% of the flux in a Gaussian distribution.

We fitted the SED of each source with a modified blackbody distribution (see equation 3.3) in order to determine the mean, column-density-weighted, line-of-sight dust temperature.

We determined a typical dust emissivity index (β), which we adopted for our cores in order to more accurately constrain the SED fitting process. While temperature and dust emissivity index can be fitted simultaneously using SCUBA-2 850µm data in conjunction with the Herschel photometric bands (see Sadavoy et al. 2013), the Herschel data alone, covering the wavelength range 160–500µm, do not provide the long-wavelength information necessary to accurately constrain both parameters. We decided to use a fixed value of β when deriving best-fit temperatures for all of our cores, including those with an 850µm detection, in order to make a fair comparison between the different sets of cores. In order to find a suitable β, we fitted SEDs to the subset of the filtered-Herschel cores with detections in 850-µm emission. We determined an SED using only the filtered-Herschel fluxes for each source, and from the best-fit SED predicted an 850-µm flux density. These predicted 850-µm flux densities were then compared to the values measured in the SCUBA-2 850-µm map. We repeated this process for a range of values of β, as well as allowing β to vary as a free parameter, in order to determine the value that best predicted the 850-µm flux densities.

Table 4.4: Derived properties of the sources found by SCUBA-2 in the L1495 region – temperature, mass, number density of molecular hydrogen, and mean deconvolved full-width at half-maximum (geometric mean of major and minor axes with beam-size subtracted in quadrature).

Source Index	Temp. (K)	Mass ($M_\odot$)	H_2 Density ($\times 10^4 \, \mathrm{cm}^{-3}$)	Deconv. FWHM (pc)
S1	14.9±0.4	0.613±0.267	6.34±2.76	0.032
S2	10.1±0.2	0.256±0.057	6.94±1.56	0.023
S3	10.9±0.2	0.420±0.114	3.96±1.08	0.033
S4	11.2±0.2	0.156±0.034	10.55±2.29	0.017
S5	10.1±0.2	0.336±0.081	8.08±1.94	0.024
S6	11.2±0.2	0.120±0.025	7.04±1.48	0.018
S7	10.6±0.2	0.110±0.023	6.88±1.41	0.018
S8	12.0±0.3	0.391±0.116	3.37±1.00	0.034
S9	11.1±0.2	0.324±0.082	3.95±1.00	0.030
S10	14.4±0.4	0.126±0.029	2.47±0.58	0.026
S11	9.3±0.2	0.196±0.043	9.38±2.04	0.019
S12	12.7±0.3	0.113±0.024	3.27±0.70	0.023
S13	14.3±0.4	0.079±0.017	2.94±0.64	0.021
S14	10.9±0.2	0.355±0.092	3.05±0.79	0.034
S15	16.1±0.5	0.026±0.005	1.67±0.34	0.017
S16	10.9±0.2	0.182±0.039	2.11±0.45	0.031
S17	11.0±0.2	0.205±0.047	3.03±0.70	0.028
S18	12.9±0.3	0.124±0.027	1.69±0.37	0.029
S19	10.7±0.2	0.109±0.022	3.72±0.76	0.021
S20	10.7±0.2	0.186±0.042	3.02±0.69	0.028
S21	11.9±0.2	0.122±0.026	1.73±0.37	0.029
S22	11.4±0.2	0.065±0.013	1.90±0.38	0.023
S23	19.6±0.7	0.023±0.005	0.69±0.15	0.023
S24	12.9±0.3	0.090±0.018	0.95±0.20	0.032
S25	13.4±0.3	0.095±0.021	1.05±0.23	0.031

For each of the values of β tested, we calculated the mean reduced χ^2 value of the SED fits. We also calculated the reduced χ^2 value of the 1:1 relation between predicted and measured 850-µm flux densities. We found that when emissivity index was allowed to vary as a free parameter, the 850-µm flux densities were generally well-predicted. We found the mean value of β when it was varied as a free parameter to be 1.3, and the standard deviation on this value to be 0.6. When β was fixed, we found that values in the range $\beta = 1.1$–1.4 gave indistinguishably good results. We therefore chose to adopt a value of dust emissivity index $\beta = 1.3 \pm 0.6$ for the remainder of this chapter.

A dust emissivity index of 1.3 is lower than that typically expected for a starless core. A wide variety of β values have been determined for starless cores. For example, Shirley et al. (2005) found $\beta =$1.8–1.9 for the starless core L1498; Friesen et al. (2005) found $\beta = 1.3$–2.1 for a sample of hot starless cores; Schnee et al. (2010) found $\beta = 2.2 \pm 0.6$ for the starless core TMC-1c; and Sadavoy et al. (2013) found $\beta =$1.6–2.0 toward cores in the Perseus molecular cloud. Our low value of β may be due to there being multiple dust temperature components along the lines of sight toward our sources, which would broaden the SEDs of the sources, and hence lower their apparent β values. This effect was discussed in detail by Martin et al. (2012). Starless cores are not expected to be isothermal sources: a temperature gradient from $\sim 15\,\mathrm{K}$ at their edges to $\sim 7\,\mathrm{K}$ in their heavily-shielded centres has been seen elsewhere (e.g. Stamatellos et al. 2007), even in the absence of external heating sources. The surrounding, more tenuous, material of the molecular cloud will be warmer still. While the spatial filtering of the SCUBA-2 observations will to some extent ameliorate this effect, there will still be some material along the line of sight not associated with the core.

Our low β might alternatively, or additionally, be the result of grain growth within the densest regions of the starless cores. Our value of β might be intermediate

Table 4.5: Derived properties of Herschel sources.

Source Index	Temp. (K)	Mass ($M_\odot$)	H_2 Density ($\times 10^4\,\mathrm{cm}^{-3}$)	Deconv. FWHM (pc)
H1	17.1±0.8	0.432±0.330	15.83±12.09	0.021
H2	20.1±1.2	0.062±0.020	6.61±2.18	0.015
H3	22.7±1.6	0.069±0.026	3.57±1.33	0.019
H4	16.4±0.8	0.109±0.038	6.95±2.40	0.017
H5	13.2±0.5	0.194±0.071	18.81±6.93	0.015
H6	14.8±0.6	0.241±0.110	6.84±3.10	0.023
H7	14.4±0.6	0.754±0.704	2.95±2.75	0.044
H8	13.6±0.5	0.298±0.140	5.80±2.72	0.026
H9	15.2±0.7	0.200±0.085	5.60±2.37	0.023
H10	14.9±0.6	0.091±0.028	6.73±2.05	0.017
H11	14.3±0.6	0.132±0.044	9.54±3.20	0.017
H12	15.5±0.7	0.122±0.043	5.72±1.99	0.019
H13	15.5±0.7	0.541±0.434	1.45±1.16	0.050
H14	16.3±0.8	0.227±0.110	2.72±1.31	0.030
H15	17.0±0.8	0.090±0.030	3.32±1.10	0.021
H16	15.7±0.7	0.210±0.094	3.44±1.54	0.027
H17	14.1±0.6	0.313±0.157	4.14±2.07	0.029
H18	16.5±0.8	0.047±0.013	5.67±1.56	0.014
H19	14.0±0.6	0.119±0.038	8.42±2.69	0.017
H20	16.7±0.8	0.063±0.019	3.83±1.13	0.018
H21	13.9±0.6	0.498±0.329	3.71±2.45	0.036
H22	16.1±0.7	0.078±0.024	4.09±1.25	0.019
H23	13.2±0.5	0.269±0.116	6.48±2.80	0.024
H24	14.9±0.6	0.128±0.044	4.66±1.60	0.021
H25	13.6±0.5	0.121±0.038	7.59±2.41	0.018
H26	13.8±0.5	0.235±0.099	4.76±2.00	0.026
H27	15.0±0.6	0.139±0.050	3.95±1.41	0.023
H28	16.1±0.7	0.434±0.310	1.37±0.97	0.048
H29	14.0±0.6	0.598±0.449	2.59±1.95	0.043
H30	14.1±0.6	0.086±0.025	8.20±2.38	0.015
H31	14.4±0.6	0.168±0.063	4.85±1.81	0.023
H32	16.0±0.7	0.060±0.017	3.97±1.13	0.017
H33	15.4±0.7	0.243±0.115	2.26±1.07	0.033
H34	16.9±0.8	0.069±0.021	2.74±0.84	0.020
H35	13.2±0.5	0.355±0.179	4.78±2.40	0.029
H36	12.6±0.5	0.312±0.139	7.62±3.40	0.024
H37	15.0±0.6	0.092±0.029	4.41±1.36	0.019
H38	15.2±0.7	0.122±0.042	3.66±1.26	0.022
H39	15.5±0.7	0.322±0.181	1.44±0.81	0.042

Table 4.5: – continued.

Source Index	Temp. (K)	Mass (M$_\odot$)	H$_2$ Density ($\times 10^4$ cm^{-3})	Deconv. FWHM (pc)
H40	13.7±0.6	0.233±0.098	4.57±1.92	0.026
H41	15.8±0.7	0.053±0.015	4.34±1.19	0.016
H42	14.3±0.6	0.720±0.642	1.21±1.08	0.059
H43	15.8±0.7	0.153±0.059	2.13±0.83	0.029
H44	14.0±0.6	0.108±0.034	5.19±1.61	0.019
H45	15.1±0.7	0.071±0.020	4.27±1.23	0.018
H46	14.7±0.6	0.051±0.013	6.11±1.61	0.014
H47	15.7±0.7	0.073±0.021	3.03±0.90	0.020
H48	17.3±0.9	0.150±0.062	1.03±0.43	0.037
H49	16.4±0.8	0.064±0.019	2.80±0.82	0.020
H50	15.0±0.6	0.104±0.034	3.50±1.13	0.022
H51	15.0±0.6	0.222±0.098	2.34±1.03	0.032
H52	14.9±0.6	0.137±0.049	3.24±1.15	0.024
H53	14.8±0.7	0.294±0.150	1.58±0.81	0.040
H54	17.1±0.8	0.074±0.023	1.99±0.63	0.023
H55	16.7±0.8	0.062±0.018	2.41±0.71	0.021
H56	16.6±0.8	0.093±0.031	2.08±0.69	0.025
H57	15.8±0.7	0.095±0.030	2.73±0.88	0.023
H58	16.8±0.8	0.037±0.010	3.10±0.82	0.016
H59	15.5±0.7	0.047±0.012	4.35±1.16	0.015
H60	15.3±0.7	0.160±0.062	1.66±0.64	0.032
H61	14.1±0.6	0.184±0.070	3.78±1.44	0.025
H62	17.0±0.8	0.115±0.042	1.44±0.53	0.030
H63	13.3±0.5	0.152±0.051	5.91±1.99	0.021
H64	16.0±0.7	0.285±0.154	1.25±0.67	0.043
H65	14.9±0.6	0.068±0.019	3.88±1.10	0.018
H66	15.3±0.7	0.236±0.111	1.39±0.65	0.039
H67	15.1±0.7	0.156±0.059	1.91±0.72	0.030
H68	15.9±0.7	0.105±0.035	1.98±0.67	0.026
H69	16.0±0.7	0.078±0.024	2.39±0.73	0.022
H70	15.3±0.7	0.109±0.036	2.58±0.86	0.024
H71	15.1±0.7	0.150±0.056	1.98±0.74	0.030
H72	14.3±0.6	0.092±0.028	4.22±1.27	0.019
H73	15.6±0.7	0.102±0.034	2.24±0.74	0.025
H74	14.3±0.6	0.089±0.027	4.62±1.38	0.019
H75	16.9±0.8	0.034±0.009	2.31±0.61	0.017
H76	14.3±0.6	0.269±0.126	2.29±1.07	0.034
H77	15.8±0.7	0.129±0.046	1.82±0.66	0.029

Source Index	Temp. (K)	Mass ($M_\odot$)	H_2 Density ($\times 10^4\,\mathrm{cm}^{-3}$)	Deconv. FWHM (pc)
H78	15.3±0.7	0.166±0.065	1.60±0.63	0.033
H79	13.4±0.5	0.096±0.028	5.82±1.71	0.018
H80	15.2±0.7	0.042±0.011	3.70±0.96	0.016
H81	15.4±0.7	0.193±0.082	0.77±0.33	0.044
H82	14.4±0.6	0.071±0.020	3.90±1.10	0.018
H83	15.1±0.7	0.067±0.019	3.18±0.90	0.019
H84	15.3±0.7	0.083±0.025	2.68±0.81	0.022
H85	15.5±0.7	0.058±0.016	2.93±0.82	0.019
H86	16.0±0.7	0.049±0.013	2.73±0.75	0.018
H87	15.6±0.7	0.194±0.083	1.19±0.51	0.038
H88	16.0±0.8	0.044±0.012	2.68±0.72	0.018
H89	15.2±0.7	0.068±0.019	2.40±0.69	0.021
H90	15.2±0.7	0.076±0.022	2.60±0.77	0.021
H91	17.1±0.8	0.050±0.014	1.76±0.50	0.021
H92	16.8±0.8	0.097±0.033	1.37±0.46	0.029
H93	16.5±0.8	0.029±0.007	2.65±0.68	0.015
H94	16.1±0.8	0.156±0.062	1.26±0.50	0.035
H95	16.3±0.8	0.036±0.009	2.47±0.65	0.017
H96	16.7±0.8	0.051±0.014	1.69±0.48	0.022
H97	17.3±0.9	0.047±0.013	1.49±0.42	0.022
H98	17.5±0.9	0.119±0.045	0.78±0.30	0.037
H99	16.4±0.8	0.134±0.051	1.13±0.43	0.034
H100	16.4±0.8	0.105±0.036	1.17±0.40	0.031
H101	15.5±0.7	0.103±0.034	1.78±0.59	0.027
H102	14.5±0.6	0.142±0.050	2.21±0.78	0.028
H103	15.9±0.7	0.039±0.010	2.14±0.56	0.018
H104	14.0±0.6	0.123±0.040	2.76±0.90	0.025
H105	16.2±0.8	0.049±0.013	1.90±0.52	0.021
H106	16.0±0.8	0.072±0.022	1.08±0.33	0.028
H107	16.4±0.8	0.076±0.023	1.19±0.37	0.028
H108	14.5±0.6	0.069±0.019	2.34±0.66	0.022
H109	15.1±0.7	0.062±0.017	1.97±0.55	0.022
H110	15.7±0.7	0.077±0.023	1.58±0.48	0.025
H111	16.4±0.8	0.049±0.014	1.51±0.42	0.022
H112	17.6±0.9	0.030±0.008	1.37±0.36	0.020
H113	15.1±0.7	0.050±0.013	2.13±0.57	0.020
H114	16.0±0.8	0.046±0.012	1.73±0.47	0.021
H115	16.5±0.8	0.032±0.008	1.67±0.43	0.019
H116	17.6±0.9	0.037±0.010	1.16±0.32	0.022
H117	16.4±0.8	0.072±0.022	1.15±0.35	0.028

Table 4.5: – continued.

Source Index	Temp. (K)	Mass ($M_\odot$)	H_2 Density ($\times 10^4\,\mathrm{cm}^{-3}$)	Deconv. FWHM (pc)
H118	17.8±0.9	0.055±0.016	0.84±0.25	0.028
H119	15.8±0.7	0.064±0.019	1.42±0.41	0.025
H120	15.0±0.7	0.047±0.013	2.29±0.61	0.019
H121	16.7±0.8	0.035±0.009	1.47±0.39	0.020
H122	17.1±0.9	0.120±0.045	0.67±0.25	0.039
H123	17.4±0.9	0.085±0.028	0.67±0.22	0.035
H124	17.4±0.9	0.051±0.015	0.84±0.24	0.027
H125	17.2±0.9	0.042±0.012	1.01±0.28	0.024
H126	16.1±0.8	0.176±0.075	0.42±0.18	0.052
H127	16.7±0.8	0.048±0.013	1.15±0.32	0.024
H128	16.6±0.8	0.106±0.037	0.76±0.27	0.036
H129	17.9±1.0	0.021±0.005	1.14±0.29	0.018
H130	16.3±0.8	0.038±0.010	1.30±0.35	0.021
H131	16.6±0.8	0.098±0.033	0.68±0.23	0.036
H132	16.8±0.8	0.024±0.006	1.29±0.33	0.019
H133	17.0±0.9	0.020±0.005	1.31±0.32	0.017
H134	16.2±0.8	0.026±0.007	1.19±0.30	0.019
H135	17.5±0.9	0.055±0.016	0.70±0.21	0.030
H136	14.4±0.6	0.035±0.009	2.14±0.54	0.018
H137	17.8±0.9	0.029±0.008	0.76±0.20	0.023
H138	14.6±0.6	0.042±0.011	1.75±0.45	0.020
H139	18.2±1.0	0.021±0.005	0.96±0.25	0.020
H140	17.0±0.9	0.030±0.008	1.11±0.29	0.021
H141	17.7±0.9	0.086±0.029	0.46±0.16	0.040
H142	16.7±0.8	0.041±0.011	0.96±0.26	0.024
H143	16.7±0.8	0.021±0.005	1.19±0.29	0.018
H144	14.8±0.7	0.062±0.017	1.31±0.37	0.025
H145	16.2±0.8	0.049±0.014	1.00±0.28	0.025
H146	17.6±0.9	0.021±0.005	0.85±0.22	0.020
H147	17.9±1.0	0.132±0.053	0.33±0.13	0.051
H148	16.7±0.8	0.064±0.019	0.60±0.18	0.033
H149	15.5±0.7	0.110±0.037	0.69±0.23	0.038
H150	17.8±0.9	0.059±0.018	0.46±0.14	0.035
H151	16.7±0.8	0.040±0.011	0.78±0.21	0.026
H152	18.0±1.0	0.012±0.003	1.04±0.25	0.016
H153	14.6±0.7	0.044±0.011	0.85±0.22	0.026
H154	17.2±0.9	0.032±0.008	0.71±0.19	0.025
H155	17.0±0.9	0.038±0.010	0.67±0.18	0.027
H156	14.6±0.6	0.036±0.009	1.60±0.41	0.020

Table 4.5: – continued.

Source Index	Temp. (K)	Mass ($M_\odot$)	H_2 Density ($\times 10^4\,\mathrm{cm}^{-3}$)	Deconv. FWHM (pc)
H157	17.4±0.9	0.041±0.011	0.56±0.16	0.029
H158	17.2±0.9	0.021±0.005	0.87±0.22	0.020
H159	15.4±0.7	0.240±0.114	0.38±0.18	0.060
H160	17.5±0.9	0.048±0.014	0.51±0.15	0.032
H161	17.0±0.9	0.055±0.016	0.49±0.14	0.034
H162	17.5±0.9	0.019±0.005	0.68±0.17	0.021
H163	17.2±0.9	0.052±0.015	0.52±0.15	0.032
H164	17.7±0.9	0.017±0.004	0.73±0.18	0.020
H165	15.8±0.8	0.086±0.027	0.52±0.16	0.038
H166	17.2±0.9	0.026±0.007	0.62±0.16	0.024
H167	15.8±0.8	0.120±0.042	0.48±0.17	0.044
H168	18.5±1.0	0.021±0.006	0.48±0.12	0.025
H169	17.7±1.0	0.030±0.008	0.63±0.17	0.025
H170	17.2±0.9	0.020±0.005	0.66±0.16	0.022
H171	17.9±1.0	0.021±0.005	0.41±0.10	0.026
H172	18.2±1.0	0.013±0.003	0.69±0.17	0.018
H173	17.7±0.9	0.043±0.012	0.40±0.11	0.033
H174	17.2±0.9	0.027±0.007	0.56±0.14	0.025
H175	17.7±0.9	0.021±0.005	0.53±0.14	0.024
H176	14.8±0.7	0.026±0.006	0.84±0.21	0.022
H177	17.0±0.9	0.046±0.013	0.42±0.12	0.033
H178	18.3±1.0	0.023±0.006	0.43±0.11	0.026
H179	18.8±1.1	0.013±0.003	0.51±0.13	0.020
H180	16.0±0.8	0.027±0.007	0.81±0.20	0.022
H181	14.5±0.7	0.023±0.006	1.14±0.28	0.019
H182	18.7±1.0	0.020±0.005	0.40±0.10	0.026
H183	17.7±1.0	0.020±0.005	0.42±0.11	0.025
H184	17.6±0.9	0.084±0.028	0.24±0.08	0.049
H185	18.8±1.1	0.072±0.024	0.15±0.05	0.055
H186	18.4±1.0	0.010±0.002	0.57±0.14	0.018
H187	18.4±1.0	0.049±0.014	0.20±0.06	0.044
H188	19.2±1.1	0.006±0.001	0.55±0.13	0.015
H189	16.5±0.9	0.007±0.002	0.84±0.20	0.014
H190	17.7±1.0	0.030±0.008	0.34±0.09	0.031
H191	17.5±0.9	0.028±0.007	0.33±0.09	0.031
H192	15.0±0.7	0.016±0.004	1.20±0.29	0.016
H193	18.8±1.1	0.024±0.006	0.21±0.06	0.034
H194	15.7±0.8	0.021±0.005	0.67±0.16	0.022
H195	18.1±1.0	0.030±0.008	0.24±0.07	0.035

Table 4.5: – continued.

Source Index	Temp. (K)	Mass (M$_\odot$)	H$_2$ Density ($\times 10^4\,\mathrm{cm}^{-3}$)	Deconv. FWHM (pc)
H196	17.9±1.0	0.016±0.004	0.35±0.09	0.025
H197	17.6±0.9	0.020±0.005	0.29±0.07	0.028
H198	19.4±1.1	0.041±0.012	0.09±0.03	0.054
H199	18.4±1.0	0.015±0.004	0.20±0.05	0.029
H200	16.7±0.9	0.015±0.004	0.29±0.07	0.026
H201	19.3±1.1	0.010±0.002	0.16±0.04	0.027
H202	19.1±1.1	0.011±0.003	0.16±0.04	0.029
H203	16.6±0.9	0.016±0.004	0.30±0.07	0.026
H204	18.1±1.1	0.004±0.001	0.32±0.08	0.016
H205	17.4±0.9	0.006±0.001	0.24±0.06	0.021
H206	20.1±1.4	0.003±0.001	0.22±0.06	0.016
H207	20.0±1.1	0.006±0.001	0.14±0.03	0.025
H208	18.2±1.1	0.005±0.001	0.24±0.06	0.019

between the value expected in molecular clouds of $\beta = 1.5$–2.0 (e.g. Draine & Lee 1984; Draine et al. 2007), and $\beta = 1.0$, expected in protoplanetary discs (Beckwith & Sargent 1991).

We fitted our sources using $\beta = 1.3$ in order to determine their dust temperatures. We then determined our source masses using the Hildebrand (1983) relation (see equation 3.4), and the sources' 850μm flux densities. Masses are given by

$$M = \frac{F_\nu(850\mu\mathrm{m})D^2}{\kappa_{\nu(850\mu\mathrm{m})}B_{\nu(850\mu\mathrm{m})}(T)},\tag{4.1}$$

where $F_\nu(850\mu\mathrm{m})$ is the flux density at 850 μm. For the SCUBA-2 sources, $F_\nu(850\mu\mathrm{m})$ was taken to be the measured SCUBA-2 850μm flux density of the source, while for the Herschel and filtered-Herschel sources, $F_\nu(850\mu\mathrm{m})$ was taken to be the flux density at 850μm as extrapolated from the best-fit SED. D is the distance to Taurus (140 pc), $B_{\nu(850\mu\mathrm{m})}(T)$ is the Planck function, and $\kappa_{\nu(850\mu\mathrm{m})}$ is the dust mass opacity, as parameterised by Beckwith et al. (1990): $\kappa_\nu = 0.1(\nu/10^{12}\mathrm{Hz})^\beta\,\mathrm{cm}^2\mathrm{g}^{-1}$ (assuming a standard dust-to-gas mass ratio of 1:100). Again, the dust emissivity index β was taken to be 1.3. Some example SED fits for sources with counterparts in all three

Table 4.6: Derived properties of filtered-Herschel sources.

Source Index	Temp. (K)	Mass ($M_\odot$)	H_2 Density ($\times 10^4\,\mathrm{cm}^{-3}$)	Deconv. FWHM (pc)
F1	15.8±0.7	0.325±0.188	8.92±5.15	0.023
F2	19.3±1.1	0.022±0.006	1.12±0.29	0.019
F3	14.7±0.6	0.246±0.112	1.21±0.55	0.041
F4	14.8±0.6	0.051±0.013	3.57±0.93	0.017
F5	14.7±0.6	0.082±0.024	1.38±0.40	0.027
F6	14.1±0.5	0.202±0.078	0.74±0.29	0.045
F7	11.2±0.3	0.144±0.041	11.99±3.45	0.016
F8	12.5±0.4	0.220±0.080	1.91±0.69	0.034
F9	110.1±0.0	0.001±0.000	0.02±0.00	0.022
F10	11.8±0.4	0.120±0.033	3.86±1.08	0.022
F11	13.1±0.4	0.095±0.027	2.17±0.61	0.025
F12	11.3±0.3	0.582±0.315	0.90±0.48	0.060
F13	10.2±0.2	0.314±0.108	6.07±2.09	0.026
F14	11.0±0.3	0.310±0.116	2.97±1.11	0.033
F15	10.9±0.3	0.101±0.026	5.24±1.32	0.019
F16	11.7±0.3	0.239±0.084	1.87±0.66	0.035
F17	11.2±0.3	0.147±0.042	6.45±1.86	0.020
F18	13.1±0.4	0.074±0.019	1.24±0.32	0.027
F19	13.0±0.3	0.096±0.026	0.43±0.11	0.042
F20	12.4±0.4	0.043±0.010	3.06±0.72	0.017
F21	12.5±0.3	0.199±0.068	0.85±0.29	0.043
F22	13.9±0.5	0.052±0.013	0.47±0.12	0.034
F23	12.9±0.4	0.036±0.008	2.85±0.66	0.016
F24	15.7±0.6	0.056±0.015	0.28±0.07	0.041
F25	13.2±0.4	0.041±0.009	1.00±0.23	0.024
F26	13.9±0.3	0.063±0.015	0.25±0.06	0.044
F27	13.3±0.4	0.085±0.023	0.73±0.19	0.034
F28	15.7±0.6	0.012±0.003	0.66±0.15	0.019
F29	10.7±0.3	0.121±0.031	4.43±1.15	0.021
F30	12.7±0.4	0.041±0.009	1.33±0.30	0.022
F31	13.6±0.5	0.016±0.004	1.78±0.41	0.014
F32	13.0±0.4	0.041±0.010	1.18±0.28	0.023
F33	15.4±0.5	0.075±0.020	0.14±0.04	0.056
F34	14.9±0.5	0.028±0.006	0.37±0.09	0.029
F35	13.7±0.4	0.048±0.011	0.71±0.17	0.028
F36	13.5±0.4	0.058±0.014	0.52±0.13	0.033
F37	16.1±0.6	0.018±0.004	0.33±0.07	0.026
F38	17.3±0.7	0.023±0.005	0.25±0.06	0.031
F39	11.1±0.2	0.138±0.037	1.80±0.48	0.030

Table 4.6: – continued.

Source Index	Temp. (K)	Mass ($M_\odot$)	H_2 Density ($\times 10^4\,\mathrm{cm}^{-3}$)	Deconv. FWHM (pc)
F40	15.3±0.6	0.036±0.009	0.55±0.13	0.028
F41	15.1±0.5	0.030±0.007	0.50±0.12	0.027
F42	12.3±0.4	0.035±0.008	1.78±0.40	0.019
F43	14.4±0.4	0.048±0.011	0.20±0.05	0.043
F44	20.5±1.0	0.007±0.002	0.10±0.02	0.029
F45	15.1±0.5	0.070±0.019	0.38±0.10	0.040
F46	12.3±0.4	0.049±0.011	1.74±0.40	0.021
F47	14.1±0.5	0.016±0.004	1.15±0.26	0.017
F48	14.8±0.5	0.050±0.013	0.30±0.08	0.038
F49	14.1±0.4	0.025±0.005	0.63±0.14	0.024
F50	11.8±0.4	0.032±0.007	1.74±0.39	0.018
F51	14.7±0.5	0.020±0.005	0.86±0.19	0.020
F52	13.7±0.4	0.025±0.006	0.74±0.16	0.023
F53	17.0±0.4	0.005±0.001	0.06±0.01	0.031
F54	15.2±0.6	0.014±0.003	0.67±0.15	0.019
F55	13.1±0.3	0.144±0.043	0.23±0.07	0.060
F56	15.4±0.5	0.025±0.006	0.32±0.07	0.030
F57	14.0±0.4	0.103±0.029	0.17±0.05	0.058
F58	16.4±0.4	0.023±0.005	0.10±0.02	0.042
F59	13.7±0.5	0.014±0.003	1.05±0.23	0.017
F60	13.2±0.5	0.015±0.003	1.27±0.28	0.016
F61	14.8±0.5	0.040±0.009	0.21±0.05	0.040
F62	12.9±0.4	0.035±0.008	0.91±0.20	0.024
F63	14.3±0.5	0.020±0.004	0.42±0.09	0.025
F64	16.4±0.6	0.022±0.005	0.23±0.05	0.032
F65	14.9±0.5	0.011±0.002	0.44±0.09	0.021
F66	15.7±0.5	0.024±0.005	0.31±0.07	0.030
F67	13.9±0.4	0.067±0.017	0.21±0.05	0.047
F68	9.5±0.3	0.098±0.025	2.35±0.60	0.024
F69	13.6±0.4	0.042±0.010	0.43±0.10	0.032
F70	13.9±0.5	0.014±0.003	0.63±0.14	0.019
F71	16.1±0.6	0.015±0.003	0.26±0.06	0.027
F72	14.2±0.4	0.020±0.004	0.41±0.09	0.025
F73	14.7±0.5	0.012±0.003	0.47±0.10	0.021
F74	15.8±0.6	0.008±0.002	0.21±0.05	0.023
F75	14.0±0.4	0.062±0.015	0.27±0.07	0.042
F76	15.0±0.5	0.019±0.004	0.36±0.08	0.026
F77	17.0±0.7	0.009±0.002	0.33±0.07	0.021

Source Index	Temp. (K)	Mass ($M_\odot$)	H_2 Density ($\times 10^4\,\mathrm{cm}^{-3}$)	Deconv. FWHM (pc)
F78	15.8±0.6	0.006±0.001	0.32±0.07	0.019
F79	13.7±0.4	0.036±0.008	0.71±0.16	0.026
F80	15.8±0.6	0.013±0.003	0.39±0.09	0.022
F81	14.7±0.4	0.036±0.008	0.24±0.05	0.037
F82	14.0±0.4	0.027±0.006	0.38±0.08	0.029
F83	14.9±0.6	0.012±0.003	0.56±0.12	0.019
F84	15.9±0.5	0.014±0.003	0.19±0.04	0.029
F85	15.5±0.6	0.011±0.002	0.24±0.05	0.025
F86	15.3±0.5	0.035±0.008	0.17±0.04	0.041
F87	15.5±0.5	0.013±0.003	0.35±0.07	0.023
F88	12.6±0.3	0.033±0.007	0.65±0.14	0.026
F89	29.3±4.7	0.000±0.000	0.04±0.01	0.013
F90	15.8±0.4	0.013±0.003	0.13±0.03	0.033
F91	16.2±0.5	0.005±0.001	0.07±0.01	0.029
F92	16.4±0.7	0.006±0.001	0.34±0.07	0.018
F93	14.6±0.4	0.014±0.003	0.22±0.05	0.027
F94	17.0±0.6	0.015±0.003	0.13±0.03	0.034
F95	14.6±0.6	0.009±0.002	0.57±0.13	0.017
F96	12.1±0.4	0.026±0.006	1.09±0.24	0.020
F97	16.0±0.5	0.052±0.014	0.18±0.05	0.046
F98	15.3±0.4	0.016±0.003	0.16±0.03	0.033
F99	13.5±0.3	0.023±0.005	0.32±0.07	0.029
F100	13.8±0.3	0.024±0.005	0.20±0.04	0.034
F101	14.6±0.4	0.021±0.004	0.24±0.05	0.031
F102	15.9±0.6	0.009±0.002	0.25±0.05	0.023
F103	14.4±0.4	0.052±0.012	0.19±0.04	0.046
F104	19.2±0.8	0.006±0.001	0.07±0.02	0.031
F105	12.7±0.3	0.158±0.048	0.26±0.08	0.059
F106	13.4±0.4	0.010±0.002	0.21±0.04	0.026
F107	12.6±0.2	0.106±0.027	0.25±0.06	0.052
F108	15.8±0.5	0.012±0.003	0.20±0.04	0.027
F109	11.7±0.3	0.041±0.009	0.49±0.10	0.031
F110	15.8±0.5	0.012±0.003	0.25±0.05	0.026
F111	15.0±0.6	0.008±0.002	0.37±0.08	0.019
F112	14.9±0.5	0.013±0.003	0.38±0.08	0.023
F113	14.7±0.4	0.019±0.004	0.34±0.07	0.027
F114	15.2±0.6	0.009±0.002	0.42±0.09	0.019
F115	16.3±0.6	0.008±0.002	0.21±0.05	0.024
F116	14.3±0.3	0.050±0.011	0.12±0.03	0.051
F117	14.5±0.4	0.042±0.010	0.22±0.05	0.040

Table 4.6: – continued.

Source Index	Temp. (K)	Mass ($M_\odot$)	H_2 Density ($\times 10^4\,\mathrm{cm}^{-3}$)	Deconv. FWHM (pc)
F118	15.6±0.5	0.011±0.002	0.24±0.05	0.025
F119	15.1±0.5	0.009±0.002	0.22±0.04	0.025
F120	13.7±0.3	0.067±0.016	0.22±0.05	0.047
F121	14.0±0.5	0.012±0.003	0.41±0.09	0.022
F122	13.8±0.4	0.022±0.005	0.35±0.07	0.028
F123	15.5±0.4	0.015±0.003	0.12±0.02	0.035
F124	14.9±0.3	0.038±0.008	0.12±0.03	0.047
F125	15.7±0.5	0.016±0.003	0.15±0.03	0.033
F126	15.8±0.5	0.025±0.006	0.17±0.04	0.037
F127	14.7±0.5	0.009±0.002	0.42±0.09	0.019
F128	15.1±0.4	0.025±0.005	0.21±0.05	0.034
F129	16.9±0.2	0.015±0.003	0.04±0.01	0.050
F130	17.6±0.9	0.002±0.001	0.15±0.04	0.017
F131	15.1±0.5	0.011±0.002	0.30±0.06	0.023
F132	16.5±0.5	0.006±0.001	0.12±0.02	0.026
F133	15.7±0.5	0.013±0.003	0.17±0.04	0.029
F134	14.4±0.3	0.020±0.004	0.15±0.03	0.035
F135	15.5±0.4	0.014±0.003	0.17±0.04	0.030
F136	17.4±0.6	0.019±0.004	0.11±0.02	0.039
F137	16.1±0.5	0.033±0.008	0.12±0.03	0.046
F138	17.0±0.6	0.010±0.002	0.13±0.03	0.029

catalogues are shown in Figure 4.9.

The mean volume density of molecular hydrogen for each source was calculated to be

$$n(H_2) = \frac{M}{\mu m_{\mathrm{H}}} \frac{1}{\frac{4}{3}\pi R^3},$$ (4.2)

where R is the equivalent deconvolved FWHM of the source. The equivalent FWHM was taken to be the geometric mean of the deconvolved major and minor FWHMs, as determined by CSAR. The deconvolution assumed a beam size of 14.1 arcsec in the case of SCUBA-2 sources and 18.1 arcsec in the case of Herschel and filtered-Herschel sources. The mean molecular weight μ was taken to be 2.86, assuming that the gas is $\sim 70\%$ H_2 by mass (Kirk et al. 2013).

4.3   Discussion

The temperatures, masses, densities and sizes of the cores detected by SCUBA-2 are listed in Table 4.4. The same information for Herschel and filtered-Herschel sources is listed in Tables 4.5 and 4.6 respectively. The properties of those sources with counterparts in another catalogue are compared with the properties of their counterparts in Figure 4.10. A source's counterpart in another catalogue is the nearest neighbour to the source in that catalogue, provided that the source and its neighbour are separated by less than the FWHM of the larger of the two sources. It can be seen from the central column of plots in Figure 4.10 that sources found in both the SCUBA-2 and the filtered-Herschel catalogues are typically found to have very similar properties. This tends to indicate that the filtering process is the correct method by which to make SCUBA-2 and Herschel data comparable.

Herschel sources are typically measured to be warmer than their SCUBA-2 and filtered-Herschel counterparts. We hypothesise that this is due to the filtering process removing much of the extended foreground and background emission originating from warmer material, thus reducing the line-of-sight temperature determined by
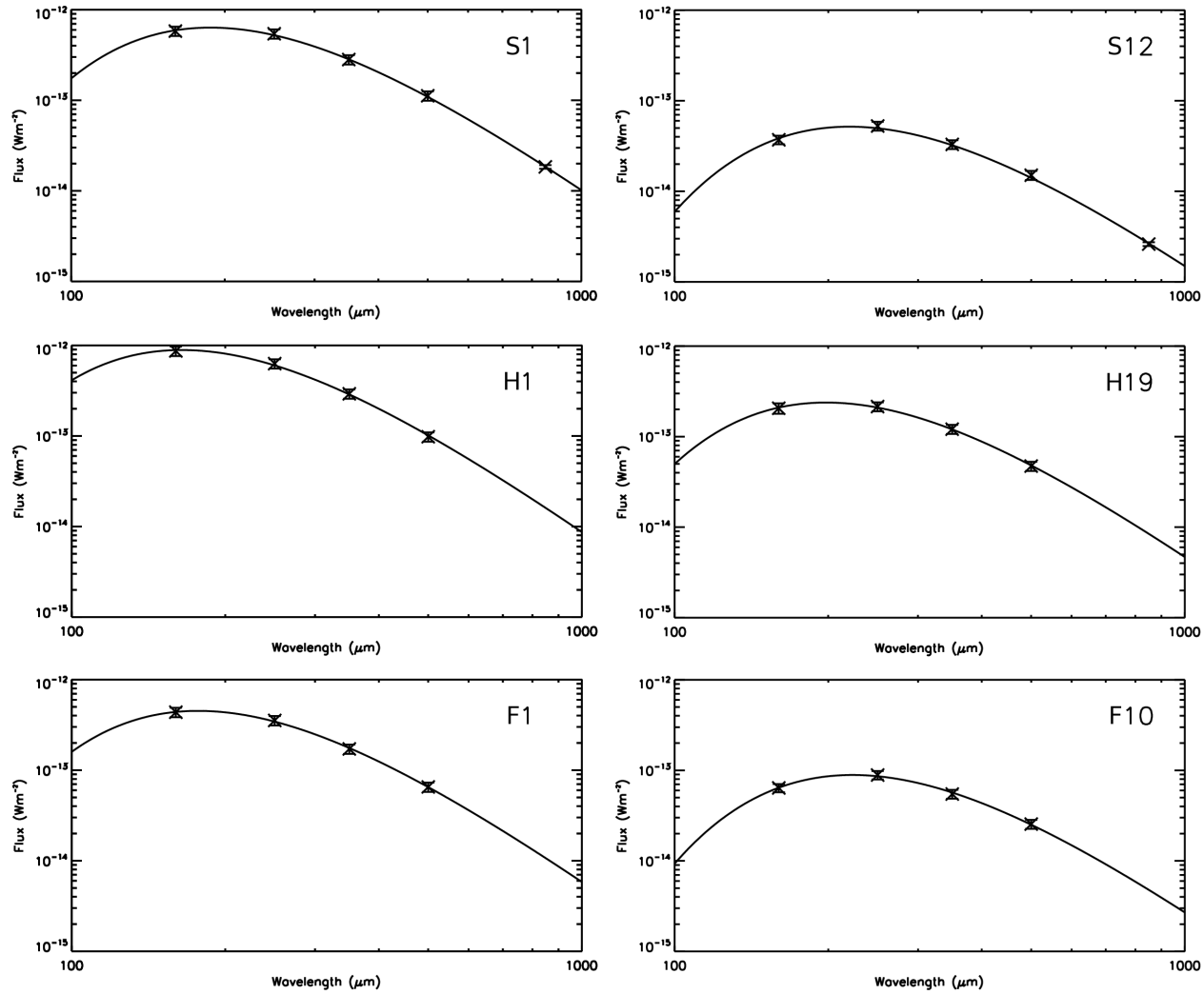
Figure 4.9: SED fits for sources S1 and S12, and their counterparts in the Herschel and filtered-Herschel catalogues (H1 and F1, and H19 and F10, respectively).
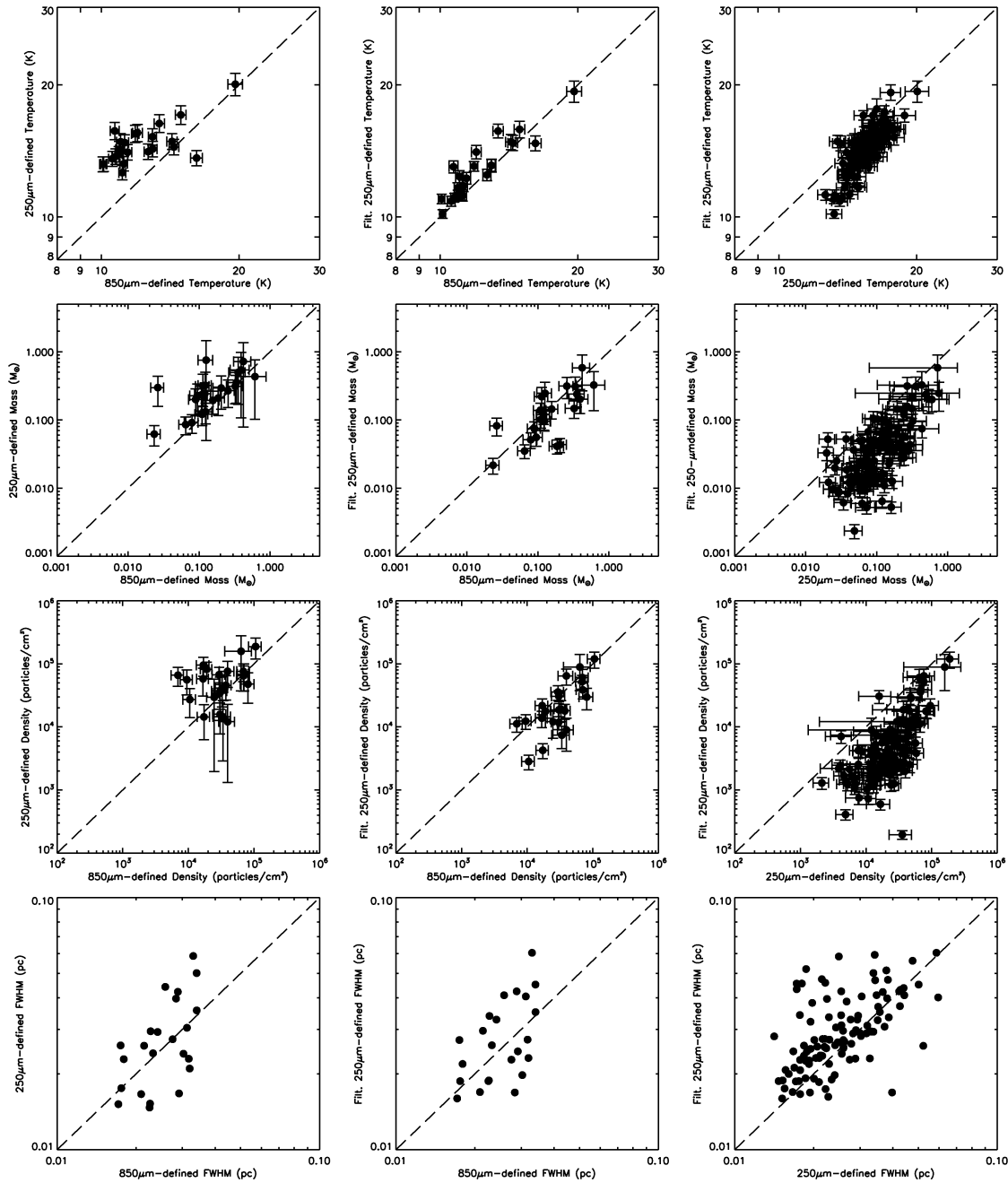
Figure 4.10: Comparison of the properties of the 23 SCUBA-2 sources with their counterpart Herschel sources (left-hand column), and filtered-Herschel sources (middle column). The 118 sources in common between the Herschel and filtered-Herschel catalogues are compared in the right-hand column. The parameters compared are temperature (top row), mass (second row), density (third row), and deconvolved FWHM size (fourth row). See text for details.
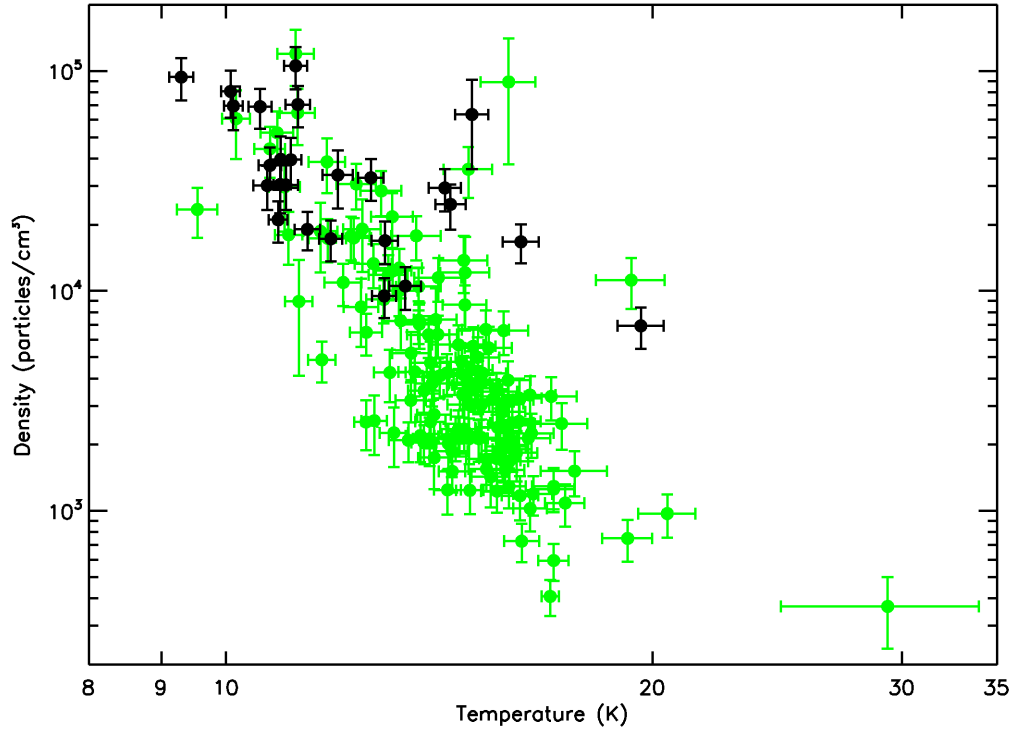
Figure 4.11: Plot of core density against temperature. Black symbols are SCUBA-2 sources, green symbols are filtered-Herschel sources. There appears to be a cut-off in density, with the minimum SCUBA-2 source density being $\sim 6 \times 10^3$ particles/cm^{-3}, while the lowest-density filtered-Herschel sources are $\sim 4 \times 10^2$ particles/cm^{-3}. However, the filtered-Herschel sources and the SCUBA-2 sources have a similar range in temperature, ~ 9–20 K, with no apparent cut-off.

the fitting process. Herschel sources are more massive and denser than their counterpart filtered-Herschel sources. Again, this is due to the removal of large-scale signal by the filtering process, although there is no apparent consistent difference in FWHM between the differently-detected sources.

Figure 4.11 shows the relationship between temperature and density for the filtered-Herschel sources and the SCUBA-2 sources. The SCUBA-2 sources follow the same density-temperature relation as the filtered-Herschel sources, $\rho \propto T^{-8.5\pm0.5}$. However, only the densest filtered-Herschel sources have a counterpart SCUBA-2 source, with the minimum SCUBA-2 source density being $\sim 3 \times 10^{-17}\,\mathrm{kgm}^{-3}$ ($\sim 6 \times 10^3$ particles/cm^3), while the lowest-density filtered-Herschel sources are $\sim 2 \times 10^{-18}\,\mathrm{kgm}^{-3}$ ($\sim 4 \times 10^2$ particles/cm^3). The filtered-Herschel sources and the SCUBA-2 sources have a similar range of temperatures, ~ 9–$20\,\mathrm{K}$.

Those SCUBA-2 sources which do not follow the temperature-density relation are S1 (L1495A-S), S10, S13, S15 and S23. All of these sources are significantly ($\sim 5\,\mathrm{K}$) warmer than might be expected from their density. Of these five sources, S1 and S23 are heated by V892 Tau (IRAS04155+2812), as discussed above. Sources S10 and S13 are being heated by IRAS04113+2758, while source S15 is associated with the IR source IRAS04111+2800G, and may in fact have an embedded YSO within it.

Figure 4.12 shows the mass-size relation for the filtered-Herschel and SCUBA-2 sources. There is no tendency for the SCUBA-2 sources to be smaller in size than the filtered-Herschel sources. However, the SCUBA-2 sources are among the most massive. The grey band shown on Figure 4.12 indicates the region of the mass/size plane which unbound, transient starless cores are expected to inhabit (Elmegreen & Falgarone 1996; André et al. 2010). A substantial fraction of the filtered-Herschel sources lie within this region. However, the SCUBA-2 sources in almost all cases occupy the region of the mass/size plot in which gravitationally bound prestellar

cores are expected to be found (c.f. André et al. 2010).

Figure 4.11 shows a clear cutoff in density below which no SCUBA-2 sources are detected. However, there appears to no similar cutoff in temperature. Figure 4.12 shows no tendency for SCUBA-2 sources to be smaller in radius than filtered-Herschel sources. This indicates that the criterion for determining whether a source detected using Herschel will be detectable with SCUBA-2 is its mass for a given size, or in other words, density.

This corresponds, in terms of the measurable parameters, effectively to surface brightness. For a given temperature, the higher column density material will produce a higher surface brightness. Also, for geometries not elongated along the line of sight, higher column density corresponds to higher volume density. Therefore, it appears that it is not mass or size alone that determines detectability with SCUBA-2, but rather a combination of mass and size that corresponds to density. The exceptions to this are those sources with associated or nearby stars or protostars, because in those cases the above assumption, that everything is at roughly similar temperature, breaks down.

Figure 4.13 shows how the minimum particle number density n to which SCUBA-2 is sensitive varies as a function of distance and temperature. A core of temperature T at distance D will be detectable in SCUBA-2 GBS data if its density is greater than or equal to n, where

$$n = n_0 \left(\frac{D}{D_0} \right)^2 \frac{e^{h\nu/k_{\mathrm{B}}T} - 1}{e^{h\nu/k_{\mathrm{B}}T_0} - 1} \tag{4.3}$$

This relation is normalised to a density sensitivity $n_0 = 6.3 \times 10^3$ particles/cm^3 at the canonical distance of the Taurus molecular cloud of $D_0 = 140\,\mathrm{pc}$ and the mean temperature of our non-externally-heated starless cores, $T_0 = 11.3\,\mathrm{K}$. The density sensitivity limit at a given distance decreases as source temperature increases.

The distances to the Taurus and Orion molecular clouds are marked on Figure 4.13. The density sensitivity limits for a 10 K core at 140 pc (close to the typical
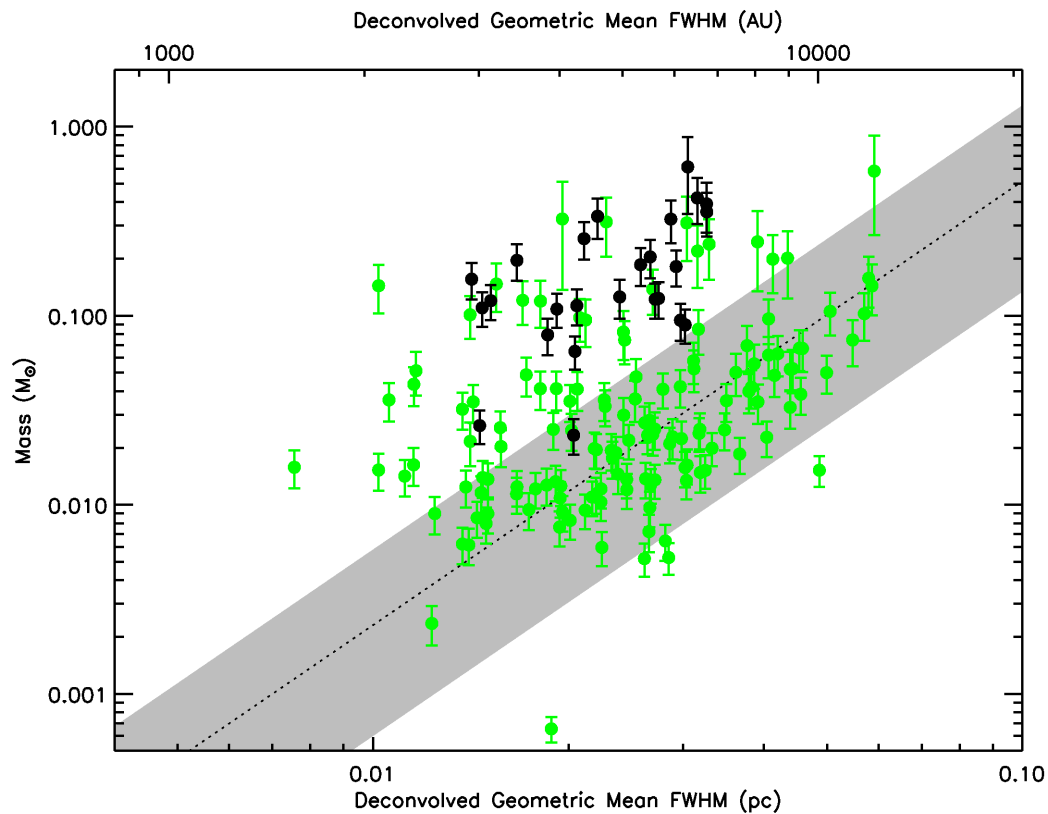
Figure 4.12: Plot of core mass against deconvolved size. Black symbols are SCUBA-2 sources, green symbols are filtered-Herschel sources. There appears to be no tendency for the SCUBA-2 sources to be smaller in size than the filtered-Herschel sources. However, the SCUBA-2 sources are among the most massive. The grey band indicates the region which unbound starless cores are expected to inhabit (Elmegreen & Falgarone 1996; André et al. 2010). A substantial fraction of the filtered-Herschel sources lie within this region. However, the SCUBA-2 sources in almost all cases occupy the region above this, in which prestellar cores are expected to be found (c.f. André et al. 2010). Note that SCUBA-2 sources occupy almost the same size range as filtered-Herschel sources.
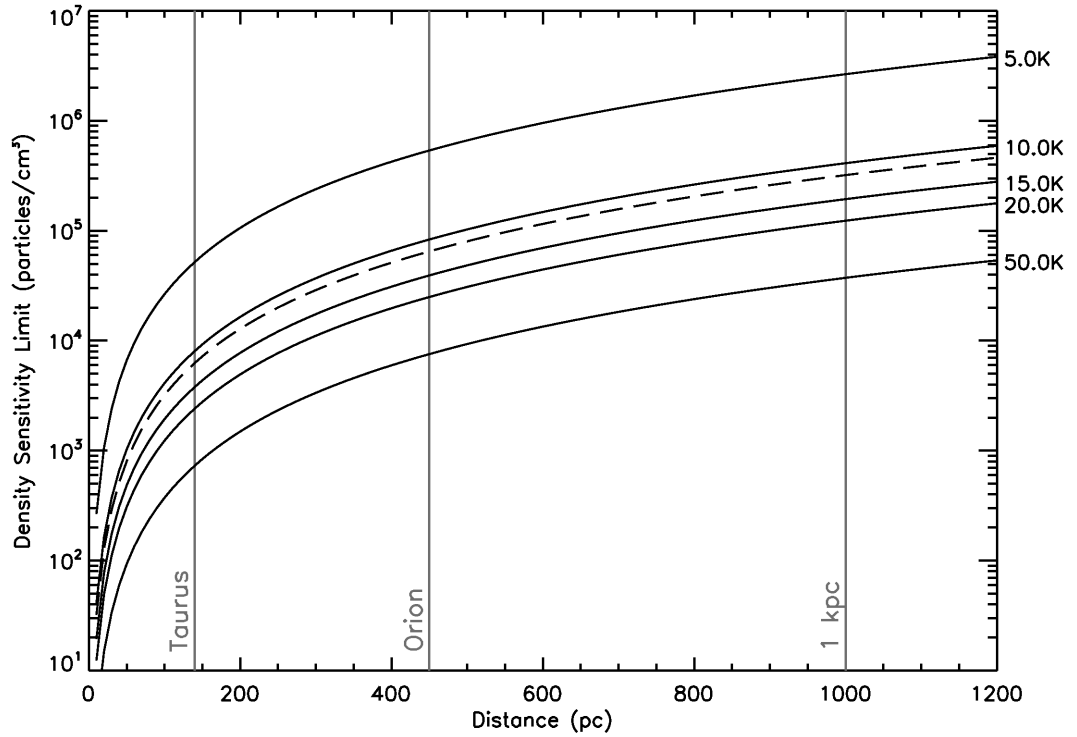
Figure 4.13: Plot of the lowest source density detectable using SCUBA-2 GBS data, as a function of distance, for various assumed source temperatures. The dashed line shows the SCUBA-2 GBS density sensitivity limit as a function of distance at the mean temperature of the non-externally heated starless cores in our sample (11.3 K). All of the relations are normalised against a density limit of $\sim 6.3 \times 10^3$ particles/cm^3 at a temperature of 11.3 K and a distance of 140 pc, as we find for the mean of the cores in Taurus in this work.

core temperature in Taurus) and a 50 K core at 450 pc (a typical core temperature in the high-mass star-forming region Orion, shown for comparison) are very similar: $\sim 8 \times 10^3$ particles/cm^3 and $\sim 7 \times 10^3$ particles/cm^3 respectively. Hence, their relative detectability in SCUBA-2 GBS data should be similar.

It is important to note that the SCUBA-2 sensitivity limits found in this chapter are those of the JCMT GBS, and not an intrinsic property of data from the instrument in general. It is possible for further data to be taken, improving the sensitivity, until the confusion limit is reached. Similarly, the Herschel data are at the (fixed) sensitivity of the HGBS, and not necessarily confusion-limited.

4.4 Energy Balance and Stability

We now estimate the magnitude of each of the terms in the virial equation, similar to the process described in Section 3.4, in order to determine the stability of our cores against collapse.

4.4.1 Gravitational potential energy

We again approximate our sources as three-dimensional, spherically-symmetric, Gaussian distributions. We determine their gravitational potential energies using equation 3.24, and the masses and core FWHM values listed in Table 4.4, taking the characteristic radius α of each core to be $\alpha = \text{FWHM}/\sqrt{8\ln2}$.

4.4.2 Internal energy

We determine the internal energy of our cores using the linewidths determined for cores in L1495 in ammonia (NH$_3$) by Seo et al. (2015). Seo et al. (2015) observed the NH$_3$ (1,1) – rest frequency 23.694 GHz – and (2,2) – rest frequency 23.723 GHz – transitions using the 100-m Robert C. Byrd Green Bank Telescope, with a beam

size of 31 arcsec and a velocity resolution of 3.05 kHz.

The integrated NH₃ emission is shown in Figure 4.14. The regions observed by Seo et al. (2015) which were also observed as part of the JCMT GBS are those identified as B7, B10 and B211 on Figure 4.14. It can be seen that the NH₃ and 850-μm continuum emission appear to be tracing the same material – the dense cores within the filament (c.f. Figure 4.3). The cores identified by Seo et al. (2015) are marked on Figure 4.14. These NH₃ cores were also extracted using CSAR (Kirk et al. 2013), and should hence be comparable to our own set of sources.

We determined which of our SCUBA-2 sources have counterparts in the Seo et al. (2015) catalogue of cores detected in ammonia emission (hereafter referred to as ammonia cores) by considering a SCUBA-2 source's counterpart ammonia core to be its nearest neighbour amongst the ammonia cores, provided that neighbour's central coordinates are separated from the SCUBA-2 core's central coordinates by less than the largest of the following quantities: the SCUBA-2 source FWHM, the ammonia core FWHM, or the 31-arcsec Green Bank beam. Of the 25 SCUBA-2 cores, 12 have counterpart ammonia cores: S1, S2, S3, S5, S6, S7, S9, S11, S12, S14, S16 and S21.

We assume that the velocity dispersions given by Seo et al. (2015) for their cores are applicable to their counterpart SCUBA-2 cores in our catalogue. For consistency with our previous assumptions, we adjust the velocity dispersions listed by Seo et al. (2015) to account for their assumption of a mean atomic weight $\mu_{Seo} = 2.33$ (where we take $\mu = 2.86$), and to assume a central core temperature of $T_{gas} = 7\,\mathrm{K}$, in keeping with our analysis of the starless cores in Ophiuchus. The linewidths are adjusted using the equation

$$\sigma_{gas}^2 = \sigma_{gas,Seo}^2 + k_{\mathrm{B}}\left(\frac{T_{gas}}{\mu m_{\mathrm{H}}} - \frac{T_{gas,Seo}}{\mu_{Seo} m_{\mathrm{H}}} + \frac{T_{gas,Seo} - T_{gas}}{m_{\mathrm{NH_3}}}\right). \qquad (4.4)$$

It should be noted that using the kinetic temperatures $T_{gas,Seo}$ rather than a gas temperature of 7 K produces minimal change in the energy balance of the cores, and

209
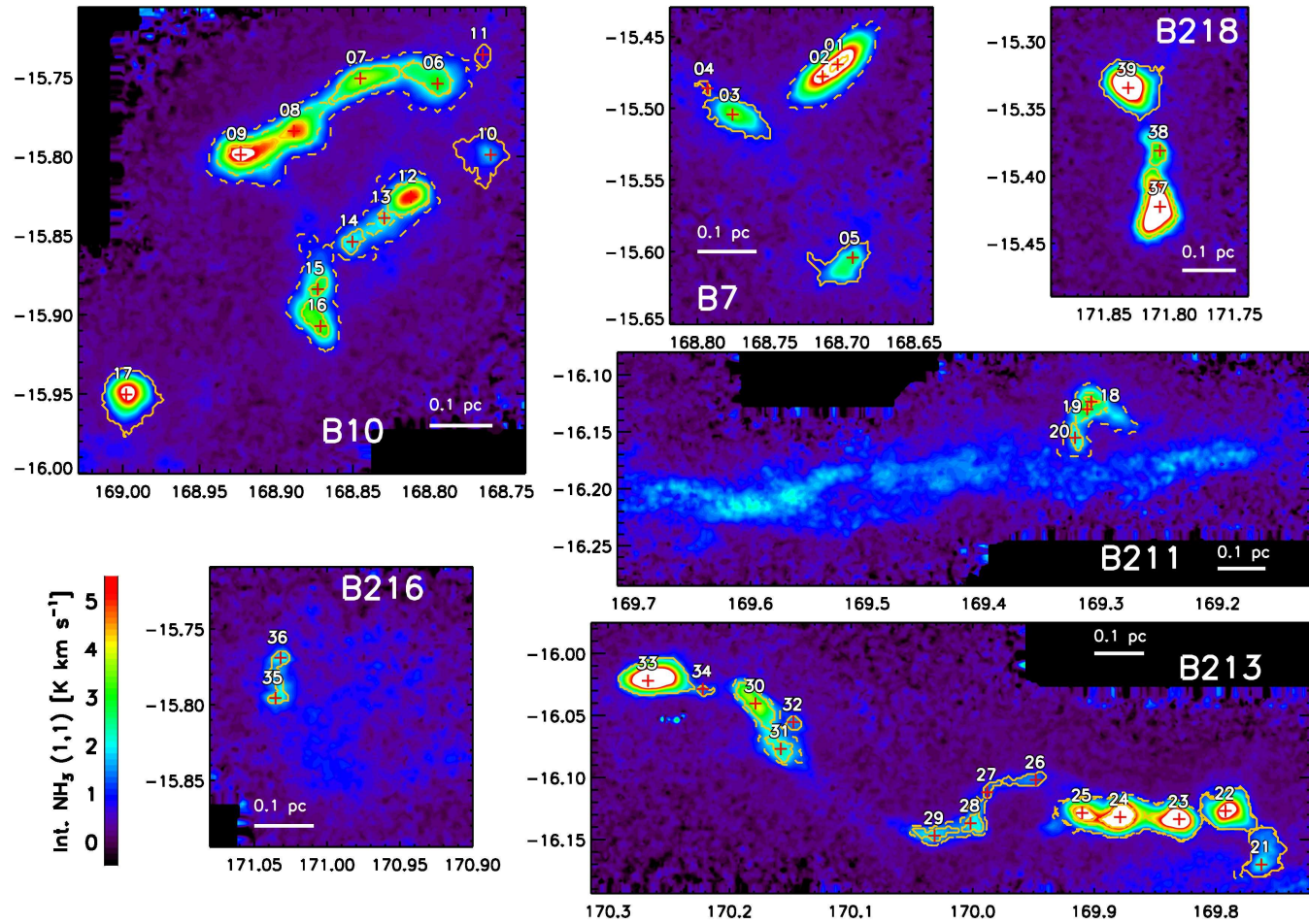
Figure 4.14: Integrated NH$_3$ (1,1) emission in the L1495 filament, with ammonia cores marked (from Seo et al. 2015).

does not change the conclusions of this analysis. We then calculated internal kinetic energies for our cores using equation 3.22.

4.4.3 External pressure energy

We determined the external pressure on our cores by determining the average velocity dispersion in HARP-B ^{12}CO J $= 3 \rightarrow 2$ emission over each core position for which data were available. The JCMT GBS HARP-B CO observations for L1495 were presented by Davis et al. (2010). The ^{12}CO and ^{13}CO data are shown in Figure 4.15. The HARP-B ^{12}CO observations cover the high-column-density regions of the head of the L1495 filament, labelled L1495 N, L1495 E, L1495 S and L1495 W in Figure 4.15, and of the north-western end of the L1495/B213/B211 filament, labelled L1495 SE in Figure 4.15. ^{13}CO emission has been observed using HARP-B in two small subsets of the area observed in ^{12}CO: the area surrounding L1495A, and a part of the L1495/B213/B211 filament not covered by the SCUBA-2 observations used in this chapter. The C^{18}O data cover the same area as the ^{13}CO data.

Davis et al. (2010) note that both ^{13}CO and C^{18}O emission is very weak in both the regions mapped, and that the ^{12}CO emission is faint, diffuse and/or optically thick. Christie et al. (2012) find that CO is severely depleted in the L1495 regions, with a depletion factor F_{dep} such that

$$F_{\mathrm{dep}} = \frac{N(\mathrm{H_2})_{\mathrm{dust}}}{N(\mathrm{H_2})_{\mathrm{CO}}} \sim 25, \tag{4.5}$$

i.e. the H$_2$ column density estimated from C^{18}O emission in starless cores in Taurus is typically 25 times smaller than that determined from dust emission. We thus do not attempt to determine the masses of our cores from any isotopologue of CO emission.

The typical mean volume densities of our SCUBA-2 cores are $\sim 10^4\,\mathrm{cm^{-3}}$ (see Table 4.4), and thus the assumption made for Ophiuchus in Section 3.4.2 that starless cores are bounded at a density of $\sim 10^5\,\mathrm{cm^{-3}}$ is clearly not valid in Taurus. In
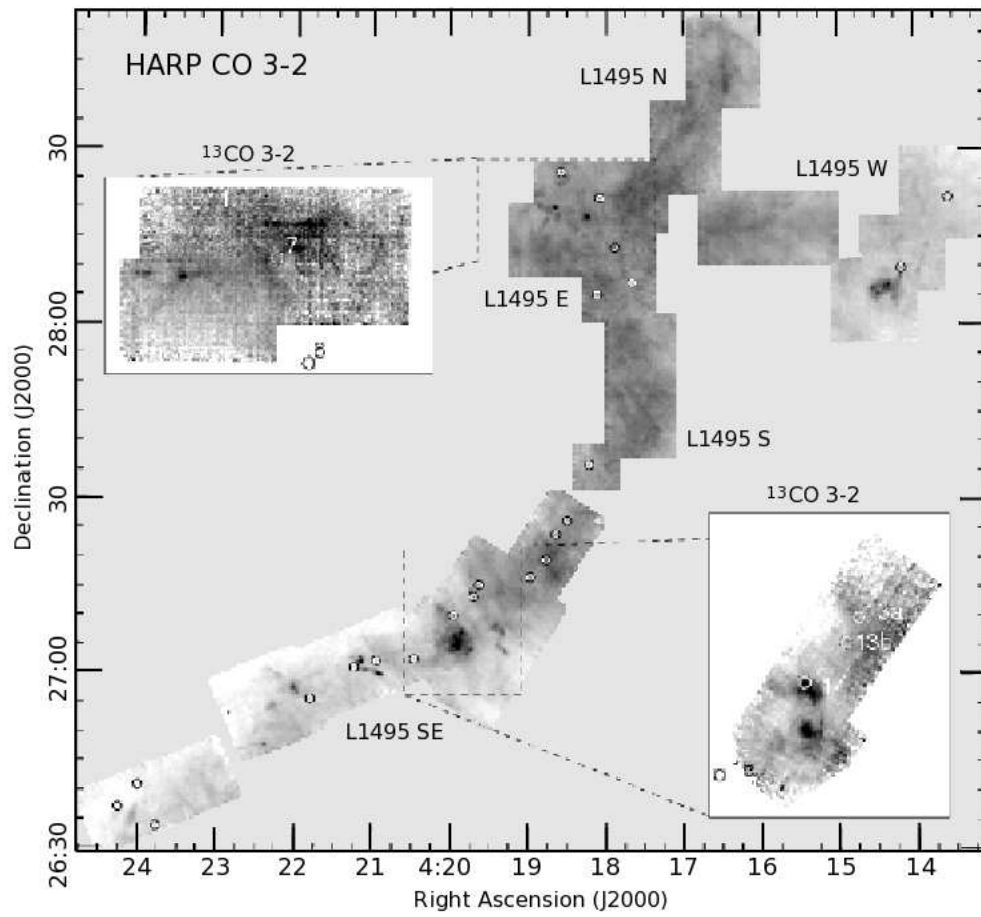
Figure 4.15: Integrated ^{12}CO J $= 3 \rightarrow 2$ emission in the L1495 filament, with integrated ^{13}CO data inset (from Davis et al. 2010).

addition, the depletion of CO in Taurus is such that a consistent velocity dispersion cannot be found for each source from the HARP-B $C^{18}O$ maps. We attempted to determine external velocity dispersions for our cores from both ^{12}CO and ^{13}CO data.

Cores in Taurus typically have similar masses to those in Ophiuchus, but larger radii. Hence, the typical densities of starless cores in Taurus will be lower than those in Ophiuchus. Star formation in Taurus appears to be proceeding in a relatively dispersed manner, and there do not appear to be any large-scale external influences on the region (such as the Sco OB2 association's effect on Ophiuchus – see Chapter 3) causing material to be 'swept up', i.e. leading to density enhancements of the sort expected in regions undergoing sequential star formation (see Section 1.2.6.1). Hence, the lower core densities seen in Taurus compared to Ophiuchus are not an unexpected result. This is discussed further in Chapter 6.

We determined velocity dispersions by fitting a single Gaussian to each pixel of ^{12}CO and ^{13}CO emission using an IDL routine utilising *mpfit* (Markwardt 2009). Fits were accepted for pixels with a signal-to-noise ratio (SNR) ≥ 5 and a reduced $\chi^2 < 10$. In an attempt to ameliorate the effects of low signal-to-noise ratio, we repeated this process with the data binned to a variety of pixel sizes: 6, 12, 24, 36 and 48 arcsec. For each core and at each pixel size, the velocity dispersion was taken to be the mean of the velocity dispersions in each good pixel covered by the aperture used for source continuum photometry, and the uncertainty on this value was taken to be the standard deviation on the mean. The velocity dispersions in ^{12}CO determined for each of the cores for which data are available are shown in Figure 4.16, while the velocity dispersions in ^{13}CO are shown in Figure 4.17, in each case as a function of re-gridded pixel size.

The velocity dispersion for each core is taken to be the weighted mean of all of the measurements for that core which have an associated uncertainty (i.e. all measurements determined from more than one pixel). As can be seen in Figure 4.16,
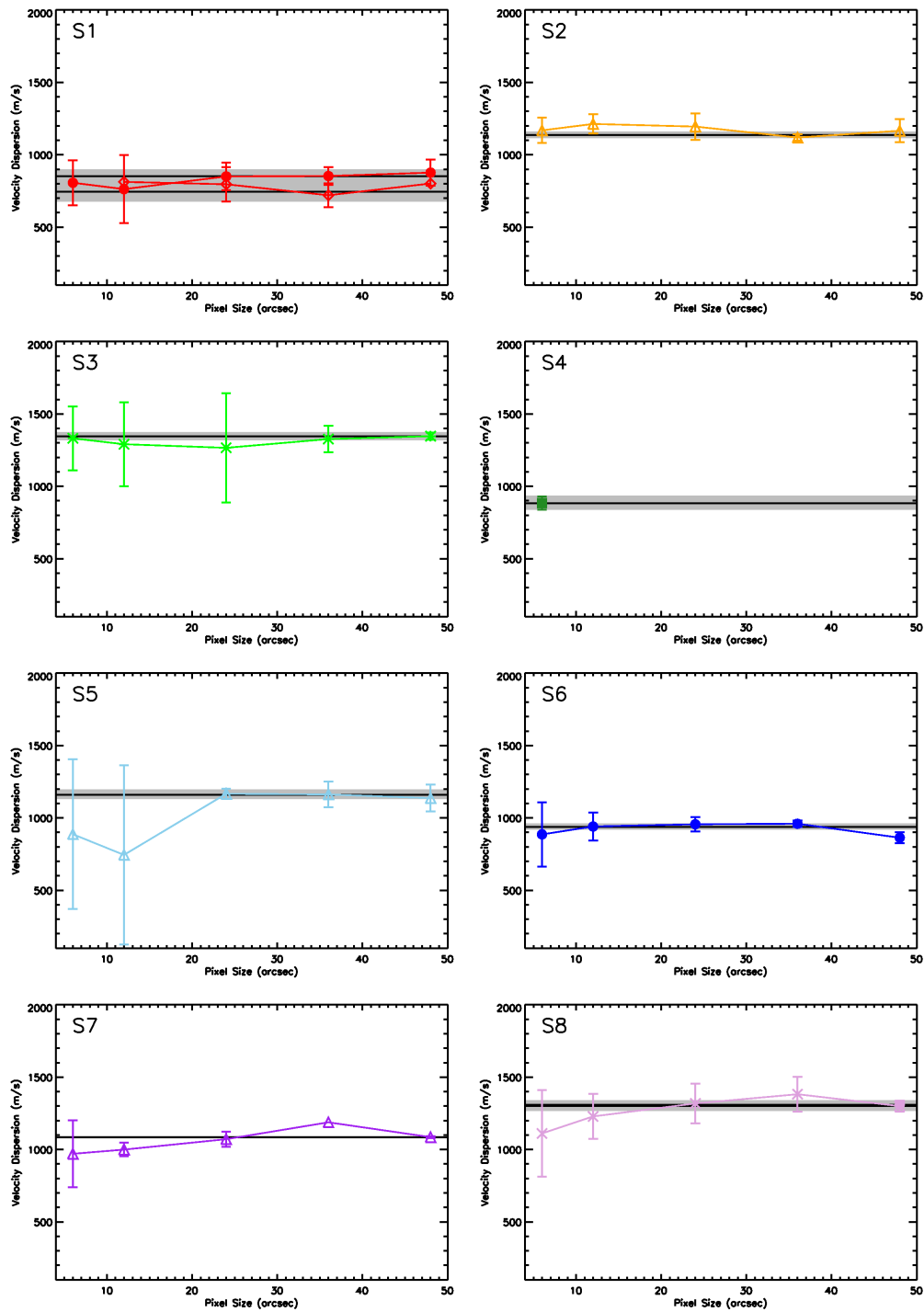
Figure 4.16: Velocity dispersion measured in ^{12}CO for the SCUBA-2 cores as a function of re-gridded pixel size. Note that S1 and S8 have two overlapping sets of HARP ^{12}CO data, and hence have two sets of data points on this plot.
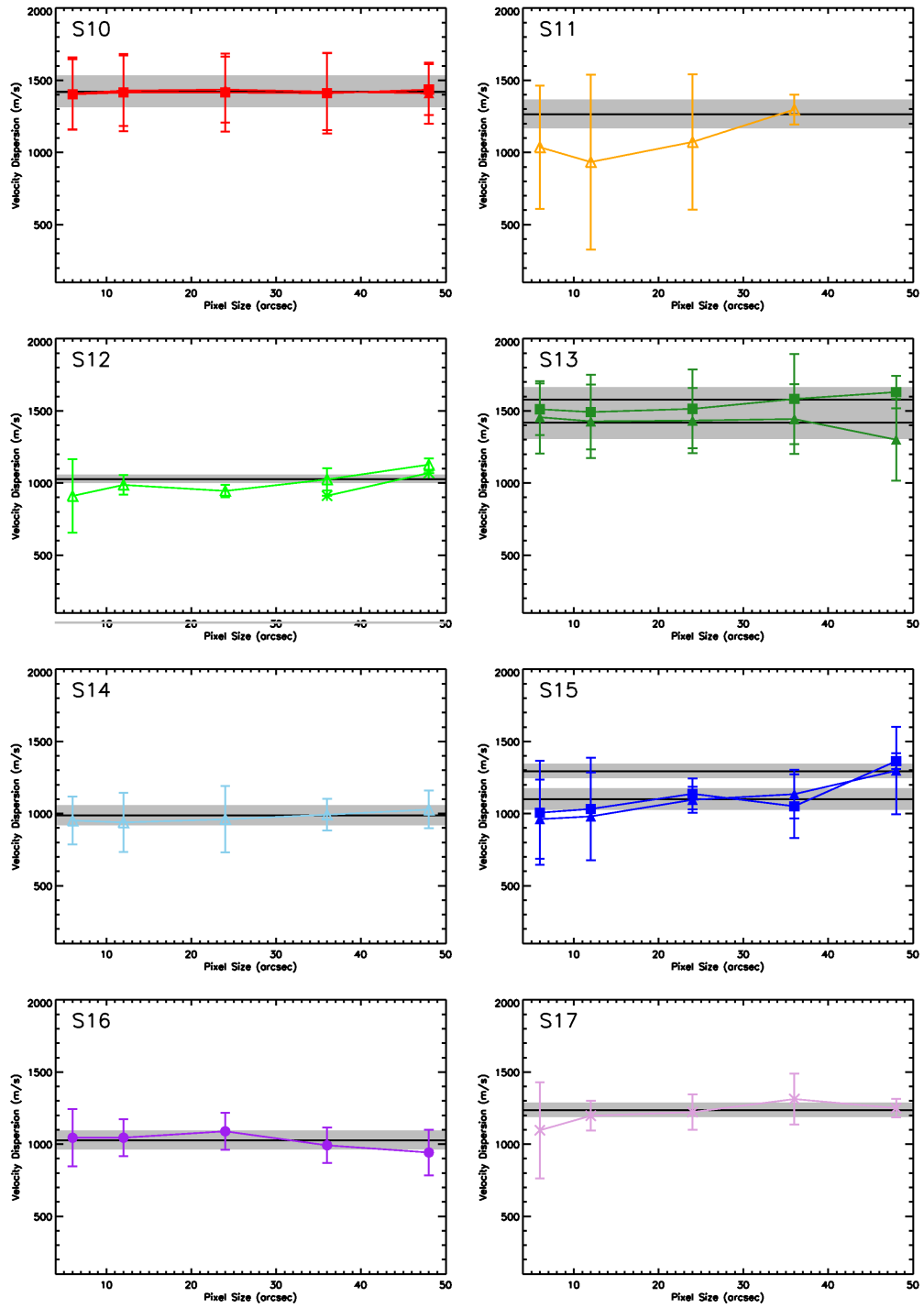
Figure 4.16: – continued. S10, S12 , S13, and S15 have two overlapping sets of HARP ^{12}CO data, and hence have two sets of data points on this plot.
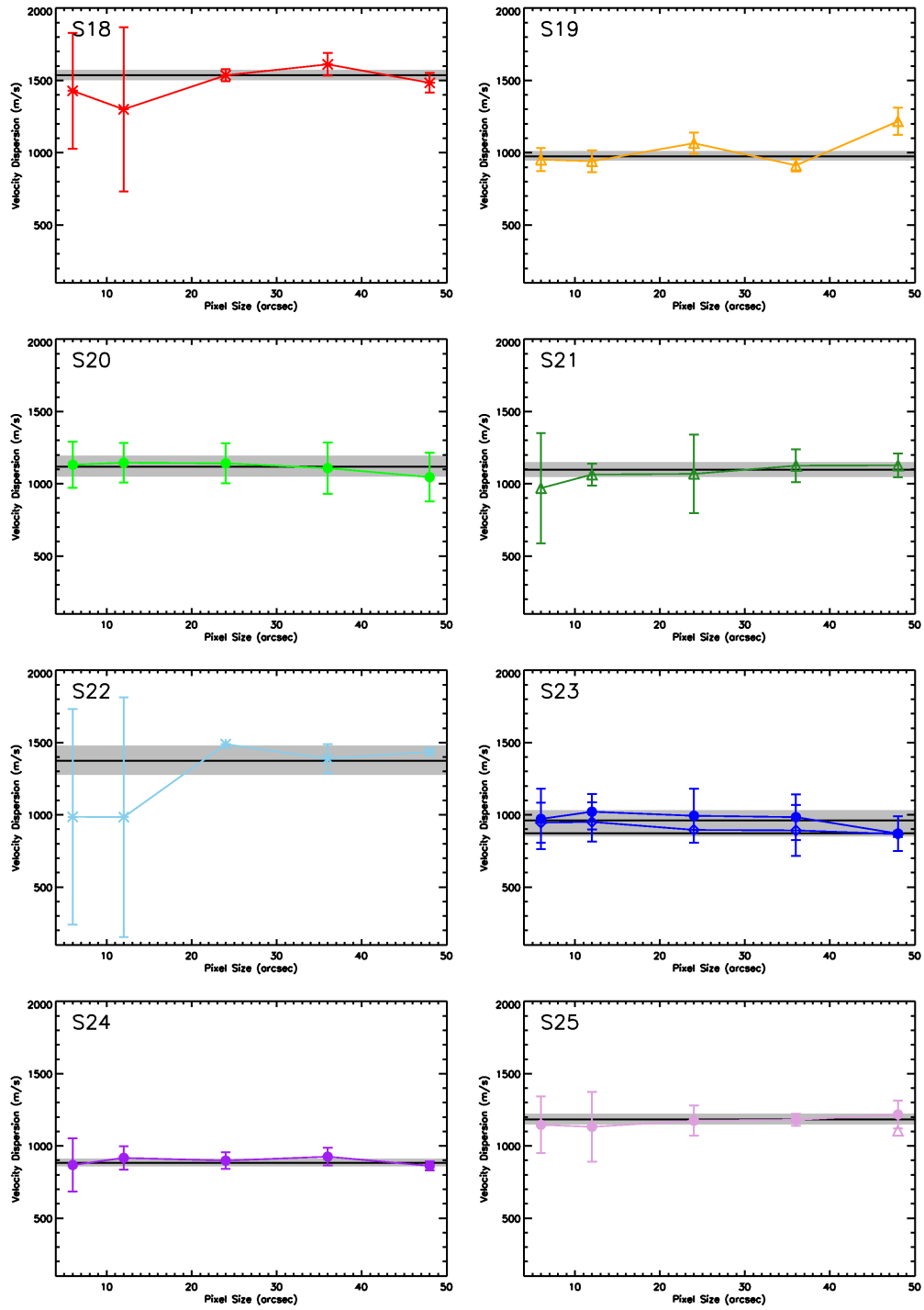
Figure 4.16: – continued. S23 and S25 have two overlapping sets of HARP ^{12}CO data, and hence have two sets of data points on this plot.

a few cores are covered by two HARP-B fields, specifically, S1, S10, S13, S15 and S23 in ^{12}CO, and S1, S6, S20, S23 and S24 in ^{13}CO. In these cases, the velocity dispersion used for further analysis is that which was determined from the larger number of measurements. If both velocity dispersions were determined from the same number of measurements – for example, core S10 in ^{12}CO, for which measurements at all wavelengths are good in both of the HARP-B fields in which the cores are observed – then a second weighted mean of the two velocity dispersions is taken.

As can be seen from Figures 4.16 and 4.17, the velocity dispersions determined from ^{12}CO observations are more consistent, and have much smaller associated uncertainties, than those determined from ^{13}CO. Additionally, all but one of the SCUBA-2 cores are covered by at least one ^{12}CO HARP-B field (the exception being S9), while only 7 are covered by a ^{13}CO field, namely S1, S6, S16, S20, S23, S24 and S25.

The velocity dispersions are corrected for the mass discrepancy between ^{12}CO and the mean gas mass in the manner described in Section 3.4.1:

$$\sigma^2_{gas,^{12}\text{CO}} = \sigma^2_{^{12}\text{CO}} + k_\text{B} T_{gas} \left(\frac{1}{\mu m_\text{H}} - \frac{1}{m_{^{12}\text{CO}}} \right) \tag{4.6}$$

where, for each source, T_{gas} is taken to be the core temperature listed in Table 4.4. As the ^{12}CO velocity dispersions are substantially supersonic, the effect of this correction is minimal.

The gas pressure in ^{12}CO is calculated very similarly to the gas pressure in C^{18}O in Section 3.4.2. Equation 3.37 is modified to

$$P_{\text{EXT}} \approx \rho_{^{12}\text{CO}} \langle \sigma^2_{gas,^{12}\text{CO}} \rangle, \tag{4.7}$$

while equation 3.38 becomes

$$r_{^{12}\text{CO}} = \alpha \sqrt{2 \ln \left(\frac{\rho_0}{\rho_{^{12}\text{CO}}} \right)}. \tag{4.8}$$

We take $\rho_{^{12}\text{CO}}$, the density at which ^{12}CO ceases to be an effective tracer, to be $10^3 \, \text{cm}^{-3}$ (Di Francesco et al. 2007), and $r_{^{12}\text{CO}}$ is the core radius at which the density
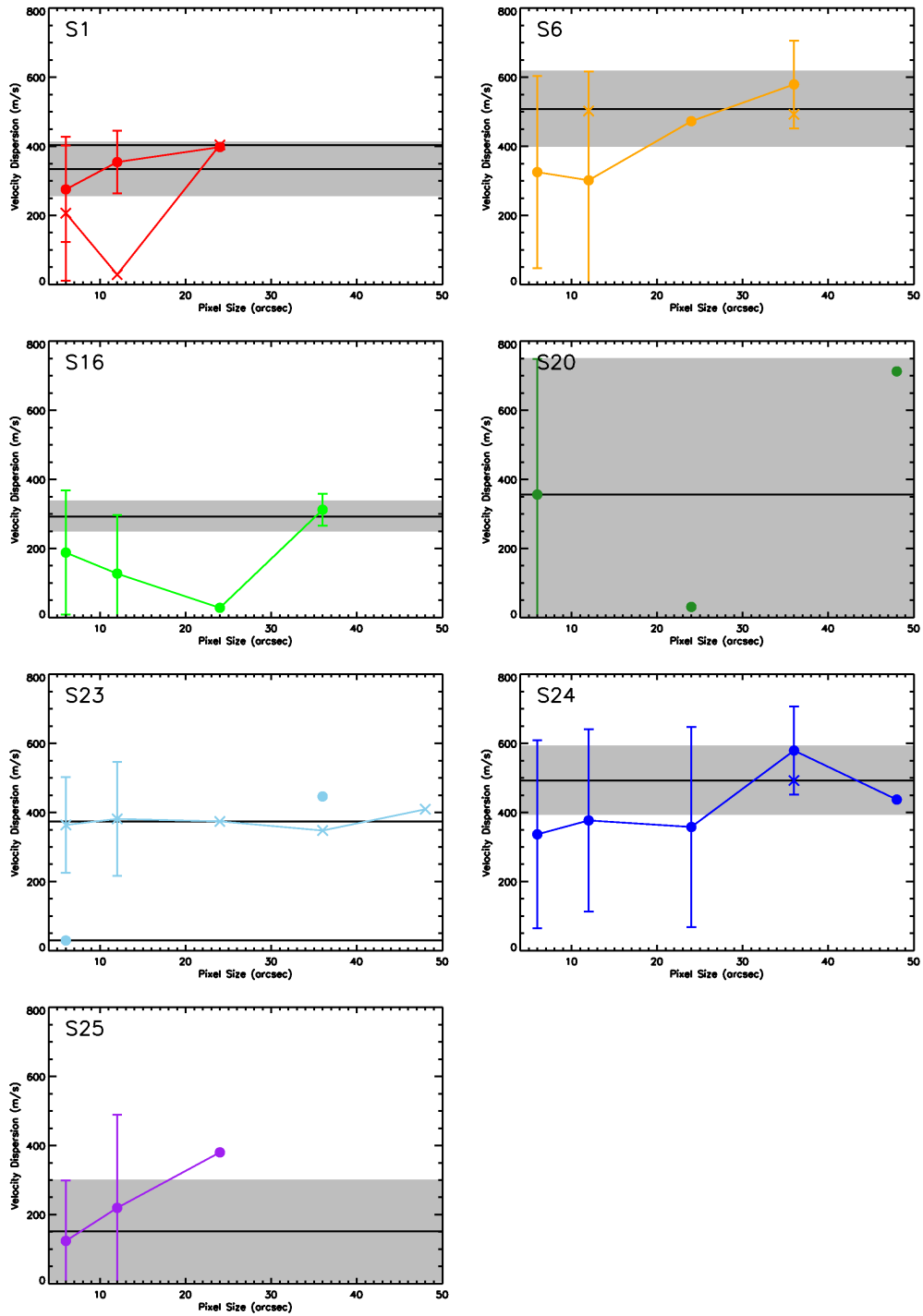
Figure 4.17: Velocity dispersion measured in ^{13}CO for the SCUBA-2 cores as a function of re-gridded pixel size. Note that S1, S23 and S24 have two overlapping sets of HARP ^{13}CO data, and hence have two sets of data points on this plot.

$\rho_{^{12}CO}$ is reached. All other symbols are as defined in Section 3.4.2. The external gas pressure term in the virial equation then becomes

$$\Omega_{\mathrm{P}} = -4\pi P_{\mathrm{EXT}} r_{^{12}CO}^3. \tag{4.9}$$

For purposes of comparison, we perform the same calculations on the cores for which ^{13}CO data are available, modifying $\sigma_{gas,^{12}CO} \rightarrow \sigma_{gas,^{13}CO}$, and choosing $\rho_{^{13}CO} = 10^4 \, \mathrm{cm}^{-3}$ (Di Francesco et al. 2007).

4.4.4 Magnetic energy density

There have been several attempts to determine the magnetic field strength of starless cores in the Taurus molecular cloud. The values obtained are summarised in Table 4.7. The magnetic field strength varies considerably between cores, and between different density tracers. We carried out the same analysis as in Chapter 3, using equation 3.45, which we repeat here:

$$\frac{\Omega_{\mathrm{M}}}{\Omega_{\mathrm{K,NT}}} = \frac{1}{3\mu_0} \frac{B_0^2}{\rho_0 \sigma_{0,\mathrm{NT}}^2}. \tag{4.10}$$

We found that the ratio of magnetic energy to non-thermal kinetic energy varies substantially, with the core TMC-1 appearing to be supported by internal kinetic energy, while L1498, L1544 and B217-2 are magnetically supported according to this analysis, with magnetic energy significantly greater than non-thermal kinetic energy in the cases of L1498 and B217-2. This suggests that magnetic energy may be of importance to the energy balance of cores in L1495, while not giving a consistent value of either B or $\Omega_{\mathrm{M}}/\Omega_{\mathrm{K,NT}}$ with which the magnetic energy term of the virial equation might be estimated or parameterised. We note this in the virial analysis below.

Table 4.7: Magnetic field strength measurements in the Taurus molecular cloud. References: T96 – Troland et al. 1996; S99 – Shinnaga et al. 1999; L01 – Levin et al. 2001; K06 – Kirk et al. 2006; T08 – Troland & Crutcher 2008. It should be noted that the Zeeman and Chandrasekhar-Fermi methods probe the line-of-sight and plane-of-sky magnetic fields respectively.

Reference	Region	B-Field (μG)	Tracer	Density (cm^{-3})	Method	σ (ms^{-1})	σ_{NT} (ms^{-1})	$\Omega_{\mathrm{M}}/\Omega_{\mathrm{K,NT}}$
T96	TMC-1	1.4	OH	$1-2 \times 10^4$	Zeeman	187 (OH)	173	$0.016 - 0.033$
S99	L1521E	160 ± 42	CCS	$10^4 - 10^5$	Zeeman	–	–	–
L01	L1498	48 ± 31	CCS	$10^4 - 10^5$	Zeeman	105 (CCS)	95	$13 - 51$
K06	L1498	10 ± 7	850μm	–	C.-F.	–	–	–
	L1517B	30 ± 10	850μm	–	C.-F.	–	–	–
T08	B217-2	13.5 ± 3.7	OH	1.7×10^3	Zeeman	200 (H$_2$)	104	49.0
	TMC-1	9.1 ± 2.2	OH	5.1×10^3	Zeeman	535 (H$_2$)	507	0.3
	L1544	10.8 ± 1.7	OH	6.6×10^3	Zeeman	204 (H$_2$)	113	2.7

4.4.5 Virial balance

We estimated the gravitational potential energy, internal energy, and external pressure energy terms in the virial equation as described above. The results of this analysis are listed in Table 4.8, and are plotted in Figure 4.18. Table 4.8 lists the source ID, the counterpart ammonia core, the velocity dispersions in NH_3 and ^{12}CO, the gravitational potential energy, internal energy, and external pressure energy terms of the virial equation, the virial balance, the magnetic field required for virial equilibrium, and the critically-stable Bonnor-Ebert mass (discussed below) for each of the SCUBA-2 cores for which data are available.

All but one of the SCUBA-2 cores are, according to this analysis, virially bound, the sole exception being the core S6, which is approximately virialised. Our cores are strongly pressure-confined, with only the core S1 consistent within error with being near equilibrium between external pressure and gravitational potential energy. In a few cases, the virial ratio is consistent within errors with the core being in virial equilibrium, but in general, the virial ratios listed in Table 4.8 would suggest that a substantial majority of our SCUBA-2 cores in L1495 are collapsing under external pressure. While not impossible, this scenario seems unlikely; visual inspection of Figures 4.1 and 4.3 does not suggest a set of cores which are substantially out of virial equilibrium with their surroundings. The L1495/B211/B213 filament in which the cores are embedded appears as a well-defined and apparently coherent structure, suggesting that it is in at least approximate virial equilibrium. Additionally, if the cores in L1495 were collapsing under pressure, one might expect to see cores in intermediate stages of collapse. However, all of our SCUBA-2 cores have similar characteristic radii and densities. Either we are fortuitously observing a newly- and simultaneously-formed set of cores precisely at the moment of onset of pressure-driven collapse, or we are missing information in our virial analysis.

Bearing in mind that our cores appear in general to be approximately equilibrium

Table 4.8: Virial stability of SCUBA-2 cores in L1495

Source ID	Seo ID	$\sigma_{\mathrm{NH3},gas}$	$\sigma_{\mathrm{^{12}CO},gas}$	$-\Omega_{\mathrm{G}}$	Ω_{K}	$-\Omega_{\mathrm{P}}$	$\frac{1}{2}\tilde{\mathcal{I}}$	B_{vir}	$\Omega_{\mathrm{M},vir}$	$\dfrac{\Omega_{\mathrm{M},vir}}{2\Omega_{\mathrm{K}}}$	M_{BE}
		\(\mathrm{(ms^{-1})}\)			\((\times 10^{41}\ \mathrm{erg})\)			$(\mu\mathrm{G})$	$(\times 10^{41}\ \mathrm{erg})$		$(\mathrm{M_\odot})$
S1	3	164.5 ± 7.5	873 ± 201	6.68	5.0	12.5	-9.2	45.1	9.2	0.93	1.06 ± 0.30
S2	12	183.7 ± 16.1	1147 ± 163	1.62	2.6	8.2	-4.6	51.9	4.6	0.90	0.37 ± 0.07
S3	17	163.5 ± 4.7	1354 ± 169	3.04	3.4	28.8	-25.1	75.9	25.1	3.74	0.36 ± 0.06
S4	$-$	$-$	900 ± 176	0.82	$-$	2.3	$-$	$-$	$-$	$-$	0.58 ± 0.13
S5	9	171.1 ± 4.7	1172 ± 164	2.68	2.9	10.1	-6.9	94.3	6.9	1.17	0.36 ± 0.07
S6	5	225.4 ± 15.4	953 ± 171	0.46	1.8	2.7	$+0.5$	$-$	$-$	$-$	0.55 ± 0.12
S7	14	195.6 ± 7.6	1096 ± 165	0.38	1.3	3.6	-1.4	41.6	1.4	0.57	0.43 ± 0.08
S8	$-$	$-$	1313 ± 179	2.55	$-$	28.2	$-$	$-$	$-$	$-$	0.46 ± 0.09
S9	18	190.4 ± 8.6	$-$	2.00	3.5	$-$	$-$	$-$	$-$	$-$	$-$
S10	$-$	$-$	1433 ± 193	0.35	$-$	13.6	$-$	$-$	$-$	$-$	0.60 ± 0.11
S11	8	164.0 ± 2.8	1273 ± 183	1.16	1.6	6.1	-4.1	30.2	4.1	1.31	0.28 ± 0.05
S12	16	160.2 ± 2.8	1043 ± 183	0.32	0.9	5.5	-4.0	35.1	4.0	2.32	0.64 ± 0.14
S13	$-$	$-$	1533 ± 192	0.17	$-$	8.7	$-$	$-$	$-$	$-$	0.55 ± 0.10
S14	6	198.4 ± 19.1	1000 ± 181	2.10	4.2	15.9	-9.6	72.4	9.6	1.16	0.49 ± 0.11
S15	$-$	$-$	1250 ± 204	0.02	$-$	2.5	$-$	$-$	$-$	$-$	0.86 ± 0.19
S16	2	161.5 ± 4.7	1039 ± 179	0.61	1.4	11.5	-9.3	93.9	9.3	3.27	0.48 ± 0.10
S17	$-$	$-$	1247 ± 175	0.85	$-$	13.7	$-$	$-$	$-$	$-$	0.40 ± 0.07
S18	$-$	$-$	1545 ± 185	0.30	$-$	19.3	$-$	$-$	$-$	$-$	0.45 ± 0.07
S19	$-$	$-$	989 ± 169	0.32	$-$	3.9	$-$	$-$	$-$	$-$	0.48 ± 0.10
S20	$-$	$-$	1131 ± 180	0.70	$-$	11.3	$-$	$-$	$-$	$-$	0.42 ± 0.08
S21	10	193.7 ± 11.4	1110 ± 182	0.29	1.4	10.0	-7.6	73.9	7.6	2.77	0.53 ± 0.10
S22	$-$	$-$	1385 ± 198	0.10	$-$	8.1	$-$	$-$	$-$	$-$	0.39 ± 0.07
S23	$-$	$-$	906 ± 225	0.01	$-$	2.3	$-$	$-$	$-$	$-$	1.76 ± 0.56
S24	$-$	$-$	901 ± 184	0.14	$-$	7.1	$-$	$-$	$-$	$-$	0.77 ± 0.19
S25	$-$	$-$	1197 ± 189	0.16	$-$	11.8	$-$	$-$	$-$	$-$	0.62 ± 0.13
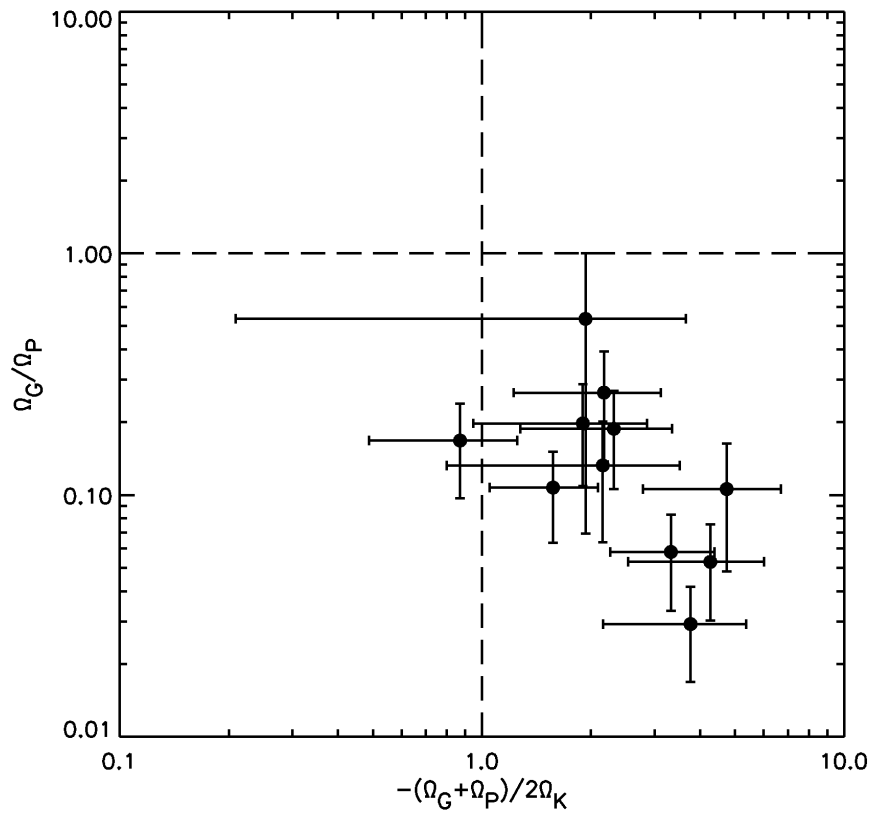
Figure 4.18: Virial stability of SCUBA-2 cores in L1495, excluding the magnetic field.

objects, and that at least some cores in Taurus may be magnetically supported (see Section 4.4.4, above), we determined the magnetic field strength required to bring each of our cores (other than S6) into virial equilibrium. For this, we assumed a constant magnetic field strength over the volume confined by ^{12}CO, and used the magnetic energy equation

$$\Omega_{\mathrm{M}} = \frac{B^2 V}{2\mu_0} = \frac{2\pi}{3\mu_0}\, B^2\, r_{12_{\mathrm{CO}}}^3 \tag{4.11}$$

to determine the magnetic field strength B_{vir} required for virial equilibrium:

$$B_{vir} = \left(-\frac{3\mu_0}{2\pi}\, r_{12_{\mathrm{CO}}}^{-3}\, (\Omega_{\mathrm{G}} + \Omega_{\mathrm{P}} + 2\Omega_{\mathrm{K}})\right)^{1/2}. \tag{4.12}$$

The B_{vir} values listed in Table 4.8 range from $\sim 30 - 100\,\mu$G. These values are consistent with the measurements of magnetic field strength in cores in Taurus in dense material ($10^4 - 10^5\,\mathrm{cm}^{-3}$) traced by CCS emission: from $48 \pm 31\,\mu$G in L1498 (Levin et al. 2001) to $160 \pm 42\,\mu$G in L1521E (Shinnaga et al. 1999). We further estimated the ratio $\Omega_{\mathrm{M},vir}/2\Omega_{\mathrm{K}}$, in order to determine whether, if our cores were virialised, the dominant mechanism for internal support would be magnetic energy or internal kinetic energy. As shown in Table 4.8, if our cores were virialised then, for every core except S6 and S7, $\Omega_{\mathrm{M},vir}/2\Omega_{\mathrm{K}} \gtrsim 1$. This would appear to suggest that the importance of magnetic energy in supporting the Taurus cores is comparable to or greater than that of the cores' internal kinetic energy.

This analysis would suggest that if our cores are indeed virialised, then they are in general supported against collapse by their internal magnetic field, rather than by their internal motions. The dominant terms in the virial equation in the cold cores in L1495 would then be Ω_{P} and Ω_{M}: cores are confined by pressure, and supported by their magnetic field. This is a different physical scenario to that which we found in Ophiuchus, where pressure and gravity are typically of similar importance to one another, and where magnetic fields are not required for the majority of the cores to be in virial equilibrium.

It must be noted that there is no requirement for all of the cores in L1495 to be virialised. In particular, the core S1 (L1495A-S) has been shown to have blue-asymmetric profiles consistent with infall (Lee et al. 2001), and is generally considered to be prestellar. However, S1 does not meet the definition of 'prestellar' used in this work, as, according to our analysis, the core is pressure-confined, with $\Omega_{\mathrm{G}}/\Omega_{\mathrm{P}} < 1$, rather than gravitationally bound. Thus, the value of B_{vir} listed for S1 in Table 4.8 is an upper limit on the true magnetic field strength in this core.

4.4.6 ^{13}CO virial analysis

A concern with the preceding analysis is the validity of the choice of ^{12}CO as the tracer of gas bounding the starless cores in L1495. One might expect that choosing a relatively low density at which the cores are bounded ($\rho_{12_{\mathrm{CO}}} = 10^3\,\mathrm{cm}^{-3}$) might result in an artificially increased Ω_{P} value (due to the large $\sigma_{gas,12_{\mathrm{CO}}}$ and $r_{12_{\mathrm{CO}}}$ which this implies), and hence that the boundedness of the cores might be overestimated. In order to test the effects of this assumption, we repeated the analysis described in Section 4.4.5, using ^{13}CO as the gas tracer and $\rho_{13_{\mathrm{CO}}} = 10^4\,\mathrm{cm}^{-3}$ as the bounding density. As the area observed in ^{13}CO by HARP-B is substantially smaller than that observed in ^{12}CO, ^{13}CO linewidths are available for only 7 of our cores, of which 3 have counterpart ammonia cores: S1, S6 and S16. As discussed in Section 4.4.3, the velocity dispersions determined from ^{13}CO emission have somewhat larger uncertainties than those determined from ^{12}CO.

The results of the ^{13}CO virial analysis are presented in Table 4.9 and Figure 4.19. The same behaviour is seen in ^{13}CO as in ^{12}CO: the cores are virially bound and pressure-confined (in the absence of magnetic field). The cores for which a virial balance can be determined occupy the same part of the virial plane as the cores for which a virial balance was determined from ^{12}CO (c.f. Figure 4.18). The virial balances of each of the three cores S1, S6 and S16 are consistent within errors

225

Table 4.9: Virial stability of SCUBA-2 cores in L1495, with external pressure determined from ^{13}CO emission.

Source ID	$\sigma_{^{13}\mathrm{CO},gas}$ (ms^{-1})	$-\Omega_\mathrm{G}$	Ω_K	$-\Omega_{\mathrm{P},^{13}\mathrm{CO}}$	$\frac{1}{2}\mathcal{I}_{^{13}\mathrm{CO}}$	$B_{vir,^{13}\mathrm{CO}}$ (μG)	$\Omega_{\mathrm{M},vir}$ ($\times10^{41}$ erg)	$\dfrac{\Omega_{\mathrm{M},vir}}{2\Omega_\mathrm{K}}$
		($\times10^{41}$ erg)						
S1	449 ± 196	6.68	5.0	14.7	-11.5	50.4	11.5	1.16
S6	535 ± 202	0.46	1.8	3.9	-0.7	18.8	0.7	0.20
S16	337 ± 174	0.61	1.4	4.1	-1.8	41.7	1.8	0.65
S20	393 ± 427	0.70	–	5.1	–	–	–	–
S23	437 ± 225	0.01	–	0.9	–	–	–	–
S24	525 ± 208	0.14	–	5.4	–	–	–	–
S25	240 ± 237	0.16	–	1.1	–	–	–	–

between ^{12}CO and ^{13}CO. S6 is virially bound in ^{13}CO, whereas it is the only one of our cores to be virialised in ^{12}CO. S16 is somewhat more bound in ^{12}CO than in ^{13}CO, while S1 occupies a very similar position in both Figures 4.18 and 4.19. In all cases the error bars on the ^{13}CO measurements are similar to or larger than those on the ^{12}CO measurements; the error bars are large enough that all of our cores are consistent with being virialised in ^{13}CO. However, the similarities between the ^{12}CO and ^{13}CO measurements suggest that our analysis is robust, and that ^{12}CO is a legitimate choice of tracer for the material confining dense cores in L1495.

4.4.7   Bonnor-Ebert stability

We determined the Bonnor-Ebert stability of our cores, in order to investigate whether the critical BE stability criterion M/M_{BE} can accurately predict the virial balance of our SCUBA-2 cores. We calculated the critically-stable BE mass using equation 1.48, considering the external pressure on our cores to be the pressure in gas traced by ^{12}CO emission, and the core temperatures to be those listed in Table 4.4.

Our critically-stable BE masses are listed in Table 4.8. Figure 4.20 compares the
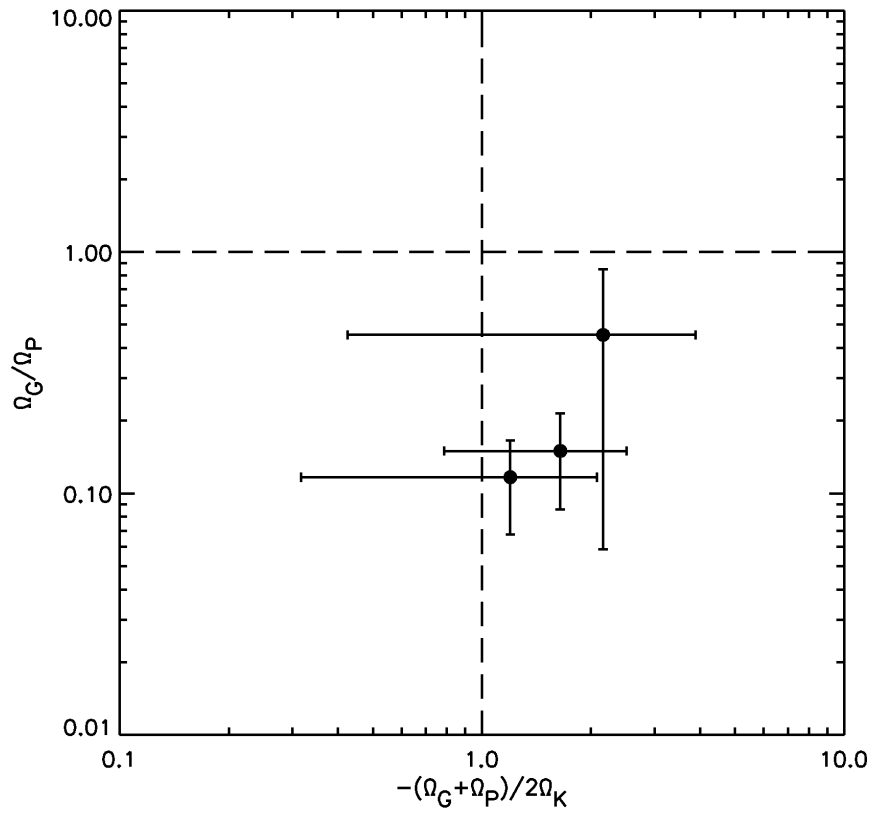
Figure 4.19: Virial stability of SCUBA-2 cores in L1495, with external pressure determined from ^{13}CO emission, excluding the magnetic field.

observed and critically-stable Bonnor-Ebert masses for our cores. The critically-stable BE masses of our cores are typically greater than the observed masses, suggesting that the cores are not gravitationally unstable. This is consistent with our virial analysis, suggesting that the BE criterion may be more applicable in Taurus than in Ophiuchus. However, in many cases, the gravitational instability of our cores appears to be overestimated by the Bonnor-Ebert criterion; in several cases, $M/M_{\mathrm{BE}} \sim 1$, which would suggest that the cores are on the brink of gravitational collapse, a result not borne out by comparison to Figure 4.18. However, as discussed above, Figure 4.18 is unlikely to accurately represent the total virial balance of our set of cores.

Care must be taken in the interpretation of Figures 4.20 and 4.18. Figure 4.20 suggests that if our cores can be modelled as BE spheres, then they have, in the majority of cases, a stable pressure-confined solution accessible to them, and hence are expected to be in equilibrium with their surroundings. This would, naïvely, support our interpretation of Figure 4.18, as demonstrating that we lack the information required to make an accurate determination of the virial state of our cores, and that the cores are in fact typically virialised. However, the mechanism by which the cores are supported against collapse is of significance to the relevance of the BE criterion. Equation 1.48 assumes that cores are supported against collapse by their internal thermal pressure. If our cores are in fact in general supported by their internal magnetic fields, as we suggest above, then the BE criterion, as given in equation 1.48, ceases to apply. The magnetic Bonnor-Ebert mass of a core with sound speed c_s, external pressure P_{EXT}, and internal magnetic field strength B is given by

$$M_{\mathrm{BE},B} = 1.18 \frac{c_s^4}{G^{3/2} \left(P_{\mathrm{EXT}} - \frac{B^2}{2\mu_0} \right)^{1/2}}. \tag{4.13}$$

This would suggest that, given that $M/M_{\mathrm{BE}} \leq 1$ for our cores and that $M_{\mathrm{BE},B} > M_{\mathrm{BE}}$ (as $B > 0$), all of our cores would have $M/M_{\mathrm{BE},B} < 1$, and have a stable, pressure-confied solution according to the magnetic Bonnor-Ebert criterion. Additionally,
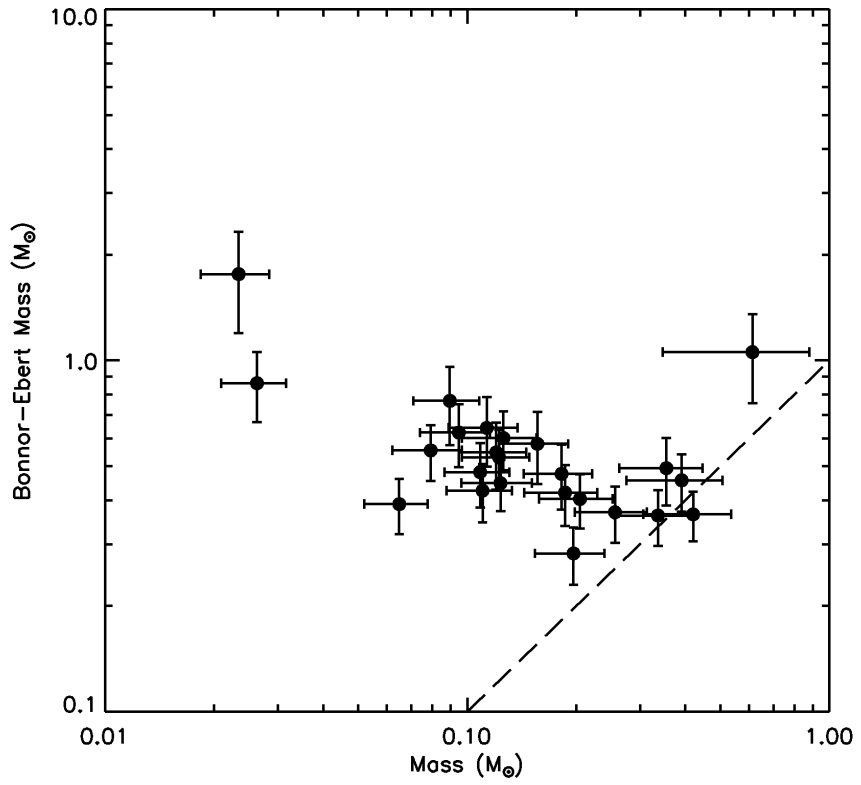
Figure 4.20: Comparison of observed mass and critically-stable Bonnor-Ebert mass for SCUBA-2 cores in L1495. Cores to the right of the dashed line are collapsing according to the critical Bonnor-Ebert criterion.

Table 4.10: Regions of L1495, with their assigned SCUBA-2 cores.

Region	Cores	Colour
L1495 East	S1, S6, S16, S20, S23, S24	Red
L1495 Centre	S2, S3, S5, S7, S11, S12, S14, S19, S21	Green
L1495 West	S4, S10, S13, S15	Blue
L1495 North	S8, S17, S25	Orange
L1495 South	S9, S18, S22	Purple

equation 1.48 does not include the contribution of non-thermal internal energy to core support (although our analysis suggests that internal kinetic energy may not be the dominant mechanism of support for our cores in many cases).

Thus, the magnetic Bonnor-Ebert criterion predicts that all of our cores are stable against collapse. The accuracy of this prediction requires a better understanding of the true virial balance of our cores. However, the blue-asymmetric line profile seen in L1495A-S (Lee et al. 2001) demonstrates that at least one of our cores is likely to be virially unstable and collapsing, suggesting that our cores may not be accurately modelled as Bonnor-Ebert spheres in all cases.

4.4.8 Regional variations

In order to determine whether the properties of our starless cores depend on their location within L1495, we divided L1495 up into five regions: East, the region containing L1495A and L1495B; Centre, the 'triangle' of filaments visible in the centre of Figures 4.1 and 4.3; West, the region shown in Figure 4.4; North, the north-western corner of Figure 4.3; and South, the southern region of Figure 4.3, the northern end of the B211/B213 filament. Each SCUBA-2 core was assigned to one of the five regions. The region assignments are given in Table 4.10. As in Chapter 3, we assigned each region a colour, also listed in Table 4.10.
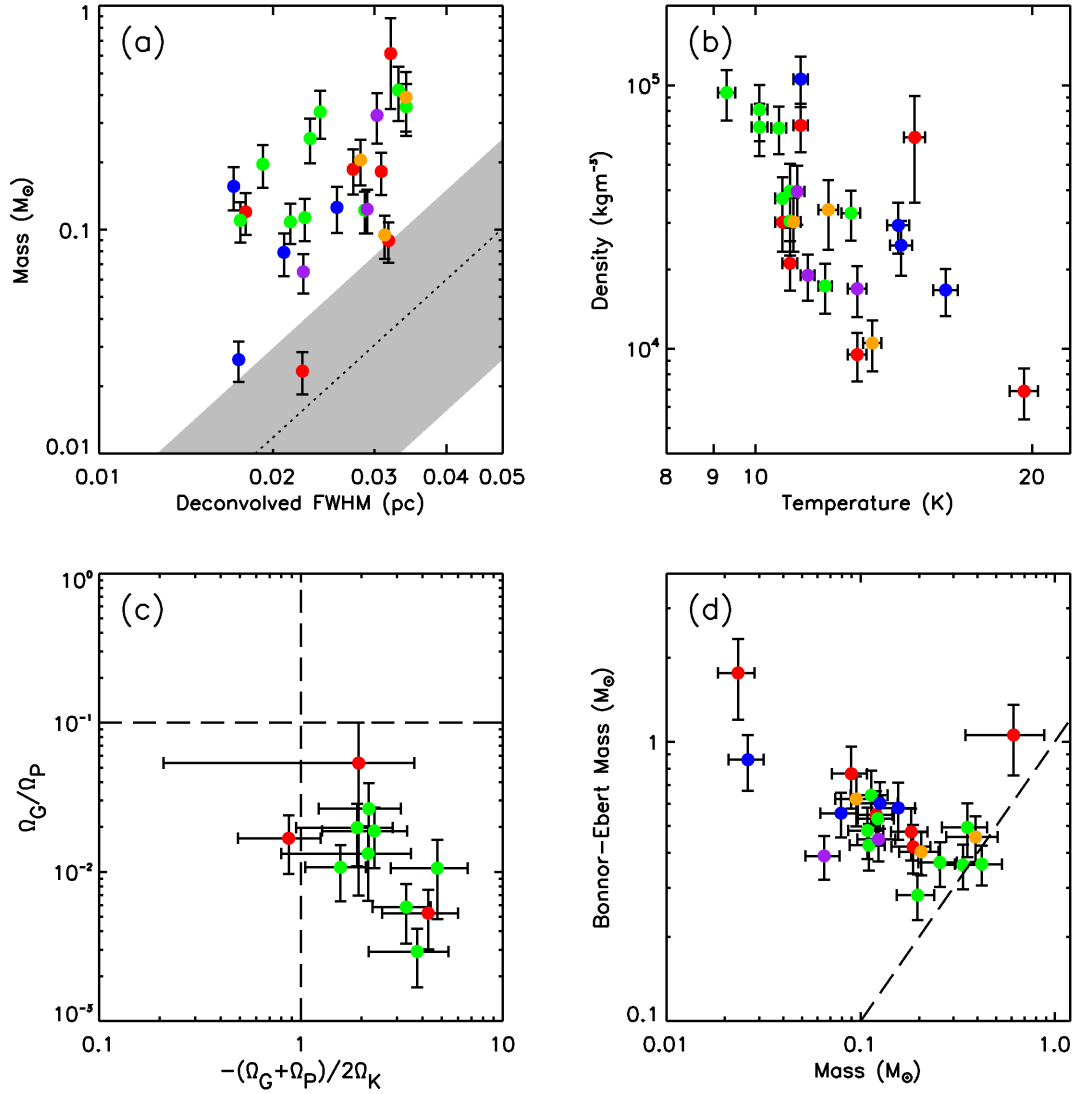
Figure 4.21: Properties of the SCUBA-2 cores, with cores colour-coded by region: (a) mass plotted against radius (c.f. Figure 4.12); (b) density plotted against temperature (c.f. 4.11); (c) gravitational/pressure energy ratio, plotted against virial ratio (c.f. Figure 4.18); (d) Bonnor-Ebert mass plotted against observed mass (c.f. Figure 4.20). Colour coding: red – L1495 East; green – L1495 Centre; blue – L1495 West; orange – L1495 North; purple – L1495 South.

Figure 4.21 reproduces Figures 4.12, 4.11, 4.18 and 4.20, with the cores colour-coded according to their region. There appears to be little correlation of core properties with region. This would suggest that the L1495 region is relatively homogeneous, with little variation in core properties across the area observed by SCUBA-2.

Some local heating effects are observed in L1495 - specifically, the heating of sources S1/L1495A-S and S23 by V892 Tau, and of S10 and S13 by IRAS04113+2758, as discussed above. However, due to the relatively dispersed nature of the cores in L1495, small-scale local effects such as these are likely to affect fewer cores than the equivalent effect in a clustered region such as Ophiuchus, as there are likely to be fewer cores in close proximity to the heating source.

The lack of a global gradient in core properties across L1495 in Figure 4.21 is consistent with the lack of any non-uniform external influences on L1495 likely to cause such a gradient (for example, there are no nearby OB associations or large PDRs likely to be influencing the region).

4.5   Summary

In this chapter we have extracted sets of cores from the SCUBA-2 850-μm, Herschel 250-μm, and spatially-filtered Herschel 250-μm data of the L1495 region of the Taurus molecular cloud. We have characterised the properties of these cores using SCUBA-2 and Herschel data sets, and have compared the cores found in the different data sets, in order to determine which property of a starless core identified by Herschel is most important in determining whether the same core would be detected with SCUBA-2. We have performed a virial analysis of the cores extracted from the SCUBA-2 850-μm map using HARP-B data and the NH_3 linewidths presented by Seo et al. (2015).

We identified sources using the CSAR source extraction algorithm. We extracted

25 sources from the regions of the SCUBA-2 850-μm map with variance $\leq 2\,(\mathrm{Jy}/6\text{-}$ arcsec pixel$)^2$, 208 sources from the Herschel 250-μm map of the same regions, and 138 sources in the equivalent spatially-filtered Herschel 250-μm map.

We determined a representative dust emissivity index of our sources of $\beta = 1.3 \pm 0.6$. This was the value of β which best predicted the SCUBA-2 850-μm flux densities of our sources from their spectral energy distribution (SED) in filtered Herschel emission. We determined mean line-of-sight temperatures for our sources by SED fitting. This then allowed an accurate mass determination to be made for each source.

We found that cores detected by SCUBA-2 and cores detected in filtered 250-μm emission have similar properties, obeying the same temperature-density relation. Cores extracted from, and characterised using, unfiltered Herschel data typically have higher temperatures and densities than their counterparts extracted from the SCUBA-2 data, due to extended emission along the line of sight which is removed by the filtering process. This further confirms that spatial filtering is necessary to accurately compare SCUBA-2 and Herschel data.

We found that SCUBA-2 detects only the densest starless cores, with no SCUBA-2 cores having densities below 6.3×10^3 particles/cm^3, an order of magnitude higher density than the least dense filtered 250-μm-detected Herschel core. There is no equivalent cut-off in temperature, with both SCUBA-2 and Herschel sources having temperatures in the range ~ 9–$20\,\mathrm{K}$. Neither are SCUBA-2 cores typically smaller in radius than Herschel cores – i.e. the spatial filtering introduced by SCUBA-2 does not appear to change the measured FWHM of a starless core observed at this distance.

Thus, we found that the criterion for whether a starless or prestellar core detected in Herschel data will also be detected in SCUBA-2 data is its density (for a given temperature). In the case of Taurus, for SCUBA-2 GBS data, this was 6×10^3

particles/cm^3. This corresponds to a cut-off in surface brightness, below which SCUBA-2 is no longer sensitive. This suggests that SCUBA-2 observations are ideal for selecting those cores in Herschel catalogues which are closest to forming stars.

We performed a virial stability analysis on the cores detected by SCUBA-2, taking the internal velocities of the cores to be those measured in NH$_3$ emission by Seo et al. (2015), and determining the external pressure from HARP-B ^{12}CO measurements. We found that all but one of the cores for which data were available were, in the absence of an internal magnetic field, virially bound and pressure-confined. We found that the magnetic field strengths required to bring our cores into virial equilibrium are in the range $\sim 30 - 100\,\mu$G, consistent with measurements of the magnetic field strength in dense gas in other parts of Taurus.

We found that the Bonnor-Ebert and magnetic Bonnor-Ebert criteria predict that the cores detected by SCUBA-2 have stable, pressure-confined configurations.

We did not find evidence for significant variation in core properties with region across L1495, except for local heating effects due to the stars V892 Tau and IRAS04113+2758.

We hypothesised that the majority of the cores detected by SCUBA-2 in L1495 are supported against collapse by their internal magnetic fields, and that the dominant terms in the virial equation in L1495 are typically internal magnetic energy and external pressure energy. This is in keeping with the theory of Palmeirim et al. (2013) and André et al. (2014) that star formation in the Taurus molecular cloud is magnetically regulated.

Chapter 5

The Cepheus Flare

The Cepheus Flare region is a collection of star-forming molecular clouds extending to $\sim 10-20$ degrees above the Galactic plane at a Galactic longitude of ~ 110 degrees (Hubble 1934). Star formation is occuring at several different distances along the line of sight toward the Cepheus Flare: at $\sim 160\,\mathrm{pc}$, where star formation is associated with the edge of the Local Bubble; at $\sim 300\,\mathrm{pc}$, associated with the Gould Belt; and at $\sim 800\,\mathrm{pc}$, associated with the Perseus arm of the Galaxy (Kun et al. 2008, and references therein). In this chapter we study the intermediate-distance material associated with the Gould Belt. There are five sets of dark clouds at intermediate distance: L1147/48/52/55/57, L1172/74, L1247/51, L1228 and L1241 (Lynds 1962). We present SCUBA-2 data for all or part of each of these regions, except L1241.

The Cepheus Flare is a sparsely-filled region in which star formation appears to be proceeding in a variety of different environments. IRAS 100µm observations of the Cepheus Flare (Miville-Deschênes & Lagache 2005) are shown in Figure 5.1, with contours of A_V extinction (Dobashi et al. 2005). It can be seen that the regions of highest visual extinction are not distributed evenly across the Cepheus Flare, but instead principally located on the north-eastern and south-western sides of the Cepheus Flare, with a central region of relatively low extinction ($A_V < 3$; Dobashi et al. 2005) in which little star formation is occurring, although there is not

a complete lack of molecular gas or young stars (Tachihara et al. 2005). Kirk et al. (2009) found that YSOs in the Cepheus Flare are typically found in small, isolated groups, with a much higher fraction of distributed YSOs (the fraction of YSOs not associated with a group) than is typical: 41% of YSOs in Cepheus are distributed, compared to an average of $\sim 10\%$ across clouds observed as part of the Spitzer c2d survey (Evans et al. 2009).

The Cepheus Flare is defined by the interaction of a collection of shells with the local ISM, of which the most significant to the evolution of the region appears to be the Cepheus Flare Shell (CFS – Grenier et al. 1989; Olano et al. 2006), an expanding supernova bubble with a radius $\sim 9.5°$, whose centre is located to the east of the Cepheus Flare at Galactic coordinates $l \sim 120°$, $b \sim 17°$. The approximate position of the CFS is marked on Figure 5.1; the shell divides the north-eastern and south-western star-forming regions. Olano et al. (2006) suggest that star formation in the eastern regions of the Cepheus Flare has been triggered by the passage of the CFS. Kirk et al. (2009) note that the current position of the CFS is consistent with that of the L1228 region, and suggest that star formation in this region is being enhanced by the interaction with the shell. A possible geometry of the clouds associated with the CFS is shown in Figure 5.2 (Kun et al. 2008). In this geometry, the various intermediate-distance dark clouds are located approximately on the current surface of the CFS. As the CFS has an approximate radius of ~ 50 pc and is located at a distance of ~ 300 pc from the Earth (Olano et al. 2006), this results in significant differences, both fractional and absolute, between the distances of the various dark clouds associated with the CFS, despite those dark clouds appearing along very similar lines of sight.
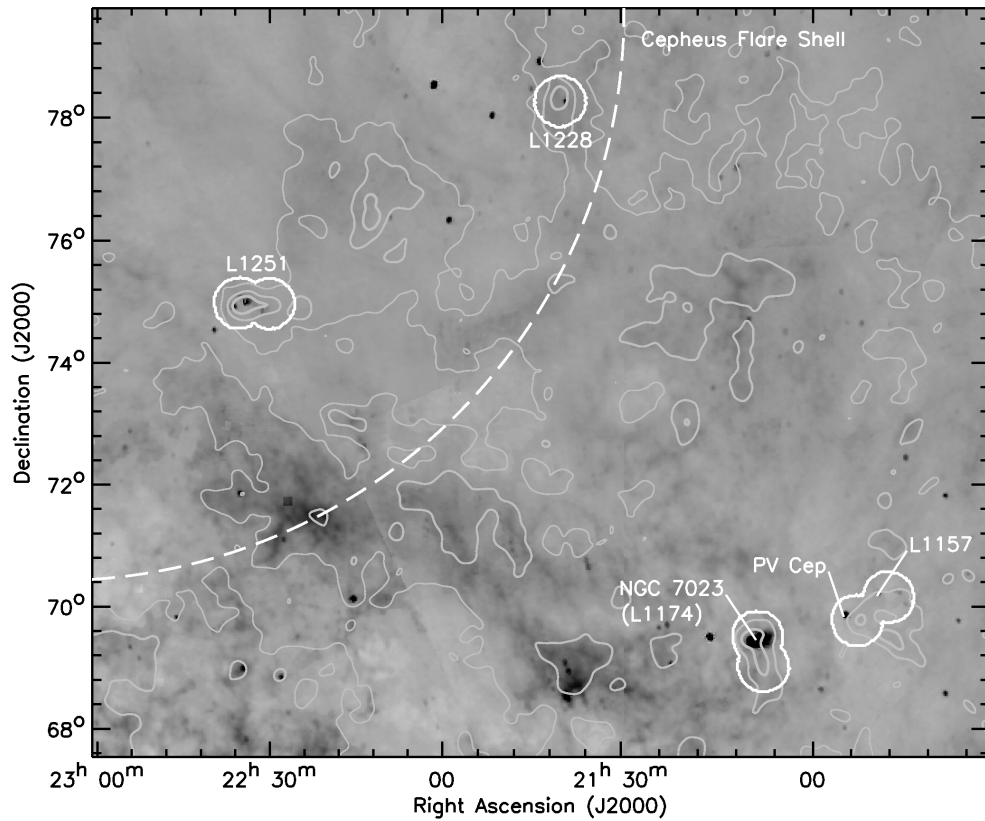
Figure 5.1: A finding chart of the Cepheus region. The greyscale image shows IRAS 100-µm emission (Miville-Deschênes & Lagache 2005). The grey contours show A_V extinction (Dobashi et al. 2005). The regions enclosed in solid white lines were observed as part of the JCMT GBS (Ward-Thompson et al. 2007). The reflection nebula L1174/NGC 7023 is marked; the L1172 region is immediately to the south. The variable star PV Cep and the protostar L1157-mm, both in the L1147/58 region, are also marked. The dashed white line shows the approximate position of the Cepheus Flare Shell (Kirk et al. 2009) – the CFS.
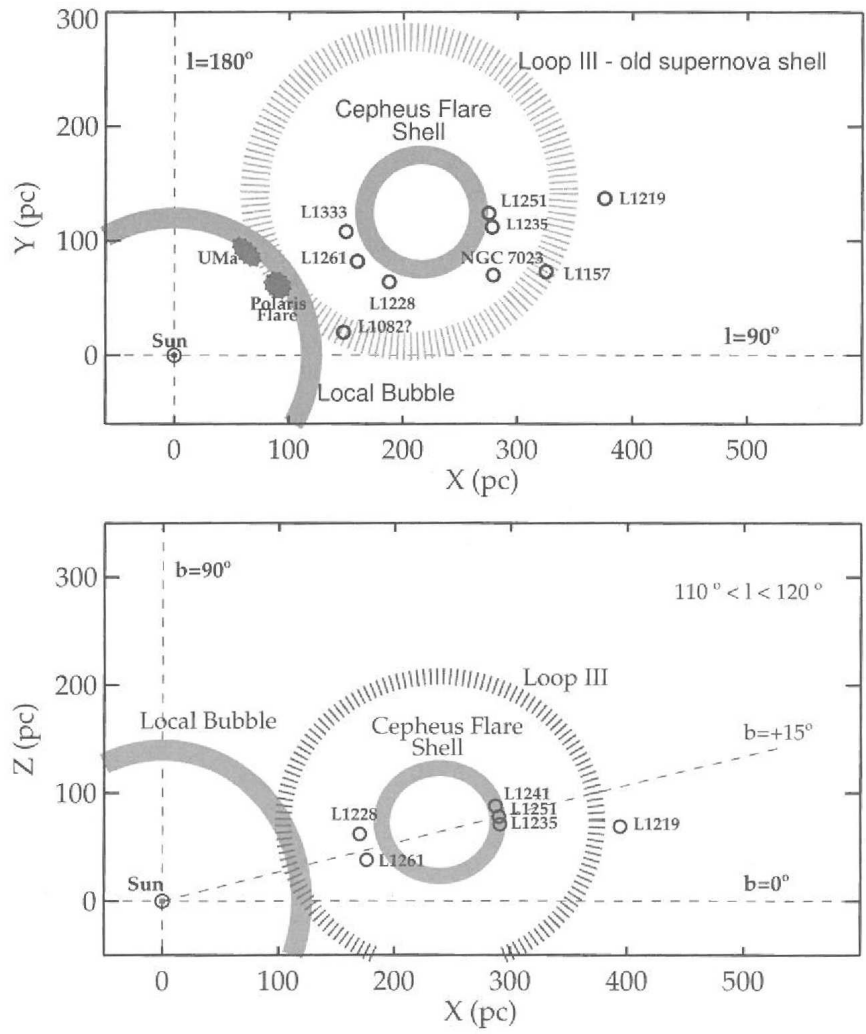
Figure 5.2: A possible geometry of the clouds associated with the CFS, from Kun et al. (2008).

Table 5.1: Cepheus regions observed as part of the JCMT GBS, with approximate central positions in equatorial and galactic coordinates listed. Distance references: L1147/58, L1172/74 – Straizys et al. (1992); L1228, L1251 – Kun et al. (2008).

Region	R.A. (J2000) (hours:min)	Dec. (J2000) (deg:arcmin)	l (deg)	b (deg)	Distance (pc)
L1147/58	21:02	+68:00	104.0	14.1	325 ± 13
L1172/74	20:41	+67:52	102.6	15.6	288 ± 25
L1251	22:34	+75:14	114.4	14.7	300^{+50}_{-10}
L1228	20:58	+77:38	111.7	20.2	200^{+100}_{-10}

5.1 Observations

The SCUBA-2 (Holland et al. 2013) observations used here form part of the JCMT GBS (Ward-Thompson et al. 2007). The Cepheus Flare was observed with SCUBA-2 in 41 observations taken between 2012 March 30 and 2014 October 24. The L1174 region was observed four times in very dry (Grade 1; $\tau_{225\,\mathrm{GHz}} < 0.05$) weather. The remainder of the regions were each observed six times in dry (Grade 2; $0.05 < \tau_{225\,\mathrm{GHz}} < 0.08$) weather, except for one region, L1147/58 East (containing the star PV Cep, discussed below), which was observed seven times.

The data were reduced as described in Section 2.1.2, using the Internal Release 2 method (Section 2.1.2; see also Mairs et al. 2015). Continuum observations at 450 and 850 µm were made using fully-sampled 30-arcmin diameter circular regions (PONG1800 mapping mode – Bintley et al. 2014). Larger regions were covered using overlapping scans. Four final output maps were produced, the central co-ordinates of which are listed in Table 5.1.

The 850-µm SCUBA-2 data of Cepheus are shown in Figures 5.3 (L1147/58), 5.4 (L1172/74), 5.5 (L1251) and 5.6 (L1228). The sources we extract from the data are marked as coloured ellipses: red in L1147/58, light green in L1174, dark green in L1172, blue in L1251, and purple in L1228. This colour coding is continued throughout this chapter.

Cepheus was not observed with HARP, and so the level of CO contamination in

the region is difficult to estimate. The only regions in the map which we expect to be substantially CO-contaminated are local to the PV Cep and L1157-mm protostars (discussed in Section 5.2.1), with which there are strong outflows associated. However, as can be seen in Figure 5.3, both PV Cep and L1157-mm are isolated objects, and CO emission from their outflows is unlikely to affect the fluxes measured for any of the other sources in the field.

5.2 Results

5.2.1 Cepheus Flare Region

As discussed above, the Cepheus Flare consists of several distinct areas of high column density, each of which is at a different distance and likely to have a different star formation history. Thus, we consider each separately in the following analysis, and summarise their properties here.

L1147/L1158 contains the Lynds dark nebulae L1147, L1148, L1152, L1155, L1157 and L1158 (Lynds 1962). This region is considered to be the least affected by the CFS, and to be forming stars with a low efficiency (Kirk et al. 2009). L1147, L1152 and L1155 were observed with SCUBA-2. All of the emission seen in the western area shown in Figure 5.3 is associated with L1152, except for the bright protostar L1157-mm and its associated outflow (Kun et al. 2008), which are discussed below. All of the emission in the eastern region of Figure 5.3 is associated with L1155, with the exception of the bright point source in the north-east, which is the star PV Cep (Li et al. 1994), discussed below.

Both L1152 and L1155 appear relatively quiescent (Kirk et al. 2009). There is some evidence that L1155 may be being externally heated: Nutter et al. (2009) found evidence for a $\sim 2\,\mathrm{K}$ temperature gradient across one of the cores in the region, L1155C, which they ascribed to the effects of the nearby A6V star BD+67

1263.

The SCUBA-2 field contains two bright PMS stars: PV Cep (R.A. (J2000) = $20^h\,45^m\,53.943^s$, Dec. (J2000) = $+67°\,57'\,38.66''$; Cutri et al. 2003) and L1157-mm (R.A. (J2000) = $20^h\,39^m\,06.2^s$, Dec. (J2000) = $+68°02'15''$; Kirk et al. 2009). PV Cep is a highly variable (Kun et al. 2009) A5 Herbig Ae/Be star (Li et al. 1994), with which an extended ouflow is associated (Reipurth et al. 1997). PV Cep has a high westerly proper motion of $\sim 20\,\mathrm{kms}^{-1}$, and is likely to have escaped from the NGC7023 cluster, which is discussed below (Goodman & Arce 2004). L1157-mm is a Class 0 protostar with an extremely strong molecular outflow (Kun et al. 2008). The outflow is highly visible in the 850-μm SCUBA-2 observations, and can be seen in Figure 5.3.

L1172/L1174 is a site of clustered star formation. The dark cloud L1174, shown in the northern part of Figure 5.4, is coincident with the NGC7023 reflection nebula – also known as the Iris Nebula (Herschel 1802), which is driven by the Herbig Ae/Be star HD200775 (R.A. (J2000) = $21^h\,01^m\,39.920^s$, Dec. (J2000) = $+68°\,09'\,47.76''$; van Leeuwen 2007), with spectral classification B2Ve (Guetter 1968). HD200775 is not visible in the SCUBA-2 data.

L1172 lies to the south of L1174, and is also shown in Figure 5.4. It is forming stars much less actively than the neighbouring L1174.

L1251, shown in Figure 5.5, consists of three submillimetre-bright regions, the western L1251A, the central L1251C and the eastern L1251E (Sato et al. 1994), surrounded by a network of filaments. L1251 appears to be actively forming stars; in particular, there is a small group of young stars, L1251B, embedded within the L1251E region (Sato et al. 1994; Lee et al. 2007). Kirk et al. (2009) suggest that star formation in L1251 may have been triggered or enhanced by the passage of the CFS $\sim 4\,\mathrm{Myr}$ ago.

L1228, shown in Figure 5.6, is a small cloud which is likely to be located on the

near side of the CFS, unlike the other clouds observed (Kun et al. 2008; see also Figure 5.2). L1228 runs $\sim 3°$ along an approximately North-South axis; as can be seen from the extinction contours in Figure 5.1, only the central part was observed by the JCMT GBS. Kirk et al. (2009) note that L1228 is at a location consistent with the current position of the CFS, and suggest that star formation here may be in the process of being enhanced by interaction with the shell.

5.2.2 Source Extraction

We identified sources in the SCUBA-2 850-µm data using CSAR (Kirk et al. 2013). We gridded each of the SCUBA-2 850-µm maps onto 6-arcsec pixels before performing the source extraction. The IR2 default pixel size is 3 arcsec at 850µm; however, the beam noise resulting from this oversampling of the data prevented CSAR from finding closed contours around sources. Source extraction was performed on the low-variance regions of the maps, where the variance, as measured in the variance array, was $< 0.005 \, (\mathrm{mJy/arcsec^2})^2$. The criteria chosen for a robustly-detected source were a peak flux density $F_\nu^{peak} \geq 5\sigma$ and a minimum of a 1σ drop in flux density between adjacent sources, where σ is the RMS noise level of the data. We adopted 1σ values of 0.041 mJy/arcsec^2 in L1174, and 0.028 mJy/arcsec^2 elsewhere on 6-arcsec pixels at 850µm. The RMS noise is highest in L1174, despite this region having been observed in the best weather, due to the presence of the NGC7023 reflection nebula (see Section 5.2.1). The bright, extended emission from NGC7023 makes it more difficult for the data reduction process to converge on a solution.

We identified 27 sources in L1147/58, 26 sources in L1174, 9 sources in L1172, 42 sources in L1251 and 20 sources in L1228. Of the 27 sources in L1147/58, 7 were rejected due to their being associated with the L1157-mm outflow, and likely to be artefacts resulting from CO contamination in the SCUBA-2 850-µm data. This left us with 20 reliable sources in L1147/58. There were no sources in other regions

which we consider to be likely to be CO artefacts.

The sources we identified in each cloud are shown on Figures 5.3–5.6. Due to the significant overlap between some of the sources, we fitted each source using the multiple-Gaussian fitting routine described in Section 3.3.1. Our sources are listed in Table 5.2.

5.2.3   Source Characterisation

Of the 117 sources in our Cepheus Flare catalogue, 23 were associated with a protostar in the K09 Spitzer catalogue. Protostar associations are listed in Table 5.3, along with the K09 source with which they are associated, the evolutionary class of that source, and alternative identifications. It should be noted that due to the greater distances of the Cepheus Flare clouds than the Taurus and Ophiuchus clouds, unlike in previous chapters, a single SCUBA-2 source in Cepheus may be associated with more than one protostellar object. In particular, source 56 contains six embedded sources, the L1251B group.

Temperatures for each of our sources were supplied by J. Keown (priv. comm.). These temperatures were determined from SED fitting to the 160μm–500μm Herschel observations taken toward the Cepheus Flare as part of the Herschel Gould Belt Survey (André et al. 2007). The Herschel data were fitted using the model

$$F_\nu = \frac{M B_\nu(T) \kappa_\nu}{D^2},\tag{5.1}$$

where F_ν is the measured flux density, $B_\nu(T)$ is the Planck function, M is the source mass, D is the distance to the source, and the Beckwith et al. (1990) parameterisation of κ_ν is used, assuming a dust emissivity index $\beta = 2.0$. The SED fitting process is described in detail by, e.g. Kirk et al. (2013), Könyves et al. (2015). It must be emphasised that the only quantity derived from the Herschel data which we use is the source temperature. We discuss our own determinations of source masses – from their SCUBA-2 850μm flux densities – below. All of our sources were
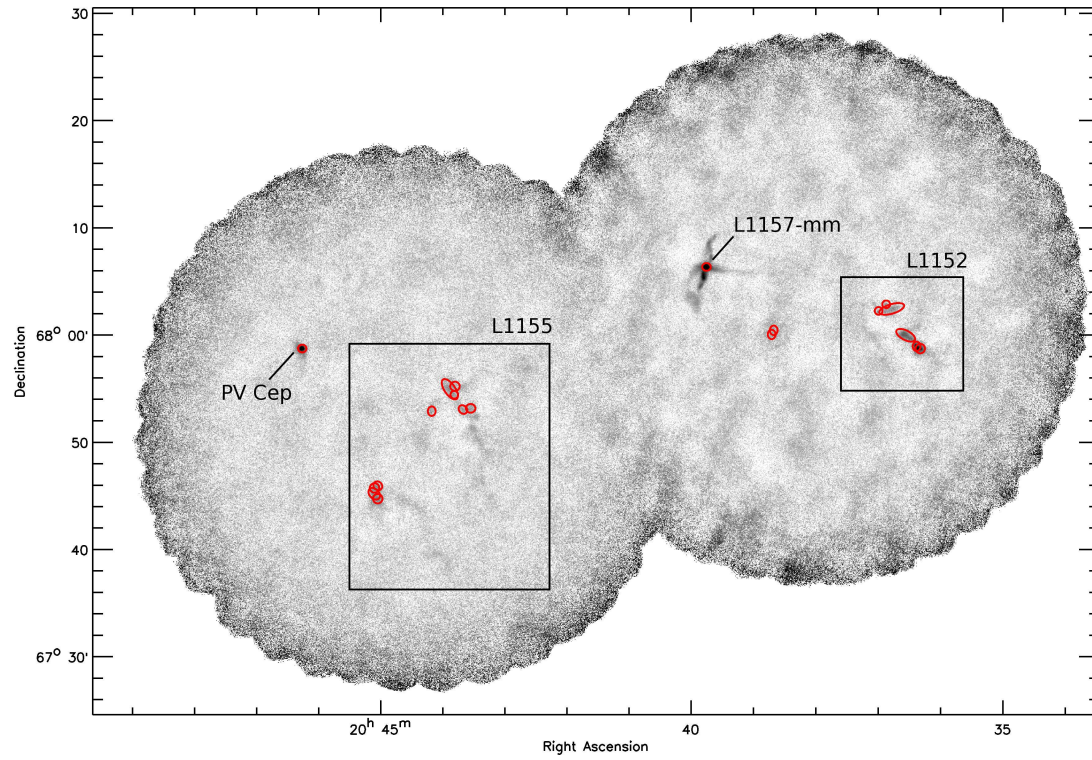
Figure 5.3: SCUBA-2 850-µm observations of the L1147/L1158 region, with sources marked.
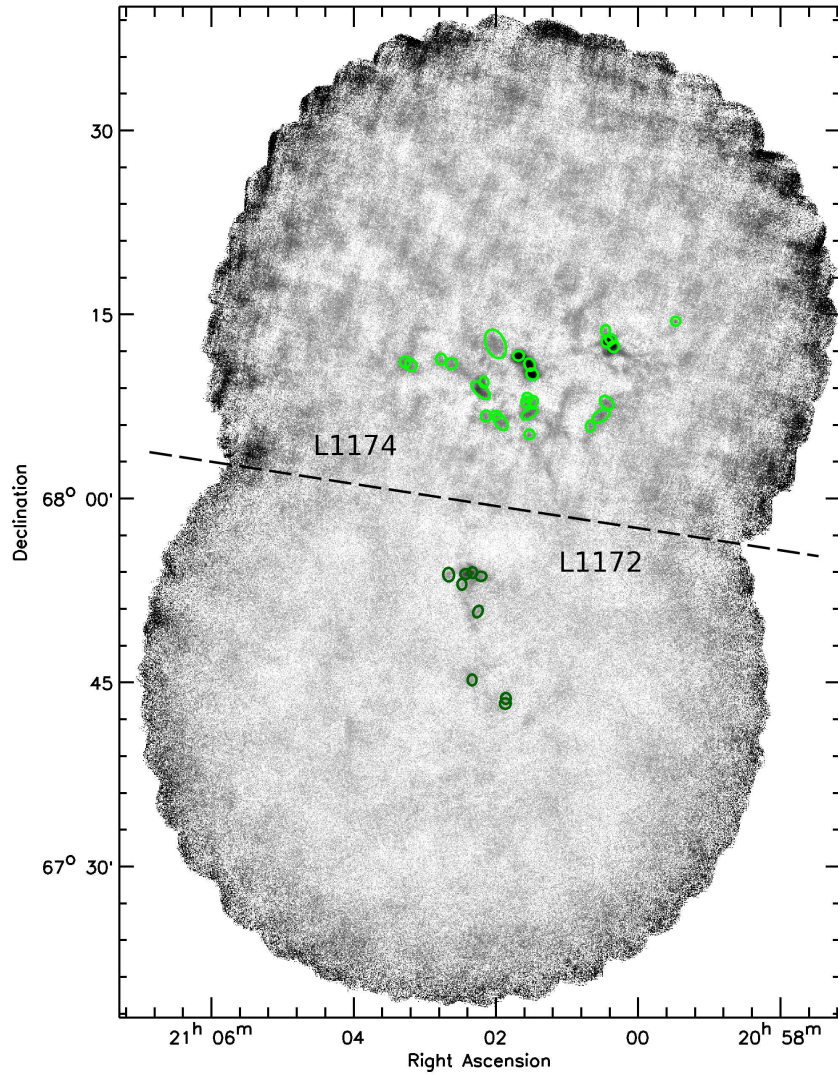
Figure 5.4: SCUBA-2 850-μm observations of the L1172 (south) and L1174 (north) regions, with sources marked.
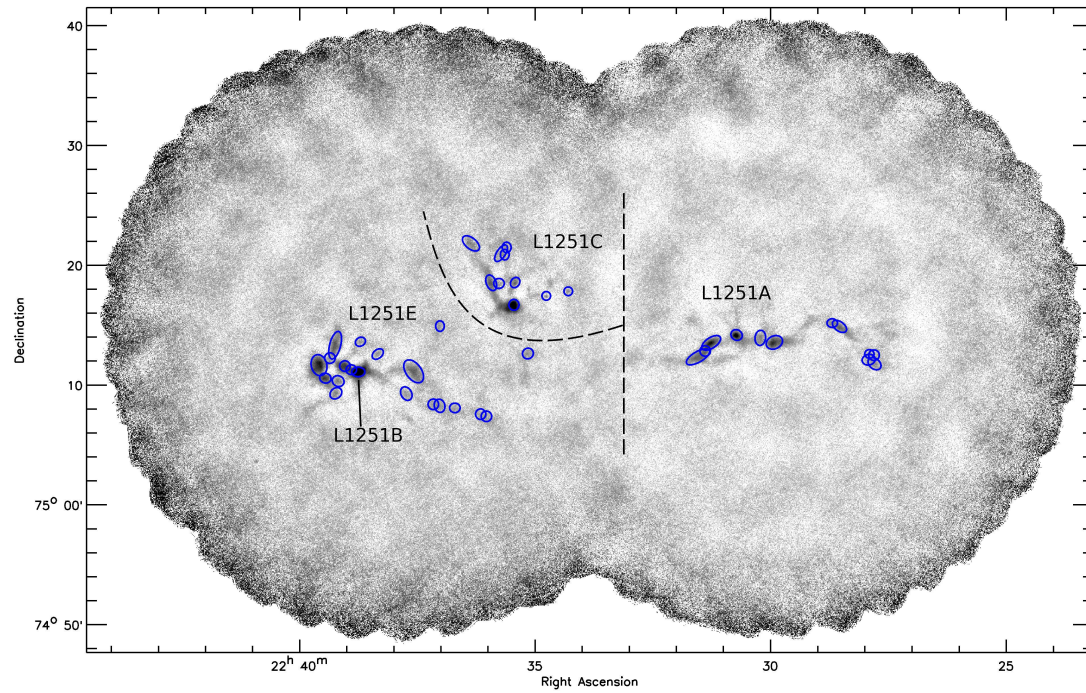
Figure 5.5: SCUBA-2 850-μm observations of the L1251 region, with sources marked.
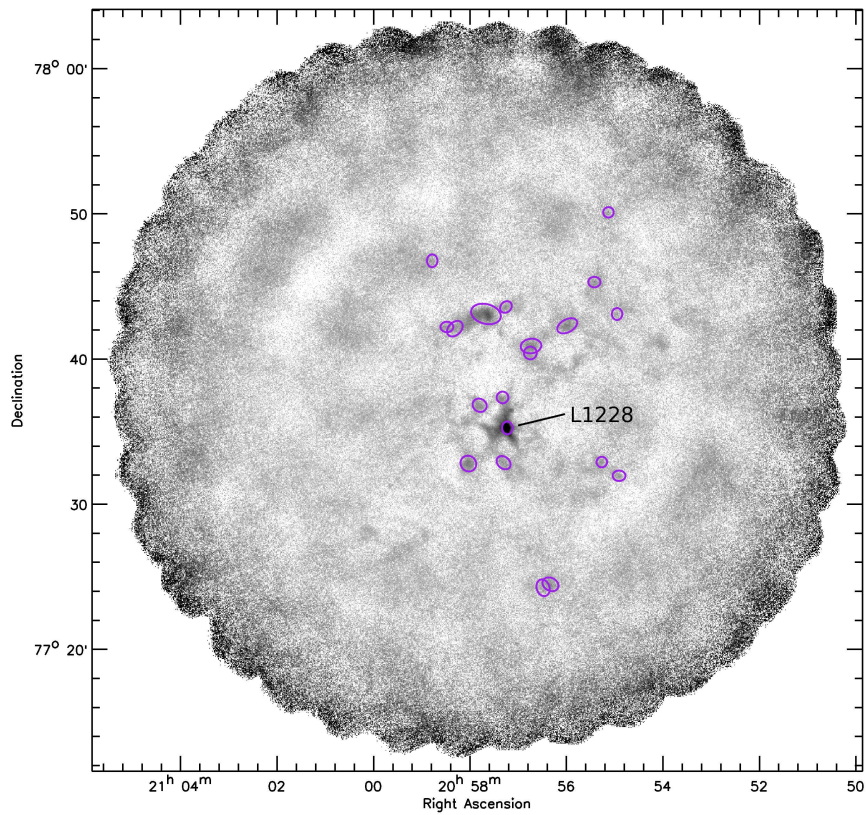
Figure 5.6: SCUBA-2 850-μm observations of the L1228 region, with sources marked.

Table 5.2: Cepheus CSAR/Multigauss Sources

Source Index	RA (J2000)	Dec (J2000)	FWHM (arcsec)	Angle (deg) (E of N)	F_ν^{peak} (mJy/arcsec^2)	F_ν^{total} (mJy)	Type	Region
1	20:39:05.28	+68:02:20.4	21.6×24.0	100.1	3.07	1804.18	Protostar	L1147/L1158
2	20:35:45.11	+67:53:02.4	21.6×26.4	5.4	0.83	538.92	Protostar	L1147/L1158
3	20:35:41.76	+67:52:48.0	26.4×26.4	–	0.78	616.97	Core	L1147/L1158
4	20:35:54.72	+67:54:10.8	57.8×26.4	152.0	0.39	679.68	Core	L1147/L1158
5	20:36:18.96	+67:56:42.0	21.6×21.6	–	0.10	51.19	Protostar	L1147/L1158
6	20:45:53.28	+67:57:39.6	23.4×21.6	170.2	1.66	951.34	Protostar	L1147/L1158
7	20:44:48.48	+67:43:12.0	26.4×26.4	–	0.16	126.40	Core	L1147/L1158
8	20:44:51.60	+67:43:40.8	37.3×26.4	125.0	0.14	153.47	Core	L1147/L1158
9	20:44:47.52	+67:44:24.0	23.1×26.4	43.0	0.12	82.48	Core	L1147/L1158
10	20:44:50.88	+67:44:13.2	26.4×26.4	–	0.16	123.73	Core	L1147/L1158
11	20:36:10.80	+67:57:14.4	21.6×21.6	–	0.16	82.55	Protostar	L1147/L1158
12	20:43:24.48	+67:53:09.6	26.4×25.7	170.0	0.07	55.01	Core	L1147/L1158
13	20:43:10.56	+67:50:60.0	26.4×24.3	10.0	0.10	73.08	Core	L1147/L1158
14	20:43:18.24	+67:50:56.4	21.6×26.4	37.5	0.10	61.99	Core	L1147/L1158
15	20:43:49.20	+67:50:60.0	21.6×26.4	173.0	0.09	59.72	Core	L1147/L1158
16	20:38:06.96	+67:55:30.0	26.4×21.6	80.0	0.06	38.63	Core	L1147/L1158
17	20:43:25.68	+67:52:22.8	21.6×21.6	177.0	0.08	40.43	Core	L1147/L1158
18	20:43:29.76	+67:52:55.2	66.4×29.8	121.7	0.13	295.49	Core	L1147/L1158
19	20:38:04.57	+67:55:51.6	21.6×26.4	0	0.04	23.08	Core	L1147/L1158
20	20:36:05.76	+67:56:45.6	72.2×26.4	19.6	0.20	430.92	Core	L1147/L1158
21	21:01:40.81	+68:12:03.6	26.4×23.7	10.0	1.33	940.18	Core	L1174
22	21:00:19.68	+68:13:22.8	22.8×26.4	100.0	0.76	519.88	Protostar	L1174
23	21:01:28.80	+68:10:33.6	29.8×26.4	147.2	1.61	1434.49	Protostar	L1174
24	21:01:30.96	+68:11:20.4	31.2×25.0	112.8	1.47	1299.64	Protostar	L1174
25	21:00:23.04	+68:13:12.0	26.4×26.4	–	1.17	925.42	Protostar	L1174
26	21:00:17.28	+68:12:46.8	26.4×26.4	–	0.99	782.71	Core	L1174

Table 5.2: – continued.

Source Index	RA (J2000)	Dec (J2000)	FWHM (arcsec)	Angle (deg) (E of N)	F_ν^{peak} (mJy/arcsec^2)	F_ν^{total} (mJy)	Type	Region
27	21:02:13.92	+68:09:14.4	57.2×26.4	127.9	0.62	1053.04	Core	L1174
28	21:02:11.04	+68:09:54.0	21.6×26.4	10.0	0.20	130.14	Core	L1174
29	21:01:28.32	+68:08:20.4	26.4×24.6	71.8	0.24	178.49	Core	L1174
30	21:03:20.16	+68:11:31.2	26.4×26.4	–	0.12	97.20	Core	L1174
31	21:03:15.12	+68:11:16.8	30.8×26.4	115.8	0.17	152.60	Core	L1174
32	20:59:22.56	+68:14:49.2	22.3×21.6	10.0	0.18	99.65	Protostar	L1174
33	21:02:00.72	+68:07:12.0	26.4×21.6	172.8	0.10	62.82	Core	L1174
34	21:01:31.20	+68:07:19.2	42.3×21.9	24.4	0.26	270.97	Core	L1174
35	21:01:34.32	+68:08:16.8	21.6×26.4	0.0	0.07	44.03	Protostar	L1174
36	21:01:31.20	+68:05:38.4	24.0×24.0	–	0.22	145.69	Core	L1174
37	21:02:48.72	+68:11:45.6	24.9×26.4	10.0	0.10	75.78	Core	L1174
38	21:00:28.56	+68:07:08.4	45.5×26.4	40.3	0.25	344.38	Core	L1174
39	21:01:56.39	+68:06:39.6	46.1×26.4	136.6	0.22	304.45	Core	L1174
40	21:02:00.96	+68:13:01.2	73.6×46.0	122.7	0.22	857.70	Core	L1174
41	21:01:32.64	+68:08:38.4	26.4×21.6	161.8	0.23	146.09	Protostar	L1174
42	21:00:24.25	+68:14:06.0	26.4×21.6	95.6	0.10	65.27	Core	L1174
43	21:00:37.92	+68:06:18.0	21.6×26.4	1.4	0.14	87.88	Core	L1174
44	21:00:23.52	+68:08:13.2	38.0×26.4	148.7	0.18	204.73	Core	L1174
45	21:02:09.12	+68:07:08.4	25.6×26.4	170.0	0.15	114.19	Core	L1174
46	21:02:39.60	+68:11:24.0	27.0×26.4	175.2	0.17	135.14	Core	L1174
47	21:02:20.64	+67:54:21.6	23.5×26.4	177.6	0.41	290.70	Protostar	L1172
48	21:02:26.40	+67:54:14.4	26.4×24.0	170.0	0.38	275.76	Protostar	L1172
49	21:02:13.20	+67:54:03.6	22.3×26.4	80.0	0.10	66.49	Core	L1172
50	21:02:20.64	+67:45:36.0	21.6×26.4	170.0	0.09	55.15	Core	L1172
51	21:01:51.60	+67:44:06.0	23.8×26.4	170.0	0.08	54.79	Core	L1172
52	21:02:15.84	+67:51:10.8	29.5×21.6	53.4	0.10	70.13	Core	L1172

Table 5.2: – continued.

Source Index	RA (J2000)	Dec (J2000)	FWHM (arcsec)	Angle (deg) (E of N)	F_ν^{peak} (mJy/arcsec^2)	F_ν^{total} (mJy)	Type	Region
53	21:01:52.08	+67:43:40.8	26.4×25.7	10.0	0.08	57.42	Core	L1172
54	21:02:29.76	+67:53:24.0	21.6×26.4	170.0	0.07	47.81	Core	L1172
55	21:02:41.28	+67:54:10.8	33.0×26.4	84.7	0.17	170.24	Core	L1172
56	22:38:47.04	+75:11:31.2	33.4×23.8	9.9	3.54	3189.74	Protostar	L1251
57	22:31:04.32	+75:13:37.2	53.7×26.4	27.2	0.92	1481.26	Protostar	L1251
58	22:39:04.56	+75:11:60.0	26.4×26.4	–	0.76	603.07	Core	L1251
59	22:38:56.16	+75:11:42.0	26.4×24.3	177.6	0.65	470.12	Core	L1251
60	22:39:38.40	+75:12:03.6	53.3×39.0	93.2	0.80	1886.04	Core	L1251
61	22:35:22.56	+75:17:06.0	27.1×25.3	80.0	1.89	1469.45	Protostar	L1251
62	22:31:12.48	+75:12:57.6	26.4×26.4	–	0.34	271.22	Core	L1251
63	22:31:22.08	+75:12:28.8	65.7×26.4	19.9	0.41	805.10	Core	L1251
64	22:39:30.00	+75:10:58.8	28.7×24.4	158.9	0.58	464.33	Core	L1251
65	22:39:16.08	+75:09:43.2	32.3×25.6	49.5	0.19	180.58	Core	L1251
66	22:28:15.36	+75:14:38.4	40.6×23.4	146.6	0.42	448.31	Core	L1251
67	22:28:24.72	+75:14:56.4	26.4×21.6	170.0	0.15	98.89	Core	L1251
68	22:35:52.32	+75:18:57.6	41.0×24.5	109.8	0.39	446.94	Core	L1251
69	22:34:39.84	+75:17:49.2	21.6×21.6	–	0.14	75.13	Protostar	L1251
70	22:35:34.08	+75:21:18.0	21.6×26.4	172.3	0.11	73.22	Core	L1251
71	22:29:41.52	+75:13:30.0	42.6×32.1	15.0	0.66	1020.02	Core	L1251
72	22:39:13.20	+75:10:44.4	30.4×26.4	163.5	0.18	165.35	Core	L1251
73	22:36:40.80	+75:08:31.2	26.4×23.8	10.0	0.08	57.28	Core	L1251
74	22:35:04.80	+75:13:01.2	27.7×26.4	29.7	0.14	116.17	Core	L1251
75	22:39:24.24	+75:12:39.6	26.4×26.4	–	0.15	121.57	Core	L1251
76	22:34:10.80	+75:18:10.8	21.6×21.6	–	0.14	72.04	Protostar	L1251
77	22:35:59.76	+75:07:48.0	26.4×26.4	–	0.09	68.76	Core	L1251
78	22:27:31.44	+75:11:24.0	36.1×25.8	143.7	0.16	170.32	Core	L1251

Table 5.2: – continued.

Source Index	RA (J2000)	Dec (J2000)	FWHM (arcsec)	Angle (deg) (E of N)	F_ν^{peak} (mJy/arcsec^2)	F_ν^{total} (mJy)	Type	Region
79	22:36:07.20	+75:07:58.8	25.7×26.4	0.0	0.08	58.93	Core	L1251
80	22:38:21.60	+75:13:01.2	31.8×21.6	39.1	0.16	125.24	Core	L1251
81	22:37:00.00	+75:15:21.6	26.4×21.6	96.8	0.09	58.00	Core	L1251
82	22:30:30.72	+75:14:13.2	29.2×25.8	146.8	1.04	884.41	Protostar	L1251
83	22:27:37.69	+75:12:14.4	23.1×21.6	10.0	0.10	56.30	Core	L1251
84	22:35:20.64	+75:18:57.6	27.3×21.6	65.4	0.32	212.18	Protostar	L1251
85	22:27:31.68	+75:12:07.2	26.4×26.4	8.4	0.06	46.62	Core	L1251
86	22:35:42.00	+75:18:54.0	26.4×24.9	10.0	0.14	101.74	Core	L1251
87	22:35:31.44	+75:21:54.0	22.1×26.4	10.0	0.09	56.59	Core	L1251
88	22:35:38.88	+75:21:25.2	47.6×21.6	64.1	0.08	92.09	Core	L1251
89	22:27:38.87	+75:11:45.6	33.3×26.4	3.3	0.10	101.74	Core	L1251
90	22:37:44.16	+75:09:43.2	35.8×26.4	129.3	0.16	168.98	Core	L1251
91	22:29:59.76	+75:13:55.2	38.1×26.4	73.9	0.20	225.32	Protostar	L1251
92	22:38:44.40	+75:14:02.4	26.4×21.6	18.2	0.13	81.97	Core	L1251
93	22:39:17.52	+75:13:44.4	71.2×27.5	77.1	0.42	937.19	Core	L1251
94	22:37:08.88	+75:08:49.2	26.4×26.4	–	0.10	77.51	Core	L1251
95	22:37:34.57	+75:11:34.8	65.6×38.3	134.0	0.38	1066.97	Core	L1251
96	22:36:18.72	+75:22:15.6	50.3×27.2	130.8	0.22	344.95	Core	L1251
97	22:37:00.71	+75:08:42.0	33.7×26.4	114.4	0.11	109.08	Core	L1251
98	20:58:02.16	+77:33:18.0	33.7×31.2	126.0	0.24	283.90	Core	L1228
99	20:57:18.24	+77:37:51.6	24.0×24.0	–	0.20	128.63	Core	L1228
100	20:56:41.28	+77:41:24.0	42.7×30.0	15.8	0.18	258.77	Core	L1228
101	20:55:54.24	+77:42:46.8	44.5×26.4	18.2	0.19	247.03	Core	L1228
102	20:57:13.68	+77:44:06.0	26.4×21.6	35.0	0.11	73.55	Core	L1228
103	20:54:49.44	+77:32:24.0	26.4×21.6	170.0	0.12	74.70	Core	L1228
104	20:56:42.24	+77:40:55.2	26.4×26.4	–	0.12	93.74	Core	L1228

Table 5.2: – continued.

Source Index	RA (J2000)	Dec (J2000)	FWHM (arcsec)	Angle (deg) (E of N)	F_ν^{peak} (mJy/arcsec^2)	F_ν^{total} (mJy)	Type	Region
105	20:54:59.04	+77:50:34.8	21.6×21.6	–	0.04	19.19	Core	L1228
106	20:57:39.60	+77:43:37.2	62.8×40.7	175.2	0.36	1032.91	Core	L1228
107	20:57:47.76	+77:37:19.2	30.0×26.5	147.4	0.17	152.64	Core	L1228
108	20:56:27.37	+77:24:43.2	35.2×26.4	118.4	0.07	71.32	Core	L1228
109	20:58:49.68	+77:47:16.8	26.2×21.6	100.0	0.07	42.66	Core	L1228
110	20:55:11.28	+77:33:21.6	21.8×21.6	55.0	0.09	50.94	Core	L1228
111	20:57:12.24	+77:35:45.6	26.4×21.8	100.5	2.20	1432.48	Protostar	L1228
112	20:55:18.48	+77:45:46.8	25.1×21.6	0.5	0.06	39.46	Core	L1228
113	20:58:19.92	+77:42:36.0	37.4×25.9	35.0	0.11	115.99	Core	L1228
114	20:54:49.44	+77:43:33.6	21.6×24.6	173.7	0.08	46.73	Core	L1228
115	20:56:18.00	+77:24:57.6	34.6×26.4	142.4	0.16	166.75	Core	L1228
116	20:58:30.24	+77:42:43.2	26.4×21.6	3.0	0.11	69.73	Core	L1228
117	20:57:17.05	+77:33:21.6	31.9×24.1	129.7	0.13	112.82	Core	L1228

Table 5.3: The protostellar sources in our catalogue, with their identification and evolutionary class from K09, and alternative identifications. With the exception of L1157-mm and stars with an identification of the form *XX* Cep, alternative identifications are given in the following order of preference: IRAS Point or Faint Source Catalogs (IRAS – Beichman et al. 1988; Moshir et al. 1992), 2MASS All-Sky Catalog of Point Sources (2MASS – Cutri et al. 2003), Spitzer Gould Belt Survey (SSTgbs – K09). For the L1251B cluster, designations from Lee et al. (2006) are also given. K09 identifications given in brackets indicate an offset between our source central coordinates and the coordinates of the K09 source greater than the JCMT 850-μm beam size, but less than the radius of the source as listed in Table 5.2.

Source ID	K09 ID	K09 Class	Alternative ID
1	134	I	L1157-mm
2	1	I	IRAS 20353+6742
5	3	II	IRAS 20359+6475
6	135	I	PV Cep
11	2	II	2MASS J2036+1165+6757093
22	17	I	SSTgbs J2100207+6813169
	(100)	F	SSTgbs J2100224+6813042
23	27	II	2MASS J21012637+6810385
	137	II	SSTgbs J2101271+6810380
24	34	I	2MASS J21013280+6811204
25	18	I	SSTgbs J2100221+6812585
	(100)	F	SSTgbs J2100224+6813042
32	15	II	FT Cep
35	(104)	F	PW Cep
41	(104)	F	PW Cep
47	49	I	IRAS 21017+6742
48	50	F	SSTgbs J2102273+6754186
	(53)	II	2MASS J21022993+6754083
56	89	I	2MASS J22384282+7511369; L1251B IRS 4
	90	I	SSTgbs J2238469+7511337; L1251B IRS 1
	92	I	2MASS J22385287+7511235; L1251B IRS 2
	107	III	IRAS 22376+7455; L1251B IRS 3
	108	III	SSTgbs J2238440+7511266; L1251B IRS 5
	109	II	2MASS J22384807+7511488; L1251B IRS 6
57	68	II	SSTgbs J2231056+7513372
61	143	I	IRAS 22343+7501
69	69	F	2MASS J22344051+7517444
76	142	F	IRAS 22331+7502
82	67	I	SSTgbs J2230318+7514094
84	(76)	II	2MASS J22351668+7518471
91	66	I	IRAS 22290+7458
111	9	F	IRAS 20582+7724; L1228

observed as part of the Herschel GBS. However, the sources on the western edge of L1152 are on the very edge of the Herschel field, and hence their temperatures may be less reliable than those in other parts of the field. Temperatures of cores without embedded sources are typically in the range 9–15 K, except in the NGC7023 region, where temperatures of up to ~ 50 K are measured.

Source masses were determined using equation 3.4, which we repeat here:

$$M = \frac{F_\nu(850\mu m)D^2}{\kappa_{\nu(850\mu m)}B_{\nu(850\mu m)}(T)},$$
(5.2)

where $F_\nu(850\mu m)$ is the best-fit model flux density at 850 µm, D is the source distance as listed in Table 5.1, $B_{\nu(850\mu m)}(T)$ is the Planck function, and $\kappa_{\nu(850\mu m)}$ is the dust mass opacity, $\kappa_\nu = 0.1(\nu/10^{12}\text{Hz})^\beta \,\text{cm}^2\text{g}^{-1}$ (Beckwith et al. 1990), where β is again taken to be 2.0.

Mean source molecular-hydrogen volume densities were determined using the equation

$$n(\text{H}_2) = \frac{M}{\mu m_\text{H}} \frac{1}{\frac{4}{3}\pi R^3},$$
(5.3)

where R is the equivalent deconvolved mean FWHM of the source. The equivalent deconvolved mean FWHM was taken to be the geometric mean of the best-fit major and minor FWHMs, with the JCMT 850µm effective beam FWHM (14.1″) subtracted in quadrature. The mean molecular weight μ was once again taken to be 2.86, assuming that the gas is $\sim 70\%$ H_2 by mass (Kirk et al. 2013).

Mean source molecular-hydrogen column densities were determined using the equation

$$N(\text{H}_2) = \frac{M}{\mu m_\text{H}} \frac{1}{\pi R^2},$$
(5.4)

with symbols defined as above.

The derived properties of our sources: temperature, mass, column density, volume density, and deconvolved FWHM, are listed in Table 5.4. As discussed in Chapter 3, for the protostellar sources in our catalogue, the temperatures, and hence the

masses, determined from the dust emission are those of the protostellar envelopes, and not of the protostars themselves. The modified blackbody model used to fit temperatures is applicable only to envelope-dominated sources; the temperatures and masses determined for the Class II and III protostars in our catalogue (listed in Table 5.3) may not be representative.

5.3   Discussion of Derived Properties

The masses and sizes of our sources are shown in Figure 5.7. As in Chapters 3 and 4, our sources typically occupy the part of the mass/size plane in which prestellar cores are expected to lie (c.f. André et al. 2010). The grey band on Figure 5.7 again shows the region in which transient, unbound starless cores are expected to lie (Elmegreen & Falgarone 1996).

The temperatures and volume densities of our sources are shown in Figure 5.8. It can be seen that with the exception of sources in L1174 – the reflection nebula – the cores in our sample have a narrow range of temperatures ($\sim 9 - 15\,\mathrm{K}$), and obey a similar temperature-density relation to the SCUBA-2 cores found in Taurus, discussed in Chapter 4.

In order to determine a mass function for each set of starless cores in our sample, we analysed the cumulative distribution functions of core masses for each region in Cepheus, using the maximum likelihood estimator for an infinite power-law distribution (Koen 2006; Maschberger & Kroupa 2009). This method is discussed in Section 3.3.4; see particularly equations 3.7–3.9. The cumulative mass distribution functions for each region of Cepheus are shown in Figure 5.9, while the cumulative mass distribution function for all of the cores in our sample is shown in Figure 5.10. The maximum-likelihood-estimator mass functions for each region are listed in Table 5.5.

As can be seen from Figure 5.9 and Table 5.5, the core mass function in each

Table 5.4: Cepheus Source Properties

Source Index	Temp. (K)	Mass (M$_\odot$)	H$_2$ Col. Density ($\times 10^{21}$ cm^{-2})	H$_2$ Vol. Density ($\times 10^6$ cm^{-3})	Deconv. FWHM (pc)
1	14.8 ± 0.2	2.43 ± 0.07	42.66 ± 1.30	36.81 ± 1.12	0.028
2	12.4 ± 0.3	0.99 ± 0.05	14.91 ± 0.80	11.93 ± 0.64	0.030
3	11.5 ± 0.2	1.31 ± 0.06	14.77 ± 0.66	10.21 ± 0.45	0.035
4	10.6 ± 0.1	1.70 ± 0.07	7.17 ± 0.31	3.03 ± 0.13	0.057
5	13.1 ± 0.2	0.08 ± 0.01	1.78 ± 0.30	1.68 ± 0.28	0.026
6	16.2 ± 0.2	1.11 ± 0.03	20.19 ± 0.58	17.75 ± 0.51	0.028
7	11.7 ± 0.0	0.26 ± 0.02	2.93 ± 0.19	2.02 ± 0.13	0.035
8	11.5 ± 0.1	0.32 ± 0.02	2.29 ± 0.16	1.26 ± 0.09	0.044
9	11.7 ± 0.1	0.17 ± 0.02	2.31 ± 0.25	1.76 ± 0.19	0.032
10	11.5 ± 0.1	0.26 ± 0.02	2.93 ± 0.21	2.02 ± 0.14	0.035
11	12.3 ± 0.0	0.15 ± 0.01	3.21 ± 0.30	3.03 ± 0.28	0.026
12	11.5 ± 0.1	0.12 ± 0.02	1.36 ± 0.19	0.96 ± 0.14	0.035
13	11.5 ± 0.0	0.15 ± 0.02	1.94 ± 0.21	1.42 ± 0.15	0.033
14	11.6 ± 0.0	0.13 ± 0.02	1.95 ± 0.24	1.56 ± 0.19	0.030
15	12.4 ± 0.0	0.11 ± 0.01	1.64 ± 0.20	1.32 ± 0.16	0.030
16	13.3 ± 0.1	0.06 ± 0.01	0.94 ± 0.18	0.75 ± 0.15	0.030
17	11.5 ± 0.1	0.09 ± 0.02	1.79 ± 0.33	1.68 ± 0.31	0.026
18	11.3 ± 0.1	0.65 ± 0.03	2.05 ± 0.11	0.75 ± 0.04	0.066
19	13.2 ± 0.0	0.04 ± 0.01	0.57 ± 0.18	0.45 ± 0.14	0.030
20	11.5 ± 0.1	0.91 ± 0.04	2.99 ± 0.14	1.12 ± 0.05	0.065
21	16.7 ± 0.5	0.82 ± 0.05	13.68 ± 0.86	11.52 ± 0.72	0.029
22	13.1 ± 0.1	0.68 ± 0.02	12.00 ± 0.39	10.40 ± 0.34	0.028
23	27.6 ± 1.5	0.60 ± 0.05	7.31 ± 0.58	5.25 ± 0.42	0.034
24	19.2 ± 1.1	0.91 ± 0.08	11.17 ± 1.04	8.07 ± 0.75	0.034
25	13.2 ± 0.1	1.19 ± 0.03	17.06 ± 0.41	13.30 ± 0.32	0.031
26	11.9 ± 0.3	1.21 ± 0.07	17.40 ± 0.94	13.57 ± 0.73	0.031
27	20.3 ± 1.4	0.68 ± 0.08	3.70 ± 0.42	1.78 ± 0.20	0.051
28	21.8 ± 0.6	0.08 ± 0.01	1.45 ± 0.17	1.31 ± 0.15	0.027
29	26.9 ± 1.1	0.08 ± 0.01	1.22 ± 0.14	1.00 ± 0.11	0.030
30	15.5 ± 0.2	0.09 ± 0.01	1.36 ± 0.17	1.06 ± 0.13	0.031
31	15.1 ± 0.2	0.16 ± 0.02	1.81 ± 0.18	1.27 ± 0.13	0.035
32	14.1 ± 0.1	0.11 ± 0.01	2.87 ± 0.33	2.97 ± 0.34	0.024
33	25.3 ± 0.3	0.03 ± 0.01	0.57 ± 0.10	0.51 ± 0.09	0.027
34	19.5 ± 0.4	0.18 ± 0.02	1.81 ± 0.15	1.17 ± 0.10	0.038
35	28.4 ± 1.2	0.02 ± 0.01	0.34 ± 0.10	0.31 ± 0.09	0.027
36	18.2 ± 0.4	0.11 ± 0.01	2.09 ± 0.22	1.87 ± 0.20	0.027
37	15.5 ± 0.0	0.07 ± 0.01	1.16 ± 0.16	0.94 ± 0.13	0.030
38	19.5 ± 0.7	0.23 ± 0.02	1.67 ± 0.16	0.92 ± 0.09	0.044
39	24.2 ± 0.6	0.15 ± 0.01	1.07 ± 0.09	0.58 ± 0.05	0.045

Table 5.4: – continued.

Source Index	Temp. (K)	Mass (M$_\odot$)	H$_2$ Col. Density ($\times 10^{21}$ cm^{-2})	H$_2$ Vol. Density ($\times 10^6$ cm^{-3})	Deconv. FWHM (pc)
40	18.8 ± 1.3	0.62 ± 0.08	1.38 ± 0.18	0.43 ± 0.06	0.079
41	31.0 ± 1.1	0.05 ± 0.01	1.01 ± 0.12	0.91 ± 0.11	0.027
42	13.2 ± 0.1	0.08 ± 0.01	1.61 ± 0.27	1.45 ± 0.25	0.027
43	21.2 ± 0.3	0.05 ± 0.01	1.02 ± 0.14	0.92 ± 0.13	0.027
44	18.9 ± 0.5	0.15 ± 0.01	1.30 ± 0.13	0.80 ± 0.08	0.040
45	23.6 ± 0.5	0.06 ± 0.01	0.88 ± 0.11	0.70 ± 0.09	0.031
46	16.3 ± 0.3	0.12 ± 0.01	1.69 ± 0.17	1.29 ± 0.13	0.032
47	12.0 ± 0.0	0.45 ± 0.01	7.56 ± 0.21	6.40 ± 0.18	0.029
48	12.1 ± 0.1	0.42 ± 0.02	6.81 ± 0.28	5.68 ± 0.23	0.029
49	11.8 ± 0.1	0.10 ± 0.01	1.91 ± 0.23	1.69 ± 0.20	0.028
50	12.9 ± 0.0	0.07 ± 0.01	1.42 ± 0.19	1.29 ± 0.17	0.027
51	12.7 ± 0.1	0.08 ± 0.01	1.27 ± 0.18	1.06 ± 0.15	0.029
52	12.5 ± 0.0	0.10 ± 0.01	1.61 ± 0.19	1.34 ± 0.15	0.029
53	12.6 ± 0.1	0.08 ± 0.01	1.20 ± 0.16	0.95 ± 0.13	0.031
54	12.3 ± 0.1	0.07 ± 0.01	1.33 ± 0.22	1.20 ± 0.20	0.027
55	12.5 ± 0.1	0.24 ± 0.01	2.58 ± 0.15	1.73 ± 0.10	0.036
56	14.9 ± 0.3	3.61 ± 0.14	39.85 ± 1.52	27.26 ± 1.04	0.036
57	11.0 ± 0.1	2.89 ± 0.09	15.59 ± 0.48	7.46 ± 0.23	0.051
58	11.1 ± 0.1	1.16 ± 0.03	15.37 ± 0.42	11.51 ± 0.31	0.032
59	13.1 ± 0.5	0.66 ± 0.06	9.83 ± 0.84	7.81 ± 0.67	0.031
60	10.3 ± 0.2	4.22 ± 0.21	14.75 ± 0.72	5.68 ± 0.28	0.063
61	18.4 ± 0.1	1.19 ± 0.02	16.04 ± 0.27	12.15 ± 0.21	0.032
62	10.8 ± 0.1	0.55 ± 0.03	7.30 ± 0.33	5.46 ± 0.25	0.032
63	11.0 ± 0.2	1.57 ± 0.07	6.72 ± 0.29	2.86 ± 0.12	0.057
64	10.2 ± 0.1	1.05 ± 0.04	13.82 ± 0.46	10.31 ± 0.35	0.033
65	11.4 ± 0.1	0.33 ± 0.02	3.45 ± 0.25	2.30 ± 0.16	0.036
66	11.1 ± 0.1	0.87 ± 0.03	7.58 ± 0.26	4.62 ± 0.16	0.040
67	11.4 ± 0.1	0.18 ± 0.01	3.18 ± 0.26	2.76 ± 0.23	0.028
68	11.4 ± 0.1	0.81 ± 0.03	6.63 ± 0.23	3.91 ± 0.14	0.041
69	13.0 ± 0.1	0.11 ± 0.01	2.64 ± 0.27	2.70 ± 0.28	0.024
70	12.4 ± 0.1	0.11 ± 0.01	2.03 ± 0.22	1.76 ± 0.19	0.028
71	10.7 ± 0.1	2.09 ± 0.07	11.78 ± 0.39	5.75 ± 0.19	0.050
72	11.1 ± 0.1	0.32 ± 0.02	3.46 ± 0.24	2.36 ± 0.16	0.036
73	12.5 ± 0.0	0.09 ± 0.01	1.35 ± 0.17	1.09 ± 0.14	0.030
74	12.0 ± 0.0	0.19 ± 0.01	2.36 ± 0.16	1.71 ± 0.12	0.034
75	11.1 ± 0.0	0.23 ± 0.02	3.09 ± 0.20	2.31 ± 0.15	0.032
76	14.4 ± 0.1	0.09 ± 0.01	2.12 ± 0.23	2.17 ± 0.24	0.024
77	13.0 ± 0.0	0.10 ± 0.01	1.30 ± 0.14	0.97 ± 0.10	0.032
78	12.1 ± 0.1	0.28 ± 0.02	2.50 ± 0.18	1.54 ± 0.11	0.039

Table 5.4: – continued.

Source Index	Temp. (K)	Mass ($M_\odot$)	H_2 Col. Density ($\times 10^{21}$ cm^{-2})	H_2 Vol. Density ($\times 10^6$ cm^{-3})	Deconv. FWHM (pc)
79	12.9 ± 0.0	0.09 ± 0.01	1.18 ± 0.15	0.90 ± 0.11	0.032
80	12.8 ± 0.0	0.18 ± 0.01	2.47 ± 0.17	1.87 ± 0.13	0.032
81	13.5 ± 0.0	0.08 ± 0.01	1.38 ± 0.18	1.20 ± 0.16	0.028
82	11.9 ± 0.1	1.49 ± 0.05	17.66 ± 0.56	12.53 ± 0.39	0.034
83	11.7 ± 0.0	0.10 ± 0.01	2.15 ± 0.28	2.07 ± 0.27	0.025
84	12.2 ± 0.1	0.34 ± 0.02	5.74 ± 0.26	4.85 ± 0.22	0.029
85	11.8 ± 0.1	0.08 ± 0.01	1.06 ± 0.18	0.79 ± 0.13	0.032
86	12.0 ± 0.1	0.17 ± 0.01	2.41 ± 0.20	1.88 ± 0.16	0.031
87	12.6 ± 0.1	0.09 ± 0.01	1.48 ± 0.20	1.26 ± 0.17	0.029
88	12.3 ± 0.1	0.15 ± 0.02	1.16 ± 0.13	0.67 ± 0.08	0.042
89	11.9 ± 0.1	0.17 ± 0.02	1.66 ± 0.18	1.07 ± 0.12	0.038
90	11.8 ± 0.1	0.29 ± 0.02	2.57 ± 0.15	1.57 ± 0.09	0.040
91	11.9 ± 0.2	0.38 ± 0.03	3.10 ± 0.22	1.82 ± 0.13	0.041
92	12.5 ± 0.0	0.13 ± 0.01	2.24 ± 0.21	1.94 ± 0.18	0.028
93	10.8 ± 0.1	1.90 ± 0.07	7.13 ± 0.27	2.84 ± 0.11	0.061
94	12.1 ± 0.0	0.13 ± 0.01	1.66 ± 0.16	1.24 ± 0.12	0.032
95	11.4 ± 0.1	1.96 ± 0.06	5.57 ± 0.17	1.93 ± 0.06	0.070
96	12.4 ± 0.1	0.54 ± 0.02	3.02 ± 0.11	1.48 ± 0.05	0.050
97	12.3 ± 0.1	0.17 ± 0.01	1.65 ± 0.14	1.05 ± 0.09	0.038
98	11.7 ± 0.1	0.22 ± 0.01	3.79 ± 0.16	3.25 ± 0.14	0.028
99	11.8 ± 0.1	0.10 ± 0.01	3.85 ± 0.25	4.97 ± 0.32	0.019
100	11.6 ± 0.1	0.20 ± 0.01	2.76 ± 0.14	2.11 ± 0.11	0.032
101	12.4 ± 0.0	0.17 ± 0.01	2.58 ± 0.12	2.07 ± 0.10	0.030
102	12.2 ± 0.1	0.05 ± 0.01	2.09 ± 0.25	2.71 ± 0.32	0.019
103	13.1 ± 0.1	0.05 ± 0.01	1.88 ± 0.20	2.44 ± 0.26	0.019
104	11.8 ± 0.1	0.07 ± 0.01	2.12 ± 0.19	2.37 ± 0.21	0.022
105	13.2 ± 0.0	0.01 ± 0.00	0.66 ± 0.25	1.01 ± 0.38	0.016
106	11.3 ± 0.2	0.86 ± 0.04	5.39 ± 0.23	2.78 ± 0.12	0.047
107	11.7 ± 0.1	0.12 ± 0.01	2.91 ± 0.19	2.99 ± 0.19	0.024
108	13.3 ± 0.1	0.04 ± 0.01	0.89 ± 0.13	0.82 ± 0.12	0.026
109	13.7 ± 0.1	0.02 ± 0.00	1.00 ± 0.18	1.31 ± 0.23	0.019
110	13.3 ± 0.1	0.03 ± 0.00	1.70 ± 0.26	2.58 ± 0.39	0.016
111	12.5 ± 0.1	0.98 ± 0.02	38.47 ± 0.64	49.75 ± 0.83	0.019
112	12.5 ± 0.0	0.03 ± 0.00	1.17 ± 0.21	1.58 ± 0.29	0.018
113	12.3 ± 0.1	0.08 ± 0.01	1.57 ± 0.13	1.42 ± 0.12	0.027
114	13.0 ± 0.0	0.03 ± 0.00	1.32 ± 0.21	1.81 ± 0.28	0.018
115	13.0 ± 0.0	0.11 ± 0.01	2.20 ± 0.11	2.06 ± 0.11	0.026
116	12.5 ± 0.1	0.05 ± 0.01	1.90 ± 0.22	2.47 ± 0.28	0.019
117	11.8 ± 0.0	0.09 ± 0.01	2.22 ± 0.17	2.33 ± 0.17	0.023
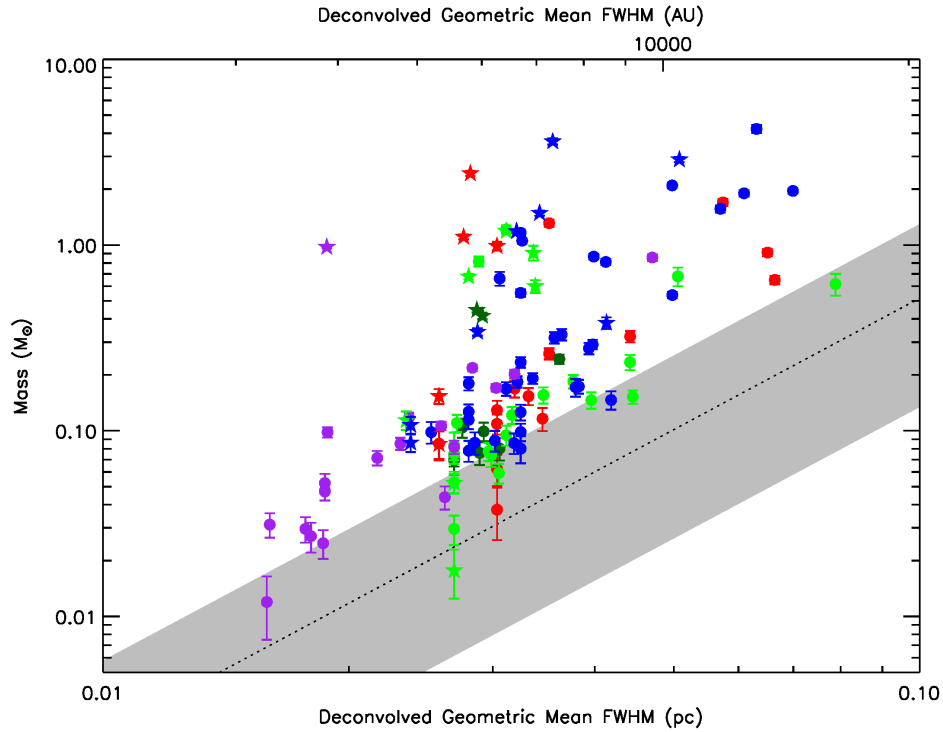
Figure 5.7: Mass/size plot for the sources in Cepheus. Circles represent starless cores; stars represent cores with embedded protostars. Red sources lie in L1147/58, light green sources in L1174, dark green sources in L1172, blue sources in L1251, and purple sources in L1228.

Table 5.5: Maximum-likelihood-estimator power law indices for cores in Cepheus

Region	α_{uml}	Mass Range
L1147/L1158	1.82 ± 0.18	$> 0.05\,\mathrm{M}_\odot$
L1174	1.99 ± 0.21	$> 0.05\,\mathrm{M}_\odot$
L1172	5.22 ± 6.47	$> 0.05\,\mathrm{M}_\odot$
L1251	1.77 ± 0.11	$> 0.05\,\mathrm{M}_\odot$
L1228	2.33 ± 0.33	$> 0.05\,\mathrm{M}_\odot$
All	1.88 ± 0.09	$> 0.08\,\mathrm{M}_\odot$
All	2.61 ± 0.27	$> 0.5\,\mathrm{M}_\odot$
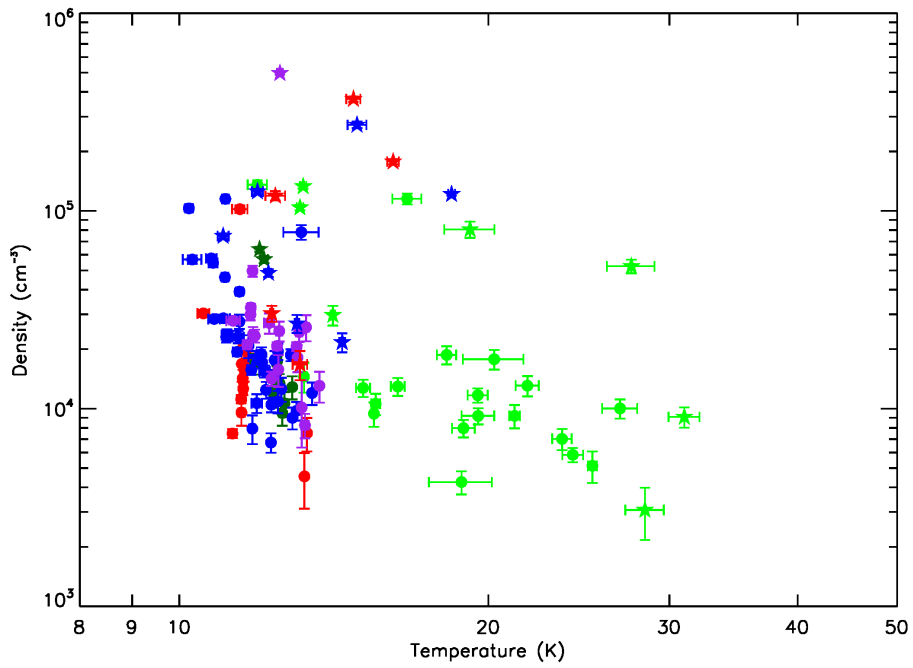
Figure 5.8: Temperature/density plot for the sources in Cepheus. Colour and symbol coding is as in Figure 5.7.

region in the Cepheus Flare can be characterised by a power law above a mass of $0.05\,M_\odot$, with the exception of L1172, in which the α_{uml} value determined is physically implausible and substantially uncertain: $\alpha_{uml,\text{L}1172} = 5.22 \pm 6.47$. This is likely to be due to the low counting statistics in L1172, rather than due any fundamental difference in the L1172 cores from the remainder of the sample – $\alpha_{uml,\text{L}1172}$ is determined from only 6 cores. The L1147/L1158, L1174 and L1251 α_{uml} values are similar, and show a sub-Salpeter high-mass CMF slope: $\alpha_{uml} = 1.82 \pm 0.18$, 1.99 ± 0.21 and 1.77 ± 0.11 respectively. The L1228 region, however, has a high-mass CMF slope of $\alpha_{uml,\text{L}1228} = 2.33 \pm 0.33$, consistent with the Salpeter IMF value, $\alpha = 2.35$ (Salpeter 1955; Chabrier 2003). Whether this difference in CMF slope is indicative of a difference in behaviour between L1228 and the remainder of the sample or merely of the small sample sizes in each region, is difficult to determine.

The cumulative mass distribution for all of the starless cores we detect in Cepheus is shown in Figure 5.10. There appears to be a break in core masses between 0.3 and $0.5\,M_\odot$, with no cores being detected in this mass range. Determining α_{uml} over the mass range $M > 0.08\,M_\odot$ gives a sub-Salpeter power-law index of 1.88 ± 0.09, with cores in the mass range $0.08 - 0.3\,M_\odot$ conforming well to a power-law distribution (see top panel of Figure 5.10). Determining α_{uml} for the high-mass cores only ($M > 0.5\,M_\odot$) gives a steeper power-law index, of 2.61 ± 0.27, marginally consistent with the Salpeter IMF. Whether these high-mass cores represent a different population is not clear. The break in core masses can be seen in Figure 5.7; inspection of Figure 5.7 further shows that these most massive cores have a higher average radius than the rest of the population. This might suggest that these more massive cores are a separate population of starless 'clumps'; objects which might be expected to fragment to form multiple starless cores. The lower-mass population of starless clumps might, due to their large radii and low masses and temperatures, be below the
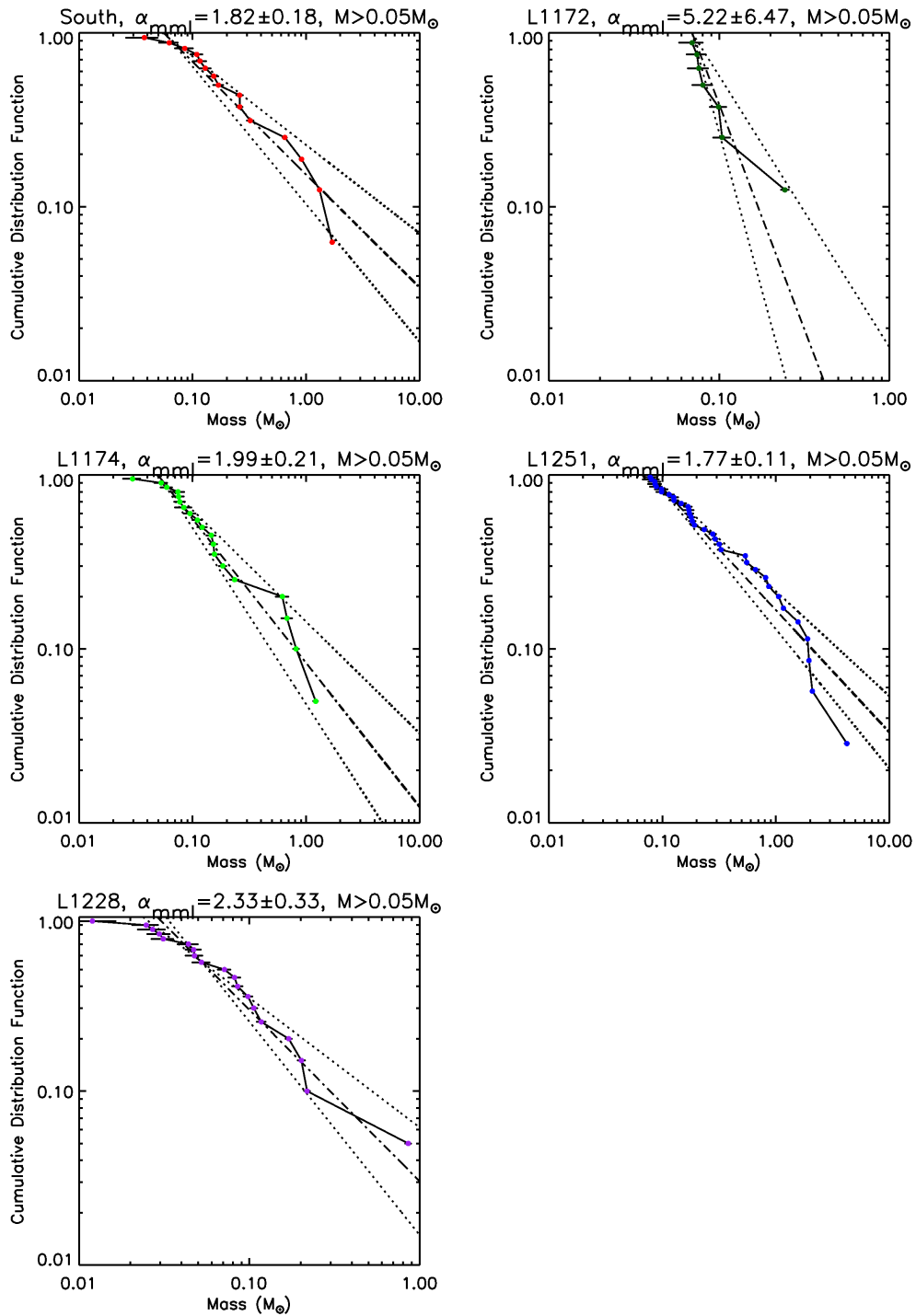
Figure 5.9: Cumulative probability plots by region. Colour coding is as in Figure 5.7.

detectability limit of SCUBA-2 (see Section 4.3). However, whether these highest-mass objects are in fact a separate population is by no means certain.

There is no *a priori* reason to expect the lower-mass-range cumulative mass distributions to obey a Salpeter power-law distribution. Figure 1.9 shows that the turn-over of the log-normal part of the CMF in the Aquila molecular cloud occurs at $\sim 0.5\,\mathrm{M_\odot}$. The mass distribution is expected to tend towards Salpeter-like behaviour at masses $\gtrsim 0.5\,\mathrm{M_\odot}$, but at masses lower than this, we should expect to see a shallower CMF slope, if the lower-mass part of the CMF can in fact be accurately characterised by a power-law (see Kroupa 2001; Chabrier 2003). Our results are consistent with this – for mass ranges $\geq 0.05\,\mathrm{M_\odot}$ we see shallow, sub-Salpeter power-law indices, whereas for the mass range $> 0.5\,\mathrm{M_\odot}$ we see a power-law behaviour consistent with the Salpeter IMF.

Furthermore, we are implicitly assuming that the mass distribution of starless cores is functionally identical to the prestellar core mass function. The mass function of starless cores will include cores which will not necessarily go on to become gravitationally-bound prestellar cores (see stability analyses in Chapters 3 and 4, and below). More massive objects are more likely to be gravitationally bound (over a relatively small range of source sizes), so the mass function of starless cores is likely to be biased toward lower-mass objects relative to the core mass function. The sub-Salpeter power-law slopes which we see in the low-mass regime could perhaps be a consequence of the majority of these cores being non-prestellar (i.e. non-gravitationally bound) starless cores.

5.4   Counting Statistics

In order to make a crude estimate of the relative level of star formation activity in the different regions of the Cepheus Flare, we compared the number of starless cores in our sample with the number of embedded (Class I and Flat) and Class II sources
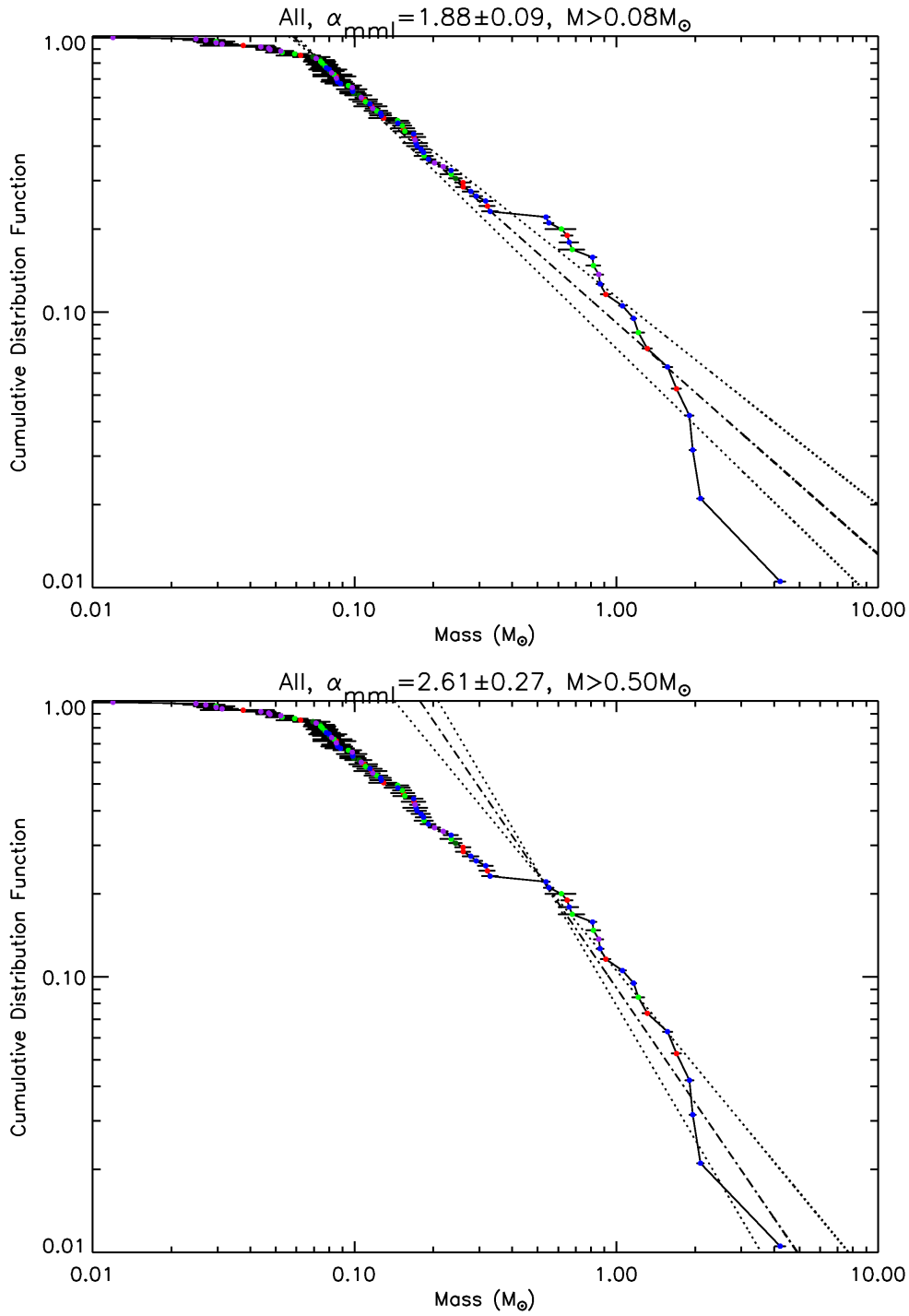
Figure 5.10: Cumulative probability plots for the starless cores in Cepheus. Top panel: power-law distribution for cores with masses $> 0.08\,M_\odot$. Bottom panel: power-law distribution for cores with masses $> 0.5\,M_\odot$. Colour coding is as in Figure 5.7.
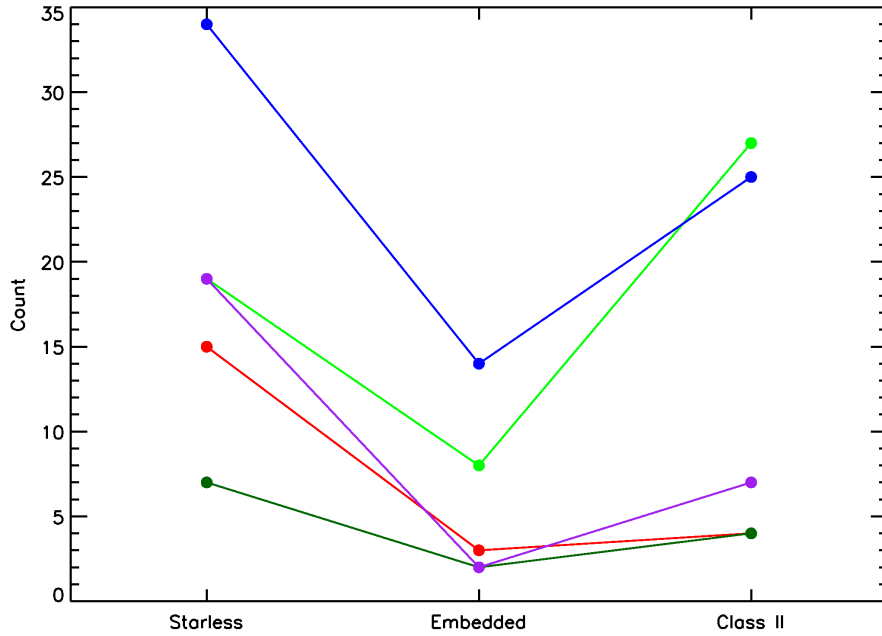
Figure 5.11: Regional statistics of absolute number of starless, embedded and Class II sources in Cepheus. Colour coding is as in Figure 5.7: red indicates L1147/58; light green, L1174; dark green, L1172; blue, L1251; purple, L1228.

detected by Kirk et al. (2009) in the same area. The absolute number counts are shown in Figure 5.11, while the counts normalised to the number of Class II sources in the region are shown in Figure 5.12.

Figure 5.11 shows that in absolute terms, L1251 contains the highest number of both starless cores and embedded sources, and the second highest number of Class II sources. L1174 contains the highest number of Class II sources; a natural result for a region in which clustered star formation has been ongoing for some time (Kun et al. 2008). L1174 has the second highest number of embedded sources after L1251, and the joint second-highest number of starless cores, along with L1228. L1228, L1147/L1158 and L1172 have low number counts of both embedded and Class II sources. This shows that the sites of ongoing active star formation, L1251 and L1174, have the highest absolute number of sources in almost all categories, while
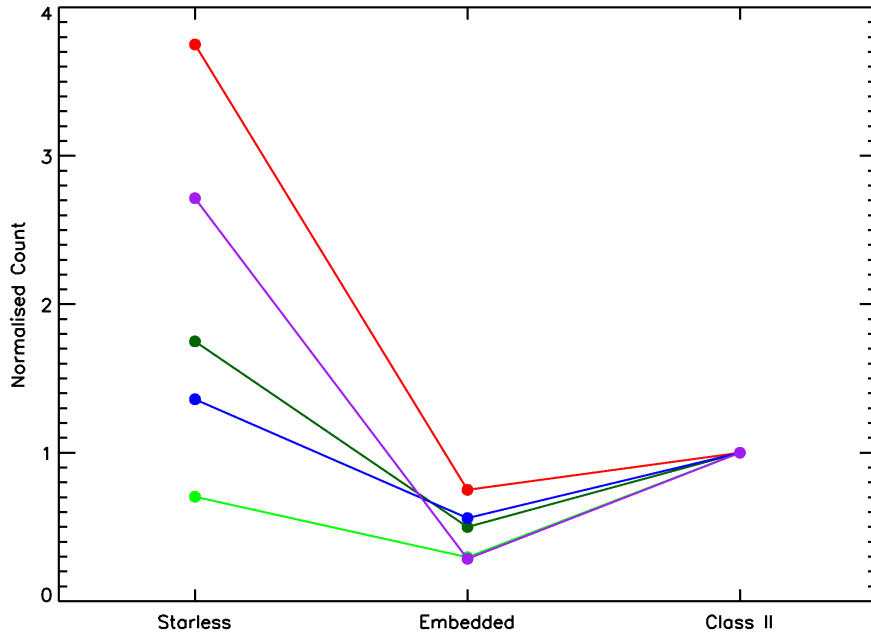
Figure 5.12: Regional counting statistics of starless, embedded and Class II sources in Cepheus, normalised to the number of Class II sources. Colour coding is as in Figure 5.11.

the regions of quiescent star formation generally have lower numbers of starless cores as well as embedded sources.

Figure 5.12 shows the number of sources of each type in each region, normalised to the number of Class II sources. Again, a difference in behaviour can be seen between the quiescent regions, L1147/L1158 and L1228, and the active regions L1174 and L1251. In the quiescent regions, there is a high ratio of starless cores to Class II sources: $\sim 3.8 : 1$ in L1148/L1157, and $\sim 2.7 : 1$ in L1228. However, in the active star-forming regions, this ratio is much lower: $\sim 1.4 : 1$ in L1251, while in L1174 Class II sources outnumber starless cores, with a ratio $\sim 0.7 : 1$. L1172 shows an intermediate behaviour, with a ratio $\sim 1.8 : 1$. However, the low counting statistics in all classes in L1172 make any interpretation of this result doubtful.

The high ratio of starless cores to embedded sources in the quiescent regions can

be interpreted in different ways. If the ratio is representative of the star-forming history of the region, it could suggest that star formation is an ongoing, inefficient process in these regions. The high ratio could, however, show that star formation in these regions is in its early stages, with only a small amount of the reservoir of available material thus far having been converted into stars.

The low ratio of starless cores to embedded sources in the active regions can be interpreted in a similar, but opposite, manner. If the low ratio is steady-state, and representative of the local star-forming history, then star formation is proceeding efficiently in L1174 and L1251, with starless cores rapidly collapsing to form stars. However, the low ratio could, alternatively, indicate that star formation in these regions is drawing to an end, with the local dense material having been depleted in the process of forming stars.

5.5   Bonnor-Ebert Stability Analysis

In an attempt to determine whether our cores are likely to be virially bound, we determined their Bonnor-Ebert critically-stable masses, assuming that the cores are confined by external pressure at a radius $R = 1 \times$ FWHM. The BE mass is then

$$M_{\mathrm{BE}} = 2.4 \frac{c_s^2}{G} R = 2.4 \frac{k_{\mathrm{B}} T}{\mu m_{\mathrm{H}} G} R. \tag{5.5}$$

The critically-stable Bonnor-Ebert masses of our cores are listed in Table 5.6, and are plotted against our observed core masses in Figure 5.13. Figure 5.13 suggests that the majority of our cores have stable, pressure-confined Bonnor-Ebert solutions.

Using equations 1.48 and 5.5, we can infer the external pressure $P_{\mathrm{EXT,BE}}$ confining our cores, if the Bonnor-Ebert model is applicable, to be

$$P_{\mathrm{EXT,BE}} = 0.242 \frac{c_s^4}{G} R^{-2} \tag{5.6}$$

where all symbols are defined as previously. The Bonnor-Ebert-predicted external
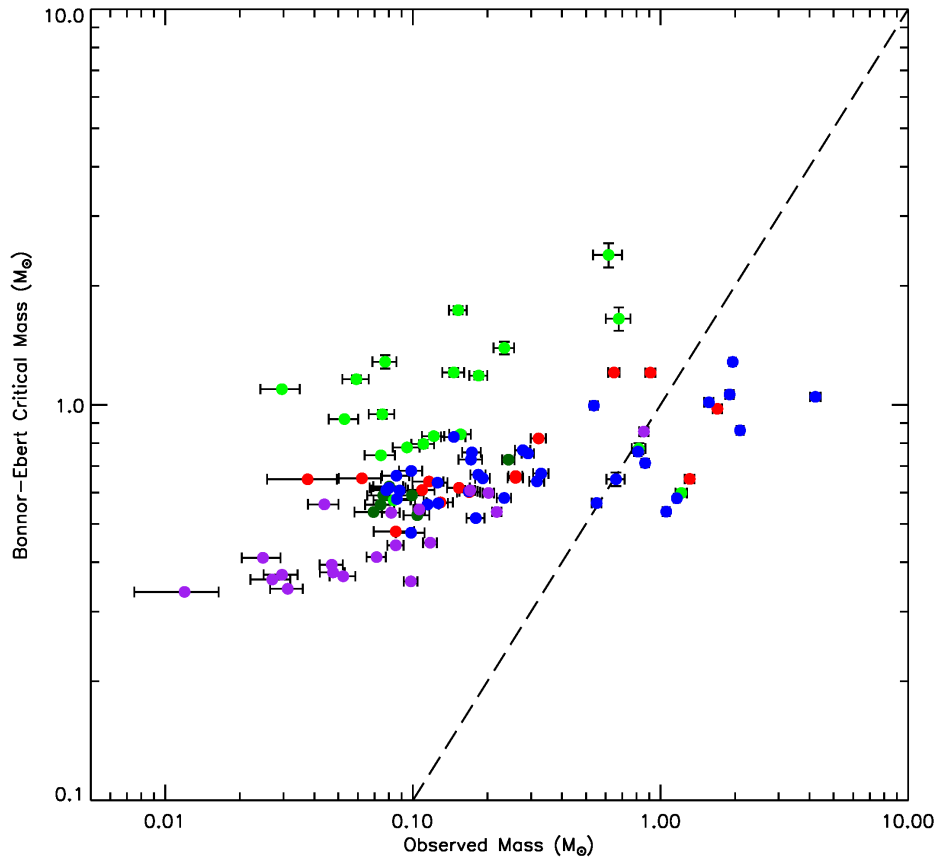
Figure 5.13: BE stability plot for cores in Cepheus. Cores to the right of the dashed line have no stable Bonnor-Ebert configuration. Colour coding is as in Figure 5.7.

pressures for our cores are listed in Table 5.6, and plotted in Figure 5.14. Figure 5.14 shows that most of our cores have similar BE-predicted external pressures, $P_{\rm EXT,BE}/k_{\rm B} \sim 1 - 5 \times 10^5 \, {\rm K cm}^{-3}$, with the exception of cores in L1174 and L1228, which this analysis suggests have external pressures $P_{\rm EXT,BE}/k_{\rm B} \sim 5 - 20 \times 10^5 \, {\rm K cm}^{-3}$. This is a not entirely unexpected result in either case. The substantially higher temperatures in L1174 than in the rest of the regions will result in elevated predicted external pressures - a result also not physically unreasonable in a reflection nebula. In the case of L1228, the elevated predicted external pressures could be considered evidence for the passage of the Cepheus Flare Shell through the region – Kirk et al. (2009) note that the current radius of the CFS is consistent with the location of L1228, and suggest that star formation might currently be being induced in L1228 by the CFS. However, care must be taken in the interpretation of this result: we adopt a distance of $\sim 200 \, {\rm pc}$ to L1228 (Kun et al. 2008), substantially different to the distances adopted to the rest of the regions, all of which are $\sim 300 \, {\rm pc}$. This results in a smaller inferred physical size for sources in L1228 than in other regions, for the same measured angular size – see Figure 5.7. Hence, given that there is no substantial difference in temperature between cores in L1228 and those in other regions, we expect to infer a higher external BE-stable pressure, as $P_{\rm EXT,BE} \propto T^2/R^2$. As discussed in Section 4.3, we expect to detect lower-density cores only at nearer distances, for the same source temperature. It may be that we are sampling a slightly different core population in L1228 than in other regions, the low-density members of which require a higher external pressure in order to be stable against dispersal. It should be noted, however, that Figure 5.8 does not show significantly lower densities in L1228 than elsewhere.
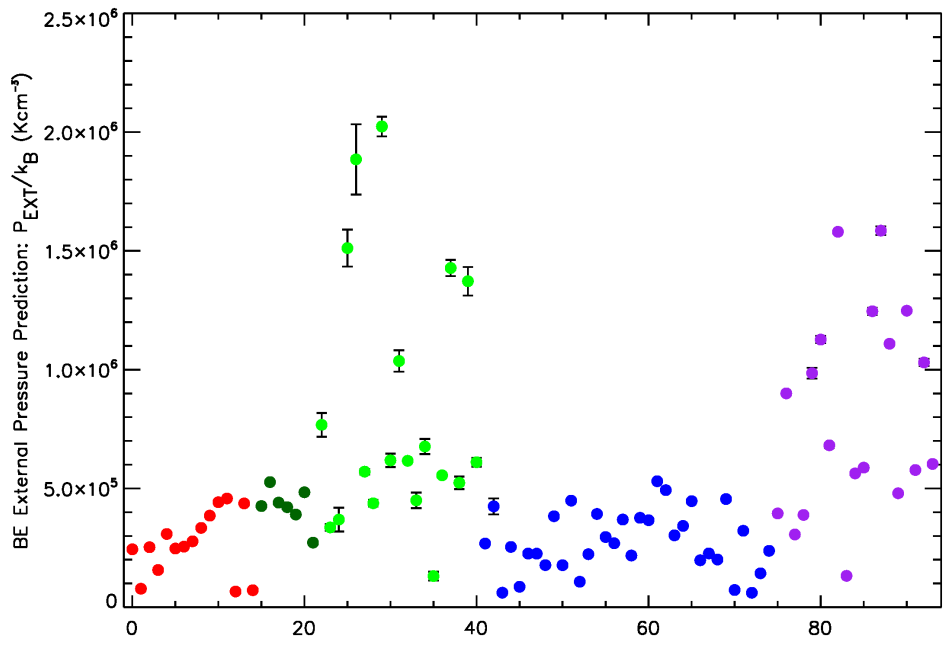
Figure 5.14: BE-stable external pressure for cores in Cepheus. Cores are arranged according to region; x axis has no physical meaning. Colour coding is as in Figure 5.7.

5.6 Energy Balance and Stability

We attempted to assess the energy balance of the starless cores in the Cepheus molecular cloud and to determine the applicability of our Bonnor-Ebert analysis by estimating the external presssure on our cores using measurements presented by Yonekura et al. (1997). Yonekura et al. (1997) conducted a large-scale ^{13}CO $J = 1 \rightarrow 0$ survey of the Cepheus Flare region using two 4-m telescopes at Nagoya University. Their observations had a resolution of 2.4 arcmin. The ^{13}CO sources identified by Yonekura et al. (1997) in the Cepheus Flare are shown in Figure 5.15. Each of the regions in our survey is entirely covered by a different, single, Yonekura et al. (1997) source: Y97 Source 8 for L1147/L1158, Y97 Source 14 for L1172 and L1174, Y97 Source 79 for L1251, and Y97 Source 66 for L1228. Thus, we can estimate only a single value for external pressure in each region, which we must assume is representative for all of the cores within that region.

We estimate the external pressure in each region from the linewidths measured by Yonekura et al. (1997) using the equation

$$P_{\text{EXT}} \approx \rho_{^{13}\text{CO}} \langle \sigma_{gas,^{13}\text{CO}} \rangle. \tag{5.7}$$

As in Chapter 4, we assume that ^{13}CO traces material up to a density $\rho_{^{13}\text{CO}} = 10^4 \, \text{cm}^{-3}$ (Di Francesco et al. 2007).

Yonekura et al. (1997) find the highest ^{13}CO linewidth in L1251, the lowest in L1147/L1158, and the same, intermediate, value in L1172, L1174 and L1228. This is in disagreement with our Bonnor-Ebert analysis, which predicted the highest external pressures to be in L1174 and L1228. It is possible that there are, locally, higher external pressures in L1174 than are captured by the low-resolution Yonekura et al. (1997) measurements. We compare the measured and BE-predicted external pressures on our sources in Figure 5.16, which shows that the measured pressure in ^{13}CO is consistently higher than that predicted by the Bonnor-Ebert model, with
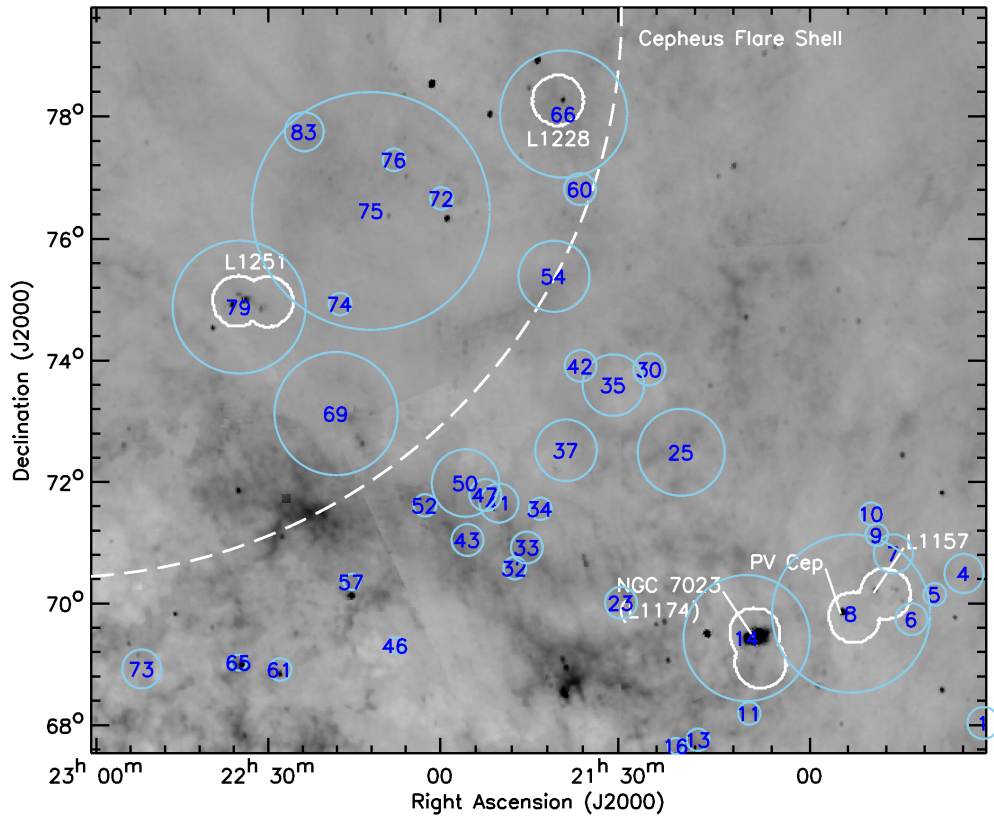
Figure 5.15: Finding chart for Yonekura et al. (1997) sources.

the exception of the few highest-BE-pressure cores in L1174 and L1228. This would suggest that our cores may not be accurately modelled as critically-stable Bonnor-Ebert spheres.

We determined external pressure energies for our cores using the equation

$$\Omega_{\mathrm{P}} = -4\pi P_{\mathrm{EXT}} r_{\mathrm{^{13}CO}}^3. \tag{5.8}$$

where $r_{\mathrm{^{13}CO}}$ is the core radius at which ^{13}CO ceases to be an effective tracer,

$$r_{\mathrm{^{13}CO}} = \alpha \sqrt{2\ln\left(\frac{\rho_0}{\rho_{\mathrm{^{13}CO}}}\right)} \tag{5.9}$$

and the central density, ρ_0 is determined using equation 3.39.

We determined gravitational potential energies for each of our cores using equation 3.24, which we repeat here,

$$\Omega_{\mathrm{G}} = -\frac{1}{2\sqrt{\pi}}\frac{GM^2}{\alpha}, \tag{5.10}$$

where M is the measured core mass and α is the modelled Gaussian width of the core.

We were able to put a lower limit on the internal energy of each of our cores by estimating the thermal kinetic energy of the core,

$$\Omega_{\mathrm{K,T}} = \frac{3}{2}Mc_s^2 = \frac{3}{2}M\frac{k_{\mathrm{B}}T}{\mu m_{\mathrm{H}}}. \tag{5.11}$$

Unless the cores in Cepheus are substantially dissimilar to those in Ophiuchus and Taurus, there is likely to be a substantial nonthermal component to the internal energy of the Cepheus cores. Hence the values given by equation 5.11 are a lower limit on the true value of Ω_{K}. The values of Ω_{G}, Ω_{P}, Ω_{K} and the virial parameter $\frac{1}{2}\ddot{\mathcal{I}}$ which we determine are listed in Table 5.6.
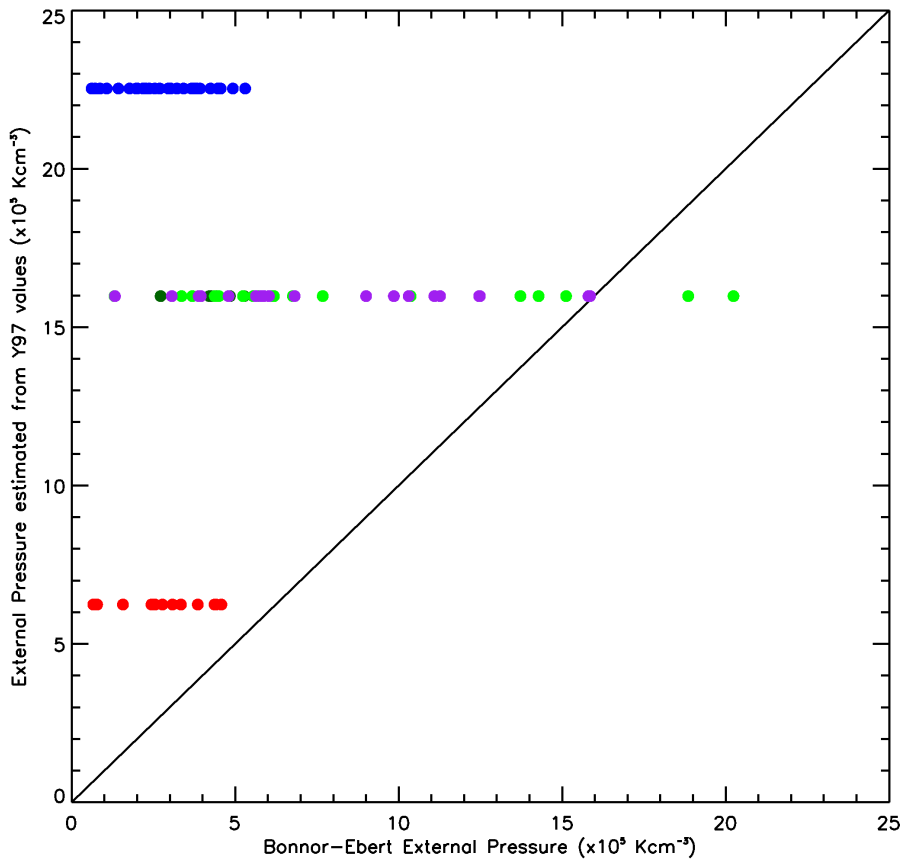
Figure 5.16: Comparison of external pressures determined from Yonekura et al. (1997) low-resolution ^{13}CO measurements and Bonnor-Ebert critically-stable pressures. The diagonal black line marks the 1:1 line. Cores to the right of the 1:1 lines have Bonnor-Ebert critically-stable pressures higher than their pressure estimated from Yonekura et al. (1997) measurements.

Table 5.6: Virial stability of cores in Cepheus

Source	$\sigma_{^{13}CO,gas}$	$P_{\mathrm{EXT}}/k_{\mathrm{B}}$	Ω_{G}	Ω_{K}	Ω_{P}	$\frac{1}{2}\ddot{\mathcal{I}}$	M_{BE}	$P_{\mathrm{EXT,BE}}/k_{\mathrm{B}}$
ID	$(\mathrm{km s^{-1}})$	$(\times 10^5\,\mathrm{K cm^{-3}})$		$(\times 10^{41}\,\mathrm{erg})$			$(M_\odot)$	$(\times 10^5\,\mathrm{K cm^{-3}})$
3	0.4	6.2	-27.82	13.0	-22.8	-24.7	0.650 ± 0.011	2.44 ± 0.08
4	0.4	6.2	-28.50	15.4	-56.6	-54.2	0.977 ± 0.013	0.78 ± 0.02
7	0.4	6.2	-1.09	2.6	-10.1	-6.0	0.661 ± 0.003	2.52 ± 0.02
8	0.4	6.2	-1.33	3.2	-14.2	-9.1	0.822 ± 0.007	1.57 ± 0.03
9	0.4	6.2	-0.51	1.7	-6.9	-4.0	0.601 ± 0.006	3.08 ± 0.06
10	0.4	6.2	-1.09	2.6	-10.1	-6.1	0.654 ± 0.005	2.47 ± 0.03
12	0.4	6.2	-0.22	1.2	-5.2	-3.2	0.640 ± 0.005	2.55 ± 0.04
13	0.4	6.2	-0.40	1.5	-6.6	-4.0	0.617 ± 0.003	2.77 ± 0.02
14	0.4	6.2	-0.31	1.3	-5.4	-3.2	0.567 ± 0.002	3.34 ± 0.03
15	0.4	6.2	-0.22	1.2	-4.8	-2.6	0.609 ± 0.001	3.85 ± 0.02
16	0.4	6.2	-0.07	0.7	-2.7	-1.4	0.652 ± 0.003	4.42 ± 0.04
17	0.4	6.2	-0.16	0.8	-3.5	-2.0	0.478 ± 0.002	4.58 ± 0.04
18	0.4	6.2	-3.60	6.3	-28.6	-19.6	1.207 ± 0.006	0.66 ± 0.01
19	0.4	6.2	-0.03	0.4	-1.3	-0.4	0.648 ± 0.001	4.37 ± 0.02
20	0.4	6.2	-7.25	9.0	-40.7	-29.9	1.206 ± 0.011	0.72 ± 0.01
21	0.7	16.0	-13.15	11.7	-33.8	-23.4	0.775 ± 0.025	7.68 ± 0.50
26	0.7	16.0	-26.86	12.5	-45.3	-47.2	0.599 ± 0.013	3.36 ± 0.15
27	0.7	16.0	-5.18	11.9	-70.6	-52.1	1.651 ± 0.112	3.69 ± 0.50
28	0.7	16.0	-0.12	1.4	-8.4	-5.7	0.947 ± 0.024	15.12 ± 0.78
29	0.7	16.0	-0.11	1.8	-8.9	-5.4	1.285 ± 0.050	18.85 ± 1.48
30	0.7	16.0	-0.16	1.3	-10.9	-8.5	0.780 ± 0.008	5.71 ± 0.11
31	0.7	16.0	-0.40	2.0	-17.5	-13.9	0.842 ± 0.013	4.38 ± 0.14
33	0.7	16.0	-0.02	0.6	-2.9	-1.6	1.096 ± 0.011	20.24 ± 0.41
34	0.7	16.0	-0.51	3.1	-21.0	-15.3	1.185 ± 0.027	6.18 ± 0.28
36	0.7	16.0	-0.25	1.7	-11.3	-8.1	0.796 ± 0.017	10.36 ± 0.45
37	0.7	16.0	-0.10	1.0	-8.6	-6.7	0.745 ± 0.001	6.16 ± 0.02
38	0.7	16.0	-0.70	3.9	-27.0	-19.8	1.392 ± 0.051	4.50 ± 0.33
39	0.7	16.0	-0.30	3.2	-15.9	-9.8	1.735 ± 0.040	6.76 ± 0.31
40	0.7	16.0	-2.74	10.0	-50.2	-32.9	2.394 ± 0.169	1.31 ± 0.18
42	0.7	16.0	-0.15	1.0	-9.2	-7.4	0.574 ± 0.003	5.55 ± 0.06
43	0.7	16.0	-0.06	1.0	-6.1	-4.2	0.920 ± 0.011	14.28 ± 0.34
44	0.7	16.0	-0.31	2.4	-16.7	-12.2	1.208 ± 0.031	5.24 ± 0.27
45	0.7	16.0	-0.07	1.2	-6.6	-4.2	1.161 ± 0.025	13.72 ± 0.60
46	0.7	16.0	-0.26	1.7	-13.6	-10.5	0.833 ± 0.013	6.10 ± 0.19
49	0.7	16.0	-0.22	1.1	-11.0	-9.1	0.526 ± 0.003	4.26 ± 0.05
50	0.7	16.0	-0.12	0.8	-8.3	-6.8	0.559 ± 0.001	5.27 ± 0.02
51	0.7	16.0	-0.11	0.8	-8.7	-7.2	0.590 ± 0.003	4.40 ± 0.05
52	0.7	16.0	-0.19	1.1	-11.1	-9.1	0.590 ± 0.002	4.21 ± 0.03
53	0.7	16.0	-0.12	0.9	-9.3	-7.6	0.621 ± 0.004	3.90 ± 0.06
54	0.7	16.0	-0.10	0.7	-7.9	-6.5	0.536 ± 0.004	4.84 ± 0.07

Table 5.6: – continued.

Source	$\sigma_{^{13}\mathrm{CO},gas}$	$P_{\mathrm{EXT}}/k_{\mathrm{B}}$	Ω_{G}	Ω_{K}	Ω_{P}	$\frac{1}{2}\ddot{\mathcal{I}}$	M_{BE}	$P_{\mathrm{EXT,BE}}/k_{\mathrm{B}}$
ID	(kms^{-1})	$(\times 10^5\,\mathrm{Kcm}^{-3})$			$(\times 10^{41}\,\mathrm{erg})$		$(\mathrm{M_\odot})$	$(\times 10^5\,\mathrm{Kcm}^{-3})$
55	0.7	16.0	-0.93	2.6	-25.5	-21.2	0.727 ± 0.004	2.72 ± 0.03
58	0.8	22.5	-23.71	11.1	-67.9	-69.4	0.580 ± 0.005	2.68 ± 0.04
59	0.8	22.5	-8.10	7.5	-48.8	-41.9	0.649 ± 0.026	4.24 ± 0.33
60	0.8	22.5	-160.37	37.5	-372.7	-458.2	1.048 ± 0.022	0.61 ± 0.03
62	0.8	22.5	-5.34	5.1	-49.8	-44.9	0.565 ± 0.006	2.54 ± 0.05
63	0.8	22.5	-24.51	14.9	-193.5	-188.2	1.014 ± 0.015	0.86 ± 0.03
64	0.8	22.5	-19.41	9.3	-65.9	-66.7	0.537 ± 0.005	2.26 ± 0.04
65	0.8	22.5	-1.69	3.2	-44.3	-39.5	0.671 ± 0.008	2.25 ± 0.06
66	0.8	22.5	-10.70	8.3	-85.4	-79.5	0.713 ± 0.005	1.77 ± 0.03
67	0.8	22.5	-0.65	1.8	-22.5	-19.6	0.517 ± 0.003	3.83 ± 0.04
68	0.8	22.5	-9.07	8.0	-86.9	-80.0	0.761 ± 0.006	1.77 ± 0.03
70	0.8	22.5	-0.27	1.2	-16.9	-14.7	0.560 ± 0.004	4.49 ± 0.06
71	0.8	22.5	-50.12	19.4	-183.7	-195.0	0.862 ± 0.010	1.07 ± 0.03
72	0.8	22.5	-1.60	3.0	-42.3	-37.8	0.640 ± 0.007	2.23 ± 0.05
73	0.8	22.5	-0.15	1.0	-14.3	-12.5	0.607 ± 0.001	3.93 ± 0.01
74	0.8	22.5	-0.62	2.0	-28.4	-25.1	0.652 ± 0.002	2.96 ± 0.02
75	0.8	22.5	-0.96	2.2	-31.4	-27.9	0.581 ± 0.002	2.69 ± 0.02
77	0.8	22.5	-0.17	1.1	-16.0	-14.0	0.681 ± 0.001	3.69 ± 0.02
78	0.8	22.5	-1.12	2.9	-42.4	-37.7	0.768 ± 0.009	2.18 ± 0.05
79	0.8	22.5	-0.13	1.0	-13.9	-12.2	0.662 ± 0.002	3.76 ± 0.02
80	0.8	22.5	-0.60	2.0	-26.5	-23.1	0.666 ± 0.003	3.66 ± 0.03
81	0.8	22.5	-0.12	0.9	-12.5	-10.8	0.609 ± 0.002	5.30 ± 0.04
83	0.8	22.5	-0.22	1.0	-13.7	-12.0	0.475 ± 0.001	4.93 ± 0.03
85	0.8	22.5	-0.11	0.8	-12.9	-11.4	0.617 ± 0.004	3.03 ± 0.04
86	0.8	22.5	-0.52	1.7	-24.3	-21.3	0.604 ± 0.005	3.42 ± 0.05
87	0.8	22.5	-0.15	0.9	-13.7	-12.0	0.578 ± 0.004	4.46 ± 0.06
88	0.8	22.5	-0.29	1.6	-22.7	-19.9	0.829 ± 0.004	1.98 ± 0.02
89	0.8	22.5	-0.44	1.8	-27.8	-24.7	0.727 ± 0.009	2.27 ± 0.05
90	0.8	22.5	-1.22	3.0	-44.3	-39.6	0.754 ± 0.003	2.01 ± 0.02
92	0.8	22.5	-0.32	1.4	-18.1	-15.7	0.564 ± 0.002	4.55 ± 0.04
93	0.8	22.5	-33.69	17.7	-235.3	-233.6	1.062 ± 0.014	0.72 ± 0.02
94	0.8	22.5	-0.28	1.3	-20.0	-17.7	0.636 ± 0.002	3.22 ± 0.02
95	0.8	22.5	-31.11	19.2	-279.8	-272.5	1.284 ± 0.012	0.61 ± 0.01
96	0.8	22.5	-3.31	5.8	-82.9	-74.7	0.996 ± 0.004	1.43 ± 0.01
97	0.8	22.5	-0.45	1.8	-28.1	-24.8	0.758 ± 0.003	2.37 ± 0.02
98	0.7	16.0	-0.96	2.2	-18.1	-14.6	0.536 ± 0.003	3.95 ± 0.05
99	0.7	16.0	-0.29	1.0	-6.6	-4.9	0.358 ± 0.002	9.00 ± 0.08
100	0.7	16.0	-0.73	2.0	-19.9	-16.6	0.599 ± 0.004	3.06 ± 0.04
101	0.7	16.0	-0.54	1.8	-16.9	-13.8	0.608 ± 0.002	3.88 ± 0.03

Table 5.6: – continued.

Source	$\sigma_{13_{CO},gas}$	$P_{\mathrm{EXT}}/k_{\mathrm{B}}$	Ω_{G}	Ω_{K}	Ω_{P}	$\frac{1}{2}\ddot{\mathcal{I}}$	M_{BE}	$P_{\mathrm{EXT,BE}}/k_{\mathrm{B}}$
ID	(kms^{-1})	$(\times 10^5\,\mathrm{Kcm}^{-3})$			$(\times 10^{41}\,\mathrm{erg})$		$(\mathrm{M}_\odot)$	$(\times 10^5\,\mathrm{Kcm}^{-3})$
102	0.7	16.0	-0.08	0.6	-4.7	-3.7	0.369 ± 0.004	9.85 ± 0.23
103	0.7	16.0	-0.07	0.5	-4.4	-3.4	0.394 ± 0.003	11.27 ± 0.15
104	0.7	16.0	-0.13	0.7	-6.7	-5.4	0.412 ± 0.003	6.82 ± 0.10
105	0.7	16.0	-0.01	0.1	-1.4	-1.1	0.337 ± 0.000	15.80 ± 0.02
106	0.7	16.0	-8.86	8.3	-75.9	-68.1	0.856 ± 0.013	1.32 ± 0.04
107	0.7	16.0	-0.33	1.2	-10.1	-8.0	0.448 ± 0.003	5.63 ± 0.09
108	0.7	16.0	-0.04	0.5	-5.0	-4.1	0.560 ± 0.005	5.88 ± 0.10
109	0.7	16.0	-0.02	0.3	-2.8	-2.2	0.410 ± 0.002	12.46 ± 0.15
110	0.7	16.0	-0.03	0.4	-2.9	-2.2	0.343 ± 0.002	15.85 ± 0.18
112	0.7	16.0	-0.02	0.3	-2.9	-2.3	0.362 ± 0.000	11.09 ± 0.02
113	0.7	16.0	-0.14	0.9	-9.0	-7.4	0.534 ± 0.003	4.80 ± 0.05
114	0.7	16.0	-0.03	0.3	-3.1	-2.4	0.372 ± 0.001	12.48 ± 0.05
115	0.7	16.0	-0.25	1.2	-10.5	-8.4	0.544 ± 0.001	5.78 ± 0.02
116	0.7	16.0	-0.07	0.5	-4.4	-3.5	0.377 ± 0.003	10.31 ± 0.15
117	0.7	16.0	-0.18	0.9	-8.1	-6.5	0.442 ± 0.001	6.03 ± 0.03

Table 5.7: Results of least-squares fitting to Figure 5.17

Region	a	b	Red. χ^2
L1147/L1158	11.4 ± 1.9	0.60 ± 0.02	11.60
L1174	28.9 ± 8.3	0.55 ± 0.03	7.63
L1172	26.4 ± 13.1	0.53 ± 0.04	0.16
L1251	36.1 ± 3.4	0.55 ± 0.01	25.31
L1228	22.3 ± 2.9	0.56 ± 0.01	3.39
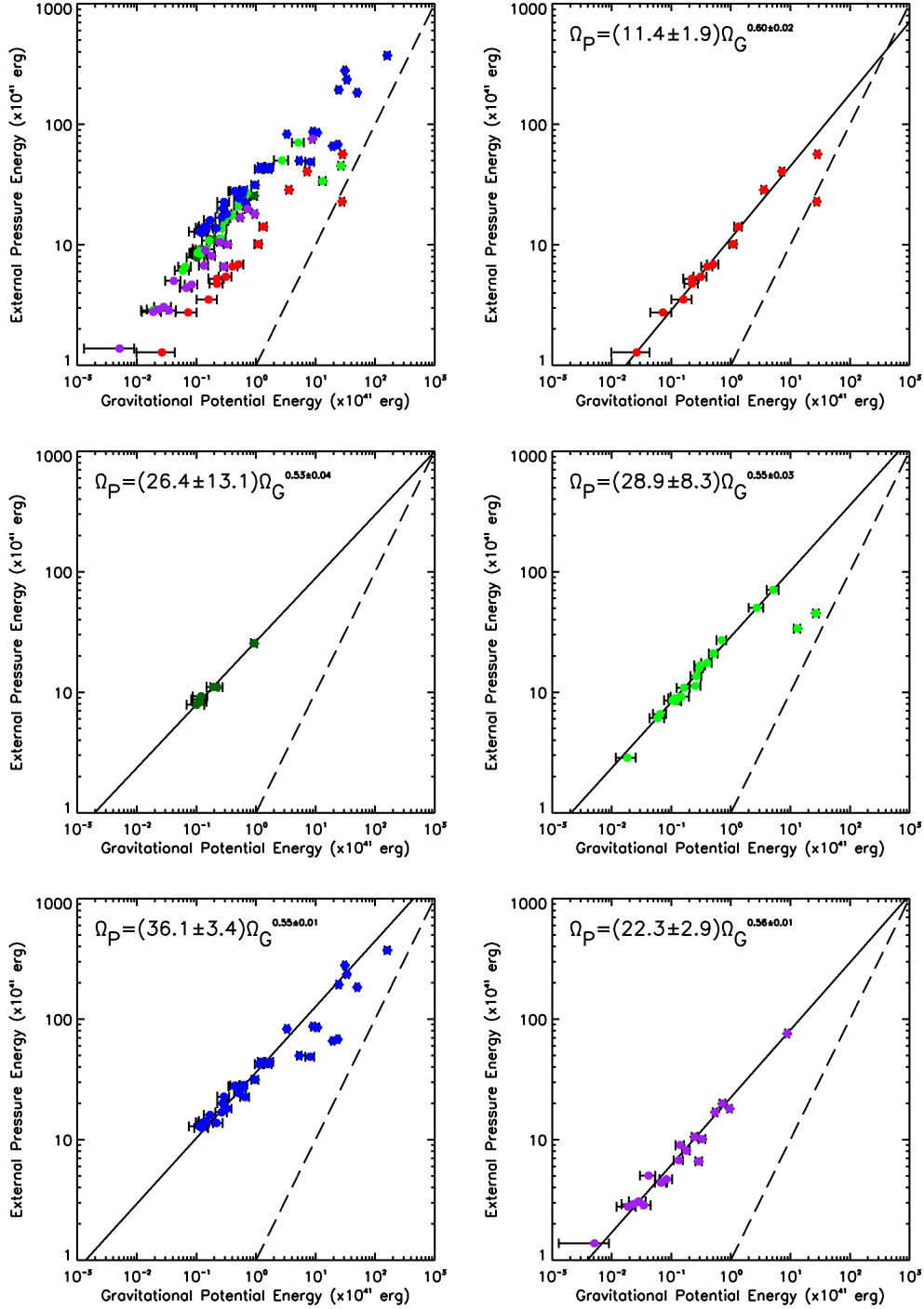
Figure 5.17: Comparison of gravitational potential energies and external pressure energies determined from Yonekura et al. (1997) measurements for our sources. The top left panel shows all of the cores. The top right panel shows the cores in L1147/58. The centre left panel shows the cores in L1172. The centre right panel shows the cores in L1174. The bottom left panel shows the cores in L1251. The bottom left panel shows the cores in L1228. In each panel, the dashed line shows the 1:1 line. For each region, the solid line shows the best-fit power-law relation between gravitational potential energy and external pressure energy of the cores.

5.6.1 Relation between gravitational potential energy and external pressure energy

The gravitational potential energies and external pressure energies are plotted against one another in Figure 5.17. It can be seen that in all but one case, $\Omega_P > \Omega_G$, i.e. our cores are generally pressure-confined. Furthermore, it can be seen that for the majority of our cores, there is a strong correlation between Ω_G and Ω_P. We fitted this relationship for each region using a non-linear least-squares fitting routine (*mpfit*; Markwardt 2009) and a power-law model:

$$\Omega_P = a\Omega_G^b. \tag{5.12}$$

The best-fit model for each region is listed in Table 5.7. The weighted average of the best-fit power-law indices is $b = 0.55 \pm 0.01$, i.e.

$$\Omega_P \propto \Omega_G^{0.55}. \tag{5.13}$$

This behaviour is a consequence of our model of external pressure energy,

$$\Omega_P = -4\pi P_{\text{EXT}}\alpha^3 \left[\ln \left(\frac{1}{2\sqrt{2}\pi^{3/2}\rho_{13\text{CO}}} \frac{M}{\alpha^3} \right) \right]^{3/2}. \tag{5.14}$$

For convenience, we define

$$k = \frac{1}{2\sqrt{2}\pi^{3/2}\rho_{13\text{CO}}}. \tag{5.15}$$

For $\rho_{13\text{CO}} = 10^4\,\text{cm}^{-3}$, $k = 1.329 \times 10^{15}\,\text{m}^3\text{kg}^{-1}$. The gravitational potential energy (equation 3.24) and external pressure energy (5.14) combine to give the ratio

$$\frac{\Omega_G}{\Omega_P} = \frac{G}{16\sqrt{2}\pi^{\frac{3}{2}}} P_{\text{EXT}}^{-1} M^2 \alpha^{-4} \ln \left(kM\alpha^{-3} \right)^{-3/2}. \tag{5.16}$$

This function has a minimum at

$$M\alpha^{-3} = \frac{\text{e}^{9/8}}{k}, \tag{5.17}$$

i.e. at that minimum,

$$\alpha \propto M^{1/3} \tag{5.18}$$

and hence equation 5.16 reduces to

$$\Omega_P \propto \Omega_G^{3/5},\tag{5.19}$$

very similar to the weighted mean $\Omega_P - \Omega_G$ index of 0.55 ± 0.01 which we measure for our cores, and within our measured range of indices (see Table 5.7).

While equation 5.19 holds exactly only at the minimum of Ω_G/Ω_P, for strongly pressure-dominated cores, Ω_G/Ω_P is a very weak function of α for a wide range of α values around $\alpha_{min} = (kMe^{-9/8})^{1/3}$. This behaviour is shown in Figure 5.18, and can be seen from the rate of change of Ω_G/Ω_P as a function of α,

$$\frac{\partial}{\partial \alpha}\left(\frac{\Omega_G}{\Omega_P}\right) = \frac{G}{16\sqrt{2}\pi^{\frac{3}{2}}}M^2 P_{EXT}^{-1}\alpha^{-5}\ln\left(kM\alpha^{-3}\right)^{-\frac{3}{2}}\left(\frac{9}{2}\ln\left(kM\alpha^{-3}\right)^{-1} - 4\right).\tag{5.20}$$

While $(G/16\sqrt{2}\pi^{1.5})M^2 P_{EXT}^{-1} \ll \alpha^5$ and $\alpha \ll (kM)^{\frac{1}{3}}$, the gradient will be small, and Ω_G/Ω_P will be a weak function of α. The first of these two requirements, $(G/16\sqrt{2}\pi^{1.5})M^2 P_{EXT}^{-1} \ll \alpha^5$, comes from the α^{-5} term in equation 5.20, which causes a steep power-law drop-off in $\partial(\Omega_G/\Omega_P)/\partial\alpha$ as α increases. The second requirement, $\alpha \ll (kM)^{\frac{1}{3}}$, is a result of the term $\ln(kM\alpha^{-3}) \to 0$ as $kM\alpha^{-3} \to 1$. As discussed in the following chapter, $kM\alpha^{-3} = 1$ means that the central density of the core is equal to the density of the surrounding material, at which point the model ceases to have any physical meaning. The result of approaching this cutoff is a sharp decrease in external pressure energy with increasing α (as shown in Figure 5.18), and hence an increase in $\partial(\Omega_G/\Omega_P)/\partial\alpha$.

The behaviour of Ω_G/Ω_P is more clearly seen by examining the Taylor expansion of equation 5.16 around its minimum, $\alpha_{min} = (kMe^{\frac{9}{8}})^{\frac{1}{3}}$. The Taylor expansion is given, up to the term in $(\alpha - \alpha_{min})^2$, by

$$\frac{\Omega_G}{\Omega_P} = \frac{G}{16\sqrt{2}\pi^{\frac{3}{2}}}\left(\frac{9}{8}\right)^{\frac{3}{2}}\left[\left(ke^{\frac{9}{8}}\right)^{\frac{4}{3}}\frac{M^{\frac{2}{3}}}{P_{EXT}} + \frac{32}{3}\left(ke^{\frac{9}{8}}\right)^{-2}\frac{(\alpha - \alpha_{min})^2}{P_{EXT}}\right]\tag{5.21}$$

which holds while $|\alpha - \alpha_{min}|/\alpha_{min} \ll 1$, and which becomes, for $k = 1.329 \times 10^{15}\,\mathrm{m^3 kg^{-1}}$,

$$\frac{\Omega_G}{\Omega_P} = 1.361 \times 10^{-32}\frac{M^{\frac{2}{3}}}{P_{EXT}} + 2.542 \times 10^{-41}\frac{(\alpha - \alpha_{min})^2}{P_{EXT}}.\tag{5.22}$$
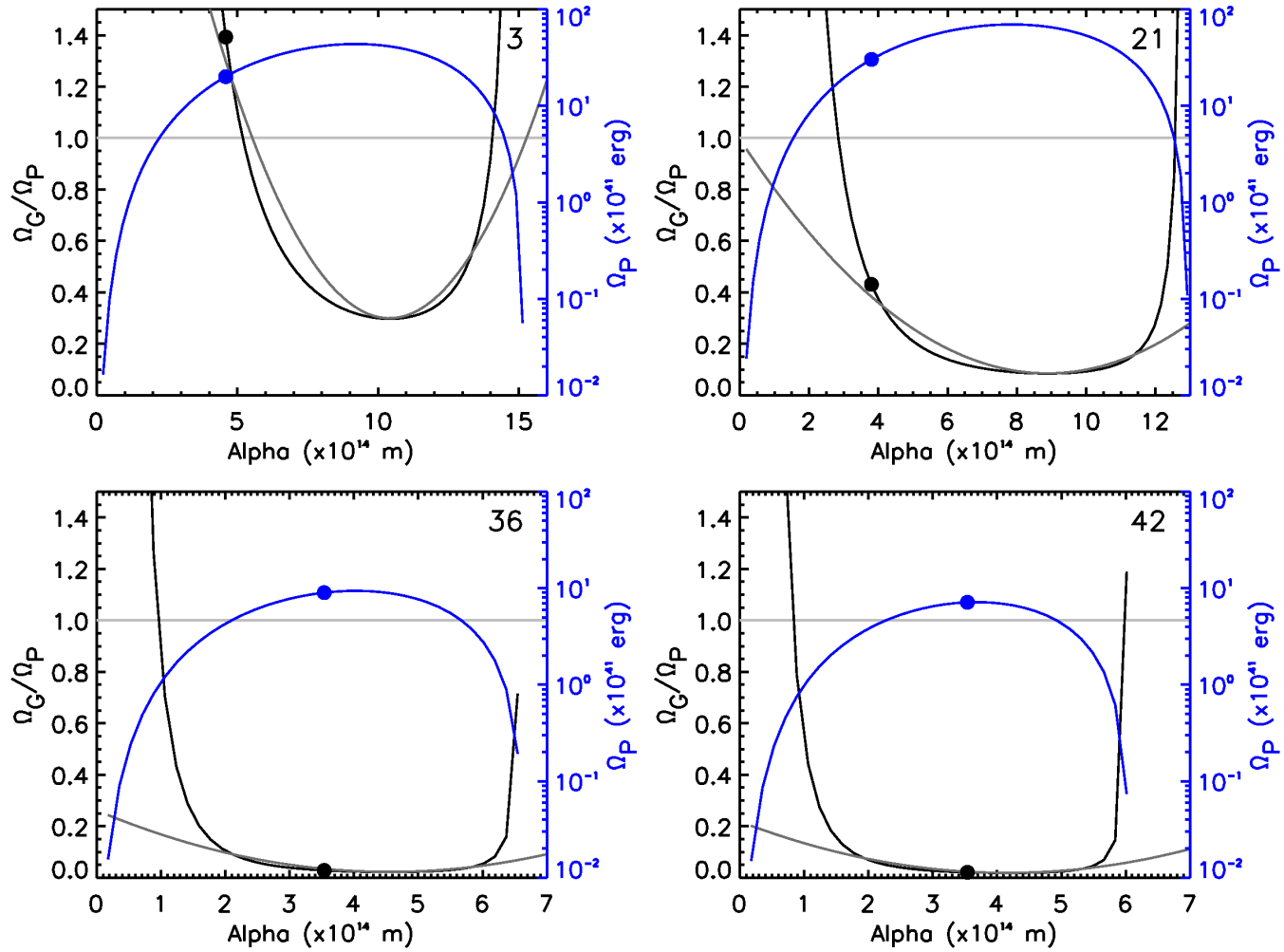
Figure 5.18: The behaviour of $\Omega_{\mathrm{G}}/\Omega_{\mathrm{P}}$ (black) and Ω_{P} (blue) as a function of Gaussian width α, for Sources 3, 21, 36 and 42. Solid circles mark measured values; lines show predicted behaviour as a function of α. The dark grey line shows the second-order Taylor expansion of $\Omega_{\mathrm{G}}/\Omega_{\mathrm{P}}$ around the minimum (see equation 5.22). The light grey line shows the point at which $\Omega_{\mathrm{G}} = \Omega_{\mathrm{P}}$.

Thus, the higher the external pressure P_{EXT}, the weaker the dependence of the $\Omega_{\text{G}}/\Omega_{\text{P}}$ ratio on α around the minimum. From this result we suggest that equation 5.19 might be expected to hold approximately for any strongly pressure-dominated core, even if it is not precisely maximally pressure-bound.

Some examples of cores which do and do not obey the relation given in equation 5.19 are shown in Figure 5.18. The top two panels show cores which do not obey the relation; the bottom two panels show cores which do. It can be seen that those cores which obey the relation are strongly pressure-confined objects, sitting in the 'flat', strongly pressure-dominated region of the $\Omega_{\text{P}}/\Omega_{\text{G}}$ curve. The cores which do not obey the relation occupy the 'transition' region of the $\Omega_{\text{P}}/\Omega_{\text{G}}$ relation, between pressure- and gravity-dominated behaviour. Those cores which do not obey equation 5.19 are the most gravitationally-dominated cores in our sample, and hence the best candidates in our sample to be gravitationally unstable and undergoing prestellar collapse. These potentially prestellar cores are: Source 3 in L1147/L1158, Sources 21 and 26 in L1174 and Sources 58, 59, 62 and 64 in L1251. Source 4 in L1147/58 and Sources 60, 66, 68 and 71 in L1251 also appear to deviate somewhat from equation 5.19. All of the cores in L1172 and L1228 obey equation 5.19, suggesting that these regions may not be forming stars as actively as the other regions.

We tested the validity of this analysis by fitting a power-law to the mass-radius relation for each region. The results are shown in Figure 5.19. We fitted only those cores which obey equation 5.19, i.e. the cores we consider to be strongly pressure-confined, for which we predict a mass-size relation $\alpha \propto M^{1/3}$. The cores which we excluded are lightly shaded in Figure 5.19. Fitting all of the strongly pressure-confined cores simultaneously, we found $\alpha \propto M^{0.37}$. Fitting each region individually gave indices of 0.39 in L1147/58, 0.43 in L1174, 0.23 in L1172, 0.28 in L1251, and 0.31 in L1228. The average of these values is 0.33 ± 0.08, very close to the predicted index of $\frac{1}{3}$, suggesting that our analysis is valid.
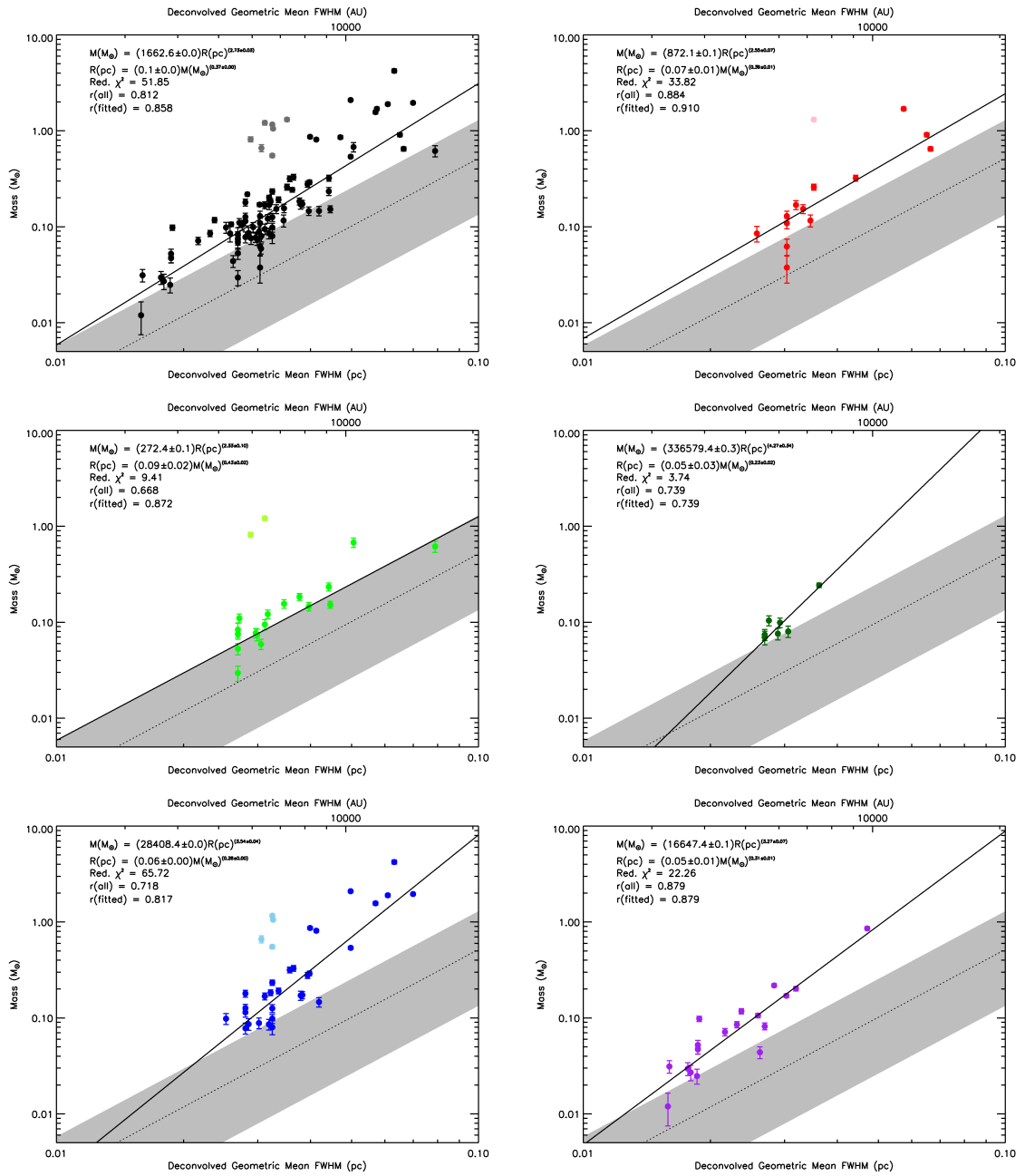
Figure 5.19: Fitted mass/size plots. Colour coding as in previous figures. Lightly-shaded points excluded from fitting, as they are candidates for gravitational instability.

We note that a mass-size relation $\alpha \propto M^{1/3}$ would imply a constant core density across all the cores in each region of our sample. Inspection of Figure 5.8 shows that while the majority of the cores to which equation 5.13 applies occupy a relatively narrow range in density, there is a clear spread. We note that we do not expect equations 5.19 and 5.18 to hold precisely for any of our cores, and the model above would apply exactly only if all of our cores were precisely maximally pressure-confined, and all bounded by a single external pressure. We do not expect either of these to be precisely the case, and so the scatter in density seen in Figure 5.8 is not an unexpected result.

It must be noted that this analysis tells us only that the cores which obey equation 5.19 are strongly pressure-confined objects, and does not tell us about their virial state. The strength of the correlations shown in Figure 5.17 is at least in part due to our assumption of a single velocity dispersion in each region of Cepheus, the result of which is that P_{EXT} is a constant over each region. While we designate some of our cores as likely to be prestellar based on this analysis, we do so based on their high ratio of gravitational energy to external pressure energy. As we discuss in the following chapter, this model typically predicts the most pressure-confined cores to be virially unstable and undergoing pressure-driven collapse. However, in this work we consider cores to be prestellar only if they are collapsing under gravity.

There are a number of well-known relations between core size, mass, internal velocity dispersion (referred to as σ_{INT} for the remainder of the chapter, for clarity) and it is worth considering whether the relation given in equation 5.18 can be derived from these. The linewidth-size relation,

$$\sigma_{\mathrm{INT}} \propto R^{\eta} \tag{5.23}$$

where for molecular clouds $\eta = 0.38$ (Larson 1981), and for cores $\eta = 0.5$ (Solomon et al. 1987), and the linewidth-mass relation,

$$\sigma_{\mathrm{INT}} \propto M^{0.2} \tag{5.24}$$

(Larson 1981), combine to give

$$R \propto M^{0.2/\eta} \tag{5.25}$$

$$\propto M^{0.4} \qquad (\eta = 0.5) \tag{5.26}$$

$$\propto M^{0.53} \qquad (\eta = 0.38). \tag{5.27}$$

Neither of these values match our measured dependence of M upon α, suggesting that this result cannot be explained using the traditional Larson relations alone.

5.6.2 Virial stability of cores in Cepheus

Our best estimate of the virial plane for Cepheus is shown in Figure 5.20. It must be stressed that the values shown for the virial ratio $-(\Omega_G + \Omega_P)/2\Omega_K$ are upper limits; Figure 5.20 shows the greatest extent to which our cores could be virially bound. Figure 5.20 shows that our cores are not thermally supported: in the absence of non-thermal internal energy and/or an internal magnetic field, $-(\Omega_G + \Omega_P) > 2\Omega_K$ in all cases. Our results suggest that there is one gravitationally-bound prestellar core amongst our sample: core 3 in L1147/L1158, for which $\Omega_G > \Omega_P$ and $-(\Omega_G + \Omega_P) > 2\Omega_K$, and which does not obey the $\Omega_P \propto \Omega_G^{0.55}$ relation.

5.7 Summary

In this chapter we have extracted sources from the SCUBA-2 data of the L1147/L1158, L1172/L1174, L1251 and L1228 regions of the Cepheus Flare. We have characterised our sources using their 850-μm flux densities and temperatures supplied by the Herschel GBS. We have compared the properties of cores in the different Cepheus Flare regions in order to determine the mode of star formation proceeeding in each region. We have determined the relative importance of gravity and external pressure in confining our cores, and have determined an upper limit on the degree to which our cores are virially bound.
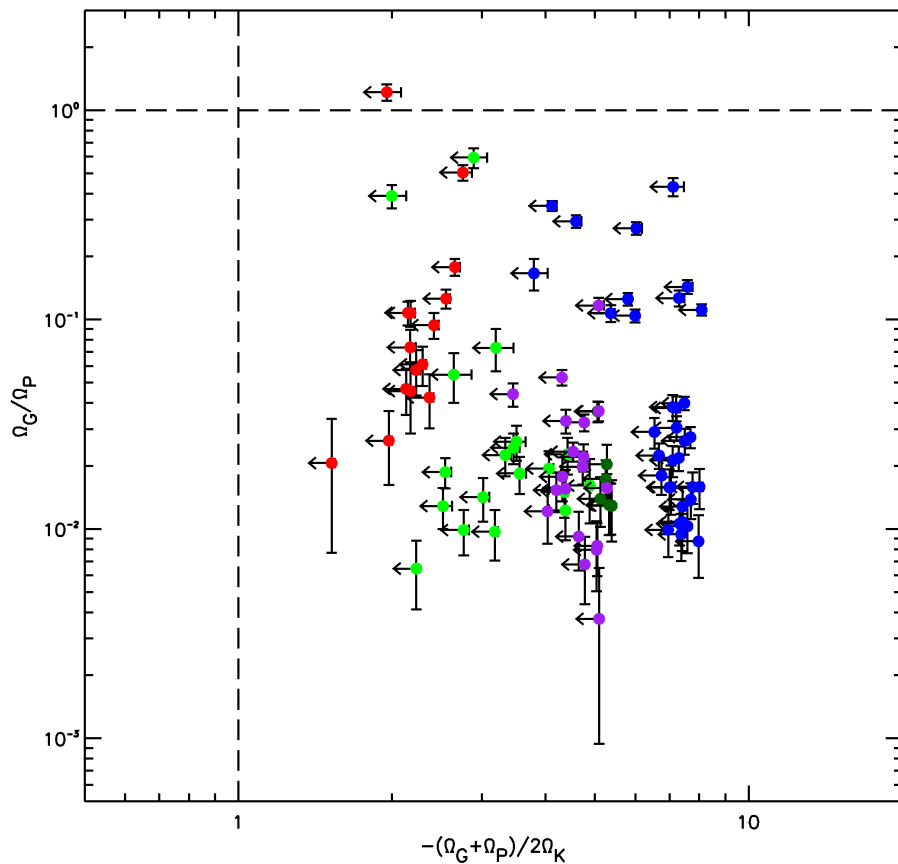
Figure 5.20: The virial stability plane for the starless cores in Cepheus. Virial stability ratio is plotted on the x axis. The ratio of gravitational potential energy to external pressure energy is plotted on the y axis. The vertical dashed line indicates the line of virial stability, with the right-hand side of the plot being bound and the left side being unbound. The horizontal dashed line marks equipartition between external pressure energy and gravitational potential energy; cores above the line are gravitationally bound, while cores below the line are pressure-confined.

We identified 117 sources across the Cepheus Flare region using the CSAR source extraction algorithm, of which 23 were associated with a protostar in the Kirk et al. (2009) Spitzer catalogue. Of our 117 sources, 20 were located in L1147/L1158, 26 in L1174, 9 sources in L1172, 42 in L1251 and 20 in L1228. We determined the best-fit flux densities of our sources using the multiple-Gaussian fitting algorithm described in Chapter 3.

We determined masses for each of our sources using our best-fit flux densities and temperatures supplied by the Herschel GBS. We found that our cores typically lie in the 'prestellar' part of the mass/size plane. Our cores typically have temperatures in the range $\sim 9 - 15\,\mathrm{K}$, with the exception of cores associated with the L1174 reflection nebula, which have temperatures up to $\sim 50\,\mathrm{K}$.

We analysed the cumulative distribution functions of core masses for each region in Cepheus, using the maximum likelihood estimator for an infinite power-law distribution, and found that the core mass function in each region shows a sub-Salpeter power-law behaviour, with the exceptions of L1228, which has a power-law index consistent with the Salpeter IMF, and L1172, for which an accurate power-law index could not be determined. Determining the power-law index over all cores, we found a sub-Salpeter value of $\alpha = 1.88 \pm 0.09$ over the mass range $M > 0.08\,\mathrm{M_\odot}$. For the highest-mass cores, we found a CMF power-law index $\alpha = 2.61 \pm 0.27$ over the mass range $M > 0.08\,\mathrm{M_\odot}$ (again determined over all cores), marginally consistent with the Salpeter IMF.

We compared the number of starless cores detected in each region with the numbers of embedded and Class II sources found by Kirk et al. (2009). We found that L1147/L1158 and L1228 have a high ratio of starless cores to Class II sources, while L1251 and L1174 have a low ratio. This is consistent with L1174 and L1251 being active sites of star formation, while L1147/L1158 and L1228 form stars in a more quiescent mode.

We determined the Bonnor-Ebert critically-stable masses of our cores, and the associated BE-critical external pressure. We found that the Bonnor-Ebert model predicts that most of our cores have stable BE solutions accessible to them. The BE model predicts higher external pressures in L1174 and in L1228 than in the other regions, although in L1228 this may be the result of the assumed distance.

We determined the external pressure on our cores using ^{13}CO velocity dispersion measurements determined by Yonekura et al. (1997). We found that almost all of our cores had substantially higher external pressures than those predicted by the Bonnor-Ebert model.

We found that all but one of our cores are pressure-confined, rather than gravitationally bound, and that for the majority of our cores there is a power-law relation between the external pressure energy and the gravitational energy, $\Omega_P \propto \Omega_P^{0.55}$. We infer from this that those of our cores which obey this relation are strongly pressure-dominated, and those which do not obey the relation are the best candidates in our sample to be undergoing gravitational collapse.

We performed a virial analysis of our cores, and found that our cores cannot be supported by internal thermal energy alone: in the absence of non-thermal internal motions or an internal magnetic field, all of our cores would be substantially virially bound and collapsing.

Chapter 6

Discussion

6.1 Comparison of regions

We now compare the properties we have measured and derived for the starless cores detected in each region in order to compare the three star-forming regions studied in this thesis. We begin by comparing the properties determined from continuum observations: size, mass, temperature and volume density. The mean, standard deviation, median, maximum and minimum values of each of these properties in each star-forming region and each sub-region (as defined in Chapters 3, 4 and 5) are listed in Tables 6.1 (temperature and mass) and 6.2 (size and density).

Figure 6.1 shows the mass/size plane, with the starless cores in Ophiuchus plotted in black, the Taurus cores plotted in red, and the Cepheus cores plotted in blue. This colour coding is maintained throughout this chapter. It can be seen from Figure 6.1 that cores in all three regions have a similar range of masses: $\langle M \rangle_{\text{Oph}} = 0.27\,\text{M}_\odot$, s.d.$=\ 0.28\,\text{M}_\odot$; $\langle M \rangle_{\text{Tau}} = 0.19\,\text{M}_\odot$, s.d.$=\ 0.14\,\text{M}_\odot$; and $\langle M \rangle_{\text{Cep}} = 0.38\,\text{M}_\odot$, s.d.$=$ $0.61\,\text{M}_\odot$. We list the mean and standard deviation values in order to illustrate the range of masses seen in each region. However, as discussed in previous chapters, the mass distribution of starless cores typically shows power-law behaviour at high masses. The relevance of the mean value of a power-law distribution is limited; the

289

Table 6.1: Regional comparison: temperature and mass

Cloud	Region	Cores	Temperature (K)					Mass (M$_\odot$)				
			Mean	S.D.	Median	Max.	Min	Mean	S.D.	Median	Max.	Min.
Ophiuchus	Oph A	7	18.6	1.5	18.4	21.7	17.2	0.66	0.41	0.75	1.30	0.26
	Oph A'	10	17.4	3.0	16.3	22.9	14.8	0.09	0.08	0.09	0.30	0.03
	Oph B1	4	12.0	0.2	12.1	12.2	11.8	0.20	0.11	0.27	0.29	0.06
	Oph B2	9	11.2	0.6	11.4	11.8	10.3	0.41	0.24	0.35	0.79	0.13
	Oph C	3	12.7	0.4	12.8	13.2	12.3	0.14	0.09	0.09	0.24	0.08
	Oph E	1	13.6	–	13.6	13.6	13.6	0.15	–	0.15	0.15	0.15
	Oph F	1	15.3	–	15.3	15.3	15.3	0.05	–	0.05	0.05	0.05
	L1688	1	11.0	–	11.0	11.0	11.0	0.36	–	0.36	0.36	0.36
	L1689 N	3	12.3	1.1	11.8	13.6	11.5	0.24	0.16	0.23	0.40	0.08
	L1689 S	6	12.5	1.1	12.5	14.3	11.3	0.12	0.08	0.12	0.25	0.04
	L1709	1	11.0	–	11.0	11.0	11.0	0.09	–	0.09	0.09	0.09
	All	**46**	**14.2**	**3.3**	**12.8**	**22.9**	**10.3**	**0.27**	**0.28**	**0.17**	**1.30**	**0.03**
Taurus	East	6	13.4	3.4	12.9	19.6	10.7	0.20	0.21	0.18	0.61	0.02
	Centre	9	10.8	1.0	10.7	12.7	9.3	0.22	0.12	0.20	0.42	0.11
	West	4	14.0	2.0	14.4	16.1	11.2	0.10	0.06	0.13	0.16	0.03
	North	3	12.1	1.2	12.0	13.4	11.0	0.23	0.15	0.20	0.39	0.10
	South	3	11.8	1.0	11.4	12.9	11.1	0.17	0.14	0.12	0.32	0.07
	All	**25**	**12.2**	**2.3**	**11.2**	**19.6**	**9.3**	**0.19**	**0.14**	**0.13**	**0.61**	**0.02**
Cepheus	L1147/58	15	11.8	0.7	11.5	13.3	10.6	0.42	0.51	0.17	1.70	0.04
	L1172	7	12.5	0.3	12.5	12.9	11.8	0.11	0.06	0.08	0.24	0.07
	L1174	19	19.1	4.1	18.9	26.9	11.9	0.26	0.32	0.12	1.21	0.03
	L1251	34	11.8	0.8	11.9	13.5	10.2	0.62	0.87	0.23	4.22	0.08
	L1228	19	12.4	0.7	12.4	13.7	11.3	0.12	0.19	0.07	0.86	0.01
	All	**94**	**13.4**	**3.4**	**12.3**	**26.9**	**10.2**	**0.38**	**0.61**	**0.15**	**4.22**	**0.01**

Table 6.2: Regional comparison: size and density

Cloud	Region	Cores	FWHM (pc)					H_2 Vol. Density ($\times 10^4\,\mathrm{cm}^{-3}$)				
			Mean	S.D.	Median	Max.	Min	Mean	S.D.	Median	Max.	Min.
Ophiuchus	Oph A	7	0.011	0.003	0.012	0.015	0.007	340.1	453.5	79.0	1039.8	29.8
	Oph A′	10	0.011	0.004	0.012	0.015	0.003	57.6	102.8	25.6	346.8	10.6
	Oph B1	4	0.010	0.003	0.012	0.012	0.005	82.9	58.0	61.4	169.5	47.7
	Oph B2	9	0.011	0.004	0.012	0.015	0.003	417.9	719.2	82.0	2100.8	37.6
	Oph C	3	0.011	0.003	0.013	0.013	0.008	33.8	15.5	39.5	45.7	16.3
	Oph E	1	0.011	–	0.011	0.011	0.011	43.3	–	43.3	43.3	43.3
	Oph F	1	0.003	–	0.003	0.003	0.003	450.1	–	450.1	450.1	450.1
	L1688	1	0.012	–	0.012	0.012	0.012	62.6	–	62.6	62.6	62.6
	L1689 N	3	0.007	0.003	0.008	0.010	0.003	1177.6	1874.7	162.4	3340.9	29.5
	L1689 S	6	0.008	0.004	0.011	0.013	0.003	170.2	198.6	72.0	469.3	21.7
	L1709	1	0.007	–	0.007	0.007	0.007	94.2	–	94.2	94.2	94.2
	All	**46**	**0.010**	**0.004**	**0.011**	**0.015**	**0.003**	**268.6**	**603.4**	**61.4**	**3340.9**	**10.6**
Taurus	East	6	0.027	0.006	0.031	0.032	0.018	3.4	2.7	3.0	7.0	0.7
	Centre	9	0.025	0.006	0.023	0.034	0.018	5.2	2.6	4.0	9.4	1.7
	West	4	0.020	0.004	0.021	0.026	0.017	4.4	4.1	2.9	10.6	1.7
	North	3	0.031	0.003	0.031	0.034	0.028	2.5	1.3	3.0	3.4	1.1
	South	3	0.027	0.004	0.029	0.030	0.023	2.5	1.2	1.9	4.0	1.7
	All	**25**	**0.026**	**0.006**	**0.026**	**0.034**	**0.017**	**4.0**	**2.7**	**3.0**	**10.6**	**0.7**
Cepheus	L1147/58	15	0.039	0.013	0.035	0.066	0.026	2.0	2.4	1.4	10.2	0.5
	L1172	7	0.030	0.003	0.029	0.036	0.027	1.3	0.3	1.3	1.7	0.9
	L1174	19	0.036	0.013	0.031	0.079	0.027	2.3	3.7	1.1	13.6	0.4
	L1251	34	0.038	0.011	0.033	0.070	0.025	2.9	2.6	1.9	11.5	0.7
	L1228	19	0.024	0.007	0.022	0.047	0.016	2.3	0.9	2.3	5.0	0.8
	All	**94**	**0.034**	**0.012**	**0.031**	**0.079**	**0.016**	**2.4**	**2.5**	**1.7**	**13.6**	**0.4**

mean will be biased towards the less common high-mass cores. The median mass in each region is more representative of the mass of a typical core. The median masses are very similar in each region: $0.17\,M_\odot$ in Ophiuchus, $0.13\,M_\odot$ in Taurus, and $0.15\,M_\odot$ in Cepheus.

Figure 6.1 further shows that while cores in Taurus and Cepheus have similar radii ($\langle\alpha\rangle_{\rm Tau} = 0.026\,{\rm pc}$, s.d.= $0.006\,{\rm pc}$; $\langle\alpha\rangle_{\rm Cep} = 0.034\,{\rm pc}$, s.d.= $0.012\,{\rm pc}$), cores in Ophiuchus are consistently smaller, with $\langle\alpha\rangle_{\rm Oph} = 0.010\,{\rm pc}$, s.d.= $0.004\,{\rm pc}$. There is no overlap in size range between Ophiuchus and either Taurus or Cepheus. While cores in Taurus and Cepheus appear to typically have comparable sizes, there is a population of high-mass and large-size cores in Cepheus which does not have an equivalent in Taurus.

This difference in core size between Ophiuchus and the other two regions, along with the lack of difference in typical core mass, results in a significantly higher core density in Ophiuchus than in either Taurus and Cepheus. Figure 6.2 plots the volume density against the temperature for our cores. Cores in Taurus and Cepheus effectively occupy the same space in the temperature/density plane, while cores in Ophiuchus are distinct. Cores in all three regions occupy a similar temperature range, $\sim 9 - 30\,{\rm K}$, although Taurus has no cores with temperature $> 20\,{\rm K}$. The three regions have very similar mean temperatures: $\langle T\rangle_{\rm Oph} = 14.2\,{\rm K}$, s.d.= $3.3\,{\rm K}$; $\langle T\rangle_{\rm Tau} = 12.2\,{\rm K}$, s.d.= $2.3\,{\rm K}$; and $\langle T\rangle_{\rm Cep} = 13.4\,{\rm K}$, s.d.= $3.4\,{\rm K}$. Cores in Taurus and Cepheus have very similar volume densities: $\langle\rho\rangle_{\rm Tau} = 4.0 \times 10^4\,{\rm cm}^{-3}$, s.d.= $2.7 \times 10^4\,{\rm cm}^{-3}$; $\langle\rho\rangle_{\rm Cep} = 2.4 \times 10^4\,{\rm cm}^{-3}$, s.d.= $2.5 \times 10^4\,{\rm cm}^{-3}$. However, the factor of $\sim 2.5 - 3$ difference in typical characteristic radius between Ophiuchus on the one hand and Taurus and Cepheus on the other results in an increase in typical core density of 1–2 orders of magnitude in Ophiuchus.

The only continuum-derived property which appears to vary substantially between the different star-forming regions is core characteristic radius (and, hence,
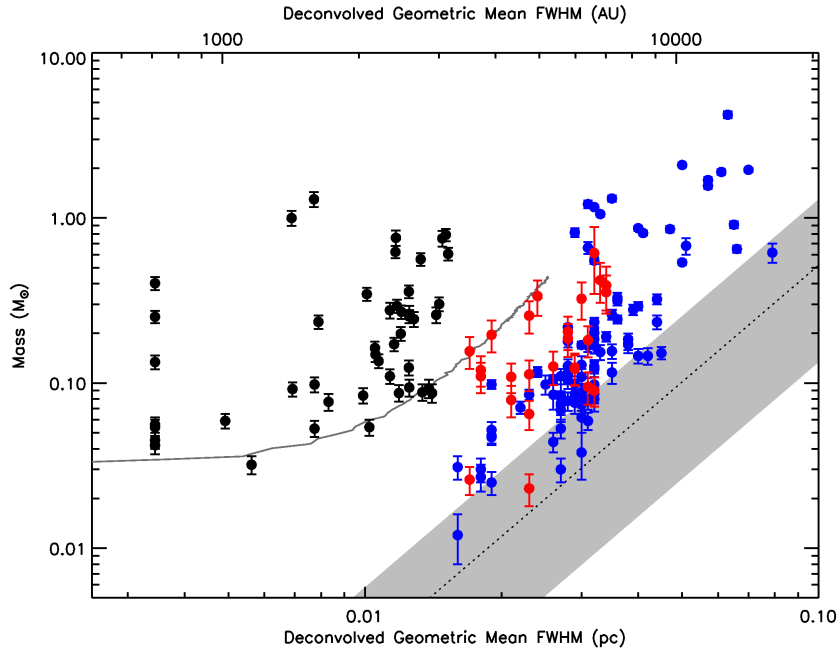
Figure 6.1: Mass-radius comparison. Black: Ophiuchus; Red: Taurus; Blue: Cepheus. Grey band: Elmegreen & Falgarone (1996). Grey line: Ophiuchus Cu-TEx 80% completeness limit. Note how the Ophiuchus cores are typically smaller in radius.
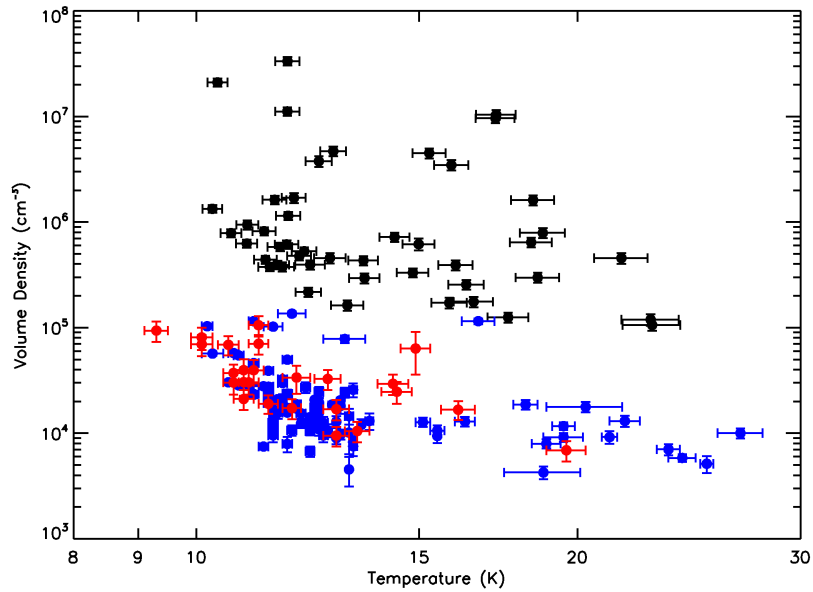
Figure 6.2: Temperature-density comparison. Black: Ophiuchus; Red: Taurus; Blue: Cepheus. Note how the Ophiuchus cores are generally higher-density.

293

core density). Figures 6.1 and 6.2 suggest that cores in Taurus and Cepheus have very similar properties, and might be considered to be part of the same population, while cores in Ophiuchus are a distinct population. This is an interesting result, particularly as Taurus and Cepheus are not particularly similar regions. Taurus is a single site of isolated star formation, while Cepheus shows star formation in several different environments: isolated and quiescent in L1147/L1158; driven or influenced by a reflection nebula in L1174; and induced by interaction with the Cepheus Flare Shell in L1251, for example. The fact that cores in disparate regions in Cepheus show similarity to cores in the Taurus molecular cloud might be explained by star formation in all of these cases apparently proceeding in a dispersed mode, whereas Ophiuchus is, at least in part, a site of clustered star formation.

Whether the difference in size between sources in Ophiuchus and sources in Taurus and Cepheus is the result of choice of source extraction algorithm must be considered, as sources were extracted from the Ophiuchus observations using CuTEx (Molinari et al. 2011), while cores in Taurus and Cepheus were extracted using CSAR (Kirk et al. 2013). However, in each region, the choice of source extraction algorithm was not arbitrary, but motivated by the physical conditions in the regions being considered. In Ophiuchus, CuTEx was chosen as the tightly-packed sources could not be separated by CSAR, which requires a closed contour around each source it identifies (Kirk et al. 2013). However, in Taurus and Cepheus, the cores are typically extended relative to the JCMT 850-µm beam, and isolated enough to have closed contours around them, making CSAR an appropriate choice.

The 80 percent completeness limit determined for Ophiuchus is shown on Figure 6.1. As discussed in Section 3.3.2, source detection with CuTEx is a function of both peak flux density and source size: the completeness limit shown on Figure 6.1 shows that the cores detected in Cepheus and Taurus have too low surface brightnesses to be detected using CuTEx, and hence CuTEx would not have been

Table 6.3: Source clustering properties

Cloud	Region	Minimum Separation (pc)		
		Mean	Median	S.D
Ophiuchus	L1688	0.073	0.043	0.101
	L1689	0.090	0.037	0.231
	All	0.114	0.039	0.388
Taurus	All	0.142	0.109	0.069
Cepheus	L1147/58	0.166	0.063	0.312
	L1172/74	0.089	0.066	0.082
	L1251	0.104	0.090	0.079
	L1228	0.109	0.097	0.075
	All	0.111	0.068	0.148

an appropriate choice of source extraction algorithm in these regions. Moreover, the completeness limit suggests that were there cores in Ophiuchus with radii similar to those seen in Taurus and Cepheus, some at least of them should have been detected with CuTEx, unless their masses were $\lesssim 0.1\,\mathrm{M_\odot}$ in every case. The CuTEx completeness limit suggests that the maximum core size seen in Ophiuchus is a physical result, and not a consequence of the choice of source extraction algorithm. This interpretation is borne out by examination of Figure 3.8, in which it can be seen that the core sizes we determine in Ophiuchus occupy the same range as those determined in previous studies (Motte et al. 1998; Simpson et al. 2011), despite these previous studies having used various different source extraction methods.

6.1.1 Clustering of sources

In the previous section, we asserted that Ophiuchus is a region of clustered star formation, while Taurus and Cepheus are dispersed. In this section, we quantify this statement. A visual inspection of the the three regions shows that sources in Ophiuchus are typically more tightly packed than those in Taurus and Cepheus (see Figures 3.4, 4.3, 4.4, 5.3, 5.4, 5.5, 5.6).
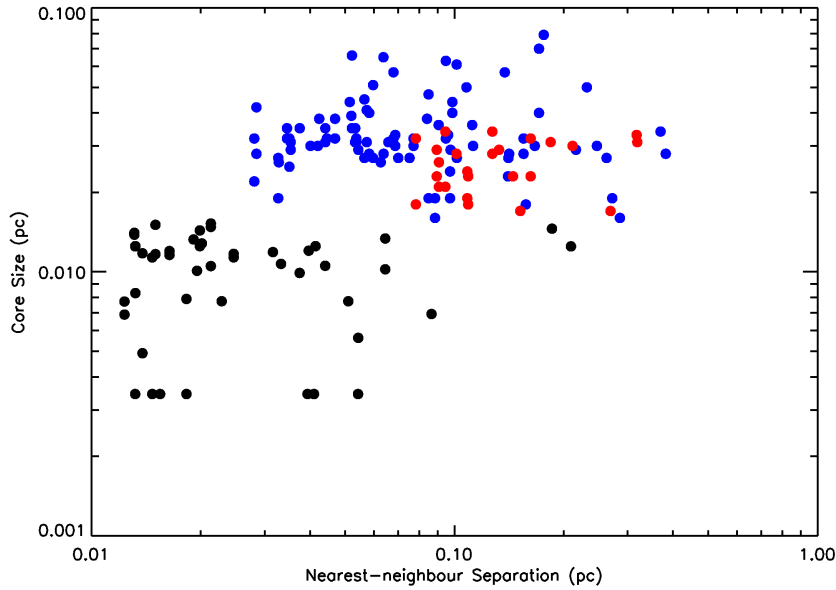
Figure 6.3: Core size against nearest-neighbour distance. Black: Ophiuchus; Red: Taurus; Blue: Cepheus.

We determined the separation between each of our sources (whether starless or protostellar) and its nearest neighbour. The results for each region are listed in Table 6.3. Nearest-neighbour separation is plotted against core size for the starless cores in our samples in Figure 6.3. Figure 6.3 shows that there are a few sources in Ophiuchus with very large separations from their nearest neighbours (in comparison with the majority of sources in Ophiuchus). These sources, lying in L1709, L1712 and L1689 East, significantly distort the mean core separation in Ophiuchus. Table 6.3 shows that the mean separation between sources in Ophiuchus is very similar to that in Cepheus, and comparable to that in Taurus, despite Figure 6.3 showing that there is a substantial population of cores in Ophiuchus with nearest-neighbour separations smaller than any seen in Taurus or Cepheus. Hence, we use the median source separation in the following discussion, as being more representative than the mean.

Figure 6.3 shows that cores in Ophiuchus typically have both smaller sizes and
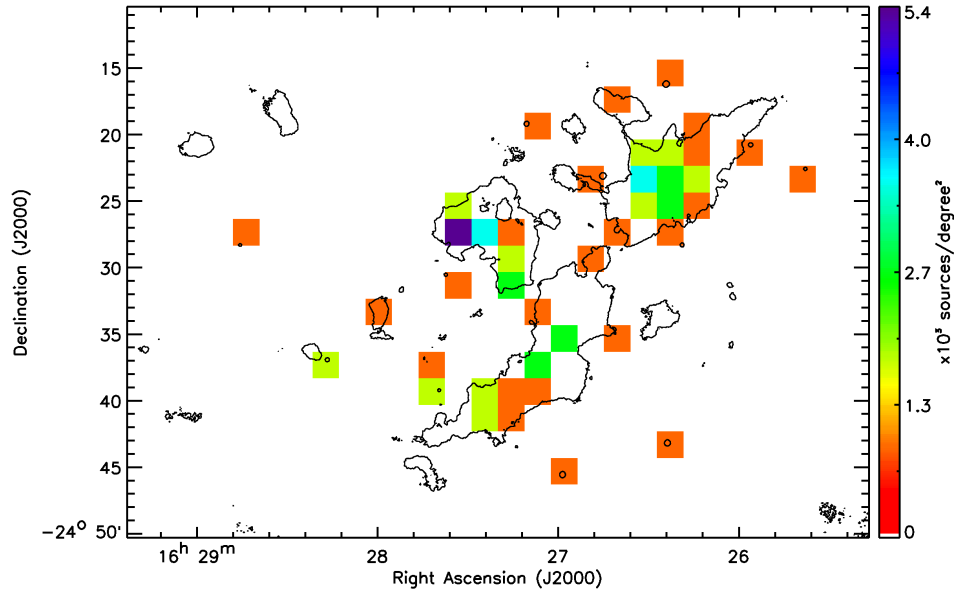
Figure 6.4: Surface density of sources in the L1688 region of Ophiuchus.

a smaller distance to their nearest neighbour than cores in Taurus and Cepheus. The populations of starless cores in Ophiuchus and Taurus are almost completely distinct from one another in terms of both their sizes and their nearest-neighbour separations. However, there is significant overlap between the nearest-neighbour separation distances in Ophiuchus and Cepheus, and also between Cepheus and Taurus.

Another sign of clustering is that as well as being closely packed, a region shows peaks in surface density of sources. If a region were to have a high, but uniform, surface density of sources, then it would not necessarily be considered to be clustered, as the sources would be evenly spaced. A sign of clustered star formation within a region is for the surface density of sources within that region to vary, with a high surface density of sources at certain sites (likely to be sites of active star formation), and a low surface density of sources elsewhere.

We determined the distribution of surface densities of sources in each region studied. The results for L1688 are shown in Figure 6.4, for L1689 and L1709 in
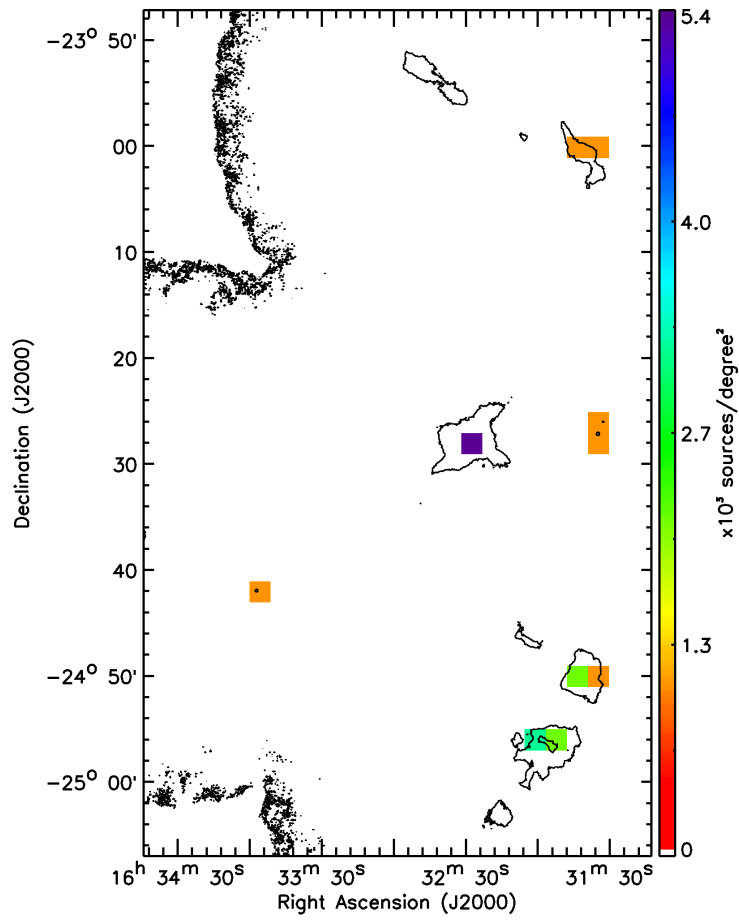
Figure 6.5: Surface density of sources in the L1689 and L1709 regions of Ophiuchus.
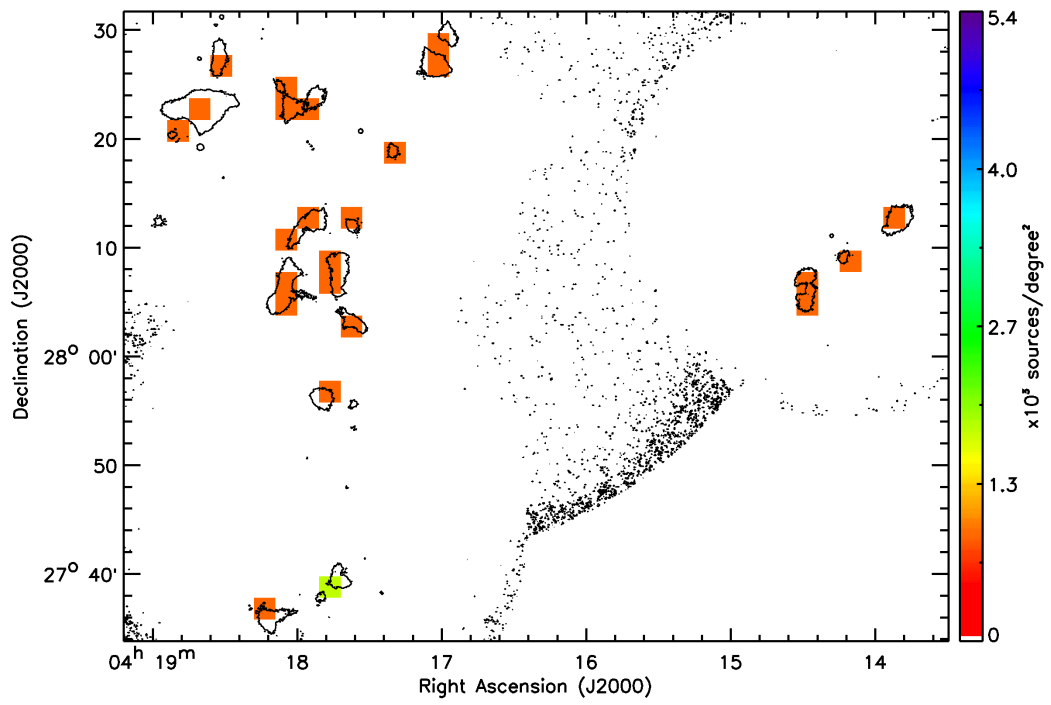
Figure 6.6: Surface density of sources in the L1495 region of Taurus.
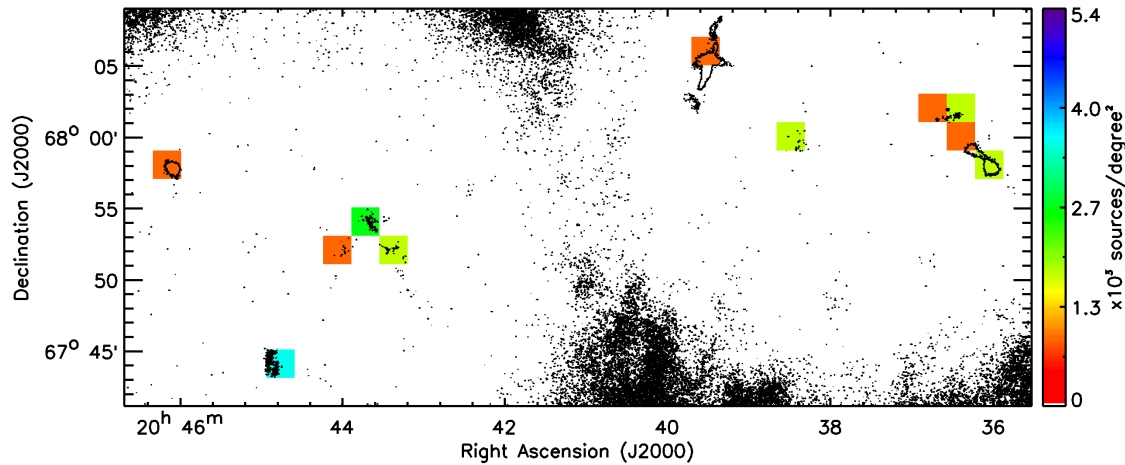
Figure 6.7: Surface density of sources in the L1147/58 region of Cepheus.

Figure 6.5, for L1495 in Figure 6.6, for L1147/58 in Figure 6.7, for L1172 and L1174 in Figure 6.8, for L1251 in Figure 6.9, and for L1228 in Figure 6.10. In each region, sources were counted in $2\,\mathrm{arcmin} \times 2\,\mathrm{arcmin}$ boxes.

The highest surface densities of sources can be found in Ophiuchus, and the lowest in Taurus, when considering surface density per unit solid angle. As these regions are at very similar distances, we can directly compare the surface densities which we observe in them. Ophiuchus also shows the greatest variation in surface density; Figures 6.4 and 6.5 show peaks in surface density of sources in Oph A, Oph B and L1689N, as well as enhancements in surface density along the Oph C-E-F 'filament' and in L1689S. Taurus, however, shows an almost perfectly flat distribution of source surface densities. All of this supports the interpretation of Ophiuchus as clustered, and Taurus as dispersed.

Direct comparison of surface densities in Cepheus to those in Taurus and Ophi-uchus is complicated by the increased distance to Cepheus compared to the other two regions. Figures 6.7, 6.8 and 6.9 show peaks in surface density of sources in
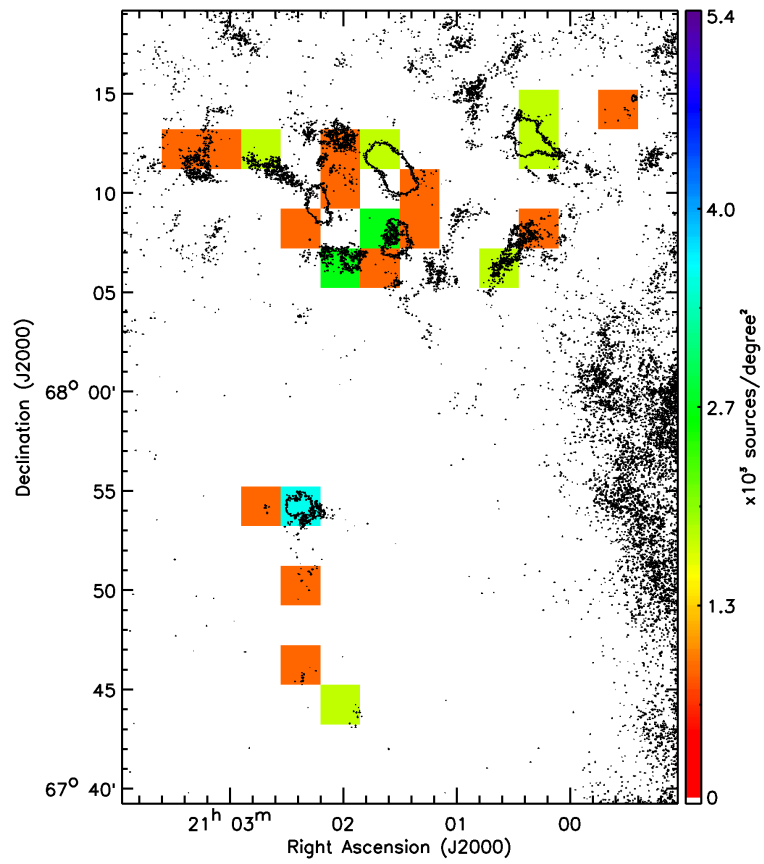
Figure 6.8: Surface density of sources in the L1172 and L1174 regions of Cepheus.
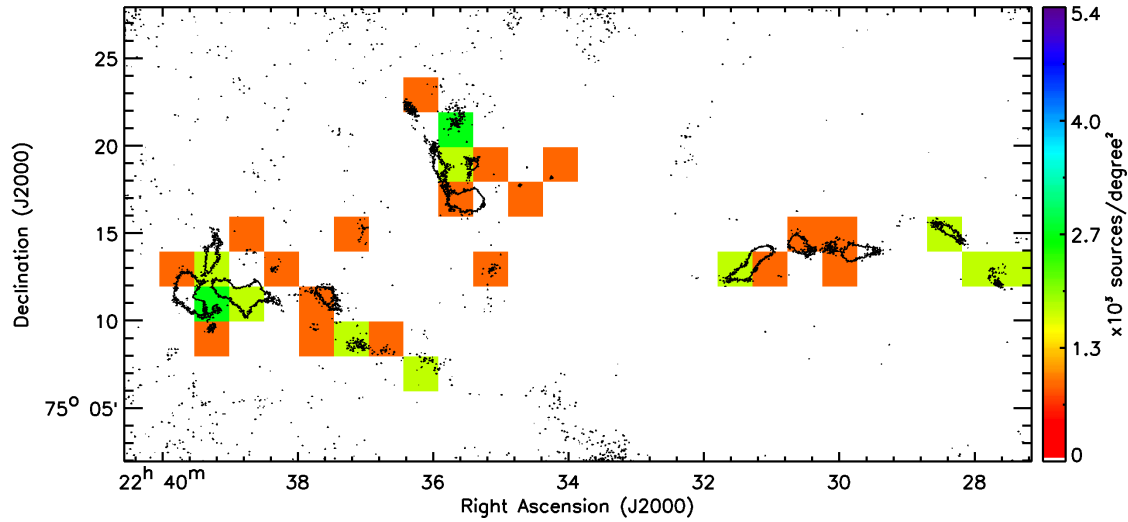
Figure 6.9: Surface density of sources in the L1251 region of Cepheus.

L1147/58, L1172 and L1174, and L1251 respectively, indicating a non-uniform distribution of sources. L1228 shows very little variation in surface density of sources (see Figure 6.10). However, despite the non-uniform source surface density distributions in most regions of Cepheus, surface densities (per unit solid angle) comparable to those in the moderately dense regions of Ophiuchus are only seen in L1172 and the southernmost region of L1155.

The increased distance to Cepheus compared to Ophiuchus has the effect of increasing the physical size of the region covered by a given solid angle. The surface density distribution of sources in Ophiuchus, shown in terms of solid angle in Figures 6.4 and 6.5, is equivalent to the range $\sim 150 - 1000\,\mathrm{pc}^{-2}$. However, in the various regions of Cepheus, a factor of $\sim 2 - 2.4$ times further from the Earth, the surface density distribution shown in Figures 6.7 to 6.10 is equivalent, in physical terms, to occupying a range $\sim 25 - 150\,\mathrm{pc}^{-2}$. Thus, while Cepheus shows some signs of clustering of sources, the source surface densities seen are almost an order of magnitude lower than those seen in Ophiuchus.

The increased distance to Cepheus also raises the possibility that the sources

302
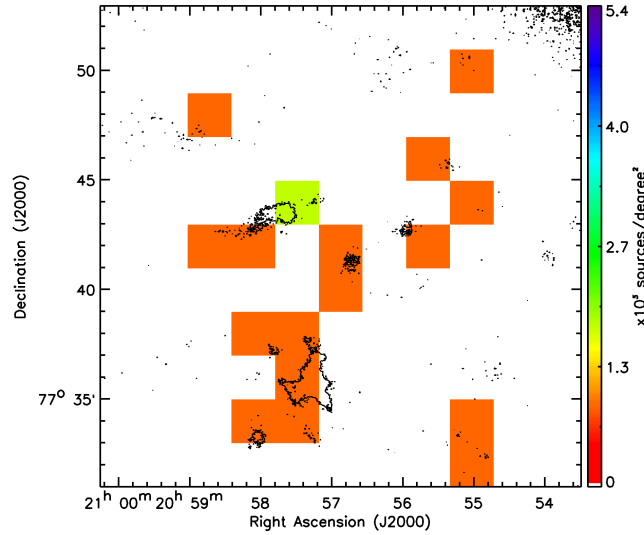
Figure 6.10: Surface density of sources in the L1228 region of Cepheus.

we are detecting are in fact multiple sources, which are not resolved by the JCMT 13.1-arcsec 850-μm beam. The larger source sizes and low source surface densities in Cepheus might thus be a distance effect: if observed at higher resolution, the clumps we observe might be resolved into multiple tightly-packed sources such as are seen in e.g Oph A or Oph B2 in Ophiuchus. This is true in at least one case: the cluster of protostars L1251B (Lee et al. 2006), which we detect as a single unresolved source. Whether this is the case for other sources is uncertain; we can discuss clustering in Cepheus only on the spatial scales which we observe with SCUBA-2.

Some regions in Cepheus are known to be clustered: the L1174/NGC7023 region is a protostellar cluster in formation (e.g. Kun et al. 2008), and L1251B contains a small cluster of protostars (Lee et al. 2006). However, as discussed at the beginning of Chapter 5, the Cepheus Flare is a large region containing a heterogeneous collection of molecular clouds. Typically, on the scales we resolve, the Cepheus Flare does not appear to have a high surface density of sources. The typical size of sources in Cepheus is comparable to those in the Taurus molecular cloud (see Figure 6.1). While there is a wide distribution in minimum source separations in Cepheus (see

Figure 6.3), the median minimum separation between sources in Cepheus is almost twice that in Ophiuchus (and slightly over half that in Taurus). Thus, we consider Cepheus to be intermediate between Ophiuchus and Taurus in the degree to which its star formation is clustered. However, the low surface density of sources and the large source sizes lead us to treat it as generally a dispersed region.

6.1.2 Variation within regions

Tables 6.1 and 6.2 list the mean, standard deviation, median, maximum and minimum temperatures, masses, sizes and densities of the starless cores in each of the sub-regions of Ophiuchus, Taurus and Cepheus, as defined in Chapters 3, 4, and 5 respectively. The variation of these properties within each molecular cloud are plotted by sub-region in Figures 6.11 (temperature), 6.12 (mass), 6.13 (FWHM) and 6.14 (density). In each of these figures, the mean value for each sub-region is plotted as a closed circle, the median is plotted as an open circle, the full range of measured values is shown as a dashed line, and the error bars on the mean value show the standard deviation divided by the square root of the number of sources, hearafter referred to as S.D./$\sqrt{N}$. The averages, range and S.D./$\sqrt{N}$ of the full region are also shown, with the mean and median plotted as closed and open stars, respectively.

Figure 6.11 shows that both mean and median core temperatures are typically $\sim 11 - 13\,\mathrm{K}$, with the exceptions of sub-regions with identifiable heating sources: Oph A and A$'$, heated by the B3-B5 star S1 and the B2V star HD147889; L1174 in Cepheus, heated by the B2V star HD200775; the eastern sub-region of Taurus, heated by the star V892 Tau; and the western sub-region of Taurus, in which some sources may be heated by the star IRAS04111+2800G. The cores in Oph E and Oph F also show slightly elevated temperatures, despite having no clear heating source; this may be the result of the high number of embedded sources in these regions, as
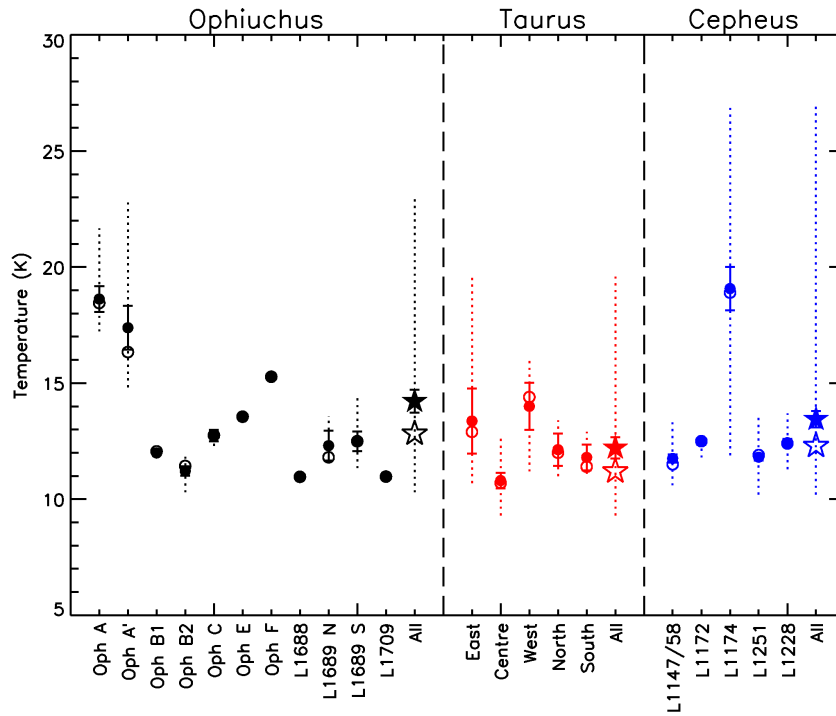
Figure 6.11: Variation of starless core temperature with sub-region within Ophiuchus (black), Taurus (red) and Cepheus (blue). Solid symbols indicate mean value; open symbols indicate median. Dashed line indicates range of values. Error bars show standard deviation divided by the square root of the total number of sources. Circles indicate values are for an individual sub-region; stars indicate values are for the entire region.
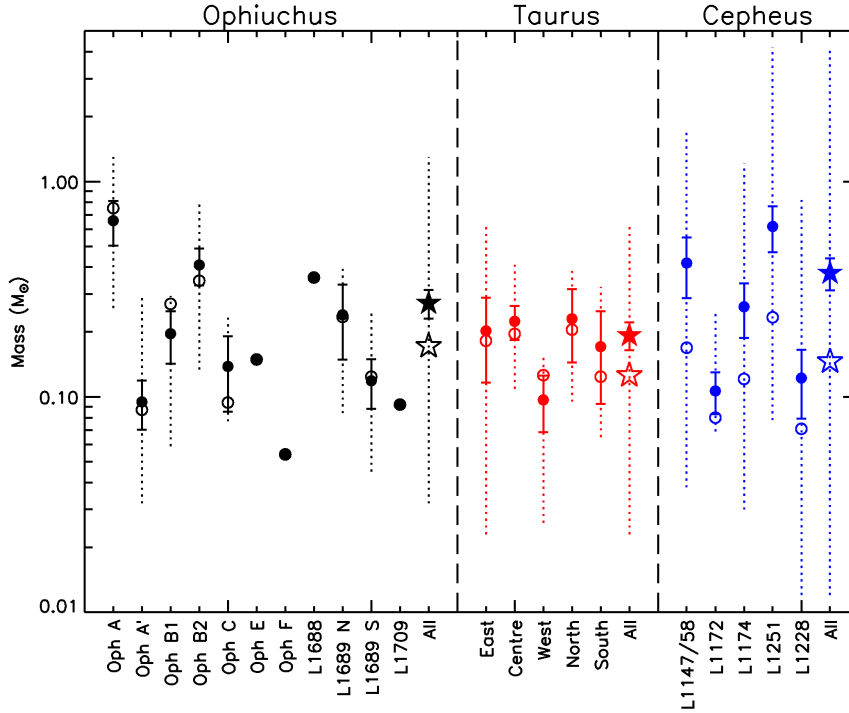
Figure 6.12: Variation of starless core mass with sub-region within Ophiuchus, Taurus and Cepheus. Colour and symbol coding as in Figure 6.11.

discussed in Chapter 3.

Figure 6.12 shows that there is a wide variation of source masses both within and between sub-regions. In Ophiuchus, Oph A and Oph B2 have somewhat larger mean and median masses than the other regions, but the range of measured masses in these two sub-regions overlaps with those of the other sub-regions of Ophiuchus – substantially so in the case of Oph B2. Mean and median core masses are very similar in every sub-region of Taurus, with the slight exception of the western sub-region, which has a maximum measured core mass of $0.16\,M_\odot$, lower than any of the other sub-regions. There is substantial variation in the core masses in Cepheus; the median values in each sub-region are similar to those in Taurus, but the range of measured masses is, in every sub-region except L1172, larger than the ranges seen in any sub-region of Taurus or Ophiuchus. The mean masses in sub-regions of Cepheus are consistently higher than the medians, suggesting that the distribution of masses
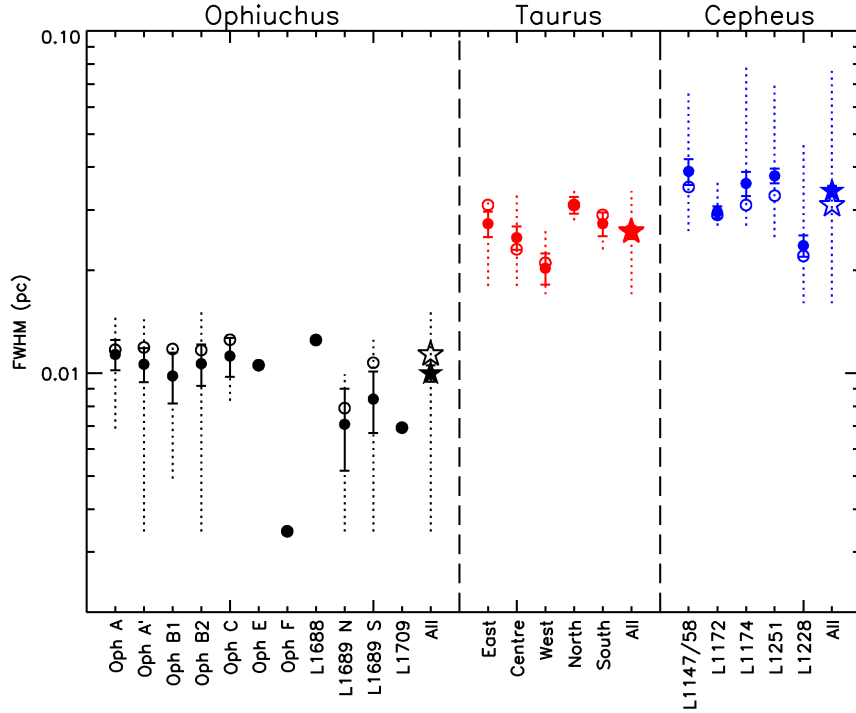
Figure 6.13: Variation of starless core deconvolved FWHM with sub-region within Ophiuchus, Taurus and Cepheus. Colour and symbol coding as in Figure 6.11.

is being skewed by a small number of high-mass cores. This is consistent with the break in behaviour of the CMF in Cepheus observed at high masses (see Figure 5.10 and discussion in Section 5.3).

As shown in Figure 6.13, mean and median source size varies very little between sub-regions. Sub-regions in Ophiuchus consistently have mean and median core FWHMs ~ 0.01 pc, although the average sizes in L1689 are slightly smaller than those in L1688. Mean core sizes in Taurus are ~ 0.03 pc in every region. Mean source sizes in Cepheus are ~ 0.04 pc for every region except L1228. This is likely to be a distance effect; we assume a distance of 200 pc to L1228, while the other sub-regions of Cepheus are taken to be at a range of distances $288 - 325$ pc. Hence, a source in L1228 will have a smaller physical size than a core with the same angular size in another region of Cepheus. While having similar average values, source sizes in Cepheus show more variation than those in Taurus.
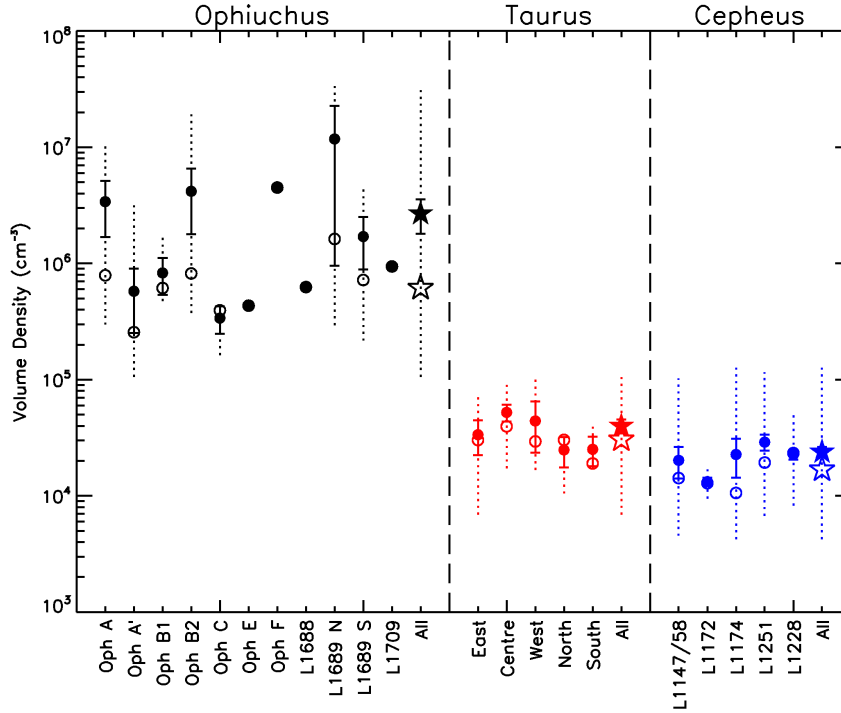
Figure 6.14: Variation of starless core volume density with sub-region within Ophiuchus, Taurus and Cepheus. Colour and symbol coding as in Figure 6.11.

Figure 6.14 shows that while there is considerable variation in source density in Ophiuchus, the median density in most sub-regions is $\sim 10^6 \, \text{cm}^{-3}$. The exception to this is Oph A′, which has a mean density $\sim 10^6 \, \text{cm}^{-3}$, but a median density $\sim 2 \times 10^5 \, \text{cm}^{-3}$; Oph A′ is the lower-density region surrounding the dense centre of Oph A, so relatively low source densities on Oph A′ are not unexpected. Oph A, Oph B2 and L1689N all contain some sources with densities $\gtrsim 10^7 \, \text{cm}^{-3}$, and have mean volume densities considerably higher than other regions. L1689S also shows a somewhat elevated mean source density, and a wide range in densities. This is consistent with our discussion of clustering in Section 6.1.1, in which Oph A, Oph B2 and L1689N were identified as being the regions in Ophiuchus with the highest surface density of sources; these are the centres of clustered regions in Ophiuchus. Both Taurus and Cepheus show little variation in mean or median source density with region; average source densities in Taurus are $\sim 2 \times 10^4 \, \text{cm}^{-3}$, while average

source densities in Cepheus are typically slightly lower, $\sim 1 \times 10^4\,\mathrm{cm}^{-3}$. Cepheus shows a slightly larger range of core densities than Taurus. However, the S.D./$\sqrt{N}$ error bars shown on Figure 6.14 are typically smaller in Cepheus than in Taurus; this apparent increase in variation is likely to be the result of the higher number of sources in Cepheus than in Taurus.

6.2 Core Evolution

In this section, we investigate whether our non-prestellar starless cores may potentially evolve to become prestellar cores, and construct possible evolutionary tracks in the virial plane. We consider the problem in the cases of both isothermal and adiabatic compression of core material.

Of the four quadrants of the virial plane shown in Figures 3.13, 4.18 and 5.20, only the upper right quadrant represents gravitationally-bound prestellar cores, collapsing and evolving away from virial equilibrium. We expect pressure-confined starless cores with a virial ratio > 1 to be evolving toward virial equilibrium. A collapsing, pressure-confined, virially-bound starless core might increase in density to the point that it becomes gravitationally bound, or might instead reach virial equilibrium with its surroundings.

We model only the 23 starless cores in Ophiuchus for which we have both internal and external velocity dispersions. These are the only cores in our samples for which we believe that the dominant terms in the energy balance have been accounted for: in Taurus, we hypothesise that the dominant mechanism for core support is the internal magnetic field (see Section 4.4.5), while in Cepheus, we do not have measurements of our cores' internal velocity dispersions, and so can only put an upper limit on the degree to which they are virially bound (see Section 5.6.2).

6.2.1 Evolutionary model

For a Gaussian density distribution $\rho = \rho_c e^{-\frac{1}{2}\left(\frac{r}{\alpha}\right)^2}$ with a central density ρ_c, and a characteristic radius α which is bounded by external pressure at a density of ρ_e at a radius r_e,

$$r_e = \alpha\sqrt{2\ln\left(\frac{\rho_c}{\rho_e}\right)}, \tag{6.1}$$

the virial ratio is given by

$$-\frac{\Omega_{\mathrm{G}} + \Omega_{\mathrm{P}}}{2\Omega_{\mathrm{K}}} = \frac{\frac{1}{2\sqrt{\pi}}\frac{GM^2}{\alpha} + 8\sqrt{2}\pi P_{\mathrm{EXT}}\alpha^3\left[\ln\left(\frac{\rho_c}{\rho_{\mathrm{C^{18}O}}}\right)\right]^{\frac{3}{2}}}{3M\sigma^2}, \tag{6.2}$$

and the ratio of gravitational to external pressure energy is given by

$$\frac{\Omega_{\mathrm{G}}}{\Omega_{\mathrm{P}}} = \frac{1}{16\sqrt{2}\pi^{\frac{3}{2}}}\frac{1}{P_{\mathrm{EXT}}}\frac{GM^2}{\alpha^4}\left[\ln\left(\frac{\rho_c}{\rho_e}\right)\right]^{-\frac{3}{2}}. \tag{6.3}$$

In keeping with our virial analysis in Chapter 3, we assume $\rho_e = \rho_{\mathrm{C^{18}O}} = 10^5\,\mathrm{cm}^{-3}$ for the cores in Ophiuchus.

For a core of fixed mass M, the central density varies with the core's characteristic radius, α, as

$$\rho_c = \frac{1}{2\sqrt{2}\pi^{3/2}}\frac{M}{\alpha^3}. \tag{6.4}$$

The velocity dispersion σ obeys the relation

$$\sigma^2(T, r_e) = \sigma_{\mathrm{T}}(T, r_e)^2 + \sigma_{\mathrm{NT}}(r_e)^2, \tag{6.5}$$

where σ_{T} is the thermal gas velocity dispersion,

$$\sigma_{\mathrm{T}} = \sqrt{\frac{k_{\mathrm{B}}T}{\mu m_{\mathrm{H}}}}, \tag{6.6}$$

and σ_{NT} is the non-thermal gas velocity dispersion.

We model the evolution of the thermal velocity dispersion with core radius in the limits of isothermal and adiabatic compression of the core material. In the isothermal case, the thermal velocity dispersion is given by

$$\sigma_{\mathrm{T}}(T) = \sigma_{\mathrm{T}}(T_0), \tag{6.7}$$

where T_0 is the initial temperature of the gas traced by N_2H^+. In keeping with the work above, we assume $T_0 = 7\,\text{K}$, as being representative of the central temperature of a prestellar core (see, e.g. Stamatellos et al. 2007).

In the adiabatic case, we assume that the gas obeys the adiabatic equation of state,

$$PV^\gamma = P_0 V_0^\gamma, \tag{6.8}$$

where $\gamma = 7/5$, assuming the gas is diatomic. If the gas is ideal then $PV \propto T$ (see Equation 1.17), and the equation of state becomes

$$T = T_0 \left(\frac{V_0}{V}\right)^{\gamma-1} = T_0 \left(\frac{V_0}{V}\right)^{\frac{2}{5}} = T_0 \left(\frac{R_0}{R}\right)^{\frac{6}{5}} = T_0 \left(\frac{r_e}{r_{e,0}}\right)^{-\frac{6}{5}}. \tag{6.9}$$

We assume that the non-thermal component of the linewidth obeys the Solomon et al. (1987) relation between the size and non-thermal internal linewidth of a starless core,

$$\sigma_{\text{NT}} \propto R^{0.5}, \tag{6.10}$$

and so

$$\sigma_{\text{NT}} = \sigma_{\text{NT},0} \left(\frac{R}{R_0}\right)^{0.5} = \sigma_{\text{NT},0} \left(\frac{r_e}{r_{e,0}}\right)^{0.5}. \tag{6.11}$$

Thus, for a given set of initial (measured) conditions, we can create adiabatic and isothermal evolutionary tracks as a function of core characteristic radius α only. Throughout this analysis, we assume that the core mass M is fixed, that the core density profile obeys a Gaussian distribution in all circumstances, that the core is bounded by a constant external pressure, and that no external disruption occurs. Figure 6.15 shows the virial stability as a function of characteristic radius of each of the starless cores in our sample for which a virial analysis can be performed.

Each panel of Figure 6.15 shows, for an individual starless core in our sample, the virial ratio, $-(\Omega_{\text{G}} + \Omega_{\text{P}})/2\Omega_{\text{K}}$ (see equation 6.2), in black and the pressure-gravity ratio, $\Omega_{\text{G}}/\Omega_{\text{P}}$ (see equation 6.3) in red, both plotted as a function of core characteristic radius α. The solid black line shows the virial ratio in the adiabatic
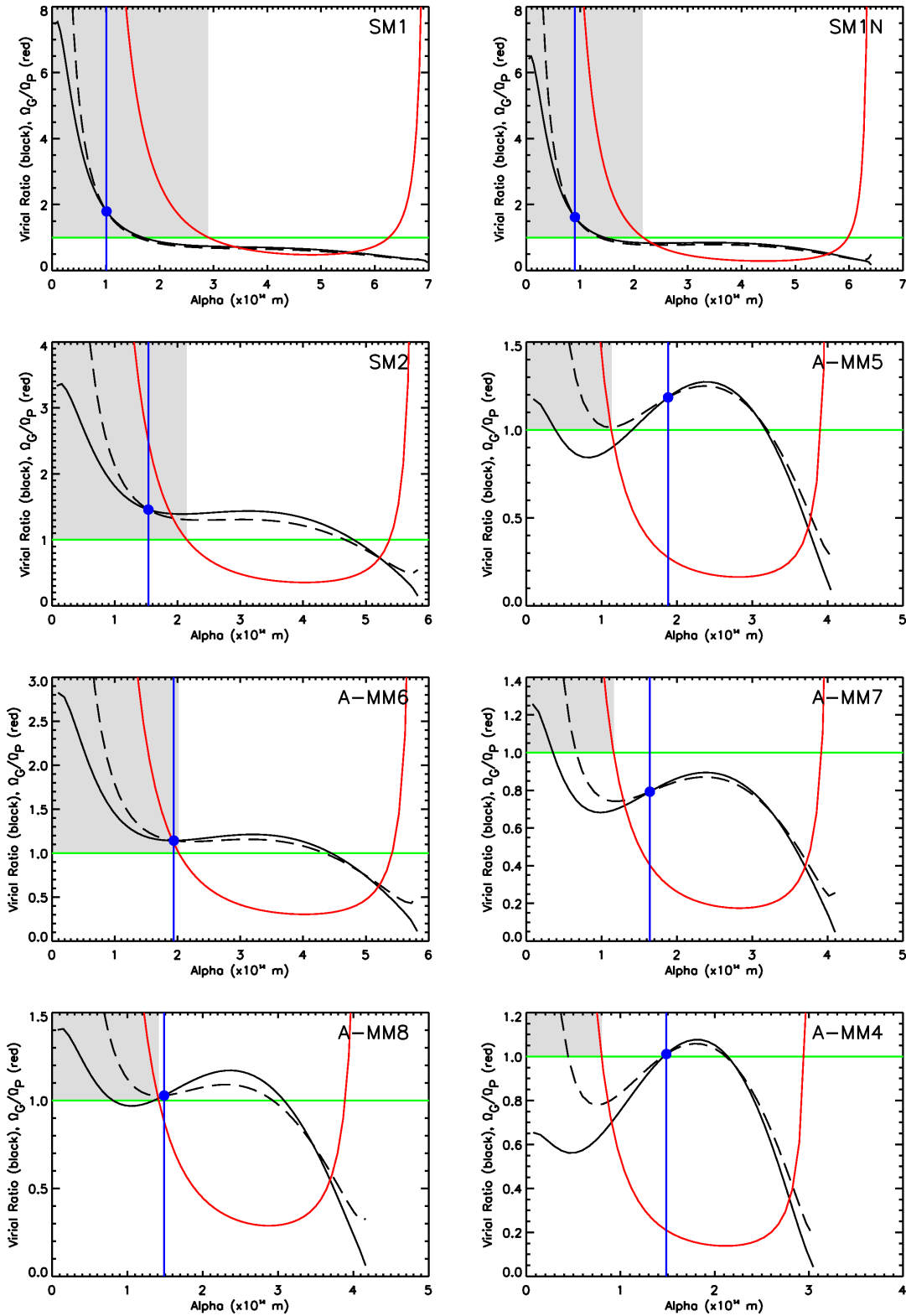
Figure 6.15: Stability as a function of characteristic radius for our cores. Solid black line shows adiabatic virial ratio; dashed black line shows – *cont'd overleaf*
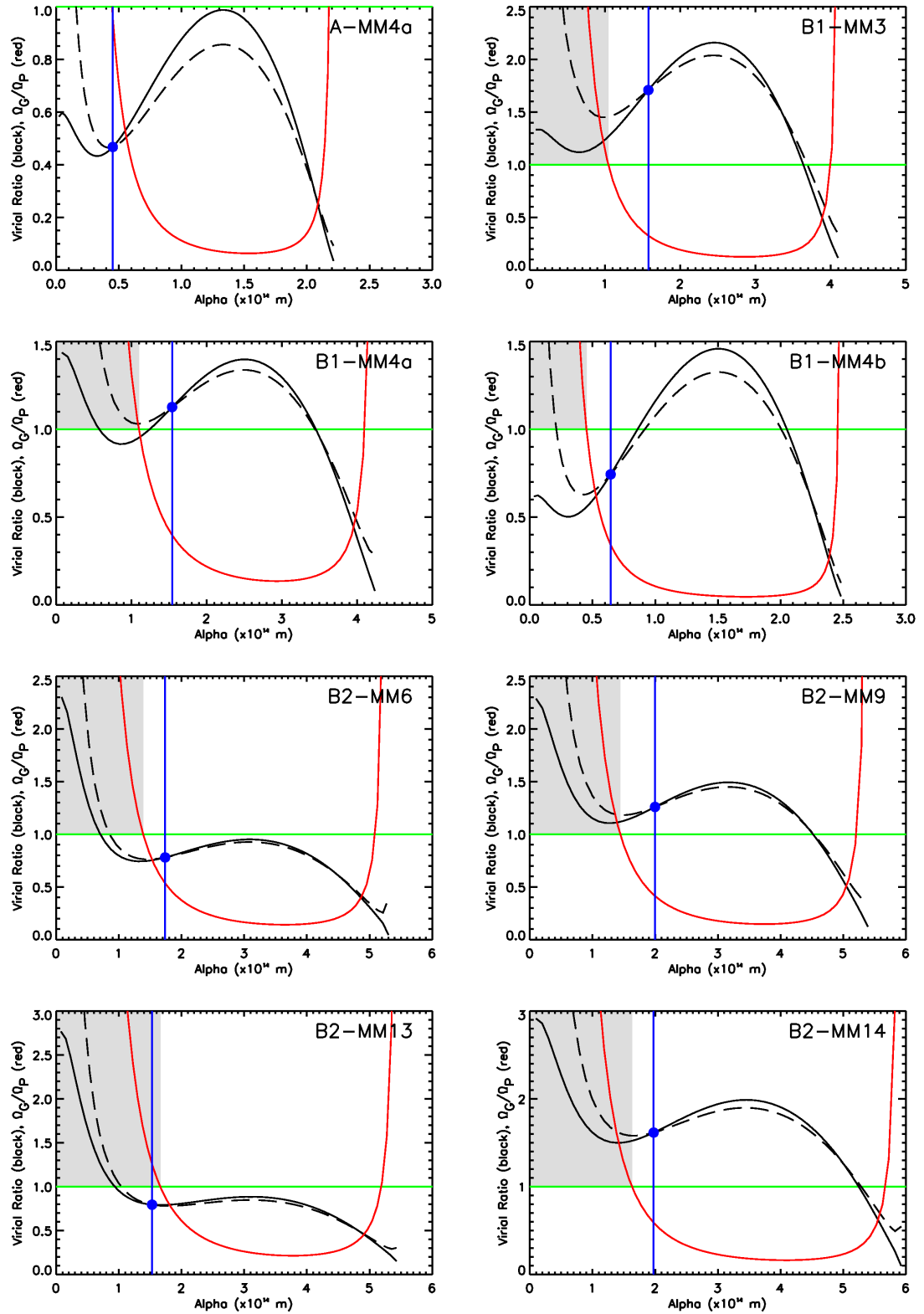
Figure 6.15: – *cont'd.* isothermal virial ratio. Red line shows ratio of gravitational potential energy to external pressure energy. Blue dot shows – *cont'd overleaf*
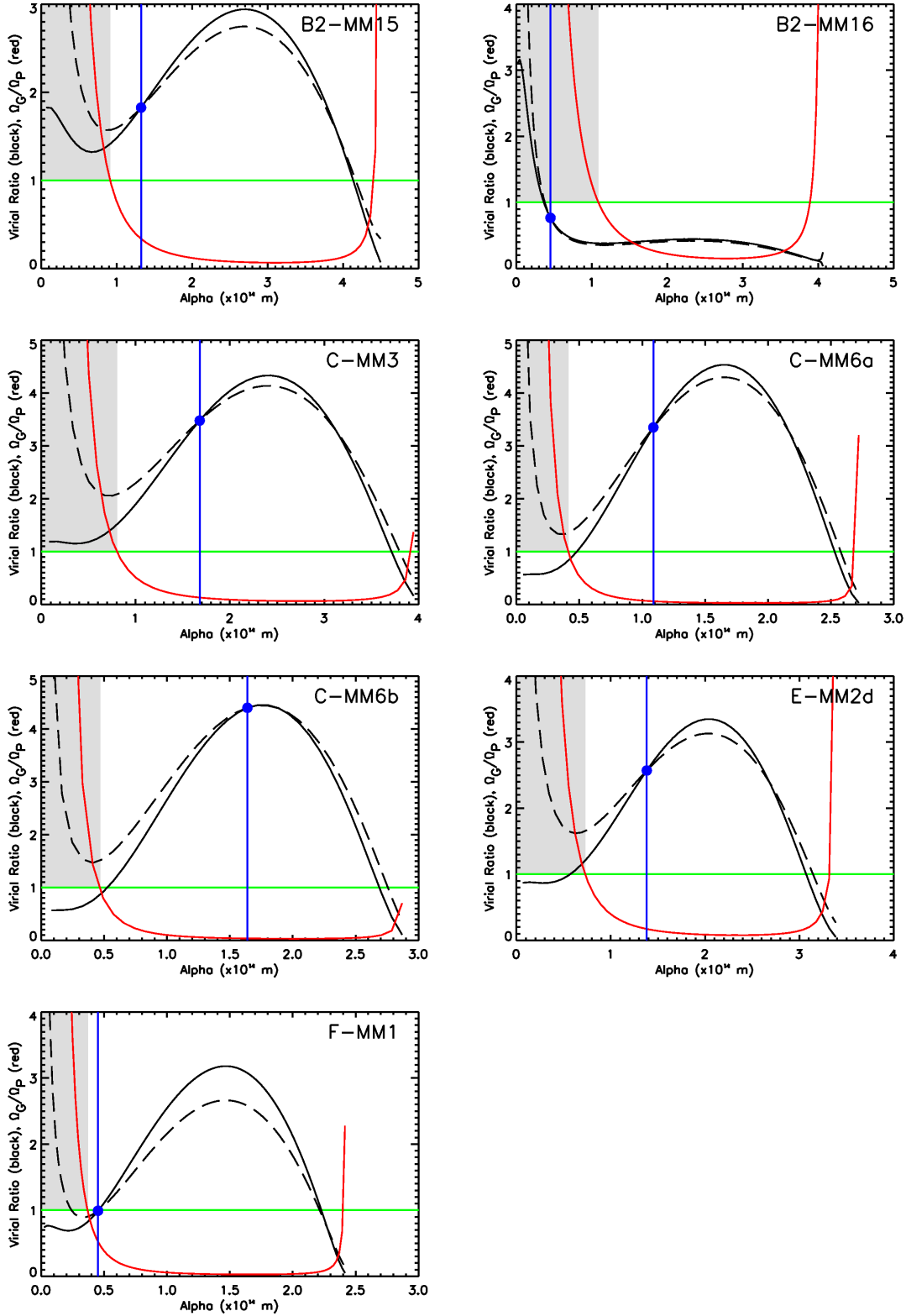
Figure 6.15: – *cont'd.* measured virial ratio. Green line shows line of virial stability. Grey shaded regions indicate parameter space occupied by prestellar cores.
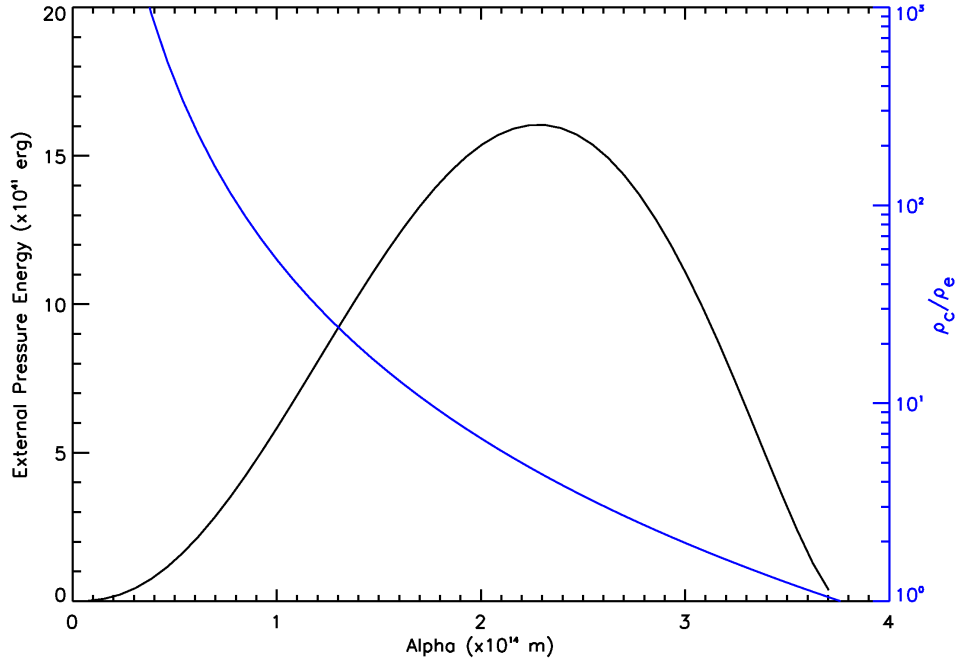
Figure 6.16: External pressure energy (black) and centre/edge density contrast (blue), plotted as a function of core characteristic radius α for a core with $M = 0.2\,\mathrm{M_\odot}$, $P_{\mathrm{EXT}}/k_{\mathrm{B}} = 1.5 \times 10^7\,\mathrm{K\,cm^{-2}}$, $T_0 = 7\,\mathrm{K}$, $\sigma_{\mathrm{NT},0} = 220\,\mathrm{ms^{-1}}$ and $\alpha_0 = 0.005\,\mathrm{pc}$.

case, while the dashed black line shows the virial ratio in the isothermal case. The blue point marks the measured virial ratio of the core, while the blue line extending from that point guides the eye to the measured value of $\Omega_{\mathrm{G}}/\Omega_{\mathrm{P}}$ on the red curve. The green line marks the line of unity, i.e. the characteristic radius or radii at which the virial ratio or pressure-gravity ratio function intersects this line, is or are where the ratio equals unity. While the virial ratio is greater than 1 the core is virially bound; while it is below the green line it is virially unbound. Similarly, while the pressure-gravity ratio is above the green line, the core is gravitationally-dominated; while it is below the green line it is pressure-dominated. The region shaded in grey is 'prestellar': where $-(\Omega_{\mathrm{G}} + \Omega_{\mathrm{P}})/2\Omega_{\mathrm{K}} > 1$ and $\Omega_{\mathrm{G}}/\Omega_{\mathrm{P}} > 1$. A core in this region will be both virially bound and confined by gravity.

As can be seen in Figure 6.15, our model for the virial parameter as a function

of α shows three regimes: (1) a gravitationally-dominated regime at small α, which will become virially bound as α approaches zero, and may be virially bound over all of its range; (2) a pressure-dominated regime at intermediate α which may be virially bound over some or all of its range; and (3) a gravitationally-dominated regime at large α which will be virially unbound. There is a maximum value of α beyond which the model is no longer physical, discussed below.

At the smallest α, gravity dominates over external pressure, as $\Omega_\mathrm{G} \propto \alpha^{-1}$, and $\Omega_\mathrm{P} \propto \alpha^3[\ln(kM\alpha^{-3})]^{1.5}$, where $k = (2\sqrt{2}\pi^{1.5}\rho_e)^{-1}$, similar to our notation in Section 5.6.1. The variation of external pressure energy with core characteristic radius α is shown in Figure 6.16. At small radii the total energy due to external pressure is small because the source is small. At intermediate α, Ω_P increases, while Ω_G continues to fall off as α^{-1}, and so the core is pressure-dominated. At large α, as the ratio ρ_c/ρ_e approaches unity, the energy due to external pressure falls off sharply. This is due to the decrease in the density contrast between the centre of the core and the pressure-confined edge (shown in blue on Figure 6.16). Gravity again dominates over external pressure, although the core will typically be virially unbound. The model's physical applicability ceases at the characteristic radius at which $\rho_c = \rho_e$, as at larger values of α, the density of the surrounding material would exceed the core central density.

6.2.2 Core evolution

When considering the evolution of the cores in our sample, we presume that any virially bound and gravitationally-dominated core $(-[\Omega_\mathrm{G}+\Omega_\mathrm{P}]/2\Omega_\mathrm{K} > 1$ and $\Omega_\mathrm{G}/\Omega_\mathrm{P} > 1)$ is prestellar and collapsing, and will evolve away from virial equilibrium to become more gravitationally bound – i.e., we expect a core which occupies the grey-shaded regions of Figure 6.15 to evolve toward smaller radii in all cases. We assume that in all other cases, cores will evolve toward virial equilibrium $(-[\Omega_\mathrm{G} + \Omega_\mathrm{P}]/2\Omega_\mathrm{K} = 1)$

– i.e. toward the green line of unity in Figure 6.15, and that a core which reaches virial equilibrium while pressure-confined will remain in or near virial equilibrium thereafter.

An effect of the functional form of Ω_{P} is, in many cases, to produce a local minimum in the virial ratio in the intermediate region between gravitationally-dominated and pressure-dominated behaviour ($\Omega_{\mathrm{G}} \sim \Omega_{\mathrm{P}}$) at small α. This minimum can be seen for every core in Figure 6.15 except the most massive, S1. As a result of this minimum, not all collapsing pressure-confined and virially bound cores will become gravitationally bound prestellar cores. Additionally, there is typically a maximum in the virial ratio at intermediate values of α, and a virially bound and pressure-confined core with large characteristic radius might expand, rather than collapse, to virial equilibrium. It should be noted, however, that all of the starless cores which we model occupy the range of values of α between zero and the maximum at intermediate α; this model may be of limited physical relevance for large values of α.

We do not expect a pressure-confined and virially bound starless core which collapses to equilibrium with its surroundings to instantaneously cease its collapse. A more realistic scenario is one in which the pressure-confined core passes virial equilibrium, continuing to collapse toward the minimum in virial ratio, until the increasing virial instability forces its collapse to halt, and then reverse. One might expect these pressure-confined starless cores without a route to gravitational instability to oscillate slightly around virial equilibrium. Keto et al. (2006) suggested, and modelled, oscillating pressure-confined starless cores as an explanation for starless cores observed to show red-asymmetric line profiles, or reversals in line-profile asymmetry.

There are four gravitationally-dominated and virially bound cores in our sample: SM1, SM1N, SM2 and A-MM6. We assume that these cores are prestellar and

collapsing, and will evolve away from virial equilibrium.

We find a variety of possible evolutionary outcomes for the pressure-confined and virially bound starless cores in our sample. We expect B1-MM3, B2-MM9, B2-MM14, B2-MM16, C-MM3, E-MM2d and A-MM8 to evolve into gravitationally-bound prestellar cores. A-MM4, we expect to collapse to virial equilibrium. A-MM5, B1-MM4a, C-MM6a and C-MM6b are ambiguous; if they were to collapse isothermally, they would become prestellar, while an adiabatic collapse would leave them in virial equilibrium with their surroundings.

Our model shows no straightforward route by which a virially-unbound pressure-confined starless core can evolve into a prestellar core while a minimum in virial ratio exists between the measured α of the core and the α required for the core to be prestellar. Cores B1-MM4b and F-MM1 will expand to reach virial equilibrium (although F-MM1 is already in almost exact virial equilibrium). If the maximum in the virial ratio due to the external pressure term is < 1, there is no way in which the core can achieve virial stability – examples of this are A-MM4a, A-MM7 and B2-MM6.

The gravitationally-dominated and virially-unbound starless cores in our sample are B2-MM13 and B2-MM16, both of which will collapse to become gravitationally bound, becoming a prestellar core without passing through the pressure-confined regime. It should be noted that B2-MM13 is very close to the virial minimum.

The predicted evolutionary outcomes of our cores are listed in Table 6.4. We emphasise that all of these evolutionary outcomes assume that there is no further accretion of mass by the core.

6.2.3   Evolutionary tracks in the virial plane

Figure 6.17 shows the loci in the virial/gravity-pressure ratio plane (see Figure 3.13) predicted by our model for a family of starless cores in the mass range 0.02–$2.0\,\mathrm{M}_{\odot}$

Table 6.4: The evolutionary outcomes predicted for each of our cores in Ophiuchus.

Core	Initial State	Confining Force	Direction of Evolution	Outcome Isothermal	Adiabatic
SM1	Bound	Gravity	Collapse	Prestellar	Prestellar
SM1N	Bound	Gravity	Collapse	Prestellar	Prestellar
SM2	Bound	Gravity	Collapse	Prestellar	Prestellar
A-MM5	Bound	Pressure	Collapse	Prestellar	Virialised
A-MM6	Bound	Gravity	Collapse	Prestellar	Prestellar
A-MM7	Unbound	Pressure	Expansion	Unstable	Unstable
A-MM8	Bound	Pressure	Collapse	Prestellar	Prestellar
A-MM4	Bound	Pressure	Collapse	Virialised	Virialised
A-MM4a	Unbound	Pressure	Expansion	Unstable	Unstable
B1-MM3	Bound	Pressure	Collapse	Prestellar	Prestellar
B1-MM4a	Bound	Pressure	Collase	Prestellar	Virialised
B1-MM4b	Unbound	Pressure	Expansion	Virialised	Virialised
B2-MM6	Unbound	Pressure	Expansion	Unstable	Unstable
B2-MM9	Bound	Pressure	Collapse	Prestellar	Prestellar
B2-MM13	Unbound	Gravity	Collapse	Prestellar	Prestellar
B2-MM14	Bound	Pressure	Collapse	Prestellar	Prestellar
B2-MM15	Bound	Pressure	Collapse	Prestellar	Prestellar
B2-MM16	Unbound	Gravity	Collapse	Prestellar	Prestellar
C-MM3	Bound	Pressure	Collapse	Prestellar	Prestellar
C-MM6a	Bound	Pressure	Collapse	Prestellar	Virialised
C-MM6b	Bound	Pressure	Collapse	Prestellar	Virialised
E-MM2d	Bound	Pressure	Collapse	Prestellar	Prestellar
F-MM1	Unbound	Pressure	Expansion	Virialised	Virialised
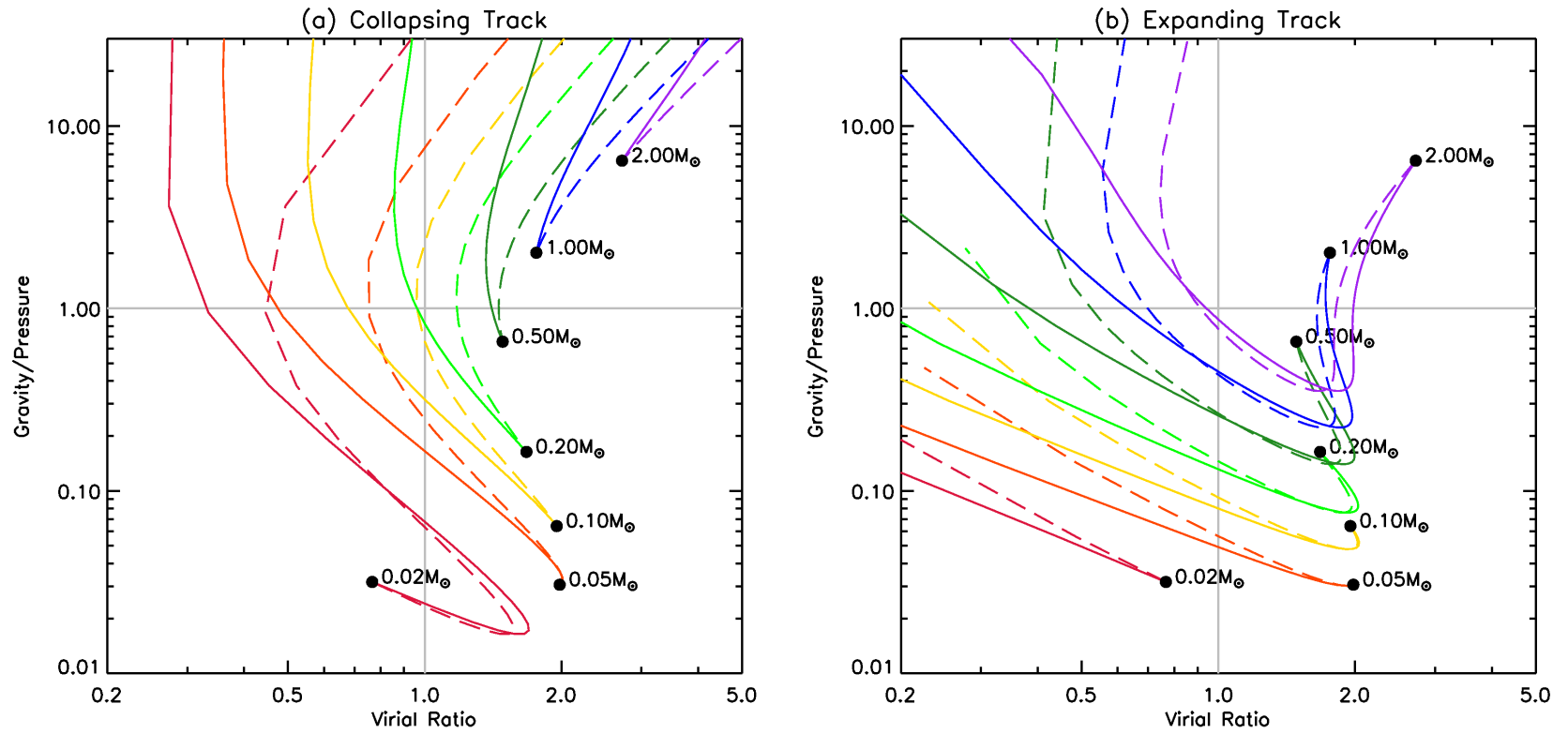
Figure 6.17: A family of loci of Equations 6.2–6.11 in the virial plane showing (a) the collapsing track and (b) the expanding track. Solid lines show adiabatic loci; dashed lines show isothermal loci. See text for details.

with external pressure $P_{\mathrm{EXT}}/k_{\mathrm{B}} = 1.5 \times 10^7 \, \mathrm{K \, cm^{-2}}$, an initial temperature of $7 \, \mathrm{K}$, an initial non-thermal linewidth of $220 \, \mathrm{m \, s^{-1}}$, and an initial characteristic radius of $0.005 \, \mathrm{pc}$. Figure 6.17a shows the collapsing tracks, with the adiabatic track shown as a solid line and the isothermal track shown as a dashed line. The expanding tracks are shown on Figure 6.17b. The two sets of tracks are separated for clarity. We propose that each core will have an evolutionary track in this plane, along the locus defined by Equations 6.2–6.11. As discussed above, unless $-(\Omega_{\mathrm{G}} + \Omega_{\mathrm{P}})/2\Omega_{\mathrm{K}} > 1$ and $\Omega_{\mathrm{G}}/\Omega_{\mathrm{P}} > 1$, we expect cores to evolve toward virial equilibrium. Thus, for each of the cores shown in Figure 6.17, only some part of the locus of Equations 6.2–6.11 is accessible, and represents an evolutionary track. The $2 \, \mathrm{M_\odot}$, $1 \, \mathrm{M_\odot}$ and $0.5 \, \mathrm{M_\odot}$ cores, we expect to follow the collapsing track indefinitely. The $0.2 \, \mathrm{M_\odot}$ core, we expect to follow the collapsing track indefinitely in the isothermal case, and collapse to virial equilibrium in the adiabatic case. We expect the $0.1 \, \mathrm{M_\odot}$ core to follow the collapsing track to virial equilibrium, as in order to access the expanding track, it would first have to increase its boundedness, and pass a maximum in virial confinement. The $0.05 \, \mathrm{M_\odot}$ core, however, we expect to follow the expanding track to virial equilibrium, as it is on the other side of the maximum in boundedness to the $0.1 \, \mathrm{M_\odot}$ core. The $0.02 \, \mathrm{M_\odot}$ core will collapse to virial equilibrium. Both the $0.02 \, \mathrm{M_\odot}$ and $0.05 \, \mathrm{M_\odot}$ cores occupy the pressure-confined region on the high-α side of the virial maximum discussed in Section 6.2.2 and seen in Figure 6.15, and as such do not have any analogues amongst our observed cores in Ophiuchus.

Figure 6.18 shows our proposed evolutionary tracks for a subset of our cores: SM1 (prestellar), C-MM3 (pressure-confined, collapsing to prestellar), A-MM5 (pressure-confined, collapsing to virialised in the adiabatic case but collapsing to prestellar in the isothermal case), B2-MM16 (unbound and gravitationally-dominated, collapsing to prestellar), B1-MM4b (unbound and pressure-dominated, expanding to virialised) and A-MM4b (unbound and marginally pressure-dominated, no accessible stable
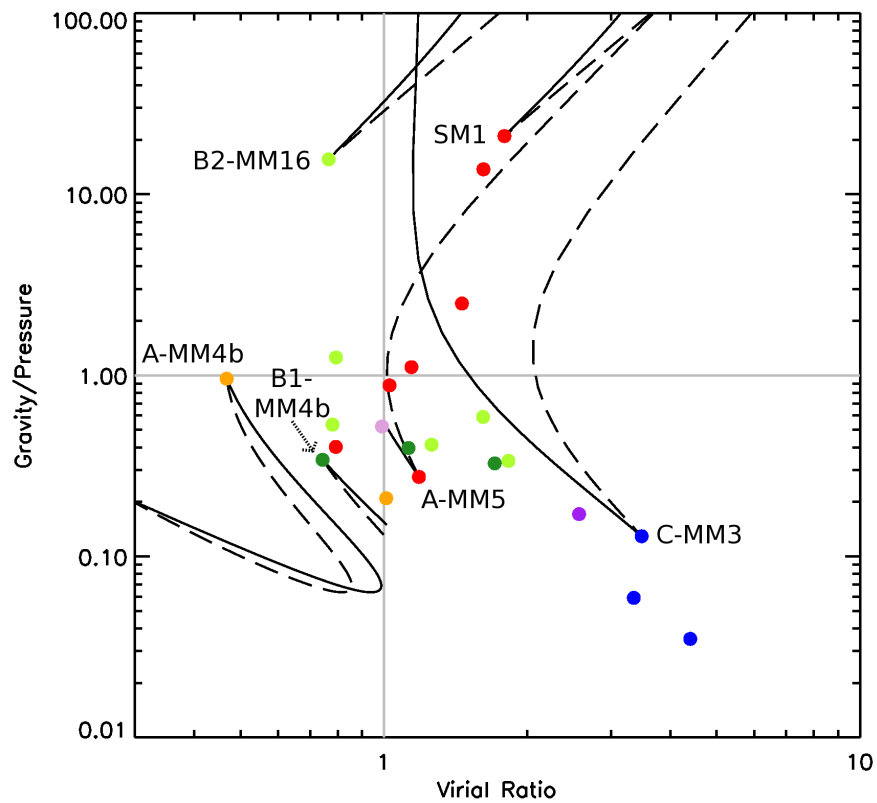
Figure 6.18: Evolutionary tracks in the virial plane, for a sample of our starless cores. All cores shown in Figure 3.13 are shown here for reference. See text for details.

solution, appears to be expanding). These are chosen to illustrate the behaviours described in Section 6.2.2, above.

6.2.4 Adiabatic vs. isothermal evolution

It can be seen in Figure 6.15 that cores collapsing under gravity do so more effectively under the assumption of isothermal collapse than under the assumption of adiabatic collapse. This is due to the core heating as it shrinks, in the adiabatic case. This causes an increase in thermal kinetic energy in the core, and hence an increase in support against collapse. When $\alpha/\alpha_0 \ll 1$, the isothermal and adiabatic virial ratios diverge dramatically. We parameterise the turbulent linewidth using a Larson-like law (Larson 1981; Solomon et al. 1987), and so in our model, turbulence decays as core size decreases, and ceases to contribute significantly to core support as the core collapses, i.e. $\sigma_{\mathrm{NT}} \to 0$ when $\alpha/\alpha_0 \ll 1$. In both the adiabatic and isothermal cases, $\Omega_{\mathrm{G}} \gg \Omega_{\mathrm{P}}$ when $\alpha/\alpha_0 \ll 1$; in the isothermal case, the expression for the virial ratio approaches

$$-\left(\frac{\Omega_{\mathrm{G}}+\Omega_{\mathrm{P}}}{2\Omega_{\mathrm{K}}}\right)_{\mathrm{isothermal}} \to \frac{1}{6\sqrt{\pi}}\frac{GM}{\sigma_{\mathrm{T}}(T_0)}\frac{1}{\alpha} \propto \alpha^{-1}: \qquad (\alpha/\alpha_0 \ll 1). \qquad (6.12)$$

However, in the adiabatic case, the small-α dependence becomes

$$-\left(\frac{\Omega_{\mathrm{G}}+\Omega_{\mathrm{P}}}{2\Omega_{\mathrm{K}}}\right)_{\mathrm{adiabatic}} \to \frac{1}{6\sqrt{\pi}}\frac{GM}{\sigma_{\mathrm{T}}(T_0)}\left(\frac{r_e}{r_{e,0}}\right)^{1.2}\frac{1}{\alpha} \propto \alpha^{0.2}\sqrt{\ln\left(kM\alpha^{-3}\right)}: \quad (\alpha/\alpha_0 \ll 1).$$
$$(6.13)$$

Thus, in the adiabatic model, we expect a decrease in the virial ratio at the very smallest radii. This is seen for some of our cores – see, for example, core B1-MM3 in Figure 6.15. It must be noted that at the smallest radii, the physical relevance of either isothermal or adiabatic collapse becomes increasingly uncertain; the decrease in virial ratio seen at the smallest radii in the adiabatic case may not be physically plausible. We stress again that this simple core model is only justified over the range of characteristic radii measured for the cores in our sample, and may not be relevant

at the smallest and largest radii, and that the model neglects further accretion of mass.

6.2.5 Non-thermal motions

We choose to parameterise the non-thermal motions of our cores as Larson-like (i.e. $\sigma_{\mathrm{NT}} \propto r_e^\eta$ – see Equation 6.11), in order to include the dissipation of turbulence expected to occur in starless cores (e.g., Klessen et al. 2005; Offner et al. 2008) in our model. For the remainder of this chapter we use η to indicate the index of the linewidth-size relation. We choose an index $\eta = 0.5$ (Solomon et al. 1987). However, other indices have been proposed – for example, for molecular clouds an index of $\eta = 0.38$ is expected (Larson 1981), while Caselli & Myers (1995) find an index $\eta = 0.21$ in high-mass star-forming regions. We investigated how our evolutionary model varies with η. We found that as the non-thermal term in Equation 6.2 becomes small at small radii, and as the dependence of the non-thermal linewidth on size is relatively weak ($\sigma_{\mathrm{NT}} \propto \alpha^{0.5}$), over the range of radii being considered, small changes in the index of Equation 6.11 do not substantially alter the expected behaviour of our cores.

While $\sigma_{\mathrm{NT}} \propto r_e^\eta$ and $0 < \eta < 1$, the behaviour of our cores does not alter significantly with varying η. An $\eta = 0$ would indicate that there is no dissipation of turbulence as the core collapses, while $\eta < 0$ would require turbulence to be enhanced, rather than dissipated, as the core decreases in size. A value of $\eta < 0.5$ implies a sub-linear increase in non-thermal kinetic energy as a function of r_e (as $\Omega_{\mathrm{K,NT}} \propto \sigma_{\mathrm{NT}}^2$). If $\eta > 0.5$, then the substantial increase in non-thermal kinetic energy with increasing α that this causes begins to destroy the maximum in virial ratio seen in the pressure-dominated regions of Figure 6.15.

The variation in the virial ratio with η is shown in Figure 6.19, for a core with
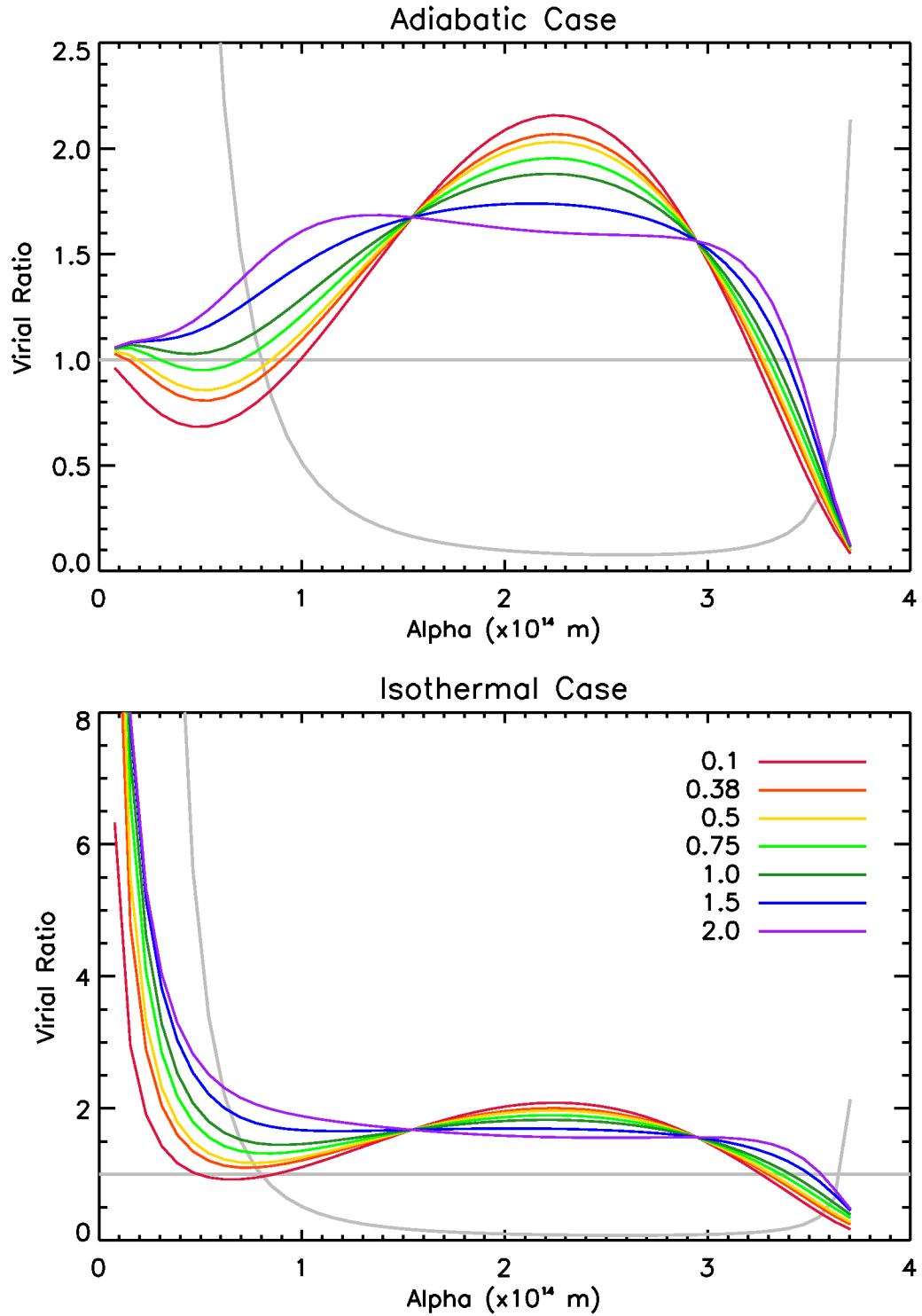
Figure 6.19: Variation in behaviour of the virial ratio with index of relationship between core size and non-thermal linewidth. Top panel: adiabatic case. Bottom panel: isothermal case. Legend shows the index η where $\sigma_{\mathrm{NT}} \propto r_e^{\eta}$. Note the similarity between the behavious resulting from the Solomon et al. (1987) index of 0.5 (yellow) and the Larson (1981) index of 0.38 (orange). The line of unity and the $\Omega_{\mathrm{G}}/\Omega_{\mathrm{P}}$ ratio are plotted in grey, for reference.

mass $0.2\,\mathrm{M_\odot}$, external pressure $P_{\mathrm{EXT}}/k_{\mathrm{B}} = 1.5 \times 10^7\,\mathrm{K\,cm^{-2}}$, and, at an initial characteristic radius of $0.005\,\mathrm{pc}$, a temperature of $7\,\mathrm{K}$ and a non-thermal internal velocity dispersion of $220\,\mathrm{ms^{-1}}$. Figure 6.19 shows that the effect of increasing η is to reduce the variation in virial ratio with α: the pressure-dominated virial maximum and the virial minimum at small radii both become less distinct as η increases. However, while $\eta < 1$, the behaviour of the virial ratio does not alter dramatically. Figure 6.19 also shows that there is only a small difference in the behaviour of the virial ratio between the Solomon et al. (1987) index of 0.5 and the Larson (1981) index of 0.38.

Thus, we choose the Solomon et al. (1987) value for the index of the relation between characteristic radius and non-thermal linewidth (i.e. $\eta = 0.5$) as being justifiable and physically plausible, while noting that varying this value within a physically reasonable range would not substantially alter our results.

6.2.6 Parameterisation of magnetic field term

We have neglected the magnetic field term in the virial equation in this analysis, due to the lack of reliable measurements of the magnetic field strength in Ophiuchus, and due to those measurements which are available suggesting that the contribution of magnetic energy to core support in Ophiuchus is only a small fraction of that of the non-thermal kinetic energy (see Section 3.4.4). However, in Chapter 4 we hypothesise that magnetic energy may be the dominant mechanism of core support in cores in Taurus. We note that the effect of the magnetic field on the virial balance of a core can be included in our model.

Assuming that the Basu (2000) relation, $B \propto n^{1/2}\sigma_{\mathrm{NT}}$, holds for our starless cores then, as discussed in Section 3.4.4, there is a constant ratio between magnetic energy and non-thermal kinetic energy, as shown in equation 3.45, which we repeat here:

$$\frac{\Omega_{\mathrm{M}}}{\Omega_{\mathrm{K,NT}}} = \frac{1}{3\mu_0}\frac{B_0^2}{\rho_0\sigma_{0,\mathrm{NT}}^2} = \Psi_{\mathrm{M}}. \tag{6.14}$$

$\Psi_{\mathrm{M}} = B_0^2/3\mu_0\rho_0\sigma_{0,\mathrm{NT}}^2$ is the ratio of magnetic energy to non-thermal kinetic energy,

from measurement of a magnetic field strength B_0 and a non-thermal linewidth $\sigma_{0,\mathrm{NT}}$ in material with a density ρ_0.

Including the magnetic term, equation 6.2 becomes

$$\text{Virial Ratio} = -\frac{\Omega_{\mathrm{G}} + \Omega_{\mathrm{P}}}{2\Omega_{\mathrm{K}} + \Omega_{\mathrm{M}}}, \tag{6.15}$$

and, if the Basu (2000) relation holds and $\Omega_{\mathrm{M}} = \Psi_{\mathrm{M}}\Omega_{\mathrm{K,NT}}$, then

$$-\frac{\Omega_{\mathrm{G}} + \Omega_{\mathrm{P}}}{2\Omega_{\mathrm{K}} + \Omega_{\mathrm{M}}} = -\frac{\Omega_{\mathrm{G}} + \Omega_{\mathrm{P}}}{2\Omega_{\mathrm{K,T}} + (2 + \Psi_{\mathrm{M}})\Omega_{\mathrm{K,NT}}}, \tag{6.16}$$

and we can continue to model the evolution of our cores as a function of characteristic radius α only, although another initial condition, initial magnetic field strength B_0, is now required.

The variation in the virial ratio with Ψ_{M} is shown in Figure 6.20, again for a core with mass $0.2\,\mathrm{M_\odot}$, external pressure $P_{\mathrm{EXT}}/k_{\mathrm{B}} = 1.5 \times 10^7\,\mathrm{K\,cm^{-2}}$, and a temperature of $7\,\mathrm{K}$ and a non-thermal internal velocity dispersion of $220\,\mathrm{ms^{-1}}$ at a characteristic radius of $0.005\,\mathrm{pc}$. We estimate Ψ_{M} for a representative initial core density of $\rho_0 = 3M/4\pi r_e^3$ and a range of magnetic field strengths B_0.

Figure 6.20 shows that for the chosen set of initial conditions, the cases of $B_0 = 0\,\mu\mathrm{G}$ ($\Psi_{\mathrm{M}} = 0$), $B_0 = 1\,\mu\mathrm{G}$ ($\Psi_{\mathrm{M}} = 2.6 \times 10^{-5}$), $B_0 = 5\,\mu\mathrm{G}$ ($\Psi_{\mathrm{M}} = 6.5 \times 10^{-4}$) and $B_0 = 10\,\mu\mathrm{G}$ ($\Psi_{\mathrm{M}} = 0.026$) are not distinguishable; the contribution of the magnetic field to the energy balance of the core is negligible. In the case $B_0 = 50\,\mu\mathrm{G}$ ($\Psi_{\mathrm{M}} = 0.065$), the effect of the magnetic energy term is visible on Figure 6.20, but not sufficient to cause more than a minimal variation in the core's evolutionary track. In the case of this core, it is not until field strengths such as $B_0 = 100\,\mu\mathrm{G}$ ($\Psi_{\mathrm{M}} = 0.26$) are reached that the energy balance begins to change significantly.

In Ophiuchus, we determined a value of $\Psi_{\mathrm{M}} = 0.11$, based on measurements by Troland et al. (1996). This is in the range that will produce a small change in the predicted evolutionary track of the core, but will change the predicted evolutionary outcome of the core only in the most marginal cases. This suggests that our neglect of the the magnetic energy term in Ophiuchus is justifiable.
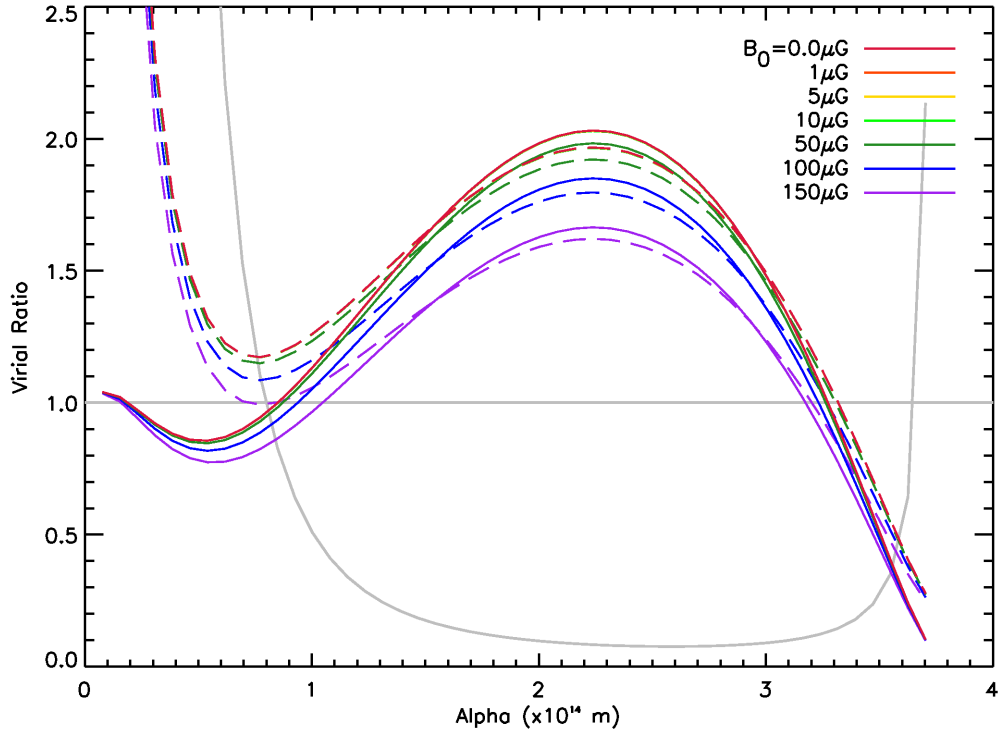
Figure 6.20: Variation in behaviour of the virial ratio with initial magnetic field strength B_0, for a core with $M = 0.2\,\mathrm{M_\odot}$, $P_{\mathrm{EXT}}/k_{\mathrm{B}} = 1.5 \times 10^7\,\mathrm{K\,cm^{-2}}$, $T_0 = 7\,\mathrm{K}$, $\sigma_{\mathrm{NT,0}} = 220\,\mathrm{ms^{-1}}$ and $\alpha_0 = 0.05\,\mathrm{pc}$. Adiabatic curves are shown as solid lines; isothermal curves are shown as dashed lines. The line of unity and the $\Omega_{\mathrm{G}}/\Omega_{\mathrm{P}}$ ratio are plotted in grey, for reference.

In Taurus, we found values of Ψ_{M} varying from $\sim 0.015 - 50$ (see Table 4.7). The applicability of this parameterisation of the magnetic energy as a fraction of the non-thermal kinetic energy in cases where $\Psi_{\mathrm{M}} \gg 1$ is not clear. This model assumes that as turbulence dissipates, so too does the magnetic field strength; if the contribution of magnetic energy to core support greatly exceeds the contribution of non-thermal kinetic energy, this assumption may not be valid. However, note that for our cores in Taurus, we expect both magnetic energy and non-thermal kinetic energy to contribute significantly to core support in most cases (see Table 4.8 and discussion in Section 4.4.5).

6.2.7   Critical discussion of the evolutionary model

All of the functions used in this model are continuous over the range $\rho_e < \rho < \rho_c$. This introduces some physically unrealistic behaviour into the model. Particularly, our parameterisation of a core's non-thermal internal velocity dispersion (equation 6.10) as dependent on core size allows both for the dissipation of turbulence as a core contracts – a physically plausible scenario (e.g., Klessen et al. 2005; Offner et al. 2008) – but also for the degree of turbulent motion in an expanding core to increase with radius. This is a less plausible situation, as there is no obvious means by which turbulence, once lost, can be regained. However, we note that this affects only the pressure-dominated and virially unbound cores in our sample which are expanding towards virial equilibrium. While the characteristic radius at which they reach virial equilibrium may be slightly larger – i.e their expansion may be a weaker function of characteristic radius – than is predicted by our model, the underlying behaviour of expansion toward equilibrium should be the same. We have further assumed that the Solomon et al. (1987) Larson-like relation between core size and non-thermal velocity dispersion applies to a single core continuously over its evolution, when this relation was determined by measurement of the velocity dispersions

of a population of objects within molecular clouds. Whether or not this assumption is valid is not certain. However, as turbulence is expected to dissipate in starless cores (e.g. Klessen et al. 2005) in some manner, and as varying the power-law index of a Larson-like relation for internal non-thermal linewidth does not significantly alter the behaviour of our cores (see Section 6.2.5 and Figure 6.19), we consider it justifiable to parameterise the dissipation of turbulence in our cores in this manner.

As discussed above, this model is valid only over the range of core radii observed in this work. Particularly, none of our cores are observed to occupy the large-α regime beyond the maximum in virial ratio which is seen for all of our cores except SM1 (see Figure 6.15) – the applicability of our model to cores with low centre-to-edge density contrasts and large characteristic radii is unclear. Furthermore, inspection of Figures 6.18 and 3.13 shows that only two of the cores in Ophiuchus – B2-MM13 and B2-MM16 – lie in the gravitationally-dominated and virially unbound quadrant of the virial plane, and that both these cores are consistent within error with being virialised. The paucity of objects in this quadrant of the plane could be explained either by a virially unbound core which is sufficiently gravitationally-dominated to be located on the small-α side of the minimum in virial ratio (i.e. where the accessible route to virial equilibrium is via further collapse – see core B2-MM16) to undergo collapse to virial equilibrium immediately upon formation. If this were the case, then the time a core would spend in the gravitationally-dominated and virially unbound quadrant of the virial plane would be very brief, and we would not expect to see large numbers of cores in that quadrant. An alternative explanation for the lack of cores in this quadrant is that formation of a gravitationally-dominated and virially unbound starless core might be either difficult or unlikely.

As molecular clouds are, on large scales, turbulent structures evolving in a non-quasistatic manner (e.g. Klessen et al. 2005), it is not surprising that many observed starless cores have non-virial-equilibrium configurations. The formation of a

pressure-bound non-equilibrium structure is not difficult to envisage, as turbulence is expected to dissipate at stagnant points in the turbulent flows within molecular clouds. This dissipation of turbulence would lead to an object with an internal velocity dispersion lower than the velocity dispersion in the surrounding material, and so the object would be confined by a high external pressure. Whether or not the object will be virially bound would depend on how effectively turbulence has been dissipated inside the object, and on the mass of the object. The formation of an object with characteristic radius small enough and mass high enough to be gravitationally dominated, yet with velocity dispersion high enough to be virially unbound, seems likely to be a rare event in this paradigm, as turbulence is expected to dissipate on small size scales (Larson 1981; Solomon et al. 1987). This might account for the apparent rarity of cores such as B2-MM16, located in the gravitationally-dominated and virially unbound quadrant of the virial plane.

This model can be usefully compared to numerical simulations of cores collapsing under external pressure. Such simulations typically assume that cores obey a Bonnor-Ebert density distribution, and typically involve the perturbation of a system which is initially in equilibrium (e.g. Foster & Chevalier 1993; Hennebelle et al. 2003). This is a somewhat different approach to our model, which considers cores as obeying a Gaussian density distribution, and models the evolution of cores which are initially in a non-equilibrium (i.e. virially unstable) state. Hennebelle et al. (2003) modelled the evolution of an initially stable Bonnor-Ebert sphere undergoing a steady increase in external pressure, in order to study protostellar collapse induced by external compression. They find that while the compression of their core is slow (i.e. when the external pressure on their core increases on a timescale much greater than the sound-crossing time of the core), the core evolves quasistatically. During the prestellar stage of the core's evolution the outer boundary of the core is pushed inward – qualitatively similar to the contraction of pressure-dominated and

virially bound cores in our model – and a modest, approximately uniform, inward velocity field is set up. However, Hennebelle et al. (2003) find that when cores are strongly compressed (i.e. the external pressure increases on a timescale shorter than the sound-crossing time), a compression wave is driven into the core, leaving behind it an inward velocity field which can become supersonic if the core compression is strong enough. This is dissimilar to our model, which assumes quasistatic core evolution throughout. Our model is thus qualitatively similar to numerical simulations of the collapse under slow compression of pressure-confined cores (Hennebelle et al. 2003). Whether the environments in the molecular clouds studied in this work allow quasistatic core evolution is not clear. However, Hennebelle et al. (2003) note that their simulations in which core compression is slow – the quasistatic case – produce results which match observational constraints on starless cores, suggesting that core evolution may be quasistatic in at least some cases.

6.2.8 Concluding remarks

It must be emphasised that the virial ratio and $\Omega_{\mathrm{G}}/\Omega_{\mathrm{P}}$ values of our cores are substantially uncertain (see error-bars on Figure 3.13). The majority of our cores have virial ratios consistent with their being virialised, and the evolutionary tracks described above are accurate only if our measurements of the core properties are precisely accurate. These evolutionary scenarios should be viewed as representative of a core with the described properties, rather than a prediction specific to the core being observed.

The key result of this analysis is that a virially-bound and pressure-confined starless core will not necessarily evolve to become gravitationally bound, and thus cannot be considered to be a prestellar core. Those of our cores for which $\Omega_{\mathrm{G}} < \Omega_{\mathrm{P}}$ which have no route to becoming gravitationally bound may be collapsing toward

or oscillating slightly about virial equilibrium. A core can only be definitively considered prestellar (i.e. about to form a protostar) if it is gravitationally unstable. Pressure confinement alone is not necessarily sufficient.

6.3   Summary

We have examined the differences in starless core properties between the Ophiuchus, Taurus and Cepheus molecular clouds. We found that cores in each region have similar temperatures and masses, but that cores in Ophiuchus are significantly smaller than those in Taurus and Cepheus. This results in typical source densities being one to two orders of magnitude higher in Ophiuchus than in the other two regions. We discussed the extent to which this may be the result of our differing choices of source extraction algorithm: CuTEx in Ophiuchus, and CSAR in Taurus and Cepheus. We concluded that: as our choice of source extraction algorithm was based on the physical conditions in Ophiuchus; as the completeness limit derived for CuTEx was such that if larger cores were present they should be detectable, unless their masses were $< 0.1\,\mathrm{M_\odot}$ in every case; and as the sizes determined for cores in Ophiuchus were comparable to those found by previous studies, our result is robust, and starless cores in Ophiuchus are indeed significantly smaller than their counterparts in Taurus and Cepheus.

We investigated the degree to which each of the three molecular clouds is clustered. We found that Ophiuchus shows the most evidence for clustered star formation, with the smallest core sizes and smallest nearest-neighbour distances between sources. We found that Ophiuchus shows peaks in its surface density of sources, associated with peaks in column density. Taurus appears to be a dispersed region, with large sources, large nearest-neighbour distances, and very little variation in surface density of sources with location. Cepheus appears to be intermediate in its degree of clustering between Ophiuchus and Taurus, although direct comparisons

are complicated by the increased distance to the Cepheus molecular clouds compared to the other two regions. There is some evidence that at least some of the sources detected in SCUBA-2 observations of Cepheus may contain multiple unresolved sources. Hence there is an additional caveat on comparisons of clustering due to the lower physical resolution at the distance of Cepheus than at the distance of Ophiuchus and Taurus. Cepheus has large sources and a range of nearest-neighbour separations overlapping with those seen in both Ophiuchus and Taurus, although nowhere in Cepheus are sources detectable at the resolution of the JCMT as closely packed as the sources in the highest-column-density regions of Ophiuchus. Cepheus shows peaks in its surface density of sources, but the increased distance to Cepheus means that the surface densities of sources seen are almost an order of magnitude lower than those seen in Ophiuchus. We concluded that Cepheus is in general a region of dispersed star formation.

We investigated the variation of starless core properties – temperature, mass, FWHM size, and volume density – with location within each of the three molecular clouds. We found that Ophiuchus has the most variation of core properties with location, as might be expected as the most clustered of our star-forming regions. Taurus shows little variation of core properties, as might be expected for a region of dispersed and relatively homogeneous star formation. Cepheus shows a wide range of core properties, but little correlation of those properties with location. In each molecular cloud, we identified heating sources to locations which show elevated core temperatures, with the exception of Oph E and Oph F in Ophiuchus, which show elevated temperatures without a clear source of external heating.

We predicted possible evolutionary scenarios for our cores, modelling the cores as having Gaussian density profiles confined by a constant external pressure at a constant external density. We modelled the evolution of the core in the cases of isothermal and adiabatic compression of core material, and found that cores collapse

334

more effectively under the assumption of isothermality than under the assumption of adiabatic collapse. We modelled the dissipation of turbulence in a collapsing core using the Solomon et al. (1987) linewidth-size relation. We investigated the magnetic field strengths required to substantially alter the evolution of our cores, parameterising the internal magnetic energy of a core as a fraction of its non-thermal kinetic energy using the Basu (2000) relation between magnetic field strength, density and non-thermal linewidth. We concluded that the magnetic field will not significantly alter core evolution while the ratio of magnetic energy to non-thermal kinetic energy is less than $\sim 25\%$.

We modelled the 23 cores in Ophiuchus for which we have both internal and external velocity dispersions. These were chosen as they are the cores for which we have the most complete measure of their virial state. We found that while some of the virially-bound pressure-confined cores in Ophiuchus are likely to evolve to become gravitationally-bound prestellar cores, many of our cores appear to be evolving toward, or oscillating around, virial equilibrium with their surroundings. A virially-bound and pressure-confined starless core will not necessarily evolve to become gravitationally bound, and hence a starless core can only be definitively considered to be prestellar if it is gravitationally unstable.

Chapter 7

Summary and Future Work

In this thesis we have identified, and characterised the properties of, starless cores in the Ophiuchus, Taurus and Cepheus Molecular Clouds. We have determined the properties of the starless cores in each region using SCUBA-2, HARP and Herschel data. We have assessed the virial stability of our starless cores, and have found, that in each of the three regions, external pressure is instrumental in confining starless cores in the majority of cases. We have constructed a model for the evolution of virially-bound and pressure-confined starless cores, and have found that these cores will not necessarily evolve to become gravitationally-bound prestellar cores, with many instead predicted to be collapsing to virial equilibrium with their surroundings.

7.1   Chapter 1: Introduction

In this chapter we introduced prestellar cores as the densest and smallest length-scale objects in the interstellar medium. We discussed the properties of molecular clouds, and introduced the current paradigm of the star-formation process. We discussed the properties of starless cores: their masses, temperatures, external pressures, magnetic field strengths, and morphologies, and the dependence of the properties of molecular cores on their local environment. The stability of starless cores was discussed and

the virial theorem was derived for a core in which gravitational potential energy, internal kinetic energy, internal magnetic energy, and energy due to external pressure contribute to the stability of the core. The Jeans and Bonnor-Ebert stability criteria were also discussed. We introduced the Initial Mass Function and Core Mass Function, and considered the possible causal link between the two. We discussed the low-mass protostellar evolutionary sequence. We described the Gould Belt of star-forming regions, and recent wide-area surveys intended to map a large fraction of its area. Finally, we outlined the structure and contents of this work.

7.2 Chapter 2: Instrumentation

In this chapter we introduced and discussed the telescopes with which data used in this work were taken: the James Clerk Maxwell Telescope (JCMT), the Herschel Space Observatory and the IRAM 30-metre telescope. We discussed the SCUBA-2 and HARP instruments on the JCMT, and the SPIRE and PACS instruments on Herschel. We discussed methods by which data from SCUBA-2 and Herschel can be meaningfully compared.

The JCMT is a 15m-diameter submillimetre telescope located at the summit of Mauna Kea. Data taken using two instruments on the JCMT – the camera SCUBA-2 and the heterodyne receiver HARP-B – are used in this work. SCUBA-2 is a 10 000-pixel submillimetre camera which takes data simultaneously at 450µm and 850µm, with effective resolutions of 9.6 arcsec and 14.1 arcsec respectively. HARP-B is a 16-pixel heterodyne receiver which operates in the frequency range 325–375 GHz ($\sim$ 800–925 µm), with an angular resolution of 14 arcsec at 345 GHz.

SCUBA-2 data reduction requires iterative modelling of the astrophysical and atmospheric signal received by the telescope, as well as correlated low-frequency noise. In order to prevent atmospheric signal being spuriously assigned as astrophysical emission in low signal-to-noise regions, a signal-to-noise based 'mask' is

used to define regions of significant astrophysical emission. In order to avoid the necessity for *a priori* knowledge of the astrophysical signal, the data reduction process is repeated twice. Firstly, the mask is defined based on simple signal-to-noise cuts in each iteration. A mask is then defined based on a signal-to-noise cut in the co-added and mosaiced first set of reductions. The fields observed are then re-reduced using this mask.

Herschel was a 3.5m-diameter submillimetre space observatory, observing in the wavelength range 70–500μm. Data taken using the SPIRE and PACS photometers were used in this work. SPIRE observed at 250μm, 350μm and 500μm, at resolutions of 18 arcsec, 25 arcsec and 36 arcsec respectively. Data were taken simultaneously using the PACS photometer, operating at 70μm and 160μm, at resolutions of 5.8 arcsec×12.1 arcsec and 11.6 arcsec×15.4 arcsec respectively.

The IRAM 30-metre telescope is a 30 m-diameter millimetre telescope located on Pico Veleta. The telescope operates in the wavelength range $\sim$ 0.9–3 mm, and has both continuum and heterodyne observing modes. IRAM 30 m observations of the N_2H^+ $J = 1 \rightarrow 0$ transition at 3 mm were used in this work.

When bringing SCUBA-2 and Herschel data to a common resolution, it is necessary to use convolution kernels based on the true telescope beams, rather than Gaussian approximations. The SCUBA-2 450-μm beam, in particular, has a substantial fraction of its power in the secondary beam, and cannot be modelled adequately as either a single- or a double-Gaussian, for the purposes of convolving the data to a common resolution with a Herschel data set. The empirically-derived convolution kernels used in this work significantly improved the previously-noted discrepancies between Herschel and SCUBA-2 450-μm flux densities.

7.3 Chapter 3: The Ophiuchus molecular cloud

In this chapter, we extracted a set of sources from the SCUBA-2 850-μm map of the Ophiuchus molecular cloud, and characterised the properties of these cores using SCUBA-2, Herschel, IRAM and HARP-B data sets.

We identified sources using the CuTEx curvature-based soure extraction algorithm, which gave us a catalogue of 93 sources, 70 of which were in the central region of the L1688 sub-cloud. Of these 93 sources, 46 were identified as protostellar, and 47 were identified as starless cores. Of the 70 sources in L1688, 47 were uniquely identified with a source in the S08 catalogue.

We determined the dust temperature of each source by SED fitting, which allowed an accurate mass determination to be made for each source. The distribution of masses of the starless cores is consistent with the expected shape of the core mass function. The low counting statistics of our sample did not allow us to accurately determine the power-law index of our core mass function, although the two slope values determined, $\alpha = 2.0 \pm 0.4$ and $\alpha = 2.7 \pm 0.4$ are both consistent with the expected behaviour of the high-mass Initial Mass Function.

We calculated the masses of our cores from N_2H^+ and $C^{18}O$ emission. We found that the mass of a core determined from 850-μm continuum emission and the mass determined from N_2H^+ emission correlate well, indicating that N_2H^+ and continuum emission are tracing the same material. The most massive cores, those in Oph A, have consistently higher continuum masses than N_2H^+ masses, indicating that, as expected, N_2H^+ emission does not trace the very densest material in prestellar cores.

We performed full virial stability analyses for the 23 cores for which both $C^{18}O$ and N_2H^+ data were available, estimating the contributions of gravitational energy, internal pressure (both thermal and non-thermal) and external pressure to the energy balance of the cores. Existing measurements of the magnetic field strength in Ophiuchus suggest that magnetic energy is unlikely to significantly alter the energy

balance of our cores. We found that most of our cores are bound or virialised, with a virial ratio ≥ 1.

We calculated the Bonnor-Ebert critically-stable masses for each of the 23 cores for which N_2H^+ data are available. We found that our cores cannot be modelled as critically-stable Bonnor-Ebert spheres, and that the Bonnor-Ebert critically-stable mass is not a good estimator of the bound state of the cores for which we can perform a full virial analysis, typically overestimating the degree to which cores are gravitationally bound.

We found that whether our cores are gravitationally bound or pressure-confined depends strongly on the region in which they are located. Cores in the centre of Oph A are gravitationally bound, while cores in Oph C and E are pressure-confined. Cores in Oph A′, B and F are in approximate equipartition between gravitational potential energy and external pressure energy, with pressure typically slightly dominating.

We see a loss of turbulence between core linewidths measured in $C^{18}O$ and core linewidths measured in N_2H^+. This supports a picture in which dissipation of turbulence occurs in the dense centres of starless cores. At the radii traced by N_2H^+ emission, turbulence is dissipating, but is not yet fully dissipated, with a transonic or mildly supersonic non-thermal component to the core linewidth still present even when the core is on the brink of gravitational collapse. The degree to which turbulence is dissipated varies between regions, with turbulence being dissipated more within Oph C, E and F than within Oph A, A′ and B.

These results show that starless cores in the Ophiuchus molecular cloud are non-equilibrium objects with complex relationships with their local environments, and that a detailed analysis of their energy balance, of the sort we have carried out here, is required in order to accurately determine their virial state. In particular, we have shown that external pressure is of key importance to the energy balance of most

341

of the densest starless cores in Ophiuchus, and thus cannot be neglected in a virial analysis.

7.4 Chapter 4: The Taurus molecular cloud

In this chapter we extracted sets of cores from the SCUBA-2 850-µm, Herschel 250-µm, and spatially-filtered Herschel 250-µm data of the L1495 region of the Taurus molecular cloud. We characterised the properties of these cores using SCUBA-2 and Herschel data sets, and compared the cores found in the different data sets, in order to determine which property of a starless core identified by Herschel is most important in determining whether the same core would be detected with SCUBA-2. We performed a virial analysis of the cores extracted from the SCUBA-2 850-µm map using HARP-B data and the NH_3 linewidths presented by Seo et al. (2015).

We identified sources using the CSAR source extraction algorithm. We extracted 25 sources from the regions of the SCUBA-2 850-µm map with variance $\leq 2\,(Jy/6$-arcsec pixel$)^2$, 208 sources from the Herschel 250-µm map of the same regions, and 138 sources in the equivalent spatially-filtered Herschel 250-µm map.

We determined a representative dust emissivity index of our sources of $\beta = 1.3 \pm 0.6$. This was the value of β which best predicted the SCUBA-2 850-µm flux densities of our sources from their spectral energy distribution (SED) in filtered Herschel emission. We determined mean line-of-sight temperatures for our sources by SED fitting. This then allowed an accurate mass determination to be made for each source.

We found that cores detected by SCUBA-2 and cores detected in filtered 250-µm emission have similar properties, obeying the same temperature-density relation. Cores extracted from, and characterised using, unfiltered Herschel data typically have higher temperatures and densities than their counterparts extracted from the SCUBA-2 data, due to extended emission along the line of sight which is removed

by the filtering process. This further confirms that spatial filtering is necessary to accurately compare SCUBA-2 and Herschel data.

We found that SCUBA-2 detects only the densest starless cores, with no SCUBA-2 cores having densities below 6.3×10^3 particles/cm^3, an order of magnitude higher density than the least dense filtered 250-µm-detected Herschel core. There is no equivalent cut-off in temperature, with both SCUBA-2 and Herschel sources having temperatures in the range ~ 9–$20\,\mathrm{K}$. Neither are SCUBA-2 cores typically smaller in radius than Herschel cores – i.e. the spatial filtering introduced by SCUBA-2 does not appear to change the measured FWHM of a starless core observed at this distance.

Thus, we found that the criterion for whether a starless or prestellar core detected in Herschel data will also be detected in SCUBA-2 data is its density (for a given temperature). In the case of Taurus, for SCUBA-2 GBS data, this was 6×10^3 particles/cm^3. This corresponds to a cut-off in surface brightness, below which SCUBA-2 is no longer sensitive. This suggests that SCUBA-2 observations are ideal for selecting those cores in Herschel catalogues which are closest to forming stars.

We performed a virial stability analysis on the cores detected by SCUBA-2, taking the internal velocities of the cores to be those measured in NH$_3$ emission by Seo et al. (2015), and determining the enternal pressure from HARP-B ^{12}CO measurements. We found that all but one of the cores for which data were available were, in the absence of an internal magnetic field, virially bound and pressure-confined. We found that the magnetic field strengths required to bring our cores into virial equilibrium are in the range $\sim 30 - 100\,\mathrm{\mu G}$, consistent with measurements of the magnetic field strength in dense gas in other parts of Taurus.

We found that the Bonnor-Ebert and magnetic Bonnor-Ebert criteria predict that the cores detected by SCUBA-2 have stable, pressure-confined configurations.

We did not find evidence for significant variation in core properties with region across L1495, except for local heating effects due to the stars V892 Tau and IRAS04113+2758.

We hypothesised that the majority of the cores detected by SCUBA-2 in L1495 are supported against collapse by their internal magnetic fields, and that the dominant terms in the virial equation in L1495 are typically internal magnetic energy and external pressure energy. This is in keeping with the theory of Palmeirim et al. (2013) and André et al. (2014) that star formation in the Taurus molecular cloud is magnetically regulated.

7.5   Chapter 5: The Cepheus Flare

In this chapter we extracted sources from the SCUBA-2 data of the L1147/L1158, L1172/L1174, L1251 and L1228 regions of the Cepheus Flare. We characterised our sources using their 850-μm flux densities and temperatures supplied by the Herschel GBS. We compared the properties of cores in the different Cepheus Flare regions in order to determine the mode of star formation proceeeding in each region. We determined the relative importance of gravity and external pressure in confining our cores, and determined an upper limit on the degree to which our cores are virially bound.

We identified 117 sources across the Cepheus Flare region using the CSAR source extraction algorithm, of which 23 were associated with a protostar in the Kirk et al. (2009) Spitzer catalogue. Of our 117 sources, 20 were located in L1147/L1158, 26 in L1174, 9 sources in L1172, 42 in L1251 and 20 in L1228. We determined the best-fit flux densities of our sources using the multiple-Gaussian fitting algorithm described in Chapter 3.

We determined masses for each of our sources using our best-fit flux densities and temperatures supplied by the Herschel GBS. We found that our cores typically lie in

the 'prestellar' part of the mass/size plane. Our cores typically have temperatures in the range $\sim 9 - 15\,\mathrm{K}$, with the exception of cores associated with the L1174 reflection nebula, which have temperatures up to $\sim 50\,\mathrm{K}$.

We analysed the cumulative distribution functions of core masses for each region in Cepheus, using the maximum likelihood estimator for an infinite power-law distribution, and found that the core mass function in each region shows a sub-Salpeter power-law behaviour, with the exceptions of L1228, which has a power-law index consistent with the Salpter IMF, and L1172, for which an accurate power-law index could not be determined. Determining the power-law index over all cores, we found a sub-Salpeter value of $\alpha = 1.88 \pm 0.09$ over the mass range $M > 0.08\,\mathrm{M_\odot}$. For the highest-mass cores, we found a CMF power-law index $\alpha = 2.61 \pm 0.27$ over the mass range $M > 0.08\,\mathrm{M_\odot}$ (again determined over all cores), marginally consistent with the Salpeter IMF.

We compared the number of starless cores detected in each region with the numbers of embedded and Class II sources found by Kirk et al. (2009). We found that L1147/L1158 and L1228 have a high ratio of starless cores to Class II sources, while L1251 and L1174 have a low ratio. This is consistent with L1174 and L1251 being active sites of star formation, while L1147/L1158 and L1228 form stars in a more quiescent mode.

We determined the Bonnor-Ebert critically-stable masses of our cores, and the associated BE-critical external pressure. We found that the Bonnor-Ebert model predicts that most of our cores have stable BE solutions accessible to them. The BE model predicts higher external pressures in L1174 and in L1228 than in the other regions, although in L1228 this may be the result of the assumed distance.

We determined the external pressure on our cores using $^{13}\mathrm{CO}$ velocity dispersion measurements determined by Yonekura et al. (1997). We found that almost all of our cores had substantially higher external pressures than those predicted by the

Bonnor-Ebert model.

We found that all but one of our cores are pressure-confined, rather than gravitationally bound, and that for the majority of our cores there is a power-law relation between the external pressure energy and the gravitational energy, $\Omega_{\mathrm{P}} \propto \Omega_{\mathrm{P}}^{0.55}$. We infer from this that those of our cores which obey this relation are strongly pressure-dominated, and those which do not obey the relation are the best candidates in our sample to be undergoing gravitational collapse.

We performed a virial analysis of our cores, and found that our cores cannot be supported by internal thermal energy alone: in the absence of non-thermal internal motions or an internal magnetic field, all of our cores would be substantially virially bound and collapsing.

7.6 Chapter 6: Discussion

In this chapter we examined the differences in starless core properties between the Ophiuchus, Taurus and Cepheus molecular clouds. We found that cores in each region have similar temperatures and masses, but that cores in Ophiuchus are significantly smaller than those in Taurus and Cepheus. This results in typical source densities being one to two orders of magnitude higher in Ophiuchus than in the other two regions. We discussed the extent to which this may be the result of our differing choices of source extraction algorithm: CuTEx in Ophiuchus, and CSAR in Taurus and Cepheus. We concluded that: as our choice of source extraction algorithm was based on the physical conditions in Ophiuchus; as the completeness limit derived for CuTEx was such that if larger cores were present they should be detectable, unless their masses were $< 0.1\,\mathrm{M}_\odot$ in every case; and as the sizes determined for cores in Ophiuchus were comparable to those found by previous studies, our result is robust, and starless cores in Ophiuchus are indeed significantly smaller than their counterparts in Taurus and Cepheus.

We investigated the degree to which each of the three molecular clouds is clustered. We found that Ophiuchus shows the most evidence for clustered star formation, with the smallest core sizes and smallest nearest-neighbour distances between sources. We found that Ophiuchus shows peaks in its surface density of sources, associated with peaks in column density. Taurus appears to be a dispersed region, with large sources, large nearest-neighbour distances, and very little variation in surface density of sources with location. Cepheus appears to be intermediate in its degree of clustering between Ophiuchus and Taurus, although direct comparisons are complicated by the increased distance to the Cepheus molecular clouds compared to the other two regions. There is some evidence that at least some of the sources detected in SCUBA-2 observations of Cepheus may contain multiple unresolved sources. Hence there is an additional caveat on comparisons of clustering due to the lower physical resolution at the distance of Cepheus than at the distance of Ophiuchus and Taurus. Cepheus has large sources and a range of nearest-neighbour separations overlapping with those seen in both Ophiuchus and Taurus, although nowhere in Cepheus are sources detectable at the resolution of the JCMT as closely packed as the sources in the highest-column-density regions of Ophiuchus. Cepheus shows peaks in its surface density of sources, but the increased distance to Cepheus means that the surface densities of sources seen are almost an order of magnitude lower than those seen in Ophiuchus. We concluded that Cepheus is in general a region of dispersed star formation.

We investigated the variation of starless core properties – temperature, mass, FWHM size, and volume density – with location within each of the three molecular clouds. We found that Ophiuchus has the most variation of core properties with location, as might be expected as the most clustered of our star-forming regions. Taurus shows little variation of core properties, as might be expected for a region of dispersed and relatively homogeneous star formation. Cepheus shows a wide range

of core properties, but little correlation of those properties with location. In each molecular cloud, we identified heating sources to locations which show elevated core temperatures, with the exception of Oph E and Oph F in Ophiuchus, which show elevated temperatures without a clear source of external heating.

We predicted possible evolutionary scenarios for our cores, modelling the cores as having Gaussian density profiles confined by a constant external pressure at a constant external density. We modelled the evolution of the core in the cases of isothermal and adiabatic compression of core material, and found that cores collapse more effectively under the assumption of isothermality than under the assumption of adiabatic collapse. We modelled the dissipation of turbulence in a collapsing core using the Solomon et al. (1987) linewidth-size relation. We investigated the magnetic field strengths required to substantially alter the evolution of our cores, parameterising the internal magnetic energy of a core as a fraction of its non-thermal kinetic energy using the Basu (2000) relation between magnetic field strength, density and non-thermal linewidth. We concluded that the magnetic field will not significantly alter core evolution while the ratio of magnetic energy to non-thermal kinetic energy is less than $\sim 25\%$.

We modelled the 23 cores in Ophiuchus for which we have both internal and external velocity dispersions. These were chosen as they are the cores for which we have the most complete measure of their virial state. We found that while some of the virially-bound pressure-confined cores in Ophiuchus are likely to evolve to become gravitationally-bound prestellar cores, many of our cores appear to be evolving toward, or oscillating around, virial equilibrium with their surroundings. A virially-bound and pressure-confined starless core will not necessarily evolve to become gravitationally bound, and hence a starless core can only be definitively considered to be prestellar if it is gravitationally unstable.

7.7 Future Work

There are various ways in which the work in this thesis could be extended.

The virial stability and energy balance could be determined in starless cores in other regions observed at part of the JCMT GBS; HARP ^{12}CO/^{13}CO/C^{18}O measurements have been taken for high-column-density regions in Orion A, Orion B, Perseus, Serpens-Aquila and IC5146. For all of these regions continuum SCUBA-2 observations have also been made; the analysis presented here could be repeated for these regions, in order to further investigate the variation in the balance of forces in starless cores between molecular clouds.

An investigation into the energy balance in high-latitude regions of isolated star formation – i.e. star formation in a non-GMC environment – might help elucidate the differences in the star formation process between clustered star formation, dispersed star formation in regions of high column density, and isolated star formation in regions of low column density. An ideal catalogue of starless cores with which to investigate this would be the Quinn (2013) Lonely Cores catalogue, a collection of high-latitude isolated starless cores observed in multiple lines. A virial analysis of the kind carried out in Chapters 3 and 4 of this work could be carried out using the data currently available. This would shed significant light on similarities and differences between truly isolated star formation and both clustered and dispersed star formation in GMCs.

In order to fully assess the virial stability of starless cores, it is necessary to place on a firm footing their internal magnetic field strengths and the relative contribution of magnetic energy to their support against collapse. An ideal instrument with which to measure the magnetic field strengths in starless cores is the POL-2 instrument on the JCMT which, at the time of writing, is undergoing final commissioning. A survey proposal aimed at mapping the highest-column-density regions of Gould Belt in polarised light is currently under review; if successful, the measurements

taken as part of this survey would provide the key missing piece of information in understanding the virial state of starless cores in nearly GMCs.

The analytical theoretical model of starless core evolution presented in the latter part of Chapter 6 could be extended to include accretion of mass onto evolving starless cores. This would generalise the model to include the full range of physical conditions in most GMCs.

Bibliography

Alves, J., Lombardi, M., & Lada, C. J. 2007, *Astron. Astrophys.*, 462, L17

Alves, J. F., Lada, C. J., & Lada, E. A. 2001, *Nature*, 409, 159

André, P. 1994, in The Cold Universe, ed. T. Montmerle, C. J. Lada, I. F. Mirabel, & J. Tran Thanh Van, 179

André, P., Belloche, A., Motte, F., & Peretto, N. 2007, *Astron. Astrophys.*, 472, 519

André, P., Di Francesco, J., Ward-Thompson, D., et al. 2014, Protostars and Planets VI, 27

André, P., Men'shchikov, A., Bontemps, S., et al. 2010, *Astron. Astrophys.*, 518, L102

André, P. & Montmerle, T. 1994, *Astrophys. J.*, 420, 837

André, P., Ward-Thompson, D., & Barsony, M. 1993, *Astrophys. J.*, 406, 122

André, P., Ward-Thompson, D., & Greaves, J. 2012, Science, 337, 69

Aniano, G., Draine, B. T., Gordon, K. D., & Sandstrom, K. 2011, *Pub. Astron. Soc. Pac.*, 123, 1218

Appenzeller, I. & Mundt, R. 1989, *Astron. Astrophys. Rev.*, 1, 291

Arzoumanian, D., André, P., Didelon, P., et al. 2011, *Astron. Astrophys.*, 529, L6

Ballesteros-Paredes, J., Klessen, R. S., & Vázquez-Semadeni, E. 2003, *Astrophys. J.*, 592, 188

Balog, Z., Müller, T., Nielbock, M., et al. 2014, Experimental Astronomy, 37, 129

Barsony, M. 1994, in Astronomical Society of the Pacific Conference Series, Vol. 65, Clouds, Cores, and Low Mass Stars, ed. D. P. Clemens & R. Barvainis, 197

Bastian, U., Finkenzeller, U., Jaschek, C., & Jaschek, M. 1983, *Astron. Astrophys.*, 126, 438

Basu, S. 2000, *Astrophys. J. Letters*, 540, L103

Bate, M. R., Bonnell, I. A., & Bromm, V. 2003, *Mon. Not. Roy. Astron. Soc.*, 339, 577

Beckwith, S. V. W. & Sargent, A. I. 1991, *Astrophys. J.*, 381, 250

Beckwith, S. V. W., Sargent, A. I., Chini, R. S., & Guesten, R. 1990, *Astron. J.*, 99, 924

Beichman, C. A., Myers, P. C., Emerson, J. P., et al. 1986, *Astrophys. J.*, 307, 337

Beichman, C. A., Neugebauer, G., Habing, H. J., Clegg, P. E., & Chester, T. J., eds. 1988, Infrared astronomical satellite (IRAS) catalogs and atlases. Volume 1: Explanatory supplement, Vol. 1

Bendo, G. J., Griffin, M. J., Bock, J. J., et al. 2013, *Mon. Not. Roy. Astron. Soc.*, 433, 3062

Benson, P. J. & Myers, P. C. 1989, *Astrophys. J. Supple.*, 71, 89

Bernard, J.-P., Paradis, D., Marshall, D. J., et al. 2010, *Astron. Astrophys.*, 518, L88

Bintley, D., Holland, W. S., MacIntosh, M. J., et al. 2014, in Society of Photo-Optical Instrumentation Engineers (SPIE) Conference Series, Vol. 9153, Millimeter, Submillimeter, and Far-Infrared Detectors and Instrumentation for Astronomy VII, ed. W. S. Holland & J. Zmuidzinas, 915303

Blaauw, A. 1956, *Astrophys. J.*, 123, 408

Blaauw, A. 1964, *Ann. Rev. Astron, Astrophys.*, 2, 213

Blaauw, A. 1991, in NATO Advanced Science Institutes (ASI) Series C, Vol. 342, NATO Advanced Science Institutes (ASI) Series C, ed. C. J. Lada & N. D. Kylafis, 125

Bok, B. J. & Reilly, E. F. 1947, *Astrophys. J.*, 105, 255

Bolatto, A. D., Wolfire, M., & Leroy, A. K. 2013, *Ann. Rev. Astron, Astrophys.*, 51, 207

Bonnell, I. A., Bate, M. R., & Zinnecker, H. 1998, *Mon. Not. Roy. Astron. Soc.*, 298, 93

Bonnor, W. B. 1956, *Mon. Not. Roy. Astron. Soc.*, 116, 351

Bontemps, S., André, P., Kaas, A. A., et al. 2001, *Astron. Astrophys.*, 372, 173

Buckle, J. V., Curtis, E. I., Roberts, J. F., et al. 2010, *Mon. Not. Roy. Astron. Soc.*, 401, 204

Buckle, J. V., Drabek-Maunder, E., Greaves, J., et al. 2015, *Mon. Not. Roy. Astron. Soc.*, 449, 2472

Buckle, J. V., Hills, R. E., Smith, H., et al. 2009, *Mon. Not. Roy. Astron. Soc.*, 399, 1026

Burstein, P., Borken, R. J., Kraushaar, W. L., & Sanders, W. T. 1977, *Astrophys. J.*, 213, 405

Caselli, P. & Myers, P. C. 1995, *Astrophys. J.*, 446, 665

Caselli, P., Walmsley, C. M., Zucconi, A., et al. 2002, *Astrophys. J.*, 565, 344

Chabrier, G. 2003, *Pub. Astron. Soc. Pac.*, 115, 763

Chandrasekhar, S. & Fermi, E. 1953a, *Astrophys. J.*, 118, 113

Chandrasekhar, S. & Fermi, E. 1953b, *Astrophys. J.*, 118, 116

Chapin, E. L., Berry, D. S., Gibb, A. G., et al. 2013, *Mon. Not. Roy. Astron. Soc.*, 430, 2545

Chen, H., Myers, P. C., Ladd, E. F., & Wood, D. O. S. 1995, *Astrophys. J.*, 445, 377

Christie, H., Viti, S., Yates, J., et al. 2012, *Mon. Not. Roy. Astron. Soc.*, 422, 968

Clausius, R. 1870, Philosophical Magazine Series 4, 40, 122

Comeron, F. & Torra, J. 1992, *Astron. Astrophys.*, 261, 94

Comeron, F. & Torra, J. 1994, *Astron. Astrophys.*, 281, 35

Comeron, F., Torra, J., & Gomez, A. E. 1992, *Astrophys. Space Sci.*, 187, 187

Crutcher, R. M. 2012, *Ann. Rev. Astron, Astrophys.*, 50, 29

Crutcher, R. M., Troland, T. H., Goodman, A. A., et al. 1993, *Astrophys. J.*, 407, 175

Currie, M. J., Draper, P. W., Berry, D. S., et al. 2008, in Astronomical Society of the Pacific Conference Series, Vol. 394, Astronomical Data Analysis Software and Systems XVII, ed. R. W. Argyle, P. S. Bunclark, & J. R. Lewis, 650

354

Curtis, E. I., Richer, J. S., & Buckle, J. V. 2010, *Mon. Not. Roy. Astron. Soc.*, 401, 455

Cutri, R. M., Skrutskie, M. F., van Dyk, S., et al. 2003, VizieR Online Data Catalog, 2246, 0

Dame, T. M., Ungerechts, H., Cohen, R. S., et al. 1987, *Astrophys. J.*, 322, 706

Daniel, F., Cernicharo, J., & Dubernet, M.-L. 2006, *Astrophys. J.*, 648, 461

Davis, C. J., Chrysostomou, A., Hatchell, J., et al. 2010, *Mon. Not. Roy. Astron. Soc.*, 405, 759

Davis, Jr., L. & Greenstein, J. L. 1951, *Astrophys. J.*, 114, 206

Dawson, J. R., Ntormousi, E., Fukui, Y., Hayakawa, T., & Fierlinger, K. 2015, *Astrophys. J.*, 799, 64

de Geus, E. J. 1992, *Astron. Astrophys.*, 262, 258

de Graauw, T., Helmich, F. P., Phillips, T. G., et al. 2010, *Astron. Astrophys.*, 518, L6

de Zeeuw, P. T., Hoogerwerf, R., de Bruijne, J. H. J., Brown, A. G. A., & Blaauw, A. 1999, *Astron. J.*, 117, 354

Dempsey, J. T., Friberg, P., Jenness, T., et al. 2013, *Mon. Not. Roy. Astron. Soc.*, 430, 2534

Di Francesco, J., André, P., & Myers, P. C. 2004, *Astrophys. J.*, 617, 425

Di Francesco, J., Evans, N. J. I., Caselli, P., et al. 2007, in Protostars and Planets V, ed. B. Reipurth, D. Jewitt, & K. K. Tucson (University of Arizona Press), 17–32

Dobashi, K., Uehara, H., Kandori, R., et al. 2005, *Pub. Astron. Soc. Japan*, 57, 1

Dobbs, C. L., Burkert, A., & Pringle, J. E. 2011, *Mon. Not. Roy. Astron. Soc.*, 413, 2935

Dolidze, M. V. & Arakelyan, M. A. 1959, AZH, 36, 444

Dottori, H. A. 1980, *Astrophys. Space Sci.*, 73, 175

Drabek, E., Hatchell, J., Friberg, P., et al. 2012, *Mon. Not. Roy. Astron. Soc.*, 426, 23

Draine, B. T., Dale, D. A., Bendo, G., et al. 2007, *Astrophys. J.*, 663, 866

Draine, B. T. & Lee, H. M. 1984, *Astrophys. J.*, 285, 89

Duarte-Cabral, A., Chrysostomou, A., Peretto, N., et al. 2012, *Astron. Astrophys.*, 543, A140

Dunham, M. M., Stutz, A. M., Allen, L. E., et al. 2014, Protostars and Planets VI, 195

Ebert, R. 1955, Zeitschrift für Astrophysik, 37, 217

Elias, J. H. 1978, *Astrophys. J.*, 224, 453

Elmegreen, B. G. & Falgarone, E. 1996, *Astrophys. J.*, 471, 816

Elmegreen, B. G. & Lada, C. J. 1977, *Astrophys. J.*, 214, 725

Elmegreen, B. G. & Scalo, J. 2004, *Ann. Rev. Astron, Astrophys.*, 42, 211

Emerson, D. 1999, Interpreting Astronomical Spectra (Wiley-VCH)

Enoch, M. L., Evans, N. J., I., Sargent, A. I., et al. 2008, *Astrophys. J.*, 684, 1240

Enoch, M. L., Evans, II, N. J., Sargent, A. I., & Glenn, J. 2009, *Astrophys. J.*, 692, 973

Enoch, M. L., Glenn, J., Evans, II, N. J., et al. 2007, *Astrophys. J.*, 666, 982

Evans, II, N. J., Allen, L. E., Blake, G. A., et al. 2003, *Pub. Astron. Soc. Pac.*, 115, 965

Evans, II, N. J., Dunham, M. M., Jørgensen, J. K., et al. 2009, *Astrophys. J. Supple.*, 181, 321

Evans, II, N. J., Rawlings, J. M. C., Shirley, Y. L., & Mundy, L. G. 2001, *Astrophys. J.*, 557, 193

Field, G. B., Goldsmith, D. W., & Habing, H. J. 1969, *Astrophys. J. Letters*, 155, L149

Foster, P. N. & Chevalier, R. A. 1993, *Astrophys. J.*, 416, 303

Frerking, M. A., Langer, W. D., & Wilson, R. W. 1982, *Astrophys. J.*, 262, 590

Friesen, R. K., Di Francesco, J., Myers, P. C., et al. 2010, *Astrophys. J.*, 718, 666

Friesen, R. K., Johnstone, D., Naylor, D. A., & Davis, G. R. 2005, *Mon. Not. Roy. Astron. Soc.*, 361, 460

Fuller, G. A. & Myers, P. C. 1992, *Astrophys. J.*, 384, 523

Garden, R. P., Hayashi, M., Hasegawa, T., Gatley, I., & Kaifu, N. 1991, *Astrophys. J.*, 374, 540

Girart, J. M., Rao, R., & Marrone, D. P. 2006, Science, 313, 812

Goldsmith, P. F., Heyer, M., Narayanan, G., et al. 2008, *Astrophys. J.*, 680, 428

Goodman, A. A. & Arce, H. G. 2004, *Astrophys. J.*, 608, 831

Goodman, A. A., Barranco, J. A., Wilner, D. J., & Heyer, M. H. 1998, *Astrophys. J.*, 504, 223

Goodman, A. A. & Heiles, C. 1994, *Astrophys. J.*, 424, 208

Gould, B. G. 1879, Resultados del Observatorio Nacional Argentino, 1, 0

Graves, S. F., Richer, J. S., Buckle, J. V., et al. 2010, *Mon. Not. Roy. Astron. Soc.*, 409, 1412

Greaves, J. S., Holland, W. S., & Pound, M. W. 2003, *Mon. Not. Roy. Astron. Soc.*, 346, 441

Greene, T. P., Wilking, B. A., André, P., Young, E. T., & Lada, C. J. 1994, *Astrophys. J.*, 434, 614

Greene, T. P. & Young, E. T. 1992, *Astrophys. J.*, 395, 516

Grenier, I. A., Lebrun, F., Arnaud, M., Dame, T. M., & Thaddeus, P. 1989, *Astrophys. J.*, 347

Griffin, M. J., Abergel, A., Abreu, A., et al. 2010, *Astron. Astrophys.*, 518, L3

Griffin, M. J., North, C. E., Schulz, B., et al. 2013, *Mon. Not. Roy. Astron. Soc.*, 434, 992

Guetter, H. H. 1968, *Pub. Astron. Soc. Pac.*, 80, 197

Guillout, P., Sterzik, M. F., Schmitt, J. H. M. M., Motch, C., & Neuhaeuser, R. 1998, *Astron. Astrophys.*, 337, 113

Hacar, A., Tafalla, M., Kauffmann, J., & Kovács, A. 2013, *Astron. Astrophys.*, 554, A55

Hayashi, C. 1961, *Pub. Astron. Soc. Japan*, 13, 450

Hayashi, C. & Hoshi, R. 1961, *Pub. Astron. Soc. Japan*, 13, 442

Hecht, E. 2001, Optics, 4th edn. (Addison-Wesley)

Helmholtz, H. 1854, On the Interaction of Natural Forces, Lecture at Kant Commemoration, Königsberg

Hennebelle, P. & Chabrier, G. 2008, *Astrophys. J.*, 684, 395

Hennebelle, P., Whitworth, A. P., Gladwin, P. P., & André, P. 2003, *Mon. Not. Roy. Astron. Soc.*, 340, 870

Henyey, L. G., Lelevier, R., & Levée, R. D. 1955, *Pub. Astron. Soc. Pac.*, 67, 154

Herbig, G. H. 1960, *Astrophys. J. Supple.*, 4, 337

Herbig, G. H. 1962, Advances in Astronomy and Astrophysics, 1, 47

Herschel, Sir, J. F. W. 1847, Results of astronomical observations made during the years 1834, 5, 6, 7, 8, at the Cape of Good Hope; being the completion of a telescopic survey of the whole surface of the visible heavens, commenced in 1825

Herschel, W. 1802, Royal Society of London Philosophical Transactions Series I, 92, 477

Herschel Observers' Manual. 2014, http://herschel.esac.esa.int/Docs/Herschel/pdf/observatory.pdf, Version 5.0.3, HERSCHEL-HSC-DOC-0876; accessed 27/04/2015

Hertzsprung, E. 1911, Publikationen des Astrophysikalischen Observatoriums zu Potsdam, 63

Heyer, M., Krawczyk, C., Duval, J., & Jackson, J. M. 2009, *Astrophys. J.*, 699, 1092

Hildebrand, R. H. 1983, Q. Jl R. astr. Soc., 24, 267

Holland, W. S., Bintley, D., Chapin, E. L., et al. 2013, *Mon. Not. Roy. Astron. Soc.*, 430, 2513

Hopkins, P. F. 2012a, *Mon. Not. Roy. Astron. Soc.*, 423, 2016

Hopkins, P. F. 2012b, *Mon. Not. Roy. Astron. Soc.*, 423, 2037

Hubble, E. 1934, *Astrophys. J.*, 79, 8

Inutsuka, S.-i. 2001, *Astrophys. J. Letters*, 559, L149

Jeans, J. H. 1928, Astronomy and Cosmogony (Cambridge University Press)

Jenness, T., Cavanagh, B., Economou, F., & Berry, D. S. 2008, in Astronomical Society of the Pacific Conference Series, Vol. 394, Astronomical Data Analysis Software and Systems XVII, ed. R. W. Argyle, P. S. Bunclark, & J. R. Lewis, 565

Jessop, N. E. & Ward-Thompson, D. 2000, *Mon. Not. Roy. Astron. Soc.*, 311, 63

Johnson, R. D. I. 2013, http://cccbdb.nist.gov/, release 16a

Johnstone, D., Wilson, C. D., Moriarty-Schieven, G., et al. 2000, *Astrophys. J.*, 545, 327

Joy, A. H. 1945, *Astrophys. J.*, 102, 168

Kelvin, L. W. T. 1861, British Association for the Advancement of Scient Reports, Part II, 27

Kenyon, S. J., Gómez, M., & Whitney, B. A. 2008, in Handbook of Star Forming Regions, Volume I, ed. B. Reipurth, 405

Keto, E., Broderick, A. E., Lada, C. J., & Narayan, R. 2006, *Astrophys. J.*, 652, 1366

Kirk, J. M., Ward-Thompson, D., & Crutcher, R. M. 2006, *Mon. Not. Roy. Astron. Soc.*, 369, 1445

Kirk, J. M., Ward-Thompson, D., Di Francesco, J., et al. 2009, *Astrophys. J. Supple.*, 185, 198

Kirk, J. M., Ward-Thompson, D., Palmeirim, P., et al. 2013, *Mon. Not. Roy. Astron. Soc.*, 432, 1424

Klein, R. I., Sandford, II, M. T., & Whitaker, R. W. 1980, *Space Sci. Rev.*, 27, 275

Klessen, R. S., Ballesteros-Paredes, J., Vázquez-Semadeni, E., & Durán-Rojas, C. 2005, *Astrophys. J.*, 620, 786

Koen, C. 2006, *Mon. Not. Roy. Astron. Soc.*, 365, 590

Kolmogorov, A. 1941, Akademiia Nauk SSSR Doklady, 30, 301

Kolmogorov, A. N. 1991, Royal Society of London Proceedings Series A, 434, 9

Könyves, V., André, P., Men'shchikov, A., & et al. 2015, *Astron. Astrophys.*

Könyves, V., André, P., Men'shchikov, A., et al. 2010, *Astron. Astrophys.*, 518, L106

Kroupa, P. 2001, *Mon. Not. Roy. Astron. Soc.*, 322, 231

Kun, M., Balog, Z., Kenyon, S. J., Mamajek, E. E., & Gutermuth, R. A. 2009, *Astrophys. J. Supple.*, 185, 451

Kun, M., Kiss, Z. T., & Balog, Z. 2008, in Handbook of Star Forming Regions, Volume I, ed. B. Reipurth, 136

Lada, C. 1987, in IAU Symp. 115, ed. M. P. . J. Jugaku (D. Reidel Publishing Co), 1–17

Larson, R. B. 1981, MNRAS, 194, 809

Lee, C. W. & Myers, P. C. 1999, *Astrophys. J. Supple.*, 123, 233

Lee, C. W., Myers, P. C., & Tafalla, M. 2001, *Astrophys. J. Supple.*, 136, 703

Lee, J.-E., Di Francesco, J., Bourke, T. L., Evans, II, N. J., & Wu, J. 2007, *Astrophys. J.*, 671, 1748

Lee, J.-E., Di Francesco, J., Lai, S.-P., et al. 2006, *Astrophys. J.*, 648, 491

Leous, J. A., Feigelson, E. D., André, P., & Montmerle, T. 1991, *Astrophys. J.*, 379, 683

Leung, C. M. 1975, *Astrophys. J.*, 199, 340

Leung, C. M. & Brown, R. L. 1977, *Astrophys. J. Letters*, 214, L73

Levin, S. M., Langer, W. D., Velusamy, T., Kuiper, T. B. H., & Crutcher, R. M. 2001, *Astrophys. J.*, 555, 850

Li, W., Evans, II, N. J., Harvey, P. M., & Colome, C. 1994, *Astrophys. J.*, 433, 199

Lindblad, P. O., Grape, K., Sandqvist, A., & Schober, J. 1973, *Astron. Astrophys.*, 24, 309

Lindblad, P. O., Palous, J., Loden, K., & Lindegren, L. 1997, in ESA Special Publication, Vol. 402, Hipparcos - Venice '97, ed. R. M. Bonnet, E. Høg, P. L. Bernacca, L. Emiliani, A. Blaauw, C. Turon, J. Kovalevsky, L. Lindegren, H. Hassan, M. Bouffard, B. Strim, D. Heger, M. A. C. Perryman, & L. Woltjer, 507–512

Liseau, R., White, G. J., Larsson, B., et al. 1999, *Astron. Astrophys.*, 344, 342

Loren, R. B. 1989, *Astrophys. J.*, 338, 902

Loren, R. B. 1989, *Astrophys. J.*, 338, 925

Lynds, B. T. 1962, *Astrophys. J. Supple.*, 7, 1

Mac Low, M.-M. & Klessen, R. S. 2004, Reviews of Modern Physics, 76, 125

Mairs, S., Johnstone, D., Kirk, H., et al. 2015, *Mon. Not. Roy. Astron. Soc.*, 454, 2557

Mamajek, E. E. 2008, Astronomische Nachrichten, 329, 10

Markwardt, C. B. 2009, in Astronomical Society of the Pacific Conference Series, Vol. 411, Astronomical Data Analysis Software and Systems XVIII, ed. D. A. Bohlender, D. Durand, & P. Dowler, 251

Marsh, K. A., Griffin, M. J., Palmeirim, P., et al. 2014, *Mon. Not. Roy. Astron. Soc.*, 439, 3683

Marsh et al. 2015, *Astron. Astrophys.*

Martin, P. G., Roy, A., Bontemps, S., et al. 2012, *Astrophys. J.*, 751, 28

Maruta, H., Nakamura, F., Nishi, R., Ikeda, N., & Kitamura, Y. 2010, *Astrophys. J.*, 714, 680

Maschberger, T. & Kroupa, P. 2009, *Mon. Not. Roy. Astron. Soc.*, 395, 931

McKee, C. F. & Ostriker, J. P. 1977, *Astrophys. J.*, 218, 148

Men'shchikov, A., André, P., Didelon, P., et al. 2012, *Astron. Astrophys.*, 542, A81

Mestel, L. & Spitzer, Jr., L. 1956, *Mon. Not. Roy. Astron. Soc.*, 116, 503

Miville-Deschênes, M.-A. & Lagache, G. 2005, *Astrophys. J. Supple.*, 157, 302

Mizuno, A., Fukui, Y., Iwata, T., Nozawa, S., & Takano, T. 1990, *Astrophys. J.*, 356, 184

Molinari, S., Schisano, E., Faustini, F., et al. 2011, A&A, 530, A133

Moshir, M., Kopman, G., & Conrow, T. A. O. 1992, IRAS Faint Source Survey, Explanatory supplement version 2

Motte, F., André, P., & Neri, R. 1998, *Astron. Astrophys.*, 336, 150

Motte, F., André, P., Ward-Thompson, D., & Bontemps, S. 2001, *Astron. Astrophys.*, 372, L41

Mouschovias, T. C. 1991, *Astrophys. J.*, 373

Mouschovias, T. C. & Ciolek, G. E. 1999, in NATO Advanced Science Institutes (ASI) Series C, Vol. 540, NATO Advanced Science Institutes (ASI) Series C, ed. C. J. Lada & N. D. Kylafis

Müller, H. S. P., Thorwirth, S., Roth, D. A., & Winnewisser, G. 2001, *Astron. Astrophys.*, 370, L49

Müller, T., Balog, Z., Nielbock, M., et al. 2014, Experimental Astronomy, 37, 253

Nakamura, F. & Li, Z.-Y. 2005, *Astrophys. J.*, 631, 411

Nakano, T. & Nakamura, T. 1978, *Pub. Astron. Soc. Japan*, 30, 671

Nutter, D., Stamatellos, D., & Ward-Thompson, D. 2009, *Mon. Not. Roy. Astron. Soc.*, 396, 1851

Nutter, D. & Ward-Thompson, D. 2007, *Mon. Not. Roy. Astron. Soc.*, 374, 1413

Nutter, D., Ward-Thompson, D., & André, P. 2006, *Mon. Not. Roy. Astron. Soc.*, 368, 1833

Offner, S. S. R., Clark, P. C., Hennebelle, P., et al. 2014, Protostars and Planets VI, 53

Offner, S. S. R., Klein, R. I., & McKee, C. F. 2008, *Astrophys. J.*, 686, 1174

Olano, C. A., Meschin, P. I., & Niemela, V. S. 2006, *Mon. Not. Roy. Astron. Soc.*, 369, 867

Olano, C. A. & Pöppel, W. G. L. 1987, *Astron. Astrophys.*, 179, 202

Ostriker, J. 1964, *Astrophys. J.*, 140, 1056

Ott, S. 2010, in Astronomical Society of the Pacific Conference Series, Vol. 434, Astronomical Data Analysis Software and Systems XIX, ed. Y. Mizumoto, K.-I. Morita, & M. Ohishi, 139

PACS Data Reduction Guide: Photometry. 2014, http://herschel.esac.esa.int/ hcss-doc-13.0/print/pacs_phot/pacs_phot.pdf, Version 11; accessed 28/04/2015

Padoan, P. & Nordlund, Å. 1999, *Astrophys. J.*, 526, 279

Padoan, P., Nordlund, A., & Jones, B. J. T. 1997, *Mon. Not. Roy. Astron. Soc.*, 288, 145

Palmeirim, P., André, P., Kirk, J., et al. 2013, *Astron. Astrophys.*, 550, A38

Panopoulou, G., Tassis, K., Blinov, D., et al. 2015, *Mon. Not. Roy. Astron. Soc.*, 452, 715

Pattle, K., Ward-Thompson, D., Kirk, J. M., et al. 2015, *Mon. Not. Roy. Astron. Soc.*, 450, 1094

Pilbratt, G. L., Riedinger, J. R., Passvogel, T., et al. 2010, *Astron. Astrophys.*, 518, L1

Pineda, J. E., Caselli, P., & Goodman, A. A. 2008, *Astrophys. J.*, 679, 481

Pineda, J. E., Goodman, A. A., Arce, H. G., et al. 2010, *Astrophys. J. Letters*, 712, L116

Pirogov, L., Zinchenko, I., Caselli, P., Johansson, L. E. B., & Myers, P. C. 2003, A&A, 405, 639

Planck Collaboration. 2011, *Astron. Astrophys.*, 536, A1

Planck Collaboration. 2014, *Astron. Astrophys.*, 571, A8

Planck HFI Core Team. 2011, *Astron. Astrophys.*, 536, A4

Plummer, H. C. 1911, *Mon. Not. Roy. Astron. Soc.*, 71, 460

Poglitsch, A., Waelkens, C., Geis, N., et al. 2010, *Astron. Astrophys.*, 518, L2

Pöppel, W. G. L. 2001, in Astronomical Society of the Pacific Conference Series, Vol. 243, From Darkness to Light: Origin and Evolution of Young Stellar Clusters, ed. T. Montmerle & P. André, 667

Pound, M. W. & Blitz, L. 1995, *Astrophys. J.*, 444, 270

Preibisch, T. & Mamajek, E. 2008, in Handbook of Star Forming Regions, Volume II, ed. B. Reipurth, 235

Press, W. H. & Schechter, P. 1974, *Astrophys. J.*, 187, 425

Pudritz, R. E., Wilson, C. D., Carlstrom, J. E., et al. 1996, *Astrophys. J. Letters*, 470, L123

Quinn, C. 2013, PhD thesis, Cardiff University

Reipurth, B., Bally, J., & Devine, D. 1997, *Astron. J.*, 114, 2708

Riley, K. F., Hobson, M. P., & Bence, S. J. 2006, Mathematical Methods for Physics and Engineering, 3rd edn. (Cambridge University Press)

Roussel, H. 2013, *Pub. Astron. Soc. Pac.*, 125, 1126

Russell, H. N. 1913, The Observatory, 36, 324

Sadavoy, S. I., Di Francesco, J., Bontemps, S., et al. 2010, *Astrophys. J.*, 710, 1247

Sadavoy, S. I., Di Francesco, J., Johnstone, D., et al. 2013, *Astrophys. J.*, 767, 126

Salpeter, E. E. 1955, *Astrophys. J.*, 121, 161

Sato, F., Mizuno, A., Nagahama, T., et al. 1994, *Astrophys. J.*, 435, 279

Schnee, S., Enoch, M., Noriega-Crespo, A., et al. 2010, *Astrophys. J.*, 708, 127

Seo, Y. M., Shirley, Y. L., Goldsmith, P., et al. 2015, *Astrophys. J.*, 805, 185

Shinnaga, H., Tsuboi, M., & Kasuga, T. 1999, in Star Formation 1999, ed. T. Nakamoto, 175–176

Shirley, Y. L., Nordhaus, M. K., Grcevich, J. M., et al. 2005, *Astrophys. J.*, 632, 982

Shu, F. H. 1977, *Astrophys. J.*, 214, 488

Shu, F. S., Adams, F. C., & Lizano, S. 1987, *Ann. Rev. Astron, Astrophys.*, 25, 23

Simpson, R. J., Johnstone, D., Nutter, D., Ward-Thompson, D., & Whitworth, A. P. 2011, *Mon. Not. Roy. Astron. Soc.*, 417, 216

Simpson, R. J., Nutter, D., & Ward-Thompson, D. 2008, *Mon. Not. Roy. Astron. Soc.*, 391, 205

Solomon, P. M., Rivolo, A. R., Barrett, J., & Yahil, A. 1987, *Astrophys. J.*, 319, 730

SPIRE Data Reduction Guide. 2014, http://herschel.esac.esa.int/hcss-doc-13.0/print/spire_drg/spire_drg.pdf, SPIRE-RAL-DOC 003248; accessed 28/04/2015

SPIRE Handbook. 2014, http://herschel.esac.esa.int/Docs/SPIRE/spire_handbook.pdf, Version 2.5, HERSCHEL-DOC-0798; accessed 28/04/2015

Spitzer, L. 1978, Physical processes in the interstellar medium

Stahler, S. W. 1983, *Astrophys. J.*, 274, 822

Stamatellos, D. & Whitworth, A. P. 2003, *Astron. Astrophys.*, 407, 941

Stamatellos, D., Whitworth, A. P., & Ward-Thompson, D. 2007, *Mon. Not. Roy. Astron. Soc.*, 379, 1390

Straizys, V., Cernis, K., Kazlauskas, A., & Meistas, E. 1992, Baltic Astronomy, 1, 149

Strom, S. E. & Peterson, D. M. 1968, *Astrophys. J.*, 152, 859

Strömgren, B. 1939, *Astrophys. J.*, 89, 526

Sugitani, K., Fukui, Y., Mizuni, A., & Ohashi, N. 1989, *Astrophys. J. Letters*, 342, L87

Swinyard, B. M., Ade, P., Baluteau, J.-P., et al. 2010, *Astron. Astrophys.*, 518, L4

Tachihara, K., Neuhäuser, R., Kun, M., & Fukui, Y. 2005, *Astron. Astrophys.*, 437, 919

Tafalla, M., Mardones, D., Myers, P. C., et al. 1998, *Astrophys. J.*, 504, 900

Testi, L. & Sargent, A. I. 1998, *Astrophys. J. Letters*, 508, L91

Tilley, D. A. & Pudritz, R. E. 2007, *Mon. Not. Roy. Astron. Soc.*, 382, 73

Troland, T. H. & Crutcher, R. M. 2008, *Astrophys. J.*, 680, 457

Troland, T. H., Crutcher, R. M., Goodman, A. A., et al. 1996, *Astrophys. J.*, 471, 302

van Leeuwen, F. 2007, *Astron. Astrophys.*, 474, 653

Vazquez-Semadeni, E. 1994, *Astrophys. J.*, 423, 681

Vázquez-Semadeni, E., Banerjee, R., Gómez, G. C., et al. 2011, *Mon. Not. Roy. Astron. Soc.*, 414, 2511

Vrba, F. J. 1977, *Astron. J.*, 82, 198

Vrba, F. J., Strom, K. M., Strom, S. E., & Grasdalen, G. L. 1975, *Astrophys. J.*, 197, 77

Walborn, N. R., Maíz-Apellániz, J., & Barbá, R. H. 2002, *Astron. J.*, 124, 1601

Walker, C. K., Lada, C. J., Young, E. T., Maloney, P. R., & Wilking, B. A. 1986, *Astrophys. J. Letters*, 309, L47

Ward-Thompson, D. 2002, Science, 295, 76

Ward-Thompson, D., André, P., Crutcher, R., et al. 2007, in Protostars and Planets V, ed. B. Reipurth, D. Jewitt, & K. K. Tucson (University of Arizona Press), 33–46

Ward-Thompson, D., André, P., & Kirk, J. M. 2002, *Mon. Not. Roy. Astron. Soc.*, 329, 257

Ward-Thompson, D., Di Francesco, J., Hatchell, J., et al. 2007, *Pub. Astron. Soc. Pac.*, 119, 855

Ward-Thompson, D., Kirk, J. M., André, P., et al. 2010, *Astron. Astrophys.*, 518, L92

Ward-Thompson, D., Nutter, D., Bontemps, S., Whitworth, A., & Attwood, R. 2006, *Mon. Not. Roy. Astron. Soc.*, 369, 1201

Ward-Thompson, D., Robson, E. I., Whittet, D. C. B., et al. 1989, *Mon. Not. Roy. Astron. Soc.*, 241, 119

Ward-Thompson, D., Scott, P. F., Hills, R. E., & André, P. 1994, *Mon. Not. Roy. Astron. Soc.*, 268, 276

Wenger, M., Ochsenbein, F., Egret, D., et al. 2000, A&AS, 143, 9

Westin, T. N. G. 1985, *Astron. Astrophys. Suppl.*, 60, 99

White, G. J., Drabek-Maunder, E., Rosolowsky, E., et al. 2015, *Mon. Not. Roy. Astron. Soc.*, 447, 1996

White, G. J., Nelson, R. P., Holland, W. S., et al. 1999, *Astron. Astrophys.*, 342, 233

Whitworth, A. P. & Ward-Thompson, D. 2001, *Astrophys. J.*, 547, 317

Wilking, B. A., Gagné, M., & Allen, L. E. 2008, in Handbook of Star Forming Regions, Volume II, ed. B. Reipurth, 351

Wilking, B. A. & Lada, C. J. 1983, *Astrophys. J.*, 274, 698

Wilking, B. A., Lada, C. J., & Young, E. T. 1989, *Astrophys. J.*, 340, 823

Williams, J. P., Blitz, L., & McKee, C. F. 2000, Protostars and Planets IV, 97

Williams, R. J. R., Ward-Thompson, D., & Whitworth, A. P. 2001, *Mon. Not. Roy. Astron. Soc.*, 327, 788

Wilson, T. L. 1999, Reports on Progress in Physics, 62, 143

Wilson, T. L., Mauersberger, R., Gensheimer, P. D., Muders, D., & Bieging, J. H. 1999, *Astrophys. J.*, 525, 343

Yonekura, Y., Dobashi, K., Mizuno, A., Ogawa, H., & Fukui, Y. 1997, *Astrophys. J. Supple.*, 110, 21

York, D. G. 1974, *Astrophys. J. Letters*, 193, L127

Young, E. T., Lada, C. J., & Wilking, B. A. 1986, *Astrophys. J. Letters*, 304, L45